Determining Pavement Design Criteria for Recycled Aggregate Base and Large Stone Subbase

MnDOT Project TPF-5(341)

Task 7 – Pavement Design Criteria

Revised Report Submission Date:
October 7 2020

DRAFT

Prepared by:
Bora Cetin
Haluk Sinan Coban
Tuncer B. Edil
Halil Ceylan
William Likos

TABLE OF CONTENTS

LIST OF TABLES ..... **vi**

LIST OF FIGURES ..... **vii**

1. TEST CELLS AND MATERIALS **1**

1.1. Test Cells 1
1.2. Materials 1

2. ADDITIONAL STUDY RELATED TO TASK 5 (PERFORMANCE MONITORING AND REPORTING) AND TASK 6 (INSTRUMENTATION) REPORTS **2**

2.1. Determination of Thermal Diffusivities (α) Based on Field Temperature Profiles 2
2.2. Comparisons Between the Volumetric Water Content (VWC) Values in the First (2017-2018) and Second (2018-2019) Freezing and Thawing Periods 11
2.3. Effect of Field Degree of Compaction (DOC) on the Performance of the Test Cells 13
2.3.1. Nuclear Density Gauge (NDG) Measurements for the Base and Subgrade Layers of the Test Cells 13
2.3.2. Effect of the Inadequate Compaction of Class 5Q Aggregate Base Layers Overlying 9-in LSSB Layers 16

3. ESTIMATION OF LABORATORY TEST RESULTS **24**

3.1. Proctor Compaction Characteristics 24
3.1.1. Uncorrected Optimum Moisture Content (OMC) and Maximum Dry Density (MDD) 24
3.1.2. Corrected Optimum Moisture Content (OMC) and Maximum Dry Density (MDD) 26
3.2. Saturated Hydraulic Conductivity (K_{sat}) 26
3.3. Soil-Water Characteristic Curve (SWCC) Parameters 27
3.3.1. Residual Volumetric Water Content (VWC) (θr) 28
3.3.2. Saturated Volumetric Water Content (VWC) (θs) 28
3.3.3. Air-Entry Pressure 28
3.4. Resilient Modulus (M_R) Characteristics 29
3.4.1. Summary Resilient Modulus (SM_R) 34
3.4.2. MEPDG Constitutive Model Coefficients (k_1, k_2, and k_3) 35
3.5. Aggregate Abrasion Characteristics 36
3.6. Reassessment of the Models Provided in Edil et al. (2012) for More General Equations 39

4. ESTIMATION OF FIELD TEST RESULTS DURING CONSTRUCTION **40**

4.1. Dynamic Cone Penetration (DCP) Parameters 40
4.1.1. Dynamic Cone Penetration Index (DCPI) 40
4.1.2. Field California Bearing Ratio (CBR) 41

DRAFT

4.2. Light Weight Deflectometer Elastic Modulus (E_{LWD}) 41
4.3. Falling Weight Deflectometer Elastic Modulus (E_{FWD}) 42
4.4. Intelligent Compaction (IC) Resilient Modulus (M_R) 44
4.4.1. Intelligent Compaction (IC) Resilient Modulus (M_R) at 10 psi (69 kPa) 44
4.4.2. Intelligent Compaction (IC) Resilient Modulus (M_R) at 30 psi (207 kPa) 48

5. PAVEMENT ME PERFORMANCE MODELS 51

5.1. General Model Inputs 52
5.2. Recycled Aggregate Base (RAB) Group 54
5.2.1. Aggregate Base Layer Design 54
5.2.2. Material Inputs 55
5.2.3. Effect of Aggregate Base Layer Thickness on Pavement Performance Prediction Models 56
5.2.4. Effect of Base Layer Aggregate Type on Pavement Performance Prediction Models 60
5.2.5. Layer Rutting at 50% Reliability 64
5.2.6. Effect of Traffic Levels on Pavement Performance Prediction Models 67
5.2.7. Recycled Aggregate Base (RAB) Layer Thicknesses Alternative to 12-in Limestone Base Layer 72
5.3. Large Stone Subbase (LSSB) Groups 77
5.3.1. Large Stone Subbase (LSSB) Layer Design 77
5.3.2. Material Inputs 78
5.3.3. Effect of Large Stone Subbase (LSSB) Thickness on Pavement Performance Prediction Models 80
5.3.4. Effect of Large Stone Subbase (LSSB) Stiffness on Pavement Performance Prediction Models 82
5.3.5. Layer Rutting at 50% Reliability 85
5.3.6. Effect of Traffic Level on Pavement Performance Prediction Models 87

6. CONCLUSIONS 91

7. RECOMMENDATIONS 93

8. REFERENCES 99

APPENDIX A. THERMAL DIFFUSIVITY (α) AND VOLUMETRIC WATER CONTENT (VWC) VALUES DETERMINED FOR 12-IN COARSE RCA (CELL 185), FINE RCA (CELL 186), LIMESTONE (CELL 188), AND RCA+RAP (CELL 189) BASE LAYERS 102

APPENDIX B. COMPARISONS BETWEEN TOP-MIDDLE AND MIDDLE-BOTTOM THERMOCOUPLES (TC) IN 12-IN BASE LAYERS 107

APPENDIX C. COMPARISONS BETWEEN THE VOLUMETRIC WATER CONTENT (VWC) VALUES IN THE FIRST (2017-2018) AND SECOND (2018-2019) FREEZING AND THAWING PERIODS 108

DRAFT

APPENDIX D. LABORATORY TEST RESULTS OF THE BASE LAYER AGGREGATES THAT WERE USED IN THE FORWARD STEPWISE REGRESSION ANALYSES 115

APPENDIX E. ALTERNATIVE MODELS TO ESTIMATE UNCORRECTED OPTIMUM MOISTURE CONTENT (OMC) AND MAXIMUM DRY DENSITY (MDD) VALUES OF AGGREGATE BASE LAYERS 120

APPENDIX F. ALTERNATIVE MODELS TO ESTIMATE CORRECTED OPTIMUM MOISTURE CONTENT (OMC) AND MAXIMUM DRY DENSITY (MDD) VALUES OF AGGREGATE BASE LAYERS 122

APPENDIX G. ALTERNATIVE MODELS TO ESTIMATE SATURATD HYDRAULIC CONDUCTIVITY (K_{sat}) VALUES OF AGGREGATE BASE LAYERS 124

APPENDIX H. SUMMARY RESILIENT MODULUS (SM_R) VS. MOISTURE CONTENT 125

APPENDIX I. SUMMARY RESILIENT MODULUS (SM_R) VS. DEGREE OF SATURATION (DOS) 127

APPENDIX J. SUMMARY RESILIENT MODULUS (SM_R) VS. VOLUMETRIC WATER CONTENT (VWC) 131

APPENDIX K. SUMMARY RESILIENT MODULUS (SM_R) VS. MATRIC SUCTION 135

APPENDIX L. ALTERNATIVE MODELS TO ESTIMATE SUMMARY RESILIENT MODULUS (SM_R) AT OPTIMUM MOISTURE CONTENT (OMC) 137

APPENDIX M. REASSESSMENT OF THE MODELS PROVIDED IN EDIL ET AL. (2012) 138

APPENDIX N. FIELD TEST RESULTS (DURING CONSTRUCTION) THAT WERE USED IN THE FORWARD STEPWISE REGRESSION ANALYSES 146

APPENDIX O. ALTERNATIVE MODELS TO ESTIMATE INTELLIGENT COMPACTION (IC) RESILIENT MODULUS (M_R) AT 207 KPA (30 PSI) 147

APPENDIX P. MONTHLY RAINFALL STATISTICS, MONTHLY CLIMATE SUMMARY, AND HOURLY AIR TEMPERATURE DISTRIBUTION BY MONTH FOR THE MNROAD TEST FACILITY 148

APPENDIX Q. GRAPHICAL AND TABULAR REPRESENTATIONS OF TRAFFIC INPUTS AND AXLE CONFIGURATION 150

DRAFT

APPENDIX R. ASPHALT LAYER PARAMETERS (LEVEL 3) IN PAVEMENT ME..... 153

APPENDIX S. ESTIMATION OF SM_R FOR SELECT GRANULAR BORROW, CLASS 6 AGGREGATE, AND CLASS 5Q AGGREGATE 157

APPENDIX T. EFFECT OF AGGREGATE BASE LAYER THICKNESS ON PAVEMENT PERFORMANCE PREDICTIONS 158

APPENDIX U. EFFECT OF BASE LAYER AGGREGATE TYPE ON PAVEMENT PERFORMANCE PREDICTIONS 174

APPENDIX V. TOTAL, ASPHALT, BASE+SUBBASE, AND SUBGRADE LAYER RUTTING AT 50% RELIABILITY FOR RECYCLED AGGREGATE BASE (RAB) GROUP 190

APPENDIX W. TOTAL AND LAYER RUTTING AT 50% RELIABILITY FOR RECYCLED AGGREGATE BASE (RAB) GROUP..... 199

APPENDIX X. EFFECT OF TRAFFIC LEVEL ON PAVEMENT PERFORMANCE PREDICTIONS..... 209

APPENDIX Y. RELATIVE AGGREGATE BASE LAYER THICKNESS 225

APPENDIX Z. EFFECT OF LARGE STONE SUBBASE (LSSB) THICKNESS ON PAVEMENT PERFORMANCE PREDICTIONS 234

APPENDIX AA. EFFECT OF LARGE STONE SUBBASE (LSSB) LAYER MODULUS ON PAVEMENT PERFORMANCE PREDICTIONS..... 248

APPENDIX AB. TOTAL, ASPHALT, BASE+SUBBASE, AND SUBGRADE LAYER RUTTING AT 50% RELIABILITY FOR LARGE STONE SUBBASE (LSSB) GROUPS..... 262

APPENDIX AC. TOTAL AND LAYER RUTTING AT 50% RELIABILITY FOR LARGE STONE SUBBASE (LSSB) GROUPS 271

APPENDIX AD. EFFECT OF TRAFFIC LEVEL ON PAVEMENT PERFORMANCE PREDICTIONS 283

APPENDIX AE. COMPARISON BETWEEN FIELD DATA AND PAVEMENT ME MODELS..... 291

APPENDIX AF. ASPHALT CONCRETE (AC) OVER AC OVERLAY DESIGNS..... 306

DRAFT

LIST OF TABLES

Table 3.1. Equations to estimate uncorrected optimum moisture content (OMC) (%) 25
Table 3.2. Equations to estimate uncorrected maximum dry density (MDD) (kN/m^3) 25
Table 3.3. Equations to estimate corrected optimum moisture content (OMC) (%) 26
Table 3.4. Equations to estimate corrected maximum dry density (MDD) (kN/m^3) 26
Table 3.5. Equations to estimate saturated hydraulic conductivity (K_{sat}) (cm/sec) 27
Table 3.6. Equation to estimate residual volumetric water content (VWC) (θr) 28
Table 3.7. Equations to estimate saturated volumetric water content (VWC) (θs) 28
Table 3.8. Equations to estimate the air-entry pressure (kPa) 29
Table 3.9. Equations to estimate summary resilient modulus (SM_R) (MPa) at optimum moisture content (OMC) 35
Table 3.10. Equations to estimate k_1 conventional fitting parameter 35
Table 3.11. Equations to estimate k_2 conventional fitting parameter 35
Table 3.12. Equations to estimate k_3 conventional fitting parameter 36
Table 3.13. Equations to estimate relative breakage (B_r) after 100 gyrations 37
Table 3.14. Equations to estimate relative breakage (B_r) after 300 gyrations 37
Table 3.15. Equations to estimate relative breakage (B_r) after 500 gyrations 38
Table 4.1. Equations to estimate dynamic cone penetration index (DCPI) (mm/blow) 41
Table 4.2. Equations to estimate field California bearing ratio (CBR) (%) 41
Table 4.3. Equations to estimate light weight deflectometer elastic modulus (E_{LWD}) (MPa) 42
Table 4.4. Equations to estimate falling weight deflectometer elastic modulus (E_{FWD}) (MPa) 43
Table 4.5. Equations to estimate intelligent compaction (IC) resilient modulus (M_R) (MPa) at 10 psi (69 kPa) 45
Table 4.6. Equations to estimate intelligent compaction (IC) resilient modulus (M_R) (MPa) at 30 psi (207 kPa) 49
Table 5.1. General design inputs for Pavement ME 52
Table 5.2. Pavement distress types, target values, and reliability levels 52
Table 5.3. Climatic parameters and regional information 53
Table 5.4. Traffic information – part 1 54
Table 5.5. Traffic information – part 2 54
Table 5.6. Material inputs used for pavement sublayers in Pavement ME models 56
Table 5.7. Summary of RAB layer thicknesses alternative to 12-in limestone base layer 77
Table 5.8. Material inputs used for pavement sublayers in Pavement ME models 79
Table 7.1. Aggregate cover thickness reduction guidance when using geosynthetics (Kwon and Tutumluer 2003; IDOT 2005) 97

DRAFT

LIST OF FIGURES

Figure 1.1. Cross-sections of the test cells (not to scale) (s. granular borrow = select granular borrow, TX = triaxial geogrid, GT = non-woven geotextile, BX = biaxial geogrid).... 1
Figure 1.2. Materials used to construct the test cells: (a) sand subgrade, (b) clay loam, (c) select granular borrow, (d) LSSB material, (e) coarse RCA, (f) fine RCA, (g) RCA+RAP, (h) limestone, (i) class 6 aggregate, and (j) class 5Q aggregate 2
Figure 2.1. Daily soil surface temperature as a sinusoidal function of time (T = temperature, A_0 = amplitude at the soil surface, T = average temperature at the soil surface) 3
Figure 2.2. Soil temperature profiles at different soil depths (Hanson et al. 2000) 3
Figure 2.3. Thermal properties of soils (λ = thermal conductivity, C = heat capacity, and α = thermal diffusivity) (Jury and Horton 2004) 4
Figure 2.4. Locations of the thermocouples (TC) and moisture probes (EC) in 12-in coarse RCA (cell 185) 5
Figure 2.5. Locations of the thermocouples (TC) and moisture probes (EC) in 18-in LSSB (cell 127) 6
Figure 2.6. Locations of the thermocouples (TC) and moisture probes (EC) in 9-in LSSB (cell 728) 6
Figure 2.7. Thermal diffusivity (α) values determined by the amplitude equation for 12-in coarse RCA base (cell 185) 7
Figure 2.8. Thermal diffusivity (α) values determined by the phase equation for 12-in coarse RCA base (cell 185) 8
Figure 2.9. Thermal diffusivity (α) values determined from top-bottom thermocouples (TCs) by the amplitude equation for 12-in base layers 8
Figure 2.10. Thermal diffusivity (α) values determined by the amplitude equation for 18-in LSSB (cell 127) 9
Figure 2.11. Thermal diffusivity (α) values determined by the phase equation for 18-in LSSB (cell 127) 9
Figure 2.12. Thermal diffusivity (α) values determined by the amplitude equation for 9-in LSSB (cell 728) 10
Figure 2.13. Thermal diffusivity (α) values determined by the phase equation for 9-in LSSB (cell 728) 10
Figure 2.14. Volumetric water content (VWC) values for the sensor at 5-in depth in 12-in fine RCA base layer (cell 186) during two freezing and thawing periods (the dates on the x-axis represent the time periods for both 2017-2018 and 2018-2019 years) 12
Figure 2.15. Volumetric water content (VWC) values for the sensor at 5-in depth in 12-in limestone base layer (cell 188) during two freezing and thawing periods (the dates on the x-axis represent the time periods for both 2017-2018 and 2018-2019 years) 12
Figure 2.16. Volumetric water content (VWC) values for the sensor at 5-in depth in 12-in RCA+RAP base layer (cell 189) during two freezing and thawing periods (the dates on the x-axis represent the time periods for both 2017-2018 and 2018-2019 years) 13

DRAFT

Figure 2.17. Relative dry density values for the base and subgrade layers (the red boxes shown for cells 127 and 227 are for class 6 aggregate base layers and those shown for cells 328-728 are for class 5Q aggregate base layers) 15
Figure 2.18. Relative moisture content values for the base and subgrade layers (the red boxes shown for cells 127 and 227 are for class 6 aggregate base layers and those shown for cells 328-728 are for class 5Q aggregate base layers)..... 16
Figure 2.19. Relative dry density values for the aggregate base layers overlying LSSB layers... 17
Figure 2.20. Relative moisture content values for the aggregate base layers overlying LSSB layers 17
Figure 2.21. Light weight deflectometer elastic modulus (E_{LWD}) of the base+subbase layers in cells 127-728..... 19
Figure 2.22. Falling weight deflectometer elastic modulus (E_{FWD}) of the base+subbase layers in cells 127-728..... 19
Figure 2.23. Intelligent compaction (IC) resilient modulus (M_R) of the base+subbase layers in cells 127-728..... 20
Figure 2.24. Base+subbase E_{FWD} of the cells 127-728 under 9,000 lb (40 kN) load (error bars represent one standard deviation of the data)..... 20
Figure 2.25. Rut depth measurements for cells 127-728 (error bars represent one standard deviation of the data) 21
Figure 2.26. International roughness index (IRI) measurements for the inside lane (main traffic) – outer wheel path (OWP)..... 22
Figure 2.27. Transverse cracking lengths in the inside lane (main traffic) of the test cells (lengths are number of unit squares shown in the distress maps)..... 23
Figure 2.28. Longitudinal cracking lengths in the inside lane (main traffic) of the test cells (lengths are number of unit squares shown in the distress maps)..... 23
Figure 3.1. Summary resilient modulus (SM_R) values at different moisture contents for coarse RCA 30
Figure 3.2. Summary resilient modulus (SM_R) values at different moisture contents for fine RCA 31
Figure 3.3. Summary resilient modulus (SM_R) values at different moisture contents for limestone..... 31
Figure 3.4. Summary resilient modulus (SM_R) values at different moisture contents for RCA+RAP 32
Figure 3.5. Summary resilient modulus (SM_R) at different matric suctions for coarse RCA 33
Figure 3.6. Summary resilient modulus (SM_R) at different matric suctions for fine RCA 33
Figure 3.7. Summary resilient modulus (SM_R) at different matric suctions for limestone..... 34
Figure 3.8. Summary resilient modulus (SM_R) at different matric suctions for RCA+RAP 34
Figure 3.9. Definitions of $PLR_{0.5}$, $PLR_{0.7}$, and median roundness parameters..... 38
Figure 4.1. (a) Light weight deflectometer elastic modulus (E_{LWD}) vs. dynamic cone penetration index (DCPI) and (b) E_{LWD} vs. field California bearing ratio (CBR)..... 42
Figure 4.2. (a) Falling weight deflectometer elastic modulus (E_{FWD}) vs. dynamic cone penetration index (DCPI) and (b) E_{FWD} vs. field California bearing ratio (CBR)..... 43
Figure 4.3. Falling weight deflectometer elastic modulus (E_{FWD}) vs. light weight deflectometer elastic modulus (E_{LWD}): (a) linear, (b) exponential, and (c) power trendline..... 44

DRAFT

Figure 4.4. Intelligent compaction (IC) resilient modulus (M_R) [at 10 psi (69 kPa)] vs. dynamic cone penetration index (DCPI): (a) linear, (b) exponential, (c) power, and (d) logarithmic relationships 45
Figure 4.5. Intelligent compaction (IC) resilient modulus (M_R) [at 10 psi (69 kPa)] vs. field California Bearing Ratio (CBR): (a) linear, (b) exponential, (c) power, and (d) logarithmic relationships 46
Figure 4.6. Intelligent compaction (IC) resilient modulus (M_R) [at 10 psi (69 kPa)] vs. light weight deflectometer elastic modulus (E_{LWD}): (a) linear, (b) exponential, (c) power trendline 47
Figure 4.7. Intelligent compaction (IC) resilient modulus (M_R) [at 10 psi (69 kPa)] vs. falling weight deflectometer elastic modulus (E_{FWD}): (a) linear, (b) exponential, and (c) power trendline 48
Figure 4.8. (a) Intelligent compaction (IC) resilient modulus (M_R) [at 30 psi (207 kPa)] vs. dynamic cone penetration index (DCPI) and (b) IC M_R [at 30 psi (207 kPa)] vs. field California bearing ratio (CBR) 49
Figure 4.9. Intelligent compaction (IC) resilient modulus (M_R) [at 30 psi (207 kPa)] vs. light weight deflectometer elastic modulus (E_{LWD}): (a) linear, (b) exponential, and (c) power trendline 50
Figure 4.10. Intelligent compaction (IC) resilient modulus (M_R) [at 30 psi (207 kPa)] vs. falling weight deflectometer elastic modulus (E_{FWD}): (a) linear, (b) exponential, and (c) power trendline 51
Figure 5.1. Locations of the six neighboring weather stations and the MnROAD LVR test facility (green pins represent the neighboring weather stations and the white flag represents the location of the MnROAD LVR) 53
Figure 5.2. Pavement ME models for coarse RCA base layer at different layer thicknesses 55
Figure 5.3. Effect of aggregate base layer thickness on (a) IRI at the end of the design life (20 years) and (b) pavement age at IRI failure 57
Figure 5.4. Effect of aggregate base layer thickness on (a) total rut depth at the end of the design life (20 years) and (b) pavement age at total rut depth failure 58
Figure 5.5. Effect of aggregate base layer thickness on (a) alligator cracking at the end of the design life (20 years) and (b) pavement age at alligator cracking failure (NF = no failure) 59
Figure 5.6. Effect of aggregate base layer thickness on (a) longitudinal cracking at the end of the design life (20 years) and (b) pavement age at longitudinal cracking failure 60
Figure 5.7. Effect of base layer aggregate type on (a) IRI at the end of the design life (20 years) and (b) pavement age at IRI failure 61
Figure 5.8. Effect of base layer aggregate type on (a) total rut depth at the end of the design life (20 years) and (b) pavement age at total rut depth failure 62
Figure 5.9. Effect of base layer aggregate type on (a) alligator cracking at the end of the design life (20 years) and (b) pavement age at alligator cracking failure (NF = no failure) 63
Figure 5.10. Effect of base layer aggregate type on (a) longitudinal cracking at the end of the design life (20 years) and (b) pavement age at longitudinal cracking failure 64
Figure 5.11. Asphalt rut depths (at 50% reliability) for the pavement models that contained sand subgrade and were subjected to 1,000 AADTT 65

DRAFT

Figure 5.12. Base+subbase rut depths (at 50% reliability) for the pavement models that contained sand subgrade and were subjected to 1,000 AADTT 66
Figure 5.13. Subgrade rut depths (at 50% reliability) for the pavement models that contained sand subgrade and were subjected to 1,000 AADTT 66
Figure 5.14. Total and layer rut depths (at 50% reliability) for the pavement models that contained sand subgrade and coarse RCA base layers and were subjected to 1,000 AADTT 67
Figure 5.15. Effect of traffic level on (a) IRI at the end of the design life (20 years) and (b) pavement age at IRI failure 68
Figure 5.16. Effect of traffic level on (a) rutting at the end of the design life (20 years) and (b) pavement age at rutting failure (NF = no failure) 69
Figure 5.17. Effect of traffic level on (a) alligator cracking at the end of the design life (20 years) and (b) pavement age at alligator cracking failure (NF = no failure) 70
Figure 5.18. Effect of traffic level on (a) longitudinal cracking at the end of the design life (20 years) and (b) pavement age at longitudinal cracking failure (NF = no failure) 71
Figure 5.19. Relative aggregate base (RAB) layer thicknesses alternative to 12-in limestone base layer in terms of (a) IRI at the end of the design life (20 years) and (b) pavement age at IRI failure 73
Figure 5.20. Relative aggregate base (RAB) layer thicknesses alternative to 12-in limestone base layer in terms of (a) rutting at the end of the design life (20 years) and (b) pavement age at rutting failure 74
Figure 5.21. Relative aggregate base (RAB) layer thicknesses alternative to 12-in limestone base layer in terms of (a) alligator cracking at the end of the design life (20 years) and (b) pavement age at alligator cracking failure (NF = no failure) 75
Figure 5.22. Relative aggregate base (RAB) layer thicknesses alternative to 12-in limestone base layer in terms of (a) longitudinal cracking at the end of the design life (20 years) and (b) pavement age at longitudinal cracking failure 76
Figure 5.23. Pavement ME models for LSSB layers at different layer thicknesses 78
Figure 5.24. Effect of LSSB layer thickness on (a) IRI at the end of the design life (20 years) and (b) pavement age at IRI failure 80
Figure 5.25. Effect of LSSB layer thickness on (a) rutting at the end of the design life (20 years) and (b) pavement age at rutting failure (NF = no failure) 81
Figure 5.26. Effect of LSSB layer thickness on (a) alligator cracking at the end of the design life (20 years) and (b) pavement age at alligator cracking failure (NF = no failure) 82
Figure 5.27. Effect of LSSB layer modulus on (a) IRI at the end of the design life (20 years) and (b) pavement age at IRI failure 83
Figure 5.28. Effect of LSSB layer modulus on (a) rutting at the end of the design life (20 years) and (b) pavement age at rutting failure (NF = no failure) 84
Figure 5.29. Effect of LSSB layer modulus on (a) alligator cracking at the end of the design life (20 years) and (b) pavement age at alligator cracking failure (NF = no failure) 85
Figure 5.30. Asphalt rut depths (at 50% reliability) for the pavement models that were subjected to 1,000 AADTT 86

DRAFT

Figure 5.31. Base+subbase rut depths (at 50% reliability) for the pavement models that were subjected to 1,000 AADTT 86
Figure 5.32. Subgrade rut depths (at 50% reliability) for the pavement models that were subjected to 1,000 AADTT 87
Figure 5.33. Total and layer rut depths (at 50% reliability) for the pavement models that contained 12-in LSSB layers and were subjected to 1,000 AADTT 87
Figure 5.34. Effect of traffic level on (a) IRI at the end of the design life (20 years) and (b) pavement age at IRI failure 88
Figure 5.35. Effect of traffic level on (a) rutting at the end of the design life (20 years) and (b) pavement age at rutting failure (NF = no failure) 89
Figure 5.36. Effect of traffic level on (a) alligator cracking at the end of the design life (20 years) and (b) pavement age at alligator cracking failure (NF = no failure) 90
Figure 7.1. Remedial thickness (above subgrade) recommendations depending on the subgrade conditions (IDOT 2005) 97
Figure 7.2. Thickness recommendations for breaker run and select crushed material (WisDOT 2019) 98

DRAFT

1. TEST CELLS AND MATERIALS

1.1. Test Cells

The test cells are located on the Minnesota Road Research Project (MnROAD) Low Volume Road (LVR), a pavement test facility owned by the MnDOT (MnDOT 2017). MnROAD LVR is a two-lane closed-loop located near westbound I-94, northwest of the Twin Cities, MN. Traffic on the MnROAD LVR was simulated by a MnROAD truck, a 5-axle tractor/trailer combination weighing 80 kip (36.3 Mg) (MnDOT 2013). The MnROAD truck traveled approximately 70 laps per day while located only in the inside lane (main traffic). The outside lane (occasional traffic) was dedicated to temperature and moisture sensors installed to investigate environmental effects. Eleven test cells were constructed in three groups: (1) a recycled aggregate base (RAB) group, (2) a large stone subbase (LSSB) group, and (3) an LSSB with geosynthetics group. The cross-sections of the test cells are provided in Figure 1.1. More detailed information about the construction of the test cells is provided in the Task 3 (construction monitoring and reporting) report.

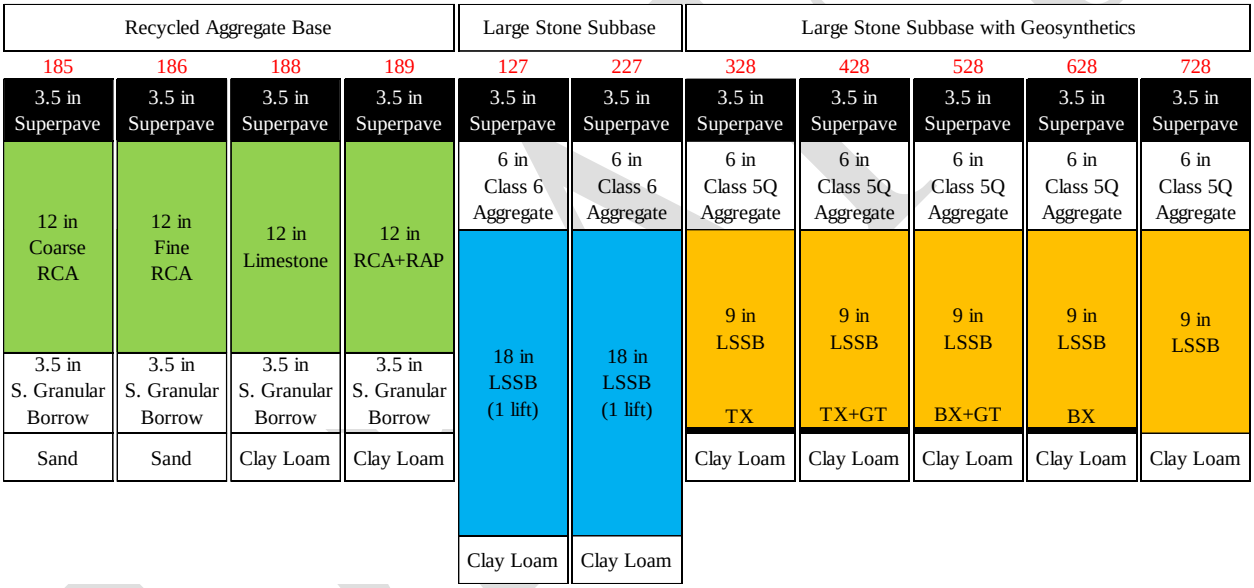


Figure 1.1. Cross-sections of the test cells (not to scale) (s. granular borrow = select granular borrow, TX = triaxial geogrid, GT = non-woven geotextile, BX = biaxial geogrid)

1.2. Materials

Ten different materials (Figure 1.2) were used to construct the test cells (Figure 1.1). The two different subgrade soils were sand subgrade and clay loam [Figures 1.2(a) and 1.2(b), respectively]. The two different subbase materials were select granular borrow (MnDOT 2018) and LSSB material (large crushed granite) [Figures 1.2(c) and 1.2(d), respectively]. The base layer aggregates were coarse recycled concrete aggregate (RCA), fine RCA, limestone, RCA and recycled asphalt pavement (RAP) mixture (RCA+RAP), class 6 Aggregate, and class 5Q Aggregate (MnDOT 2018) [Figures 1.2(e), 1.2 (f), 1.2 (g), 1.2 (h), 1.2 (i), and 1.2 (j), respectively]. More detailed information about the index and engineering properties of these materials is provided in the Task 4 (laboratory testing) report.

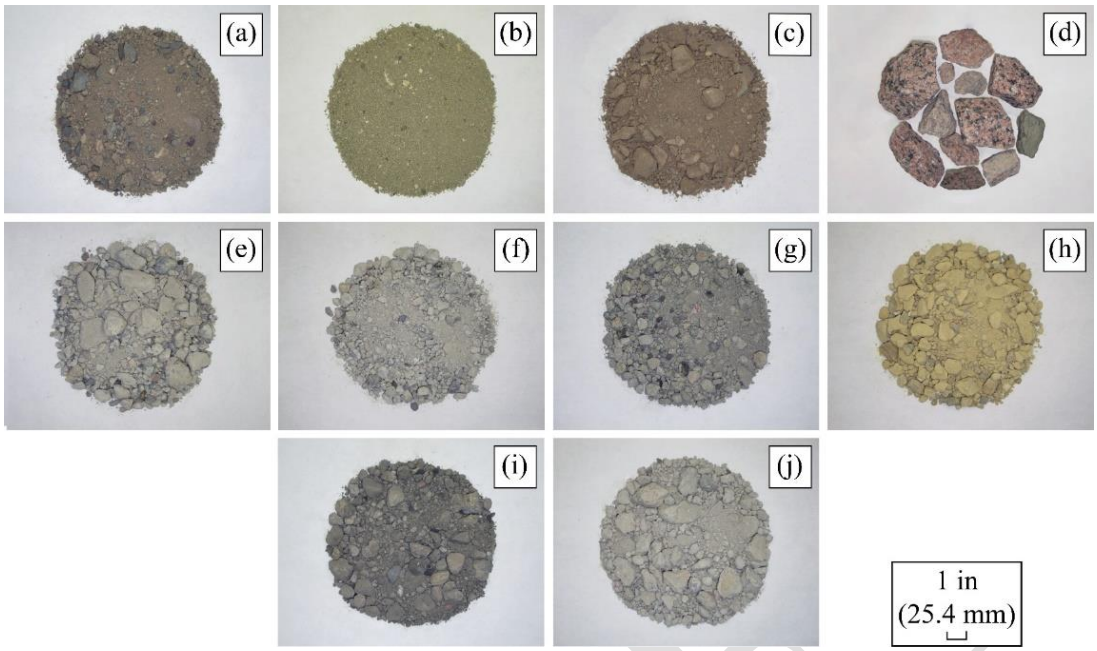


Figure 1.2. Materials used to construct the test cells: (a) sand subgrade, (b) clay loam, (c) select granular borrow, (d) LSSB material, (e) coarse RCA, (f) fine RCA, (g) RCA+RAP, (h) limestone, (i) class 6 aggregate, and (j) class 5Q aggregate

2. ADDITIONAL STUDY RELATED TO TASK 5 (PERFORMANCE MONITORING AND REPORTING) AND TASK 6 (INSTRUMENTATION) REPORTS

2.1. Determination of Thermal Diffusivities (α) Based on Field Temperature Profiles

In one-dimensional conduction heat transfer theory, the analytical solution used to determine the soil temperature at a specific depth (z) and time (t) is shown in Equation (1) (Horton et al. 1983).

$$T(z,t) = \overline{T} + A_0 e^{-z\sqrt{\frac{\omega}{2\alpha}}} \sin\left(\omega t - z\sqrt{\frac{\omega}{2\alpha}} + C_4\right) \quad (1)$$

where $\overline{T}$ is the average temperature at the soil surface, A_0 is the amplitude at the soil surface, ω is the radial frequency $\left(\frac{2\pi}{p}\right)$, p is the period, α is the thermal diffusivity, and C_4 is the phase constant.

The theory described by Equation (1) has several assumptions that may affect the accuracy of the estimations made from field temperature profiles, including the following:

- Heat flow by conduction only,
- One-dimensional heat flow,
- The soil is homogeneous,
- The soil is semi-infinite in space,
- The soil surface temperature is a sinusoidal function of time (Figures 2.1 and 2.2), and
- The sine wave is assumed to be repeating (Figure 2.2).

DRAFT

In the given theory, the amplitude (A) decreases as soil depth increases and the sinusoidal-like temperature curve shifts to the right as soil depth increases due to the phase constant (C_4) (Figure 2.2) (Hanson et al. 2000). Time is required for heat transfer from higher elevations (closer to the surface) to lower elevations (deeper levels).

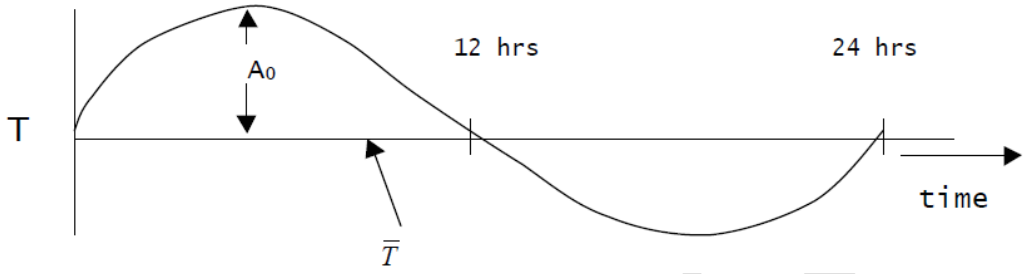


Figure 2.1. Daily soil surface temperature as a sinusoidal function of time (T = temperature, A_0 = amplitude at the soil surface, $\overline{T}$ = average temperature at the soil surface)

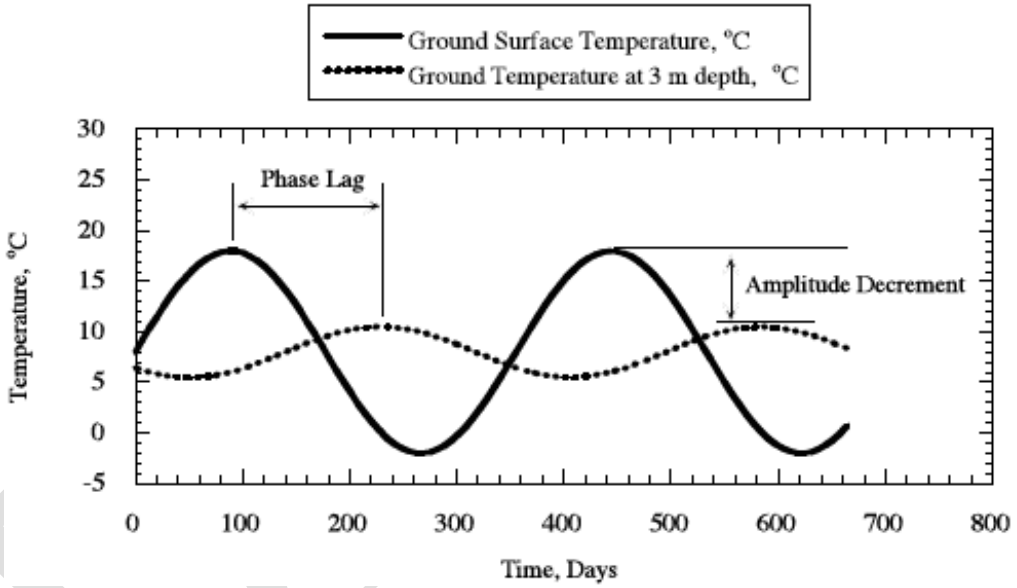


Figure 2.2. Soil temperature profiles at different soil depths (Hanson et al. 2000)

Thermal conductivity (λ), volumetric heat capacity (C), and thermal diffusivity (α) are the three thermal properties of soils. λ is defined as a soils' ability to conduct heat, and C is defined as the amount of heat required to increase the temperature of a mass of soil by 1°C. α is defined as the ratio between λ and C, as shown in Equation (2). Volumetric water content (VWC) of a soil affects its λ and C properties, as shown in Figure 2.3. Since both λ and C are affected by soil VWC, α is also affected by soil VWC (Figure 2.3). λ, C, and α of soils can be measured through laboratory testing by using a thermal properties analyzer such as a Decagon KD2 Pro. In addition to laboratory testing, α can also be determined from soil temperature profiles recorded in the field by temperature sensors (e.g., thermocouples used in this project). Amplitude and phase equations derived from Equation (1) and provided in Equations (3) and (4), respectively, can be used to determine soil α in the field.

$$\alpha = \frac{\lambda}{C} \tag{2}$$

where α is the thermal diffusivity, λ is the thermal conductivity, and C is the volumetric heat capacity.

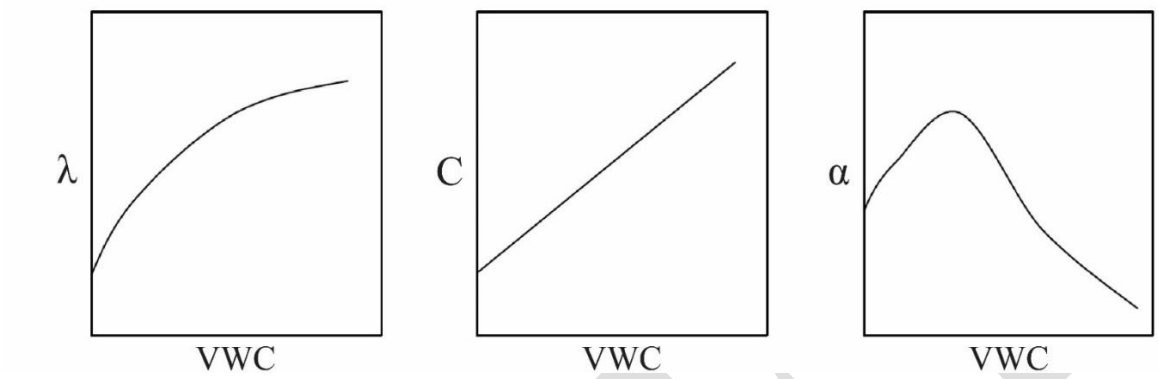


Figure 2.3. Thermal properties of soils (λ = thermal conductivity, C = heat capacity, and α = thermal diffusivity) (Jury and Horton 2004)

$$\alpha = \left(\frac{\omega}{2}\right)\left[\frac{z_2 - z_1}{\ln\left(\frac{A_1}{A_2}\right)}\right]^2 \tag{3}$$

$$\alpha = \left(\frac{1}{2\omega}\right)\left[\frac{z_2 - z_1}{\Delta t_{max}}\right]^2 \tag{4}$$

where ω is the radial frequency $\left(\frac{2\pi}{p}\right)$, p is the period, z_1 and z_2 are the two elevations where the measurements are taken, A_1 and A_2 are the amplitudes measured at z_1 and z_2, and Δt_{max} is the time difference between maximum temperatures at z_1 and z_2.

Amplitude and phase equations, provided in Equations (3) and (4), respectively, were used to determine α values based on field temperature profiles throughout coarse RCA base (cell 185), fine RCA base (cells 186), limestone base (cell 188), RCA+RAP base (cell 189), and LSSB layers (cells 127 and 728) [detailed information about soil temperature profiles obtained from field measurements is provided in the Task 5 (performance monitoring and reporting) and Task 6 (instrumentation) report]. As shown in Figure 2.1, there should be 12 hours of daytime and 12 hours of nighttime to obtain more reliable results by using the one-dimensional conduction heat transfer theory. Since equinoxes, dates when day and night are of equal length (12 hours/each), occur in March (around March 21) and September (around September 23), α values of the selected pavement sublayers were determined only near those dates.

In 12-in coarse RCA (cell 185), fine RCA (cell 186), limestone (cell 188), and RCA+RAP (cell 189) base layers, there were three thermocouples (TCs): (1) top TC, (2) middle TC, and (3) bottom TC. Figure 2.4 is an example that shows the locations of the TC sensors in 12-in coarse RCA (cell

DRAFT

185). Since the α values of soil are affected by the VWC of soils, evaluating the moisture probe readings, if taken close to the TC sensors, could also be beneficial in understanding the α values calculated by the amplitude equation [Equation (3)] and phase equation [Equation (4)]. In the same base layers, there were two moisture probes (ECs): (1) top EC and (2) bottom EC. Figure 2.4 is also an example that shows the locations of the EC sensors in 12-in coarse RCA (cell 185). The EC sensors were at the same locations in 12-in fine RCA (cell 186), limestone (cell 188), and RCA+RAP (cell 189) base layers; therefore, their locations are not shown separately. The top EC and bottom EC sensors were close to the top TC and bottom TC sensors, respectively. In 18-in LSSB layer (cell 127), there were four TC sensors: (1) top TC, (2) middle 1 TC, (3) middle 2 TC, and (4) bottom TC (Figure 2.5). In 9-in LSSB layer (cell 728), there were three TC sensors: (1) top TC, (2) middle TC, and (3) bottom TC (Figure 2.6). There were no EC sensors in any of the LSSB layers [Figure 2.5 for 18-in LSSB layer (cell 127) and Figure 2.6 for 9-in LSSB layer (cell 728)]. More information regarding the locations of these sensors is provided in the Task 3 (construction monitoring and reporting), Task 5 (performance monitoring and reporting), and Task 6 (instrumentation) reports.

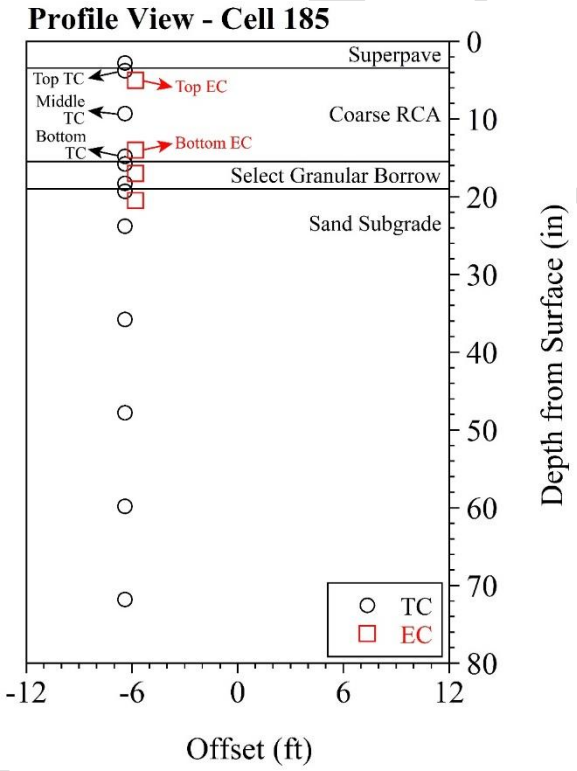


Figure 2.4. Locations of the thermocouples (TC) and moisture probes (EC) in 12-in coarse RCA (cell 185)

DRAFT

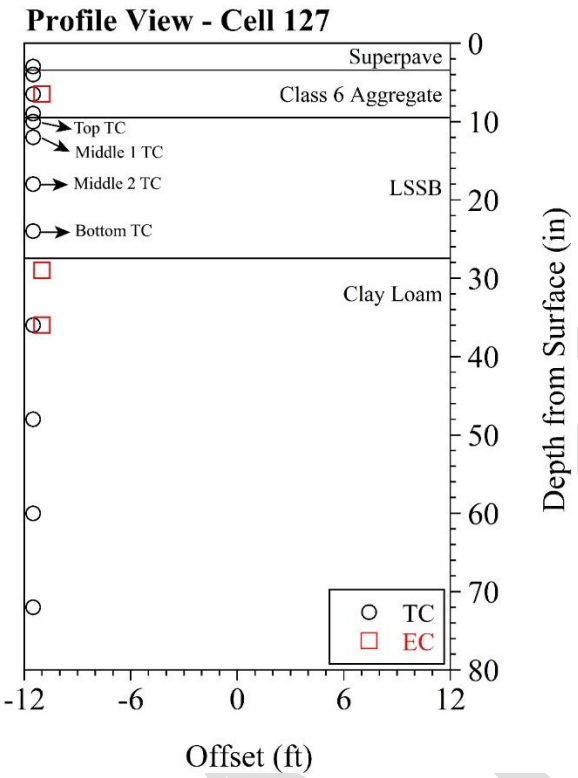


Figure 2.5. Locations of the thermocouples (TC) and moisture probes (EC) in 18-in LSSB (cell 127)

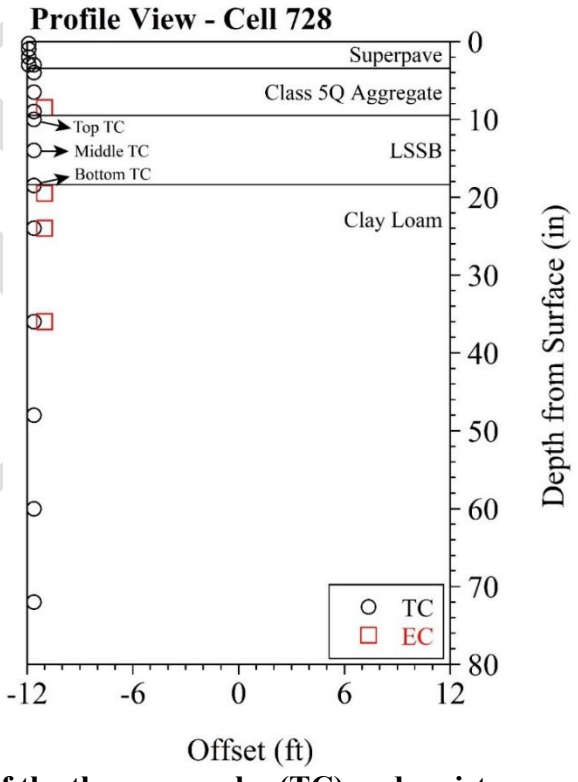


Figure 2.6. Locations of the thermocouples (TC) and moisture probes (EC) in 9-in LSSB (cell 728)

DRAFT

For 12-in coarse RCA (cell 185), fine RCA (cell 186), limestone (cell 188), and RCA+RAP (cell 189) base layers, overall, the α values determined by the amplitude equation [Equation (3)] were located in a smaller range than those calculated by the phase equation [Equation (4)]. Figures 2.7 and 2.8 are examples that show the α values determined by the amplitude and phase equations, respectively, for 12-in coarse RCA base layer (cell 185). The α values determined for 12-in fine RCA (cell 186), limestone (cell 188), and RCA+RAP (cell 189) base layers are provided in Appendix A. The VWC values (median) around the equinox dates were also determined for 12-in base layers (Appendix A); however, no consistent trend was observed between the VWC values and the α values.

Overall, 12-in limestone (cell 188) base layer exhibited higher α values (between 40 and 53 cm^2/h) than the other 12-in base layers in cell 185 (coarse RCA) (between 26 and 31 cm^2/h), cell 186 (fine RCA) (between 24 and 31 cm^2/h), and cell 189 (RCA+RAP) (between 28 and 35 cm^2/h). This could be due to two reasons: (1) different thermal properties of the materials and (2) different VWC values in the base layers (Figure 2.3). As stated previously, no consistent trend was observed between the VWC values and the α values, so it was speculated that 12-in limestone (cell 188) exhibited higher α values than other 12-in base layers because of limestone's different thermal properties. Figure 2.9 is an example that shows the α values calculated from top-bottom TC sensors in 12-in base layers. Comparisons between top-middle and middle-bottom TC sensors in 12-in base layers are provided in Appendix B.

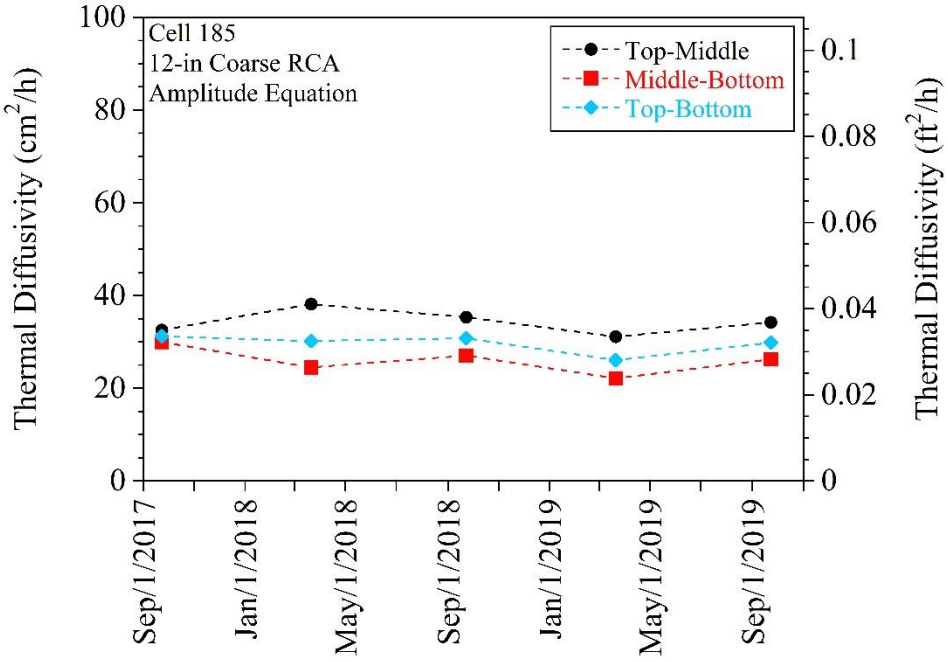


Figure 2.7. Thermal diffusivity (α) values determined by the amplitude equation for 12-in coarse RCA base (cell 185)

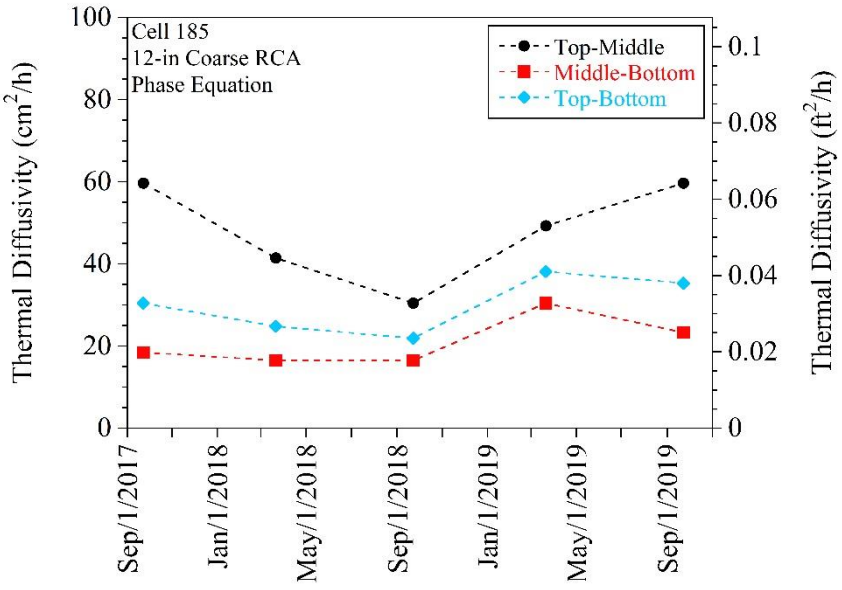


Figure 2.8. Thermal diffusivity (α) values determined by the phase equation for 12-in coarse RCA base (cell 185)

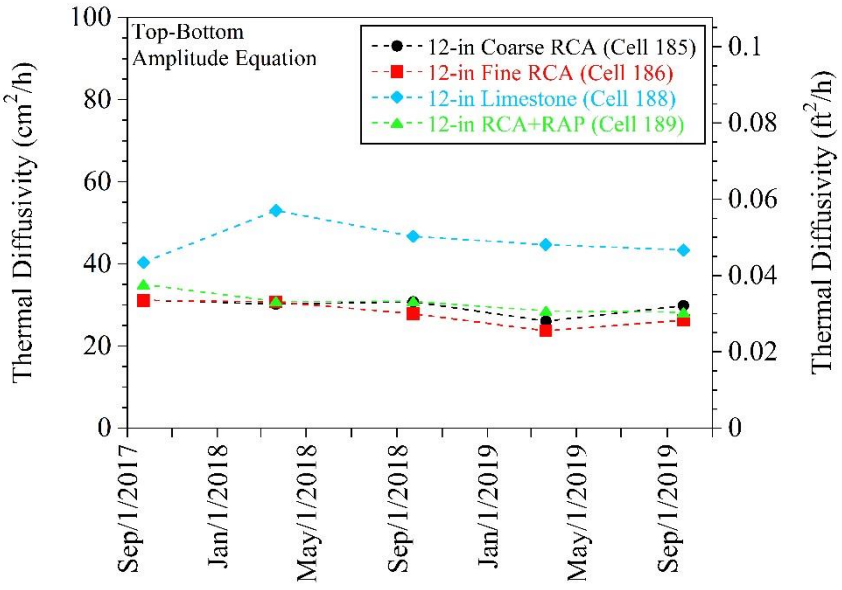


Figure 2.9. Thermal diffusivity (α) values determined from top-bottom thermocouples (TCs) by the amplitude equation for 12-in base layers

The α values determined by the amplitude equation [Equation (3)] and phase equation [Equation (4)] for 18-in LSSB layer in cell 127 are provided in Figures 2.10 and 2.11, respectively. Only the top, middle 1, and middle 2 TC sensors were considered for the calculation since the bottom and middle 2 TC sensors exhibited similar temperature profiles. As explained previously, as soil depth increases, amplitude reduces (Figure 2.2), and soil temperatures at deeper elevations tend to be similar to one another. No comparison between the α values and VWC values could be made since 18-in LSSB layer in cell 127 did not contain any EC sensors (Figure 2.5).

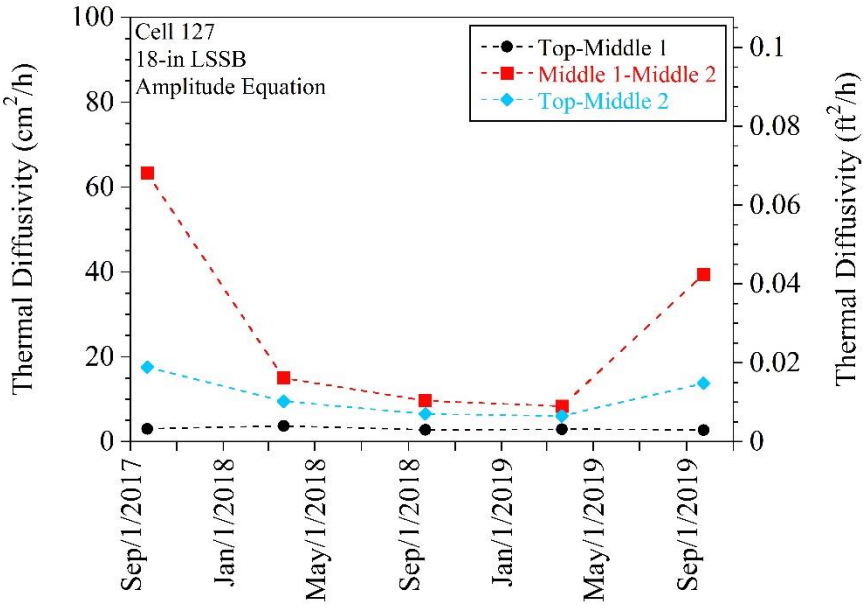


Figure 2.10. Thermal diffusivity (α) values determined by the amplitude equation for 18-in LSSB (cell 127)

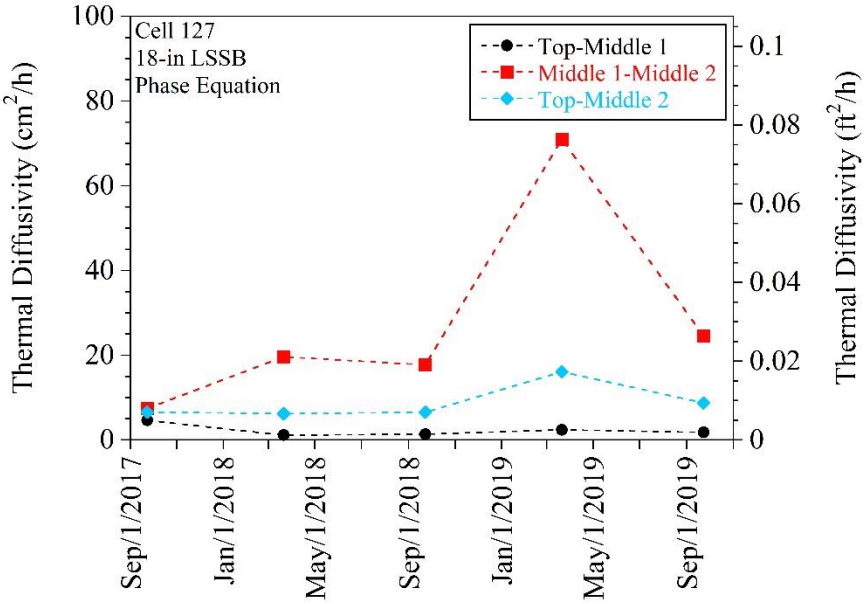


Figure 2.11. Thermal diffusivity (α) values determined by the phase equation for 18-in LSSB (cell 127)

The α values determined by the amplitude equation [Equation (3)] and phase equation [Equation (4)] for 9-in LSSB layer in cell 728 are provided in Figures 2.12 and 2.13, respectively. Only the top and middle TC sensors were considered because the bottom TC sensor and the middle TC sensor exhibited similar temperature profiles. As explained previously, as soil depth increases, amplitude diminishes, and soil temperature profiles become similar to one another (Figure 2.2). No comparison between the α values and VWC values could be made since 9-in LSSB layer in cell 728 did not contain any EC sensors (Figure 2.6).

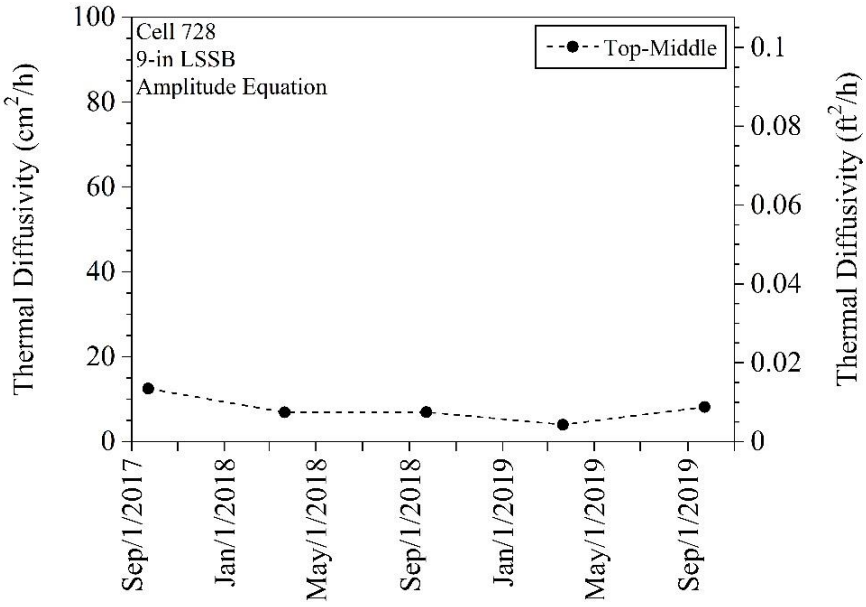


Figure 2.12. Thermal diffusivity (α) values determined by the amplitude equation for 9-in LSSB (cell 728)

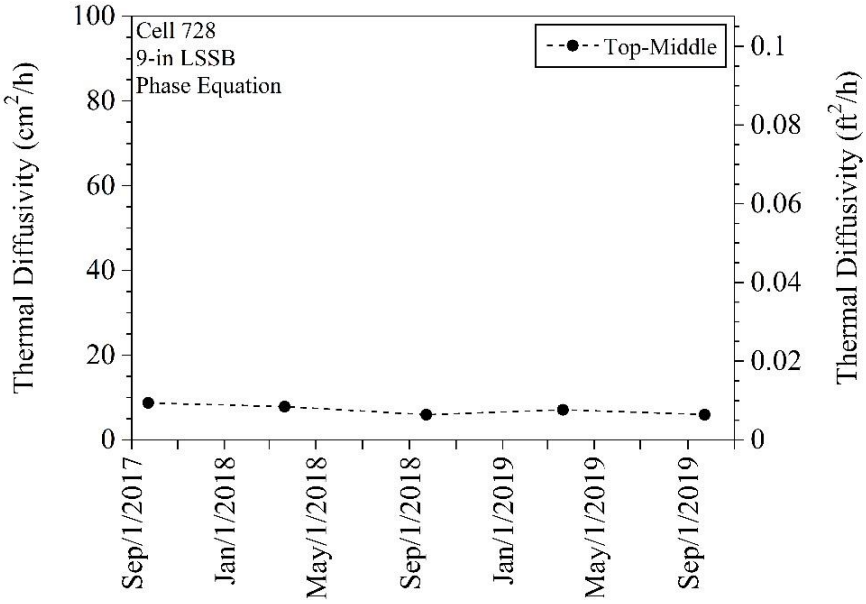


Figure 2.13. Thermal diffusivity (α) values determined by the phase equation for 9-in LSSB (cell 728)

Thermal properties of soils would affect the freeze-thaw (F-T) durability and frost penetration depth of pavement sublayers. For more reliable evaluation of the thermal properties of soils (λ, C, and α), laboratory testing rather than using the amplitude [Equation (3)] and phase equations [Equation (4)] is recommended. As described previously, the one-dimensional conduction heat transfer theory is based on several assumptions that would affect the reliability of such equations in determining soil α. However, determining the λ, C, and α properties of soils is beyond the scope of this project; therefore, it was not included in this study.

2.2. Comparisons Between the Volumetric Water Content (VWC) Values in the First (2017-2018) and Second (2018-2019) Freezing and Thawing Periods

In the previous task report, which was the combination of the Task 5 (performance monitoring and reporting) and Task 6 (instrumentation) reports, frost penetration depths were determined based on soil temperature profiles recorded over more than two years for cells 185 (12-in coarse RCA), 186 (12-in fine RCA), 188 (12-in limestone), 189 (12-in RCA+RAP), 127 (18-in LSSB), and 728 (9-in LSSB). From those results, all of the frost penetration depths observed during the 2018-2019 winter were deeper than those observed during the 2017-2018 winter [differences between the maximum frost penetration depths in these winters were between 0.15-0.62 ft (0.05-0.19 m)]. It was also observed that the winter in 2018-2019 (freezing periods occurred between 116 and 124 days) was longer than that in 2017-2018 (freezing periods occurred between 83 and 94 days). However, no significant differences were observed between the two years in terms of the duration of the thawing periods (between 15 and 28 days for the 2017-2018 spring and between 17 and 27 days for the 2018-2019 spring). For this task report, an effort was made to compare VWC values during the first (2017-2018) and second (2018-2019) freezing and thawing periods. Since the EC sensors were prone to stop working properly when the ground was frozen, no specific evaluation was made for such differences between VWC values recorded during the December-February periods.

When liquid water begins to freeze and transform into ice, its dielectric constant (about 80) begins to diminish, which also reduces the dielectric constant of the soil medium. Therefore, freezing events can be detected by noting sudden reductions in VWC values over time. When the soil has become fully frozen, its dielectric constant tends to stay constant because there will be no change in the liquid water content under such conditions. Following freezing and fully frozen conditions, thawing events can be determined by noting sudden increases in VWC values over time. It is expected that data obtained by the moisture probes would be compatible with data collected by the thermocouples and properly demonstrate the freezing and thawing periods (Genc 2019).

For cell 185 (12-in coarse RCA), VWC readings could not be taken from any of the pavement sublayers after Oct 2017 due to the malfunctioning of the moisture probes embedded in the test cell; therefore, no comparisons could be made between the VWC values during two freezing and thawing periods. For cell 186 (12-in fine RCA), the only consistent VWC readings could be taken from the top EC sensor in 12-in fine RCA base layer. For cell 186 (12-in fine RCA), no continuous VWC readings could be taken from the select granular borrow subbase (sensor was at 17-in depth) and the bottom of the fine RCA base layer (sensor was at 14-in depth). Also, the EC sensor embedded in the sand subgrade layer (sensor was at 20.5-in depth) exhibited highly fluctuated data, possibly indicating malfunctioning of that sensor, too.

For 12-in fine RCA (cell 186), limestone (cell 188), and RCA+RAP (cell 189) base layers, the VWC values before both freezing periods were similar to one another. The VWC values after both thawing periods were also similar. The only difference was that the thawing period in 2018-2019 started around 15 days later than that in 2017-2018 because the 2018-2019 winter was longer. Figures 2.14, 2.15, and 2.16 are examples showing the VWC values for the EC sensors at 5-in depths in 12-in fine RCA (cell 186), limestone (cell 188), and RCA+RAP (cell 189) base layers, respectively. The comparisons for the other EC sensors are provided in Appendix C.

DRAFT

For cells 127 (18-in LSSB) and 728 (9-in LSSB), since there were no EC sensors embedded in the LSSB layers, no comparison could be made for those layers. However, comparisons for 6-in class 6 aggregate base layer (cell 127), class 5Q aggregate base layer (cell 728), and clay loam subgrade layers (both cells 127 and 728) were made and are provided in Appendix C.

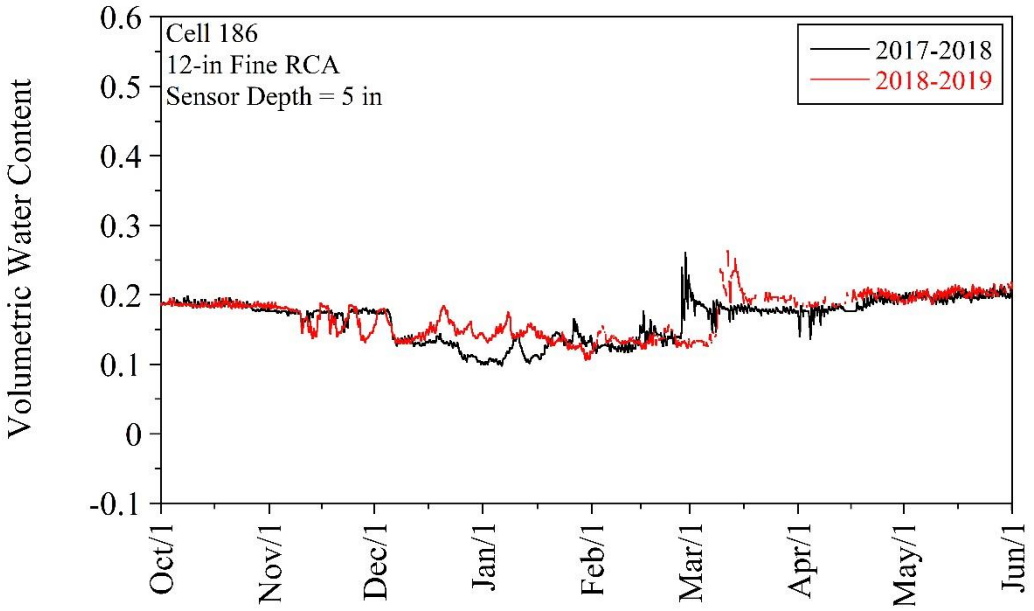


Figure 2.14. Volumetric water content (VWC) values for the sensor at 5-in depth in 12-in fine RCA base layer (cell 186) during two freezing and thawing periods (the dates on the x-axis represent the time periods for both 2017-2018 and 2018-2019 years)

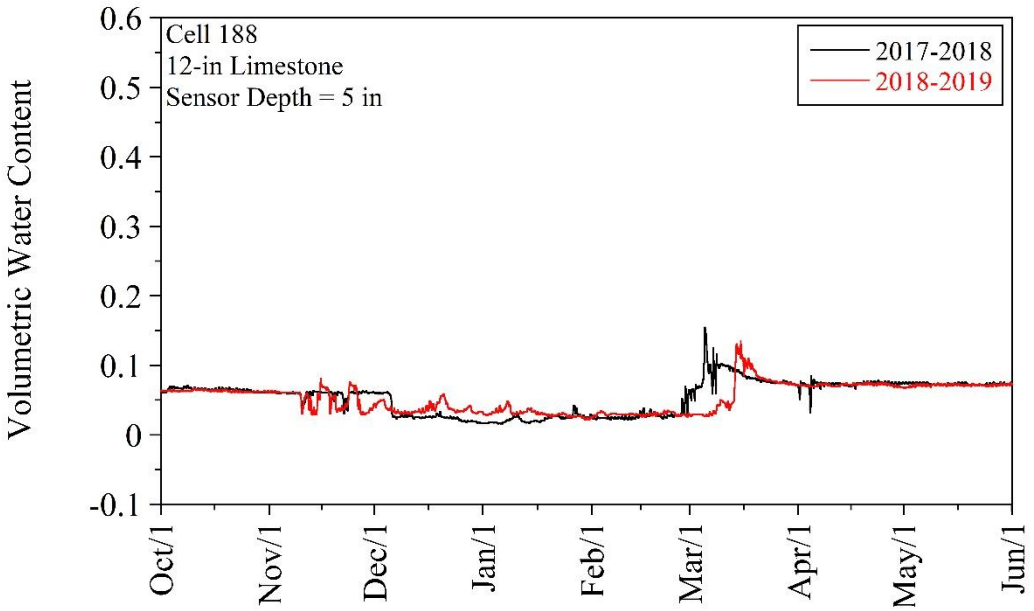


Figure 2.15. Volumetric water content (VWC) values for the sensor at 5-in depth in 12-in limestone base layer (cell 188) during two freezing and thawing periods (the dates on the x-axis represent the time periods for both 2017-2018 and 2018-2019 years)

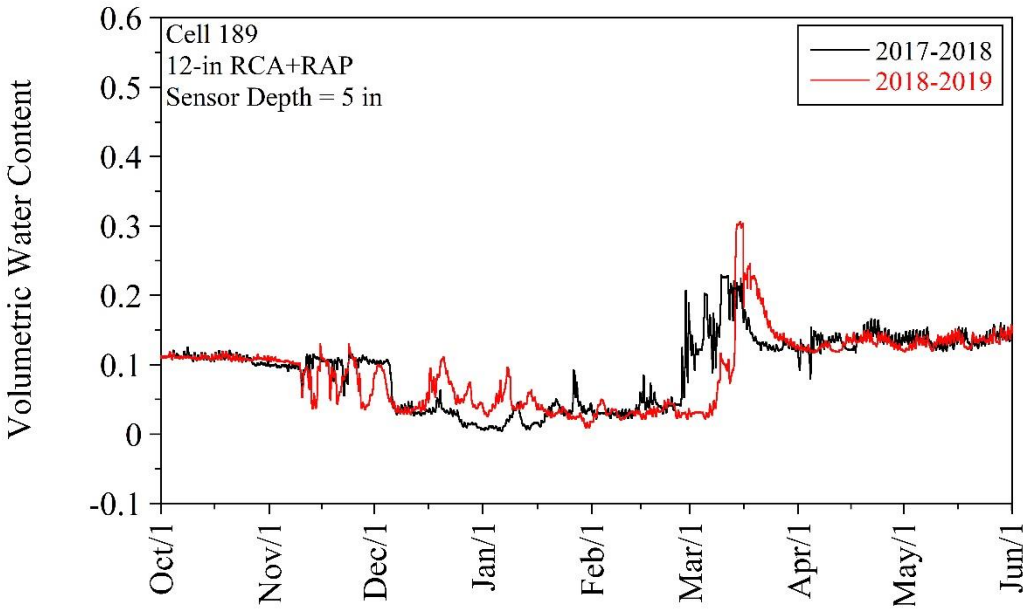


Figure 2.16. Volumetric water content (VWC) values for the sensor at 5-in depth in 12-in RCA+RAP base layer (cell 189) during two freezing and thawing periods (the dates on the x-axis represent the time periods for both 2017-2018 and 2018-2019 years)

2.3. Effect of Field Degree of Compaction (DOC) on the Performance of the Test Cells

2.3.1. Nuclear Density Gauge (NDG) Measurements for the Base and Subgrade Layers of the Test Cells

Modified Proctor compaction test results [maximum dry density (MDD) and optimum moisture content (OMC)] and in-situ nuclear density gauge (NDG) measurements were compared for subgrade and base layers to determine the relative dry density (i.e., field degree of compaction) and relative moisture content values. NDG tests could not be performed for the subgrade layers in cells 127 (18-in LSSB), 227 (18-in LSSB), 328 (9-in LSSB + TX), 428 (9-in LSSB + TX+GT), 528 (9-in LSSB + BX+GT), 628 (9-in LSSB + BX), and 728 (9-in LSSB) since a very non-traditional subgrade preparation procedure was followed during the construction of these cells to create a weak subgrade with a dynamic cone penetration index (DCPI) value between 2.5 and 3.5 in/blow (63.5 and 89 mm/blow) (ASTM D6951) for the upper 1 ft (0.3 m) of the clay loam subgrade soil [in fact, no field testing (except DCP) was performed on the prepared subgrade layers not to disturb these layers]. For NDG measurements to be valid, particles bigger than 38 mm (1 ½ in) should not be more than 40% of test material by weight (Roads and Maritime Services 2015). Since 64% of the particles in the LSSB material was larger than 38 mm (1 ½ in), NDG measurements were not taken for LSSB cells (cells 127 to 728). For all the subbase layers, a quality compaction method, in which the compacted layer was visually observed for consolidation, pumping, and lateral movement, was used (MnDOT 2018). Detailed information regarding the NDG measurements is provided in the Task 3 (construction monitoring and reporting) report. Figures 2.17 and 2.18 summarize the relative dry density and relative moisture content values for the base and subgrade layers, respectively.

DRAFT

The sand subgrade layer in cell 185 (12-in coarse RCA) exhibited lower relative dry density values (between 89 and 99%) than the clay loam subgrade layers in cells 188 (12-in limestone) and 189 (12-in RCA+RAP) (between 94 and 112%) (Figure 2.17). In general, the relative moisture content values of these subgrade layers were lower than 100%. (Figure 2.18). All three subgrade layers exhibited similar calibrated in-place moisture content values (between 1.6 and 5.3%). However, since the OMC of the sand subgrade (5.6%) was lower than that of clay loam (10%) [per Task 4 (laboratory testing) report], the sand subgrade layer in cell 185 (12-in coarse RCA) exhibited higher relative moisture content values (median value of 85%) than the clay loam subgrade layers in cells 188 (12-in limestone) and 189 (12-in RCA+RAP) (median values of 26 and 39%, respectively) (Figure 2.18).

The relative dry density values of 12-in coarse RCA (cell 185), fine RCA (cell 186), limestone (cell 188), and RCA+RAP (cell 189) base layers were between 88% and 100% (Figure 2.17). The relative moisture content values of these base layers were lower than 100%, indicating that each base layer was compacted at the dry side of the OMC of the corresponding material (Figure 2.18), so MDD values could not be obtained and lower relative dry density values were observed (Kazmee and Tutumluer 2015). Overall, the relative dry density values of 12-in coarse RCA base layer (cell 185) were lower than those of 12-in fine RCA (cell 186), limestone (cell 188), and RCA+RAP (cell 189) base layers. However, since different materials were used in 12-in aggregate base layers, no specific comparison was made between the NDG measurements and the performance of these layers.

The relative dry density values of the class 6 aggregate base layers (cells 127 and 227) (between 91 and 95%) were higher than those of the class 5Q aggregate base layers (cells 328, 428, 528, 628, and 728) (between 78 and 92%) (Figure 2.17). Similar to the 12-in aggregate base layers, each 6-in aggregate base layer [class 6 aggregate (cells 127-227) and class 5Q aggregate (cells 328-728) base layers] was compacted at the dry side of the OMC of the corresponding material [the relative moisture content values of the class 6 aggregate (cells 127-227) and class 5Q aggregate (cells 328-728) base layers were lower than 100%)] (Figure 2.18).

During compaction, lower relative dry density values were expected to be observed for materials containing large voids associated with large particles due to particle reorientation (Kazmee and Tutumluer 2015). It was concluded that 9-in LSSB layers could not provide a stable foundation for the class 5Q aggregate base layers, and therefore, reduced the effectiveness of compaction for the class 5Q aggregate base layers due to the reorientation of large particles during compaction. By considering that the main contribution of the geosynthetics placed beneath 9-in LSSB layers would be to the subgrade layers, placing geosynthetics on top of 9-in LSSB layers would improve the stability of 9-in LSSB layers during compaction of the class 5Q aggregate base layers due to improved load distribution. A similar result was not observed with 18-in LSSB layers, possibly indicating that 18-in LSSB layers were more suitable for pavement construction than 9-in LSSB layers. Higher layer stiffness would be expected for thicker layers because of improvement in load distribution with an increase in the layer thickness (Tanyu et al. 2003).

Specifically, the 6-in class 5Q aggregate base layer in cell 528 (overlying 9-in LSSB layer) exhibited lower relative dry density values compared to the other 6-in class 5Q aggregate base layers (overlying 9-in LSSB layers) in cells 328, 428, 628, and 728. In addition, the relative

DRAFT

moisture content values of 6-in class 5Q aggregate base layer (overlying 9-in LSSB layer) in cell 528 were lower than those of the other class 5Q aggregate base layers (overlying 9-in LSSB layers) in cells 328, 428, 682, and 728. Compacting drier soil at the same compaction energy is expected to result in lower compacted dry density due to the lack of lubricant effect provided by the water. Therefore, lower relative dry density values observed in the class 5Q aggregate base layer (overlying 9-in LSSB layer) in cell 528 were possibly due to the lack of sufficient water in the aggregate matrix.

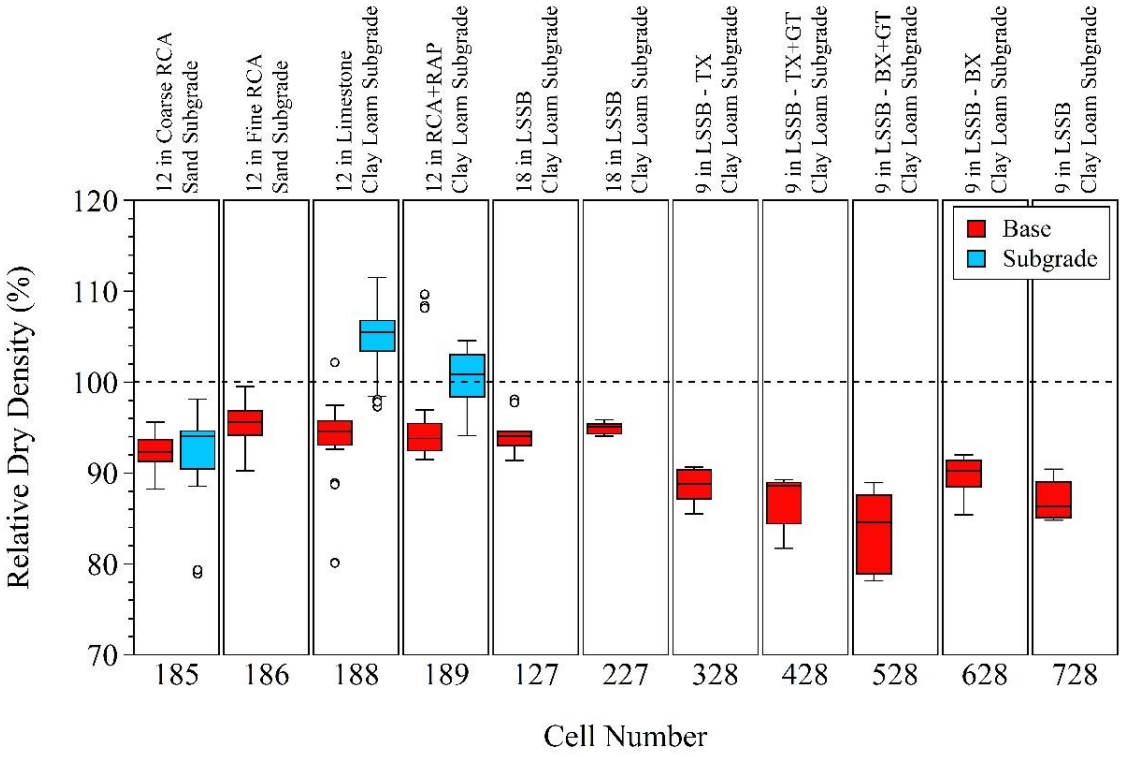


Figure 2.17. Relative dry density values for the base and subgrade layers (the red boxes shown for cells 127 and 227 are for class 6 aggregate base layers and those shown for cells 328-728 are for class 5Q aggregate base layers)

DRAFT

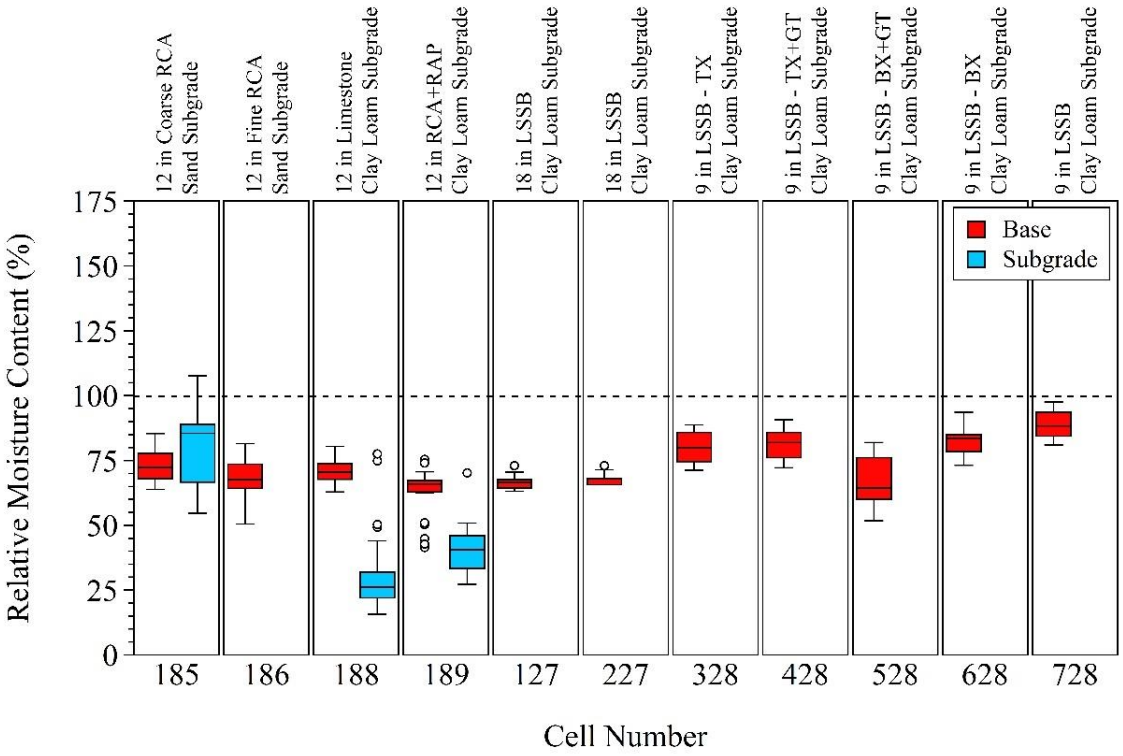


Figure 2.18. Relative moisture content values for the base and subgrade layers (the red boxes shown for cells 127 and 227 are for class 6 aggregate base layers and those shown for cells 328-728 are for class 5Q aggregate base layers)

2.3.2. Effect of the Inadequate Compaction of Class 5Q Aggregate Base Layers Overlying 9-in LSSB Layers

As previously shown in Figure 2.17, the relative dry density values of all of the aggregate base layers were lower than 95%-100%. Specifically, the relative dry density values of 6-in class 5Q aggregate base layers overlying 9-in LSSB layers were lower than other base layers due to the instability of 9-in LSSB layers under compaction. To focus on the effect of the instability of 9-in LSSB layers under compaction on the performance of the test cells, Figures 2.17 and 2.18 were revised into Figures 2.19 and 2.20, respectively.

DRAFT

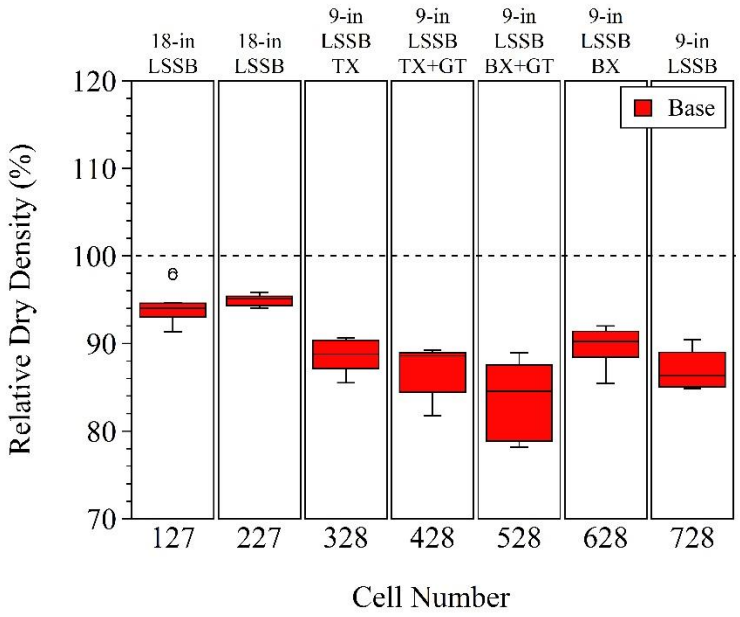


Figure 2.19. Relative dry density values for the aggregate base layers overlying LSSB layers

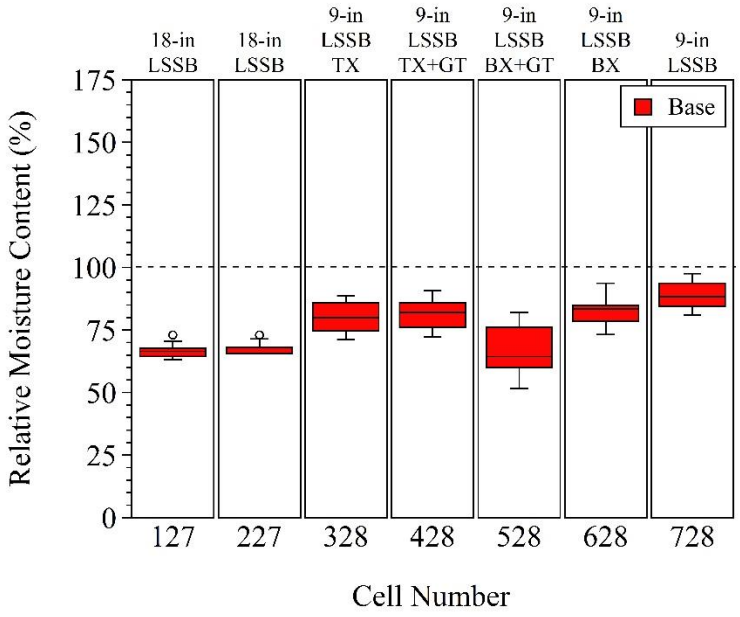


Figure 2.20. Relative moisture content values for the aggregate base layers overlying LSSB layers

Figures 2.21, 2.22, and 2.23 show light weight deflectometer (LWD) elastic modulus (E_{LWD}), falling weight deflectometer (FWD) elastic modulus (E_{FWD}), and intelligent compaction (IC) resilient modulus (M_R) values, respectively, for the base+subase layers through cells 127-728 [these results were taken from the Task 3 (construction monitoring and reporting) report]. As can be seen in these figures, the base+subbase layers in cells 127 and 227 (6-in class 6 aggregate base + 18-in LSSB layers) generally provided greater stiffness than the base+subbase layers of cells 328-728 (6-in class 5Q aggregate base + 9-in LSSB layers). There were two principal reasons for this: (1) 18-in LSSB provided better structural support than 9-in LSSB due to higher thickness

(Tanyu et al. 2003) and (2) class 6 aggregate base layers overlying 18-in LSSB layers were better compacted than class 5Q aggregate base layers overlying 9-in LSSB layers. LWD, FWD, and IC test results (Figures 2.21, 2.22, and 2.23, respectively) exhibited that stiffness trends were similar to the trends observed in relative dry density values (Figure 2.19). Specifically, the base+subbase layer in cell 528 (class 5Q aggregate base + 9-in LSSB layers) exhibited the lowest base+subbase stiffness compared to the similar base+subbase layers in cells 328, 428, 628, and 728. This occurred because the class 5Q aggregate base layer in cell 528 exhibited the lowest relative dry density compared to the other class 5Q aggregate base layers in cells 328, 428, 628, and 728 (Figure 2.19). Therefore, it was concluded that the structural benefits of the geosynthetics could not be clearly observed by LWD, FWD, and IC testing due to the overall instability of 9-in LSSB layers and lower relative dry density of 6-in class 5Q aggregate base layers. In addition, it was also speculated that the loads applied by LWD, FWD, or IC testing were insufficient to permit observation of the structural benefits of geosynthetics. A heavy weight deflectometer (HWD), a type of FWD equipment applying higher loads, could be used for this purpose.

As discussed in the Task 3 (construction monitoring and reporting) report, after the placement of 9-in LSSB layers over clay loam subgrade layers, subgrade soil pumping into 9-in LSSB layers was observed in the originally constructed test cells (cells 128 and 228) under construction traffic. In addition, as the construction of those originally constructed test cells (cells 128 and 228) continued, rutting was observed in the aggregate base and asphalt layers when subjected to construction traffic. To overcome these subgrade soil pumping and rutting issues, the originally constructed test cells (cells 128 and 228) were excavated to their subgrade layers for reconstruction. Cell 228 could not be fully removed because of the presence of near-surface utilities in an area to the east, so around 130 ft (39.6 m) of that cell was kept in place and renumbered as cell 728. The newly designed test cells were named as cells 328, 428, 528, and 628. During reconstruction, geosynthetics were placed on top of the clay loam subgrade layers in cells 328, 428, 528, and 628 to improve load distribution and separate the clay loam subgrade and the LSSB layers. The placement of the geosynthetics provided important benefits such as improving workability and the rest of the construction was completed without any further problem related to subgrade soil pumping and rutting. As stated previously, the area where cell 728 was located could not be reconstructed due to near-surface utilities, so no geosynthetics were placed there. However, even without placement of any geosynthetics, no observable issue was encountered in cell 728. While no field data was available to make a scientific evaluation of this behavior, it was speculated that the top 1 ft (0.3 m) of the clay loam subgrade layer in cell 728 was not as loose as that of other clay loam subgrade layers underlying 9-in LSSB layers. Therefore, for cell 728, upward movement of the clay loam subgrade soil and downward movement of the LSSB particles were expected to be limited. While another factor could be the effect of the existing underground utilities on the pavement responses with respect to loading, no specific investigation was performed on this matter. Forensic analysis is recommended to better understand the behavior of the 9-in LSSB layers including cell 728.

In fact, it would be highly possible that if no loosening had been applied to the top 1 ft (0.3 m) of the clay loam subgrade layer in the originally constructed test cells (cells 128 and 228), no severe subgrade soil pumping or base/asphalt rutting would have been observed. Since the loosened clay loam subgrade thickness [1 ft (0.3 m)] was thicker than the 9-in LSSB layers, the clay loam subgrade soil could reach up to the top of the 9-in LSSB layers in the originally constructed test

DRAFT

cells (cells 128 and 228). However, since the 18-in LSSB layers were thicker than the loosened clay loam subgrade thickness [1 ft (0.3 m)], no subgrade soil pumping was observed on the surface of the 18-in LSSB layers during construction. On the other hand, it seemed quite possible that the loosened clay loam subgrade soil mixed with the large stones at some degree in 18-in LSSB. The reason why rutting was not observed during construction in the test cells constructed with 18-in LSSB layers (cells 127 and 228) could be the greater structural support provided by 18-in LSSB compared to 9-in LSSB (Tanyu et al. 2003).

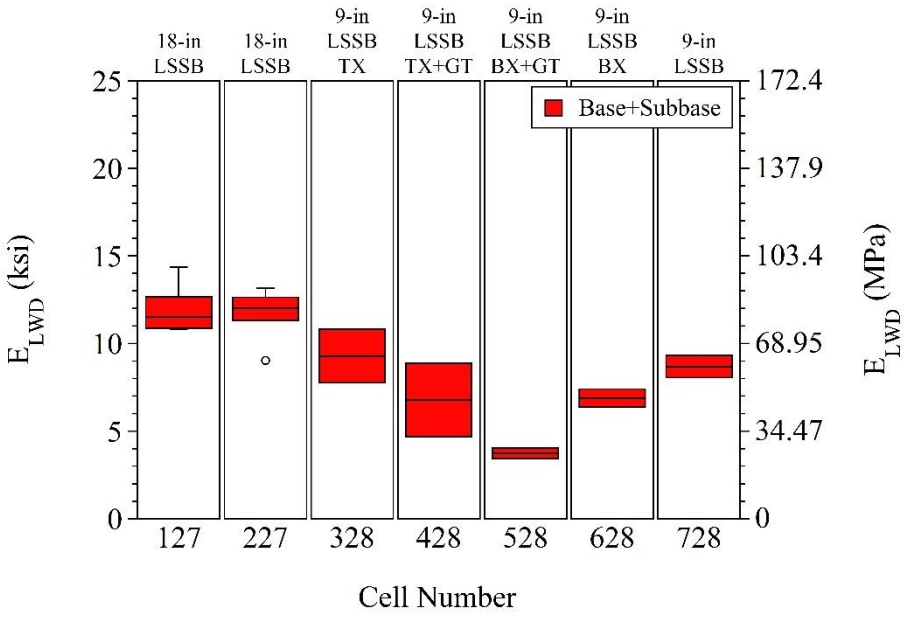


Figure 2.21. Light weight deflectometer elastic modulus (E_{LWD}) of the base+subbase layers in cells 127-728

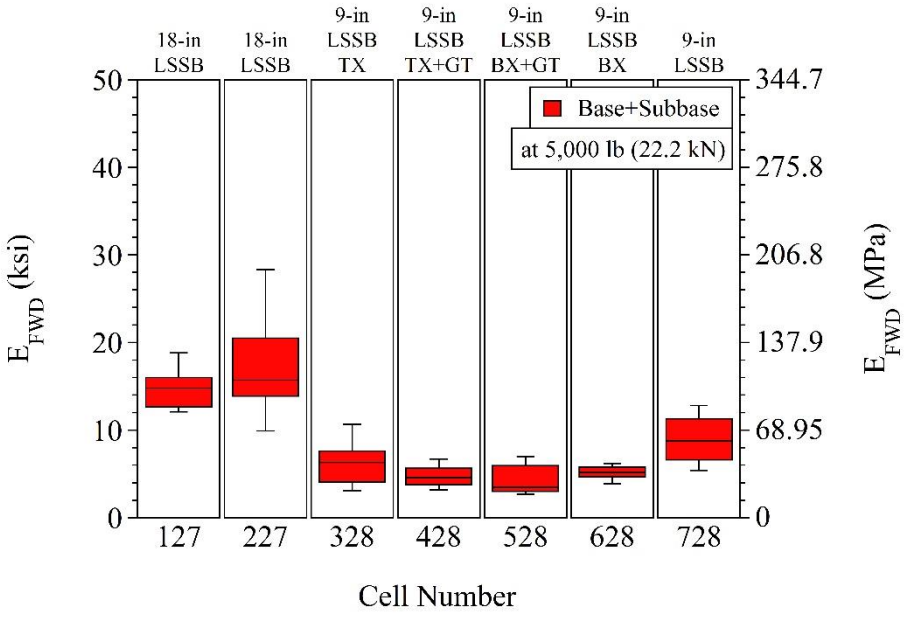


Figure 2.22. Falling weight deflectometer elastic modulus (E_{FWD}) of the base+subbase layers in cells 127-728

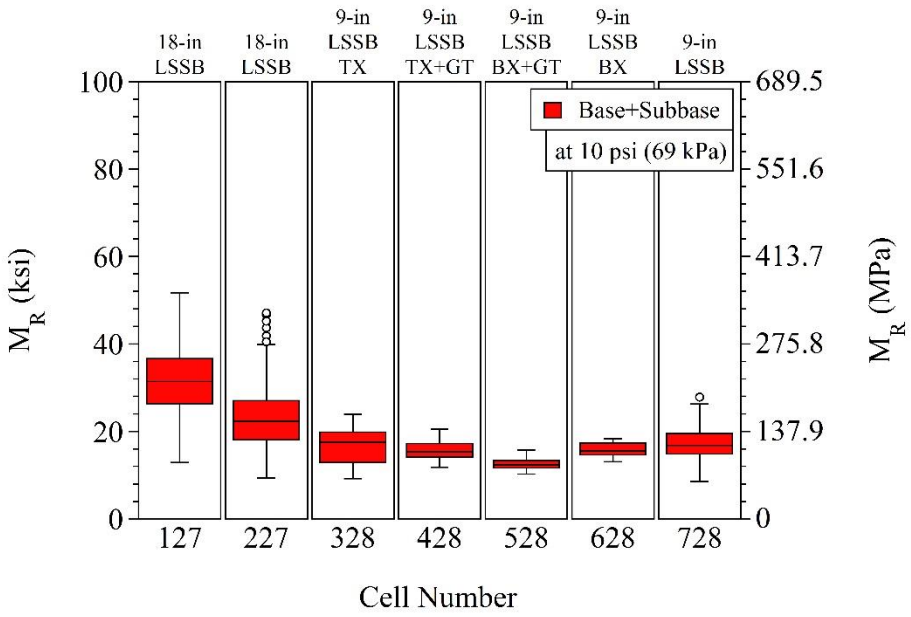


Figure 2.23. Intelligent compaction (IC) resilient modulus (M_R) of the base+subbase layers in cells 127-728

In terms of the long-term base+subbase E_{FWD} values in the inside lanes (main traffic) of the test cells (Figure 2.24) [these values were taken from the Task 5 (performance monitoring and reporting) and Task 6 (instrumentation) report], the base+subbase layers in cells 127 and 227 (6-in class 6 aggregate base + 18-in LSSB layers) exhibited higher stiffness than those in cells 328, 428, 528, 628, and 728 (6-in class 5Q aggregate base + 9-in LSSB layers). This indicated that 18-in LSSB layers should be more preferable than 9-in LSSB layers in pavement foundations systems. Overall, no consistent trend was observed between the relative dry density values of the test cells (Figure 2.19) and their base+subbsae E_{FWD} values (Figure 2.24).

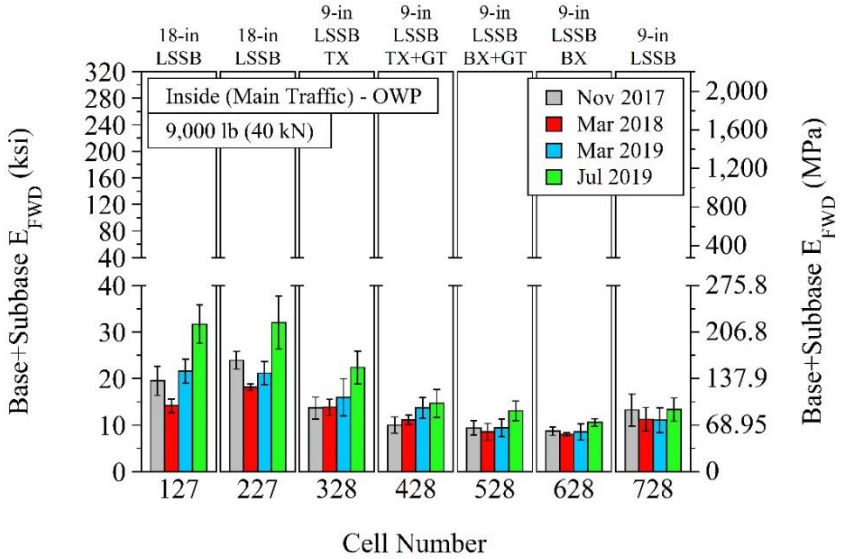


Figure 2.24. Base+subbase E_{FWD} of the cells 127-728 under 9,000 lb (40 kN) load (error bars represent one standard deviation of the data)

In terms of the long-term rutting observed in the inside lanes (main traffic) of the test cells (Figure 2.25) [rutting observations were taken from the Task 5 (performance monitoring and reporting) and Task 6 (instrumentation) report and more information can be found in that report], cells 328 (9-in LSSB – TX), 428 (9-in LSSB – TX+GT), 528 (9-in LSSB – BX+GT), and 628 (9-in LSSB – BX) exhibited greater rutting than the other cells. This was because the 9-in LSSB layers and class 5Q aggregate base layers could not be compacted properly during construction due to the nature of the large stones and lack of structural support provided by 9-in LSSB layers (as a result of inadequate layer thickness). In fact, cells 328 (9-in LSSB – TX) and 628 (9-in LSSB BX) exhibited shallower rut depths than cells 428 (9-in LSSB – TX+GT) and 528 (9-in LSSB – BX+GT). As shown in Figure 2.19, lower in-situ dry density values were observed for the class 5Q aggregate base layers in cells 428 (9-in LSSB – TX+GT) and 528 (9-in LSSB – BX+GT) compared to those observed in cells 328 (9-in LSSB – TX) and 628 (9-in LSSB – BX). Thus, it resulted in higher rutting values for cells 428 (9-in LSSB – TX+GT) and 528 (9-in LSSB – BX+GT) compared to cells 328 (9-in LSSB – TX) and 628 (9-in LSSB – BX). The least rutting was observed in cell 728 (9-in LSSB). It was previously speculated that the top 1 ft (0.3 m) of the clay loam subgrade layer in cell 728 was not as loose as other clay loam subgrade layers underlying 9-in LSSB layers and this could possibly be the reason why the least rutting was observed in cell 728 (9-in LSSB).

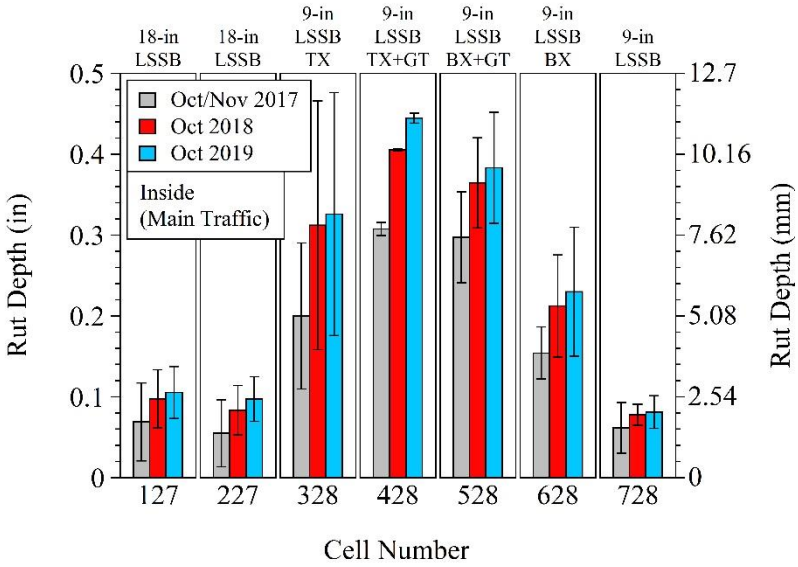


Figure 2.25. Rut depth measurements for cells 127-728 (error bars represent one standard deviation of the data)

International roughness index (IRI) measurements for the inside lane (main traffic) – OWP of the test cells are provided in Figure 2.26 [these measurements were taken from the Task 5 (performance monitoring and reporting) and Task 6 (instrumentation) report and more detailed information can be found in that report]. Cells 628 (9-in LSSB – BX) and 728 (9-in LSSB) exhibited higher IRI values than the other cells. Overall, except for cell 728 (9-in LSSB), all other IRI values were lower than 2.68 m/km (170 in/mile), which indicated that the ride quality was acceptable throughout all the test cells except cell 728 (9-in LSSB) according to the FHWA [detailed information is provided in the Task 5 (performance monitoring and reporting) and Task 6 (instrumentation) report]. For cell 728 (9-in LSSB), while the initial IRI values were lower than

2.68 m/km (170 in/mile) in Oct 2017, the values slightly exceeded that criterion over time, which indicated that the ride quality was unacceptable. No consistent trend was observed between the relative dry density values of the test cells (Figure 2.19) and their long-term IRI values (Figure 2.26).

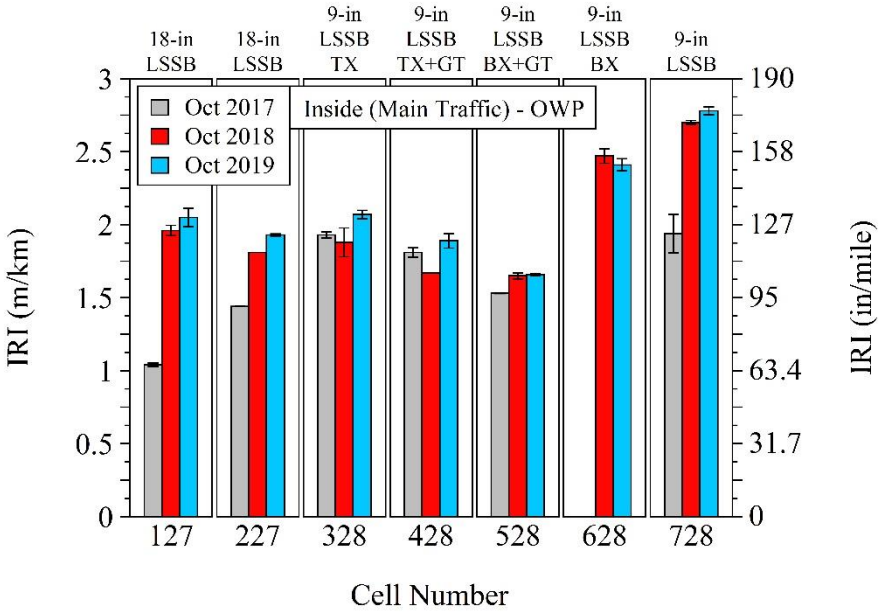


Figure 2.26. International roughness index (IRI) measurements for the inside lane (main traffic) – outer wheel path (OWP)

Figures 2.27 summarizes transverse cracking behavior in the inside lane (main traffic) of the test cells [this information was taken from the Task 5 (performance monitoring and reporting) and Task 6 (instrumentation) report and more detailed information can be found in that report]. Transverse cracking was observed only in cells 227 (18-in LSSB), 328 (9-in LSSB – TX), 528 (9-in LSSB – BX+GT), and 728 (9-in LSSB). While no change was observed in the transverse cracking length in cells 227 (18-in LSSB), 328 (9-in LSSB – TX), and 728 (9-in LSSB) after March/April 2019, the crack length increased in cell 528 (9-in LSSB – BX+GT) after that testing period. While this increasing transverse cracking length in cell 528 (9-in LSSB + BX+GT) could be due to the lower relative dry density values of the cell (Figure 2.19), no consistent trend was observed between these two parameters.

Figure 2.28 summarizes longitudinal cracking behavior in the inside lane (main traffic) of the test cells [this information was taken from the Task 5 (performance monitoring and reporting) and Task 6 (instrumentation) report and more detailed information can be found in that report]. Crack locations were just to the right of the centerline (non-wheel path). Longitudinal cracking was observed only in the inside lane (main traffic) of cells 328 (9-in LSSB – TX), 528 (9-in LSSB – BX+GT), and 728 (9-in LSSB). While the shortest longitudinal cracking (total length) was observed in cells 328 (9-in LSSB – TX), the longest cracking (total length) was observed in cell 528 (9-in LSSB – BX+GT). Although the higher longitudinal cracking length in cell 528 (9-in LSSB – BX+GT) could possibly be due to the lower relative dry density values of the cell (Figure 2.19), no consistent trend was observed between these two parameters.

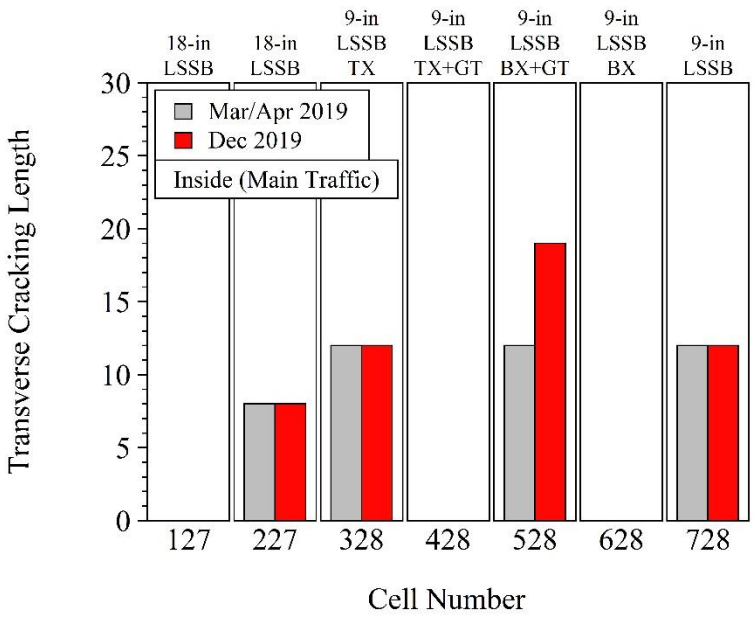


Figure 2.27. Transverse cracking lengths in the inside lane (main traffic) of the test cells (lengths are number of unit squares shown in the distress maps)

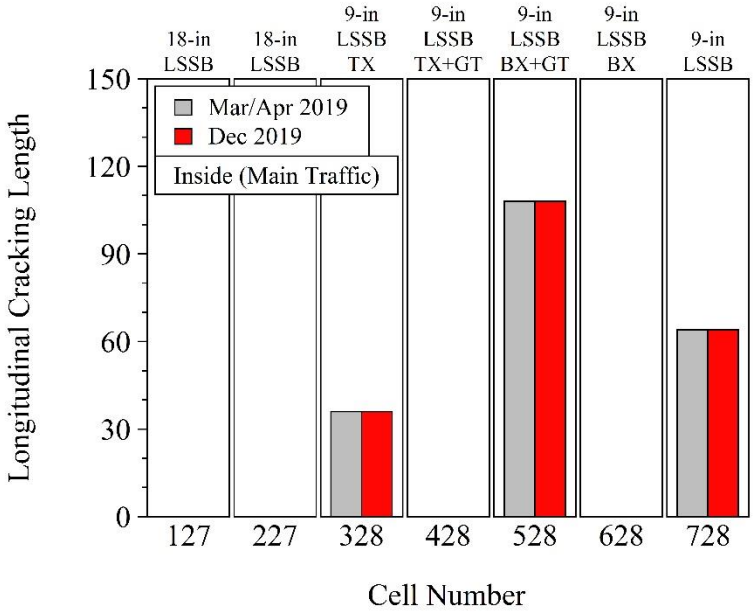


Figure 2.28. Longitudinal cracking lengths in the inside lane (main traffic) of the test cells (lengths are number of unit squares shown in the distress maps)

3. ESTIMATION OF LABORATORY TEST RESULTS

For the estimation of laboratory test results, a forward stepwise regression technique, which is one of the two stepwise regression methods (the other method is known as backward stepwise regression) was used to obtain simple and easily interpretable models (Edil et al. 2012; Bareither et al. 2008). Initially, a significance level of 0.05 [alpha (α) = 0.05 (95% confidence)], was used to determine whether the model was statistically significant. The p-value of each parameter in the model and the significance F value of the whole model must be smaller than 0.05 for statistical significance. However, when no statistically significant model could be determined at $\alpha = 0.05$, the confidence level was reduced to 90% ($\alpha = 0.1$). The statistical significance of the intercept, which was the constant value in the model, was ignored. In addition, all of the statistically significant models were checked for physical significance. In addition, all of the statistically significant models were checked for physical significance. The sample size for all of the regression analyses shown in this section (section 3) was six (each base layer aggregate was one sample) except the analyses performed to estimate resilient modulus (M_R) of the base layer aggregates. For the estimation of the M_R of the base layer aggregates, the sample size was only four since the M_R tests were performed only on coarse RCA, fine RCA, limestone, and RCA+RAP materials.

Forward stepwise regression analyses were performed only for the base layer aggregates in all the test cells (Figure 1.1). These base layer aggregates were coarse RCA, fine RCA, limestone, RCA+RAP, class 6 aggregate, and class 5Q aggregate (Figure 1.2). Detailed information regarding laboratory test results of these aggregates is provided in the Task 4 (laboratory testing) report. In addition, summaries of the laboratory test results of the base layer aggregates that were used in the forward stepwise regression analyses are provided in Appendix D.

3.1. Proctor Compaction Characteristics

For aggregates, determining Proctor compaction characteristics consisted of two stages: (1) conventional Proctor testing [modified Proctor compaction testing was used in this project (ASTM D1557)] and (2) correction of unit weight and water content for soils containing oversize particles (ASTM D4718). The optimum moisture content (OMC) and maximum dry density (MDD) parameters determined only through conventional modified Proctor compaction testing (ASTM D1557) are referred to as "uncorrected OMC" and "uncorrected MDD", respectively, hereinafter. On the other hand, the OMC and MDD parameters determined after applying the correction for oversize particles (ASTM D4718) are referred to as "corrected OMC" and "corrected MDD", respectively, hereinafter.

3.1.1. Uncorrected Optimum Moisture Content (OMC) and Maximum Dry Density (MDD)

Tables 3.1 and 3.2 summarize the most convenient equations that can be used to estimate uncorrected optimum moisture content (OMC) and maximum dry density (MDD) values of the base layer aggregates, respectively. All of the equations listed in Tables 3.1 and 3.2 are statistically significant at $\alpha = 0.05$. Additional equations, which are less convenient than those provided in Tables 3.1 and 3.2 but still can be used, are provided in Appendix E.

DRAFT

Table 3.1. Equations to estimate uncorrected optimum moisture content (OMC) (%)

Equation	R^2	Adj. R^2	Std. Error
0.3740*Fine Absorption (%) - 7.4767*Fine Apparent G_s + 0.4845*C_c + 25.5829	1	1	0.12
-10.1413*Fine SSD G_s - 0.8009*Asphalt Binder Content by Extraction (%) + 34.1067	1	0.99	0.15
-7.8353*Fine OD G_s - 0.0271*Sand (%) + 28.0680	1	0.99	0.17
0.4022*Fine Absorption (%) - 5.8618*Fine Apparent G_s + 21.9079	0.98	0.96	0.38
-7.5866*Fine OD G_s + 26.3385	0.97	0.96	0.39
-10.0533*Fine SSD G_s + 33.3040	0.91	0.89	0.67
0.4404*Fine Absorption (%) + 6.4150	0.86	0.83	0.84
1.9516*Coarse Absorption (%) + 3.0264	0.83	0.79	0.93
0.1411*Residual Mortar Content (%) + 6.1902	0.8	0.75	1.01
-19.1560*Coarse OD G_s + 56.8998	0.78	0.73	1.06
-22.9161*Coarse SSD G_s + 68.0771	0.72	0.65	1.2

G_s = specific gravity; C_c = coefficient of curvature; SSD = saturated-surface-dry; OD = oven-dry

Table 3.2. Equations to estimate uncorrected maximum dry density (MDD) (kN/m^3)

Equation	R^2	Adj. R^2	Std. Error
6.2770*Combined OD G_s - 1.5330*D_{10} (mm) + 5.6493	1	0.99	0.1
-0.3473*Uncorrected OMC (%) + 0.0079*C_u + 22.8208	1	0.99	0.11
8.4437*Combined SSD G_s - 0.2150*D_{30} (mm) - 0.3574	0.99	0.98	0.15
9.5728*Combined SSD G_s - 0.4428*Gravel-to-Sand Ratio - 2.8983	0.99	0.98	0.18
4.5679*Fine OD G_s + 9.9306	0.98	0.97	0.21
-0.2100*Fine Absorption (%) + 5.1046*Fine Apparent G_s + 8.2741	0.98	0.96	0.25
-1.8681*Coarse Absorption (%) + 0.6488*D_{30} (mm) + 25.2969	0.97	0.96	0.25
-0.3256*Fine Absorption (%) - 0.9333*Asphalt Binder Content by Extraction (%) + 23.0652	0.96	0.94	0.31
-0.5755*Uncorrected OMC (%) + 25.5324	0.92	0.90	0.39
12.2566*Coarse OD G_s - 10.2530	0.89	0.86	0.46
-0.0887*Residual Mortar Content (%) + 22.1542	0.88	0.85	0.48
15.0737*Coarse SSD G_s - 18.4532	0.86	0.83	0.51
-1.1371*Coarse Absorption (%) + 23.8381	0.78	0.73	0.64
-0.2432*Fine Absorption (%) + 21.7656	0.73	0.66	0.71

OD = oven-dry; SSD = saturated-surface-dry; G_s = specific gravity; C_u = coefficient of uniformity; OMC = optimum moisture content. To determine the combined G_s values, the weighted average of the G_s values of the coarse [> No. 4 sieve (4.75 mm)] and fine (< No. 4) fractions of the materials were used.

DRAFT

3.1.2. Corrected Optimum Moisture Content (OMC) and Maximum Dry Density (MDD)

Tables 3.3 and 3.4 summarize the most convenient equations that can be used to estimate corrected optimum moisture content (OMC) and maximum dry density (MDD) values of the base layer aggregates, respectively. All of the equations listed in Tables 3.3 and 3.4 are statistically significant at $\alpha = 0.05$. Additional equations, which are not as convenient as those provided in Tables 3.3 and 3.4 but still can be used, are provided in Appendix F.

Table 3.3. Equations to estimate corrected optimum moisture content (OMC) (%)

Equation	R^2	Adj. R^2	Std. Error
0.5026*Combined Absorption (%) - 6.0058*Fine Apparent G_s + 22.0333	0.96	0.94	0.41
-9.1895*Combined OD G_s + 30.5418	0.92	0.91	0.51
-8.1230*Fine SSD G_s + 28.2286	0.89	0.86	0.61
-5.9208*Fine OD G_s + 22.1405	0.88	0.85	0.64
0.5912*Combined Absorption (%) + 5.9768	0.79	0.73	0.85

G_s = specific gravity; OD = oven-dry; SSD = saturated-surface-dry. To determine the combined G_s or absorption values, the weighted average of the G_s or absorption values of the coarse [> No. 4 sieve (4.75 mm)] and fine (< No. 4) fractions of the materials were used.

Table 3.4. Equations to estimate corrected maximum dry density (MDD) (kN/m^3)

Equation	R^2	Adj. R^2	Std. Error
5.4563*Combined OD G_s - 0.4420*Asphalt Binder Content by Ignition (%) + 8.7018	0.99	0.99	0.12
6.4234*Combined OD G_s + 0.0551*D_{60} (mm) + 4.8986	0.99	0.98	0.16
3.2017*Fine OD G_s - 0.7433*Asphalt Binder Content by Ignition (%) + 15.1387	0.99	0.98	0.16
5.6348*Fine SSD G_s + 0.0264*Gravel (%) + 5.7557	0.98	0.96	0.23
4.1482*Fine OD G_s + 0.0345*Gravel (%) + 9.4952	0.98	0.96	0.22
8.5169*Combined SSD G_s - 0.5435	0.96	0.95	0.24
6.4424*Combined OD G_s + 5.2901	0.95	0.94	0.29
-0.6590*Corrected OMC (%) + 26.3182	0.91	0.88	0.39
5.6169*Fine SSD G_s + 7.0948	0.89	0.86	0.43
3.9711*Fine OD G_s + 11.5752	0.83	0.79	0.53
12.4780*Coarse SSD G_s - 11.5034	0.66	0.58	0.74

OD = oven-dry; G_s = specific gravity; SSD = saturated-surface-dry; OMC = optimum moisture content. To determine the combined G_s values, the weighted average of the G_s values of the coarse [> No. 4 sieve (4.75 mm)] and fine (< No. 4) fractions of the materials were used.

3.2. Saturated Hydraulic Conductivity (K_{sat})

Forward stepwise regression analyses were performed only to correlate saturated hydraulic conductivity (K_{sat}) values of the base layer aggregates determined by falling head permeability

DRAFT

testing at 100% degree of compaction (DOC). Table 3.5 summarizes the most convenient equations that can be used to estimate K_{sat} values of the base layer aggregates. All of the equations listed in Table 3.5 are statistically significant at $\alpha = 0.05$. Additional equations, which are not as convenient as those provided in Table 3.5 but still can be used, are provided in Appendix G.

Table 3.5. Equations to estimate saturated hydraulic conductivity (K_{sat}) (cm/sec)

Equation	R^2	Adj. R^2	Std. Error
0.002992*e - 0.000136*Fine Apparent G_s - 0.000222	1	1	7.16E-06
0.002635*e - 2.26E-05*Corrected MDD (kN/m^3) - 1.89E-05	1	1	7.7E-06
0.002534*e + 1.78E-05*Corrected OMC (%) - 0.000611	1	1	8.98E-06
-0.000190*Corrected MDD (kN/m^3) + 0.001358*Combined Apparent G_s + 0.000523	1	0.99	1.25E-05
0.005083*n - 0.000844	0.99	0.99	1.75E-05
0.003073*e - 0.000598	0.99	0.98	1.9E-05
-0.000183*Corrected MDD (kN/m^3) + 0.000933*Fine Apparent G_s + 0.001539	0.98	0.96	2.95E-05
0.016696*e^3/(1+e) - 4.05*E-05	0.96	0.95	3.36E-05
5.52E-05*Combined Absorption (%) - 4.50E-05	0.91	0.89	4.71E-05
7.80E-05*Corrected OMC (%) - 0.000464	0.81	0.76	6.99E-05
-0.000716*Combined OD G_s + 0.001917	0.75	0.68	8.07E-05
2.90E-05*Fine Absorption (%) + 3.46E-05	0.75	0.68	8.1E-05
-0.000106*Corrected MDD (kN/m^3) + 0.002409	0.72	0.65	8.46E-05
-0.0004586*Fine OD G_s + 0.001257	0.71	0.63	8.72E-05
-9.74E-05*Uncorrected MDD (kN/m^3) + 0.002195	0.68	0.6	9.06E-05
5.77E-05*Uncorrected OMC (%) - 0.000309	0.66	0.58	9.33E-05

e = void ratio [based on corrected MDD and apparent specific gravity (G_s)]; n = porosity [n = e/(1+e)]; G_s = specific gravity; MDD = maximum dry density; OMC = optimum moisture content; OD = oven-dry. To determine the combined G_s or absorption values, the weighted average of the G_s or absorption values of the coarse [> No. 4 sieve (4.75 mm)] and fine (< No. 4) fractions of the materials were used.

3.3. Soil-Water Characteristic Curve (SWCC) Parameters

Forward stepwise regression analyses were performed only to correlate soil-water characteristic curve (SWCC) parameters of the base layer aggregates determined by pressure plate and activity meter tests at 100% DOC. As stated in the Task 4 (laboratory testing) report, the van Genuchten model (van Genuchten 1980) [Equation (5)] was used to plot SWCC curves of the base layer aggregates. Among the parameters shown in Equation (5), forward stepwise regression analyses were performed only to estimate the residual VWC (θ_r) and the saturated VWC (θ_s). Forward stepwise regression analyses were also run to estimate air-entry pressure (or bubbling pressure) values required to initiate desaturation of the largest pores in the soils/aggregates (Fredlund and Rahardjo 1993).

DRAFT

$$\Theta = \frac{\theta - \theta_r}{\theta_s - \theta_r} = \left[\frac{1}{1 + (\alpha\psi)^n}\right]^m \quad (5)$$

where Θ is the normalized VWC, θ is the soil VWC, θ_r is the residual VWC, θ_s is the saturated VWC, Ψ is the matric suction (kPa), and α, n, and m are the van Genuchten fitting parameters (van Genuchten 1980).

3.3.1. Residual Volumetric Water Content (VWC) (θ_r)

Table 3.6 shows the only equation that can be used to estimate the θ_r values of the base layer aggregates, and it is statistically significant at $\alpha = 0.1$.

Table 3.6. Equation to estimate residual volumetric water content (VWC) (θ_r)

Equation	R^2	Adj. R^2	Std. Error
#-0.0100*Corrected OMC (%) + 0.1127	0.55	0.44	0.02

OMC = optimum moisture content
#statistically significant at alpha = 0.1

3.3.2. Saturated Volumetric Water Content (VWC) (θ_s)

Table 3.7 shows the equations that can be used to estimate the θ_s values of the base layer aggregates. The equations listed in Table 3.7 are statistically significant at $\alpha = 0.05$.

Table 3.7. Equations to estimate saturated volumetric water content (VWC) (θ_s)

Equation	R^2	Adj. R^2	Std. Error
-0.1382*Combined OD Gs + 0.0213*C_c + 0.5672	0.91	0.85	0.01
0.0271*Coarse Absorption (%) + 0.1845	0.9	0.88	0.01
0.0018*Residual Mortar Content (%) + 0.2315	0.77	0.71	0.01
0.0116*Uncorrected OMC (%) + 0.1647	0.76	0.7	0.01
-0.0188*Uncorrected MDD (kN/m^3) + 0.6526	0.72	0.65	0.02
-0.2413*Coarse OD Gs + 0.8718	0.7	0.62	0.02
-0.0848*Fine OD Gs + 0.4632	0.68	0.6	0.02

OD = oven-dry; G_s = specific gravity; C_c = coefficient of curvature; OMC = optimum moisture content; MDD = maximum dry density. To determine the combined G_s values, the weighted average of the G_s values of the coarse [> No. 4 sieve (4.75 mm)] and fine (< No. 4) fractions of the materials were used.

3.3.3. Air-Entry Pressure

Table 3.8 shows the equations that can be used to estimate the air-entry pressure values of the base layer aggregates. The equations listed in Table 3.8 are statistically significant at $\alpha = 0.05$. However, further evaluation would be required to check the physical significance of the equations shown in Table 3.8.

DRAFT

Table 3.8. Equations to estimate the air-entry pressure (kPa)

Equation	R^2	Adj. R^2	Std. Error
48.5469*e - 2.2888*Coarse Absorption (%) - 0.1958*Fines (%) - 1.2909	1	0.99	0.15
78.8067*n - 1.4732*Coarse Absorption (%) - 9.0649	0.97	0.94	0.38
46.0499*e - 1.3624*Coarse Absorption (%) - 5.1737	0.96	0.93	0.41
31.5864*e - 0.6861*D_{30} (mm) - 4.7364	0.93	0.89	0.53
52.2180*n - 0.7107*D_{30} (mm) - 7.2297	0.93	0.88	0.56

e = void ratio [based on corrected MDD and apparent specific gravity (G_s)]; n = porosity [n = e/(1+e)]

3.4. Resilient Modulus (M_R) Characteristics

Laboratory resilient modulus (M_R) tests were performed on coarse RCA, fine RCA, limestone, RCA+RAP, sand subgrade, and clay loam subgrade materials per AASHTO T 307 by the University of Texas at El Paso (UTEP). Since no information regarding resilient modulus (M_R) testing for the base layer aggregates was given in the Task 4 (laboratory testing) report, the test methodology used for the base layer aggregates will be explained in the following. Nazarian et al. (2020) provides more information regarding M_R testing for sand subgrade and clay loam subgrade.

The base layer aggregates were air-dried, and aggregations were broken up rigorously to preserve the natural size of the aggregate particles. Since the aggregates were classified as Type I (AASHTO T 307), 152 mm by 305 mm cylindrical specimens were prepared. Variation in compaction moisture content affects the degree of saturation (DOS) of aggregates and changes pore water pressure or matric suction in the aggregates (Dawson et al. 2000). Such changes in aggregates affect their M_R significantly (Edil et al. 2012). To determine the relationship between the moisture content (or matric suction) and M_R values, the aggregates were compacted with modified Proctor effort at different moisture contents (dry side of OMC, OMC, and wet side of OMC) in six lifts of equal mass with a 4.5-kg impact hammer. Duplicate specimens were prepared for each compaction moisture content and mellowed for 24 hours prior to testing. Elastic deformations, recorded during the last five cycles of each loading sequence, were considered and the model introduced by Ooi et al. (2004) was used to determine the M_R. The model introduced by Ooi et al. (2004) is known as the modified MEPDG model [Equation (6)]. Most of the highway agencies use the conventional MEPDG model [Equation (7)]. To convert the modified MEPDG model [Equation (6)] into the conventional MEPDG model [Equation (7)], the modified fitting parameters (k_1', k_2', and k_3') [Equation (6)] were converted into the conventional fitting parameters (k_1, k_2, and k_3) [Equation (7)] (Nazarian et al. 2015). Conversions of the fitting parameters are shown in Equations (8), (9), and (10) for $k_1' \rightarrow k_1$, $k_2' \rightarrow k_2$, and $k_3' \rightarrow k_3$, respectively.

$$M_R' = k_1' P_a \left(\frac{\theta}{P_a} + 1\right)^{k_2'} \left(\frac{\tau_{oct}}{P_a} + 1\right)^{k_3'} \quad (6)$$

$$M_R = k_1 P_a \left(\frac{\theta}{P_a}\right)^{k_2} \left(\frac{\tau_{oct}}{P_a} + 1\right)^{k_3} \quad (7)$$

DRAFT

where P_a is the atmospheric pressure, θ is the bulk stress ($\theta = \sigma_1 + \sigma_2 + \sigma_3 = \sigma_1 + 2\sigma_3 = \sigma_d + 3\sigma_3$), σ_1, σ_2, and σ_3 are the principal stresses, σ_d is the deviator stress ($\sigma_d = \sigma_1 - \sigma_3$), τ_{oct} is the octahedral shear stress [$\tau_{oct} = 1/3\sqrt{(\sigma_1 - \sigma_2)^2 + (\sigma_1 - \sigma_3)^2 + (\sigma_2 - \sigma_3)^2} = (\sqrt{2}/3)\sigma_d$], and k_1', k_2', k_3' are modified fitting parameters, and k_1, k_2, and k_3 are the conventional fitting parameters.

$$k_1' = k_1 e^{-1.32k_2} \quad (8)$$

$$k_2' = 1.88k_2 \quad (9)$$

$$k_3' = k_3 \quad (10)$$

where k_1', k_2', k_3' are modified fitting parameters, and k_1, k_2, k_3 are the conventional fitting parameters.

NCHRP 1-28A suggests that an M_R at θ = 214 kPa (31 psi) and τ_{oct} = 52 kPa (7.5 psi) can be considered to be a summary M_R (SM_R) for base layer aggregates (Mazari et al. 2014; Nazarian et al. 2015). Figures 3.1, 3.2, 3.3, and 3.4 summarize the SM_R values at various moisture content values for coarse RCA, fine RCA, limestone, and RCA+RAP, respectively. In these figures, linear trendlines were added to show SM_R as a function of moisture content. More figures showing exponential, logarithmic, and power relationships between SM_R and moisture content are provided in Appendix H. Appendices I and J contain more figures showing SM_R vs. degree of saturation (DOS) and SM_R vs. VWC, respectively. Overall, it was concluded that increasing the moisture content, DOS, or VWC yielded lower M_R values. It was also concluded that this result was in agreement with findings in the literature.

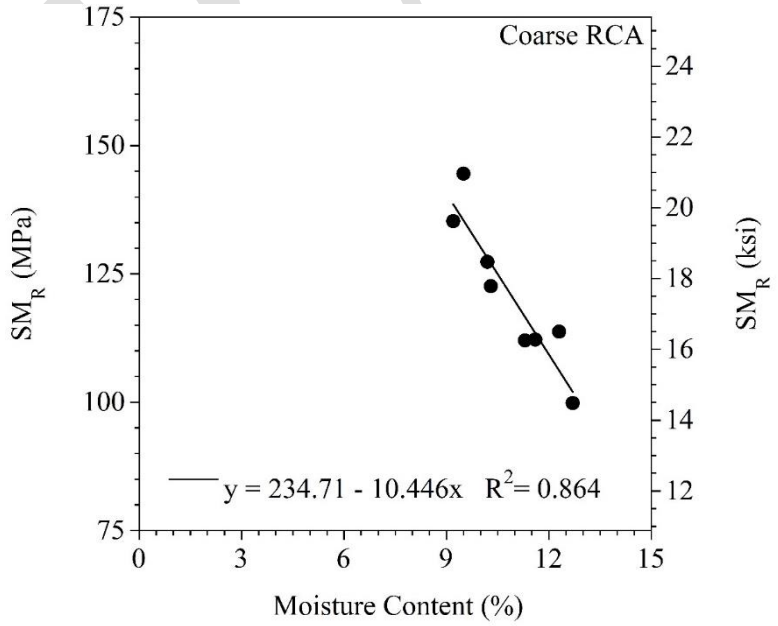


Figure 3.1. Summary resilient modulus (SM_R) values at different moisture contents for coarse RCA

DRAFT

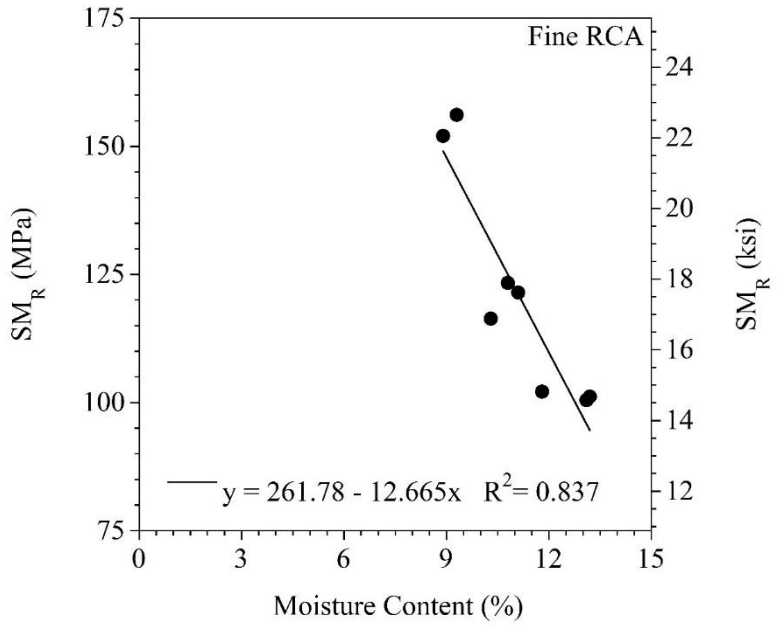


Figure 3.2. Summary resilient modulus (SM_R) values at different moisture contents for fine RCA

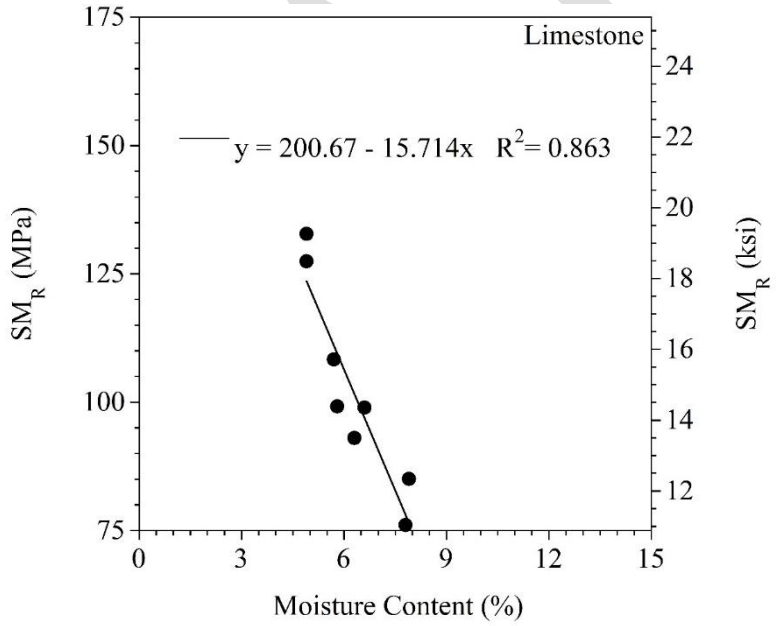


Figure 3.3. Summary resilient modulus (SM_R) values at different moisture contents for limestone

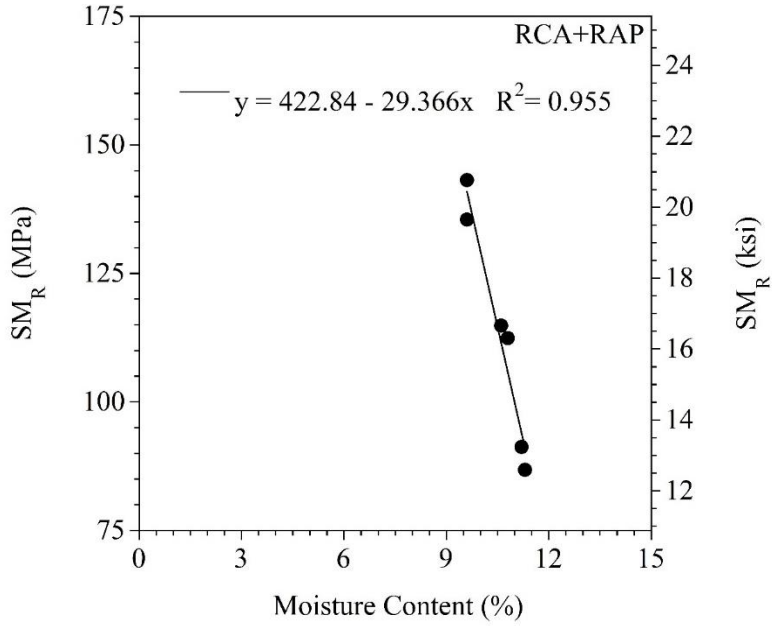


Figure 3.4. Summary resilient modulus (SM_R) values at different moisture contents for RCA+RAP

Soil suction is composed of osmotic suction and matric suction (Mehrotra 2014). Khoury et al. (2004) stated that changes in M_R of unsaturated soils/aggregates were mostly affected by changes in matric suction. Previous studies have indicated that M_R was better correlated to matric suction than to moisture content (Edil et al. 2012; Ba et al. 2013; Nokkaew 2014; Mehrotra 2014; Nazarian et al. 2015; Banerjee et al. 2020; Chu 2020). In a soil/aggregate matrix, matric suction affects the stress existing in the soil/aggregate particle with pore water pressure (Ba et al. 2013; Nokkaew 2014; Chu 2020). In addition, a force that reinforces the particle bonding is generated by matric suction (Chu 2020). Overall, soil/aggregate M_R is expected to increase when the matric suction in soil/aggregate matrix increases (Edil et al. 2012; Mehrotra 2014).

The effect of matric suction on M_R of unsaturated soils/aggregates depends on the air-entry pressure. In a study performed by Banerjee et al. (2020), for ML and CH soils (ASTM D2487), while considerable increases in the M_R values were observed at matric suctions higher than air-entry pressures of the soils, no significant changes in the M_R values were observed at matric suctions lower than the air-entry pressures of the soils.

In this study, an effort was made to compare the SM_R values determined for coarse RCA, fine RCA, limestone, and RCA+RAP with the matric suction values, determined from the SWCC properties of these materials [detailed information regarding the SWCC of these aggregates is provided in the Task 4 (laboratory testing) report]. Figures 3.5, 3.6, 3.7, and 3.8 show the relationships between the SM_R and matric suction for coarse RCA, fine RCA, limestone, and RCA+RAP, respectively. In these figures, logarithmic trendlines were added to show SM_R as a function of matric suction. In addition, air-entry pressure values, determined from the SWCC properties of the aggregates, were also added to these figures. More figures showing linear, exponential, and power relationships between SM_R and matric suction are provided in Appendix K. Unlike in the study performed by Banerjee et al. (2020), all the matric suction values were higher than the air-entry pressures of the base layer aggregates, i.e., no M_R data presented at matric

suctions lower than the air-entry pressures of the base layer aggregates. Since all the matric suction values were higher than the air-entry pressures of the base layer aggregates, higher SM_R values were observed at higher matric suctions (Banerjee et al. 2020).

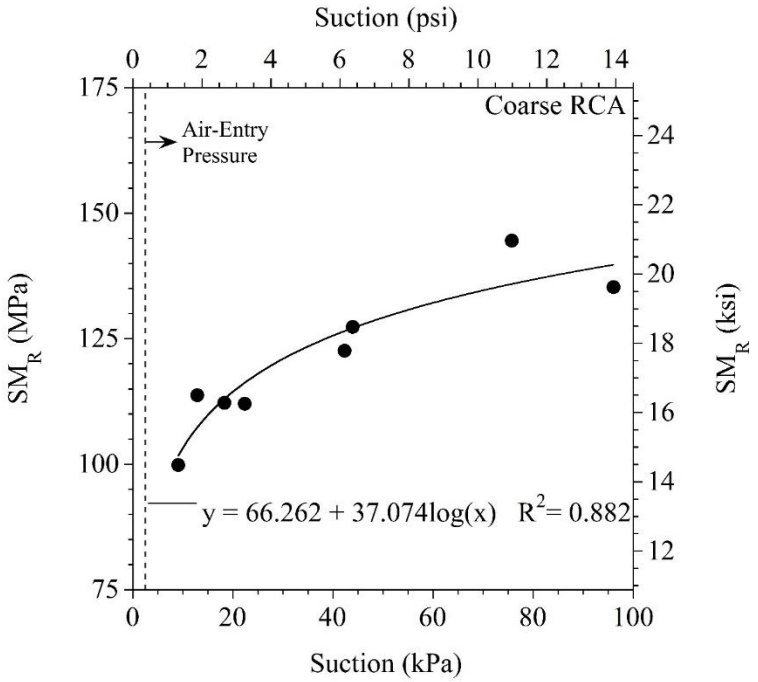


Figure 3.5. Summary resilient modulus (SM_R) at different matric suctions for coarse RCA

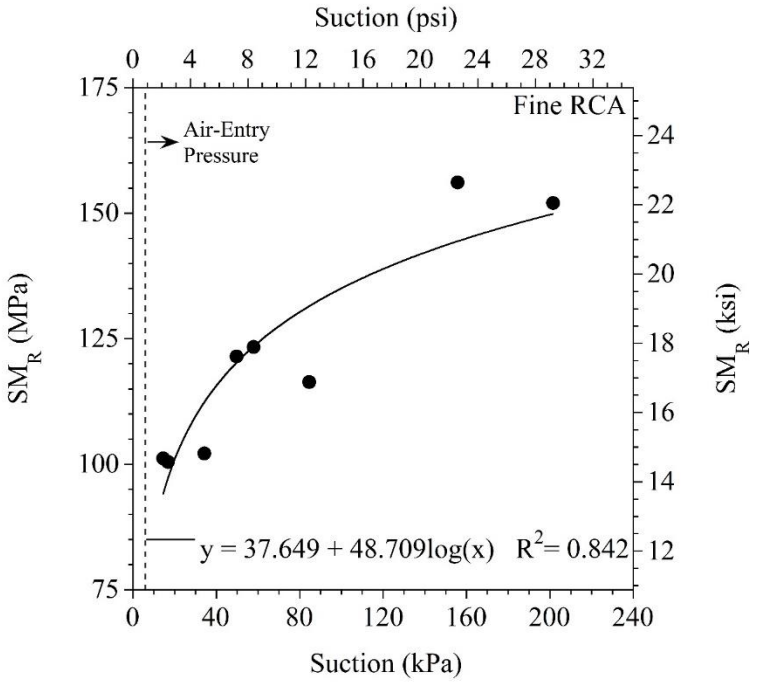


Figure 3.6. Summary resilient modulus (SM_R) at different matric suctions for fine RCA

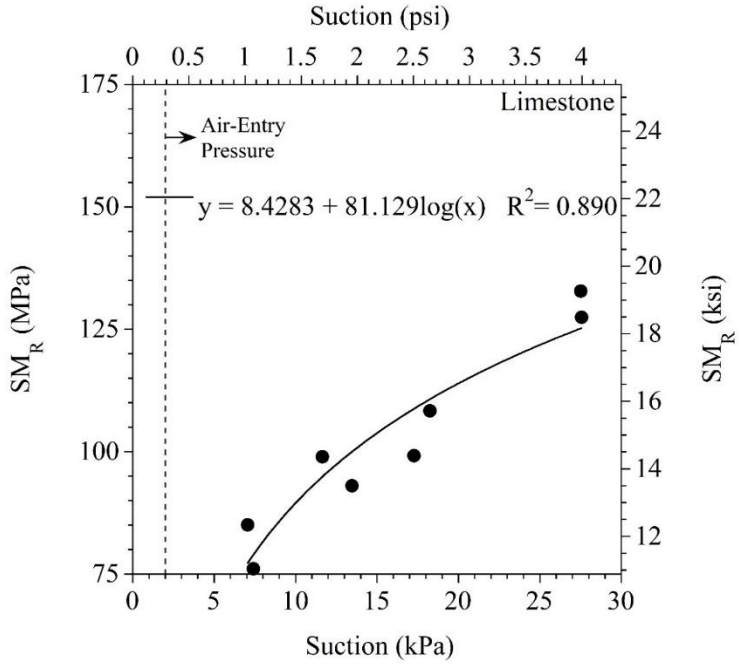


Figure 3.7. Summary resilient modulus (SM_R) at different matric suctions for limestone

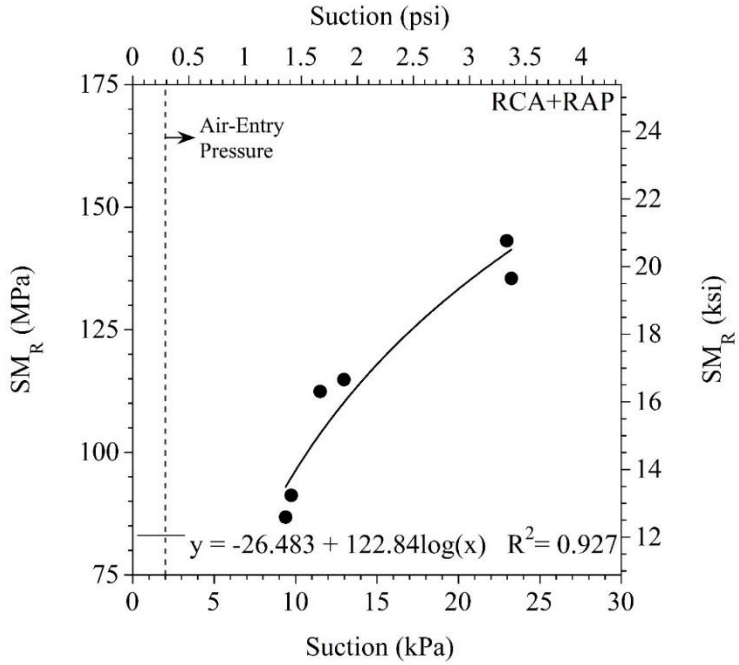


Figure 3.8. Summary resilient modulus (SM_R) at different matric suctions for RCA+RAP

3.4.1. Summary Resilient Modulus (SM_R)

Table 3.9 summarizes the most convenient equations that can be used to estimate SM_R at optimum moisture content (OMC). All of the equations listed in Table 3.9 are statistically significant at $\alpha = 0.05$. More equations, which are not as convenient as those provided in Table 3.9 but still can be used, are provided in Appendix L.

Table 3.9. Equations to estimate summary resilient modulus (SM_R) (MPa) at optimum moisture content (OMC)

Equation	R^2	Adj. R^2	Std. Error
0.9121*Residual Mortar Content (%) + 95.0309	1	1	0.51
13.9035*Coarse Absorption (%) + 69.9919	0.99	0.99	1.32
5.4794*Uncorrected OMC (%) + 61.4114	0.98	0.97	2.19
-39.5364*Fine OD G_s + 201.5303	0.97	0.95	2.8
-118.4860*Coarse OD G_s + 409.3854	0.95	0.92	3.73
-8.4659*Uncorrected MDD (kN/m^3) + 284.6113	0.94	0.91	3.89
-143.1262*Coarse SSD G_s + 482.0049	0.92	0.88	4.61
2.4855*Fine Absorption (%) + 95.5617	0.92	0.88	4.62

OMC = optimum moisture content; OD = oven-dry; SSD = saturated-surface-dry; G_s = specific gravity; MDD = maximum dry density

3.4.2. MEPDG Constitutive Model Coefficients (k_1, k_2, and k_3)

Tables 3.10, 3.11, and 3.12 summarize the equations that can be used to estimate k_1, k_2, and k_3 conventional fitting parameters [Equation (7)]. All of the equations listed in Tables 3.10, 3.11, and 3.12 are statistically significant at $\alpha = 0.05$.

Table 3.10. Equations to estimate k_1 conventional fitting parameter

Equation	R^2	Adj. R^2	Std. Error
11.6644*Fine Absorption (%) + 16.1631*D_{30} (mm) + 731.5558	1	1	0.73
83.7374*Coarse Absorption (%) + 153.4469*Fine Apparent G_s + 173.1523	1	1	0.26
13.4873*Fine Absorption (%) + 738.4029	0.96	0.94	16.51
70.6962*Coarse Absorption (%) + 614.7812	0.92	0.87	24.80

G_s = specific gravity

Table 3.11. Equations to estimate k_2 conventional fitting parameter

Equation	R^2	Adj. R^2	Std. Error
-0.5822*Combined Apparent G_s - 0.0136*Corrected MDD (kN/m^3) + 2.250	1	1	0
-0.5946*Combined Apparent G_s + 0.0092*Corrected OMC (%) + 1.9211	1	1	0
-0.4716*Fine Apparent G_s + 0.0061*Combined Absorption (%) + 1.6280	1	1	0
-0.7294*Combined Apparent G_s + 2.3626	0.98	0.97	0.01
-0.5161*Fine Apparent G_s + 1.7773	0.96	0.93	0.02

G_s = specific gravity; MDD = maximum dry density; OMC = optimum moisture content. To determine the combined G_s or absorption values, the weighted average of the G_s or absorption values of the coarse [> No. 4 sieve (4.75 mm)] and fine (< No. 4) fractions of the materials were used.

DRAFT

Table 3.12. Equations to estimate k_3 conventional fitting parameter

Equation	R^2	Adj. R^2	Std. Error
0.2190*Fine Apparent G_s + 0.0048*Combined Absorption (%) - 0.6708	1	1	0
0.5910*Fine Apparent G_s + 0.7889*k_2 - 1.9552	1	1	0

G_s = specific gravity; k_2 = conventional fitting parameter. To determine the combined absorption values, the weighted average of the absorption values of the coarse [> No. 4 sieve (4.75 mm)] and fine (< No. 4) fractions of the materials were used.

3.5. Aggregate Abrasion Characteristics

To evaluate degradation during compaction, breakage potential (B_p), total breakage (B_t), and relative breakage (B_r) parameters, as described by Hardin (1985), were used in the Task 4 (laboratory testing) report. B_p is defined as the area between the initial gradation curve (before compaction) and the line defining the upper limit of silt size (0.075 mm) (Hardin 1985). B_t is defined as the area between initial (before compaction) and final (after compaction) gradation curves (Hardin 1985). B_p and B_t are relative areas compared to the unit area, which is the area of one log cycle (Hardin 1985). B_r is the ratio between the B_t and B_p.

According to Hardin (1985), the larger the particle size, the higher the B_p value. Based on the test results provided in the Task 4 (laboratory testing) report, coarse RCA and class 5Q aggregate exhibited higher B_p than other materials due to their gradation characteristics. In fact, the highest B_p was observed with class 5Q aggregate, which was the coarsest aggregate. According to these results, coarse RCA and class 5Q aggregate would be expected to exhibit higher B_t than other materials because less stress is required to break up larger particles compared to finer particles (Hardin 1985).

In the literature, it is stated that an increase in the residual mortar content can yield an increase in aggregate degradation through crushing and degradation of porous mortar (de Juan and Gutiérrez 2009; Butler et al. 2011; Bhasya and Bharatkumar 2018). Therefore, coarse RCA and class 5Q aggregate exhibited higher B_t because of not only their coarser gradations but also their high residual mortar content. Since both coarse RCA and class 5Q aggregates may have gravel size cemented aggregates that could instantly break down under compaction pressure, these two aggregates exhibited higher B_t values. These two aggregates also exhibited higher B_r values than other aggregates.

In this study, an effort was made to model abrasion characteristics of the base layer aggregates. To do so, B_r values of the base layer aggregates were considered. Tables 3.13, 3.14, and 3.15 summarize the equations that can be used to estimate B_r after 100, 300, and 500 gyrations. All of the equations listed in Table 3.13, 3.14, and 3.15 are statistically significant at $\alpha = 0.1$.

DRAFT

Table 3.13. Equations to estimate relative breakage (B_r) after 100 gyrations

Equation	R^2	Adj. R^2	Std. Error
-0.0702*Coarse OD G_s + 0.0048*$PLR_{0.5}$ (%) + 0.1524	0.98	0.96	0
-0.1056*Coarse OD G_s - 0.6655*Median Roundness + 0.7250	0.97	0.96	0
0.0005*Residual Mortar Content (%) + 0.0042*$PLR_{0.5}$ (%) - 0.0281	0.96	0.94	0
-0.1052*Coarse OD G_s + 0.0022*$PLR_{0.7}$ (%) + 0.1451	0.95	0.91	0
#0.0007*Residual Mortar Content (%) - 0.5216*Median Roundness + 0.3519	0.94	0.9	0
0.0008*Residual Mortar Content (%) + 0.0096	0.76	0.7	0.01
-0.0986*Coarse OD G_s + 0.2713	0.69	0.61	0.01
0.0067*$PLR_{0.5}$ (%) - 0.0407	0.69	0.61	0.01

OD = oven-dry; G_s = specific gravity; $PLR_{0.5}$ = percent less rounded than 0.5; $PLR_{0.7}$ = percent less rounded than 0.7 (the definitions of $PLR_{0.5}$, $PLR_{0.7}$, and median roundness are provided in Figure 3.9). For the distribution shown in Figure 3.9, the number of particles was considered instead of the volume of particles. If the volume of particles was considered, particle size would affect the particle shape distributions. To avoid this, the number of particles was used in order to evaluate the distributions. More detailed information can be found in the Task 4 (laboratory testing) report.

#statistically significant at alpha = 0.1

Table 3.14. Equations to estimate relative breakage (B_r) after 300 gyrations

Equation	R^2	Adj. R^2	Std. Error
-0.1327*Coarse OD G_s - 1.1803*Median Roundness + 1.1357	1	0.99	0
-0.1324*Coarse OD G_s + 0.0040*$PLR_{0.7}$ (%) + 0.0992	0.99	0.98	0
0.0009*Residual Mortar Content (%) - 0.9992*Median Roundness + 0.6665	0.98	0.97	0
0.0009*Residual Mortar Content (%) + 0.0033*$PLR_{0.7}$ (%) - 0.2066	0.96	0.94	0
#0.0006*Residual Mortar Content (%) + 0.0066*$PLR_{0.5}$ (%) - 0.0485	0.9	0.84	0.01
0.0095*$PLR_{0.5}$ (%) - 0.0630	0.71	0.64	0.01
#0.0010*Residual Mortar Content (%) + 0.0109	0.64	0.55	0.01
#-0.1203*Coarse OD G_s + 0.3312	0.53	0.42	0.01

OD = oven-dry; G_s = specific gravity; $PLR_{0.5}$ = percent less rounded than 0.5; $PLR_{0.7}$ = percent less rounded than 0.7 (the definitions of $PLR_{0.5}$, $PLR_{0.7}$, and median roundness are provided in Figure 3.9). For the distribution shown in Figure 3.9, the number of particles was considered instead of the volume of particles. If the volume of particles was considered, particle size would affect the particle shape distributions. To avoid this, the number of particles was used in order to evaluate the distributions. More detailed information can be found in the Task 4 (laboratory testing) report.

#statistically significant at alpha = 0.1

DRAFT

Table 3.15. Equations to estimate relative breakage (B_r) after 500 gyrations

Equation	R^2	Adj. R^2	Std. Error
0.0009*Residual Mortar Content (%) + 0.0083*$PLR_{0.5}$ (%) - 0.0601	0.94	0.91	0.01
0.0014*Residual Mortar Content (%) - 1.0793*Median Roundness + 0.7221	0.94	0.9	0.01
#0.0014*Residual Mortar Content (%) + 0.0035*$PLR_{0.7}$ (%) - 0.2165	0.92	0.86	0.01
#-0.1121*Coarse OD G_s + 0.0096*$PLR_{0.5}$ (%) + 0.2258	0.9	0.84	0.01
#-0.1836*Coarse OD G_s - 1.3319*Median Roundness + 1.3744	0.89	0.82	0.01
#-0.1832*Coarse OD G_s + 0.0044*$PLR_{0.7}$ (%) + 0.2075	0.88	0.8	0.01
0.0014*Residual Mortar Content (%) + 0.0139	0.73	0.66	0.01
0.0128*$PLR_{0.5}$ (%) - 0.0827	0.69	0.62	0.01
#-0.1697*Coarse OD G_s + 0.4665	0.57	0.47	0.02

OD = oven-dry; G_s = specific gravity; $PLR_{0.5}$ = percent less rounded than 0.5; $PLR_{0.7}$ = percent less rounded than 0.7 (the definitions of $PLR_{0.5}$, $PLR_{0.7}$, and median roundness are provided in Figure 3.9). For the distribution shown in Figure 3.9, the number of particles was considered instead of the volume of particles. If the volume of particles was considered, particle size would affect the particle shape distributions. To avoid this, the number of particles was used in order to evaluate the distributions. More detailed information can be found in the Task 4 (laboratory testing) report.

#statistically significant at alpha = 0.1

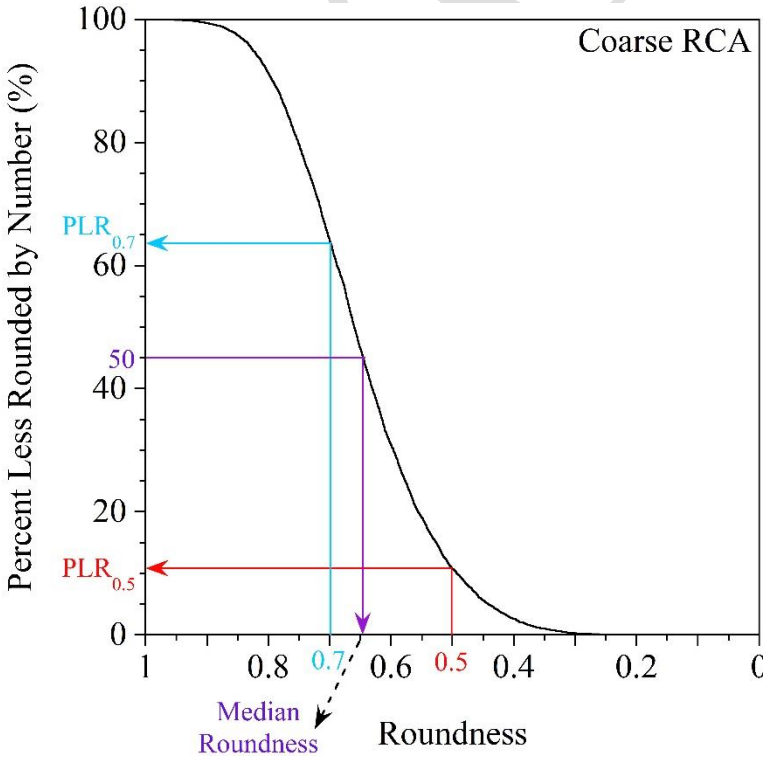


Figure 3.9. Definitions of $PLR_{0.5}$, $PLR_{0.7}$, and median roundness parameters

DRAFT

3.6. Reassessment of the Models Provided in Edil et al. (2012) for More General Equations

Edil et al. (2012) conducted a study on recycled aggregates that were collected from different sources throughout the US. Thus, it was considered that it would be useful to retrieve the data and analysis results provided in Edil et al. (2012) and evaluate whether they can be combined together to expand the database for recycled aggregate materials. The laboratory test results that are summarized in Appendix D [also reported in the Task 4 (laboratory testing) report in detail] and the laboratory test results from Edil et al. (2012) in Appendix M were combined to obtain more general equations to predict engineering properties of these materials by considering simple index properties. The test methods were first compared to see whether they were similar, and after the comparisons forward stepwise regression analyses were run to obtain more general equations to estimate the uncorrected OMC and MDD values of the materials. However, no satisfactory equations were determined because some of the laboratory data [coarse & fine oven-dry (OD) specific gravity (G_s), coarse & fine saturated-surface-dry (SSD) G_s, coarse apparent G_s, fine absorption, and combined absorption values of the aggregates] were not available in Edil et al. (2012). In Edil et al. (2012), the G_s of aggregates were determined by ASTM D854, which can only give fine apparent G_s. However, in this study, ASTM C127 and C128 were followed to obtain oven-dry (OD), saturated-surface-dry (SSD), apparent, and combined G_s values for both coarse and fine fractions of the aggregates. In addition, in this study, coarse, fine, and combined absorption values of the aggregates were reported (ASTM C127 and C128) while only the coarse absorption (ASTM C127) was reported in Edil et al. (2012). Lastly, in this study, a method developed by Abbas et al. (2008) was used to determine the residual mortar content of the aggregates (the method is defined as the combination of freeze-thaw testing and aggregate soundness testing by using a saturated sodium sulfate solution). In Abbas et al. (2008), for each aggregate, 2000 g of the particles retained on a 1-in sieve (if any), 2000 g of the particles retained on a 3/4-in sieve (if any), 1000 g of the particles retained on a 3/8-in sieve, and 1000 g of the particles retained on a No. 4 sieve were collected. This method gave the opportunity to consider a wide range of gravel fractions to determine residual mortar content. However, in Edil et al. (2012), a method described in Nokkaew (2014) was used to determine mortar contents of RCA materials by immersing 500 g of specimen in a 10% HCl solution for 24 h. The specimens were then sieved through a 5-mm sieve and aggregate weight loss was calculated (Gokce 2001; Nokkaew 2014). Due to the smaller specimen size in the method described in Nokkaew (2014), the mortar content values reported in Edil et al. (2012) may not be as representative as the residual mortar content values reported in this study. However, since no direct comparisons between the two test methods to determine the residual mortar content of RCA materials was made in this study, the previous statement was left as speculation.

The M_R test results reported in this study and in Edil et al. (2012) could not be combined for further analysis. While NCHRP 1-28A was followed for the test specimens compacted at 95% MDD in Edil et al. (2012), AASHTO T 307 was used for the test specimens compacted at 100% MDD in this study. In addition, while the NCHRP model (NCHRP 2004) was used in Edil et al. (2012), the modified MEPDG method (Ooi et al. 2004) [Equation (6)] was used in this study to analyze the test data. As stated by Mazari et al. (2014) and Nazarian et al. (2015), since these test methods differed in loading time, stress sequence, and type and location of the linear variable displacement transducers (LVDT), different M_R values were obtained by these two test methods (Mazari et al. 2014), and therefore, their results could not be combined.

DRAFT

In addition to the equations provided in this section, uncorrected OMC, uncorrected MDD, and SM_R [expressed as SRM in Edil et al. (2012)] models provided in Edil et al. (2012) were reassessed. However, those assessments were not included in the main context of this study but reported in Appendix M. Additionally, the revised correlations generated using the data provided by Edil et al. (2012) are also provided in Appendix M.

4. ESTIMATION OF FIELD TEST RESULTS DURING CONSTRUCTION

Forward stepwise regression technique was also used to obtain simple and easily interpretable models for the estimation of field test results collected during construction (Bareither et al. 2008; Edil et al. 2012). The median values [the middle value in a sorted (ascending or descending) list of values] of the test results (obtained from NDG, DCP, LWD, FWD, and IC testing) provided in Task 3 (construction monitoring and reporting) were used in the regression analyses. The sample size for all of the regression analyses shown in this section (section 4) was eleven (there were eleven test cells). Initially, a significance level of 0.05 [alpha (α) = 0.05 (95% confidence)], was used to determine whether the model was statistically significant. The p-value of each parameter in the model and the significance F value of the whole model must be smaller than 0.05 for statistical significance. However, when no statistically significant model could be determined at α = 0.05, the confidence level was reduced to 90% (α = 0.1). The statistical significance of the intercept, which was the constant value in the model, was ignored. In addition, all of the statistically significant models were checked for physical significance.

Forward stepwise regression analyses were only performed for the base or base+subbase layers in all the test cells (Figure 1.1). Detailed information regarding the laboratory test results of all the research materials (Figure 1.2) is provided in the Task 4 (laboratory testing) report (Appendix D also contains information about the summaries of the laboratory test results for the base layer aggregates). Summaries of the field test results that were used in the forward stepwise regression analyses are provided in Appendix N. Detailed information regarding the field tests performed during construction and their results is provided in the Task 3 (construction monitoring and reporting) report.

4.1. Dynamic Cone Penetration (DCP) Parameters

4.1.1. Dynamic Cone Penetration Index (DCPI)

Table 4.1 summarizes the equations that can be used to estimate the dynamic cone penetration index (DCPI) values of the constructed test cells. All of the equations listed in Table 4.1 are statistically significant at α = 0.05.

DRAFT

Table 4.1. Equations to estimate dynamic cone penetration index (DCPI) (mm/blow)

Equation	R^2	Adj. R^2	Std. Error
-1.6462*Median NDG Dry Density (kN/m^3) + 11.3118*Combined OD G_s + 13.2990	0.63	0.54	0.91
-0.2650*Median Relative MDD (%) + 33.2674	0.56	0.51	0.94

NDG = nuclear density gauge; OD = oven-dry; G_s = specific gravity; MDD = maximum dry density. To determine the combined G_s values, the weighted average of the G_s values of the coarse [> No. 4 sieve (4.75 mm)] and fine (< No. 4) fractions of the materials were used.

4.1.2. Field California Bearing Ratio (CBR)

Table 4.2 provides the equation that can be used to estimate field California bearing ratio (CBR) based on the DCPI values collected by dynamic cone penetrometer (DCP) [Equation (11) (ASTM D6951)]. The equation shown in Table 4.2 is statistically significant at $\alpha = 0.05$.

Table 4.2. Equations to estimate field California bearing ratio (CBR) (%)

Equation	R^2	Adj. R^2	Std. Error
0.8407*Median Relative MDD (%) - 51.3895	0.53	0.48	3.17

MDD = maximum dry density

$$\text{CBR (\%)} = \frac{292}{\text{DCP}^{1.12}} \text{ for DCP in mm/blow} \quad (11)$$

4.2. Light Weight Deflectometer Elastic Modulus (E_{LWD})

Table 4.3 summarizes the equations that can be used to estimate light weight deflectometer elastic modulus (E_{LWD}) values based on laboratory and field testing. The equations listed in Table 4.3 are statistically significant at $\alpha = 0.05$. The equations that show E_{LWD} as a linear function of DCPI or CBR in Table 4.3 are also graphically illustrated in Figure 4.1.

DRAFT

Table 4.3. Equations to estimate light weight deflectometer elastic modulus (E_{LWD}) (MPa)

Equation	R^2	Adj. R^2	Std. Error
31.7980*Median NDG Dry Density (kN/m^3) - 217.5777*Combined OD G_s - 14.4437	0.81	0.76	11.25
27.6348*Median NDG Dry Density (kN/m^3) - 240.6255*Combined SDD G_s + 145.4250	0.73	0.67	13.26
34.2796*Median NDG Dry Density (kN/m^3) - 144.5733*Fine OD G_s - 251.1844	0.73	0.66	13.33
33.7399*Median NDG Dry Density (kN/m^3) - 198.3377*Fine SSD G_s - 92.1880	0.72	0.65	13.51
5.1192*Median Relative MDD (%) - 398.1386	0.71	0.68	13.01
24.4016*Median NDG Dry Density (kN/m^3) - 9.7645*Combined Absorption (%) - 435.6365	0.64	0.55	15.44
-13.2604*Median DCPI (mm/blow) + 189.5575	0.6	0.56	15.31
4.0215*Median CBR (%) - 32.8065	0.59	0.54	15.56

NDG = nuclear density gauge; OD = oven-dry; Gs = specific gravity; SSD = saturated-surface-dry; MDD = maximum dry density; DCPI = dynamic cone penetration index; CBR = field California bearing ratio. To determine the combined G_s or absorption values, the weighted average of the G_s or absorption values of the coarse [> No. 4 sieve (4.75 mm)] and fine (< No. 4) fractions of the materials were used.

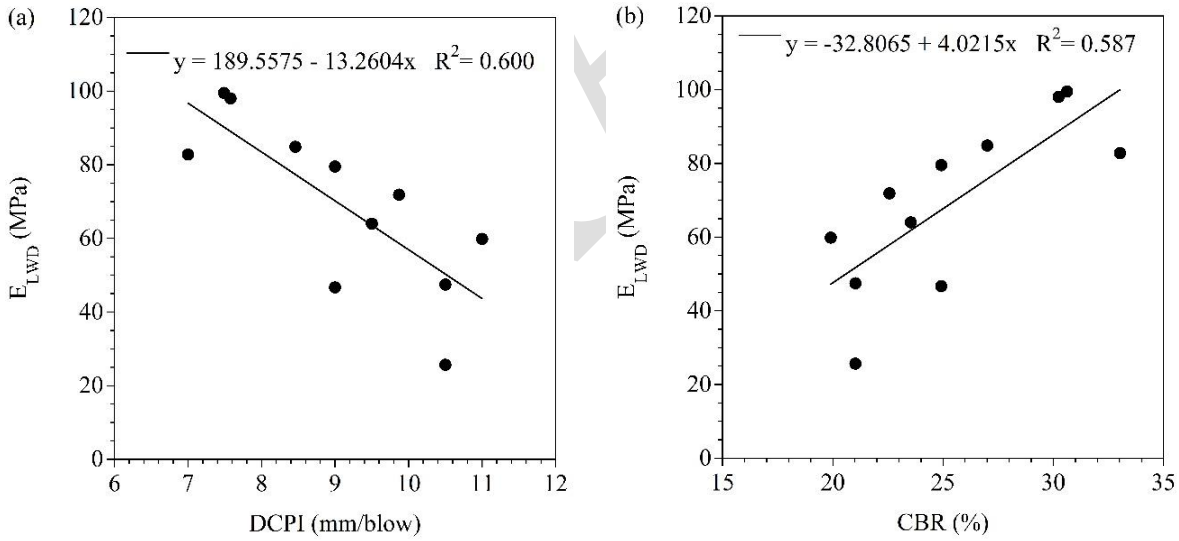


Figure 4.1. (a) Light weight deflectometer elastic modulus (E_{LWD}) vs. dynamic cone penetration index (DCPI) and (b) E_{LWD} vs. field California bearing ratio (CBR)

4.3. Falling Weight Deflectometer Elastic Modulus (E_{FWD})

Table 4.4 summarizes the equations that can be used to estimate falling weight deflectometer elastic modulus (E_{FWD}) values based on laboratory and field testing. The equations listed in Table 4.4 are statistically significant at $\alpha = 0.05$. The equations that show E_{FWD} as a linear function of DCPI, CBR, or E_{LWD} in Table 4.4 are also graphically illustrated in Figures 4.2 (for E_{FWD} vs. DCPI

or CBR) and 4.3 (for E_{FWD} vs. E_{LWD}). In addition to the linear relationship between E_{FWD} and E_{LWD} (Table 4.4), Figure 4.3 also shows E_{FWD} as exponential and power functions of E_{LWD}.

Table 4.4. Equations to estimate falling weight deflectometer elastic modulus (E_{FWD}) (MPa)

Equation	R^2	Adj. R^2	Std. Error
2.2010*Median E_{LWD} (MPa) + 20.8064*Combined Absorption (%) - 21.8024*Median NDG Moisture Content (%) - 30.8626	0.95	0.93	15.7
-40.4818*D_{30} (mm) + 21.5511*Fine Absorption (%) + 31.0942*Median NDG Dry Density (kN/m^3) - 563.7491	0.95	0.92	17.07
2.2769*Median E_{LWD} (MPa) + 11.8182*Combined Absorption (%) - 1.8902*Median Relative OMC (%) + 4.5147	0.94	0.92	17.37
1.8589*Median E_{LWD} (MPa) + 16.4004*Combined Absorption (%) - 165.2143*D_{10} (mm) - 86.5880	0.94	0.91	18.11
2.4732*Median E_{LWD} (MPa) + 9.7178*Combined Absorption (%) - 136.4322	0.89	0.86	22.87
2.3858*Median E_{LWD} (MPa) - 76.4845	0.8	0.78	29.04
16.1040*Median Relative MDD (%) + 10.1868*Fine Absorption (%) - 1461.9277	0.77	0.72	32.71
10.6542*Median CBR (%) - 181.6171	0.58	0.53	42.02
-34.4403*Median DCPI (mm/blow) + 401.2251	0.57	0.52	42.51
11.7122*Median Relative MDD (%) - 980.6099	0.52	0.47	44.69

E_{LWD} = light weight deflectometer elastic modulus; NDG = nuclear density gauge; OMC = optimum moisture content; MDD = maximum dry density; CBR = field California bearing ratio; DCPI = dynamic cone penetration index. To determine the combined absorption values, the weighted average of the absorption values of the coarse [> No. 4 sieve (4.75 mm)] and fine (< No. 4) fractions of the materials were used.

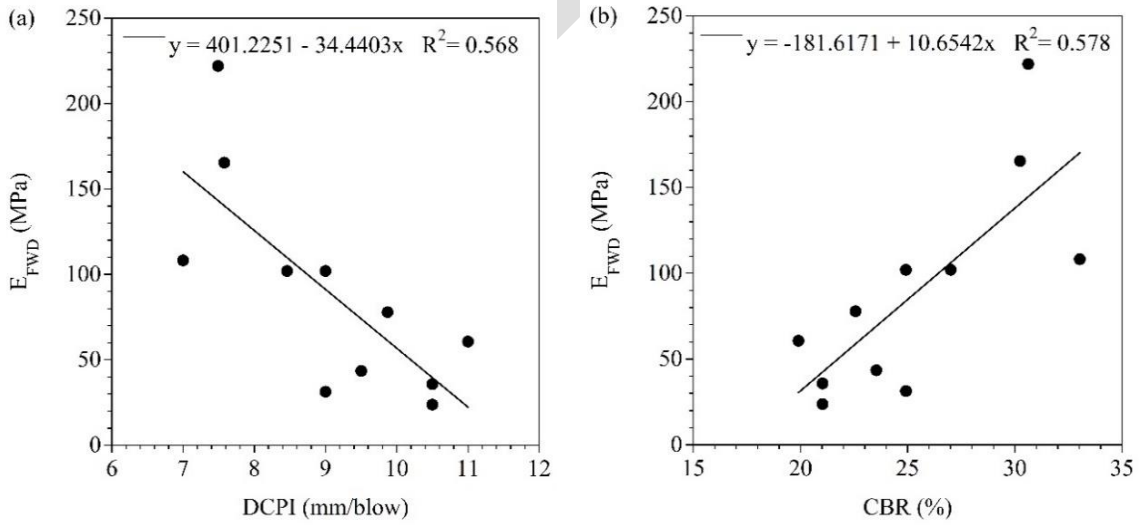


Figure 4.2. (a) Falling weight deflectometer elastic modulus (E_{FWD}) vs. dynamic cone penetration index (DCPI) and (b) E_{FWD} vs. field California bearing ratio (CBR)

DRAFT

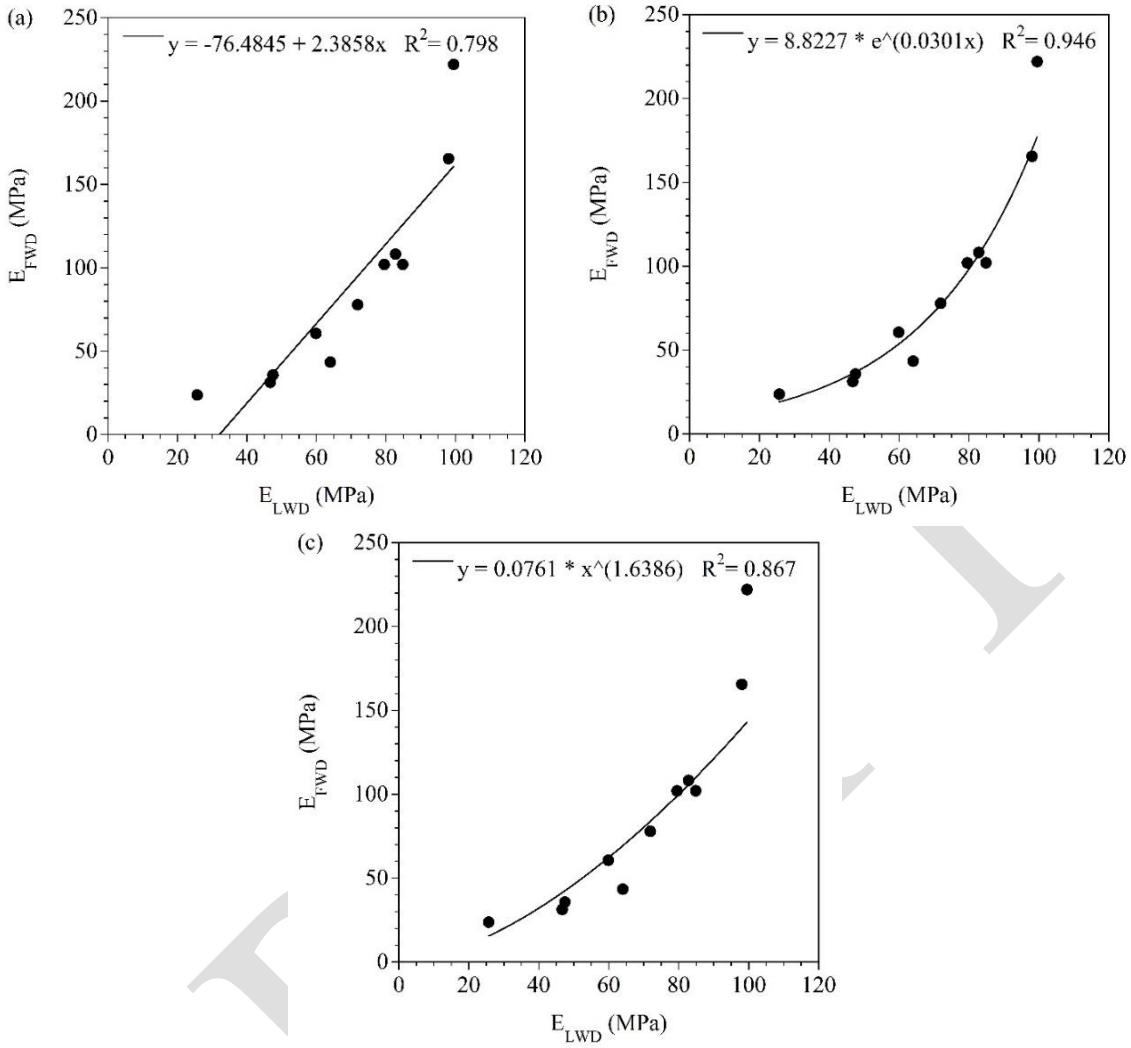


Figure 4.3. Falling weight deflectometer elastic modulus (E_{FWD}) vs. light weight deflectometer elastic modulus (E_{LWD}): (a) linear, (b) exponential, and (c) power trendline

4.4. Intelligent Compaction (IC) Resilient Modulus (M_R)

4.4.1. Intelligent Compaction (IC) Resilient Modulus (M_R) at 10 psi (69 kPa)

Table 4.5 summarizes the equations that can be used to estimate intelligent compaction (IC) M_R at 10 psi (69 kPa) based on laboratory and field testing. The equations listed in Table 4.5 are statistically significant at $\alpha = 0.05$. The equations that show IC M_R [at 10 psi (69 kPa)] as a linear function of DCPI, CBR, E_{LWD}, or E_{FWD} in Table 4.5 are also graphically illustrated in Figures 4.4 (for IC M_R vs. DCPI), 4.5 (for IC M_R vs. CBR), 4.6 (for IC M_R vs. E_{LWD}), and 4.7 (for IC M_R vs. E_{FWD}). In addition to the linear relationship between the parameters, Figures 4.4, 4.5, 4.6, and 4.7 also show nonlinear relationships between the parameters.

Table 4.5. Equations to estimate intelligent compaction (IC) resilient modulus (M_R) (MPa) at 10 psi (69 kPa)

Equation	R^2	Adj. R^2	Std. Error
1.0258*Median E_{FWD} (MPa) + 69.5686	0.91	0.9	20.93
2.5583*Median E_{LWD} (MPa) - 16.5596	0.79	0.77	31.62
16.8683*Median Relative MDD (%) + 10.4512*Fine Absorption (%) - 1461.9308	0.73	0.66	38.29
-35.2625*Median DCPI (mm/blow) + 480.5413	0.52	0.46	48.46
12.3625*Median Relative MDD (%) - 968.1201	0.5	0.45	49.04
10.5220*Median CBR (%) - 106.4179	0.49	0.43	49.81

E_{FWD} = falling weight deflectometer elastic modulus; E_{LWD} = light weight deflectometer elastic modulus; MDD = maximum dry density; DCPI = dynamic cone penetration index; CBR = field California bearing ratio

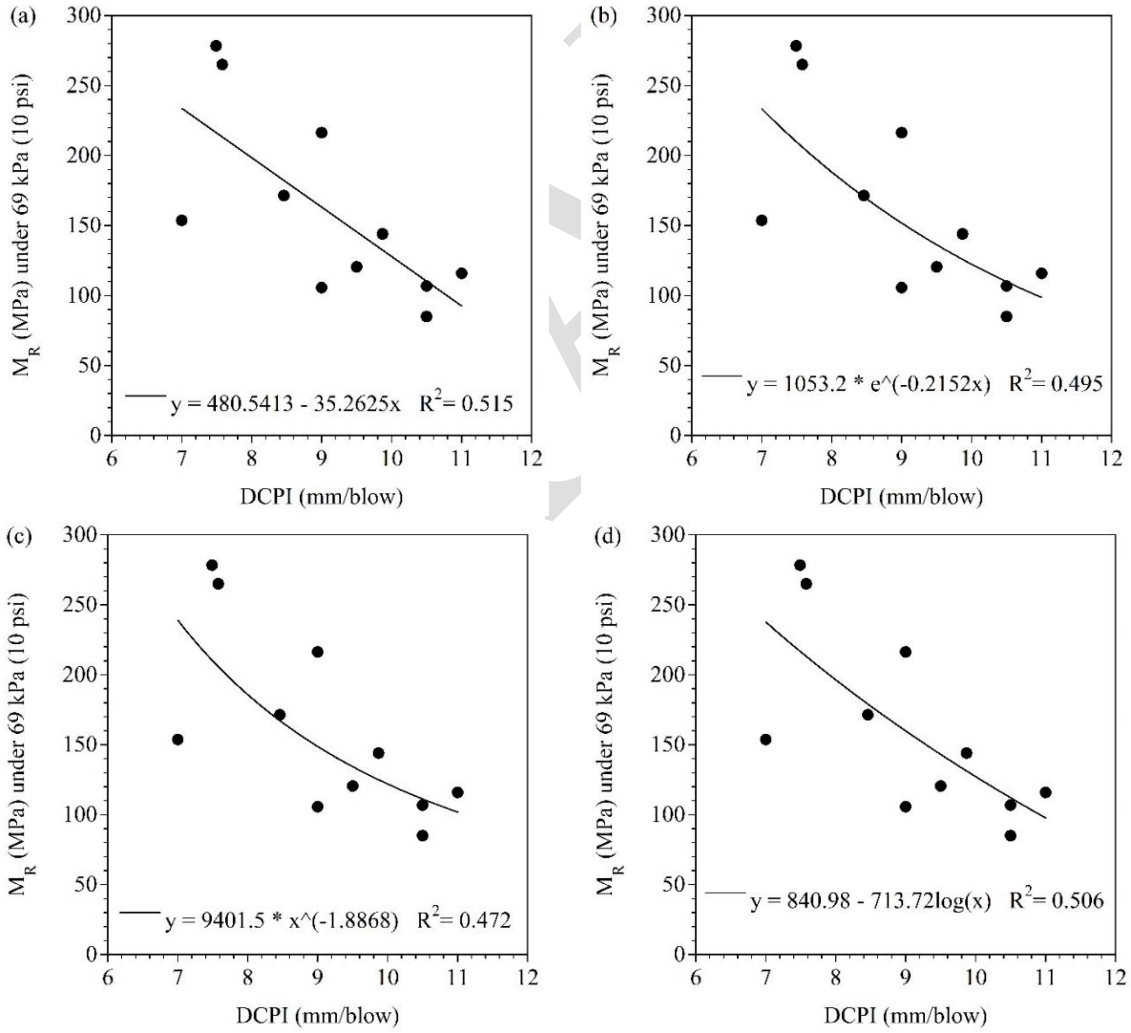


Figure 4.4. Intelligent compaction (IC) resilient modulus (M_R) [at 10 psi (69 kPa)] vs. dynamic cone penetration index (DCPI): (a) linear, (b) exponential, (c) power, and (d) logarithmic relationships

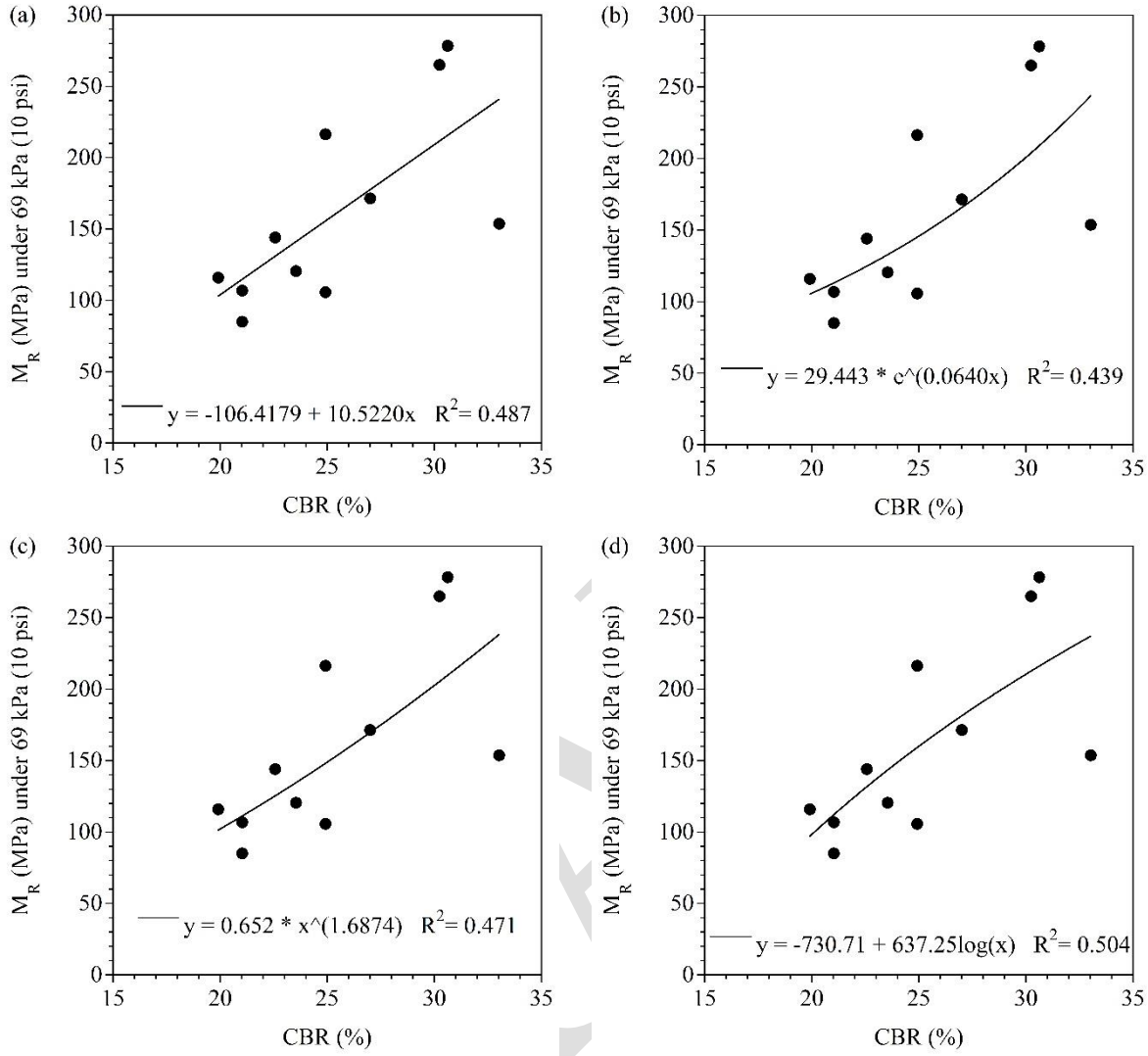


Figure 4.5. Intelligent compaction (IC) resilient modulus (M_R) [at 10 psi (69 kPa)] vs. field California Bearing Ratio (CBR): (a) linear, (b) exponential, (c) power, and (d) logarithmic relationships

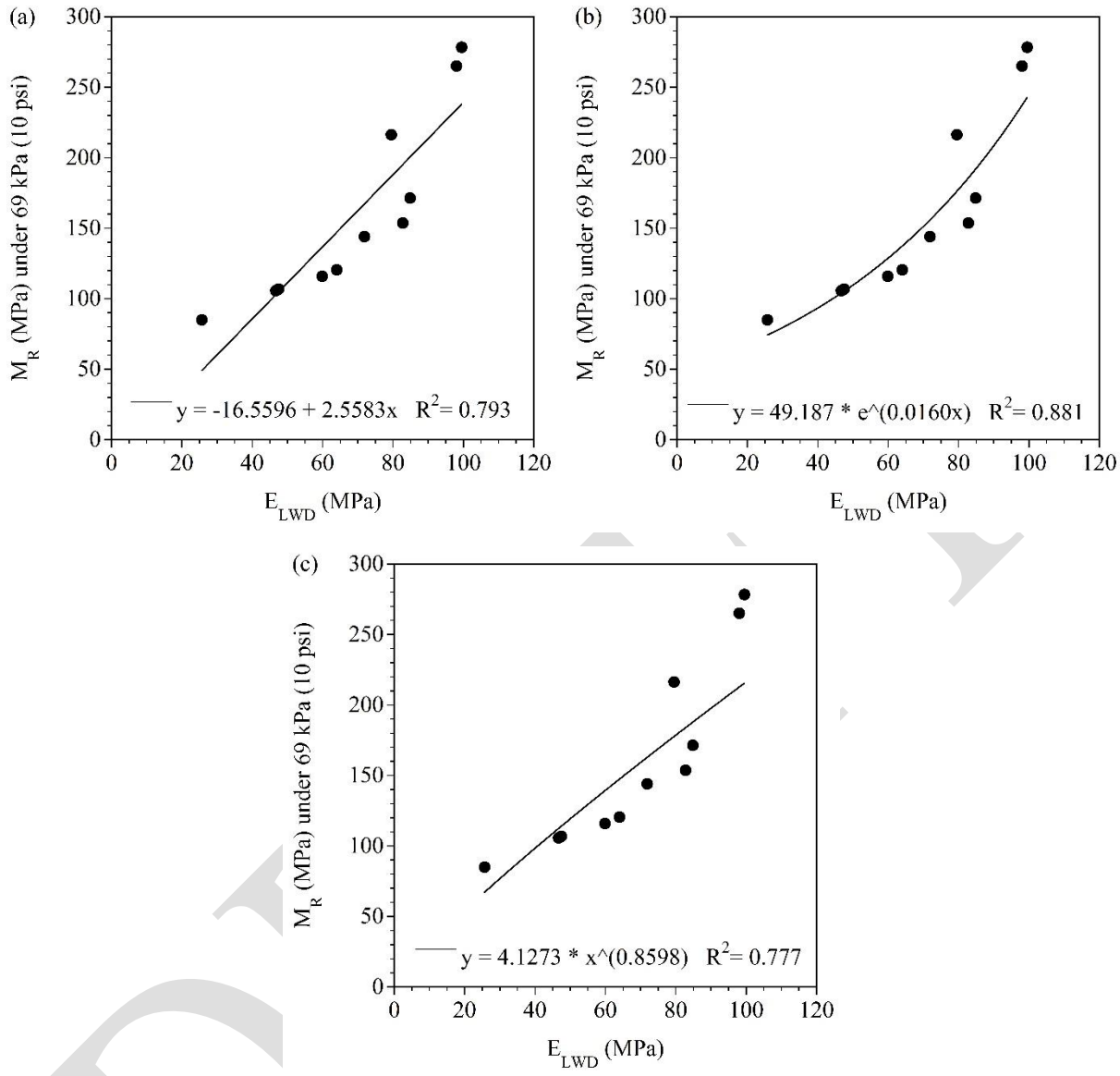


Figure 4.6. Intelligent compaction (IC) resilient modulus (M_R) [at 10 psi (69 kPa)] vs. light weight deflectometer elastic modulus (E_{LWD}): (a) linear, (b) exponential, (c) power trendline

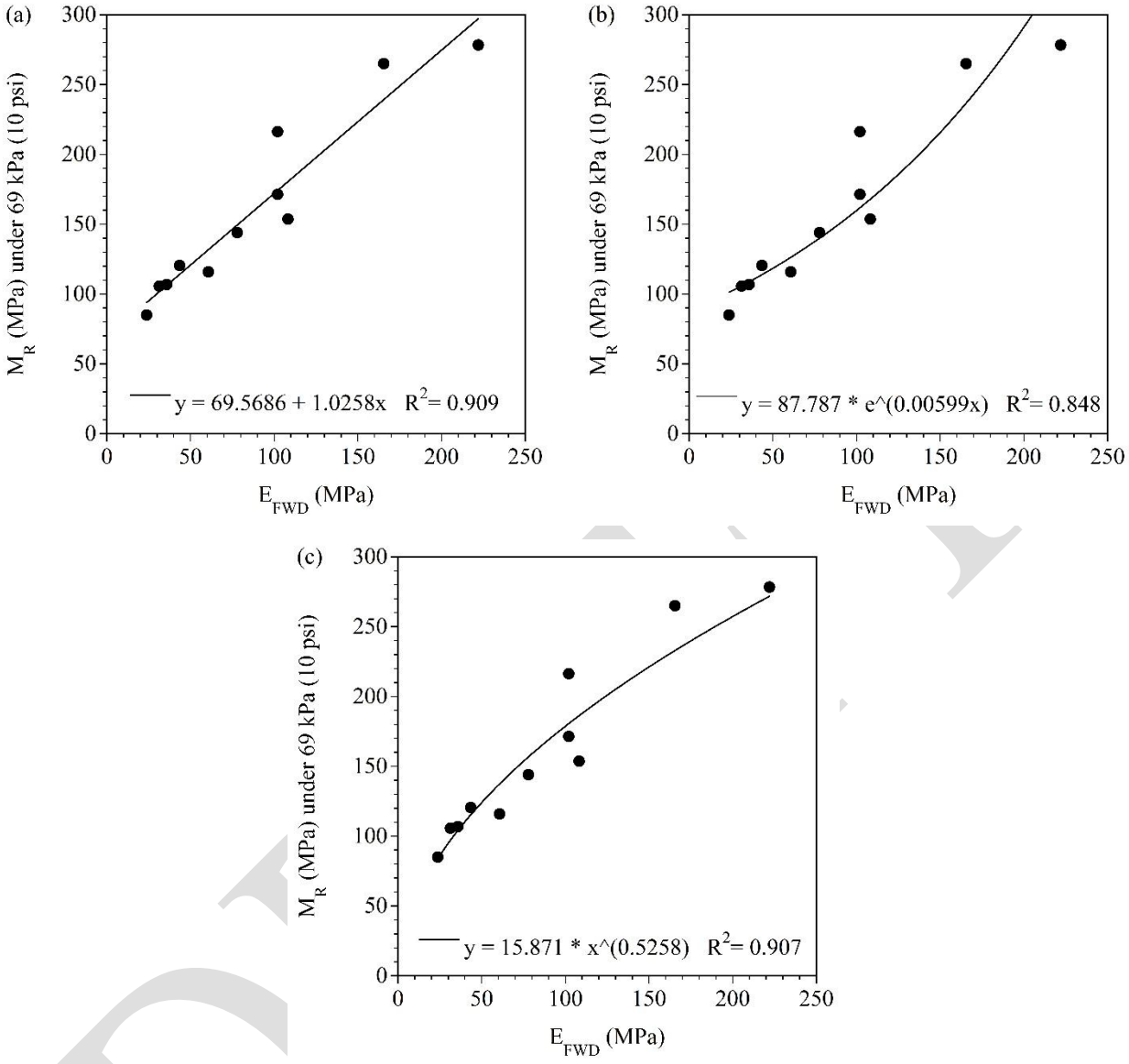


Figure 4.7. Intelligent compaction (IC) resilient modulus (M_R) [at 10 psi (69 kPa)] vs. falling weight deflectometer elastic modulus (E_{FWD}): (a) linear, (b) exponential, and (c) power trendline

4.4.2. Intelligent Compaction (IC) Resilient Modulus (M_R) at 30 psi (207 kPa)

Table 4.6 summarizes the most convenient equations that can be used to estimate intelligent compaction (IC) M_R at 30 psi (207 kPa) based on laboratory and field testing. Other equations that are not as convenient as those listed in Table 4.6 are provided in Appendix O. The equations listed in Table 4.6 are statistically significant at $\alpha = 0.05$. The equations that show IC M_R [at 30 psi (207 kPa)] as a linear function of DCPI, CBR, E_{LWD}, or E_{FWD} in Table 4.6 are also graphically illustrated in Figures 4.8 (for IC M_R vs. DCPI or CBR), 4.9 (for IC M_R vs. E_{LWD}), and 4.10 (for IC M_R vs. E_{FWD}). In addition to the linear relationship between IC M_R [at 30 psi (207 kPa)] and E_{LWD} or E_{FWD} (Table 4.5), Figures 4.9 and 4.10 also show IC M_R [at 30 psi (207 kPa)] as exponential and power functions of E_{LWD} and E_{FWD}, respectively.

Table 4.6. Equations to estimate intelligent compaction (IC) resilient modulus (M_R) (MPa) at 30 psi (207 kPa)

Equation	R^2	Adj. R^2	Std. Error
1.2907*Median M_R at 69 kPa (MPa) - 50.5300	0.99	0.99	9.97
1.3445*Median E_{FWD} (MPa) + 37.4498	0.93	0.92	24.5
3.2745*Median E_{LWD} (MPa) - 70.0008	0.77	0.75	43.25
21.5095*Median Relative MDD (%) + 14.9378*Fine Absorption (%) - 1924.9268	0.72	0.65	50.79
-44.8505*Median DCPI (mm/blow) + 563.6878	0.49	0.44	64.28
13.5485*Median CBR (%) - 187.0635	0.48	0.42	65.21
15.0695*Median Relative MDD (%) - 1219.1306	0.44	0.38	67.41

M_R = resilient modulus; E_{FWD} = falling weight deflectometer elastic modulus; E_{LWD} = light weight deflectometer elastic modulus; MDD = maximum dry density; DCPI = dynamic cone penetration index; CBR = field California bearing ratio

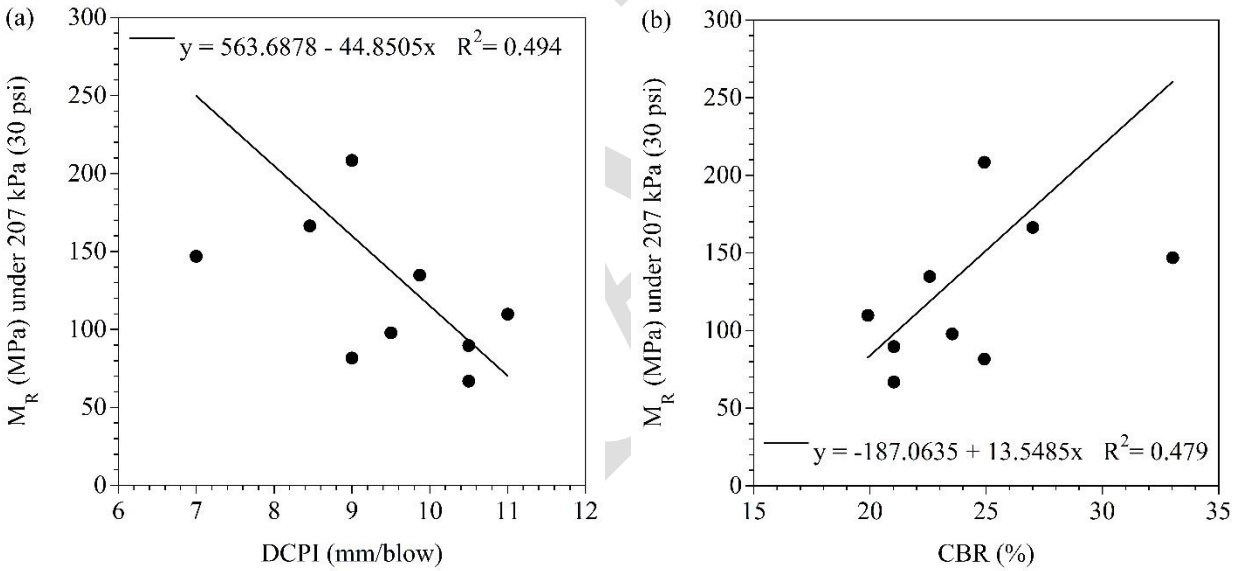


Figure 4.8. (a) Intelligent compaction (IC) resilient modulus (M_R) [at 30 psi (207 kPa)] vs. dynamic cone penetration index (DCPI) and (b) IC M_R [at 30 psi (207 kPa)] vs. field California bearing ratio (CBR)

DRAFT

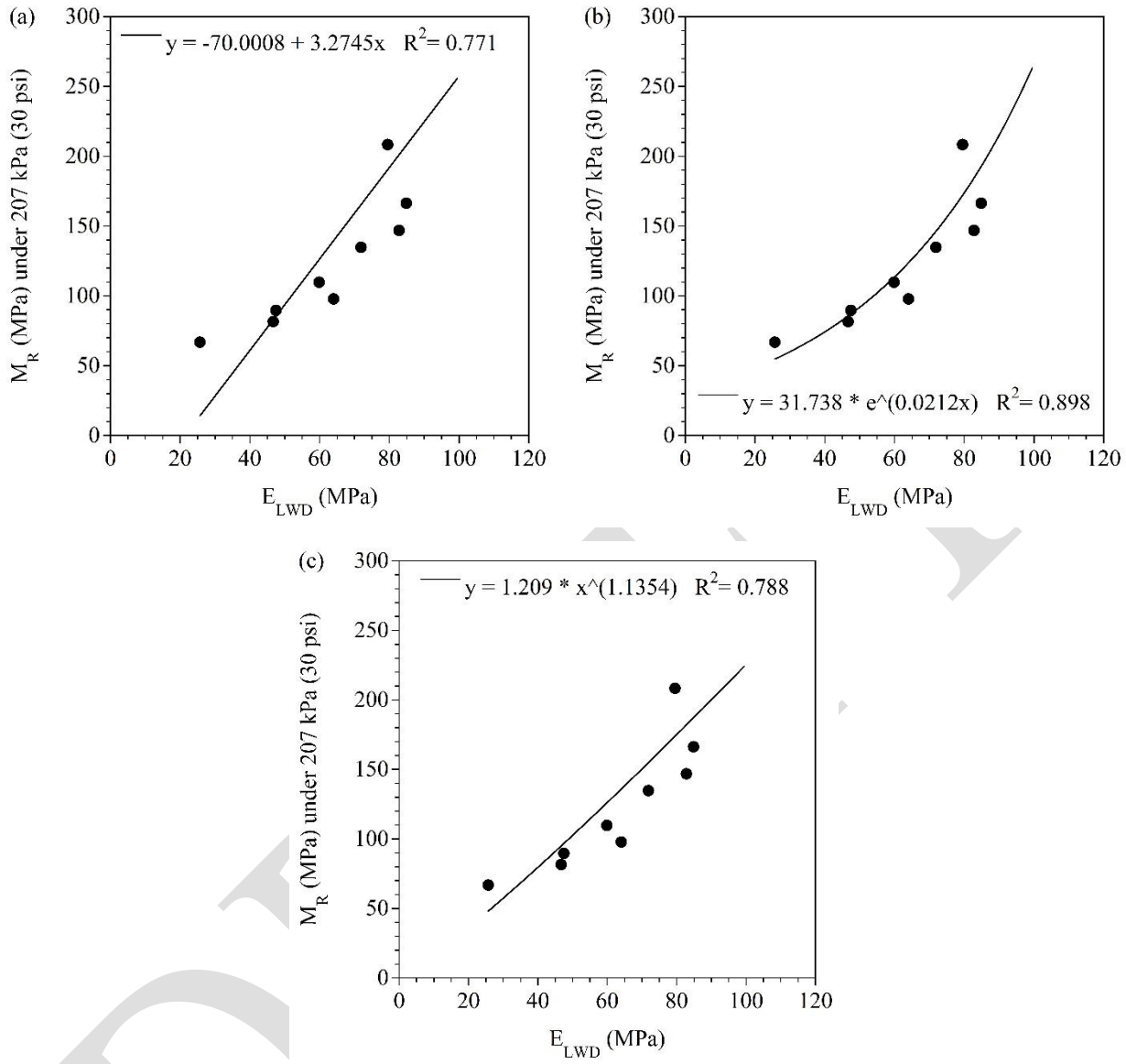


Figure 4.9. Intelligent compaction (IC) resilient modulus (M_R) [at 30 psi (207 kPa)] vs. light weight deflectometer elastic modulus (E_{LWD}): (a) linear, (b) exponential, and (c) power trendline

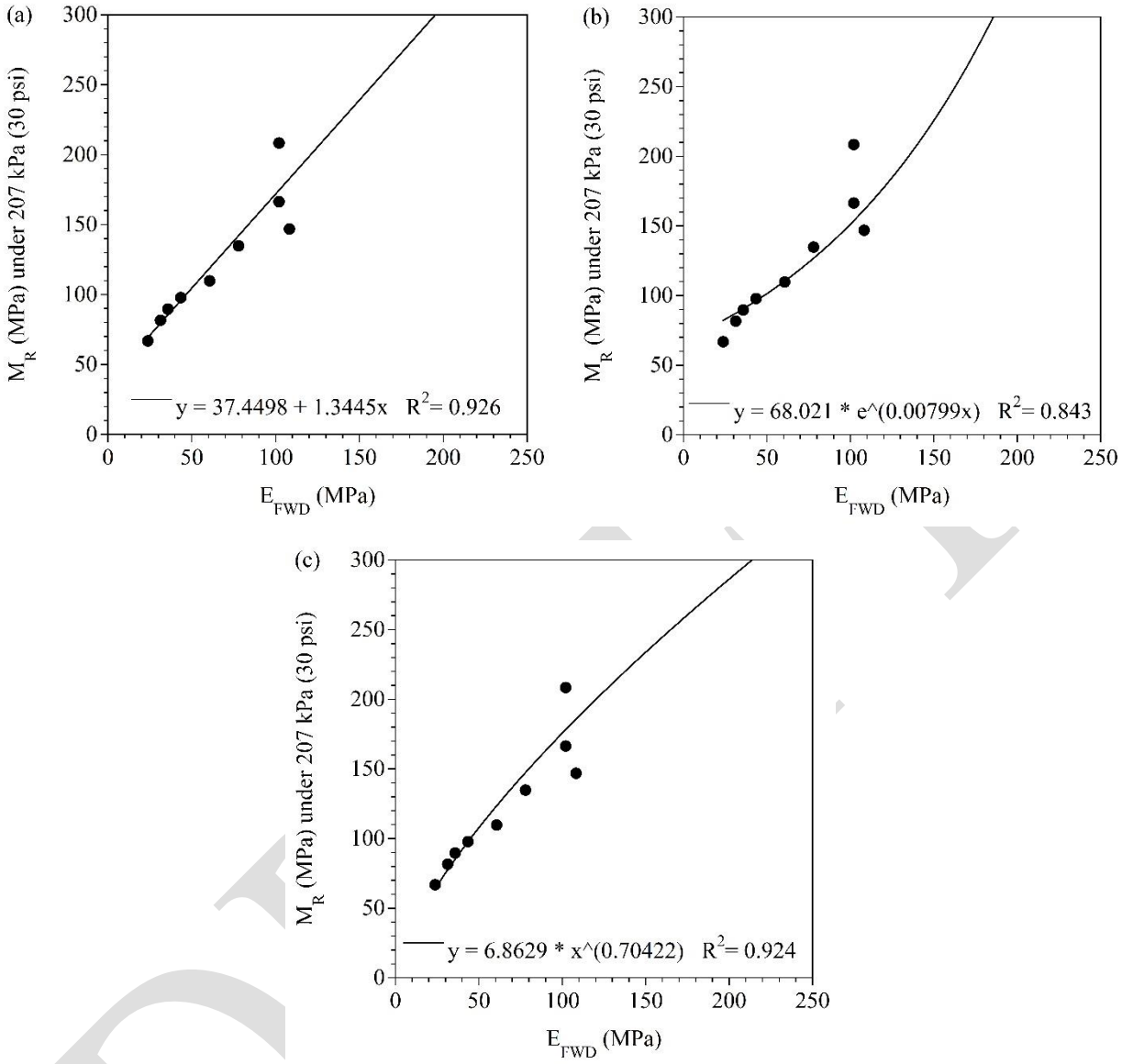


Figure 4.10. Intelligent compaction (IC) resilient modulus (M_R) [at 30 psi (207 kPa)] vs. falling weight deflectometer elastic modulus (E_{FWD}): (a) linear, (b) exponential, and (c) power trendline

5. PAVEMENT ME PERFORMANCE MODELS

The AASHTOWare Pavement ME Design program (version 2.5.5) was used to provide recommendations on pavement base and subbase layer thicknesses. The following sections give detailed information about general model inputs, material inputs, and evaluation of the performance prediction models. Since the use of local calibration is not within the scope of this study, global (default) calibration was used in the analyses.

5.1. General Model Inputs

General design inputs are summarized in Table 5.1. The design life of flexible pavement models was determined to be 20 years (Velasquez et al. 2009; Ceylan et al. 2015). For the base and pavement construction dates, actual construction dates of the test cells (Figure 1.1) were used [detailed information about the construction timeline is provided in the Task 3 (construction monitoring and reporting) report]. The initial international roughness index (IRI) value was determined to be 63 in/mile (Izevbekhai and Akkari 2011; Ceylan et al. 2015).

Table 5.1. General design inputs for Pavement ME

Parameter	Input/Value
Design Life (years)	20
Design Type	Flexible
Base Construction	August, 2017
Pavement Construction	September, 2017
Traffic Opening	September, 2017
Initial IRI (in/mile)	63

IRI = international roughness index

Target values and reliability levels for different pavement distresses are summarized in Table 5.2. For all distresses, a reliability level of 90% was used. According to the FHWA, while IRI values lower than 2.68 m/km (170 in/mile) might be acceptable in terms of ride quality, values greater than 2.68 m/km (170 in/mile) are considered unacceptable (Elbheiry et al. 2011). Therefore, the terminal IRI value was determined to be 170 in/mile (Elbheiry et al. 2011). Other pavement distress target values were selected based on Ceylan et al. (2015).

Table 5.2. Pavement distress types, target values, and reliability levels

Parameter	Target Value	Reliability (%)
Terminal IRI (in/mile)	170	90
AC Bottom-Up Fatigue Cracking (% lane area)	25	90
AC Thermal Cracking (ft/mile)	1,000	90
AC Top-Down Fatigue Cracking (ft/mile)	2,000	90
Permanent Deformation – AC Only (in)	0.25	90
Permanent Deformation – Total Pavement (in)	0.75	90

IRI = international roughness index; AC = asphalt concrete

Climatic parameters and regional information are summarized in Table 5.3. The MnROAD LVR test facility, where the test cells (Figure 1.1) were located, was selected, and to enable specific selection of the MnROAD LVR test facility, a virtual weather station was created by selecting six neighboring weather stations. The coordinates and the locations of the neighboring weather stations are shown in Table 5.3 and Figure 5.1, respectively. Water table depth was selected to be 10 ft based on Schwartz et al. (2011). Monthly rainfall statistics, monthly climate summary, and hourly air temperature distribution by month for the MnROAD LVR test facility location are provided in Appendix P.

DRAFT

Table 5.3. Climatic parameters and regional information

Parameter	Input/Value	Coordinates
Climate Location	MnROAD LVR	45.5016205, -93.7609675
		45.001088, -93.7521709
		45.5003105, -93.1249918
		45.0003614, -93.1247624
		45.4994913, -94.3722707
		45.0000331, -94.368383
Mean Annual Air Temperature (°F)	43.8	
Mean Annual Precipitation (in)	39	
Freezing Index (°F – days)	1894	
Average Annual Number of Freeze/Thaw Cycles	80	
Water Table Depth (ft)	10	

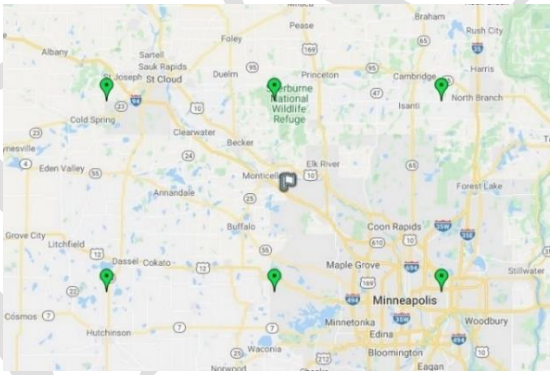


Figure 5.1. Locations of the six neighboring weather stations and the MnROAD LVR test facility (green pins represent the neighboring weather stations and the white flag represents the location of the MnROAD LVR)

Traffic information is provided in two parts in Tables 5.4 and 5.5. Operational speed was determined to be 50 mph (Izevbekhai and Akkari 2011; Schwartz et al. 2011) (Table 5.4). Truck traffic category (TTC) was selected to be 4 (level 3 default vehicle distribution) (Schwartz et al. (2011) with a default growth factor of 3% (linear) (Table 5.4). Five different traffic levels were used (Table 5.5) (Schwartz et al. 2011). Average annual daily truck traffic (AADTT) values of 100, 500, and 1,000 represented low traffic levels (Table 5.5) (Schwartz et al. 2011). In addition, AADTT values of 7,500 and 25,000 represented medium and high traffic levels, respectively (Table 5.5) (Schwartz et al. 2011). Graphical and tabular representations of the traffic inputs are provided in Appendix Q.

DRAFT

Table 5.4. Traffic information – part 1

Parameter	Input/Value
Operational Speed (mph)	50
Truck Traffic Category (TTC)	4 (Level 3)
Growth Factor (%)	3 (Linear)

Table 5.5. Traffic information – part 2

Parameter	Low Traffic			Medium Traffic	High Traffic
	100 AADTT	500 AADTT	1,000 AADTT	7,500 AADTT	25,000 AADTT
Number of Lanes in Design Direction	1	2	2	3	3
Percent of Trucks in Design Direction (%)	50	50	50	50	50
Percent of Trucks in Design Lane (%)	100	75	75	55	50

AADTT = average annual daily truck traffic

5.2. Recycled Aggregate Base (RAB) Group

5.2.1. Aggregate Base Layer Design

In the MnROAD LVR test facility, the recycled aggregate base (RAB) group contained the test cells built with 12-in coarse RCA (cell 185), fine RCA (cell 186), limestone (cell 188), and RCA+RAP (cell 189) base layers. To evaluate the effect of aggregate base layer thickness on pavement performance using Pavement ME, thinner aggregate base layers (10 in, 8 in, 6 in, and 4 in) were modeled in addition to the original aggregate base layer thickness of 12 in. In addition, as can be seen in Figure 1.1 for the RAB group, while two of the test cells contained sand subgrade layers (cells 185 and 186), the other two test cells contained clay loam subgrade layers (cells 188 and 189). In Pavement ME, first, coarse RCA, fine RCA, limestone, and RCA+RAP base layers were placed on sand subgrade layers. Then, the same base layers were placed on clay loam subgrade layers. Asphalt and subbase layer thicknesses were kept the same as the original (3.5 in/each). Figure 5.2 is an example that shows different coarse RCA base layer thicknesses that were modeled with Pavement ME.

DRAFT

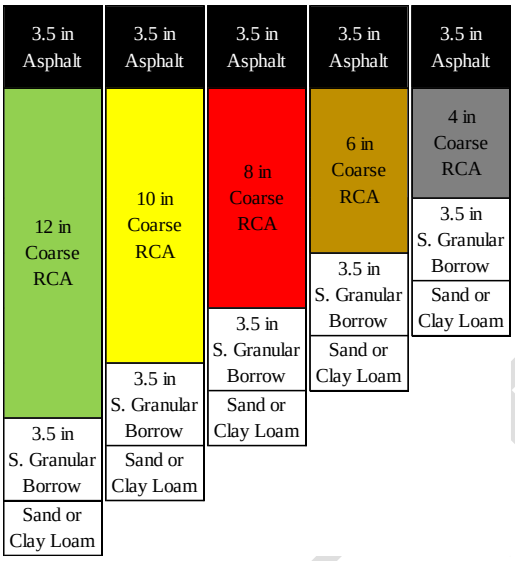


Figure 5.2. Pavement ME models for coarse RCA base layer at different layer thicknesses

5.2.2. Material Inputs

Van Deusen et al. (2018) reported that the asphalt mixture type used in the construction of the test cells (Figure 1.1) was 12.5 mm nominal maximum aggregate size (NMAS) Superpave performance grade (PG) 58S-34 [58 = maximum pavement design temperature (°C), S = standard traffic level, -34 = minimum pavement design temperature (°C)]. Therefore, for modeling the asphalt layers, Superpave PG 58-34 was selected (level 3). Appendix R provides detailed information about the level 3 parameters for the modeled asphalt layer.

Table 5.6 summarizes the input parameters for aggregate base, subbase, and subgrade layers that were used in the models. For each pavement sublayer, the coefficient of lateral earth pressure (K_0) was kept at the default (0.5). For M_R inputs of the aggregate base and subgrade layers, the previously explained actual SM_R values were used (level 2). For select granular borrow subbase layers, no laboratory M_R testing was performed, so the equations that were found to estimate the SM_R values for coarse RCA, fine RCA, limestone, and RCA+RAP (Table 3.9 and Appendix L) were used to estimate select granular borrow's SM_R (Appendix S). After using the suitable equations to estimate the SM_R values of select granular borrow, the median SM_R value (12,888.8 psi) was determined and compared with the SM_R values of other materials. After comparison, the estimated SM_R value of select granular borrow (12,888.8 psi) was determined to be in an acceptable range, and therefore, it was used in the models (Table 5.6). In addition, no K_{sat} testing was performed for select granular borrow. Unlike the procedure followed to estimate the SM_R of select granular borrow [as stated previously, the correlations shown in Table 3.9 and Appendix L were used to estimate the SM_R of select granular borrow], the K_{sat} (2.71E-03 ft/hr) value for select granular borrow material was predicted by the Pavement ME program in level 2 analysis (Table 5.6). Lastly, as described previously, the SWCC characteristics of the materials were determined using the van Genuchten model (van Genuchten 1980) [Equation (5)] in this study. Since the Pavement ME program uses the Fredlund and Xing (1994) SWCC model, the SWCC inputs [a_f, b_f, c_f, h_r fitting parameters (Fredlund and Xing 1994)] were not user-defined for any of the materials listed in Table 5.6.

DRAFT

Table 5.6. Material inputs used for pavement sublayers in Pavement ME models

Parameter		Coarse RCA Base	Fine RCA Base	Lime-stone Base	RCA+ RAP Base	Select Granular Borrow Subbase	Sand Subgrade	Clay Loam Subgrade
AASHTO Classification		A-1-a	A-1-a	A-1-b	A-1-a	A-1-b	A-1-b	A-6
Poisson's Ratio		0.35	0.35	0.35	0.35	0.35	0.4	0.4
M_R (psi)		18,129	17,760.9	13,926.3	16,487.7	12,888.8[#]	11,336.1	8,630.9
LL		0	32.7	17.9	27.4	18.9	19.9	36.3
PI		0	0	0	0	0	0	12.4
Corrected MDD (pcf)		128.6	121.7	143.2	125.8	140.3	137.7	124.9
K_{sat} (ft/hr)		3.15E-02	5.73E-02	5.74E-03	2.44E-02	2.71E-03[*]	3.24E-02	1.62E-05
Combined OD G_s		2.25	2.17	2.66	2.28	2.62	2.6	2.68
Corrected OMC (%)		9.5	11.1	6.3	9.1	5.3	5.6	10
Percent Passing (%)	No. 200	3.4	7.1	15.1	8.6	12.4	12.6	59.7
	No. 100	5.3	10.8	20.1	12.4	14.4	16.9	68.9
	No. 60	7.6	15	23.8	17.2	20.1	24.4	77.6
	No. 40	11.4	21.1	27.1	24.2	32.6	38.2	84.6
	No. 20	18.2	30.6	30.5	32.6	48	53.6	90.1
	No. 10	26.7	43.6	35.9	43.5	59.9	62.8	94
	No. 4	38.3	61.7	47.7	59	68.9	72.4	96.9
	3/8 in	53.3	81	64.7	75.8	77.4	81.5	98.4
	3/4 in	75.4	99.7	95	99.3	93.3	95.8	99.4
	1 in	85.1	100	100	100	100	99.9	99.5
	1 1/2 in	100	100	100	100	100	100	100
	2 in	100	100	100	100	100	100	100
	2.5 in	100	100	100	100	100	100	100
	3 in	100	100	100	100	100	100	100

M_R = resilient modulus; LL = liquid limit; PI = plasticity index; MDD = maximum dry density; K_{sat} = saturated hydraulic conductivity; OD = oven-dry; G_s = specific gravity; OMC = optimum moisture content. To determine the combined G_s values, the weighted average of the G_s values of the coarse [> No. 4 sieve (4.75 mm)] and fine (< No. 4) fractions of the materials were used.
[#]Determined based on the M_R models developed in this study (Table 3.9 and Appendix L)
[*]Not user-defined

5.2.3. Effect of Aggregate Base Layer Thickness on Pavement Performance Prediction Models

As stated previously, base layer thicknesses ranging between 4 in and 12 in were used in the models (Figure 5.2) to evaluate the effect of the aggregate base layer thickness on long-term pavement performance prediction models. Overall, for all types of base layer aggregates, increasing the aggregate base layer thickness decreased pavement distresses at the end of typical flexible pavement design life (20 years) and increased the service life of pavements (service life is defined

as the pavement age at failure). Figures 5.3, 5.4, 5.5, and 5.6 are examples that show the effect of the base layer thickness on IRI, rutting, alligator cracking, and longitudinal cracking, respectively, for the pavement models that contained sand subgrade layers and were subjected to 1,000 AADTT. More results for other pavement models are provided in Appendix T.

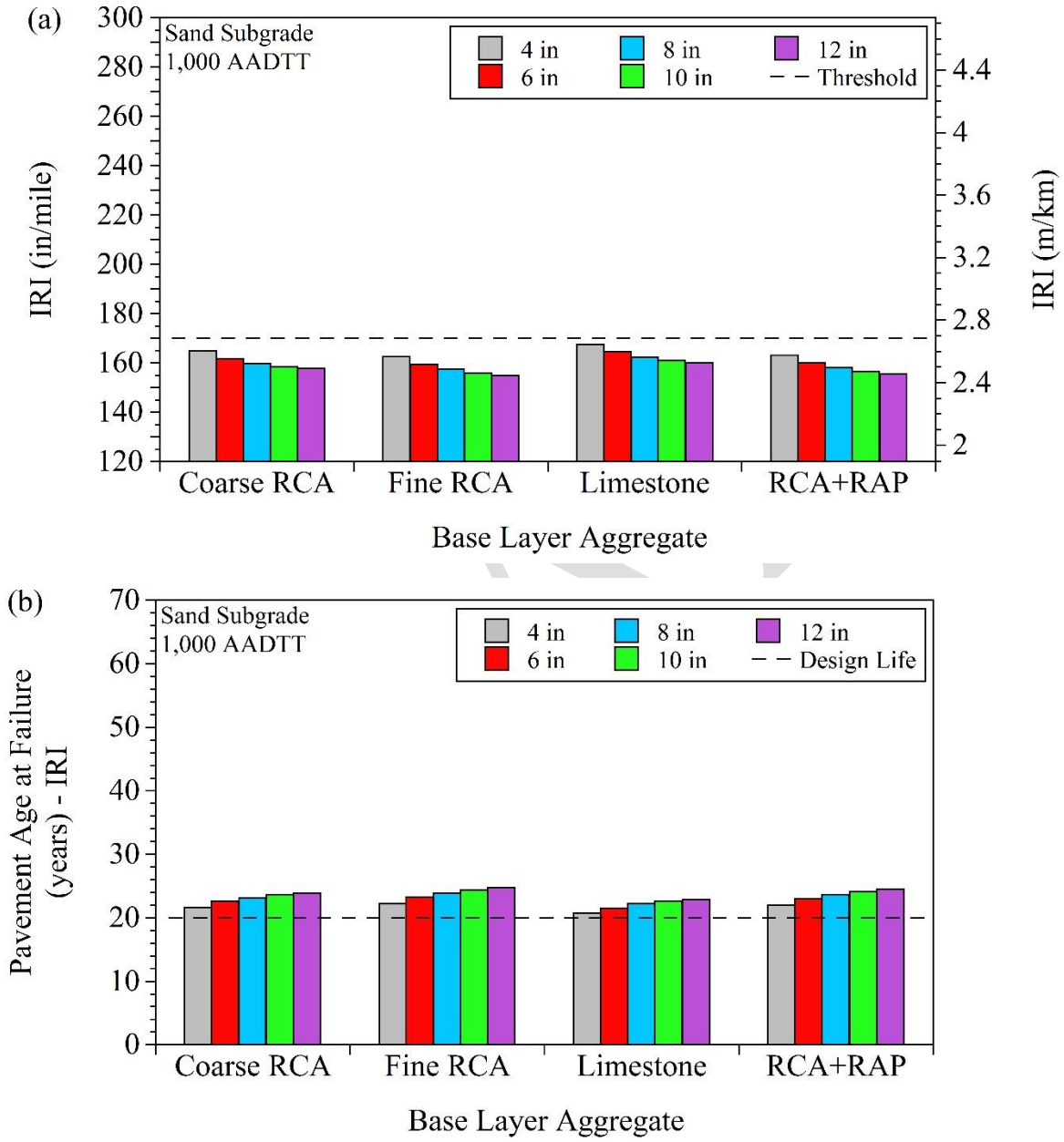


Figure 5.3. Effect of aggregate base layer thickness on (a) IRI at the end of the design life (20 years) and (b) pavement age at IRI failure

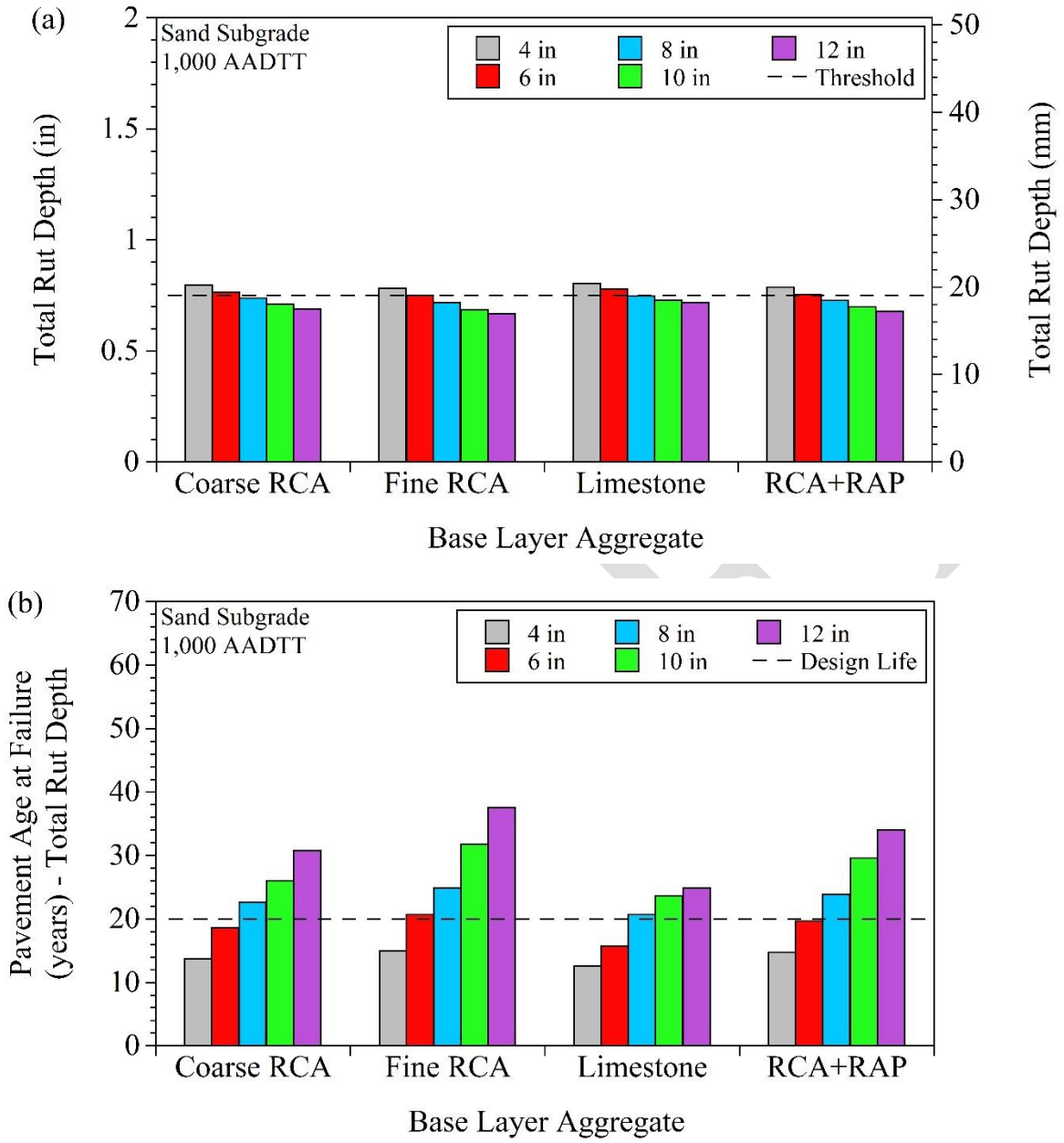


Figure 5.4. Effect of aggregate base layer thickness on (a) total rut depth at the end of the design life (20 years) and (b) pavement age at total rut depth failure

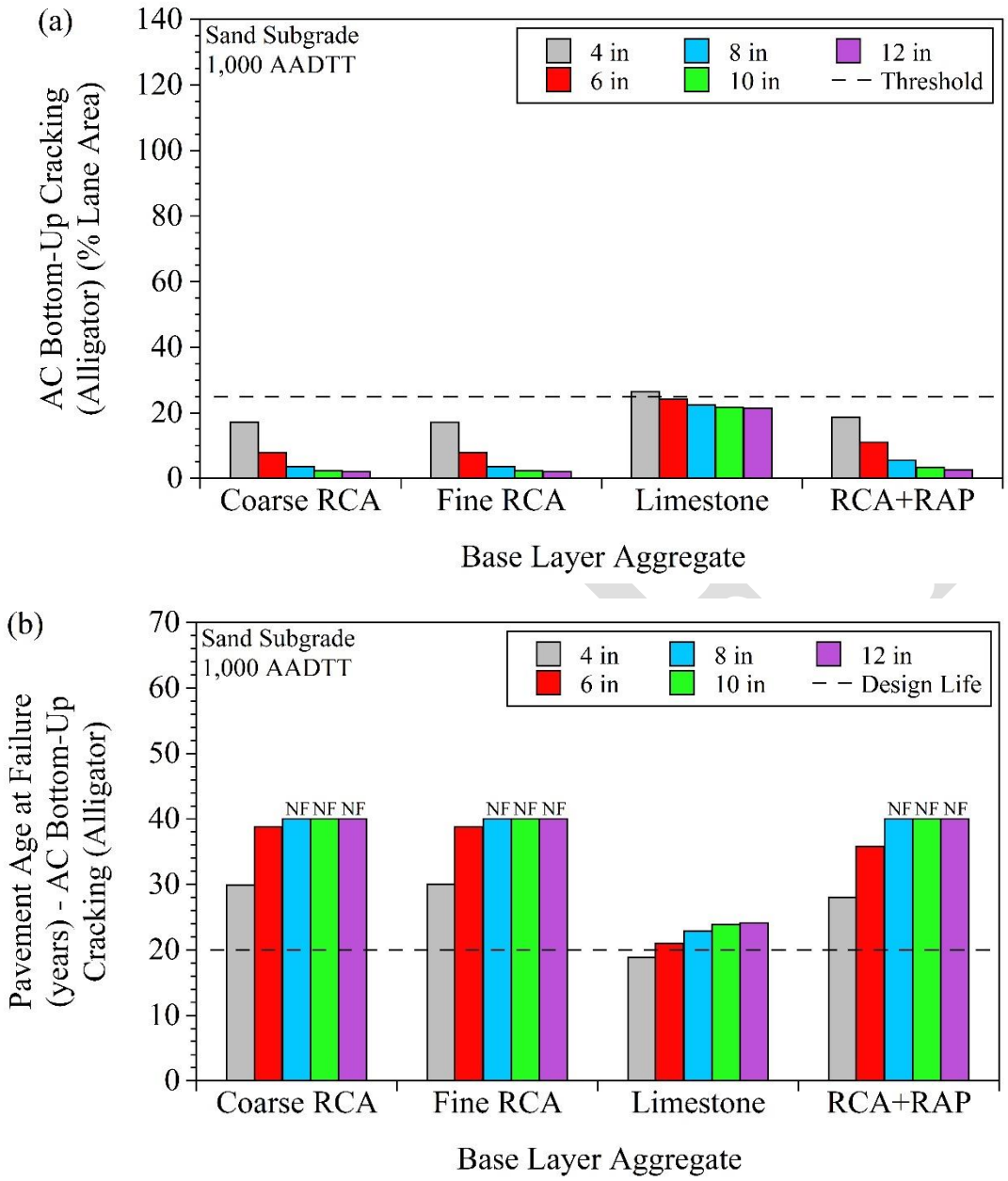


Figure 5.5. Effect of aggregate base layer thickness on (a) alligator cracking at the end of the design life (20 years) and (b) pavement age at alligator cracking failure (NF = no failure)

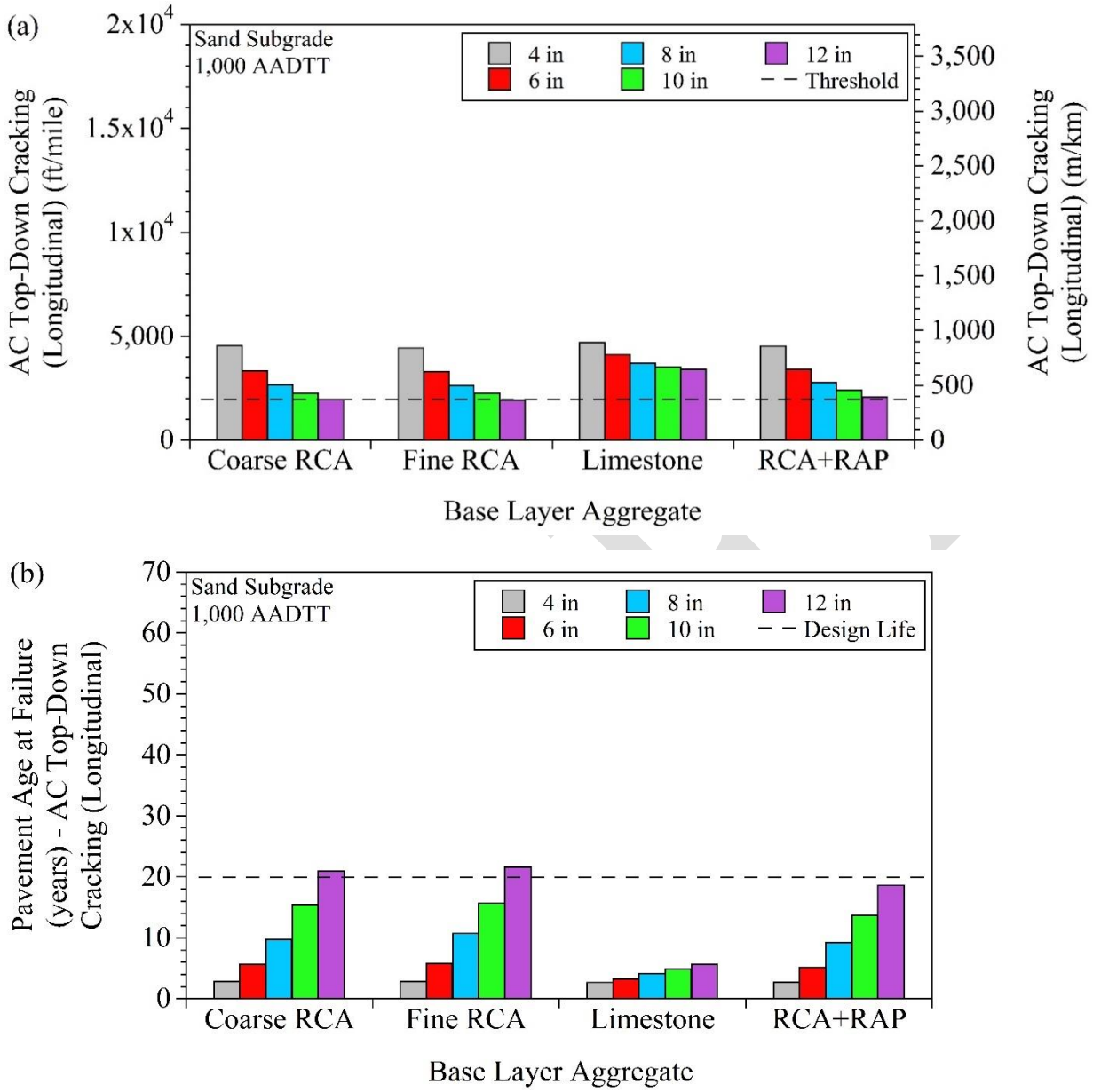


Figure 5.6. Effect of aggregate base layer thickness on (a) longitudinal cracking at the end of the design life (20 years) and (b) pavement age at longitudinal cracking failure

5.2.4. Effect of Base Layer Aggregate Type on Pavement Performance Prediction Models

As stated previously, coarse RCA, fine RCA, limestone, and RCA+RAP were used to model the aggregate base layers at each different layer thickness (12, 10, 8, 6, and 4 in) (Figure 5.2). Overall, for all base layer thicknesses, it was observed that using limestone resulted in higher pavement distresses at the end of the pavement design period (20 years) and lower pavement service life. Figures 5.7, 5.8, 5.9, and 5.10 are examples that show the effect of the base layer aggregate type on IRI, rutting, alligator cracking, and longitudinal cracking, respectively, for pavement models that contained sand subgrade layers and were subjected to 1,000 AADTT. More results for other pavement models can be found in Appendix U.

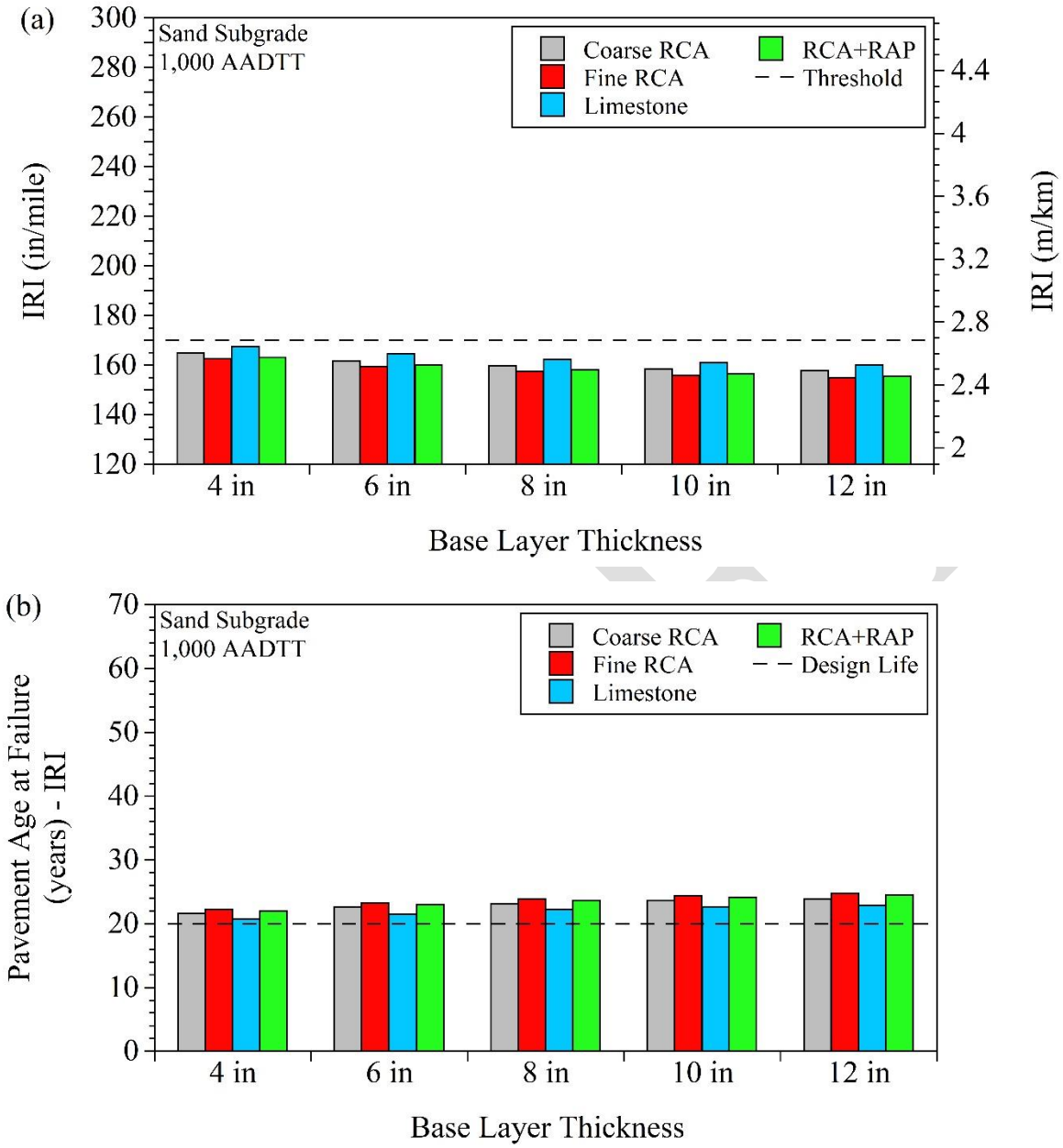


Figure 5.7. Effect of base layer aggregate type on (a) IRI at the end of the design life (20 years) and (b) pavement age at IRI failure

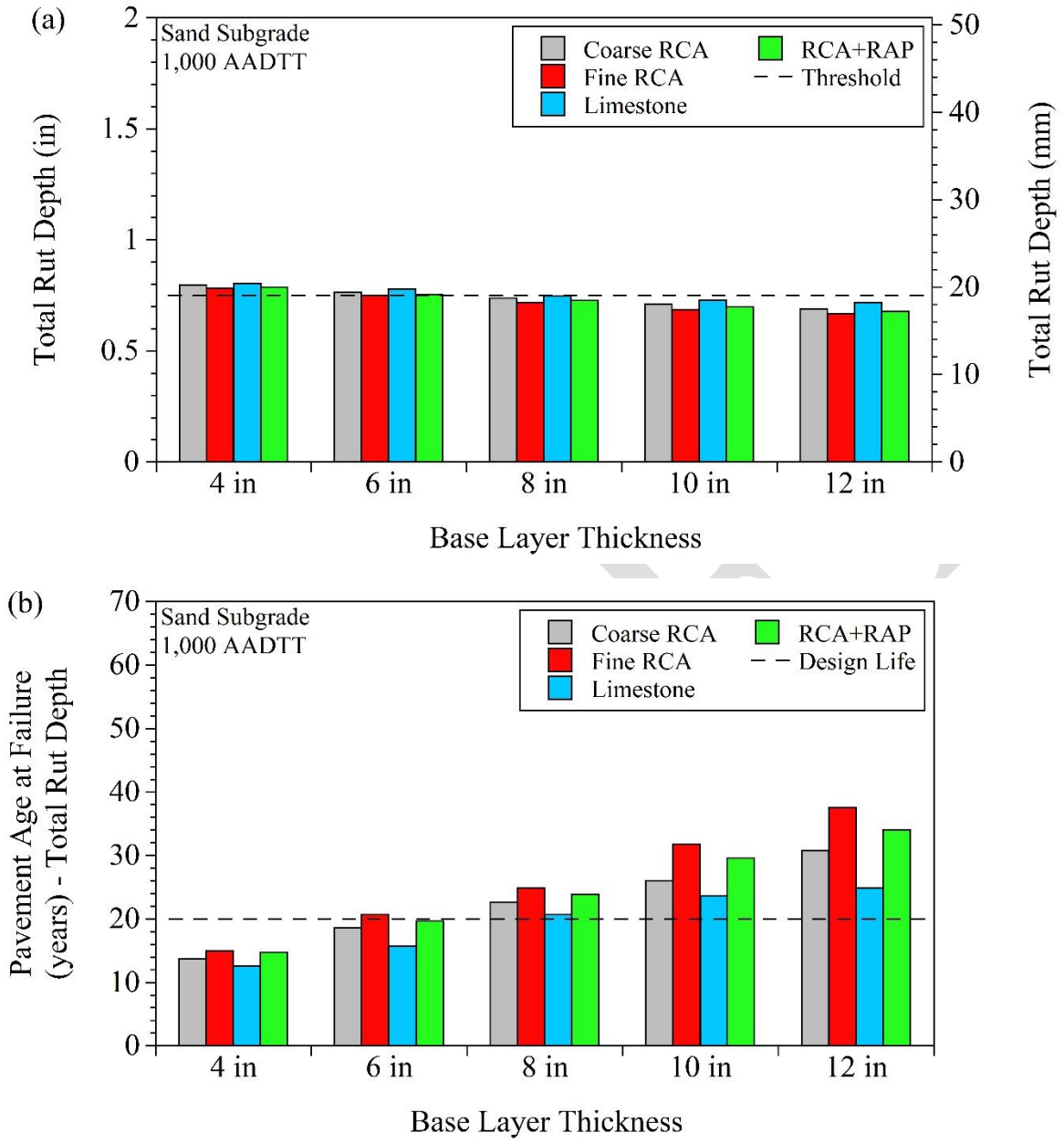


Figure 5.8. Effect of base layer aggregate type on (a) total rut depth at the end of the design life (20 years) and (b) pavement age at total rut depth failure

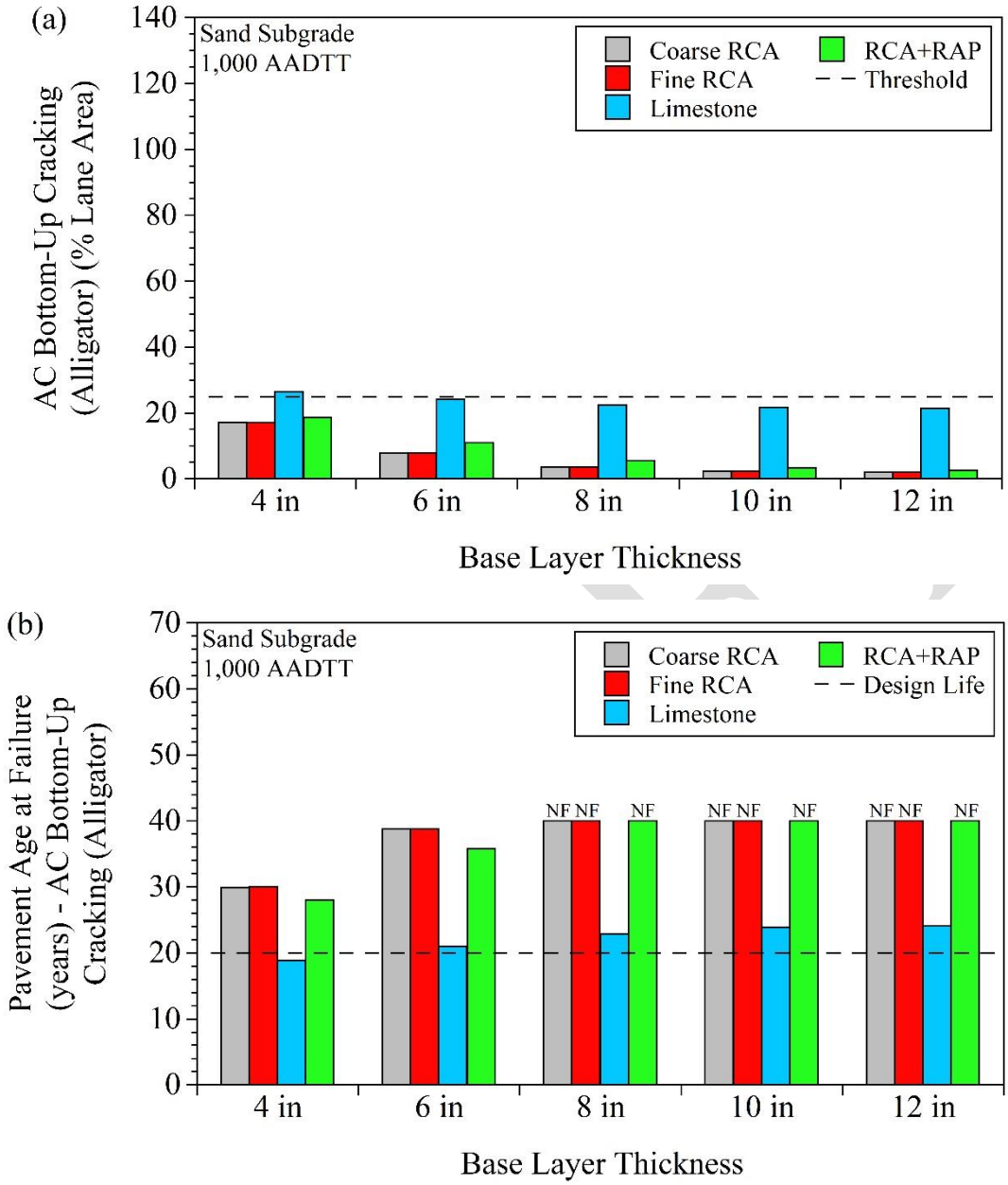


Figure 5.9. Effect of base layer aggregate type on (a) alligator cracking at the end of the design life (20 years) and (b) pavement age at alligator cracking failure (NF = no failure)

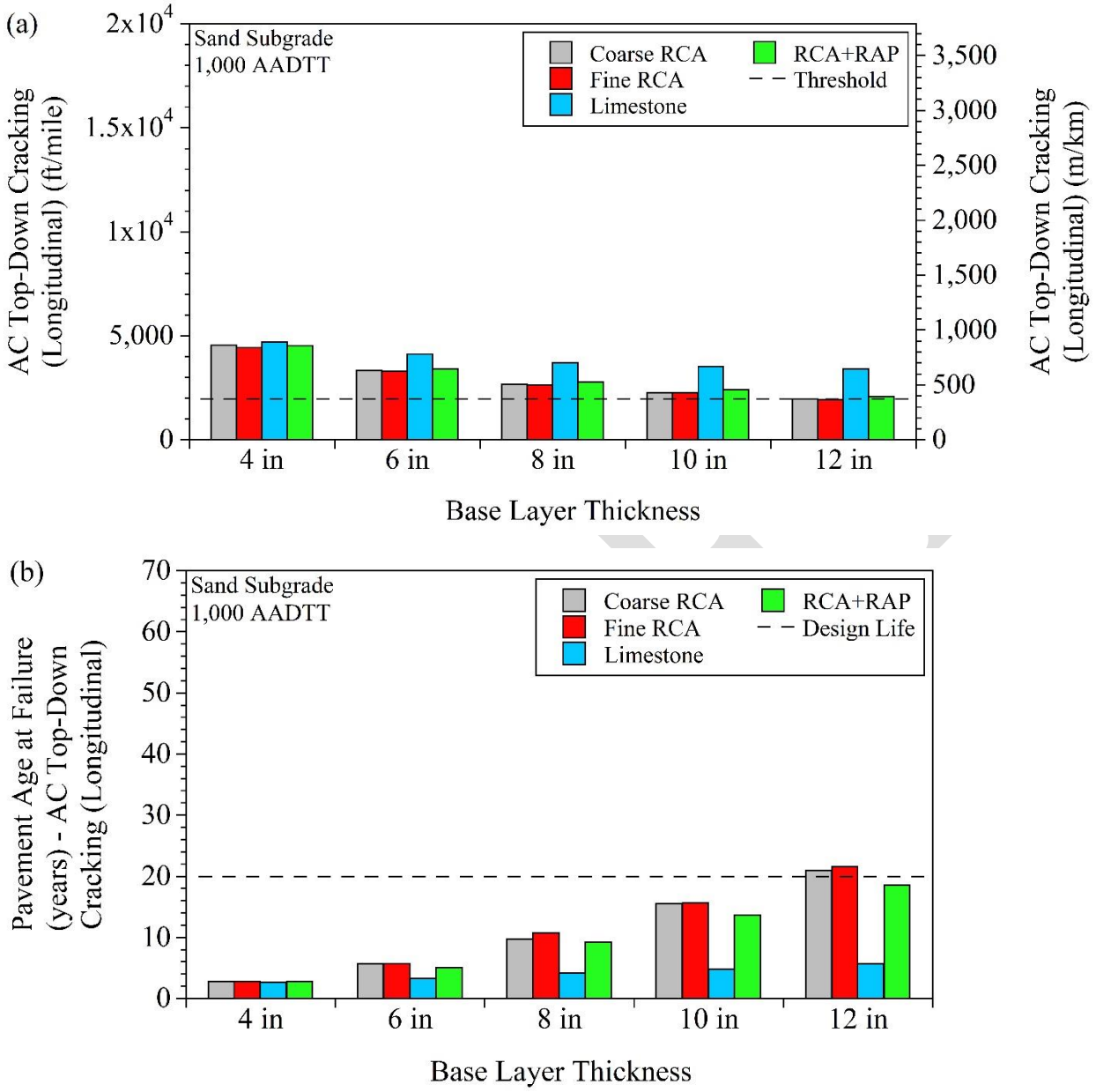


Figure 5.10. Effect of base layer aggregate type on (a) longitudinal cracking at the end of the design life (20 years) and (b) pavement age at longitudinal cracking failure

5.2.5. Layer Rutting at 50% Reliability

Layer rutting for asphalt, base+subbase, and subgrade layers was also evaluated at 50% reliability (Pavement ME can only give 50% reliability for layer rutting). For asphalt layer rutting, the asphalt layers overlying limestone base layers (at different thicknesses) provided slightly higher asphalt rutting. However, overall, it could be said that no significant difference was observed among the asphalt layers placed on coarse RCA, fine RCA, limestone, and RCA+RAP base layers (at different thicknesses) in the modeling results.

For base+subbase layer rutting, overall, limestone base+select granular borrow subbase layers yielded higher rutting than the other base+subbase layers (for each base layer thickness). For subgrade layer rutting, the sand subgrade layers underlying limestone base+select granular borrow subbase layers yielded slightly lower rutting. Figures 5.11, 5.12, and 5.13 are examples that show the asphalt, base+subbase, and subgrade rutting for the pavement models that contained sand subgrade layers and were subjected to 1,000 AADTT. More results for other pavement modeling results are provided in Appendix V.

As expected, it was observed from the model results that the highest amount of layer rutting was observed in subgrade layers. In addition, increasing the aggregate base layer thickness increased the base+subbase rutting overall. However, it should be kept in mind that the higher rutting in thicker layers does not mean that the thicker layer's performance is lower than the thinner layer's performance. Figure 5.14 is an example that shows total, asphalt, base+subbase, and subgrade rutting for the pavement models that contained sand subgrade and coarse RCA base layers and were subjected to 1,000 AADTT (more results for other pavement models are provided in Appendix W). As can be seen in Figure 5.14, although there was a slight increase in base+subbase layer rutting with an increase in the base layer thickness, the subgrade layer rutting reduced significantly. These are the model results. However, in real life, a similar result would be observed because increased base layer thickness tends to improve the load distribution mechanism and reduce the amount of loads that are applied on the subgrade layers. Reduced loading on subgrade layers yields lower subgrade rutting. Since subgrade layer rutting is the major contributor to the total pavement rutting, reduced subgrade layer rutting reduces total rutting.

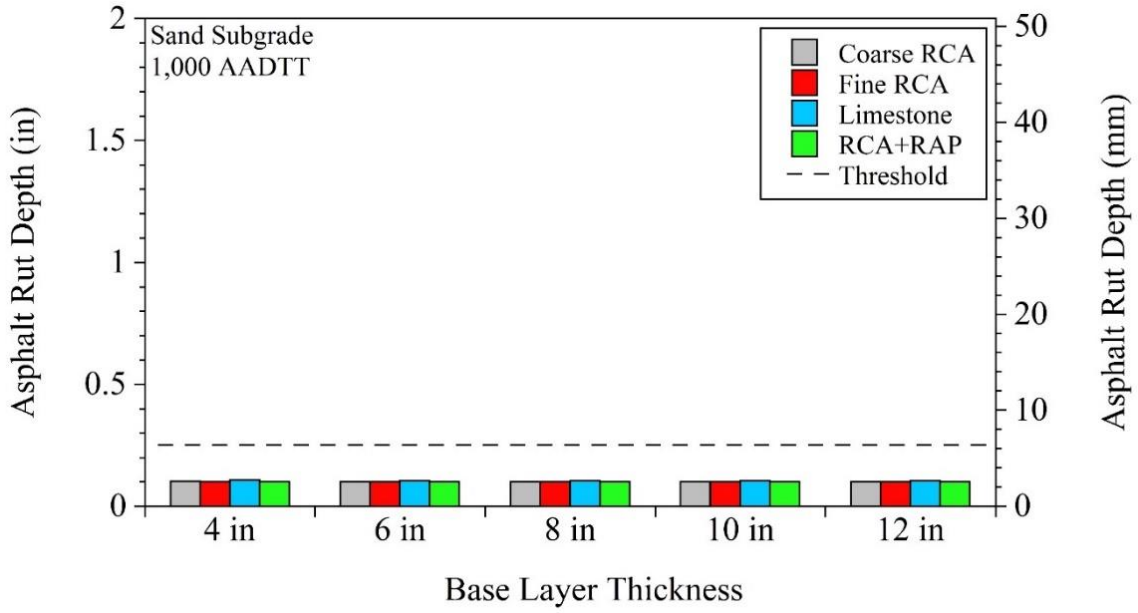


Figure 5.11. Asphalt rut depths (at 50% reliability) for the pavement models that contained sand subgrade and were subjected to 1,000 AADTT

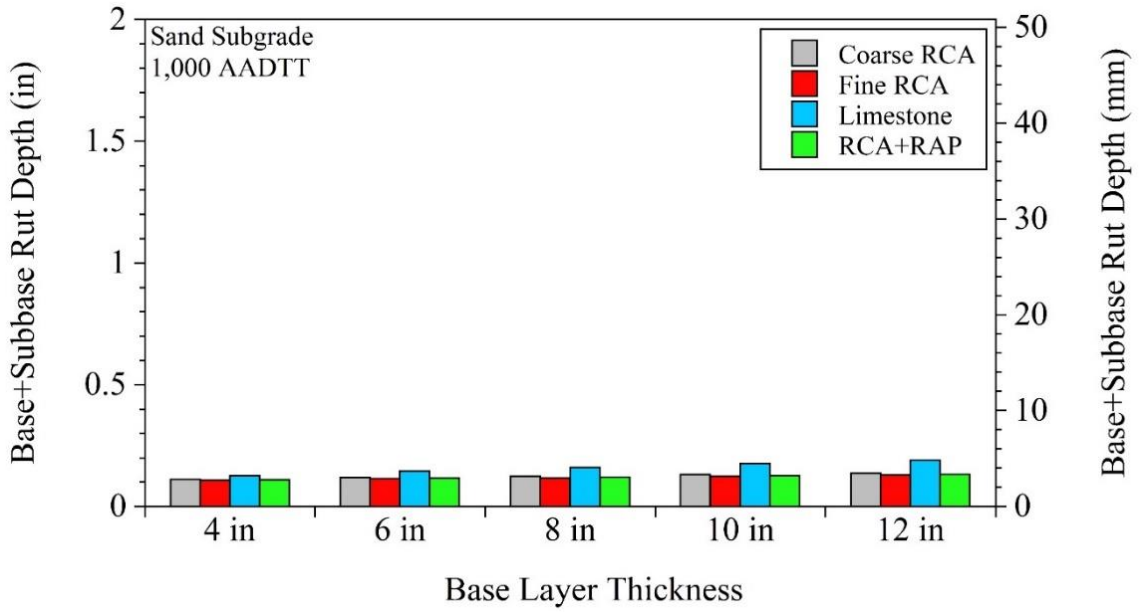


Figure 5.12. Base+subbase rut depths (at 50% reliability) for the pavement models that contained sand subgrade and were subjected to 1,000 AADTT

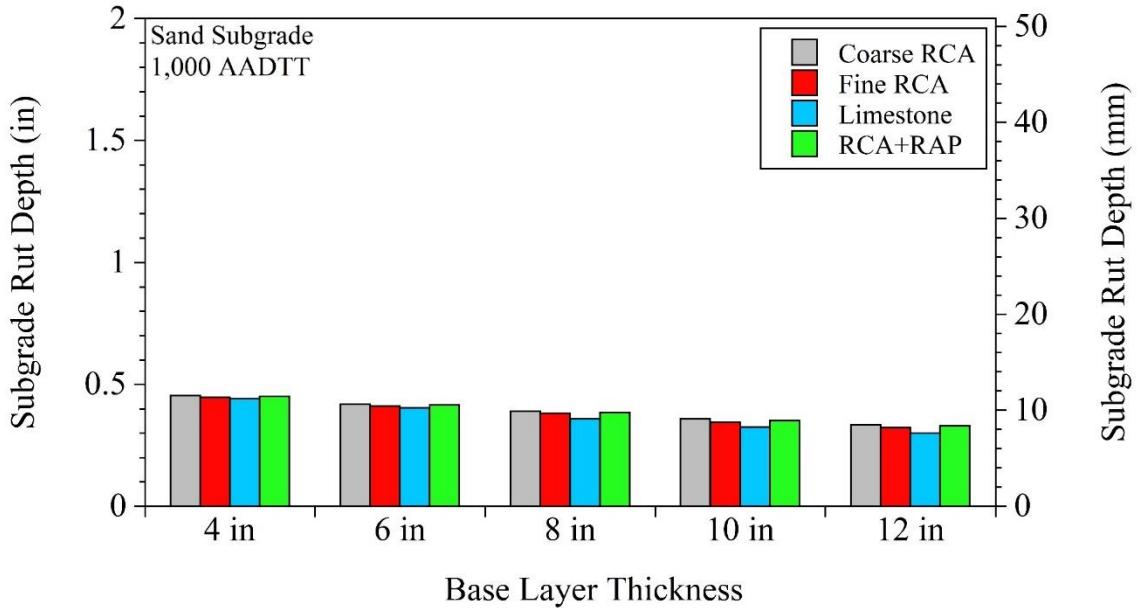


Figure 5.13. Subgrade rut depths (at 50% reliability) for the pavement models that contained sand subgrade and were subjected to 1,000 AADTT

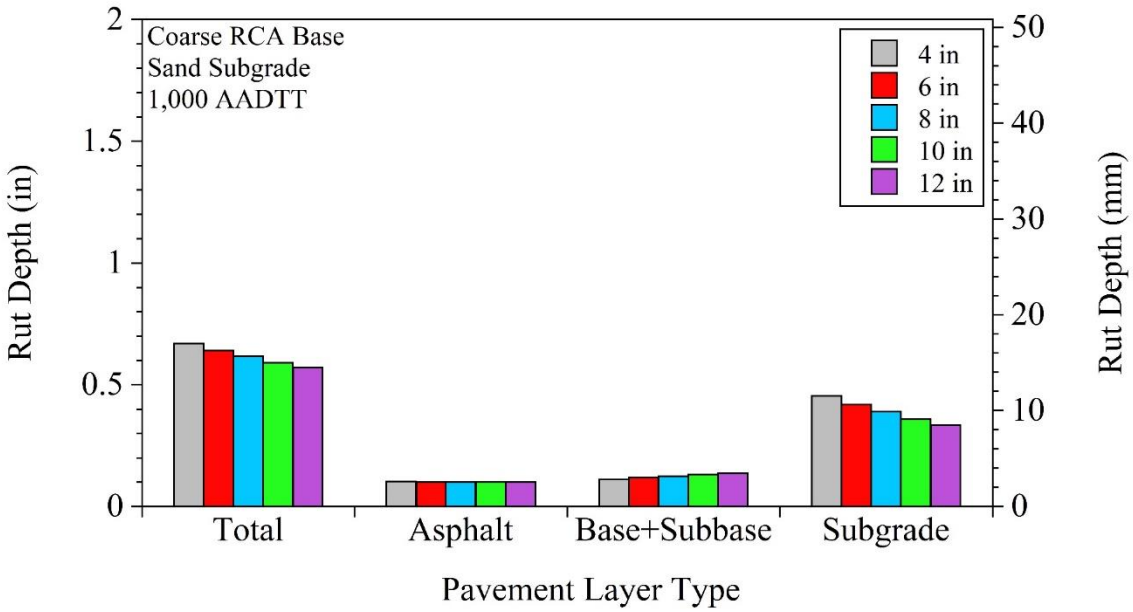


Figure 5.14. Total and layer rut depths (at 50% reliability) for the pavement models that contained sand subgrade and coarse RCA base layers and were subjected to 1,000 AADTT

5.2.6. Effect of Traffic Levels on Pavement Performance Prediction Models

As stated previously, five different traffic levels were applied to the models (Table 5.5). Overall, as expected, increasing the AADTT level yielded greater pavement distresses and shorter pavement service life. Performance prediction models exhibited that while acceptable pavement distresses and service lives were obtained at 100, 500, and 1,000 AADTT levels (low traffic), excessive failures occurred at 7,500 (medium traffic) and 25,000 (high traffic) AADTT levels (Table 5.5). Since the test cells were located in the MnROAD LVR and were designed as low volume road sections, it could be concluded that the model results complied with the actual case. Figures 5.15, 5.16, 5.17, and 5.18 are examples that show the effect of traffic levels on IRI, rutting, alligator cracking, and longitudinal cracking, respectively, for pavement models that contained sand subgrade layers and 12-in aggregate base layers. More results for other pavement models are provided in Appendix X.

DRAFT

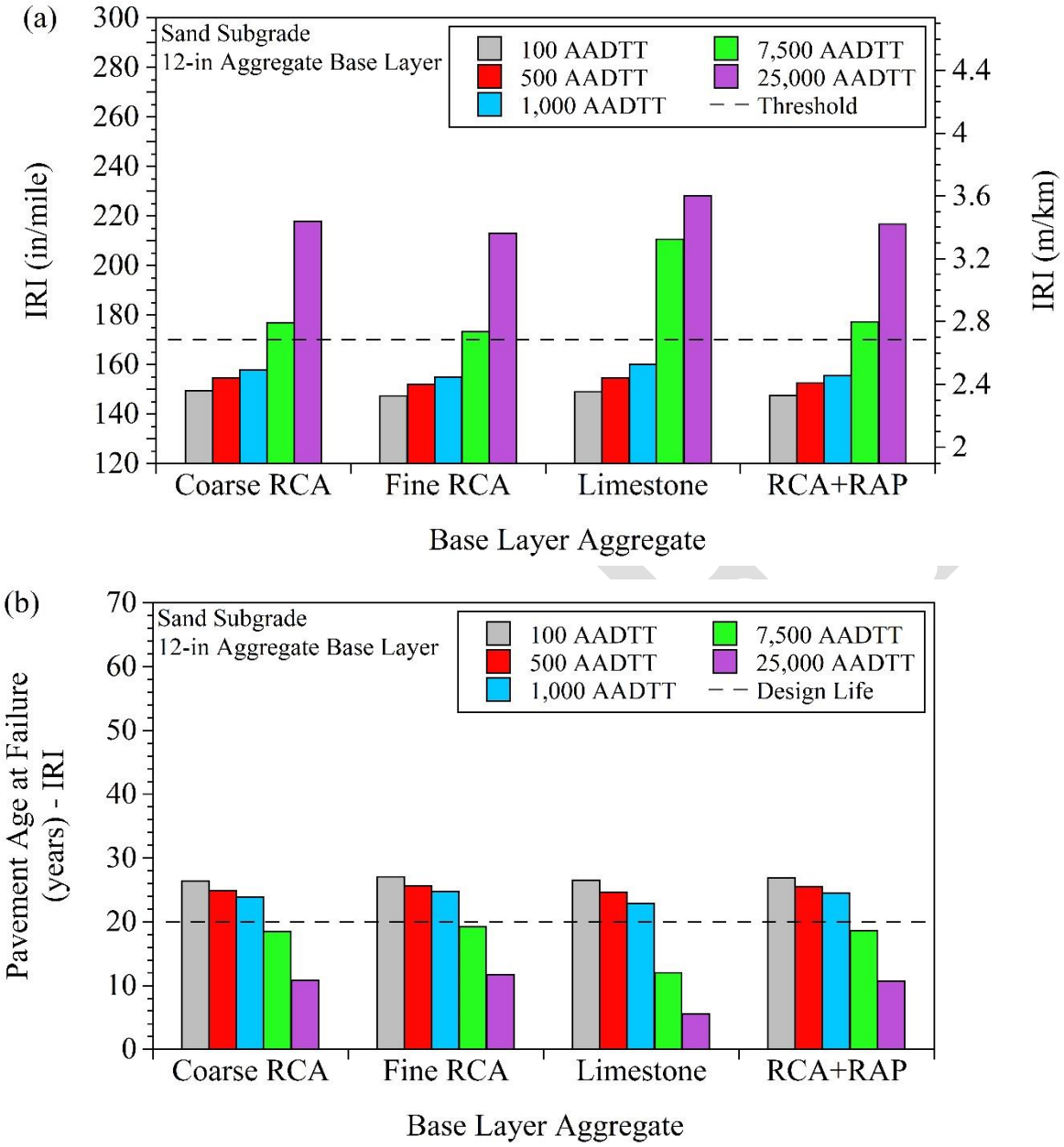


Figure 5.15. Effect of traffic level on (a) IRI at the end of the design life (20 years) and (b) pavement age at IRI failure

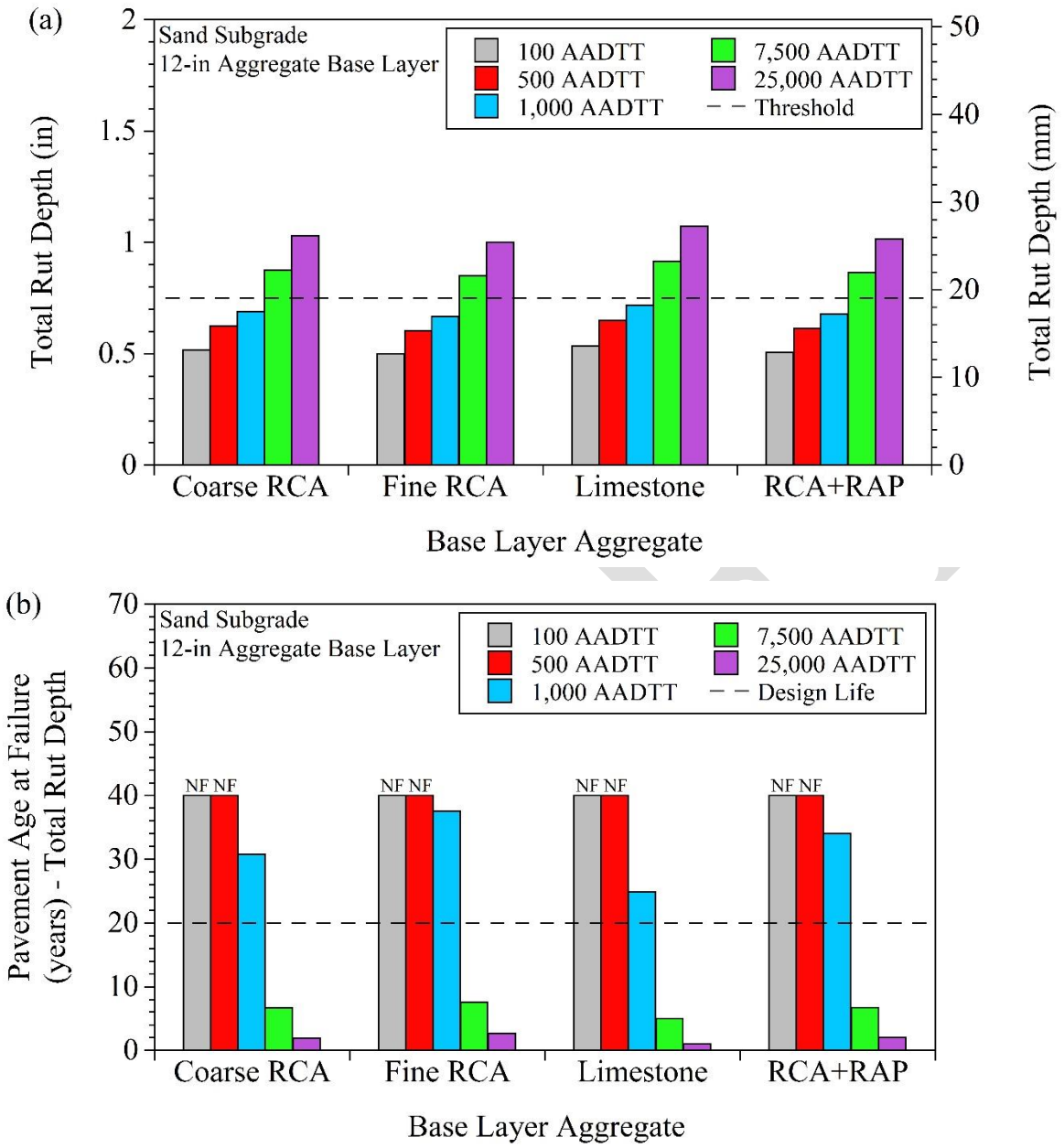


Figure 5.16. Effect of traffic level on (a) rutting at the end of the design life (20 years) and (b) pavement age at rutting failure (NF = no failure)

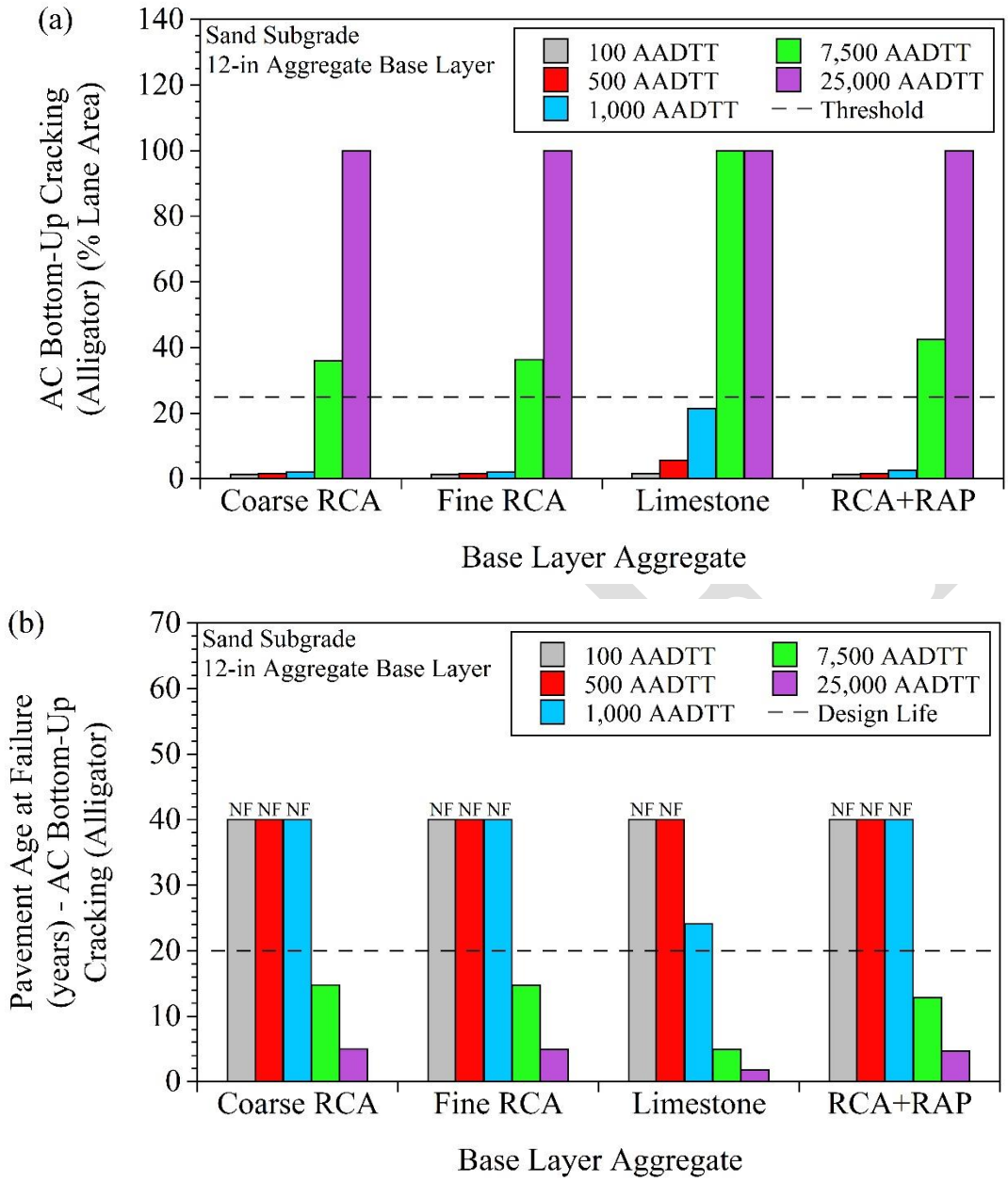


Figure 5.17. Effect of traffic level on (a) alligator cracking at the end of the design life (20 years) and (b) pavement age at alligator cracking failure (NF = no failure)

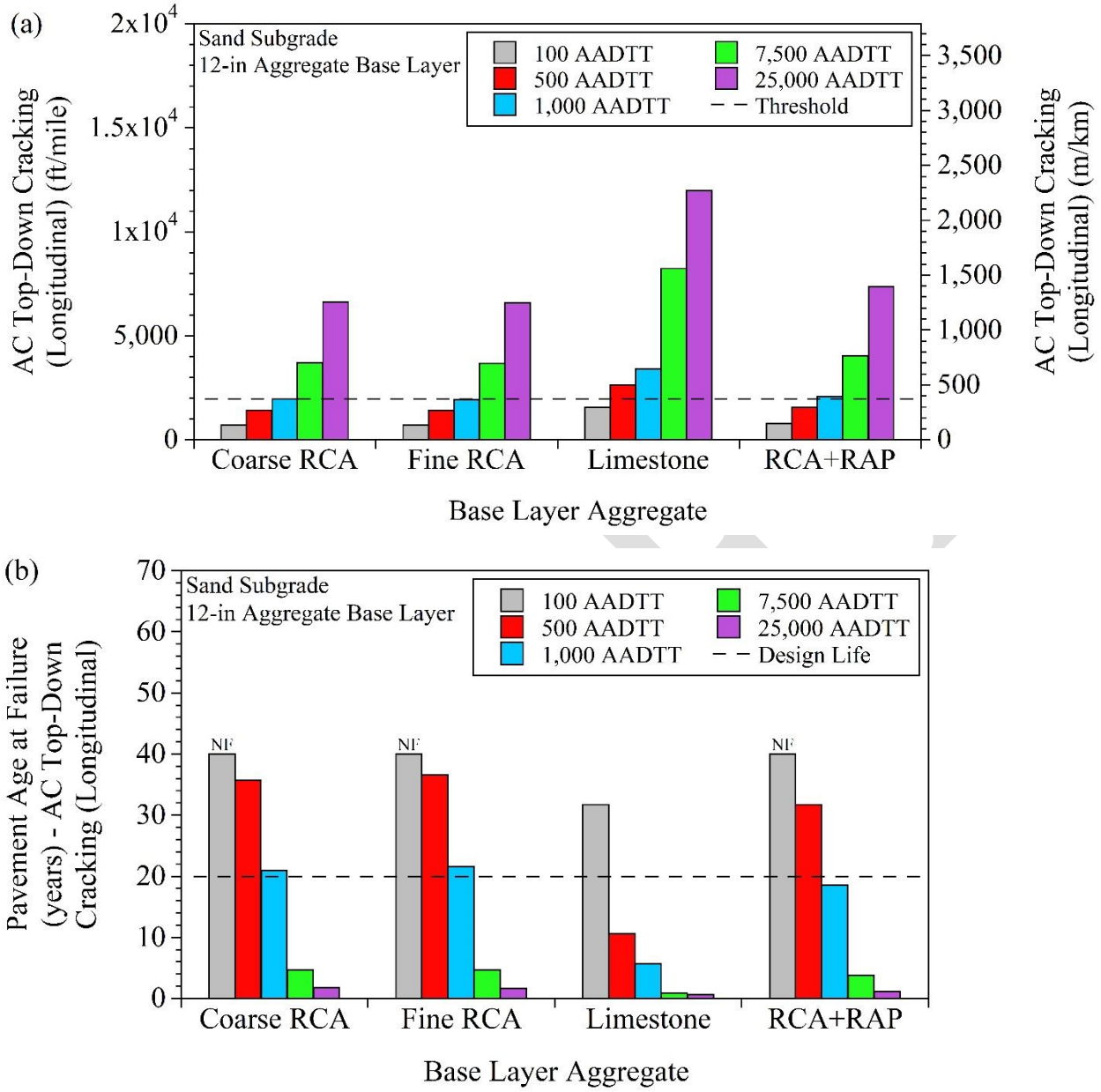


Figure 5.18. Effect of traffic level on (a) longitudinal cracking at the end of the design life (20 years) and (b) pavement age at longitudinal cracking failure (NF = no failure)

5.2.7. Recycled Aggregate Base (RAB) Layer Thicknesses Alternative to 12-in Limestone Base Layer

To make thickness recommendations for RAB layers constructed with coarse RCA, fine RCA, and RCA+RAP, the pavement performance prediction models for the pavements that contained 12-in limestone base layer were compared to those for the pavements that contained RAB layers at different thicknesses (ranging from 4 in to 12 in). Since it was previously discussed that AADTT levels of 7,500 and 25,000 yielded excessive pavement distresses and the overall designs of the pavement models were more suitable for lower traffic levels, comparisons were made only for the pavement models that were subjected to low traffic levels [100, 500, and 1,000 AADTT (Table 5.5)].

Overall, based on the models, it was concluded that thinner RAB layers (4, 6, 8, or 10 in) could be constructed with coarse RCA, fine RCA, or RCA+RAP materials instead of constructing a 12-in limestone base layer. This was mainly due to the input SM_R values used for coarse RCA (18,129 psi), fine RCA (17,760.9 psi), and RCA+RAP (16,487.7 psi) base layers all of which were higher than those used for limestone base layers (13,926.3 psi). Figures 5.19, 5.20, 5.21, and 5.22 are examples that show relative aggregate base (RAB) layer thicknesses as alternatives to 12-in limestone base layers in terms of IRI, rutting, alligator cracking, and longitudinal cracking, respectively [for pavement models that contained sand subgrade layers and were subjected to 1,000 AADTT]. More results for other pavement models are provided in Appendix Y. A summary of all RAB layer thicknesses alternative to 12-in limestone base layer based on different pavement distresses is provided in Table 5.7.

Based on the IRI predictions, while the input SM_R value used for coarse RCA (18,129 psi) was higher than those used for fine RCA (17,760.9 psi) and RCA+RAP (16,487.7 psi), the model results showed that the fine RCA and RCA+RAP base layers could be even thinner than coarse RCA base layers (Table 5.7). This demonstrated that not only the input SM_R value, but also other input parameters (e.g., K_{sat} and gradation) could be important for the determination of the base layer design thickness. Based on rutting predictions, similar alternative RAB thicknesses (10 in) were determined for the sections built with RAB layers on sand subgrade layers. However, for the RAB layers overlying clay loam subgrade layers, rutting predictions showed that fine RCA and RCA+RAP base layers could be 4-in thick and coarse RCA base layer could be 6-in thick. Based on alligator cracking predictions, the alternative RAB layer thicknesses were 4 in. Lastly, based on longitudinal cracking predictions, while 6 in was the alternative layer thickness for coarse RCA and fine RCA base layers, it was 8 in for RCA+RAP base layers.

DRAFT

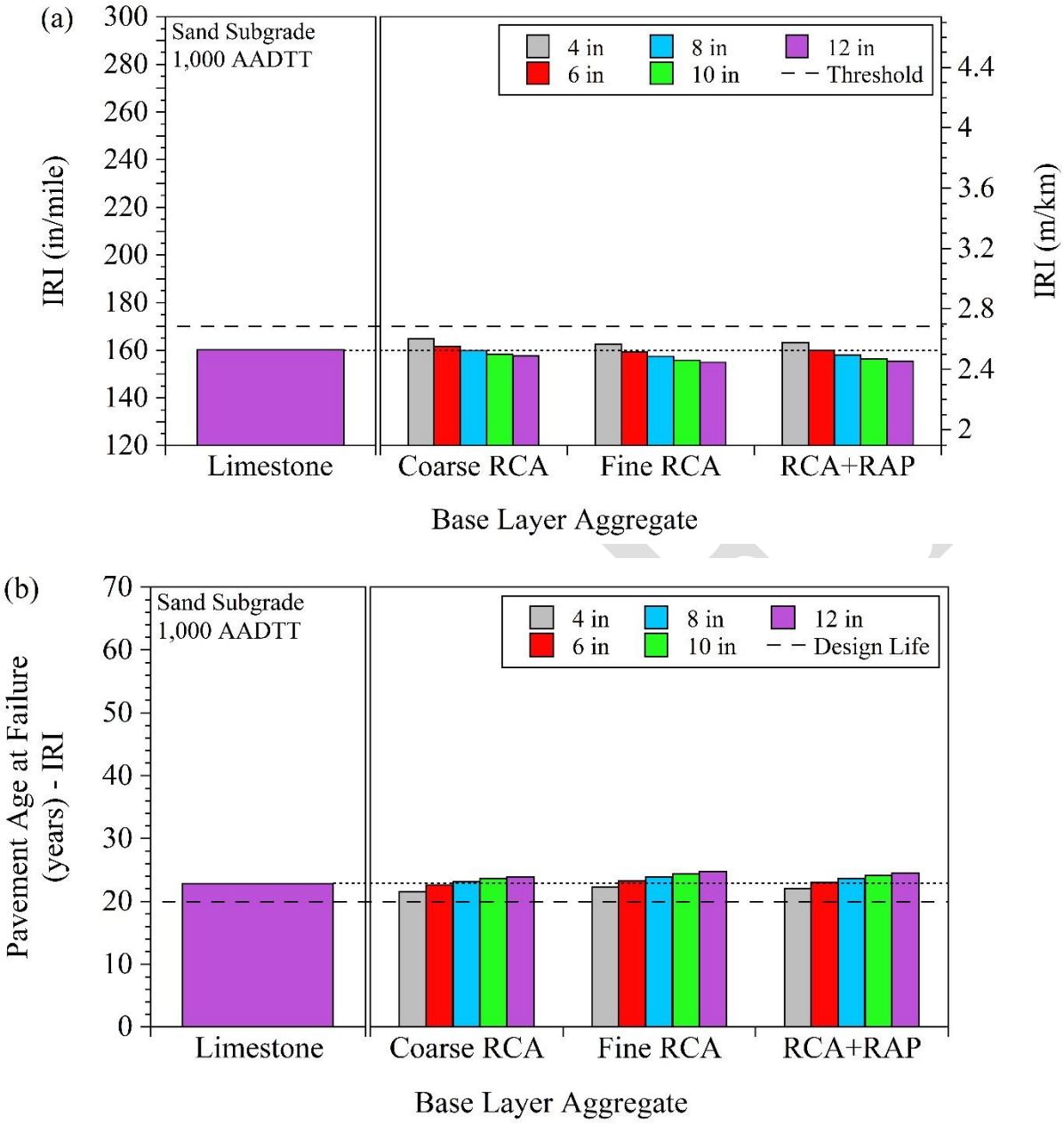


Figure 5.19. Relative aggregate base (RAB) layer thicknesses alternative to 12-in limestone base layer in terms of (a) IRI at the end of the design life (20 years) and (b) pavement age at IRI failure

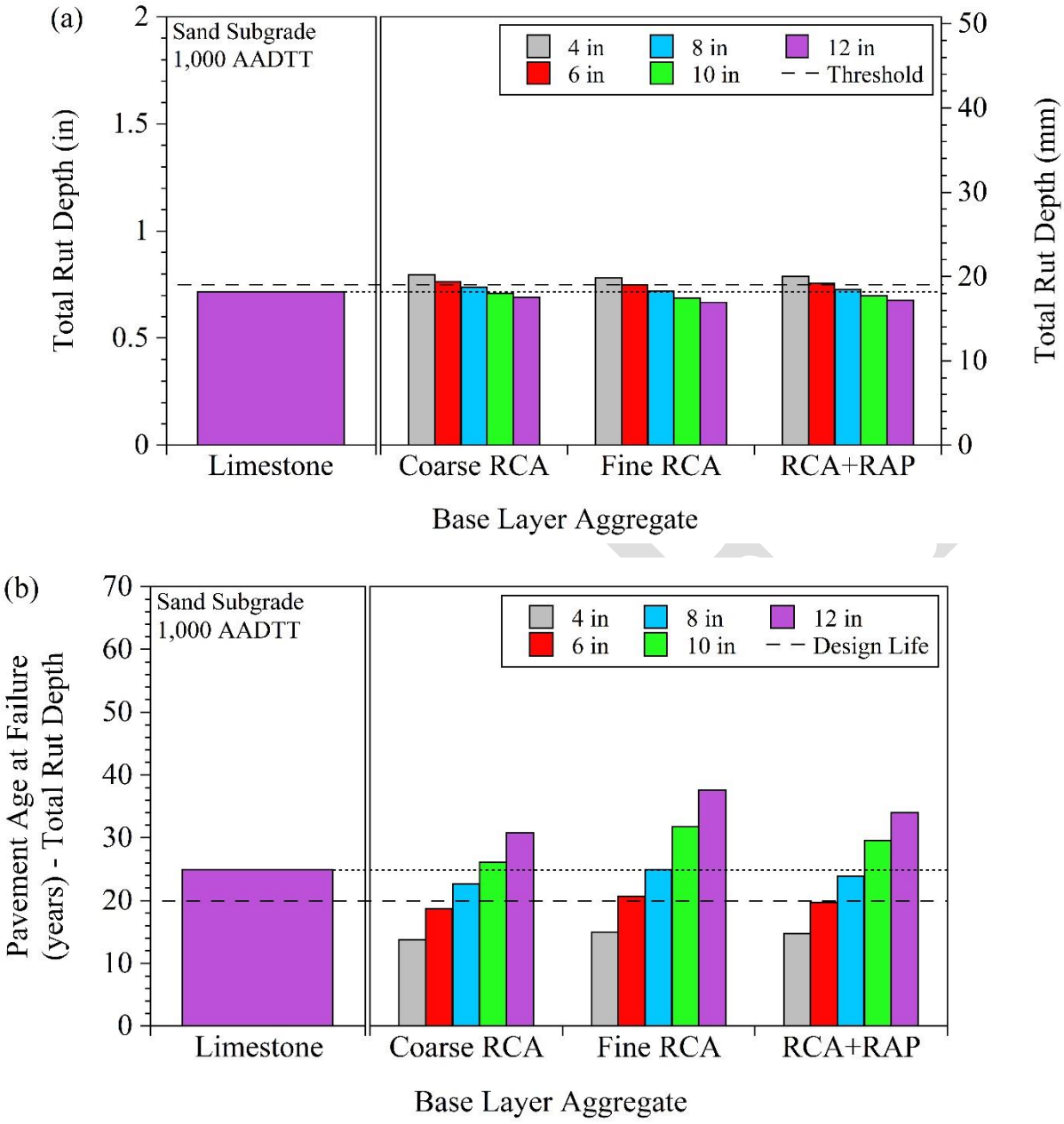


Figure 5.20. Relative aggregate base (RAB) layer thicknesses alternative to 12-in limestone base layer in terms of (a) rutting at the end of the design life (20 years) and (b) pavement age at rutting failure

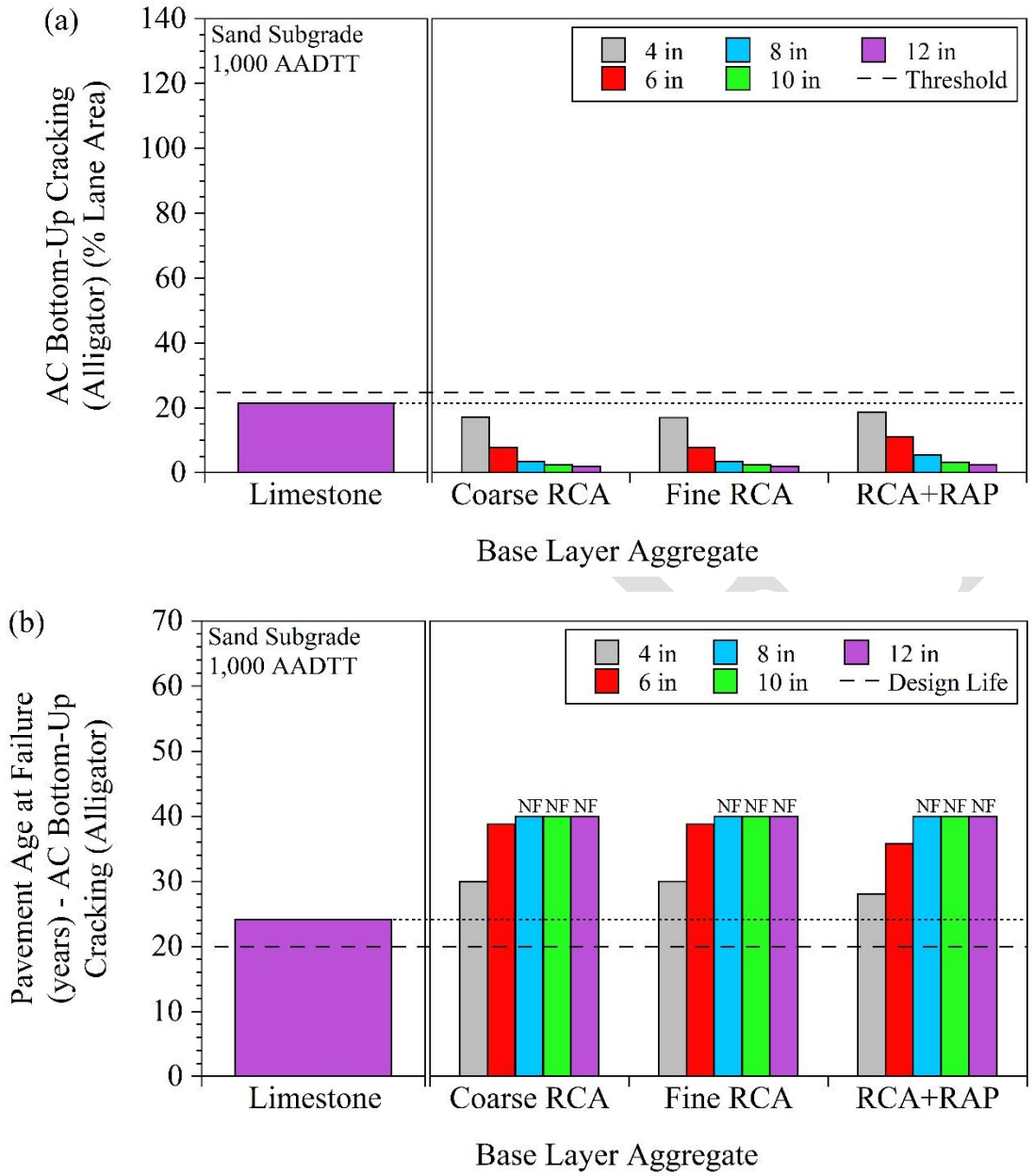


Figure 5.21. Relative aggregate base (RAB) layer thicknesses alternative to 12-in limestone base layer in terms of (a) alligator cracking at the end of the design life (20 years) and (b) pavement age at alligator cracking failure (NF = no failure)

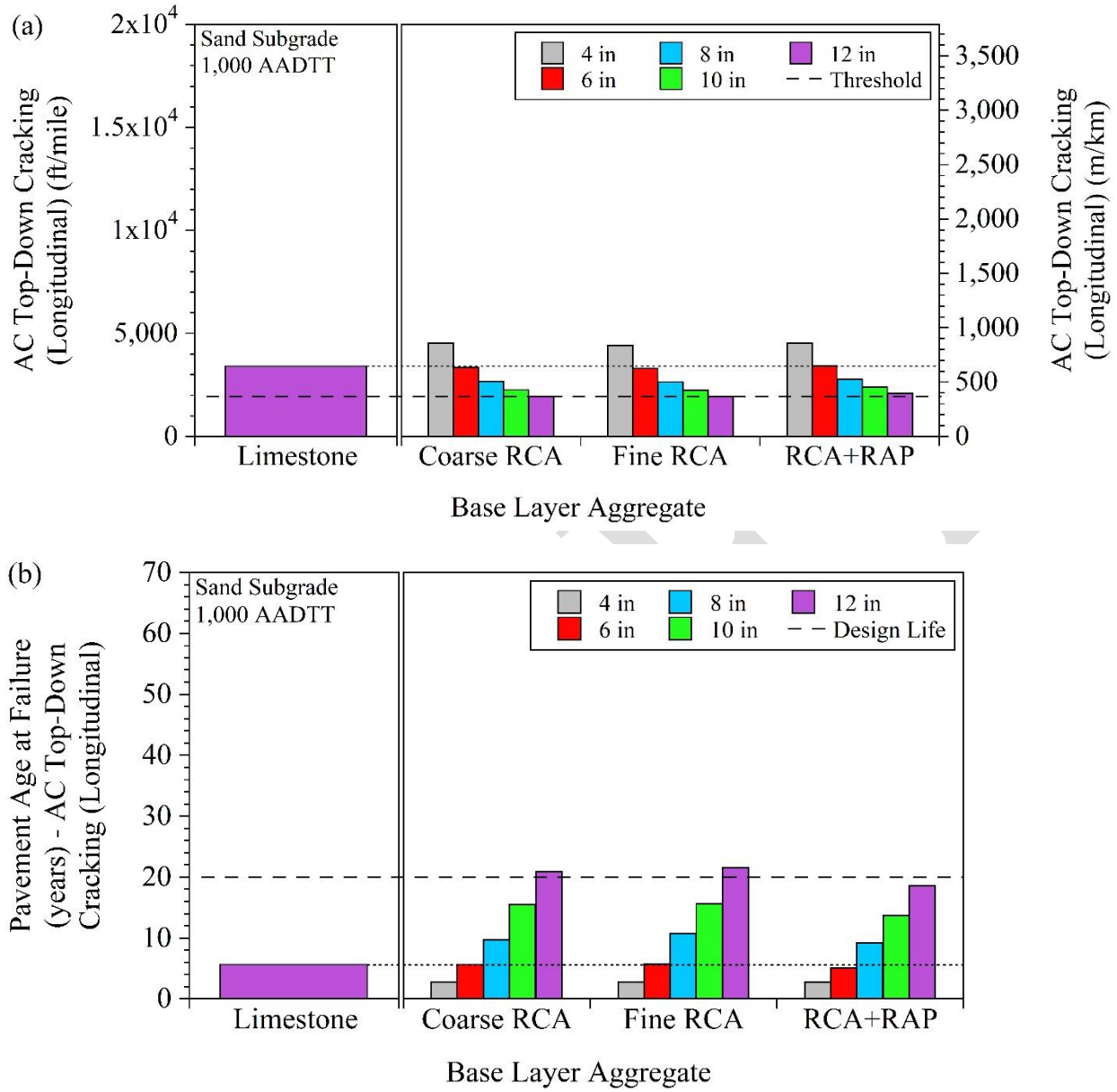


Figure 5.22. Relative aggregate base (RAB) layer thicknesses alternative to 12-in limestone base layer in terms of (a) longitudinal cracking at the end of the design life (20 years) and (b) pavement age at longitudinal cracking failure

Table 5.7. Summary of RAB layer thicknesses alternative to 12-in limestone base layer

AADTT Level	Recycled Aggregate Base (RAB) Layer Thickness Alternative to 12-in Limestone (in)							
	Alter-native Material	Based on IRI		Based on Rutting		Based on Alligator Cracking		Based on Longitudinal Cracking
		Sand Subgrade	Clay Loam Subgrade	Sand Subgrade	Clay Loam Subgrade	Sand Subgrade	Clay Loam Subgrade	Sand Subgrade
100	Coarse RCA	12	10	10	6	4	4	6
	Fine RCA	10	6	10	4	4	4	6
	RCA+ RAP	10	4	10	4	4	4	8
500	Coarse RCA	12	8	10	6	4	4	6
	Fine RCA	8	6	10	4	4	4	6
	RCA+ RAP	8	6	10	4	4	4	8
1,000	Coarse RCA	8	6	10	6	4	4	6
	Fine RCA	6	6	10	4	4	4	6
	RCA+ RAP	6	4	10	4	4	4	8

AADTT = average annual daily truck traffic; IRI = international roughness index

5.3. Large Stone Subbase (LSSB) Groups

5.3.1. Large Stone Subbase (LSSB) Layer Design

In the MnROAD LVR test facility, LSSB layers were constructed at two different thicknesses: (1) 18-in LSSB layers (cells 127 and 227) and (2) 9-in LSSB layers (cells 328-728). To evaluate the effect of the LSSB layer thickness on pavement performance prediction models in Pavement ME, 12-in LSSB and 15-in LSSB layers were also modeled in addition to the original LSSB layer thicknesses (18 in and 9 in). In addition, as can be seen in Figure 1.1 for the LSSB groups, while cells 127 and 227 (18-in LSSB) contained class 6 aggregate base layers, cells 328-728 (9-in LSSB) contained class 5Q aggregate base layers. In Pavement ME, first, 6-in class 6 aggregate base layers were placed on top of the LSSB layers [asphalt layer thicknesses were kept as original (3.5 in), and similar clay loam subgrade layers were used]. Then, 6-in class 5Q aggregate base layers were placed on top of the LSSB layers. Figure 5.23 is an example that shows different LSSB layer thicknesses that were modeled on top of the clay loam subgrade layers.

DRAFT

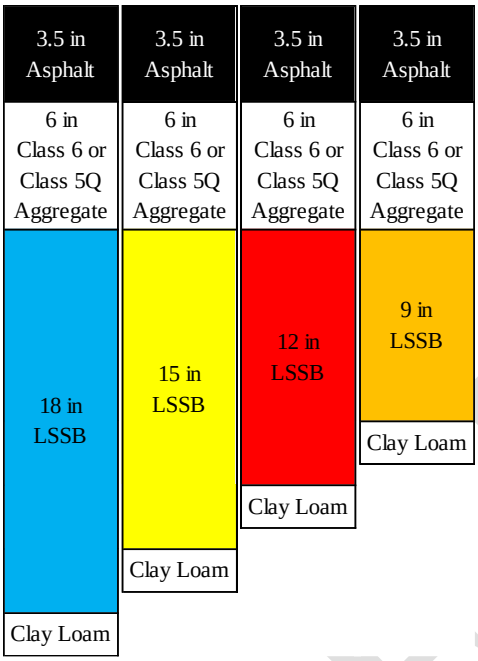


Figure 5.23. Pavement ME models for LSSB layers at different layer thicknesses

5.3.2. Material Inputs

Similar to the RAB group, Superpave PG 58-34 was selected (level 3) to model the 3.5-in asphalt layers. Appendix R provides detailed information about level 3 parameters for the modeled asphalt layer. Table 5.8 summarizes the input parameters (level 2) for aggregate base, LSSB, and clay loam subgrade layers that were used in the models.

For each pavement sublayer, the coefficient of lateral earth pressure (K_0) was kept at its default value (0.5). Since no laboratory M_R tests were performed for class 6 aggregate and class 5Q aggregate, the equations were found to estimate the SM_R for coarse RCA, fine RCA, limestone, and RCA+RAP (Table 3.9 and Appendix L) were used for class 6 aggregate and class 5Q aggregate to estimate their SM_R values (Appendix S). After using the equations suitable to estimate the SM_R values of class 6 aggregate and class 5Q aggregate, the median SM_R values (16,478.9 psi and 18,651.1 psi for class 6 aggregate and class 5Q aggregate, respectively) were determined and compared with the SM_R values of coarse RCA (18,129 psi), fine RCA (17,760.9 psi), limestone (13,926.3 psi), and RCA+RAP (16,487.7 psi). Since the comparison showed that the estimated SM_R values of class 6 aggregate (16,478.9 psi) and class 5Q aggregate (18,651.1 psi) were in an acceptable range, they were used in the modeling analyses (Table 5.8).

For the SM_R of LSSB layers, based on the literature, three SM_R levels were used in the modeling analyses: (1) 10,000 psi, (2) 30,000 psi, and (3) 50,000 psi. MDD, K_{sat}, and OMC values for the LSSB layers were not user-defined, and their values, provided by the Pavement ME program during level 2 analysis, were used for LSSB (80 pcf for MDD, 1.18E+03 ft/hr for K_{sat}, and 0% for OMC). The input parameters for clay loam subgrade layers were identical to those used in the models created for the RAB group. Lastly, as described previously, the SWCC characteristics of the materials were determined by the van Genuchten model (van Genuchten 1980) [Equation (5)] in this study. Since the Pavement ME program uses the Fredlund and Xing (1994) SWCC model,

DRAFT

the SWCC inputs [a_f, b_f, c_f, h_r fitting parameters (Fredlund and Xing 1994)] were not user-defined for class 6 aggregate, class 5Q aggregate, and clay loam subgrade (no matric suction would be expected for LSSB due to the presence of large stones).

Table 5.8. Material inputs used for pavement sublayers in Pavement ME models

Parameter		Class 6 Aggregate Base	Class 5Q Aggregate Base	LSSB	Clay Loam Subgrade
AASHTO Classification		A-1-a	A-1-a	A-1-a	A-6
Poisson's Ratio		0.35	0.35	0.35	0.4
M_R (psi)		16,478.9[#]	18,651.1[#]	10,000 psi[+] 30,000 psi[+] 50,000 psi[+]	8,630.9
LL		27.4	0	0	36.3
PI		0	0	0	12.4
Corrected MDD (pcf)		128.5	128	80*	124.9
K_{sat} (ft/hr)		2.26E-02	3.44E-02	1.18E+03*	1.62E-05
Combined OD G_s		2.35	2.28	2.60	2.68
Corrected OMC (%)		8.3	9.6	0*	10
Percent Passing (%)	No. 200	6.3	3.2	0.1	59.7
	No. 100	9.3	4.8	0.1	68.9
	No. 60	14.6	6.8	0.2	77.6
	No. 40	23.9	10.4	0.2	84.6
	No. 20	37.1	15.8	0.3	90.1
	No. 10	49.3	22.8	0.4	94
	No. 4	64.9	34.1	0.4	96.9
	3/8 in	79.9	48.4	0.9	98.4
	3/4 in	98.3	76.1	6.3	99.4
	1 in	100	89.3	13.1	99.5
	1 1/2 in	100	100	35.8	100
	2 in	100	100	70.2	100
	2.5 in	100	100	96.9	100
	3 in	100	100	100	100

M_R = resilient modulus; LL = liquid limit; PI = plasticity index; MDD = maximum dry density; K_{sat} = saturated hydraulic conductivity; OD = oven-dry; G_s = specific gravity; OMC = optimum moisture content. To determine the combined G_s values, the weighted average of the G_s values of the coarse [> No. 4 sieve (4.75 mm)] and fine (< No. 4) fractions of the materials were used.

[#]Determined based on the M_R models developed in this study (Table 3.9, and Appendices L and S)

[*]Not user-defined (level 2)

[+]Estimated based on the literature to provide a wide range of M_R values

DRAFT

5.3.3. Effect of Large Stone Subbase (LSSB) Thickness on Pavement Performance Prediction Models

As stated previously, LSSB layer thicknesses ranging between 9 in and 18 in were used in the modeling analyses (Figure 5.2) to evaluate the effect of the LSSB layer thickness on long-term pavement performance predictions. For IRI, no consistent trend was observed between the IRI predictions and LSSB layer thickness. On the other hand, increasing the LSSB layer thickness generally decreased rutting and alligator cracking at the end of the pavement design life (20 years). Figures 5.24, 5.25, and 5.26 are examples that show the effect of the LSSB thickness on IRI, rutting, and alligator cracking, respectively, for the pavement models that contained class 6 aggregate base layers and were subjected to 1,000 AADTT. More results for other pavement modeling analyses are provided in Appendix Z.

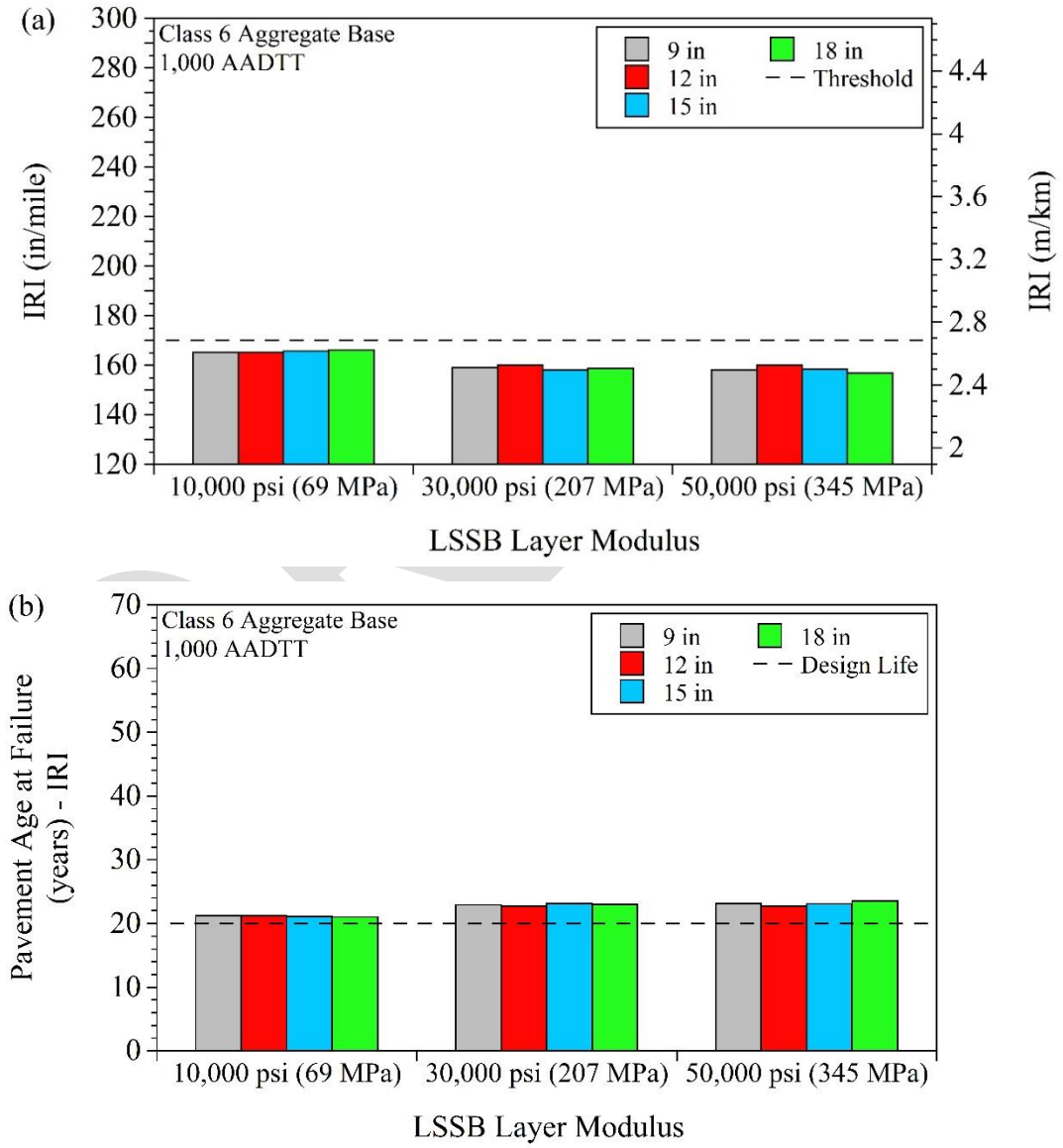


Figure 5.24. Effect of LSSB layer thickness on (a) IRI at the end of the design life (20 years) and (b) pavement age at IRI failure

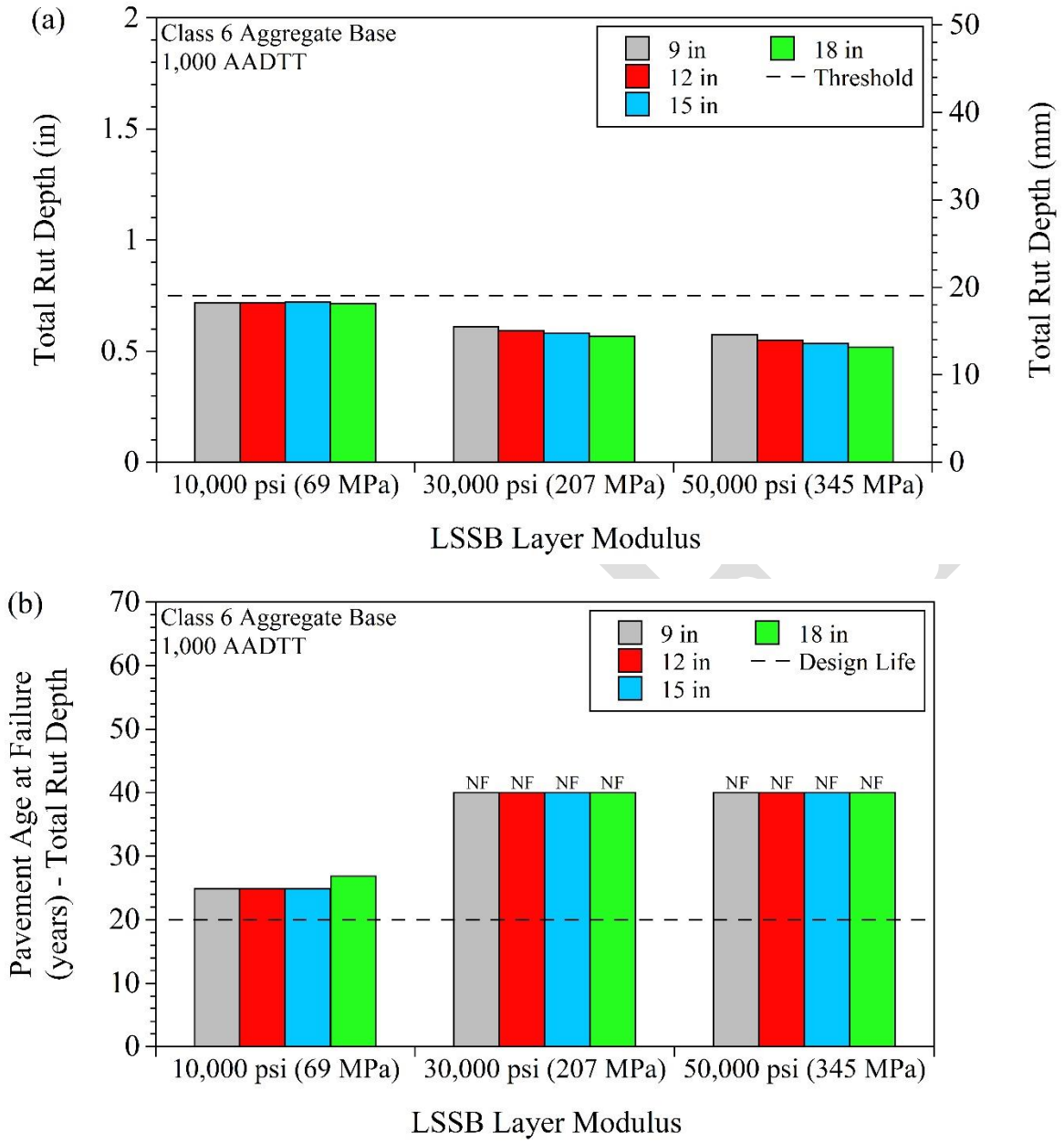


Figure 5.25. Effect of LSSB layer thickness on (a) rutting at the end of the design life (20 years) and (b) pavement age at rutting failure (NF = no failure)

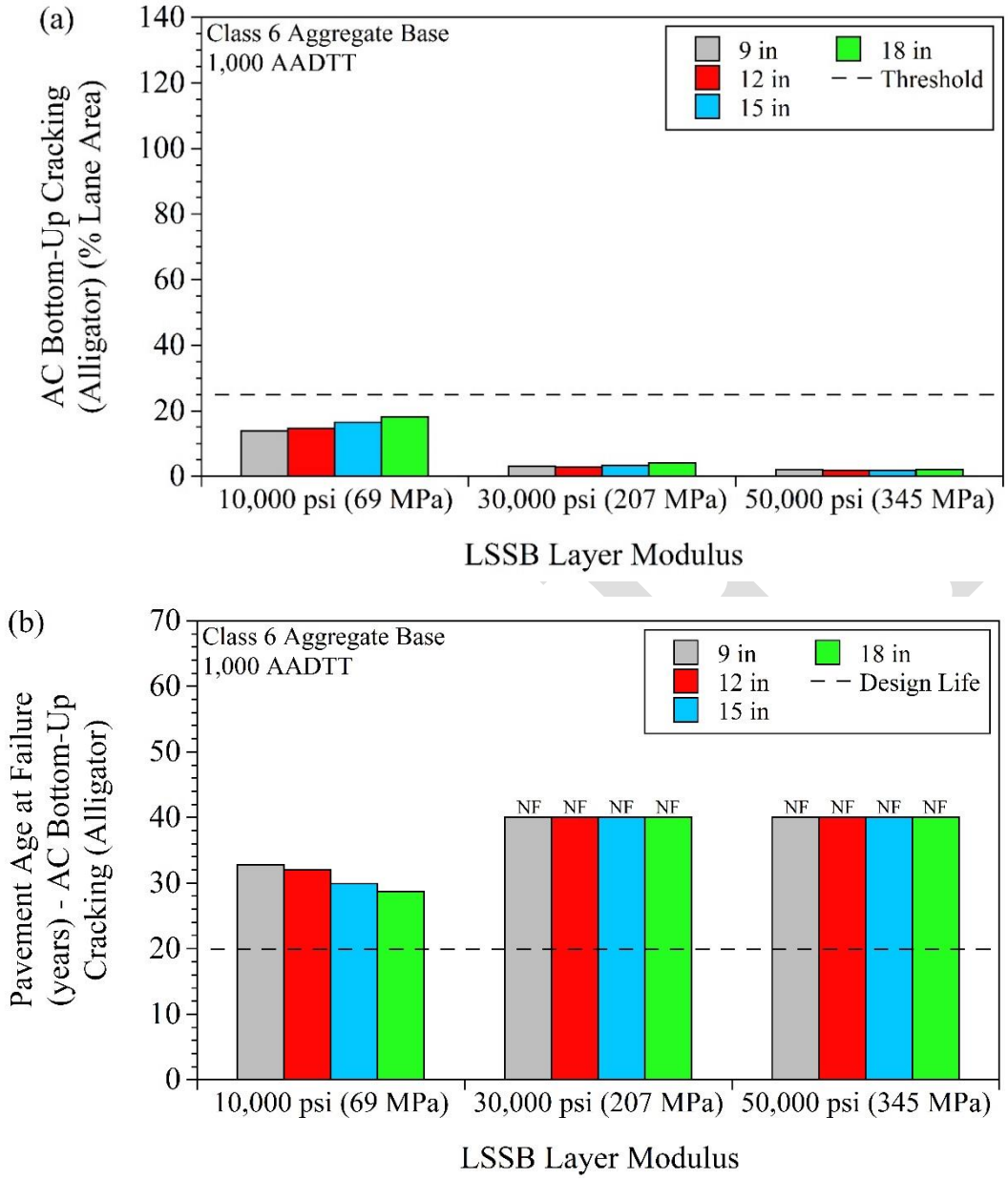


Figure 5.26. Effect of LSSB layer thickness on (a) alligator cracking at the end of the design life (20 years) and (b) pavement age at alligator cracking failure (NF = no failure)

5.3.4. Effect of Large Stone Subbase (LSSB) Stiffness on Pavement Performance Prediction Models

As stated previously, three different SM_R values were used in the models for LSSB: (1) 10,000 psi, (2) 30,000 psi, and (3) 50,000 psi. Overall, it was concluded that increasing the LSSB SM_R value resulted in lower pavement distress at the end of the pavement design life (20 years) and an increase in pavement service life. Figures 5.27, 5.28, and 5.29 are examples that show the effect of LSSB M_R on IRI, rutting, and alligator cracking, respectively, for the pavement models that contained class 6 aggregate base layers and were subjected to 1,000 AADTT. More results for other pavement modeling analyses are provided in Appendix AA.

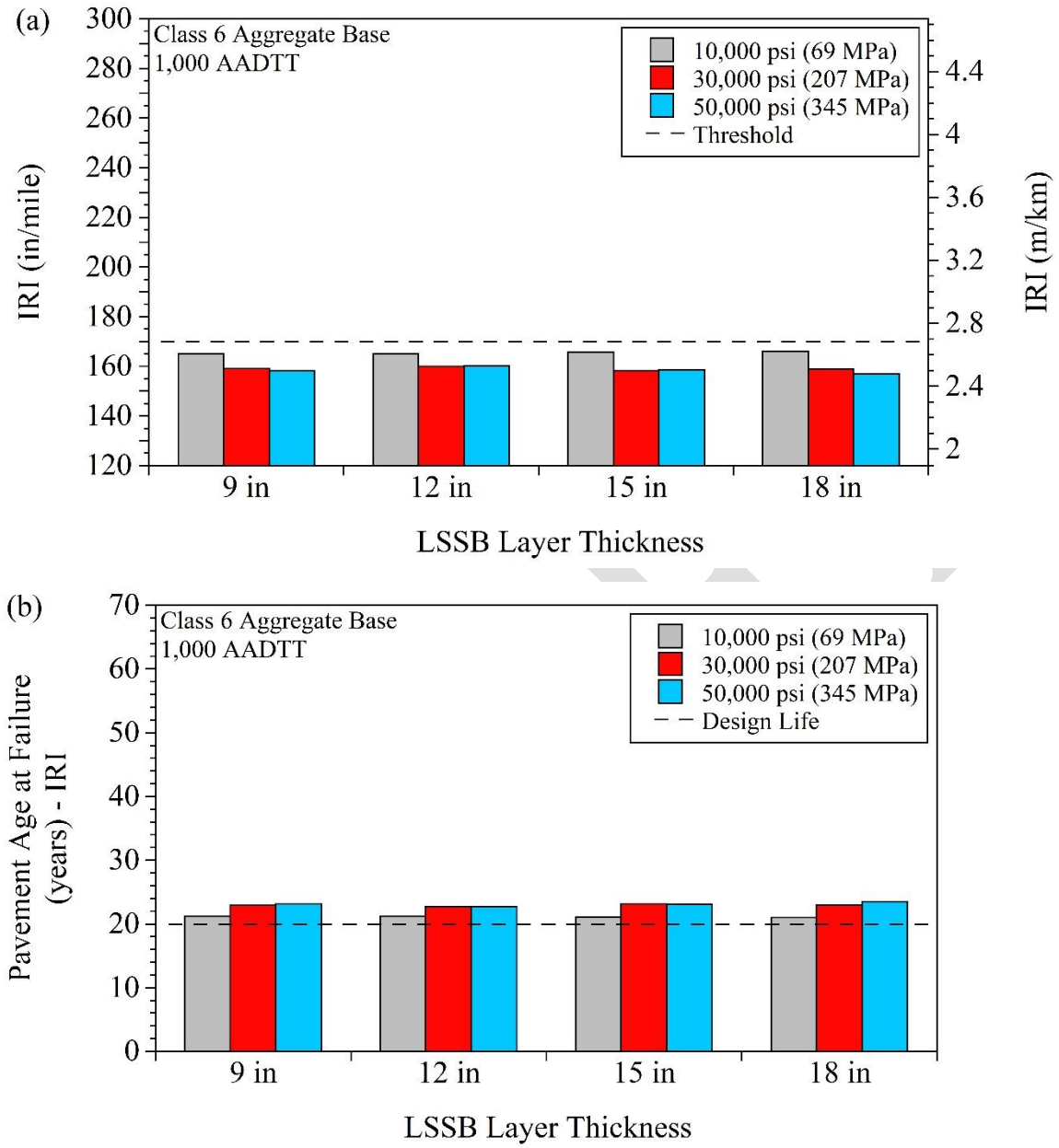


Figure 5.27. Effect of LSSB layer modulus on (a) IRI at the end of the design life (20 years) and (b) pavement age at IRI failure

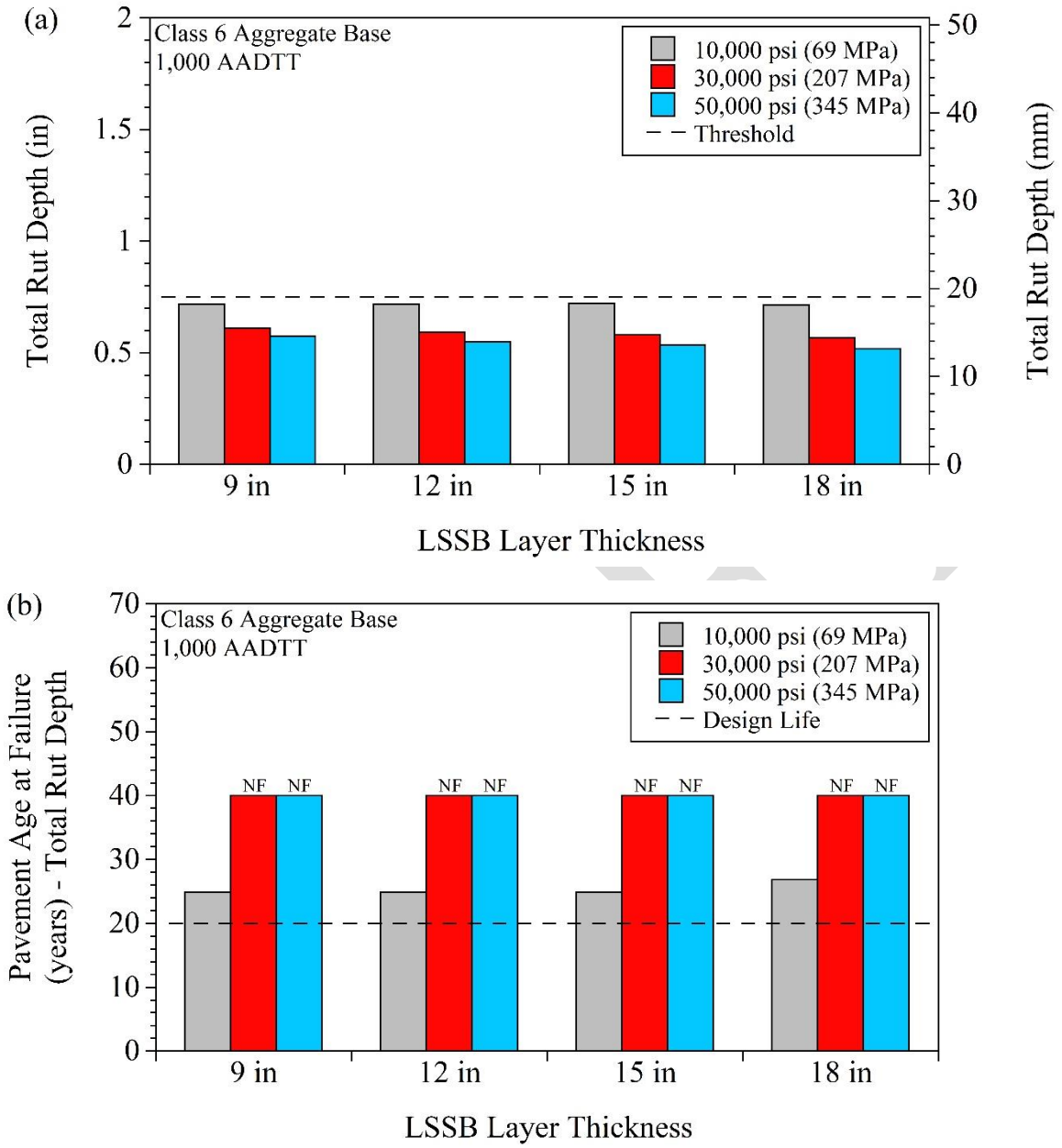


Figure 5.28. Effect of LSSB layer modulus on (a) rutting at the end of the design life (20 years) and (b) pavement age at rutting failure (NF = no failure)

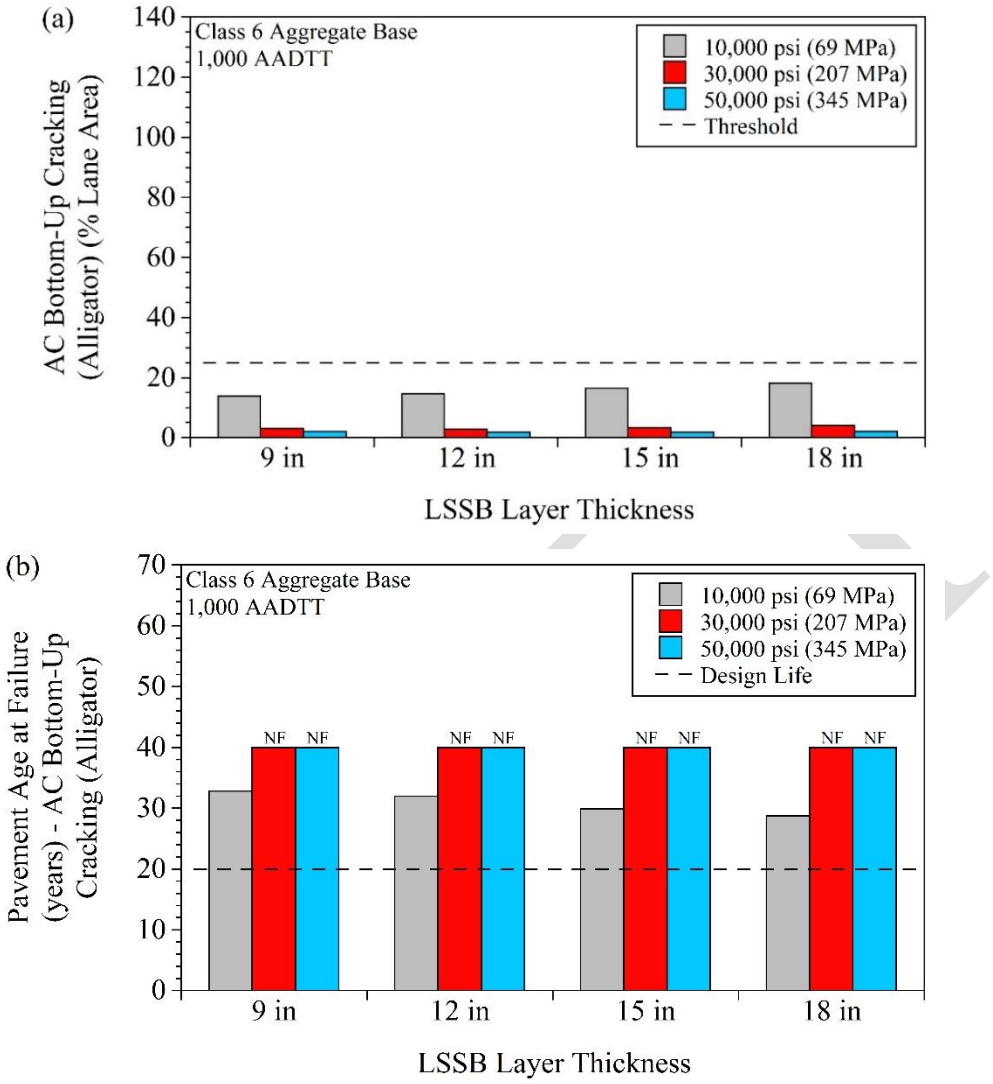


Figure 5.29. Effect of LSSB layer modulus on (a) alligator cracking at the end of the design life (20 years) and (b) pavement age at alligator cracking failure (NF = no failure)

5.3.5. Layer Rutting at 50% Reliability

Layer rutting for asphalt, base+subbase, and subgrade was also evaluated at 50% reliability (Pavement ME can only give 50% reliability for layer rutting) based on the outputs obtained from Pavement ME. For asphalt layer rutting, there was generally no significant difference between the asphalt layers placed on LSSB layers at different thicknesses and with different M_R values in the modeling analyses.

For base+subbase layer rutting, increasing the LSSB thickness generally yielded higher LSSB layer rutting. For subgrade layer rutting, the subgrade layers underlying thinner LSSB layers exhibited higher rutting. Figures 5.30, 5.31, and 5.32 are examples that show the asphalt, base+subbase, and subgrade rut depths for the pavement models that contained class 6 aggregate base layers and were subjected to 1,000 AADTT. More results for other pavement modeling analyses are provided in Appendix AB.

As expected, the modeling analyses showed that the highest layer rutting was observed in the subgrade layers. In addition, increasing the LSSB M_R value decreased both base+subbase and subgrade layer rutting. It was concluded that the model results complied with general expectations. Figure 5.33 is an example that shows the total, asphalt, base+subbase, and subgrade rutting for the pavement models that contained class 6 aggregate base layers and were subjected to 1,000 AADTT. More results for other pavement modeling analyses are provided in Appendix AC.

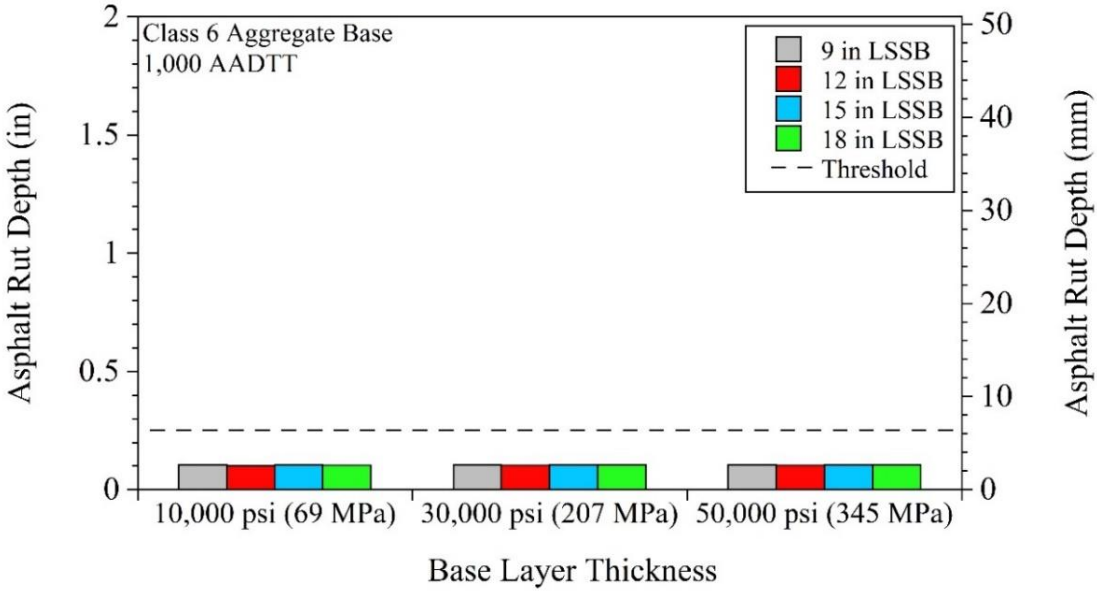


Figure 5.30. Asphalt rut depths (at 50% reliability) for the pavement models that were subjected to 1,000 AADTT

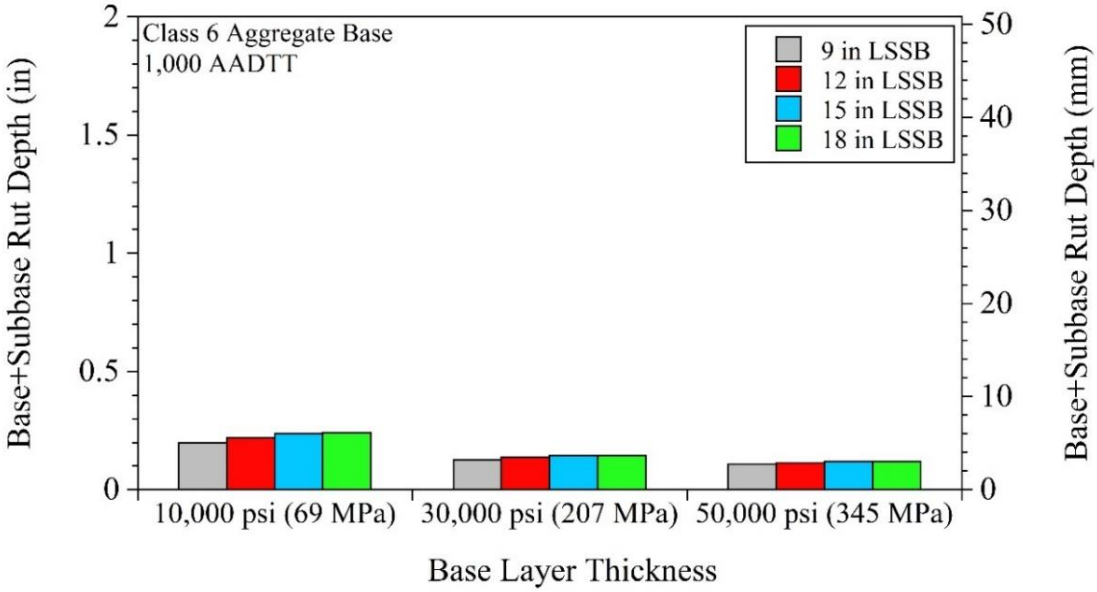


Figure 5.31. Base+subbase rut depths (at 50% reliability) for the pavement models that were subjected to 1,000 AADTT

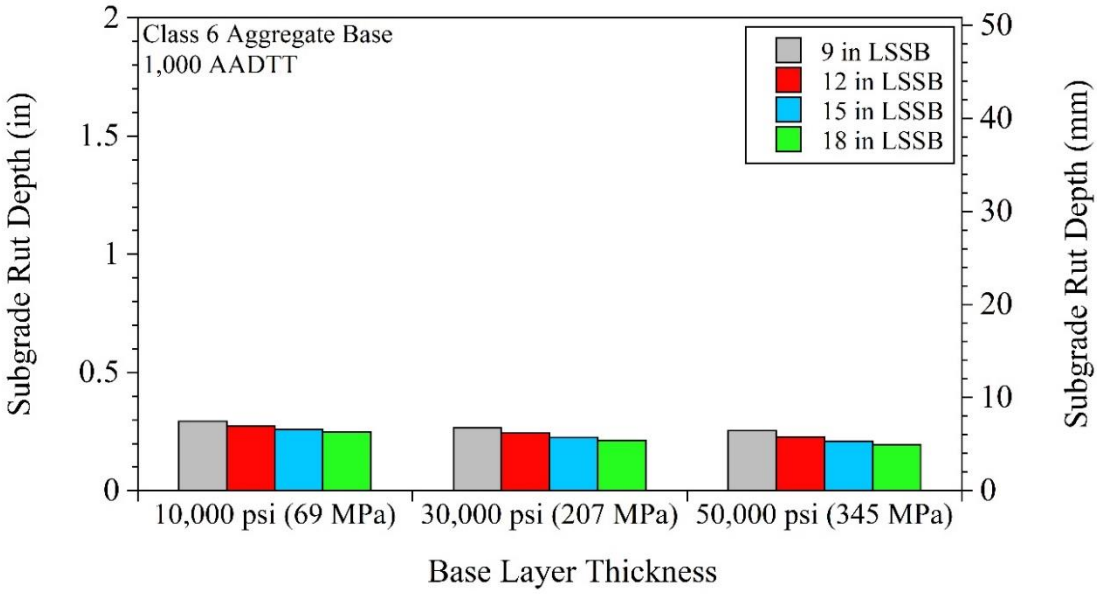


Figure 5.32. Subgrade rut depths (at 50% reliability) for the pavement models that were subjected to 1,000 AADTT

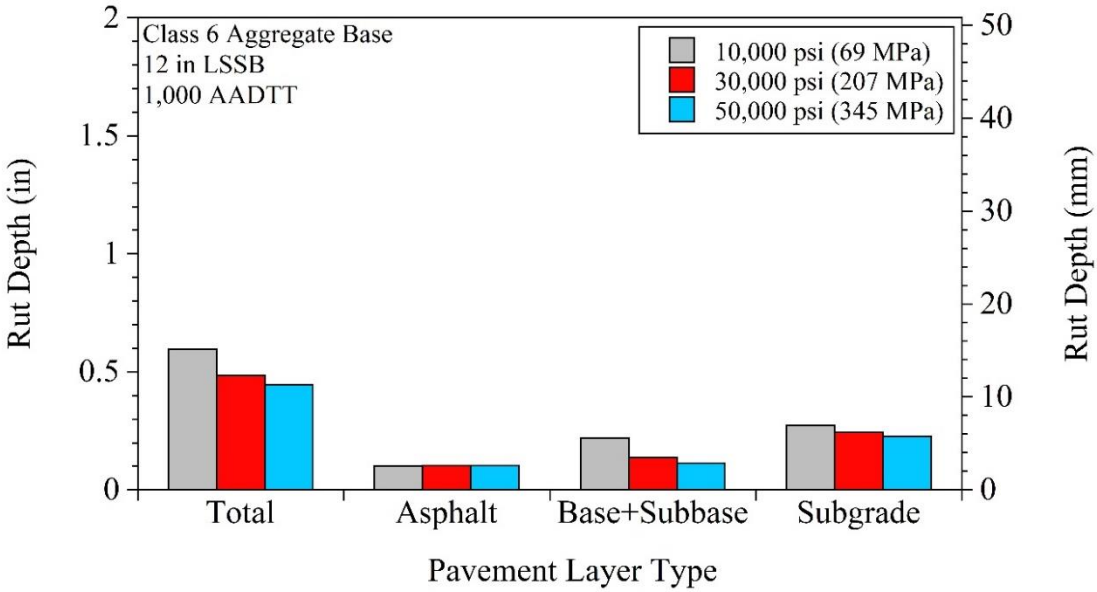


Figure 5.33. Total and layer rut depths (at 50% reliability) for the pavement models that contained 12-in LSSB layers and were subjected to 1,000 AADTT

5.3.6. Effect of Traffic Level on Pavement Performance Prediction Models

Similar to the observations made for the RAB group, increasing the AADTT level yielded greater pavement distresses and shorter pavement service life. Figures 5.34, 5.35, and 5.36 are examples that show the effect of traffic levels on IRI, rutting, and alligator cracking, respectively, for pavement modeling analyses that contained class 6 aggregate base layers and LSSB layers having an SM_R of 10,000 psi. More results for other pavement modeling analyses are provided in Appendix AD.

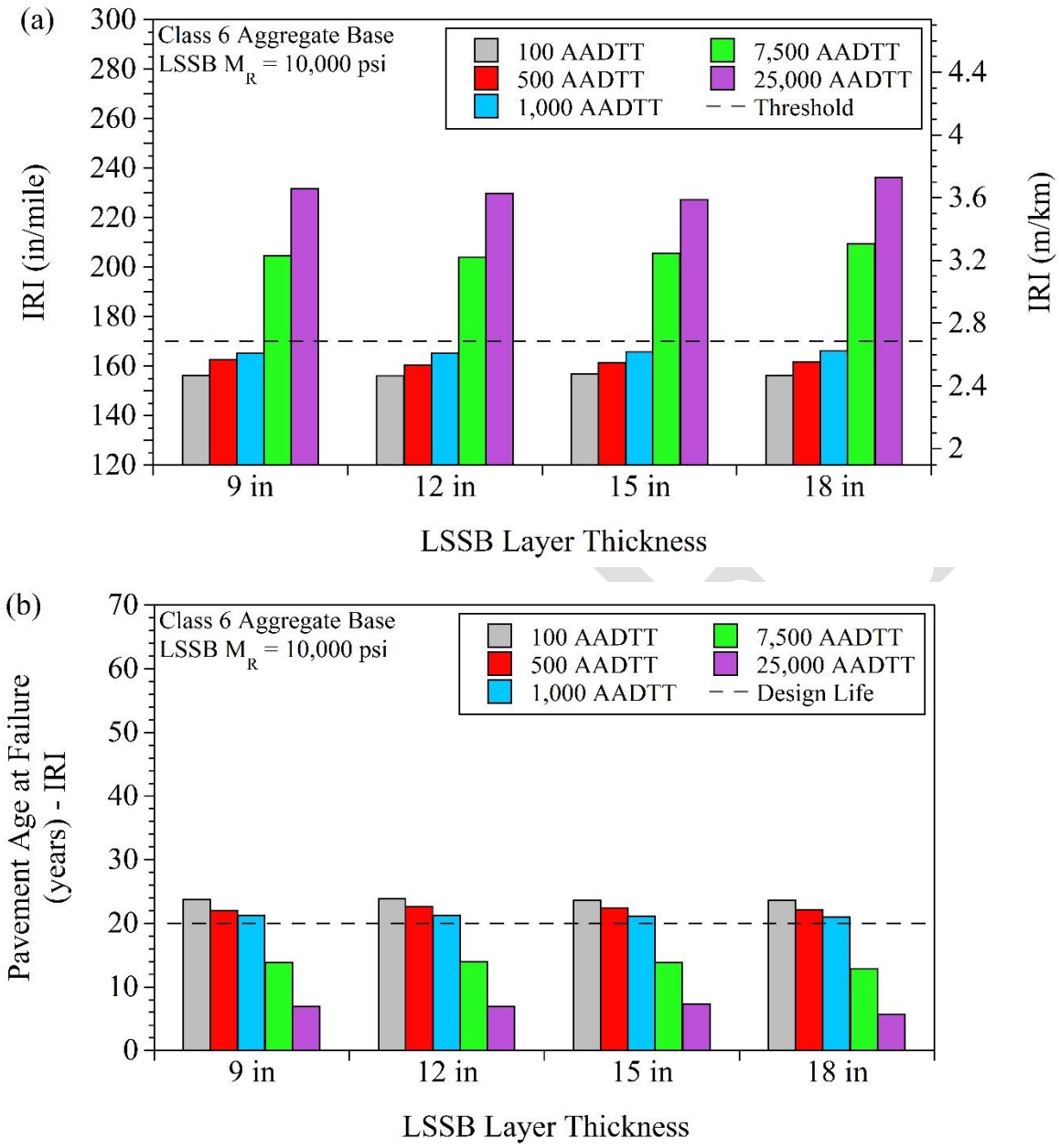


Figure 5.34. Effect of traffic level on (a) IRI at the end of the design life (20 years) and (b) pavement age at IRI failure

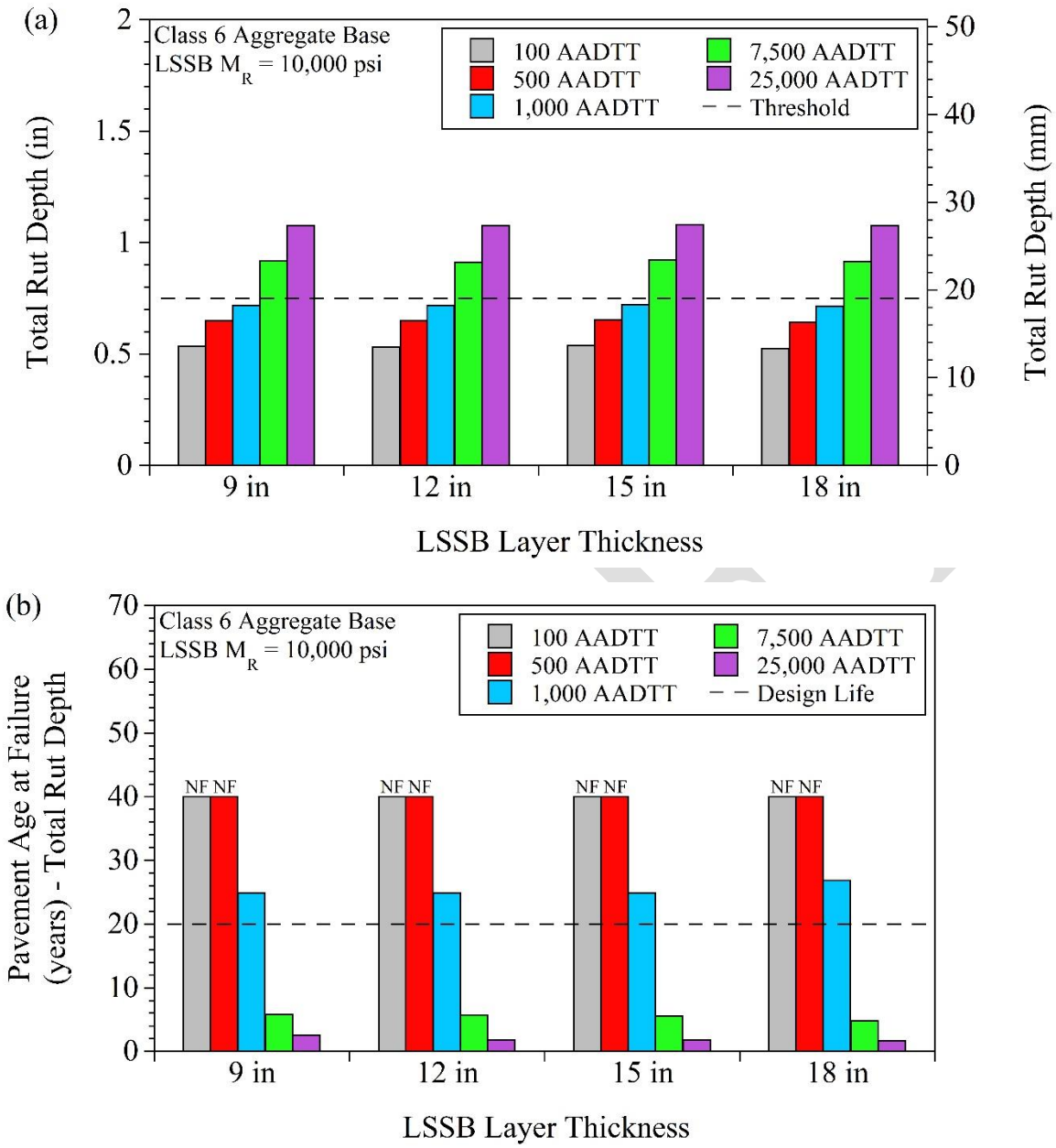


Figure 5.35. Effect of traffic level on (a) rutting at the end of the design life (20 years) and (b) pavement age at rutting failure (NF = no failure)

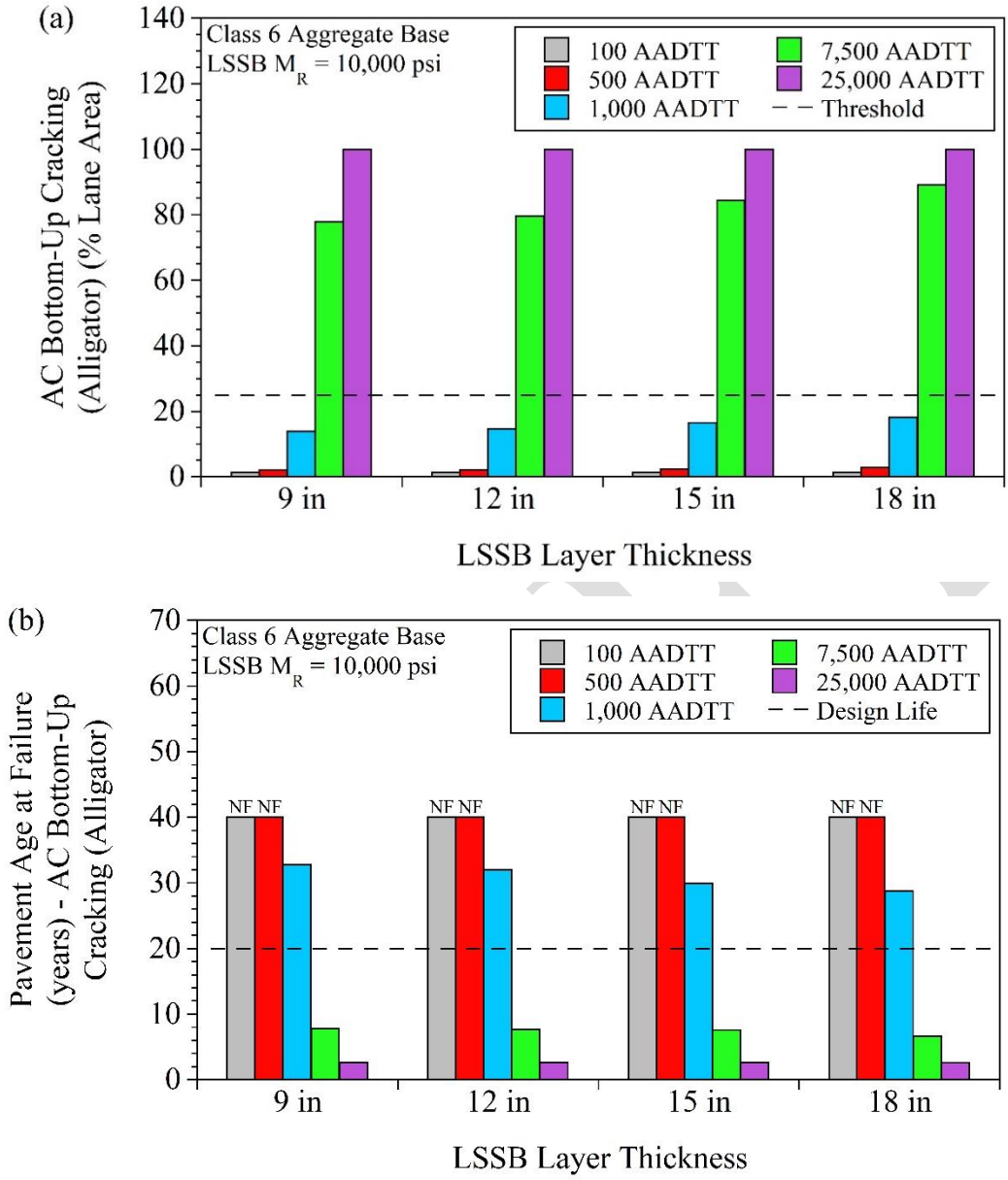


Figure 5.36. Effect of traffic level on (a) alligator cracking at the end of the design life (20 years) and (b) pavement age at alligator cracking failure (NF = no failure)

In addition to all the Pavement ME analyses shown above, an effort was made to compare the actual field data obtained from the MnROAD test facility with that of the Pavement ME models. The Pavement ME models were not calibrated with the local calibrations since that is outside the scope of this study. Therefore, no perfect match would be expected between the field data and the models. These comparisons were not included in the main context of this study. Appendix AE contains information about comparison between field data and model data.

An effort was also made to analyze pavement overlays [asphalt concrete (AC) over AC] for the originally constructed test cells (Figure 1.1). However, the results of those analyses were not included in the main context of this study and are provided in Appendix AF.

6. CONCLUSIONS

- Stepwise regression analysis results revealed that the common parameters that could be used to estimate the uncorrected and corrected optimum moisture content (OMC) and maximum dry density (MDD) values of base layer aggregates used in this study (coarse RCA, fine RCA, limestone, RCA+RAP, class 5Q aggregate, and class 6 aggregate) are specific gravity (G_s), absorption, and gradation characteristics. Residual mortar content could also be used to estimate uncorrected OMC and MDD values of base layer aggregates containing RCA.

- For estimation of saturated hydraulic conductivity (K_{sat}), stepwise regression analysis results showed that G_s, absorption, OMC and MDD (both uncorrected and corrected), and void ratio/porosity parameters could be used. To calculate the void ratio or porosity, G_s and MDD of the aggregate must be known [$e = (G_s\gamma_w/\gamma_d) - 1$ and $e = e/(1 + e)$]. Therefore, knowledge of the G_s, absorption, or Proctor compaction parameters is more critical in estimating the K_{sat} properties of the base layer aggregates. However, it should be kept in mind that since aggregate base layers were compacted at lower dry densities than MDD in the field, the models may not be representative for field conditions.

- Residual volumetric water content (VWC) (θ_r), saturated VWC (θ_s), and air-entry pressure parameters, which are soil-water characteristic curve (SWCC) parameters, could also be estimated by using the index properties of the base layer aggregates. It was also found that corrected OMC could be used to estimate θ_r. For the estimation of θ_s, it was found that G_s, absorption, residual mortar content, and uncorrected OMC and MDD could be used. To estimate air-entry pressures, void ratio/porosity, absorption, and gradation could be used. However, further evaluation would be required to check the physical significance of the equations found to estimate the air-entry pressures.

- As expected, the M_R values of the base layer aggregates were inversely related to the moisture contents in their matrices. Since the degree of saturation (DOS) and VWC of the base layer aggregates were affected by the moisture content in their matrices, M_R values and DOS or VWC values were also inversely related to each other. On the other hand, there was a direct relationship between the M_R values of the base layer aggregates and the matric suctions presented in the aggregate matrices (matric suctions were higher than the air-entry pressures).

- It was determined that G_s, absorption, uncorrected OMC and MDD, and residual mortar content could be used to estimate the summary resilient modulus (SM_R) values of the base layer aggregates. For the estimation of k_1, k_2, and k_3 (conventional MEPDG fitting parameters), G_s and absorption could commonly be used.

- It was determined that the breakage characteristics of the base layer aggregates were affected by not only their gradations, but also their coarse oven-dry (OD) G_s, residual mortar content, and roundness characteristics. The stepwise regression analyses revealed that the relative breakage (B_r) of the base layer aggregates increased with their residual mortar content. In addition, it was determined that the B_r and coarse OD G_s or roundness of the base layer aggregates were inversely related.

DRAFT

- The laboratory test results obtained in this study and Edil et al. (2012) were combined to obtain more general equations to estimate the uncorrected OMC and MDD of the base layer aggregates. However, no satisfactory equations could be developed, possibly due to unavailable data about oven-dry (OD), saturated-surface-dry (SSD), apparent, and combined G_s values for both coarse and fine fractions of the aggregates in Edil et al. (2012). In addition, fine and combined absorption values of the aggregates were not reported in Edil et al. (2012). The stepwise regression analyses performed in this study revealed that the most commonly used index properties to estimate the Proctor compaction characteristics were G_s and absorption. Therefore, it was concluded that understanding the G_s and absorption properties of the base layer aggregates were very important to predict the compaction characteristics and other engineering properties of the base layer aggregates.

- Overall, it was concluded that the base dynamic cone penetration index (DCPI), the base field California bearing ratio (CBR), the base+subbase light weight deflectometer elastic modulus (E_{LWD}), the base+subbase falling weight deflectometer elastic modulus (E_{FWD}), and the base+subbase intelligent compaction (IC) M_R values were all related to one another. While base+subbase E_{LWD}, E_{FWD}, and IC M_R values were inversely related to the base DCPI values, they were directly related to the base field CBR values. In addition, the base+subbase E_{LWD}, E_{FWD}, and IC M_R values were directly related to one another. Therefore, it was concluded that the results obtained from relatively simpler field tests (e.g., DCP and/or LWD tests) could be used to estimate the results of relatively more advanced field tests (e.g., FWD and IC tests).

- Based on the Pavement ME analyses performed for the recycled aggregate base (RAB) group:

  - Increasing the aggregate base layer (coarse RCA, fine RCA, limestone, RCA+RAP) thicknesses decreased the predicted pavement distress values at the end of the flexible pavement design life (20 years) and increased pavement service life.

  - Using limestone in the aggregate base layer models (at different thicknesses) resulted in greater pavement distresses at the end of the pavement design period (20 years) and lower pavement service life in the Pavement ME models than the recycled aggregates.

  - There was no significant difference in rutting between the asphalt layers placed on coarse RCA, fine RCA, limestone, and RCA+RAP base layers (at different thicknesses). For base+subbase layer rutting, overall, limestone base+select granular borrow subbase layers yielded higher rutting than the other base+subbase layers (for each base layer thickness). For subgrade layer rutting, the sand subgrade layers underlying limestone base+select granular borrow subbase layers yielded slightly lower rutting depths than those underlying coarse RCA, fine RCA, and RCA+RAP base+select granular borrow subbase layers. On the other hand, the clay loam subgrade layers underlying limestone base+select granular borrow subbase layers yielded higher rutting depths than those underlying coarse RCA, fine RCA, and RCA+RAP base+select granular borrow subbase layers. As expected, model results showed that the highest layer rutting was observed in subgrade layers. In addition, increasing the aggregate base layer thickness increased the overall base+subbase rutting. An increase in the aggregate base layer thickness resulted in a decrease in subgrade layer rutting.

DRAFT

- As expected, increasing the AADTT level yielded greater pavement distresses and shorter pavement service life. While performance prediction models showed that acceptable pavement distresses and service lives were obtained at 100, 500, and 1,000 AADTT levels (low traffic), excessive failures occurred at 7,500 (medium traffic) and 25,000 (high traffic) AADTT levels.

- It was concluded that thinner RAB layers (4, 6, 8, or 10 in) could be constructed with coarse RCA, fine RCA, or RCA+RAP materials rather than constructing a 12-in limestone base layer depending on the distress values that are of interest to an agency.

- Based on the Pavement ME analyses performed for the large stone subbase (LSSB) groups:

  - No consistent trend was observed between IRI predictions and LSSB layer thickness. On the other hand, increasing the LSSB layer thickness generally decreased rutting and alligator cracking at the end of the pavement design life (20 years).

  - It was concluded that increasing the LSSB SM_R value resulted in lower pavement distresses at the end of the pavement design life (20 years) and increased pavement service life.

  - There was no significant difference between the rutting of the asphalt layers placed on LSSB layers at different thicknesses and having different M_R values in the models. For base+subbase layer rutting, increasing the LSSB thickness resulted in greater LSSB layer rutting. The subgrade layers underlying thinner LSSB layers exhibited higher rutting. As expected, the greatest amount of layer rutting was observed in subgrade layers. In addition, increasing the LSSB M_R value decreased both base+subbase and subgrade layer rutting.

  - Similar to the observations made for the RAB group, increasing the AADTT level yielded greater pavement distresses and shorter pavement service life.

7. RECOMMENDATIONS

Material selection for recycled aggregate base (RAB) layers

- In this study, for the materials containing RCA (all the base layer aggregates except limestone), the oven-dry specific gravity (OD G_s) values were ranging between 2.17 and 2.35 (OD G_s of limestone was 2.66). The water absorption was ranging between 3.86% and 8.65% for the materials containing RCA (water absorption of limestone was 1.72%). In addition, the residual mortar contents of those materials were ranging between 20.1% and 37.1% (residual mortar content of RCA was 1.3%). As can be seen from these results, the aggregates used in this study could be separated by assessing just their OD G_s, absorption, and residual mortar content values. RCA materials tend to exhibit lower G_s (due to their porous structure) and higher absorption (due to their porous structure, hydrophilicity, and unhydrated cement content).

- The following relationship was observed between the water absorptions of the base layer aggregates used in this study: fine RCA > coarse RCA > class 5Q aggregate > RCA+RAP > class 6 aggregate > limestone. The materials containing RCA (all the aggregates except

DRAFT

limestone) may attract more water due to their higher absorption capacity and hydrophilicity. An increase in the water-holding capacity of aggregate base layers constructed with RCA materials may increase the amount of water available to freeze throughout the layer. Such an increase in water content can increase frost heaving and thaw settlement, and thereby, reduce the overall freeze-thaw (F-T) durability. In this study, since RCA+RAP and class 6 aggregate exhibited lower absorption than fine RCA, coarse RCA, and class 5Q aggregate, it can be affirmed that RCA can be mixed with RAP to reduce the absorption and hydrophilicity. In this study, the absorption values of limestone, RCA+RAP, and class 6 aggregate were 1.7%, 4.3%, and 3.9%, respectively. Therefore, it can be recommended to mix RCA with RAP with a maximum of 4.3% absorption. In addition, coarser RCA materials (coarse RCA and class 5Q aggregate) would be preferable than fine RCA because their absorption values (7% and 6.3% for coarse RCA and class 5Q aggregate, respectively) were relatively lower than that of fine RCA (8.65%). Therefore, it can be recommended that an RCA material should not have an absorption value higher than 7%.

- It can be concluded that any base layer aggregate with asphalt binder contents higher than 3% (per the ignition method) and 1.5% (per the quantitative extraction method) would exhibit hydrophobic properties, resulting in materials with higher freeze-thaw durability and better drainage properties.

- The following relationship was observed with respect to breakage (due to compaction) of the base layer aggregates used in this study: class 5Q aggregate > coarse RCA > fine RCA > class 6 aggregate > RCA+RAP > limestone. It was concluded that not only gradation but also the residual mortar content and roundness of aggregate particles affected the breakage characteristics of the base layer aggregates. It was observed that coarser RCA materials (coarse RCA and class 5Q aggregate) exhibited greater breakage. In addition, due to their higher residual mortar contents, class 5Q aggregate and coarse RCA exhibited higher breakage. Lastly, it was concluded that breakage increases as the roundness of the particles decreases (angularity increases) overall. Higher breakage of particles may decrease the permeability of aggregate base layers, possibly negatively affecting long-term pavement performance. Breakage of RCA materials may also cause a release of unhydrated cement content that then presents in the RCA particle's matrix. While this may further improve the stiffness of RCA later, it may also increase the potential for tufa formation, and drainage properties of aggregate base layers constructed with RCA can be reduced as a result of the tufa formation. Due to the high breakage of coarse RCA and class 5Q aggregate, the field degree of compaction (DOC) of coarse-grained RCA materials can be lowered (e.g., between 90% and 95%). For coarse-grained RCA materials, the gradation after compaction is recommended to use to consider breakage.

- The following relationship was observed between the saturated hydraulic conductivity (K_{sat}) of the base layer aggregates used in this study: fine RCA > class 5Q aggregate > coarse RCA > RCA+RAP > class 6 aggregate > limestone. It was concluded that there was a direct relationship between the aggregate's void ratio/porosity and K_{sat}. It was concluded that fine RCA yielded the highest void ratio/porosity and can be used if greater K_{sat} is preferred in the pavement structure.

DRAFT

In summary, the following material selection can be recommended to build RAB layers from the most preferred to least preferred: (1) fine RCA, (2) coarse RCA, (3) RCA+RAP, (4) limestone.

Material selection for large stone subbase (LSSB) layers

- The LSSB material used in this study (large crushed granite) to construct LSSB layers was poorly graded. During the construction of the pavement test cells containing LSSB layers, subgrade soil pumping and base/asphalt rutting were observed. Poorly graded large stones contain large voids that weak subgrade soil can move into. Large voids can also cause excessive particle reorientation during compaction and cause a less stable foundation for the construction of the upper layers. By using well-graded large stones, such problems could be reduced. A well-graded structure can provide a packed structure with fewer voids so that weak subgrade soils cannot easily move into the voids. In addition, such a packed LSSB structure can provide a more stable foundation for construction and compaction of aggregate base layers placed on top of the LSSB layers.

Recycled aggregate base (RAB) design

- Different agencies may assign different priorities to pavement distresses (IRI, rutting, alligator cracking, or longitudinal cracking or a combination of several distresses) in optimizing their pavement design. Therefore, in this study, RAB thicknesses, possibly considered as an alternative to 12-in limestone, were evaluated with respect to different pavement distress mechanisms, and the results were summarized to provide guidance to the agencies. Based on the pavement ME models that were created in this study, instead of 12-in limestone base layers, RAB layers as thin as 4 in could be satisfactorily constructed.

- RCA materials may attract more water due to their higher absorption capacity and hydrophilicity. In addition, tufa formation may be observed because of carbonation, possibly reducing the permeability of RCA materials. To minimize water-related issues associated with RCA materials, highly permeable subbase layers can be placed beneath the RCA base layers. In addition, suitable geosynthetic(s) can be placed between the base and subbase layers or in the middle of the base layers to improve drainage.

- Due to the relatively higher breakage of RCA materials compared to virgin aggregates, gradation after compaction is recommended to be used to consider breakage, particularly for coarse-grained RCA materials.

- In Pavement ME, the fundamental materials inputs for base layer aggregates are resilient modulus (M_R), maximum dry density (MDD) (corrected MDD is preferred), optimum moisture content (OMC) (corrected OMC is preferred), saturated hydraulic conductivity (K_{sat}), specific gravity (G_s) [oven-dry (OD) G_s is preferred], and gradation. In this study, several equations with both statistical and physical significance were provided for the estimation of summary M_R (SM_R), corrected OMC and MDD, and K_{sat}. Among those equations, the common parameters were determined to be G_s and absorption. This study showed that the G_s and absorption parameters, determined by ASTM C127 and C128, can be used to estimate the other material inputs required for pavement design.

DRAFT

Large stone subbase (LSSB) design

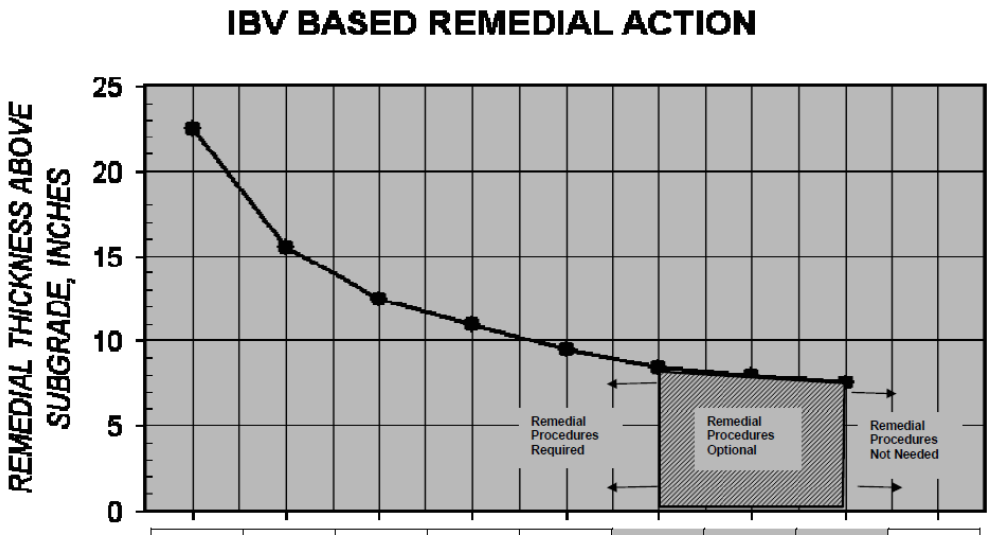
- As stated previously, geosynthetics had to be placed in the field to minimize subgrade soil pumping and base/asphalt rutting in the test cells containing 9-in LSSB layers. However, no significant problem was observed in constructing 18-in LSSB layers. In addition, while LSSB layers would be expected to show good drainage properties, conditions that could lower their permeability (e.g., contamination by subgrade soil pumping) should be considered. Special care must be taken during construction of thinner LSSB layers, and placement of geosynthetic(s) between the thinner LSSB layers and weak subgrade layers should be considered.

- In this study, placement of the geosynthetics between 9-in LSSB layers and clay loam subgrade layers were indeed found to provide important benefits such as workability improvement because the rest of the construction was completed without a problem regarding subgrade soil pumping and rutting. However, structural benefits of the geosynthetics could not be observed clearly using light weight deflectometer (LWD), falling weight deflectometer (FWD), or intelligent compaction (IC) testing due to the lower relative dry density of the class 5Q aggregate base layers. In addition, the loads applied by LWD, FWD, or IC testing were not sufficient to allow observation of the structural benefits of the geosynthetics. Therefore, no specific recommendation could be made for the selection of the most suitable geosynthetics. A heavy weight deflectometer (HWD), which is a type of FWD equipment providing higher loads, could be used for this purpose.

- Coarse-grained aggregates can interlock between grid openings of geogrids and the interlocking mechanism increases the integrity and stiffness of pavement layers. If placement of geogrids between an LSSB layer and a clay loam subgrade layer is intended, special attention must be given to the geogrid aperture size. There are only a few geogrids with grid apertures suitable for use with large stones to provide adequate interlocking. In this study, Tensar TriAx TX190L (triaxial geogrid) and Tensar BX1300 (biaxial geogrid) were used. Tensar TriAx TX190L had a rib pitch of 60 mm (2.4 in). Aperture dimensions of Tensar BX1300 were 46 mm (1.8 in) in machine direction (MD) and 64 mm (2.5 in) in cross-machine direction (XMD).

- Figure 7.1 provided by the Illinois Department of Transportation (IDOT) Subgrade Stability Manual (2005) shows remedial thickness (above subgrade) recommendations depending on the strength/stiffness of subgrades. In this study, a very non-traditional subgrade preparation procedure was followed during construction to create a weak subgrade with a dynamic cone penetration index (DCPI) value between 2.5 and 3.5 in/blow (63.5 and 89 mm/blow) (ASTM D6951) for the upper 1 ft (0.3 m) of the clay loam subgrade soil. According to Figure 7.1, the sufficient LSSB layer thickness would be between 15 in and 20 in for the subgrade DCPI range of 2.5-3.5 in/blow (63.5 and 89 mm/blow). Figure 7.1 also reveals that an 18-in LSSB layer is more sufficient than a 9-in LSSB layer.

DRAFT



IBV	1	2	3	4	5	6	7	8	9
Cone Index(CI)	40	80	120	160	200	240	280	320	360
Shear Strength (psi)	2.25	4.50	6.75	9.00	11.25	13.50	15.75	18.00	20.25
Qu (tsf)	0.32	0.64	1.00	1.28	1.60	1.94	2.24	2.56	2.88
Rate (in./Blow)	4.6	2.6	2.0	1.5	1.3	1.1	1.0	0.9	0.8
Rate (Blows/6")	1.3	2.3	3.0	4.0	4.6	5.5	6.0	6.7	7.5
Treatment Thickness	22.5	15.5	12.5	11	9.5	8.5	8	7.5	0

Figure 7.1. Remedial thickness (above subgrade) recommendations depending on the subgrade conditions (IDOT 2005)

- From the same manual (IDOT 2005), Table 7.1 also provides aggregate cover thickness reduction guidance when using geosynthetics [the table was developed by Kwon and Tutumluer (2003)]. According to Table 7.1, a 12-in LSSB with geotextile or geogrid could be constructed instead of constructing an 18-in LSSB without geosynthetics. In addition, instead of constructing a 9-in LSSB with geogrid, a 12-in LSSB could be constructed with geotextile or without any geosynthetics (Table 7.1).

Table 7.1. Aggregate cover thickness reduction guidance when using geosynthetics (Kwon and Tutumluer 2003; IDOT 2005)

IBV/CI	Aggregate Cover without Geosynthetics in. (mm)	Aggregate Cover with Geotextile in. (mm)	Aggregate Cover with Geogrid in. (mm)
1/40	22 (560)	16 (405)	15 (375)
1.5/60	18 (450)	12 (300)	12 (300)
2/80	16 (400)	12 (300)	10 (250)
3/120	12 (300)	12 (300)	9 (230)

- Wisconsin DOT's Facilities Development Manual (FDM) (2019) also provides thickness recommendations for breaker run (100% passing through a 6-inch sieve) and select crushed material (90-100% passing through a 5-in sieve, 20-50% passing through a 1½-in sieve, and 0-10% passing through a No. 10 sieve). Figure 7.2 shows recommended thicknesses for breaker run stone and select crushed material with or without geogrids. As can be seen from Figure 7.2, instead of constructing a 16-in large stone layer without any geogrid, a 12-in large stone layer with a geogrid could be constructed.

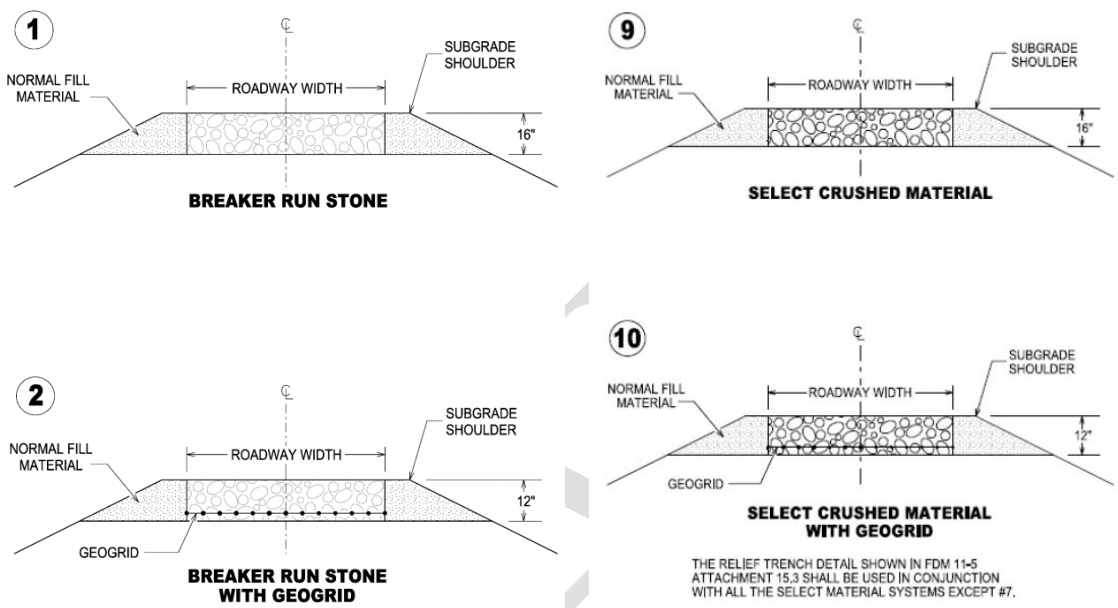


Figure 7.2. Thickness recommendations for breaker run and select crushed material (WisDOT 2019)

- While agencies or engineers might consider placing geocomposite layers in the middle of LSSB layers to improve lateral drainage, field monitoring during construction revealed that two-lift construction was not practical for LSSB layers (for 18-in LSSB layers, the original plan was to construct one of the LSSB layers in one lift and another one in two lifts), so placing a geocomposite between two LSSB lifts would not be practical and should be avoided.

- As stated previously, class 5Q aggregate base layers overlying 9-in LSSB layers could not be compacted effectively due to the instability of 9-in LSSB layers under loading. Such a problem was not observed in class 6 aggregate base layers overlying 18-in LSSB layers. Therefore, the LSSB layer thickness must be sufficient to provide sufficient structural support. If not, geosynthetic(s) can be placed on top of the LSSB layers to provide reinforcement before the placement of the base layers. Using geosynthetic(s) on top of LSSB layers can help to distribute load more effectively and increase the stability of LSSB layers under loading. Another option would be to consider SM_R values at a lower degree of compaction (DOC) (as low as 80%) for the base layers overlying 9-in LSSB layers during the design process, optimizing the thickness of the aggregate base layer overlying the 9-in LSSB layer.

8. REFERENCES

Abbas, A., Fathifazl, G., Isgor, O. B., Razaqpur, A. G., Fournier, B., & Foo, S. (2008). Proposed method for determining the residual mortar content of recycled concrete aggregates. *Journal of ASTM International*, *5*(1), 1-12.

Ba, M., Nokkaew, K., Fall, M., & Tinjum, J. M. (2013). Effect of matric suction on resilient modulus of compacted aggregate base courses. *Geotechnical and Geological Engineering*, *31*(5), 1497-1510.

Banerjee, A., Puppala, A. J., Congress, S. S., Chakraborty, S., Likos, W. J., & Hoyos, L. R. (2020). Variation of Resilient Modulus of Subgrade Soils over a Wide Range of Suction States. *Journal of Geotechnical and Geoenvironmental Engineering*, *146*(9), 04020096.

Bareither, C.A., Edil, T.B., Benson, C.H. and Mickelson, D.M. (2008). "Geological and Physical Factors Affecting the Friction Angle of Compacted Soils." *Journal of Geotechnical and Geoenvironmental Engineering,* No.10, pp. 1476-1489.

Bhasya, V., & Bharatkumar, B. H. (2018). Mechanical and Durability Properties of Concrete Produced with Treated Recycled Concrete Aggregate. *ACI Materials Journal*, *115*(2).

Butler, L., West, J. S., & Tighe, S. L. (2011). Quantification of recycled concrete aggregate (RCA) properties for usage in bridges and pavements: An Ontario case study. In *presentation at the Innovative Developments in Sustainable Pavements Session of the 2011 Annual Conf. of the Transport, Assoc. of Canada, Edmonton, Alberta*.

Ceylan, H., Gopalakrishnan, K., & Kim, S. (2015). Investigation of AASHTOWare Pavement ME Design/DARWinME Performance Prediction Models for Iowa Pavement Analysis and Design.

Chu, X. (2020). A Review on the Resilient Response of Unsaturated Subgrade Soils. *Advances in Civil Engineering*, *2020*.

Dawson, A. R., Mundy, M. J., & Huhtala, M. (2000). European research into granular material for pavement bases and subbases. *Transportation Research Record*, *1721*(1), 91-99.

de Juan, M. S., & Gutiérrez, P. A. (2009). Study on the influence of attached mortar content on the properties of recycled concrete aggregate. *Construction and building materials*, *23*(2), 872-877.

Edil, T. B., Tinjum, J. M., & Benson, C. H. (2012). Recycled Unbound Materials. Report No. 2012-35. Minnesota Department of Transportation. St. Paul, MN.

Elbheiry, M. R., Kandil, K. A., & Kotb, A. S. (2011). *Investigation of factors affecting pavement roughness* (Doctoral dissertation, Arab Academy for Science and Technology and Maritime Transport).

Fredlund, D. G., & Rahardjo, H. (1993). *Soil mechanics for unsaturated soils*. John Wiley & Sons.

Fredlund, D. G., & Xing, A. (1994). Equations for the soil-water characteristic curve. *Canadian geotechnical journal*, *31*(4), 521-532.

Genc, D. (2019). Development, installation and preliminary data collection of an environmental sensor system for freeze–thaw monitoring under granular-surfaced roadways.

Gokce, A. 2001, "Investigation of the Parameters Controlling Frost Resistance of Recycled Aggregate Concrete," Doctoral Thesis, Nigata University.

Hanson, J. L., Edil, T. B., & Yesiller, N. (2000). Thermal properties of high water content materials. In *Geotechnics of High Water Content Materials*. ASTM International.

Hardin, B. O. (1985). Crushing of soil particles. *Journal of geotechnical engineering*, *111*(10), 1177-1192.

Horton, R., Wierenga, P. J., & Nielsen, D. R. (1983). Evaluation of Methods for Determining the Apparent Thermal Diffusivity of Soil Near the Surface 1. *Soil Science Society of America Journal*, *47*(1), 25-32.

Illinois Department of Transportation (IDOT). (2005). Subgrade Stability Manual. IDOT Bureau of Bridges and Structures.

Izevbekhai, B. I., & Akkari, A. (2011). *Pervious concrete test cells on MnROAD low-volume road*. Minnesota Department of Transportation, Research Services Section.

Jury, W.A. & Horton R. (2004). Soil Physics. John Wiley & Sons. Hoboken, NJ.

Kazmee, H., Mishra, D., & Tutumluer, E. (2015). Sustainable alternatives in low volume road base course applications evaluated through accelerated pavement testing. In *IFCEE 2015* (pp. 409-418).

Khoury, N. N., and Zaman, M. M., "Correlation between Resilient Modulus, Moisture Variation, and Soil Suction for Subgrade Soils." *Transportation Research Record: Journal of the Transportation Research Board* 1874, no. 1 (2004): 99–107.

Kwon, J., and Tutumluer, E. (2003). "Use of Geosynthetics in Working Platform and Pavement Construction," Unpublished White Paper, Project IHR-30, Department of Civil & Environment Engineering, UIUC.

Mazari, M., Navarro, E., Abdallah, I., & Nazarian, S. (2014). Comparison of numerical and experimental responses of pavement systems using various resilient modulus models. *Soils and Foundations*, *54*(1), 36-44.

Mehrotra, A. (2014). Evaluating the influence of moisture variation on resilient modulus for unsaturated pavement subgrades.

MnDOT (2013a). MnROAD Semi Tractor Trailer, https://www.dot.state.mn.us/mnroad/data/pdfs/MnROADSemiDescriptions(March%202013).pdf

MnDOT (2017). *MnROAD safer, smarter, sustainable pavements through innovative research*. MnDOT, St. Paul, MN.

MnDOT (2018). Standard Specifications for Construction (2018 Edition). Minnesota Department of Transportation, St. Paul, MN.

Moosazedh, J. & Witczak, M. (1981). "Prediction of Subgrade Moduli for Soil that Exhibits Nonlinear Behavior." Journal of Transportation Research Board, No.810, Washington, D.C., pp. 10-17.

Nazarian, S., Fathi, A., Tirado, C., Kreinovich, V., Rocha, S., & Mazari, M. (2020). Evaluating Mechanical Properties of Earth Material During Intelligent Compaction. *NCHRP Research Report*, (933).

Nazarian, S., Mazari, M., Abdallah, I. N., Puppala, A. J., Mohammad, L. N., & Abu-Farsakh, M. Y. (2015). *Modulus-based construction specification for compaction of earthwork and unbound aggregate*. Washington, DC: Transportation Research Board.

NCHRP. (2004). "Laboratory Determination of Resilient Modulus for Flexible Pavement Design." NCHRP Research Results Digest, National Academies of Sciences, Engineering, and Medicine. Washington, DC.

Nokkaew, K. (2014). Hydraulic Properties of Recycled Pavement Aggregates and Effect of Soil Suction on Resilient Modulus for Pavement Design (Doctoral dissertation, University of Wisconsin-Madison).

Occupational Safety and Health Administration (OSHA), 2014. *Classification of soils for excavations*. Method No. ID-194. Physical Measurements Team, Industrial Hygiene Chemistry Division, OSHA Salt Lake Technical Center, Salt Lake City, UT.

Ooi, P. S., Archilla, A. R., & Sandefur, K. G. (2004). Resilient modulus models for compacted cohesive soils. *Transportation research record*, *1874*(1), 115-124.

Schwartz, C. W., Li, R., Kim, S., Ceylan, H., & Gopalakrishnan, K. (2011). Sensitivity evaluation of MEPDG performance prediction.

Tanyu, B. F., Kim, W. H., Edil, T. B., & Benson, C. H. (2003). Comparison of laboratory resilient modulus with back-calculated elastic moduli from large-scale model experiments and FWD tests on granular materials. In *Resilient modulus testing for pavement components*. ASTM International.

Van Deusen, D., Burnham, T., Dai, S., Geib, J., Hanson, C., Izevbekhai, B., Johnson, E., Palek, L., Siekmeier, J., Vrtis, M., & Worel, B. (2018). Report on 2017 MnROAD Construction Activities. Report MN/RC 2018-16. Minnesota Department of Transportation, St. Paul, MN.

Van Genuchten, M. T. (1980). A closed-form equation for predicting the hydraulic conductivity of unsaturated soils. *Soil science society of America journal*, *44*(5), 892-898.

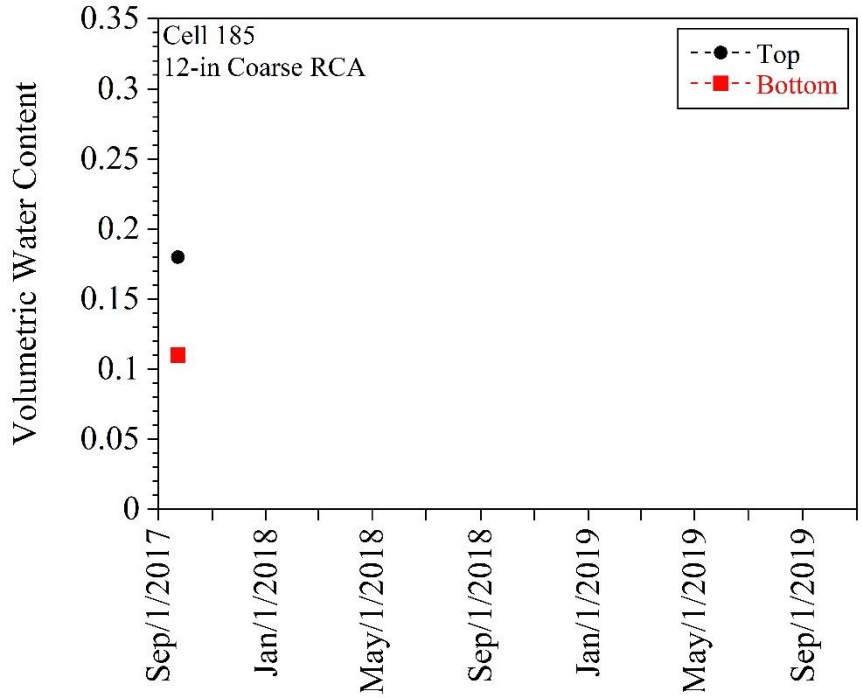
Velasquez, R., Hoegh, K., Yut, I., Funk, N., Cochran, G., Marasteanu, M., & Khazanovich, L. (2009). Implementation of the MEPDG for new and rehabilitated pavement structures for design of concrete and asphalt pavements in Minnesota.

WisDOT (2019). Facilities Development Manual (FDM). Wisconsin Department of Transportation, Madison, WI.

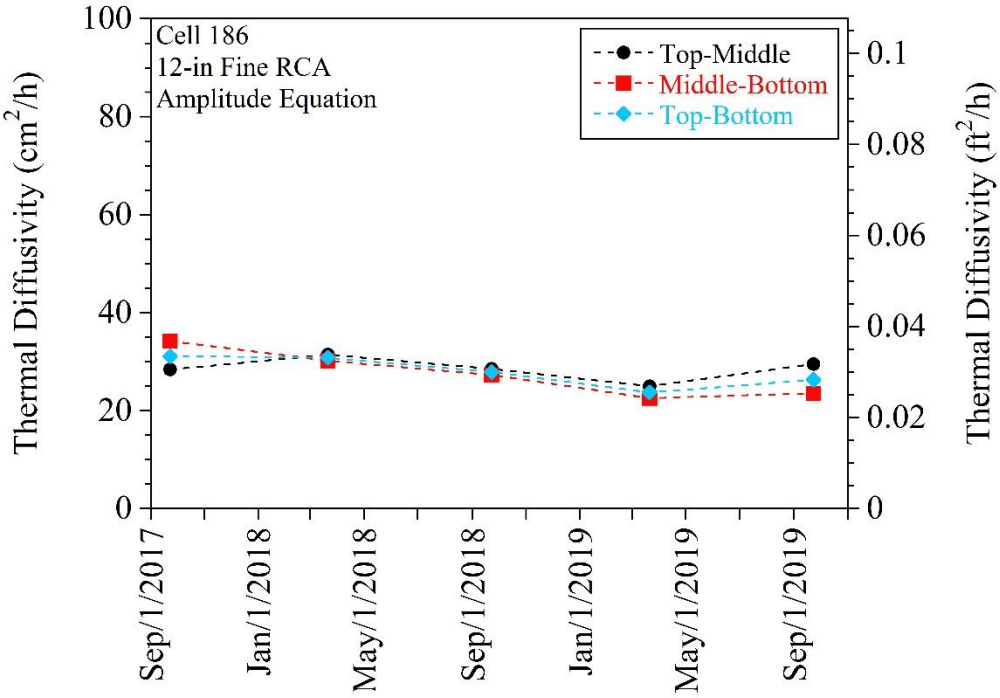
DRAFT

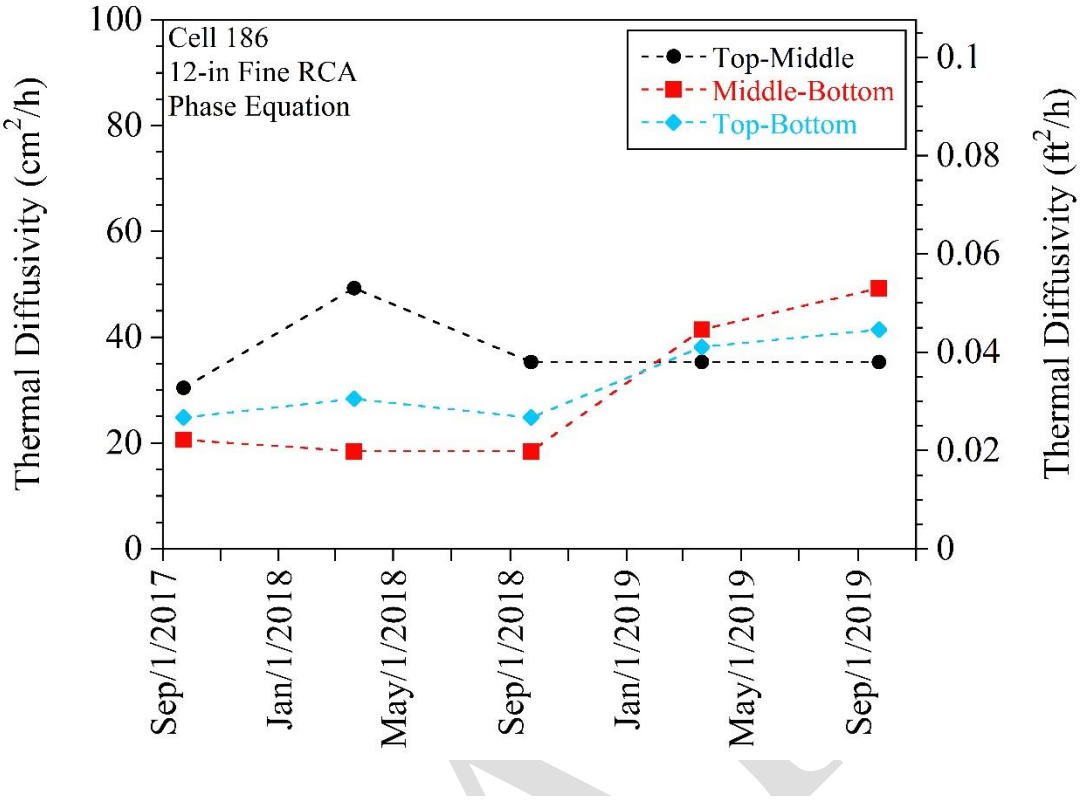
APPENDIX A. THERMAL DIFFUSIVITY (α) AND VOLUMETRIC WATER CONTENT (VWC) VALUES DETERMINED FOR 12-IN COARSE RCA (CELL 185), FINE RCA (CELL 186), LIMESTONE (CELL 188), AND RCA+RAP (CELL 189) BASE LAYERS

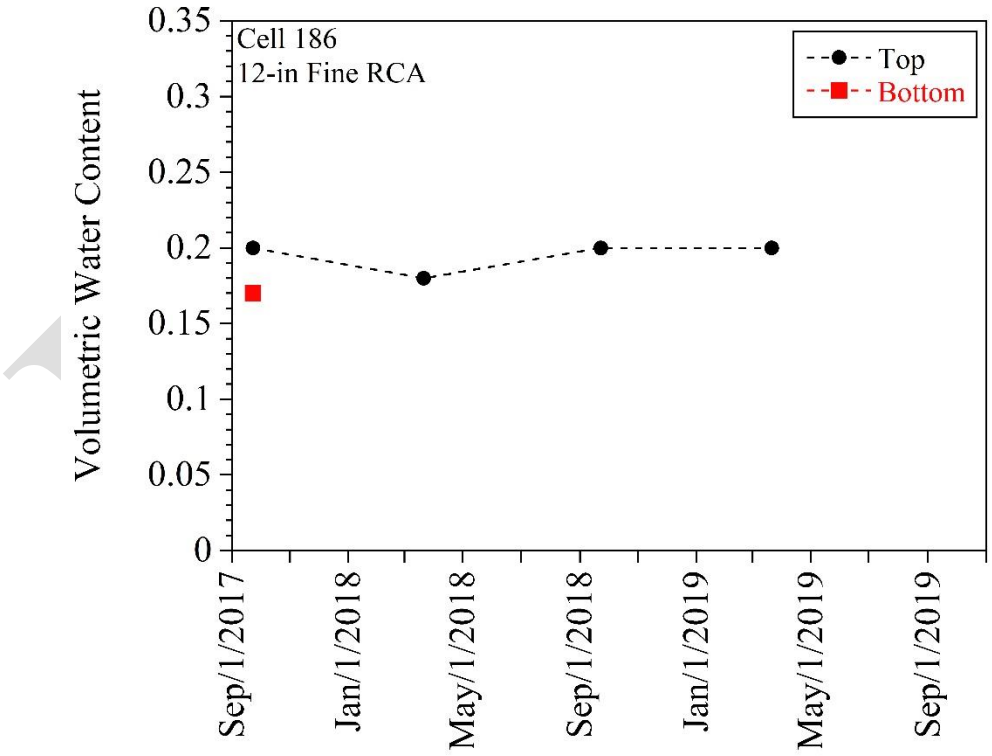
For 12-in coarse RCA (cell 185):



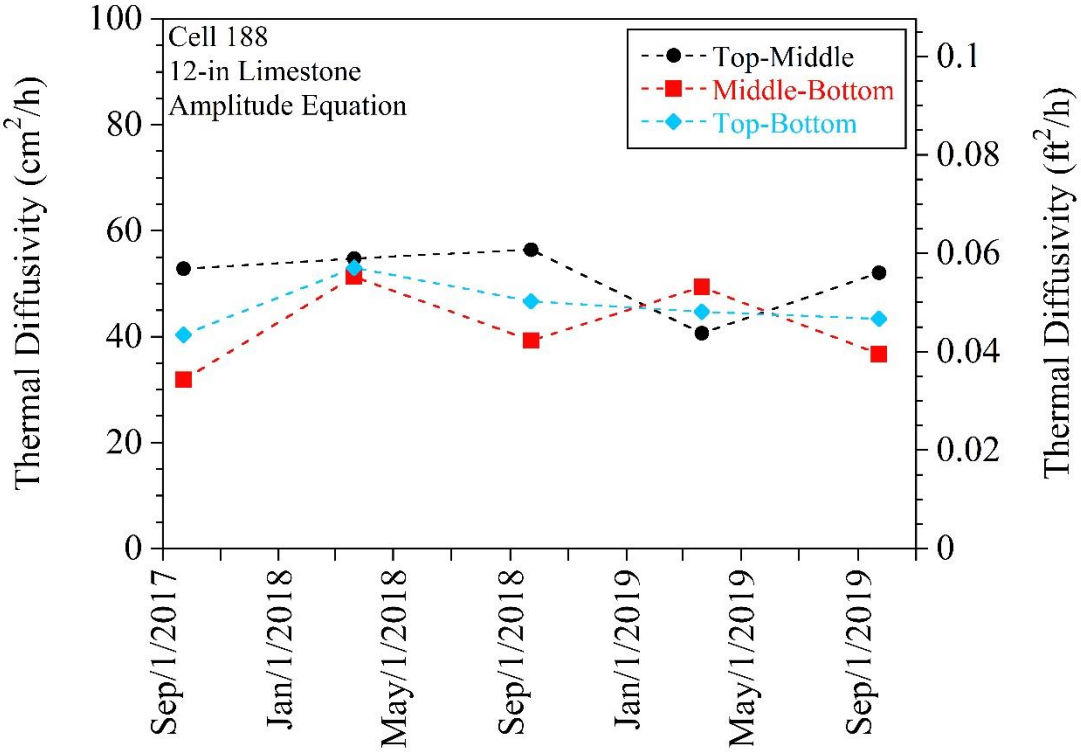
For 12-in fine RCA (cell 186):

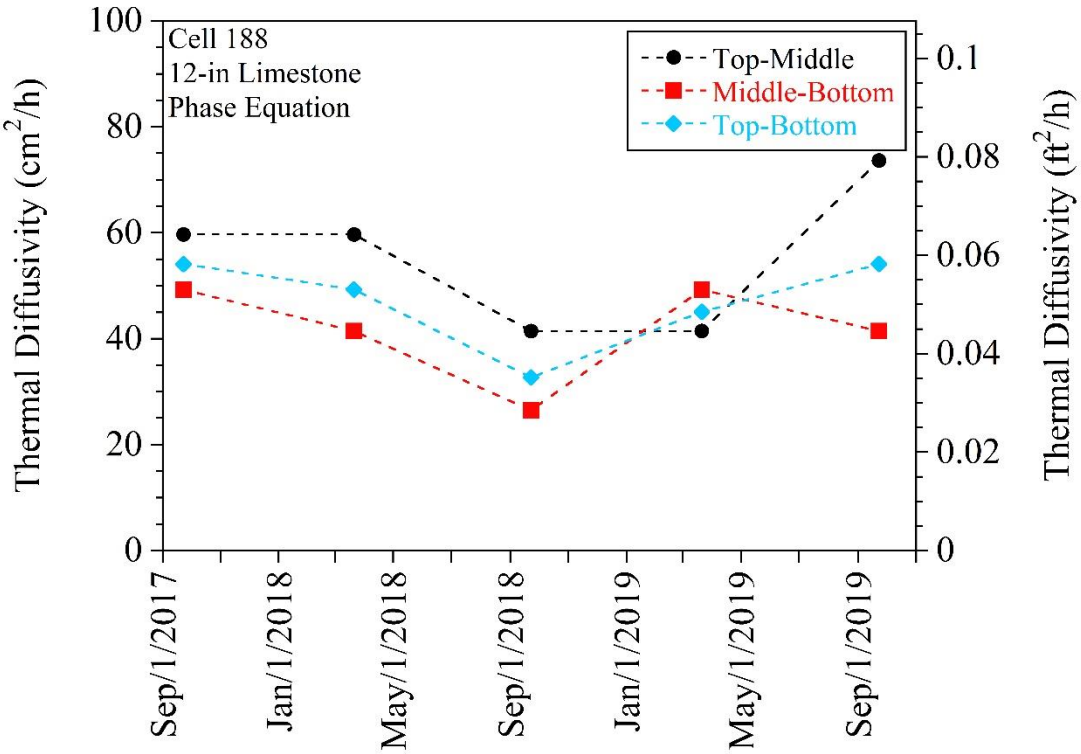


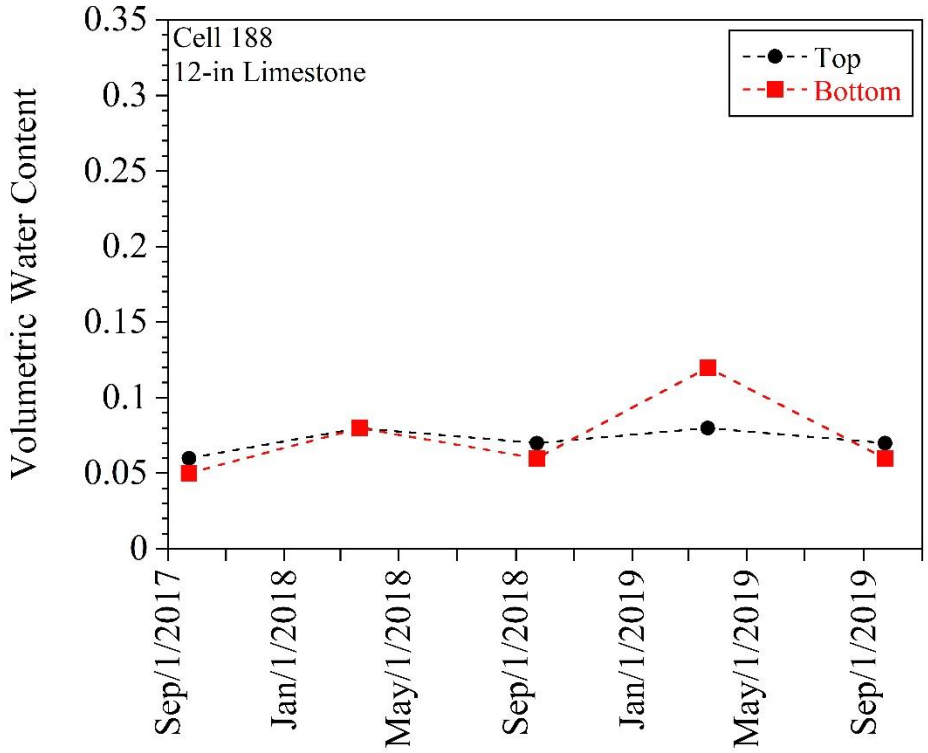

Cell 186
12-in Fine RCA
Phase Equation
Top-Middle
Middle-Bottom
Top-Bottom
Thermal Diffusivity (cm²/h)
Thermal Diffusivity (ft²/h)
100
80
60
40
20
0
0.1
0.08
0.06
0.04
0.02
0
Sep/1/2017
Jan/1/2018
May/1/2018
Sep/1/2018
Jan/1/2019
May/1/2019
Sep/1/2019


Cell 186
12-in Fine RCA
Top
Bottom
Volumetric Water Content
0.35
0.3
0.25
0.2
0.15
0.1
0.05
0
Sep/1/2017
Jan/1/2018
May/1/2018
Sep/1/2018
Jan/1/2019
May/1/2019
Sep/1/2019

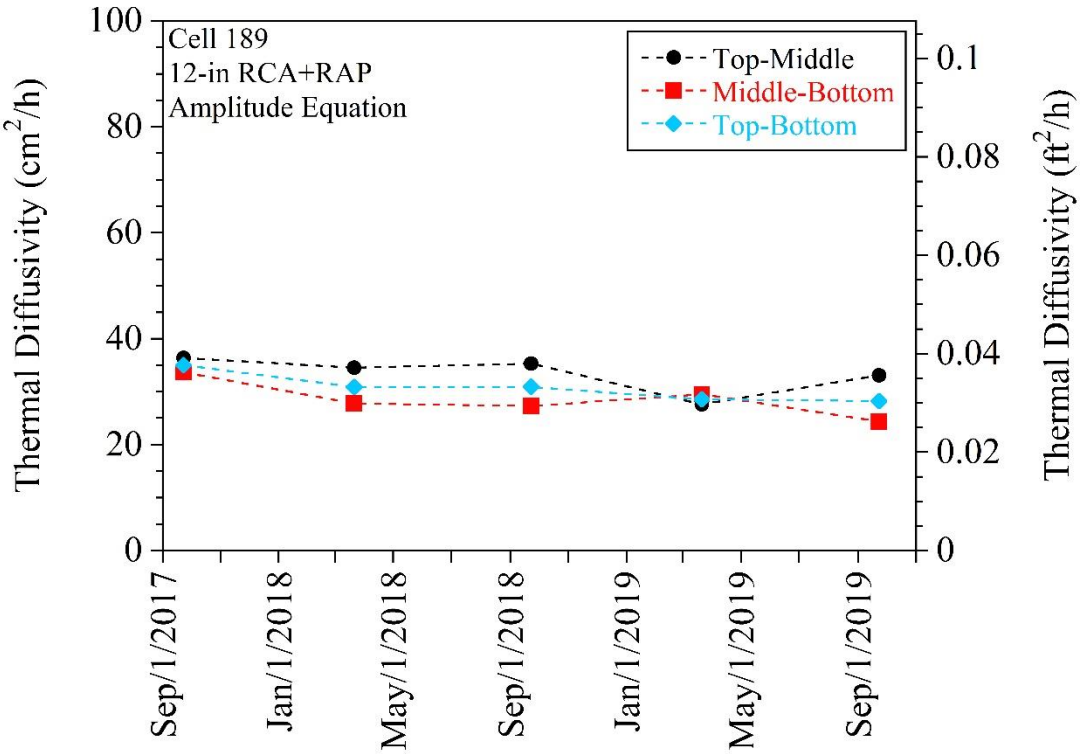
For 12-in limestone (cell 188):

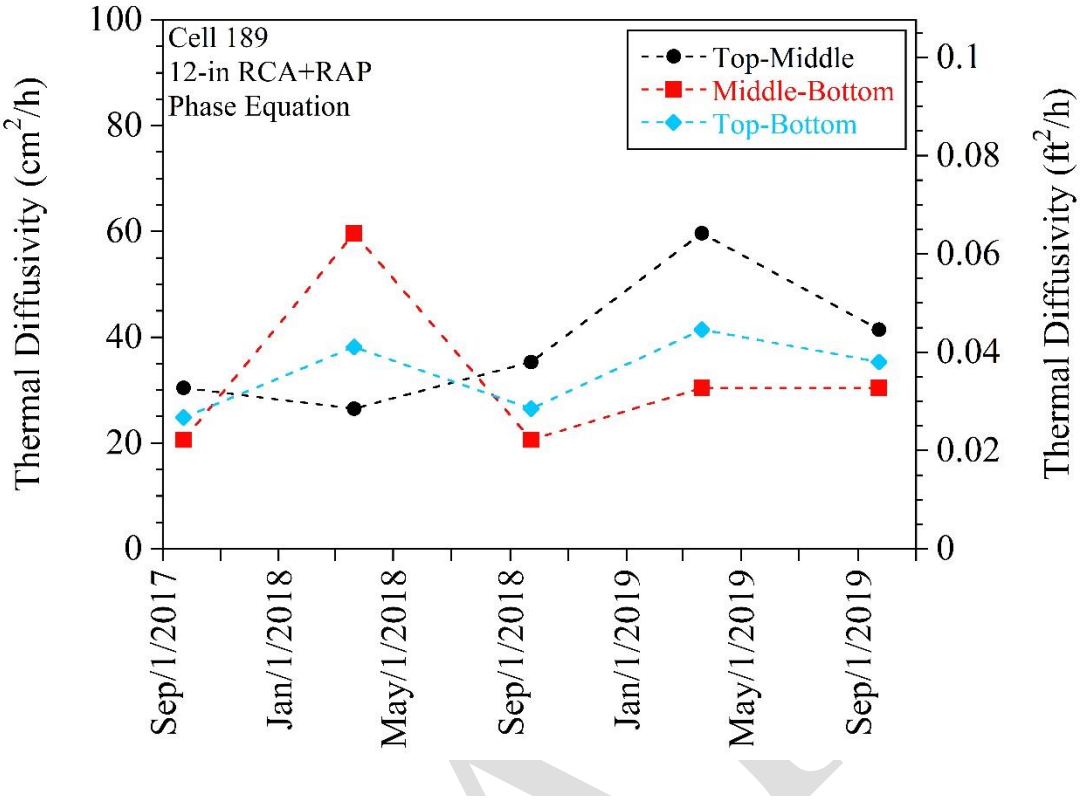


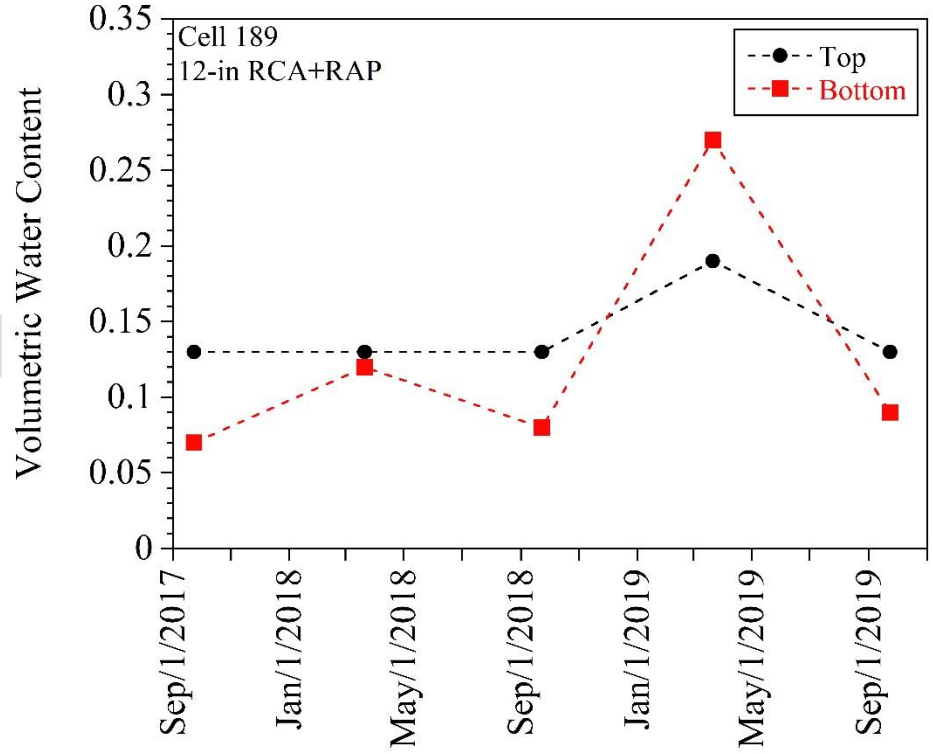




For 12-in RCA+RAP (cell 189):

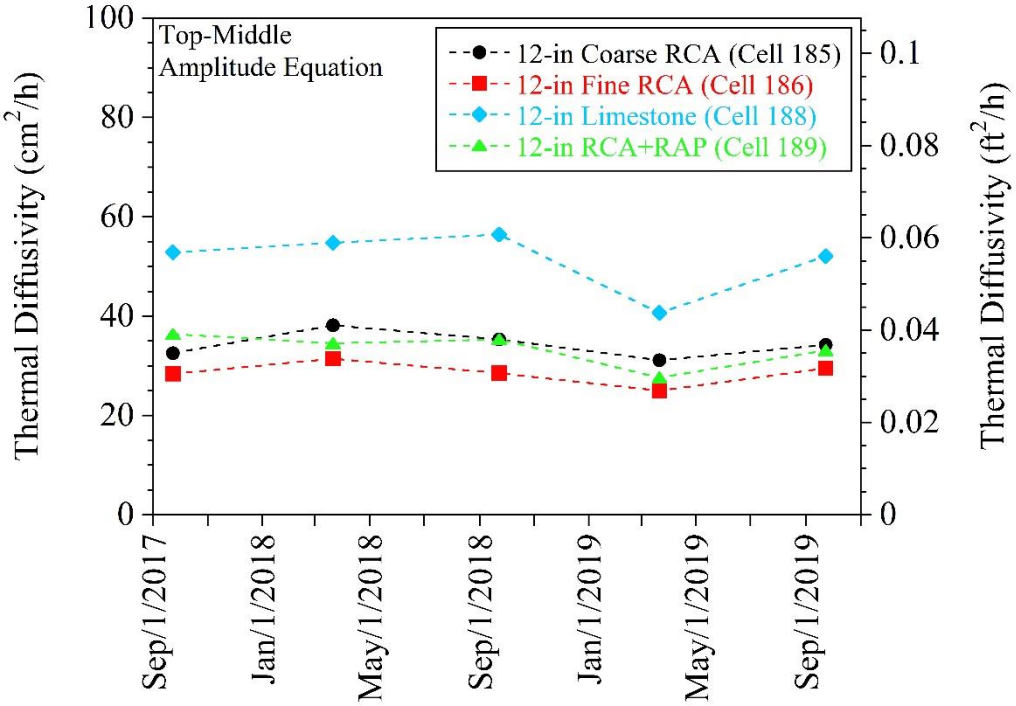



Cell 189
12-in RCA+RAP
Phase Equation
Top-Middle
Middle-Bottom
Top-Bottom
Thermal Diffusivity (cm²/h)
Thermal Diffusivity (ft²/h)
100
80
60
40
20
0
0.1
0.08
0.06
0.04
0.02
0
Sep/1/2017
Jan/1/2018
May/1/2018
Sep/1/2018
Jan/1/2019
May/1/2019
Sep/1/2019

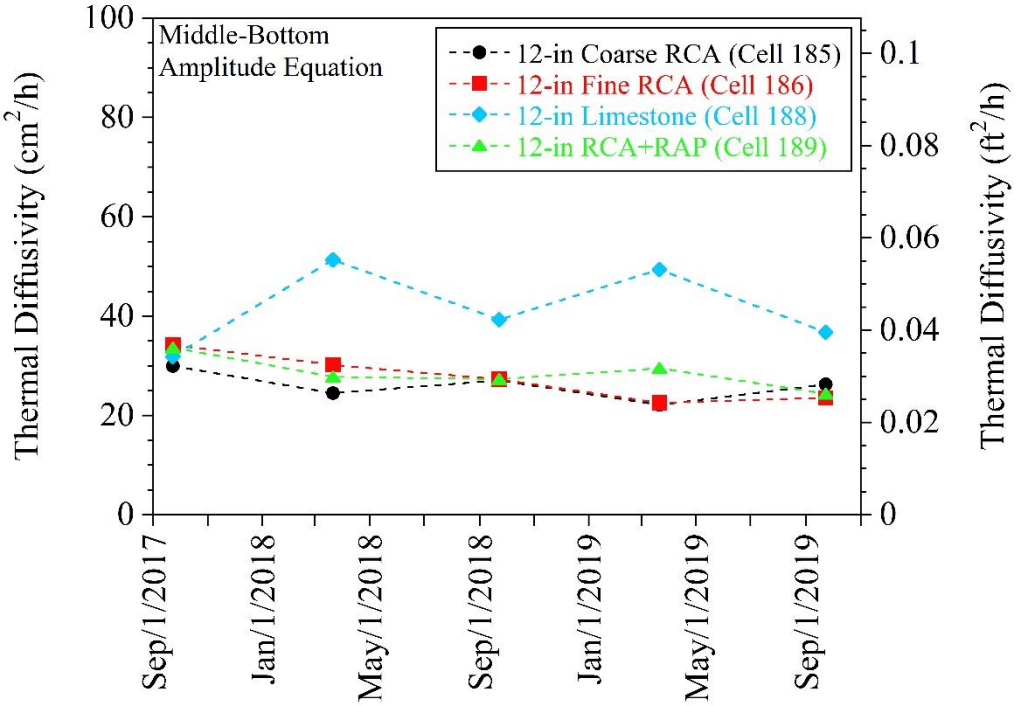

Cell 189
12-in RCA+RAP
Top
Bottom
Volumetric Water Content
0.35
0.3
0.25
0.2
0.15
0.1
0.05
0
Sep/1/2017
Jan/1/2018
May/1/2018
Sep/1/2018
Jan/1/2019
May/1/2019
Sep/1/2019

APPENDIX B. COMPARISONS BETWEEN TOP-MIDDLE AND MIDDLE-BOTTOM THERMOCOUPLES (TC) IN 12-IN BASE LAYERS

For top-middle TC sensors:

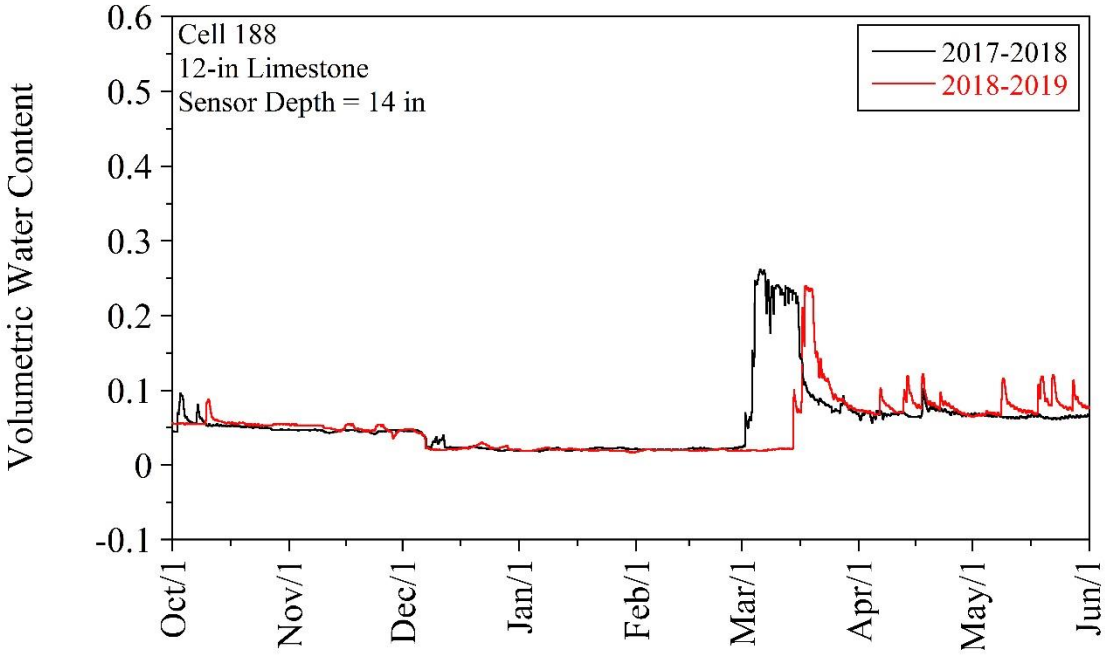


For middle-bottom TC sensors:

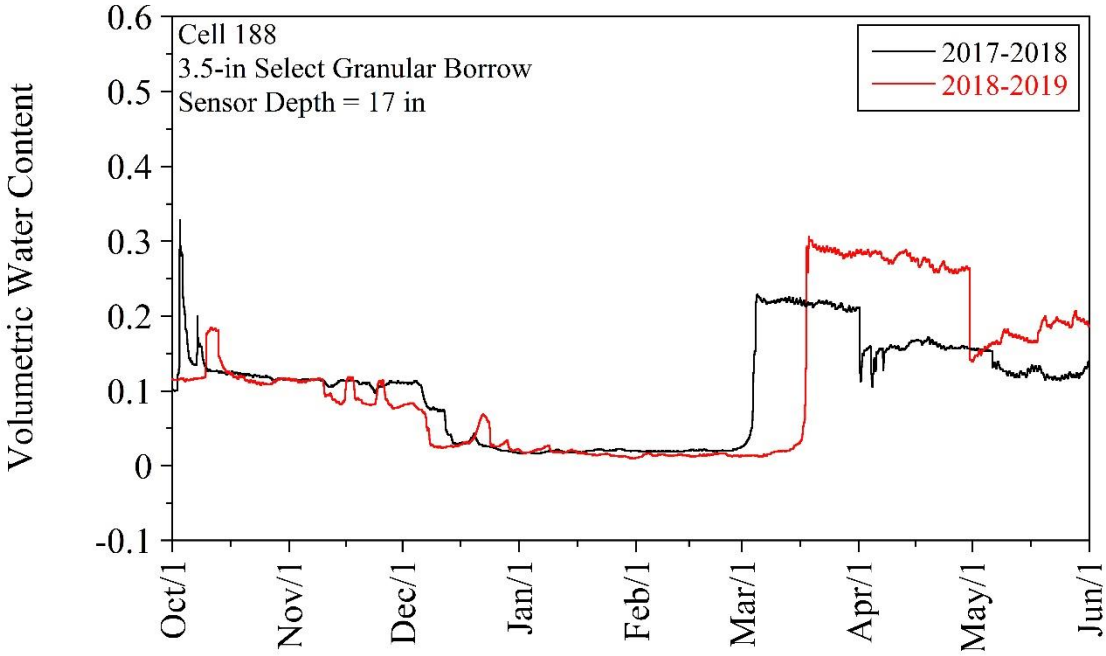


APPENDIX C. COMPARISONS BETWEEN THE VOLUMETRIC WATER CONTENT (VWC) VALUES IN THE FIRST (2017-2018) AND SECOND (2018-2019) FREEZING AND THAWING PERIODS

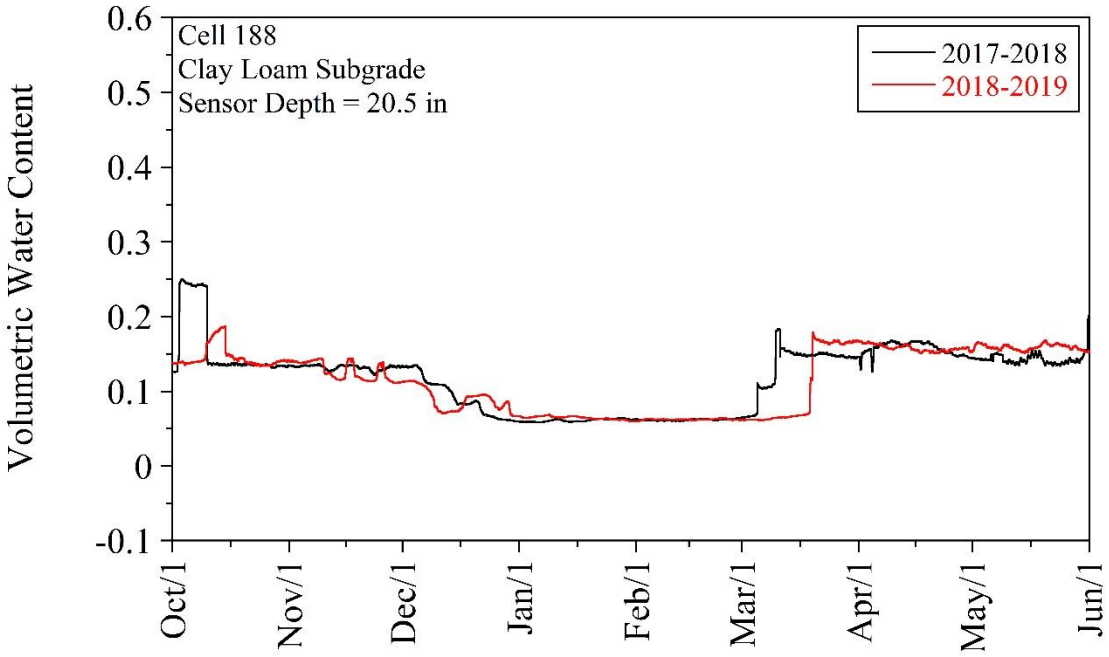
For cell 188:



(the dates on the x-axis represent the time periods for both 2017-2018 and 2018-2019 yeas)

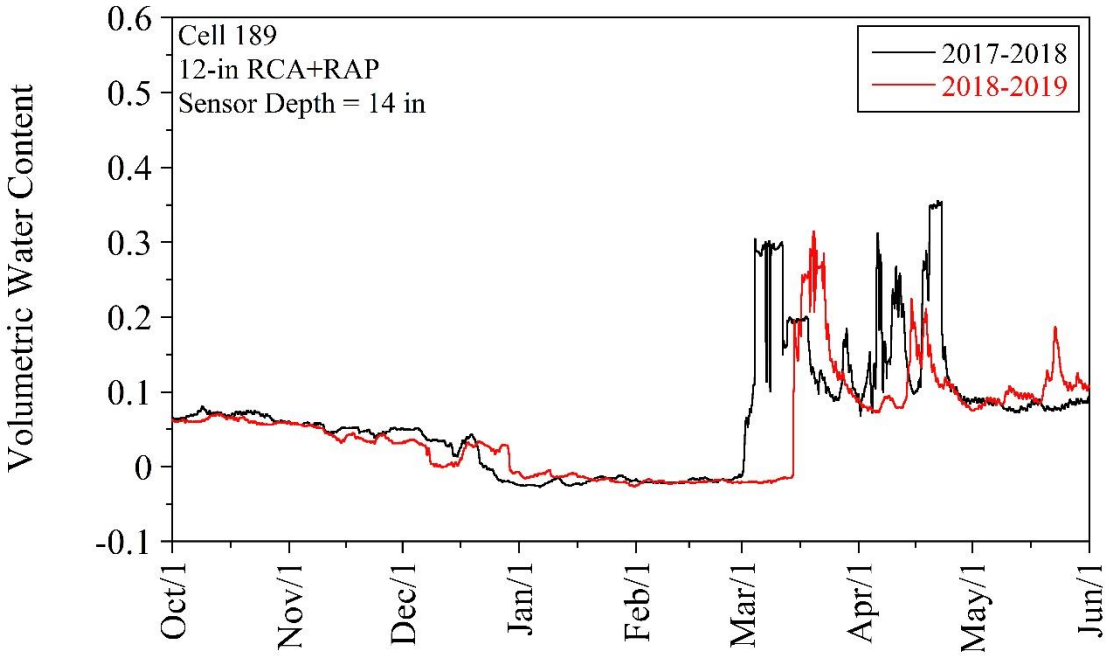


(the dates on the x-axis represent the time periods for both 2017-2018 and 2018-2019 yeas)

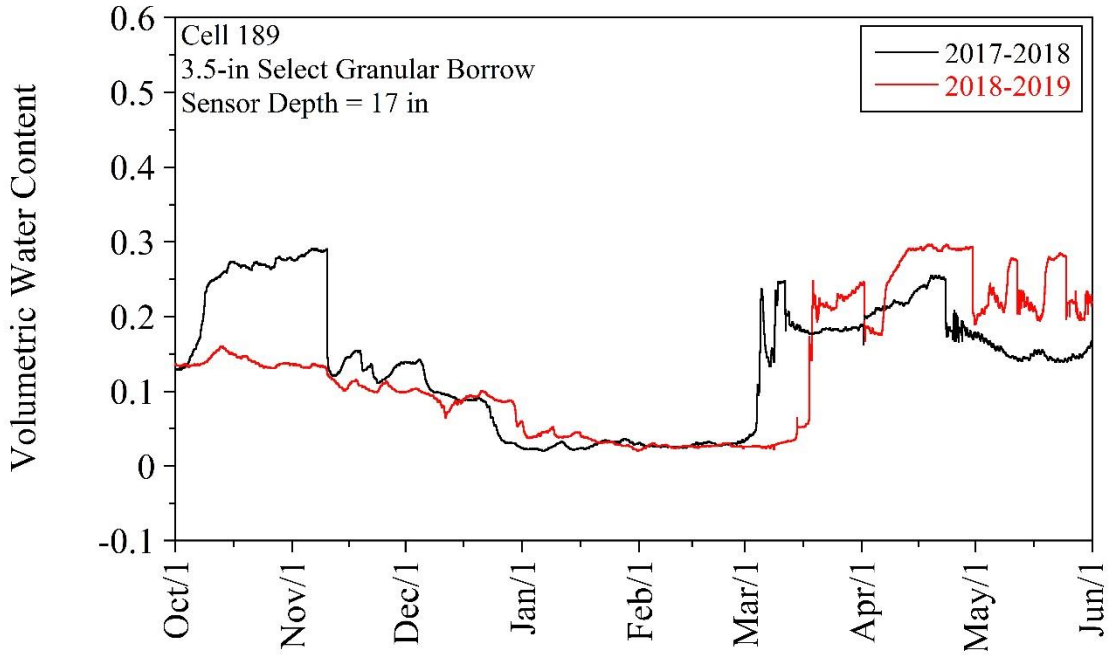


(the dates on the x-axis represent the time periods for both 2017-2018 and 2018-2019 yeas)

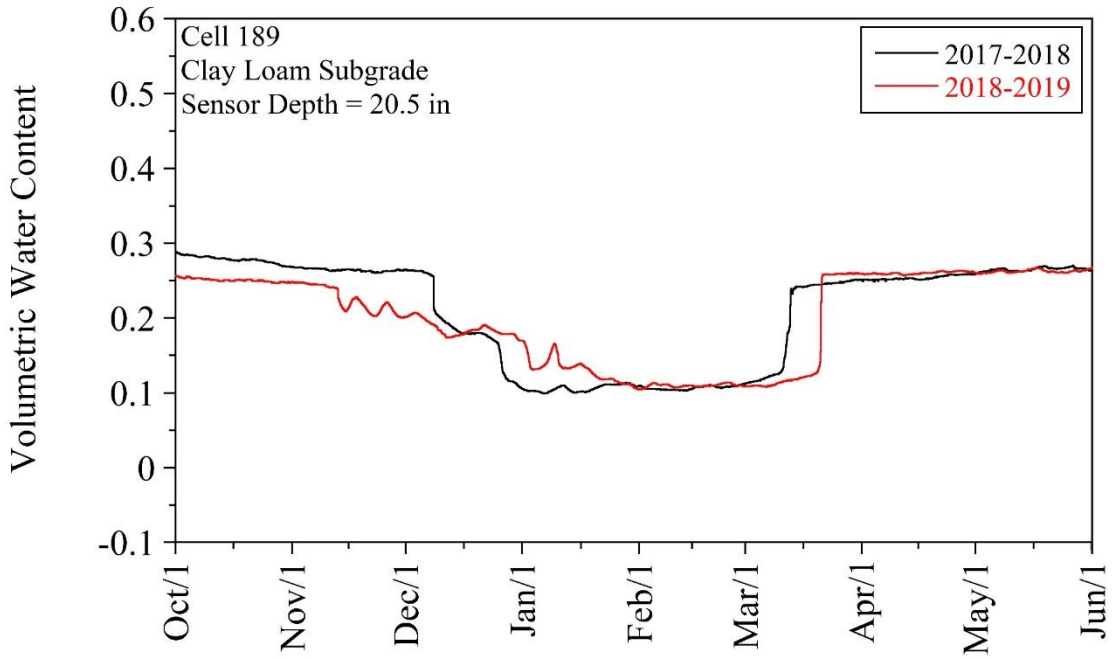
For cell 189:



(the dates on the x-axis represent the time periods for both 2017-2018 and 2018-2019 yeas)

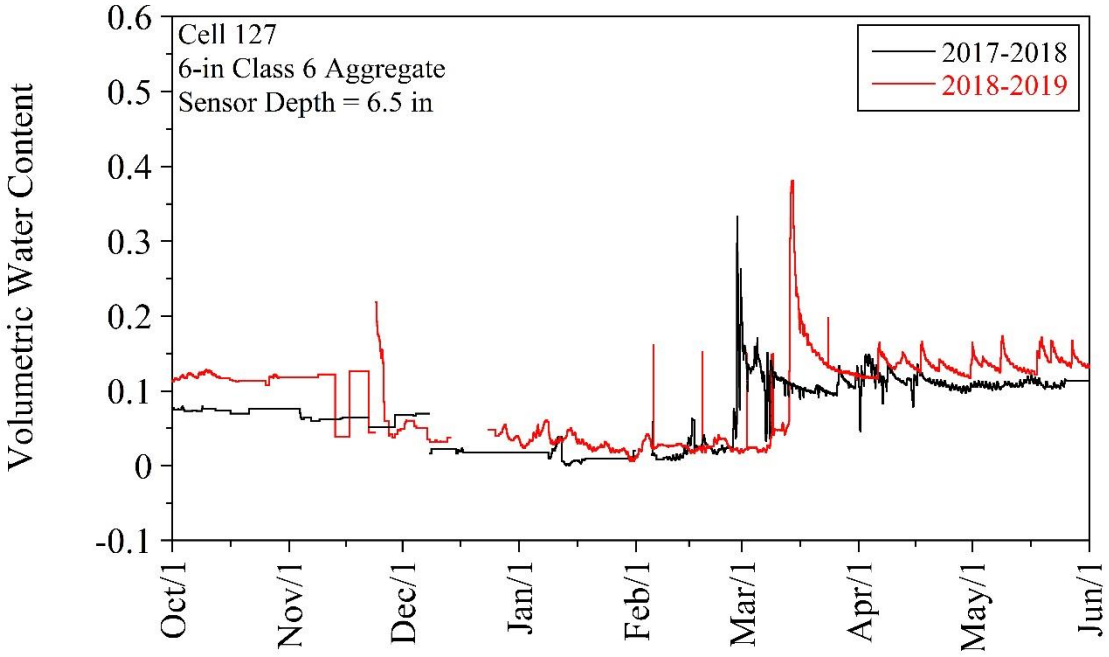


(the dates on the x-axis represent the time periods for both 2017-2018 and 2018-2019 yeas)

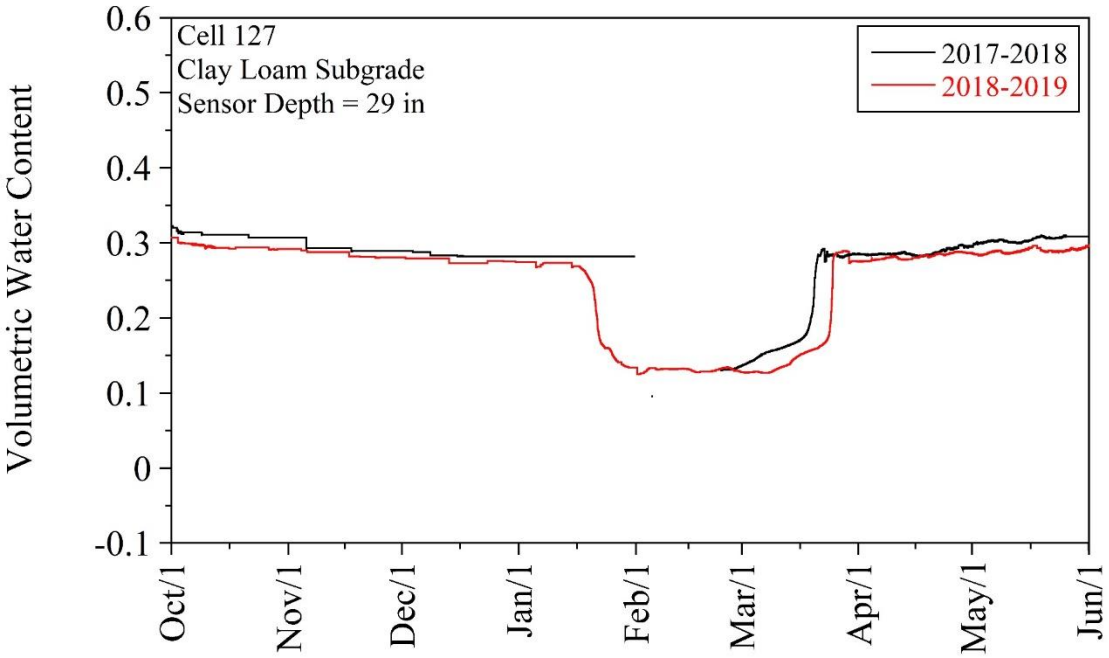


(the dates on the x-axis represent the time periods for both 2017-2018 and 2018-2019 yeas)

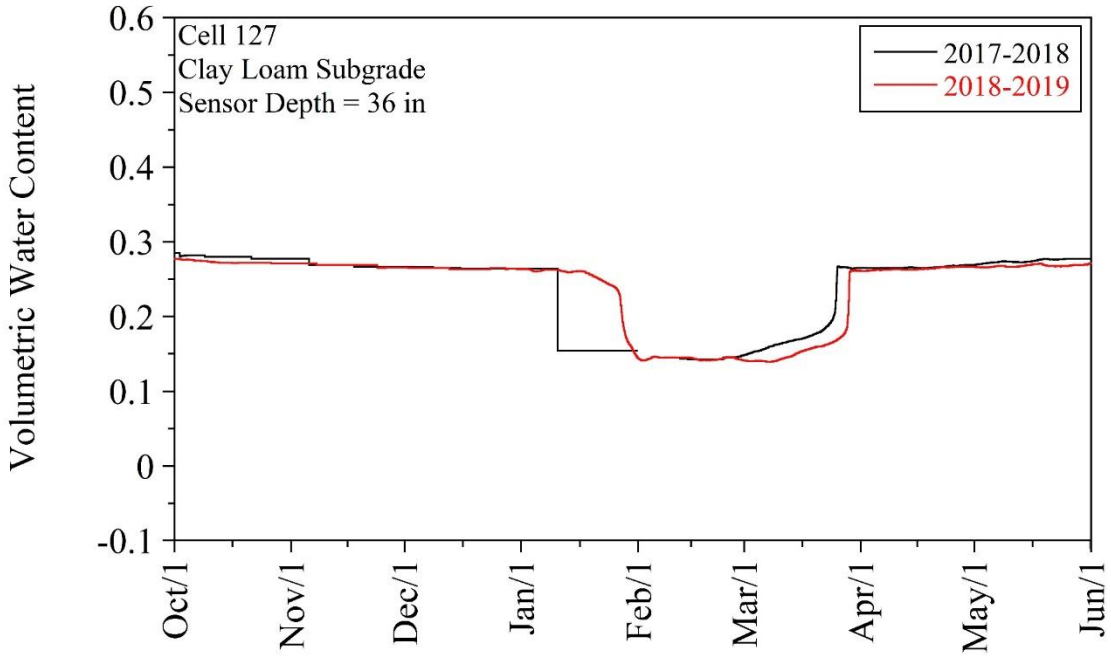
For cell 127:



(the dates on the x-axis represent the time periods for both 2017-2018 and 2018-2019 yeas)

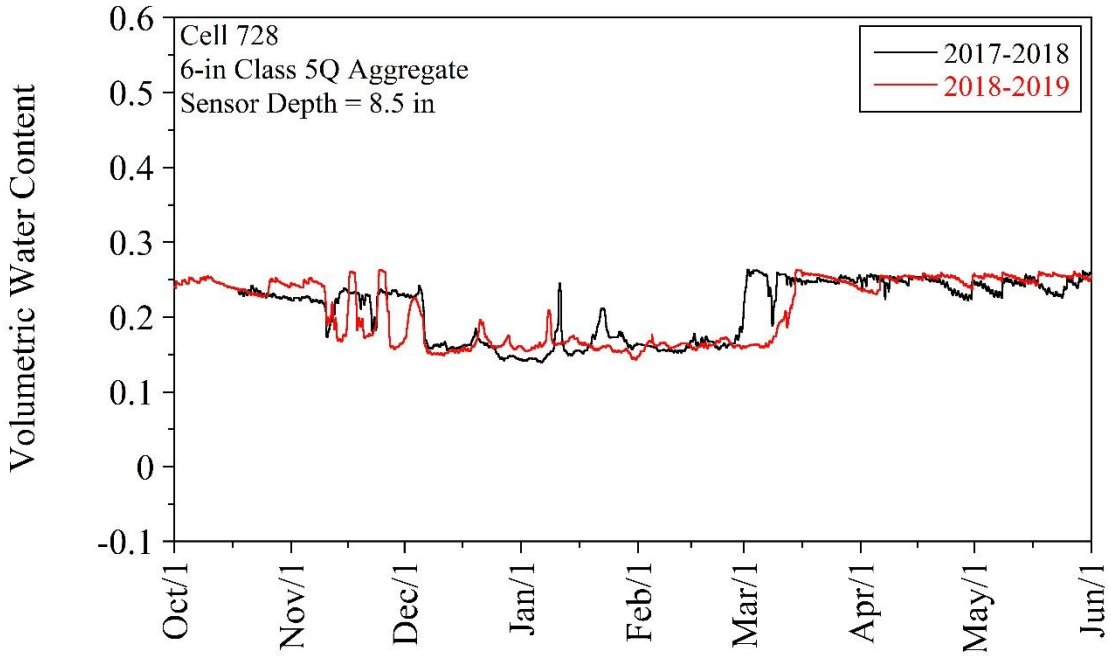


(the dates on the x-axis represent the time periods for both 2017-2018 and 2018-2019 yeas)

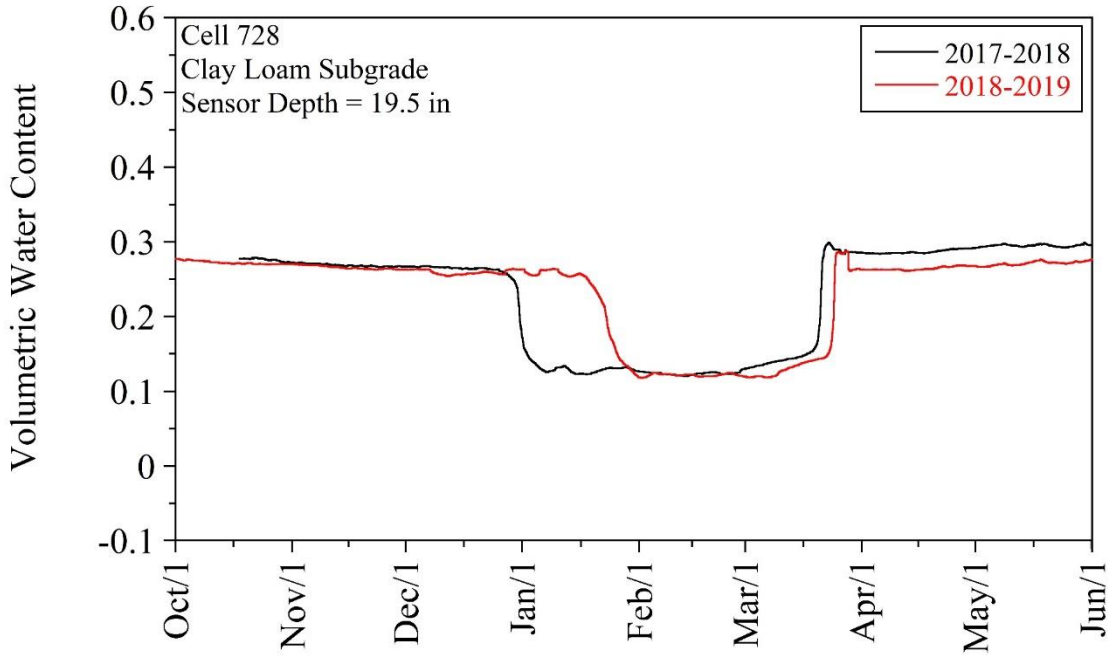


(the dates on the x-axis represent the time periods for both 2017-2018 and 2018-2019 yeas)

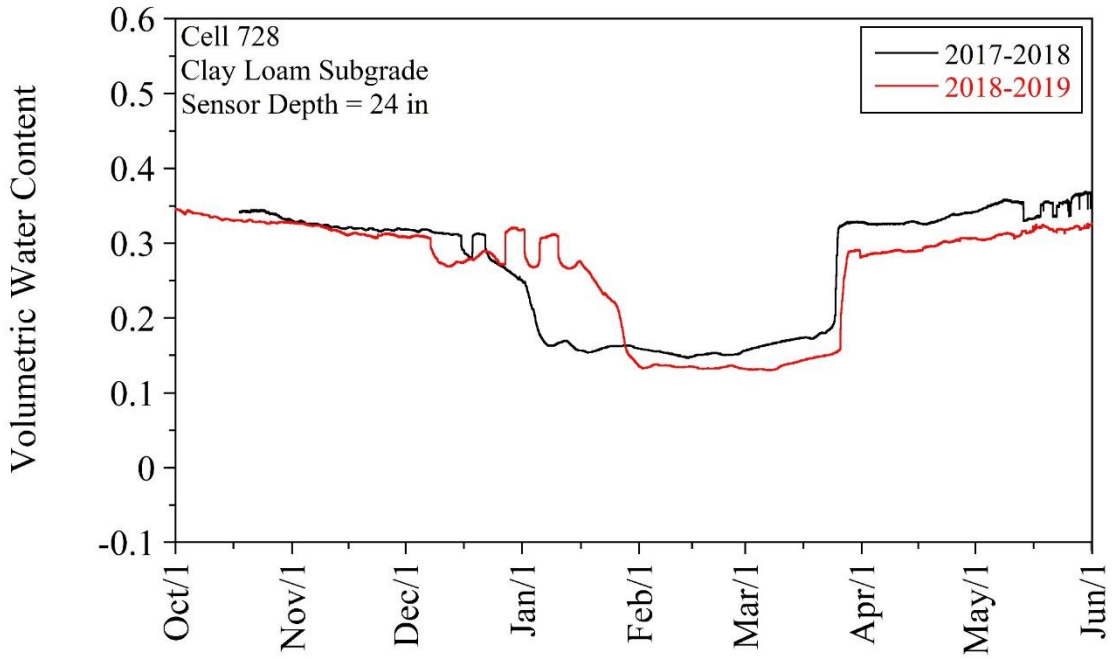
For cell 728:



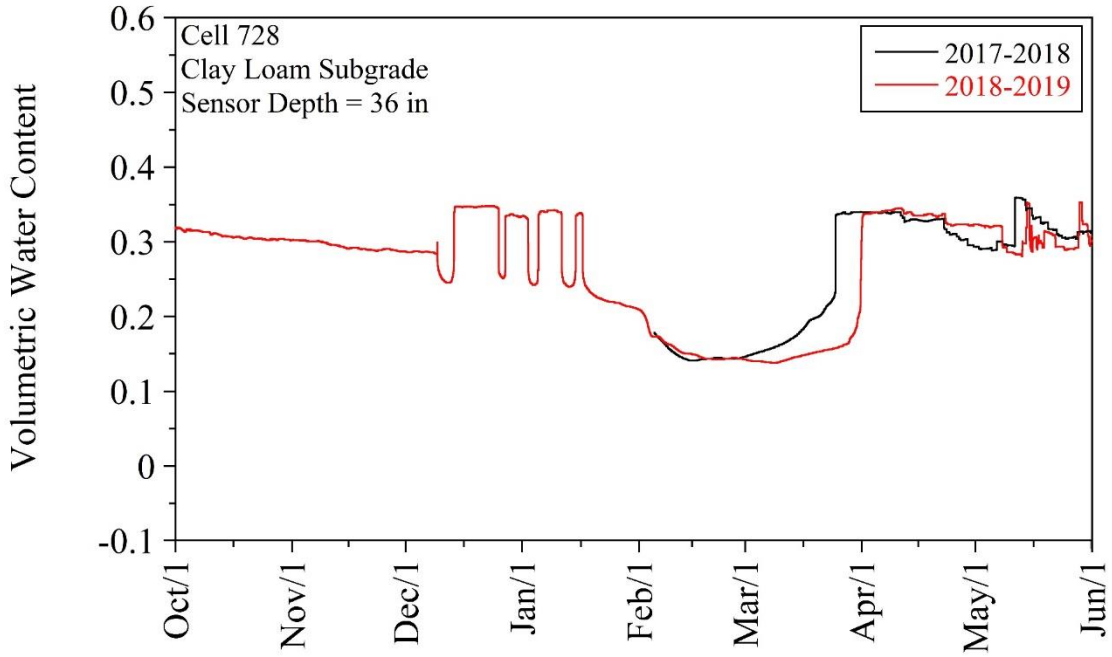
(the dates on the x-axis represent the time periods for both 2017-2018 and 2018-2019 yeas)



(the dates on the x-axis represent the time periods for both 2017-2018 and 2018-2019 yeas)



(the dates on the x-axis represent the time periods for both 2017-2018 and 2018-2019 yeas)



(the dates on the x-axis represent the time periods for both 2017-2018 and 2018-2019 yeas)

DRAFT

APPENDIX D. LABORATORY TEST RESULTS OF THE BASE LAYER AGGREGATES THAT WERE USED IN THE FORWARD STEPWISE REGRESSION ANALYSES

Gradation characteristics:

Material	Gravel (%)	Sand (%)	Gravel-to-Sand Ratio	Fines (%)	D_{10} (mm)	D_{30} (mm)	D_{50} (mm)	D_{60} (mm)	C_u	C_c
Coarse RCA	61.7	34.9	1.77	3.4	0.36	2.79	8.45	12.37	34.49	1.75
Fine RCA	38.3	54.6	0.7	7.1	0.13	0.82	2.98	4.49	33.93	1.12
Limestone	52.3	32.6	1.6	15.1	0.04	0.78	5.39	8.19	211.31	1.91
RCA+RAP	41	50.4	0.81	8.6	0.1	0.71	3.15	5.05	49.41	0.98
Class 6 Agg.	35.1	58.6	0.6	6.3	0.16	0.61	2.12	3.88	23.82	0.6
Class 5Q Agg.	65.9	30.9	2.13	3.2	0.4	3.75	10.05	13.49	33.69	2.6

Fines = silt and clay; D_{10} = effective particle size; D_{30} = particle size at which 30% of the particles are finer; D_{50} = median particle diameter; D_{60} = particle size at which 60% of the particles are finer; C_u = coefficient of uniformity; C_c = coefficient of curvature

Atterberg limits:

Material	LL	PL	PI
Coarse RCA	NA	NA	NP
Fine RCA	32.7	NA	NP
Limestone	17.9	NA	NP
RCA+RAP	27.4	NA	NP
Class 6 Agg.	27.4	NA	NP
Class 5Q Agg.	NA	NA	NP

LL = liquid limit; PL = plastic limit; PI = plasticity index; NA = not available; NP = non-plastic

Oven-dry (OD) specific gravity (G_s):

Material	Coarse OD G_s	Fine OD G_s	Combined OD G_s
Coarse RCA	2.4	2	2.25
Fine RCA	2.45	1.99	2.17
Limestone	2.65	2.68	2.66
RCA+RAP	2.47	2.15	2.28
Class 6 Agg.	2.45	2.3	2.35
Class 5Q Agg.	2.39	2.07	2.28

OD = oven-dry; G_s = specific gravity

DRAFT

Saturated-surface-dry (SSD) specific gravity (G_s):

Material	Coarse SSD G_s	Fine SSD G_s	Combined SSD G_s
Coarse RCA	2.49	2.24	2.4
Fine RCA	2.54	2.23	2.35
Limestone	2.7	2.72	2.71
RCA+RAP	2.54	2.26	2.38
Class 6 Agg.	2.52	2.4	2.44
Class 5Q Agg.	2.5	2.27	2.42

SSD = saturated-surface-dry; G_s = specific gravity

Apparent specific gravity (G_s):

Material	Coarse Apparent G_s	Fine Apparent G_s	Combined Apparent G_s
Coarse RCA	2.65	2.61	2.64
Fine RCA	2.7	2.6	2.64
Limestone	2.79	2.8	2.79
RCA+RAP	2.67	2.42	2.52
Class 6 Agg.	2.64	2.55	2.58
Class 5Q Agg.	2.68	2.59	2.65

G_s = specific gravity

Absorption:

Material	Coarse Absorption (%)	Fine Absorption (%)	Combined Absorption (%)
Coarse RCA	4.05	11.68	6.97
Fine RCA	3.7	11.73	8.65
Limestone	1.91	1.51	1.72
RCA+RAP	3.09	5.22	4.34
Class 6 Agg.	3	4.32	3.86
Class 5Q Agg.	4.62	9.62	6.32

DRAFT

Proctor compaction parameters, void ratio (e), and porosity (n)

Material	Uncorrected MDD (kN/m^3)	Uncorrected OMC (%)	Corrected MDD (kN/m^3)	Corrected OMC (%)	e	n
Coarse RCA	19.31	11.3	20.19	9.48	0.28	0.22
Fine RCA	19.1	11.1	19.12	11.07	0.35	0.26
Limestone	22.34	6.2	22.49	6.28	0.22	0.18
RCA+RAP	19.73	10	19.76	9.97	0.25	0.2
Class 6 Agg.	20.14	8.3	20.19	8.26	0.25	0.2
Class 5Q Agg.	19.26	11	20.11	9.63	0.29	0.23

MDD = maximum dry density; OMC = optimum moisture content; e = void ratio [based on corrected MDD and apparent specific gravity (G_s)]; n = porosity [n = e/(1+e)]

Asphalt binder and residual mortar contents:

Material	Asphalt Binder Content by Ignition (%)	Asphalt Binder Content by Extraction (%)	Residual Mortar Content (%)
Coarse RCA	2.02	0.1	33.4
Fine RCA	2.98	0.38	29.6
Limestone	1.61	0.35	1.3
RCA+RAP	3.18	1.58	20.1
Class 6 Agg.	3.17	1.77	25.6
Class 5Q Agg.	2.15	0.28	37.1

Width-to-length ratio sphericity:

Material	Median Sphericity	$PLS_{0.9}$ (%)	$PLS_{0.7}$ (%)	$PLS_{0.5}$ (%)	$PLS_{0.3}$ (%)	$PLS_{0.1}$ (%)
Coarse RCA	0.769729034	88	28	1	0	0
Fine RCA	0.758298649	90	32	2.5	0	0
Limestone	0.775580109	88	26	1	0	0
RCA+RAP	0.763247555	90.5	30	2	0	0
Class 6 Agg.	0.759657917	90	32	2	0	0
Class 5Q Agg.	0.756547947	90.5	33	2	0	0

$PLS_{0.9}$ = percent less spherical than 0.9; $PLS_{0.7}$ = percent less spherical than 0.7; $PLS_{0.5}$ = percent less spherical than 0.5; $PLS_{0.3}$ = percent less spherical than 0.3; $PLS_{0.1}$ = percent less spherical than 0.1

DRAFT

Roundness:

Material	Median Roundness	$PLR_{0.9}$ (%)	$PLR_{0.7}$ (%)	$PLR_{0.5}$ (%)	$PLR_{0.3}$ (%)	$PLR_{0.1}$ (%)
Coarse RCA	0.660245895	99.5	64	11	0.5	0
Fine RCA	0.657135606	99.5	66	9.5	0	0
Limestone	0.649245381	99.5	67.5	10	0	0
RCA+RAP	0.663714975	100	63.5	8.5	0	0
Class 6 Agg.	0.663310677	99	63.5	10	0	0
Class 5Q Agg.	0.641065776	100	70	12.5	0	0

$PLR_{0.9}$ = percent less rounded than 0.9; $PLR_{0.7}$ = percent less rounded than 0.7; $PLR_{0.5}$ = percent less rounded than 0.5; $PLR_{0.3}$ = percent less rounded than 0.3; $PLR_{0.1}$ = percent less rounded than 0.1

Relative breakage (B_r):

Material	B_r After 100 Gyrations	B_r After 300 Gyrations	B_r After 500 Gyrations
Coarse RCA	0.03407	0.03801	0.06440
Fine RCA	0.02577	0.03413	0.05325
Limestone	0.01421	0.01848	0.02582
RCA+RAP	0.02146	0.02436	0.02777
Class 6 Agg.	0.02677	0.02942	0.03870
Class 5Q Agg.	0.04644	0.06259	0.07820

B_r = relative breakage

Saturated hydraulic conductivity (K_{sat}) and soil-water characteristic curve (SWCC) parameters:

Material	K_{sat} (cm/sec)	Residual VWC	Saturated VWC	Air-Entry Pressure (kPa)
Coarse RCA	2.67E-04	0	0.2804	2.5
Fine RCA	4.85E-04	0	0.2887	6
Limestone	4.86E-05	0.0406	0.2366	2
RCA+RAP	2.06E-04	0.0048	0.2764	2
Class 6 Agg.	1.91E-04	0.0502	0.2607	3
Class 5Q Agg.	2.91E-04	0.0318	0.317	1.75

K_{sat} = saturated hydraulic conductivity; VWC = volumetric water content

DRAFT

Resilient modulus (M_R):

Material	M_R (MPa)	k_1	k_2	k_3
Coarse RCA	124.99	913	0.44	-0.07
Fine RCA	122.46	882	0.45	-0.06
Limestone	96.02	762	0.32	-0.05
RCA+RAP	113.68	803	0.51	-0.12
Class 6 Agg.	NA	NA	NA	NA
Class 5Q Agg.	NA	NA	NA	NA

M_R = resilient modulus; k_1, k_2, and k_3 = MEPDG M_R model fitting parameters; NA = not available

DRAFT

APPENDIX E. ALTERNATIVE MODELS TO ESTIMATE UNCORRECTED OPTIMUM MOISTURE CONTENT (OMC) AND MAXIMUM DRY DENSITY (MDD) VALUES OF AGGREGATE BASE LAYERS

For uncorrected optimum moisture content (OMC):

Equation	R^2	Adj. R^2	Std. Error
-13.7918*Combined OD G_s - 0.1033*Sand (%) - 0.1434*D_{50} (mm) + 47.0832	1	1	0
-13.7114*Combined OD G_s - 0.0854*Sand (%) - 0.2107*D_{30} (mm) + 45.6781	1	1	0.02
-13.5679*Combined OD G_s - 0.0760*Sand (%) - 1.3958*D_{10} (mm) + 44.8785	1	1	0.04
-13.7779*Combined OD G_s - 0.1166*Sand (%) - 0.0477*Gravel (%) + 49.2062	1	1	0.02
-13.7779*Combined OD G_s - 0.0689*Sand (%) + 0.0477*Fines (%) + 44.4357	1	1	0.05
-10.2402*Fine SSD G_s - 0.6206*Asphalt Binder Content by Extraction (%) + 0.2358*C_c + 33.8534	1	1	0.05
0.3288*Fine Absorption (%) - 9.1184*Fine Apparent G_s + 0.3155*C_c - 0.4603*Asphalt Binder Content by Extraction (%) + 30.7698	1	1	0.05
-12.6425*Combined OD G_s - 0.0632*Sand (%) + 41.8871	1	1	0
-7.6245*Fine OD G_s + 0.4420*C_c + 25.7617	1	1	0.14
-11.8099*Fine SSD G_s - 0.9615*Asphalt Binder Content by Ignition (%) + 39.8574	1	0.99	0.18
-19.6912*Combined SSD G_s - 1.7824*Asphalt Binder Content by Ignition (%) + 62.3518	0.99	0.98	0.29
-13.6173*Combined OD G_s - 1.2124*Asphalt Binder Content by Ignition (%) + 44.4507	0.99	0.97	0.32
-10.9676*Combined OD G_s + 0.1602*D_{60} (mm) + 33.9536	0.98	0.97	0.35
-10.8351*Combined OD G_s + 0.2065*D_{50} (mm) + 33.8059	0.98	0.97	0.35
-11.7264*Combined OD G_s + 0.9328*C_c + 35.5972	0.98	0.97	0.35
-17.0353*Combined SSD G_s - 0.0793*Sand (%) + 54.8267	0.98	0.97	0.36
-15.6546*Combined SSD G_s + 1.2149*C_c + 46.1668	0.97	0.95	0.45
-14.0096*Combined SSD G_s + 0.2540*D_{50} (mm) + 42.5928	0.97	0.94	0.49
-10.9123*Combined OD G_s + 35.0921	0.96	0.92	0.56
0.7431*Combined Absorption (%) + 5.7034	0.87	0.84	0.81
-13.6175*Combined SSD G_s + 42.9932	0.83	0.79	0.93

G_s = specific gravity; SSD = saturated-surface-dry; OD = oven-dry; C_c = coefficient of curvature

DRAFT

For uncorrected maximum dry density (MDD):

Equation	R^2	Adj. R^2	Std. Error
6.3812*Combined SSD G_s - 0.4756*Coarse Absorption (%) + 5.9683	1	1	0.07
5.4082*Combined OD G_s - 0.3449*Coarse Absorption (%) + 8.5401	1	0.99	0.09
6.5823*Combined OD G_s - 0.1496*D_{30} (mm) + 4.8677	1	0.99	0.1
4.9439*Combined OD G_s - 0.0304*Residual Mortar Content (%) + 9.1974	1	0.99	0.11
4.5928*Fine SSD G_s - 0.0280*Residual Mortar Content (%) + 9.8594	1	0.99	0.11
5.4125*Combined OD G_s + 0.0730*Fines (%) + 6.8279	0.99	0.99	0.12
5.6446*Combined SSD G_s - 0.0401*Residual Mortar Content (%) + 7.1398	0.99	0.98	0.16
9.5737*Combined SSD G_s - 0.3991*C_c - 2.8669	0.99	0.98	0.17
9.0361*Combined SSD G_s - 0.0852*D_{50} (mm) - 1.6901	0.99	0.98	0.17
7.9065*Combined SSD G_s - 2.0737*D_{10} (mm) + 1.0323	0.99	0.98	0.18
9.0976*Combined SSD G_s - 0.0648*D_{60} (mm) - 1.7844	0.99	0.98	0.19
-0.2085*Fine Absorption (%) + 6.9277*Combined Apparent G_s + 3.2383	0.97	0.96	0.25
-1.3568*Coarse Absorption (%) + 0.8841*Gravel-to-Sand Ratio + 23.4612	0.97	0.95	0.26
-1.3618*Coarse Absorption (%) + 0.7804*C_c + 23.4353	0.97	0.95	0.27
6.9110*Combined OD G_s + 3.8658	0.97	0.96	0.23
-1.5319*Coarse Absorption (%) + 0.1977*D_{50} (mm) + 24.1188	0.97	0.94	0.29
-0.3613*Combined Absorption (%) + 4.5591*Fine Apparent G_s + 10.0660	0.96	0.93	0.33
-1.0944*Coarse Absorption (%) - 0.7557*Asphalt Binder Content by Ignition (%) + 25.5955	0.96	0.93	0.33
-1.4842*Coarse Absorption (%) + 0.1448*D_{60} (mm) + 23.8709	0.96	0.93	0.33
-0.3588*Combined Absorption (%) + 6.1792*Combined Apparent G_s + 5.5866	0.96	0.92	0.33
-0.3175*Combined Absorption (%) + 11.6006*Coarse Apparent G_s - 9.5334	0.96	0.93	0.33
-1.4232*Coarse Absorption (%) + 0.0446*Gravel (%) + 22.6210	0.96	0.93	0.33
8.9049*Combined SSD G_s - 1.8244	0.94	0.92	0.34
-0.4286*Combined Absorption (%) + 22.2548	0.77	0.71	0.65

G_s = specific gravity; SSD = saturated-surface-dry; OD = oven-dry; C_c = coefficient of curvature

DRAFT

APPENDIX F. ALTERNATIVE MODELS TO ESTIMATE CORRECTED OPTIMUM MOISTURE CONTENT (OMC) AND MAXIMUM DRY DENSITY (MDD) VALUES OF AGGREGATE BASE LAYERS

For corrected optimum moisture content (OMC):

Equation	R^2	Adj. R^2	Std. Error
0.9066*Uncorrected OMC (%) - 0.3036*D_{60} (mm) + 0.8947*C_c + 1.4338	1	1	0.11
0.8501*Uncorrected OMC (%) - 0.1533*D_{60} (mm) + 2.1258	0.97	0.96	0.34
1.0244*Uncorrected OMC (%) - 5.5904*D_{10} (mm) + 0.3445	0.97	0.95	0.37
0.8580*Uncorrected OMC (%) - 0.1930*D_{50} (mm) + 1.8711	0.97	0.94	0.4
0.8252*Uncorrected OMC (%) - 0.0470*Gravel (%) + 3.4571	0.97	0.94	0.4
0.9422*Uncorrected OMC (%) - 0.5206*D_{30} (mm) + 0.8448	0.96	0.94	0.41
-11.7635*Combined SSD G_s + 37.9200	0.88	0.85	0.64
0.7499*Uncorrected OMC (%) + 1.8796	0.84	0.8	0.74

OMC = optimum moisture content; C_c = coefficient of curvature; SSD = saturated-surface-dry; G_s = specific gravity

DRAFT

For corrected maximum dry density (MDD):

Equation	R^2	Adj. R^2	Std. Error
1.3991*Uncorrected MDD (kN/m^3) + 0.8096*D_{50} - 3.4342*Gravel-to-Sand Ratio - 7.6185	1	1	0.04
-0.4399*Uncorrected OMC (%) - 1.2115*Asphalt Binder Content by Ignition (%) - 2.1556*Fine Apparent G_s + 33.1997	1	1	0.05
0.9264*Uncorrected MDD (kN/m^3) + 0.0938*D_{60} (mm) + 1.0596	1	0.99	0.1
1.1356*Uncorrected MDD (kN/m^3) + 3.3492*D_{10} (mm) - 3.0446	0.99	0.99	0.13
0.9375*Uncorrected MDD (kN/m^3) + 0.1195*D_{50} (mm) + 0.9394	0.99	0.99	0.14
0.8999*Uncorrected MDD (kN/m^3) + 0.0297*Gravel (%) + 0.8753	0.99	0.99	0.14
1.0342*Uncorrected MDD (kN/m^3) + 0.3132*D_{30} (mm) - 0.8455	0.99	0.98	0.14
0.8580*Uncorrected MDD (kN/m^3) + 0.5861*Gravel-to-Sand Ratio + 2.4342	0.99	0.98	0.16
-0.3939*Uncorrected OMC (%) - 0.9332*Asphalt Binder Content by Ignition (%) + 26.4608	0.99	0.98	0.17
-0.4655*Uncorrected OMC (%) - 0.0494*Sand (%) + 26.9591	0.99	0.98	0.18
0.8015*Uncorrected MDD (kN/m^3) - 0.0310*Sand (%) + 5.6495	0.98	0.97	0.2
0.7185*Uncorrected MDD (kN/m^3) - 0.6171*Asphalt Binder Content by Ignition (%) + 7.5096	0.98	0.97	0.2
3.6328*Fine OD G_s - 0.0368*Sand (%) + 13.9284	0.98	0.96	0.22
5.0802*Fine SSD G_s - 0.0290*Sand (%) + 9.6254	0.98	0.96	0.23
4.2779*Fine OD G_s + 0.1074*D_{60} (mm) + 10.0510	0.98	0.96	0.23
5.7675*Fine SSD G_s + 0.0815*D_{60} (mm) + 6.0954	0.98	0.96	0.23
1.4339*Uncorrected MDD (kN/m^3) + 0.7989*Coarse Absorption (%) - 11.0475	0.98	0.96	0.23
-0.5524*Uncorrected OMC (%) + 0.0475*Gravel (%) + 23.3136	0.97	0.96	0.24
3.9122*Fine OD G_s + 0.6678*Gravel-to-Sand Ratio + 10.8568	0.97	0.95	0.26
4.3220*Fine OD G_s + 0.1350*D_{50} (mm) + 10.0800	0.97	0.95	0.26
-0.5099*Uncorrected OMC (%) + 0.9094*Gravel-to-Sand Ratio + 24.0760	0.97	0.94	0.27
-0.5817*Uncorrected OMC (%) + 0.1881*D_{50} (mm) + 24.9159	0.96	0.93	0.31
0.8848*Uncorrected MDD (kN/m^3) + 2.6339	0.88	0.85	0.44
-0.4764*Uncorrected OMC (%) + 24.9076	0.71	0.63	0.69

MDD = maximum dry density; OMC = optimum moisture content; G_s = specific gravity; SSD = saturated-surface-dry

DRAFT

APPENDIX G. ALTERNATIVE MODELS TO ESTIMATE SATURATD HYDRAULIC CONDUCTIVITY (K_{sat}) VALUES OF AGGREGATE BASE LAYERS

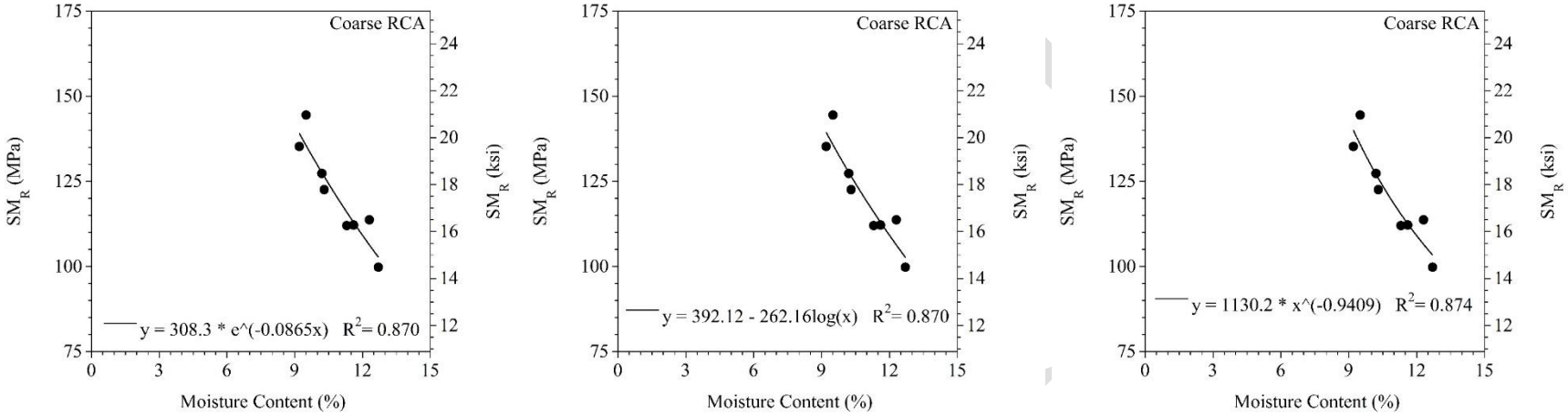
Equation	R^2	Adj. R^2	Std. Error
0.001581*Corrected MDD (kN/m^3) - 0.012708*Combined Apparent G_s + 0.046235*n - 0.008281	1	1	4.23E-06
0.002988*e - 0.000185*Combined Apparent G_s - 8.53E-05	1	1	7.14E-06
0.002735*e - 0.000165*Combined SSD G_s - 9.97E-05	1	1	9.99E-06

MDD = maximum dry density; G_s = specific gravity; e = void ratio [based on corrected MDD and apparent specific gravity (G_s)]; n = porosity [n = e/(1+e)]; SSD = saturated-surface-dry

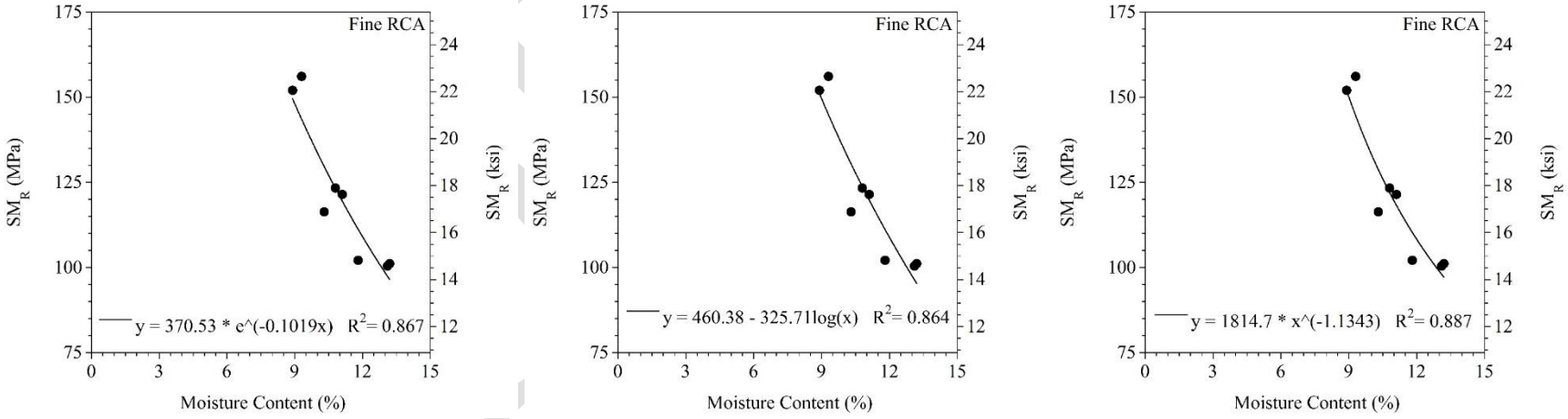
DRAFT

APPENDIX H. SUMMARY RESILIENT MODULUS (SM_R) VS. MOISTURE CONTENT

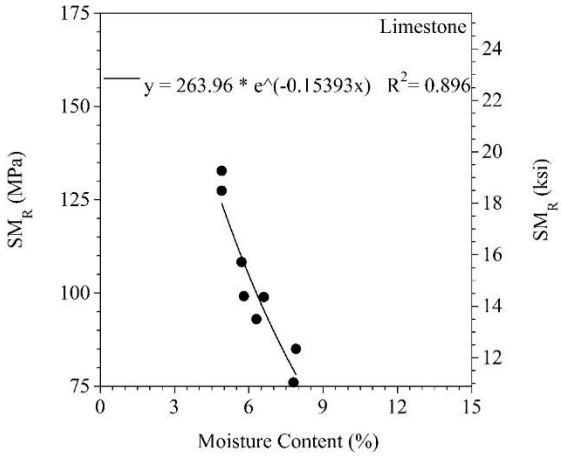
For coarse RCA:

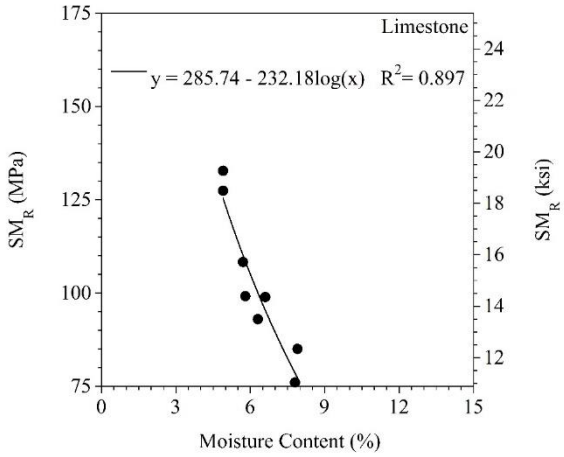


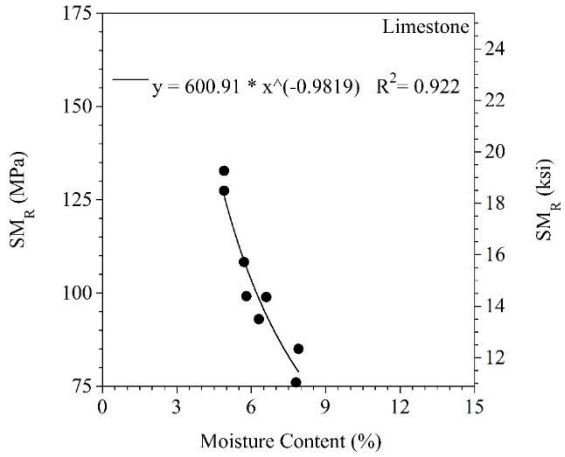
For fine RCA:



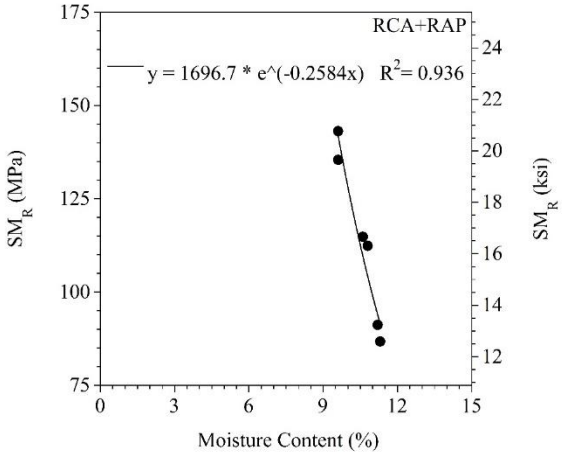
For limestone:

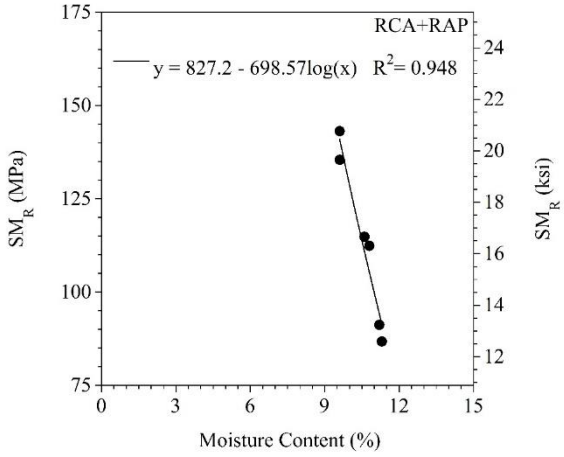


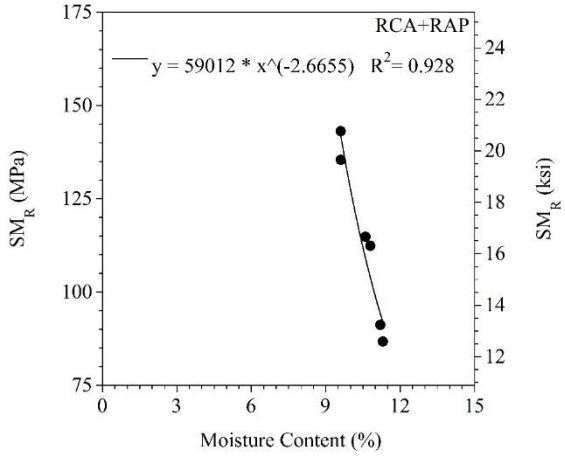




For RCA+RAP:

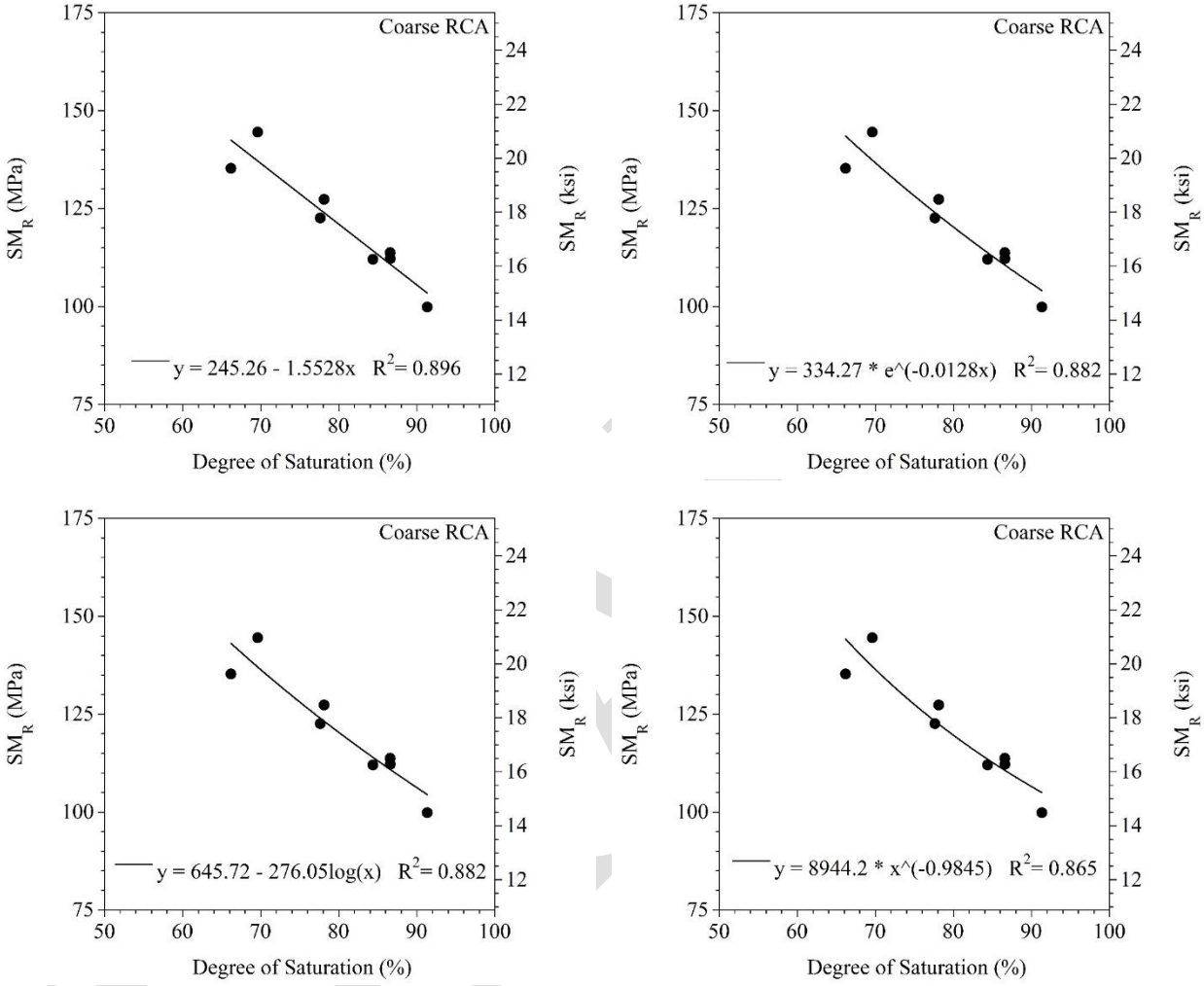




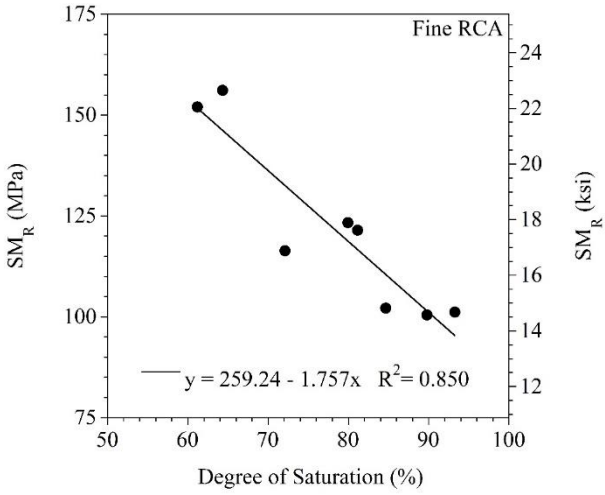


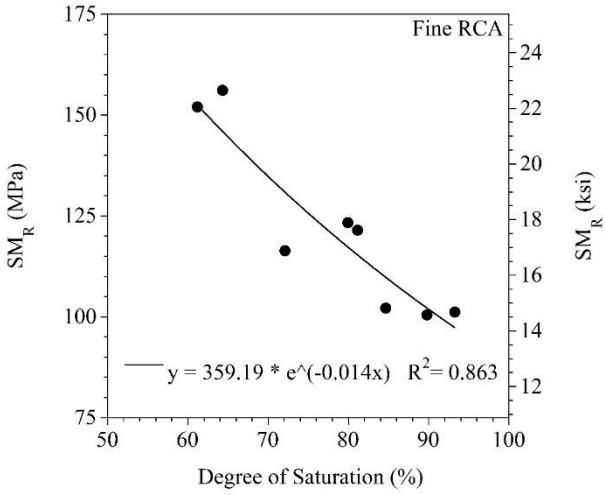
APPENDIX I. SUMMARY RESILIENT MODULUS (SM_R) VS. DEGREE OF SATURATION (DOS)

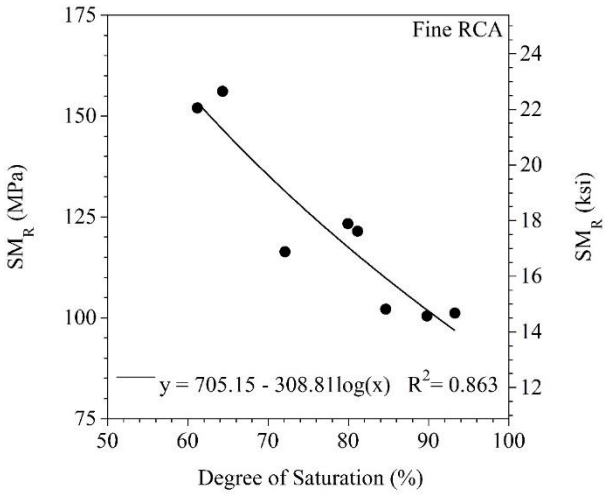
For coarse RCA:

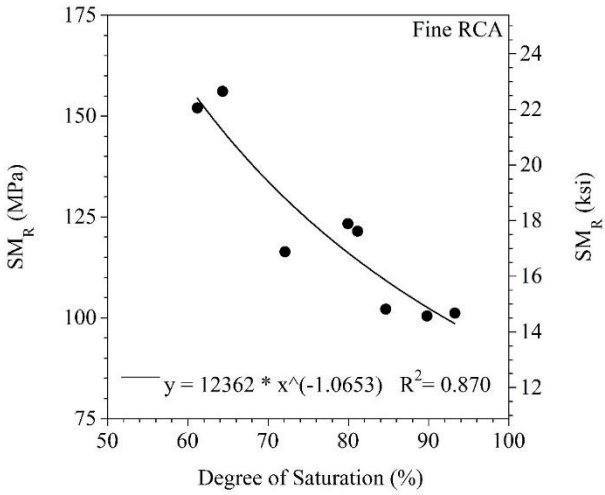


For fine RCA:



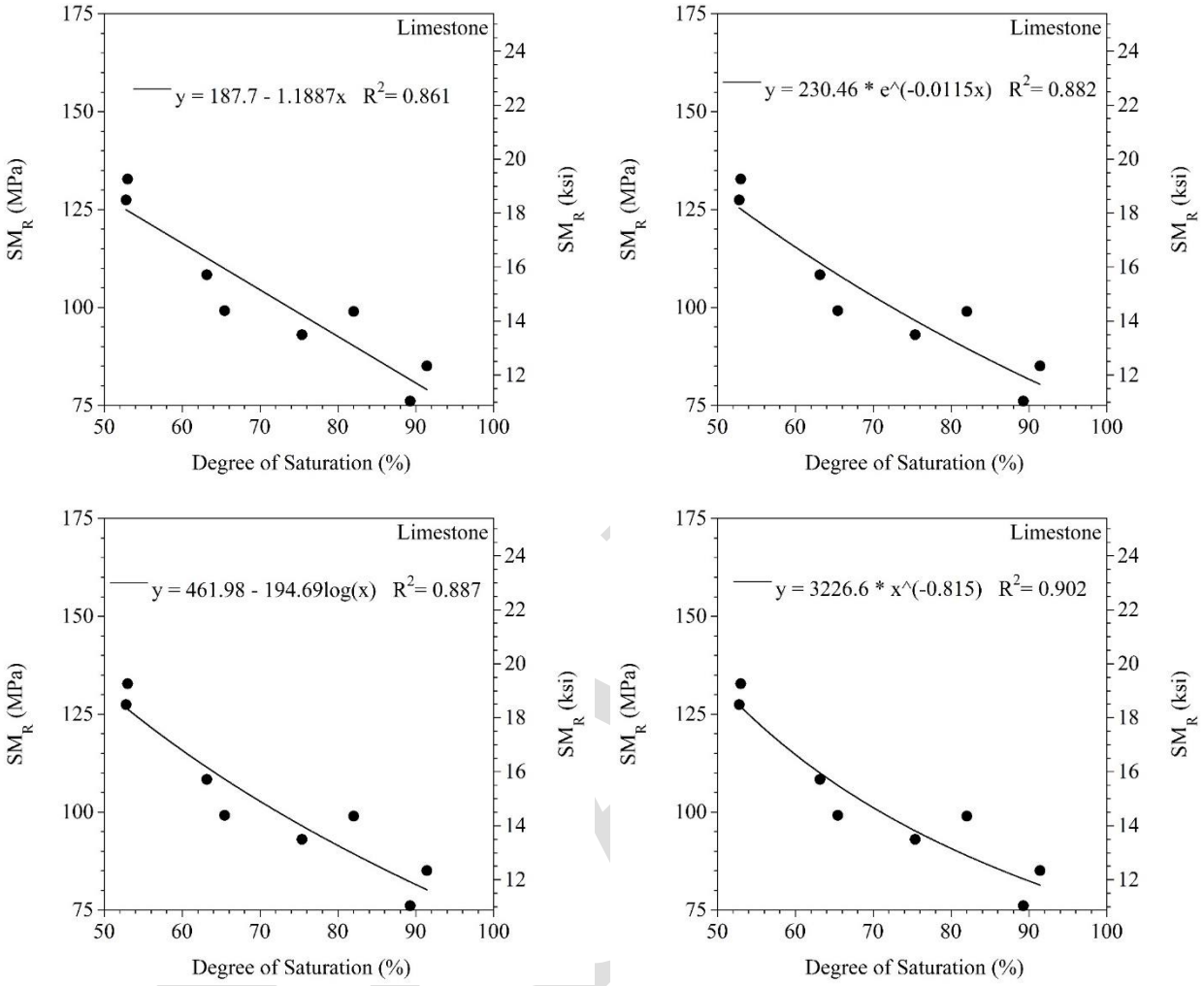






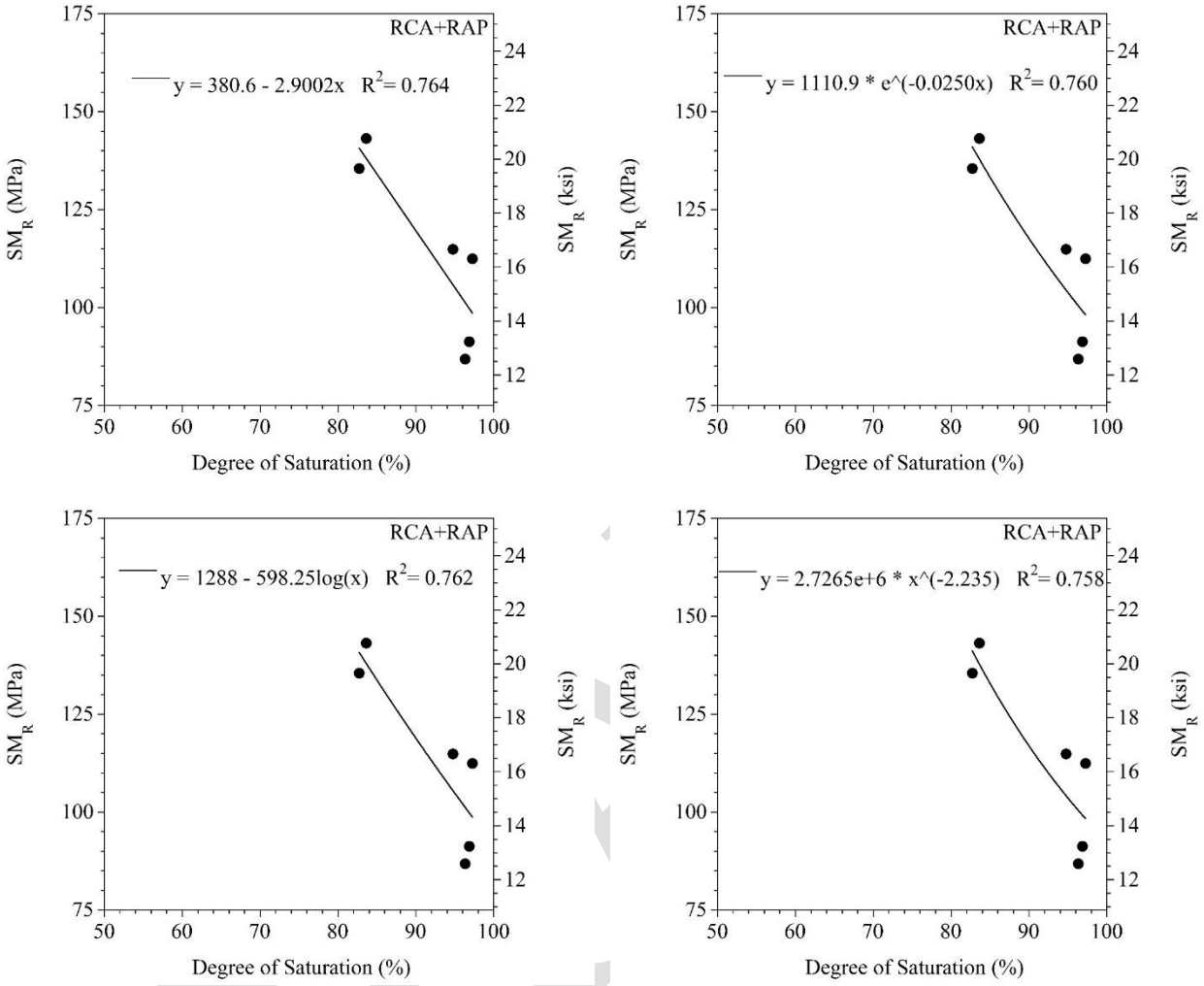
DRAFT

For limestone:



DRAFT

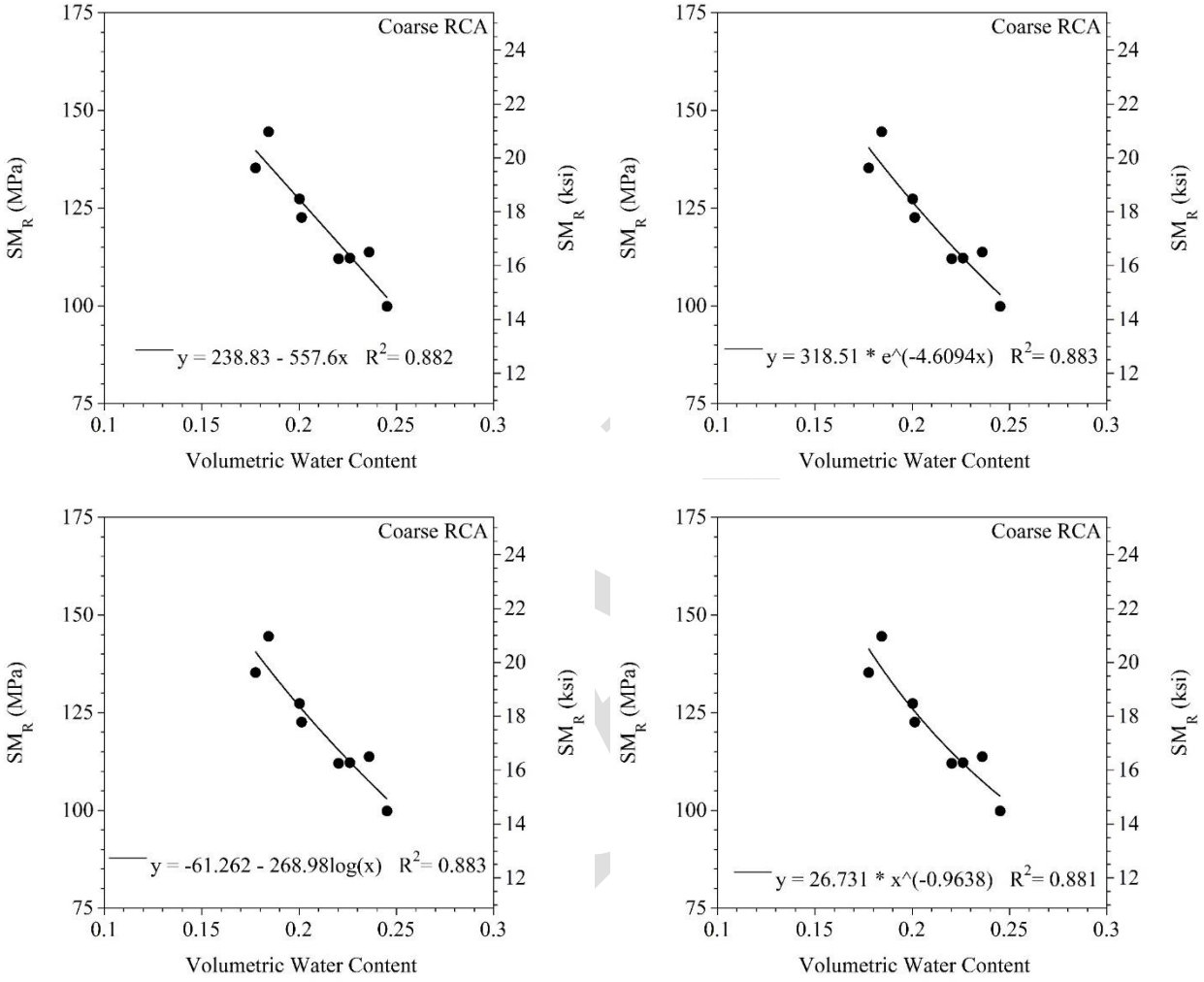
For RCA+RAP:



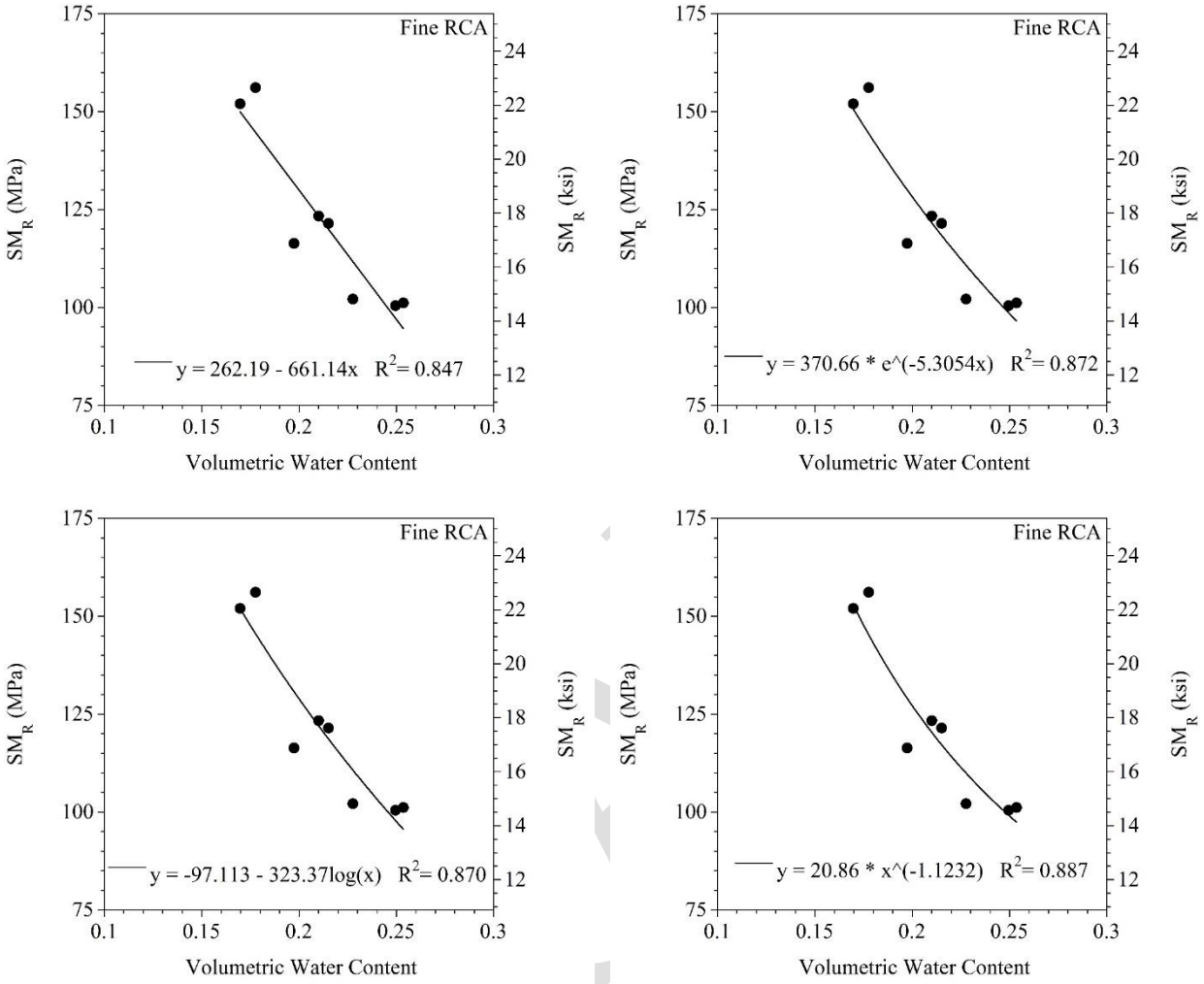
DRAFT

APPENDIX J. SUMMARY RESILIENT MODULUS (SM_R) VS. VOLUMETRIC WATER CONTENT (VWC)

For coarse RCA:

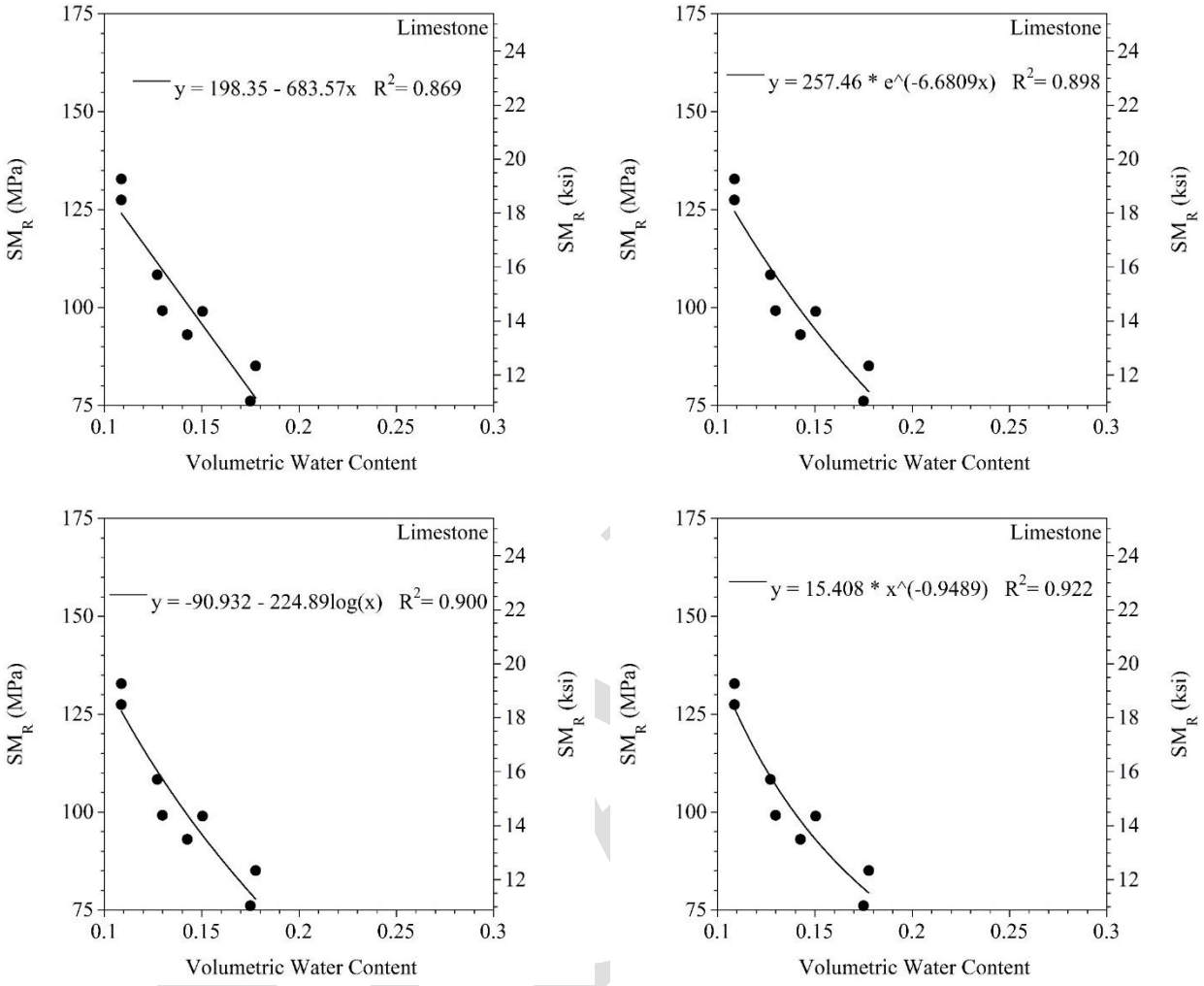


Fine RCA:



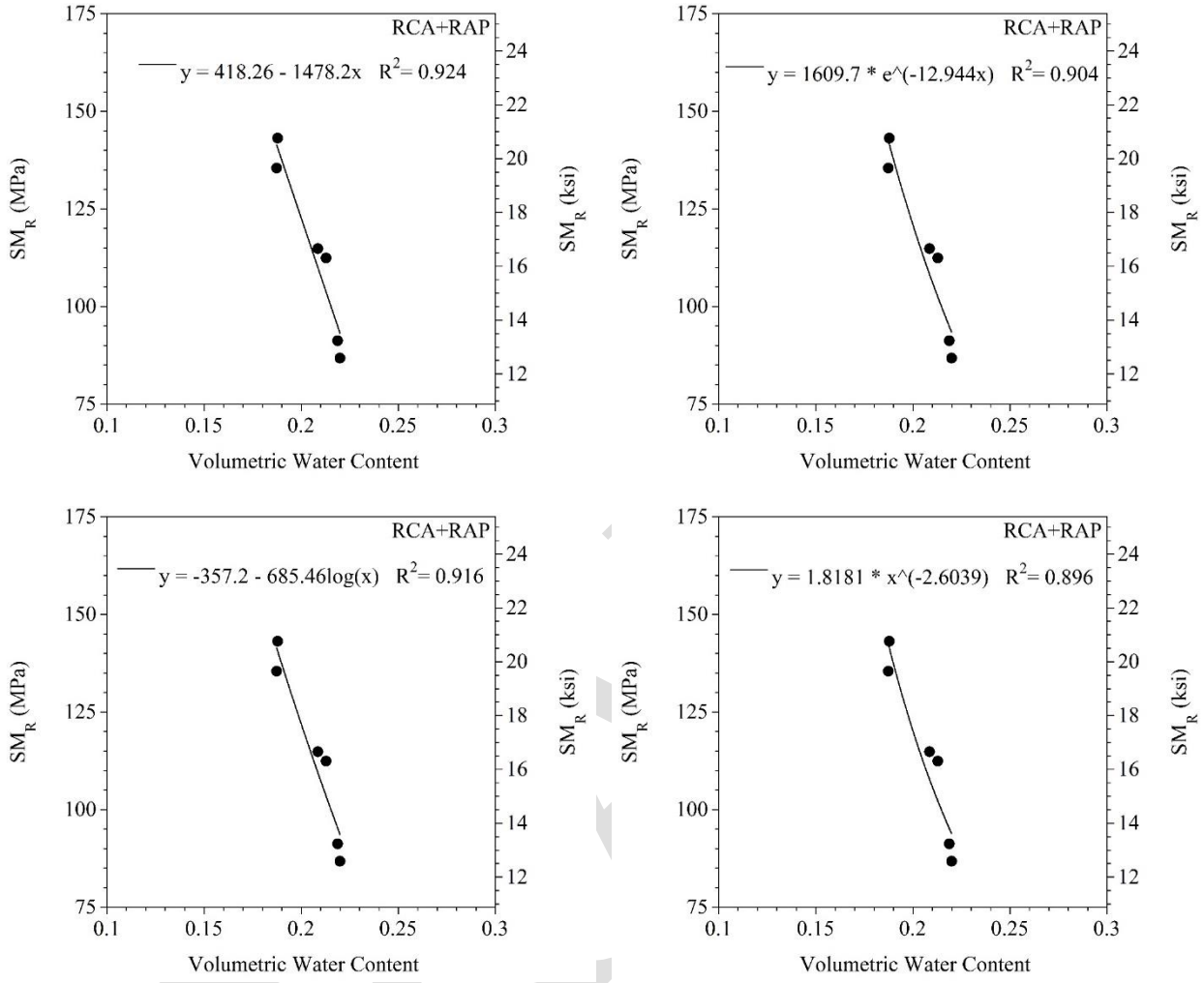
DRAFT

For limestone:



DRAFT

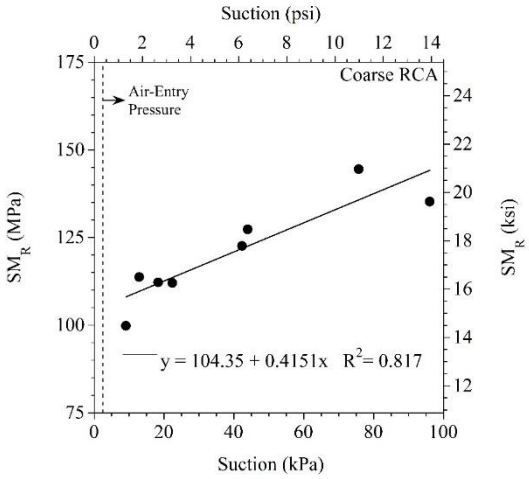
For RCA+RAP:

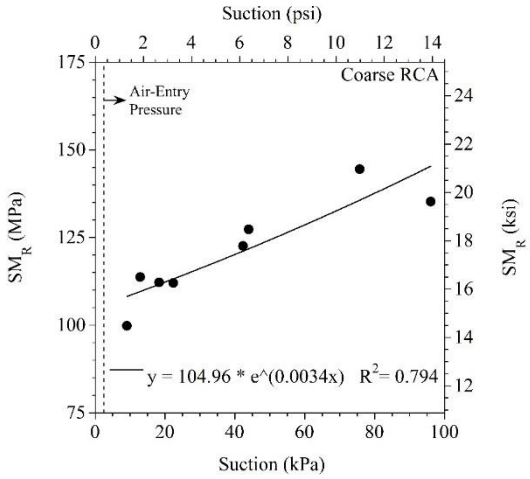


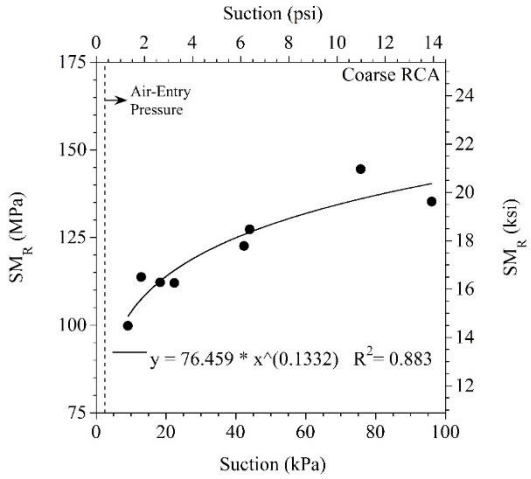
DRAFT

APPENDIX K. SUMMARY RESILIENT MODULUS (SM_R) VS. MATRIC SUCTION

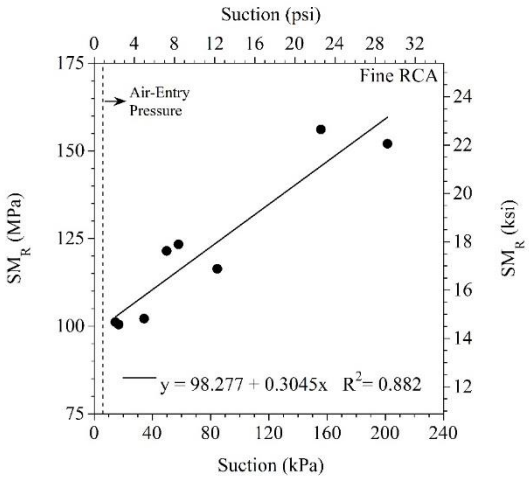
For coarse RCA:

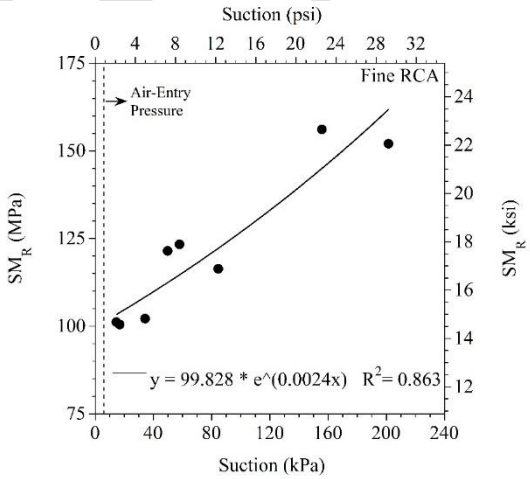


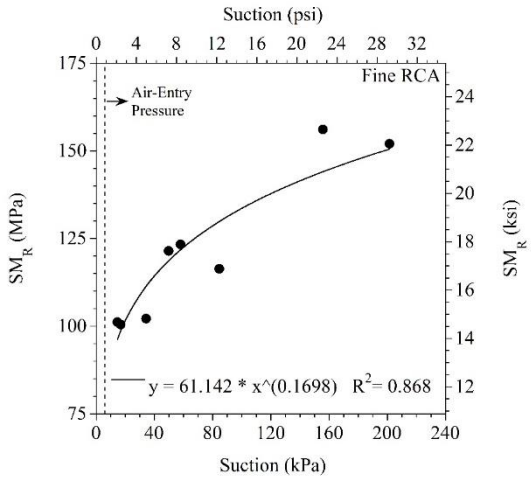




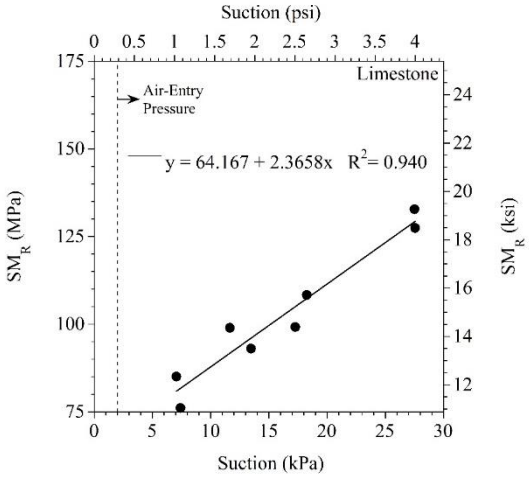
For fine RCA:

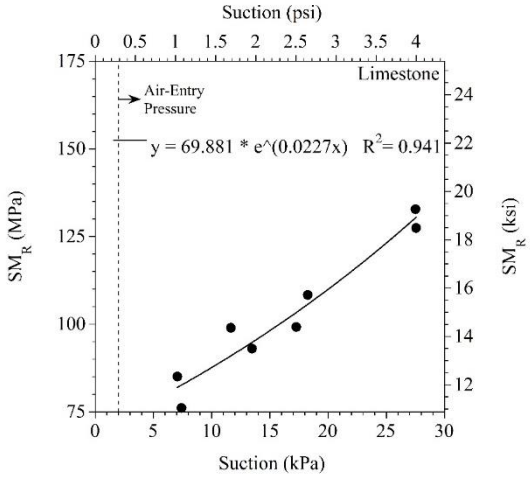


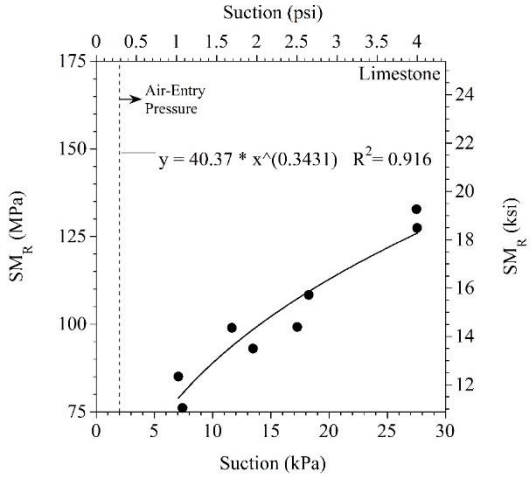




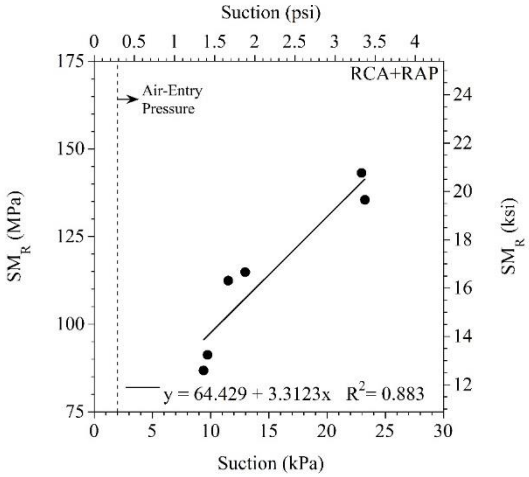
For limestone:

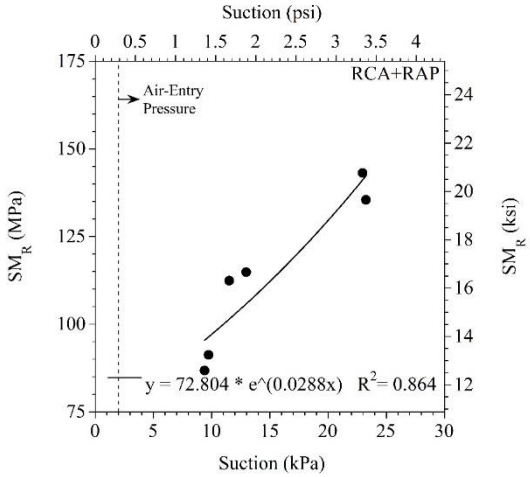


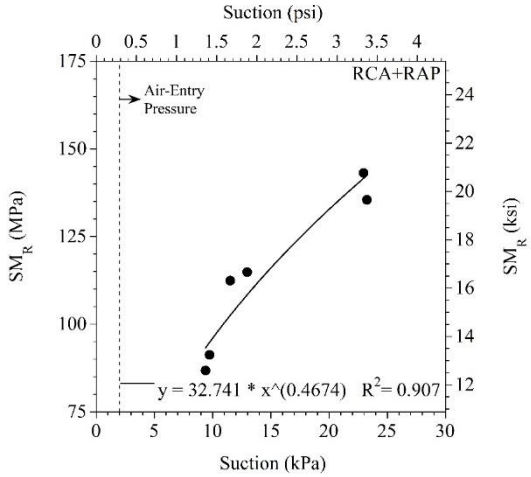




For RCA+RAP:







APPENDIX L. ALTERNATIVE MODELS TO ESTIMATE SUMMARY RESILIENT MODULUS (SM_R) AT OPTIMUM MOISTURE CONTENT (OMC)

Equation	R^2	Adj. R^2	Std. Error
-8.5917*Uncorrected MDD (kN/m^3) + 3.0558*$PLR_{0.5}$ (%) + 257.3496	1	1	0.25
-209.7556*Coarse SSD G_s + 3.7592*$PLR_{0.7}$ (%) + 407.9011	1	1	0.48
-68.7070*Combined OD G_s - 3.6657*$PLS_{0.9}$ (%) + 601.7242	1	1	0.45
-56.4223*Combined OD G_s + 246.2814	0.91	0.86	4.89

MDD = maximum dry density; SSD = saturated-surface-dry; OD = oven-dry; G_s = specific gravity; $PLR_{0.5}$ = percent less rounded than 0.5; $PLR_{0.7}$ = percent less rounded than 0.7; $PLS_{0.9}$ = percent less spherical than 0.9

DRAFT

APPENDIX M. REASSESSMENT OF THE MODELS PROVIDED IN EDIL ET AL. (2012)

Index properties, compaction characteristics, and summary resilient modulus (SRM) values based on power function [Equation (M1)] for the materials used in Edil et al. (2012) are shown in Tables M1, M2, and M3, respectively. The empirical correlations reported by Edil (2012) were reevaluated.

Table M1. Index properties of the materials (Edil et al. 2012)

Material	States	D_{10} (mm)	D_{30} (mm)	D_{50} (mm)	D_{60} (mm)	C_u	C_c	G_s	Absorption (%)	Asphalt Content /Mortar Content (%)	Impurities (%)	Gravel (%)	Sand (%)	Fines (%)	USCS	AASHTO
Class 5 Aggregate	MN	0.1	0.4	1.0	1.7	21	1.4	2.57	_	_	0.25	22.9	67.6	9.5	GW-GM	A-1-b
Blend	MN	0.2	0.6	1.5	2.8	13	0.5	_	_	_	0.36	32.7	63.8	3.4	SP	A-1-b
RCA	MN	0.1	0.4	1.0	1.7	21	1.4	2.39	5.0	55	0.87	31.8	64.9	3.3	SW	A-1-a
	MI	0.4	4.1	9.7	12.3	35	3.9	2.37	5.4	_	0.35	68.5	28.3	3.2	GP	A-1-a
	CO	0.1	0.6	2.8	4.9	66	1.1	2.28	5.8	47	0.26	40.9	46.3	12.8	SC	A-1-b
	CA	0.3	1.7	4.8	6.8	22	1.4	2.32	5.0	37	0.26	50.6	47.1	2.3	GW	A-1-a
	TX	0.4	6.5	13.3	16.3	38	6.0	2.27	5.5	45	0.86	76.3	21.6	2.1	GW	A-1-a
	OH	0.2	1.2	3.4	5.3	34	1.7	2.24	6.5	65	0.16	43.2	49.5	7.3	SW-SM	A-1-a
	NJ	0.2	0.5	2.0	5.1	28	0.3	2.31	5.4	_	1.67	41.2	54.6	4.3	SP	A-1-b
RAP	MN	0.3	0.7	1.6	2.3	7	0.7	2.41	1.8	7.1	0.06	26.3	71.2	2.5	SP	A-1-a
	CO	0.4	0.9	2.2	3.3	9	0.7	2.23	3.0	5.9	0.09	31.7	67.7	0.7	SP	A-1-a
	CA	0.3	1.3	3.0	4.2	13	1.2	2.56	2.0	5.7	0.33	36.8	61.4	1.8	SW	A-1-a
	TX	0.7	2.5	5.4	7.9	11	1.1	2.34	1.3	4.7	0.05	41.0	44.9	1.0	SW	A-1-a
	OH	0.5	1.6	2.9	3.8	7	1.3	2.43	0.6	6.2	0.06	32.1	66.2	1.7	SW	A-1-a
	NJ	1.0	2.8	4.9	5.9	6	1.3	2.37	2.1	5.2	0.48	50.9	48.4	0.7	GW	A-1-a
	WI	0.6	1.4	2.7	3.6	6	0.9	2.37	1.5	6.2	0.08	30.9	68.5	0.5	SP	A-1-b
RPM	NJ	0.5	2.1	5.8	8.7	18	1.0	2.35	2.6	4.3	0.04	55.7	43.6	0.6	GW	A-1-b
	MI	0.4	1.7	4.6	6.5	17	1.1	2.39	1.7	5.3	0.13	49.3	50.4	0.4	SW	A-1-b

D_{10} = effective size; D_{30} = particle size for 30% finer; D_{50} = median particle size; D_{60} = particle size for 60% finer; C_u = coefficient of uniformity; C_c = coefficient of curvature; G_s = specific gravity; USCS = unified soil classification system; AASHTO: the American Association of State Highway and Transportation Officials

Note 1: Asphalt content determined for RAP/RPM and mortar content determined for available RCA. RPM was a recycled pavement material that included HMA and base layer aggregate and possibly some subgrade soil like in full-depth reclamation.

Note 2: Particle size analysis conducted following ASTM D 422, G_s determined by ASTM D 854, Absorption of coarse aggregate were determined by ASTM C127-07, USCS classification determined by ASTM D 2487, AASHTO classification determined by ASTM D 3282, asphalt content determined by ASTM D 6307

Note 3: Blend consists of 50% RCA (MN) and 50% Class 5 aggregate obtained at MNROAD field site

Table M2. Maximum dry unit weight and optimum water content of the materials (Edil et al. (2012)

Specimens	States	Optimum Water Content W_{opt} (%)	Maximum Dry Unit Weight γ_{dmax} (kN/m^3)
Class 5 Aggregate	MN	8.9	20.1
Blend*	MN	8	21.3
RCA	MN	11.2	19.5
	MI	8.7	20.8
	CO	11.9	18.9
	CA	10.4	19.9
	TX	9.2	19.7
	OH	11.8	19.4
	NJ	9.5	19.8
RAP	MN	6.7	20.8
	CO	5.7	20.7
	CA	6.1	20.7
	TX	8	20.3
	OH	8.8	19.8
	NJ	6.5	20.4
	WI	7.3	20
RPM	MI	5.2	21.5
	NJ	6.3	20.6

Note: Blend consists of 50% RCA (MN) and 50% Class 5 aggregate obtained at MNROAD field site

Table M3. Summary resilient modulus (SRM), power function model fitting parameters k_1 and k_2, and plastic strain [based on Equation (M1)] (Edil et al. 2012)

Material	States	External			Internal			Plastic Strain (%)	SRM_{INT}/SRM_{EXT}
		k_1	k_2	SRM (MPa)	k_1	k_2	SRM(MPa)		
Class 5 Aggregate	MN	14.9	0.43	152	43.2	0.47	525	1.60	3.5
Blend*	MN	18.2	0.43	182	50.2	0.49	675	1.05	3.7
RCA	MN	18.5	0.44	189	38.3	0.54	680	0.63	3.6
	MI	14.3	0.46	171	40.7	0.54	715	0.80	4.2
	CO	17.4	0.43	175	41.5	0.49	580	0.73	3.3
	CA	15.2	0.46	178	33.0	0.54	627	0.70	3.5
	TX	9.1	0.54	164	17.6	0.64	549	0.83	3.3
	OH	12.6	0.48	163	27.7	0.56	554	0.57	3.4
	NJ	22.0	0.42	208	49.6	0.50	735	0.55	3.5
RAP	MN	23.0	0.39	180	26.3	0.61	674	1.35	3.7
	CO	25.6	0.37	184	75.0	0.41	673	1.47	3.7
	CA	12.3	0.49	173	36.4	0.53	627	1.16	3.6
	TX	21.6	0.42	198	52.4	0.52	776	1.38	3.9
	OH	15.6	0.48	197	42.7	0.52	699	1.32	3.6
	NJ	23.5	0.41	209	54.6	0.48	715	2.13	3.4
	WI	29.5	0.41	266	65.0	0.51	968	0.89	3.6
RPM	MI	14.7	0.46	168	43.5	0.50	631	1.49	3.8
	NJ	26.3	0.43	264	61.6	0.52	989	1.26	3.8

Note: Plastic strains were determined for base materials from M_R testing by using the measured permanent deformations from the internal LVDTs with the power function model (Table 3.5). Plastic strains were calculated as the sum of the plastic strains for each loading sequence during resilient modulus test by excluding the plastic strains in the conditioning phase (Sequence 1).

The power function model proposed by Moosazedh and Witczak (1981):

$$M_R = k_1 \theta^{k_2} \quad \text{(M1)}$$

where M_R is the resilient modulus, θ is the bulk stress, and k_1 and k_2 are empirical fitting parameters.

In Edil et al. (2012), based on the index properties (Table M1) and compaction characteristics (Table M2) of the materials, the forward stepwise regression technique was performed by using multiple linear regressions to develop correlations (models) to predict the compaction characteristics of RCA and RAP based on their gradation characteristics (Table M4). A significance level of 0.05 [or alpha (α) = 0.05], which gives 95% confidence, was used to determine whether the model is statistically significant. In Edil et al. (2012), it was stated that all the independent variables used in the models shown in Table M4 had p-values smaller than 0.05, which showed the statistical significance of those variables. As can be seen in Table M4, for both RCA and RAP materials, W_{opt} was a function of C_u and absorption. In addition, γ_{dmax} was a function of W_{opt}.

Table M4. Equations to estimate optimum moisture content (W_{opt}) and maximum dry density (γ_{dmax}) of the materials (Edil et al. 2012)

Materials	Compaction Characteristics	Correlation Equations	R^2
RCA	W_{opt} (%)	-0.064 *Cu + 0.763 *$Absorption(\%)$ + 7.75	0.65
	γ_{dmax} (kN/m^3)	-0.374 *$W_{opt}(\%)$ + 23.6	0.83
RAP	W_{opt} (%)	-0.0626 *Cu - 1.349 *$Absorption(\%)$ + 9.84	0.92
	γ_{dmax} (kN/m^3)	-0.289* W_{opt} (%) + 22.42	0.83

W_{opt} = optimum moisture content; γ_{dmax} = maximum dry density; C_u = coefficient of uniformity

An effort was made to reassess the equations given in Table M4 using the data generated in Edil et a. (2012). First, the actual (based on the laboratory test results) and estimated (based on the equations given in Table M4) W_{opt} and γ_{dmax} values were compared. Figure M1 shows the actual W_{opt} vs. predicted W_{opt} for RCA and RAP. Figure M2 shows the actual γ_{dmax} vs. predicted γ_{dmax} for RCA and RAP. Based on Figures M1 and M2, it was observed that while the models for W_{opt} of RAP and γ_{dmax} of RCA and RAP were somewhat successful, the W_{opt} model of RCA was not satisfactory.

DRAFT

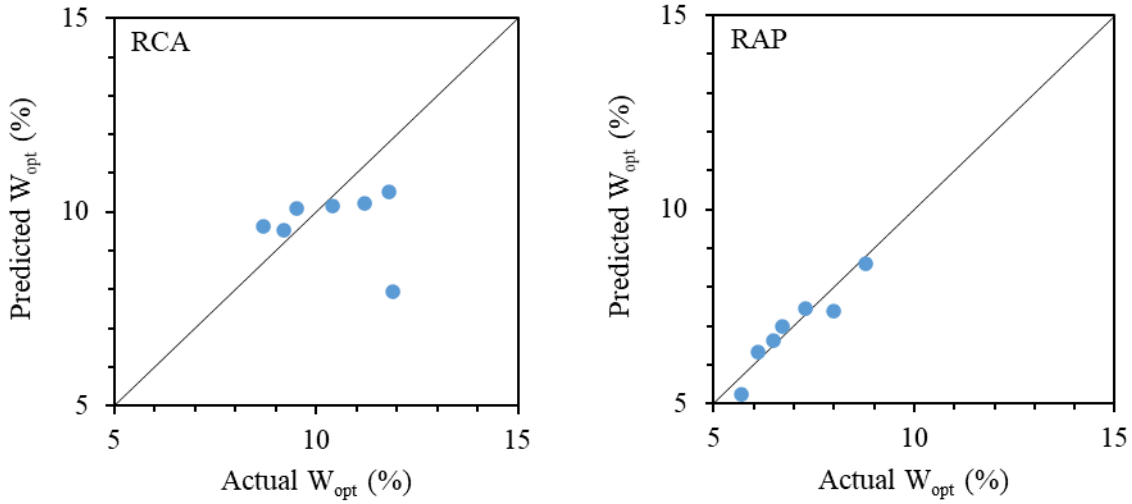


Figure M1. Actual W_{opt} vs. predicted W_{opt} for RCA (left) and RAP (right)

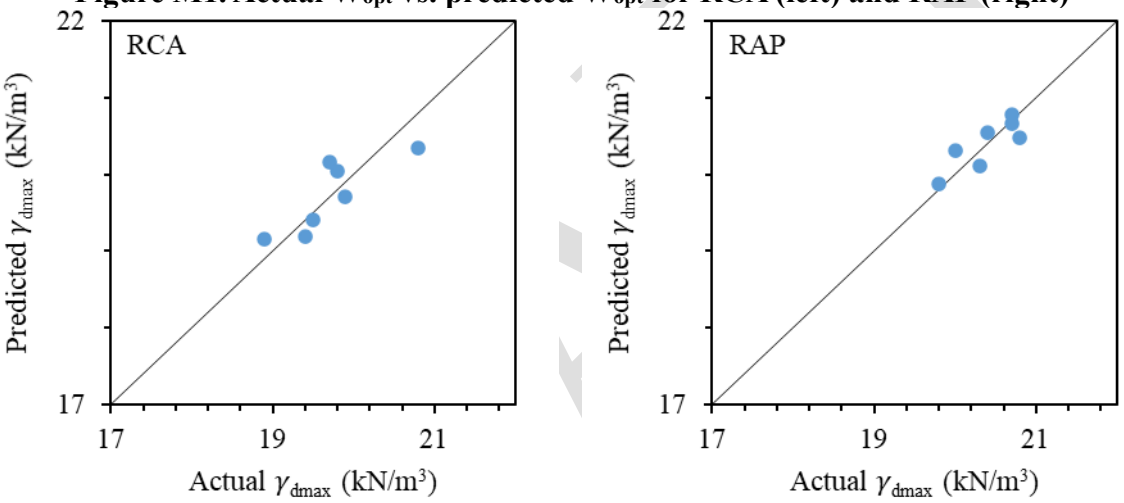


Figure M2. Actual γ_{dmax} vs. predicted γ_{dmax} for RCA (left) and RAP (right)

The data generated by Edil et al (2012) were used to develop models that were the most convenient with statistical significance. To do so, forward stepwise regression technique, described previously, was used by considering all the parameters shown in Tables M1 and M2, and new models were established.

Table M5 summarizes the new equations to estimate W_{opt}. According to Table M4, W_{opt} was a function of C_u and absorption for both RCA and RAP materials. However, as can be seen from Table M5, there was no equation that contained both C_u and absorption parameters. For RCA, neither C_u nor absorption was statistically significant (Table M5). For RAP, while absorption was statistically significant, C_u was insignificant. The combination of G_s and absorption was found to be statistically significant for RAP materials. In addition to separate regression analyses for RCA and RAP materials, these materials were combined with each other and with class 5 aggregate to establish more models (Table M5).

Table M6 summarizes the new equations to estimate γ_{dmax}. According to Table M4, γ_{dmax} was a function of W_{opt} for both RCA and RAP. As can be seen from Table M6, both equations shown in

Table M4 were statistically significant. In Table M4, the R^2 values of both models were reported as 0.83. However, after reassessing the reported equations, it was found that multiple R values, which were 0.83, were reported instead of R^2 values. According to Table M6, the correct R^2 values were 0.690 and 0.694 for RCA and RAP, respectively. In addition to separate regression analyses for RCA and RAP materials, these materials were combined with each other and with class 5 aggregate to establish more models (Table M6).

Table M5. New equations to estimate optimum moisture content (W_{opt}) (%) of the materials

Material	Equation	R^2	Adj. R^2	Std. Error
RCA	-8.2941*D_{10} (mm) + 12.4000	0.67	0.6	0.81
RAP	-1.3891*Absorption (%) + 9.4552	0.9	0.88	0.38
	-1.5831*Absorption (%) - 3.5587*G_s + 18.2910	0.99	0.98	0.16
RCA and RAP	0.7619*Absorption (%) + 5.9300	0.55	0.52	1.45
	0.0889*C_u + 6.7750	0.54	0.5	1.48
	0.4642*Fines (%) + 7.2345	0.54	0.5	1.48
	#0.0769*Mortar Content (%) + 7.0368	0.81	0.79	1.04
RCA, RAP, and Class 5	#0.0725*Mortar Content (%) + 7.2647	0.76	0.73	1.12
	#0.0598*Mortar Content (%) + 0.1864*Fines (%) + 6.8460	0.84	0.81	0.94
RCA and Class 5	#0.0482*Mortar Content (%) - 0.3237*D_{30} (mm) + 9.1488	0.92	0.86	0.49
	#0.0472*Mortar Content (%) - 0.4115*C_c + 9.5007	0.93	0.88	0.44

#RCA-MI and RCA-NJ materials were removed because their mortar contents were not reported

Table M6. New equations to estimate maximum dry density (γ_{dmax}) (kN/m^3) of the materials

Material	Equation	R^2	Adj. R^2	Std. Error
RCA	-0.3743*W_{opt} (%) + 23.6015	0.69	0.63	0.35
	3.4559*D_{10} (mm) + 18.8750	0.57	0.49	0.42
RAP	-0.2900* W_{opt} (%) + 22.4195	0.69	0.63	0.23
	0.4714*Absorption (%) + 0.2977*Fines (%) + 19.1788	0.90	0.85	0.15
RCA and RAP	-0.2413* W_{opt} (%) + 22.1494	0.74	0.72	0.31
	#-0.0179*Mortar Content (%) + 20.3795	0.64	0.61	0.37
RCA, RAP, and Class 5	-0.2410* W_{opt} (%) + 22.1531	0.74	0.72	0.30
	#-0.0172*Mortar Content (%) + 20.3453	0.62	0.59	0.36
RCA and Class 5	-0.3557* W_{opt} (%) + 23.3907	0.70	0.65	0.33

#RCA-MI and RCA-NJ materials were removed because their mortar contents were not reported

In Edil et al. (2012), based on the index properties (Table M1), compaction characteristics (Table M2), and SRM values (based on power function) of the materials, the forward stepwise regression technique was performed by using multiple linear regressions to develop correlations (models) to

DRAFT

predict the SRM values (based on power function) (Table M3). A significance level of 0.05 [or alpha (α) = 0.05], which gives 95% confidence, was used to determine whether the model is statistically significant. In Edil et al. (2012), it was stated that all the independent variables used in the models shown in Table M7 had p-values smaller than 0.05, which showed the statistical significance of those variables.

Table M7. Equations to estimate the summary resilient modulus (SRM) of the materials determined by the power function model (Edil et al. 2012)

Materials	Summary Resilient Modulus (SRM) (Mpa)	Correlation Equations	R^2
RCA	SMR_{EXT}	171.646-(3.482*D_{30}) + (22.378*Impurities %)	0.89
	SMR_{INT}	14683.478 - (36.764*D_{30}) - (72.719*Wopt)	0.89
RAP	SMR_{EXT}	(117.493 * D_{30}) + (19.472 *γ_{dmax} + (27.128 * Asphalt Content(%)) - (18.510 * Absorption(%)) -427.329	0.99
	SMR_{INT}	(-2268.783)-(285.884*Fines %)+(628.742*Asphalt content (%))+ (201.107*D_{60})-(483.158*G_s)-(58.243*Absorption (%))	0.99

D_{30} = particle size for 30% finer; W_{opt} = optimum moisture content; γ_{dmax} = maximum dry density; G_s = specific gravity

An effort was made to reassess the equations given in Table M7. First, the actual (based on the laboratory test results) and estimated (based on the equations given in Table M7) SMR values were compared. Figure M3 shows the actual SRM based on external linear variable differential transformer (LVDT) (SRM_{EXT}) vs. predicted SRM_{EXT} for RCA and RAP. Figure M4 shows the actual SRM based on internal linear LVDT (SRM_{INT}) vs. predicted SRM_{INT} for RCA and RAP. Based on Figures M3 and M4, it was observed that while the models for RCA were somewhat successful, the models for RAP was not satisfactory.

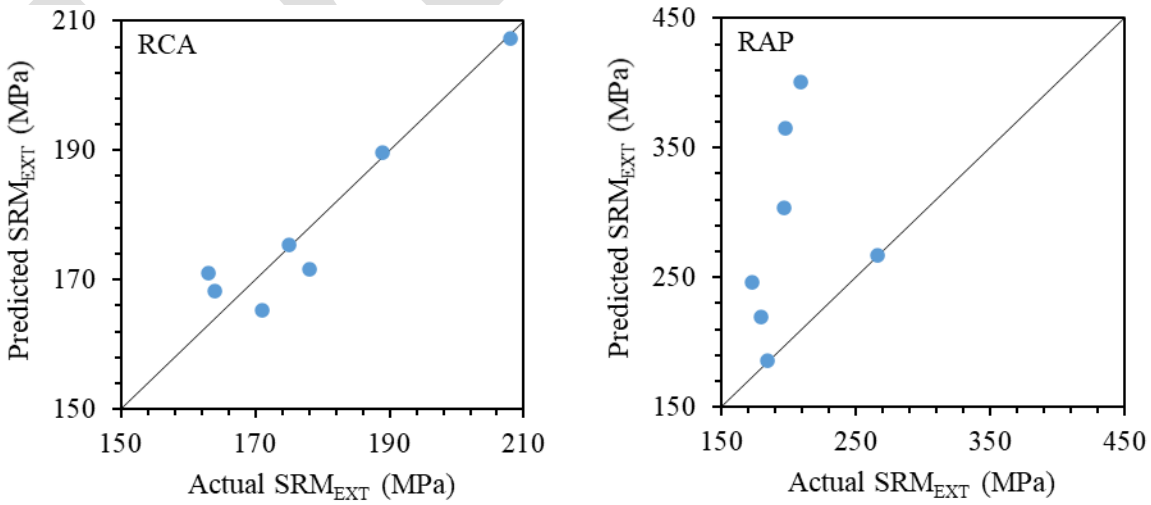


Figure M3. Actual SRM_{EXT} vs. predicted SRM_{EXT} for RCA (left) and RAP (right)

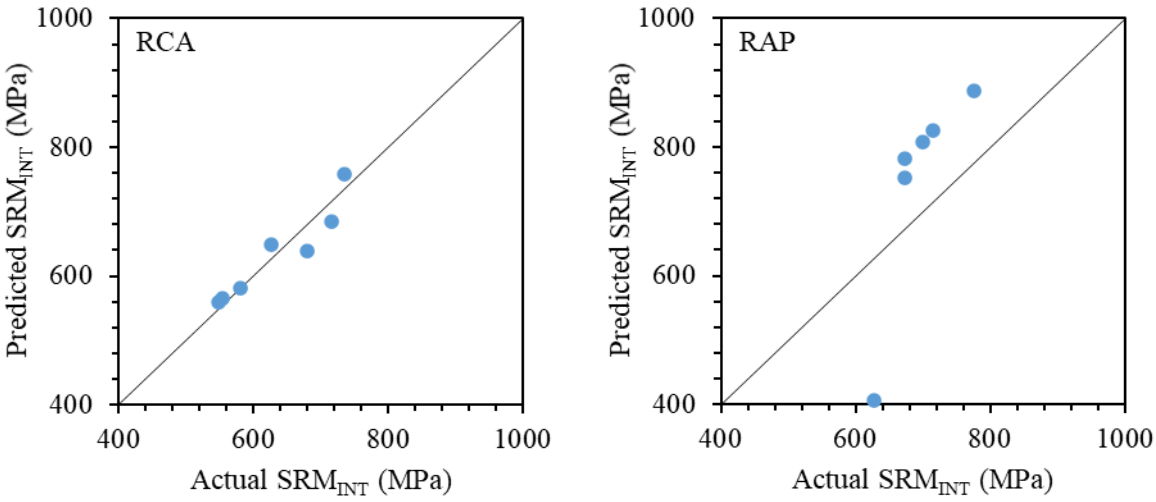


Figure M4. Actual SRM_{INT} vs. predicted SRM_{INT} for RCA (left) and RAP (right)

The data generated by Edil et al (2012) were used to develop models that are the most convenient with statistical significance. The forward stepwise regression method was performed by using multiple linear regressions to develop correlations (models) to predict the SRM values (based on power function) (Table M3).

Table M8 summarizes the new equations to estimate SRM_{EXT}. According to Table M7, the SRM_{EXT} of RCA materials was a function of D_{30} and impurities. As can be seen from Table M8, both D_{30} and impurities were statistically significant for SRM_{EXT} of RCA. In addition, Table M8 shows that not only D_{30} but also C_c can be used in combination with impurities to estimate SRM_{EXT} of RCA. While Table M7 shows a complex equation to estimate SRM_{EXT} of RAP, reassessment of the laboratory data revealed that none of those parameters was statistically significant. Therefore, no statistically significant equation could be found for SRM_{EXT} of RAP. In addition to the separate regression analyses for RCA and RAP materials, these materials were combined with each other and with class 5 aggregate to establish more models. Among the combinations, only the combination of RCA and class 5 aggregate provided an equation (Table M8).

Table M9 summarizes the new equations to estimate SRM_{INT}. According to Table M7, the SRM_{INT} of RCA materials was a function of D_{30} and W_{opt}. As can be seen from Table M9, both D_{30} and W_{opt} were statistically significant for SRM_{INT} of RCA. In addition, Table M9 shows that G_s can also be used to estimate SRM_{INT} of RCA. While Table M7 shows a complex equation to estimate SRM_{INT} of RAP, reassessment of the laboratory data revealed that none of those parameters had a statistical significance. Thus, any equation, which are statistically significant, could not be found for SRM_{INT} of RAP. In addition to the separate regression analyses for RCA and RAP materials, these materials were combined with each other and with class 5 aggregate to establish more models. However, no statistically significant equations could be found for the combinations (Table M9).

DRAFT

Table M8. New equations to estimate SRM_{EXT} (MPa) of the materials

Material	Equation	R^2	Adj. R^2	Std. Error
RCA	23.0770*Impurities (%) + 163.6812	0.63	0.55	10.58
	21.0281*Impurities (%) - 4.3410*C_c + 174.7761	0.92	0.88	5.5
	22.0836*Impurities (%) - 3.5436*D_{30} (mm) + 171.9035	0.89	0.84	6.31
RAP	No Equation			
RCA and RAP	No Equation			
RCA, RAP, and Class 5	No Equation			
RCA and Class 5	28.1646*Impurities (%) + 159.6937	0.62	0.55	11.6

C_c = coefficient of curvature

Table M9. New equations to estimate SRM_{INT} (MPa) of the materials

Material	Equation	R^2	Adj. R^2	Std. Error
RCA	1091.5850*G_s - 1888.8350	0.59	0.5	54.10
	-36.8275*D_{30} (mm) – 72.9428*W_{opt} (%) + 1470.7646	0.89	0.83	31.37
RAP	No Equation			
RCA and RAP	No Equation			
RCA, RAP, and Class 5	No Equation			
RCA and Class 5	No Equation			

G_s = specific gravity; W_{opt} = optimum moisture content

DRAFT

APPENDIX N. FIELD TEST RESULTS (DURING CONSTRUCTION) THAT WERE USED IN THE FORWARD STEPWISE REGRESSION ANALYSES

Cell Number	Median NDG Moisture Content (%)	Median NDG Dry Density (kN/m^3)	Median Relative OMC (%)	Median Relative MDD (%)	Median DCPI (mm/blow)	Median CBR (%)	Median E_{LWD} (MPa)	Median E_{FWD} (MPa)	Median IC M_R at 69 kPa (MPa)	Median IC M_R at 207 kPa (MPa)
185	6.86	18.65	72.33	92.34	7.58	30.24	98.06	165.47	265.04	305.98
186	7.5	18.27	67.71	95.59	7.49	30.62	99.52	222.01	278.43	311.51
188	4.43	21.28	70.53	94.62	8.46	27.01	84.85	102.04	171.48	166.4
189	6.57	18.53	65.91	93.79	9.87	22.57	71.88	77.91	144.05	134.81
127	5.49	18.99	66.46	94.07	9	24.92	79.52	102.04	216.39	208.48
227	5.62	19.2	68.1	95.08	7	33.03	82.79	108.25	153.74	146.92
328	7.7	17.86	79.99	88.79	9.5	23.54	64.03	43.44	120.51	97.87
428	7.89	17.82	81.94	88.6	9	24.92	46.7	31.37	105.7	81.65
528	6.2	17.01	64.38	84.58	10.5	21.03	25.68	23.79	85.02	66.87
628	8.03	18.15	83.4	90.25	10.5	21.03	47.49	35.85	106.88	89.65
728	8.5	17.36	88.28	86.31	11	19.91	59.88	60.67	115.96	109.82

NDG = nuclear density gauge; OMC = optimum moisture content; MDD = maximum dry density; DCPI = dynamic cone penetration index; CBR = field California bearing ratio; E_{LWD} = light weight deflectometer elastic modulus; E_{FWD} = falling weight deflectometer elastic modulus; IC M_R = intelligent compaction resilient modulus

DRAFT

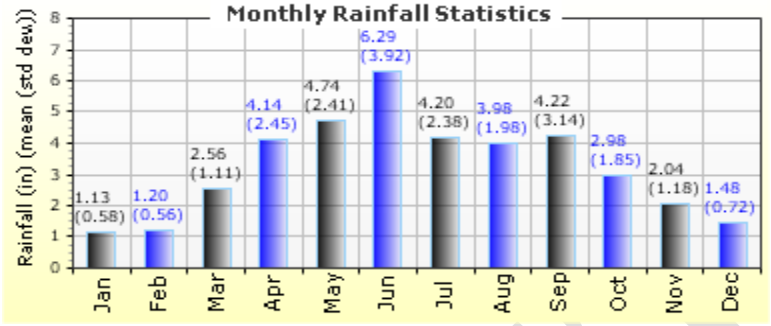
APPENDIX O. ALTERNATIVE MODELS TO ESTIMATE INTELLIGENT COMPACTION (IC) RESILIENT MODULUS (M_R) AT 207 KPA (30 PSI)

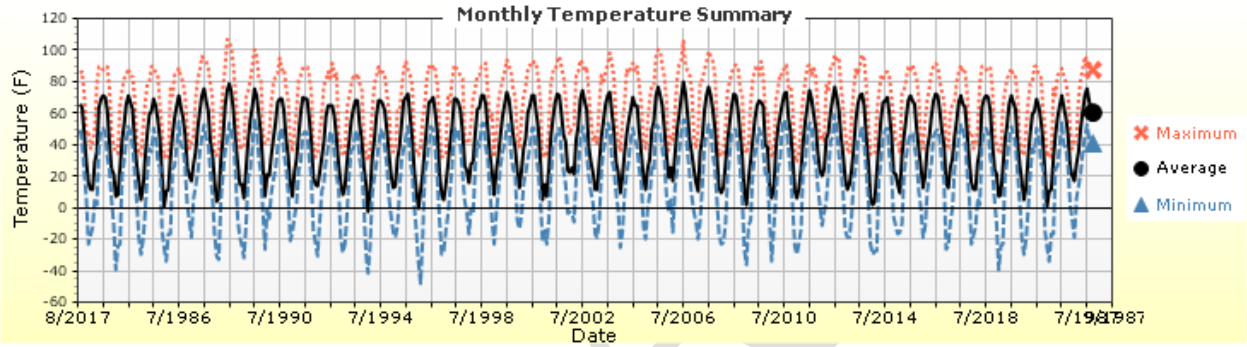
Equation	R^2	Adj. R^2	Std. Error
3.0066*Median E_{LWD} (MPa) + 30.0589*Combined Absorption (%) - 31.5527*Median NDG Moisture Content (%) - 3.6529	0.94	0.91	25.65
3.1960*Median E_{LWD} (MPa) + 16.8517*Fine Absorption (%) - 31.3564*Median NDG Moisture Content (%) + 15.5679	0.94	0.91	26.01
1.8399*Median E_{LWD} (MPa) + 26.0419*Fine Absorption (%) - 86.9710*Coarse Absorption (%) + 154.2450	0.93	0.9	27.54
3.2263*Median E_{LWD} (MPa) + 10.2064*Fine Absorption (%) - 2.8517*Median Relative OMC (%) + 62.4653	0.93	0.9	27.68
3.4006*Median E_{LWD} (MPa) + 14.0113*Combined Absorption (%) - 156.4348	0.87	0.83	34.92
3.4875*Median E_{LWD} (MPa) + 7.8616*Fine Absorption (%) - 146.8084	0.87	0.83	35.04

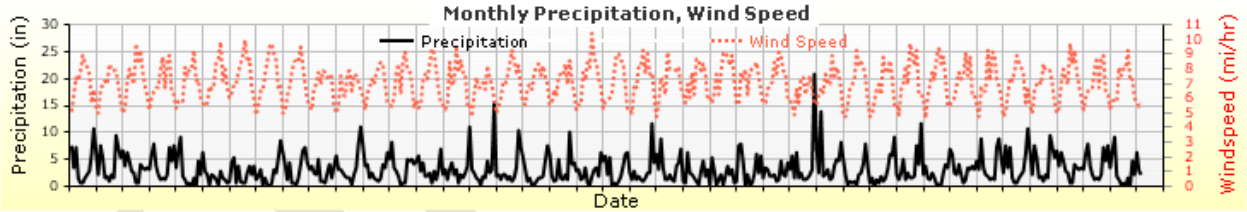
E_{LWD} = light weight deflectometer elastic modulus; OMC = optimum moisture content; NDG = nuclear density gauge

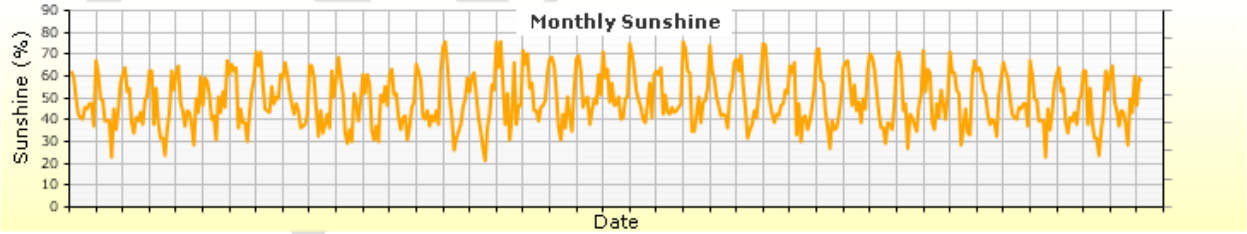
DRAFT

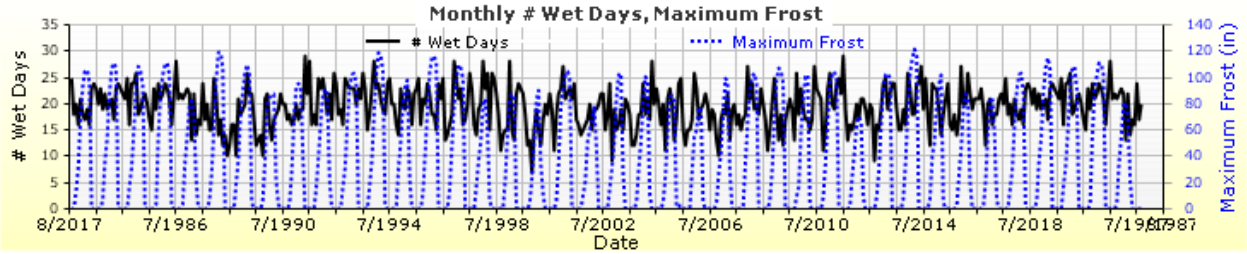
APPENDIX P. MONTHLY RAINFALL STATISTICS, MONTHLY CLIMATE SUMMARY, AND HOURLY AIR TEMPERATURE DISTRIBUTION BY MONTH FOR THE MNROAD TEST FACILITY



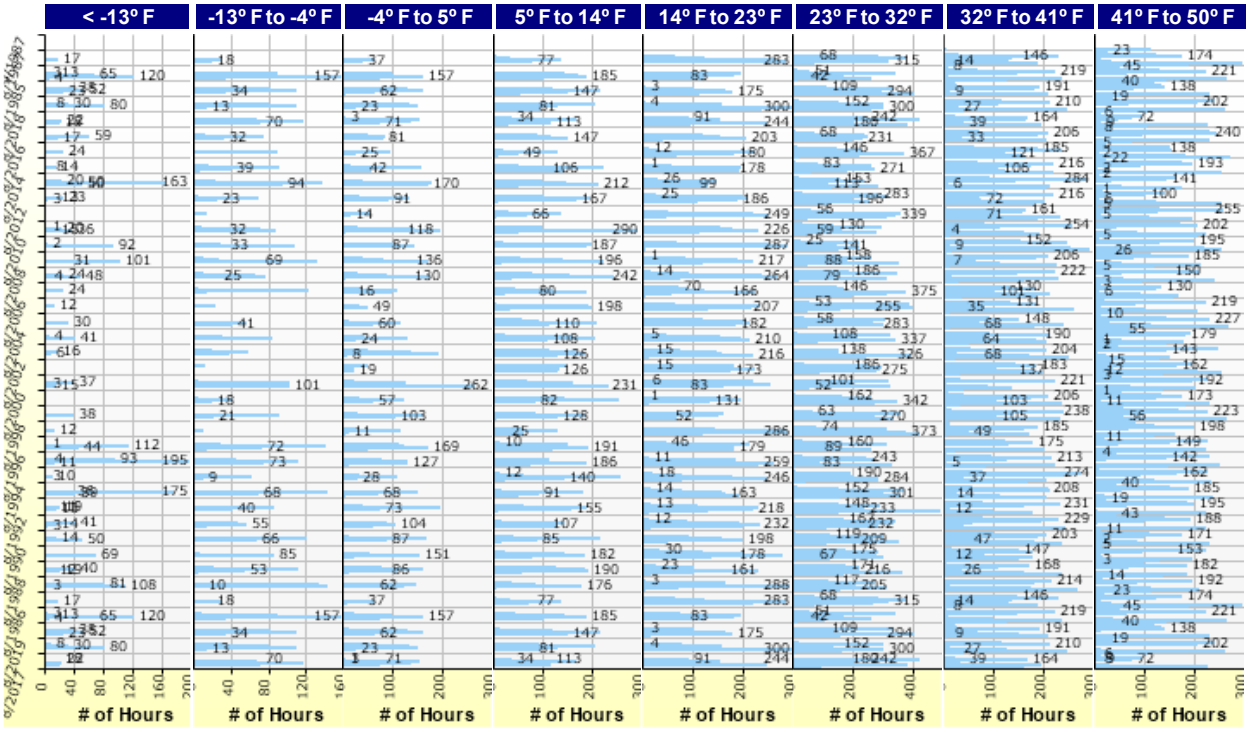


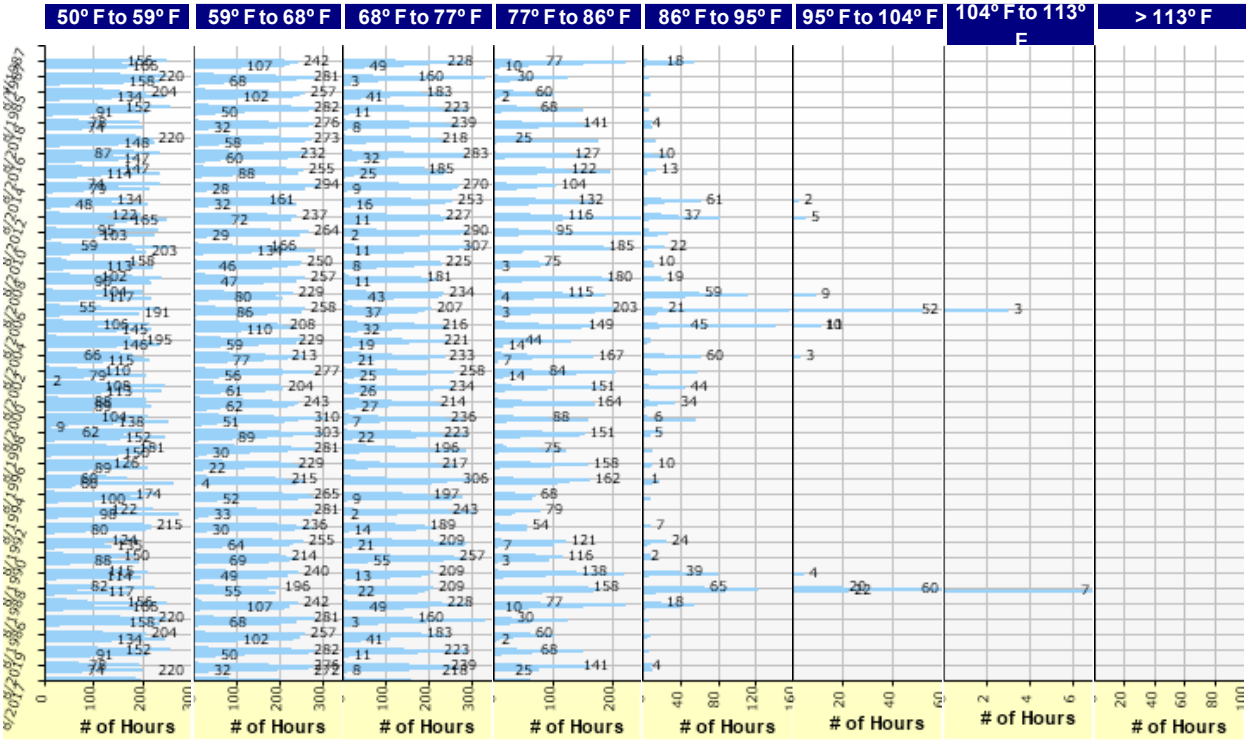




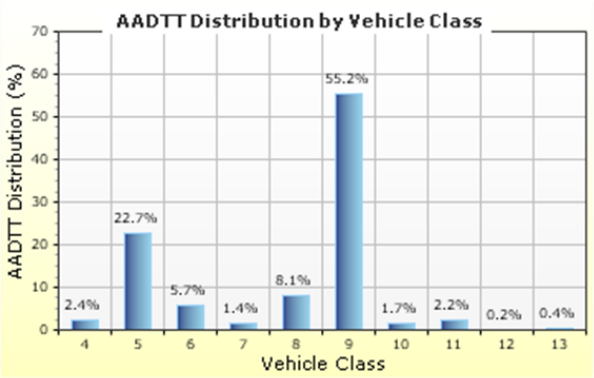


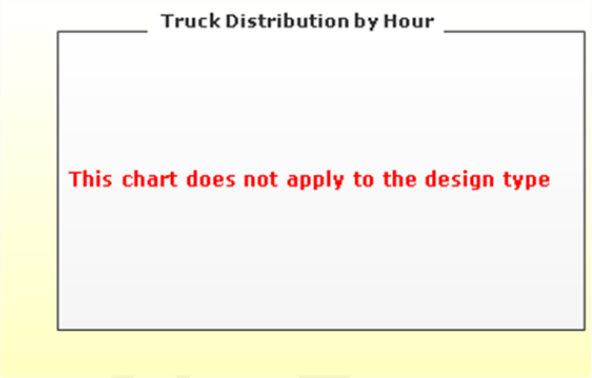
Hourly Air Temperature Distribution by Month:

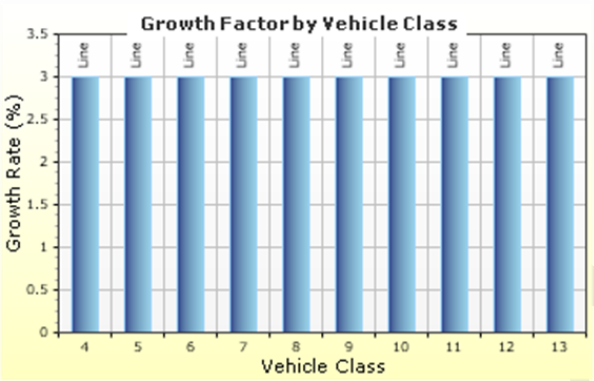


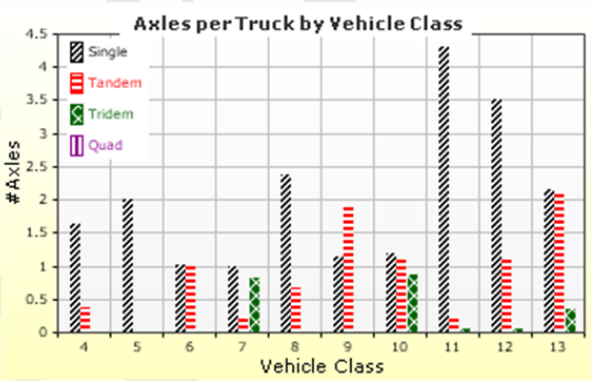


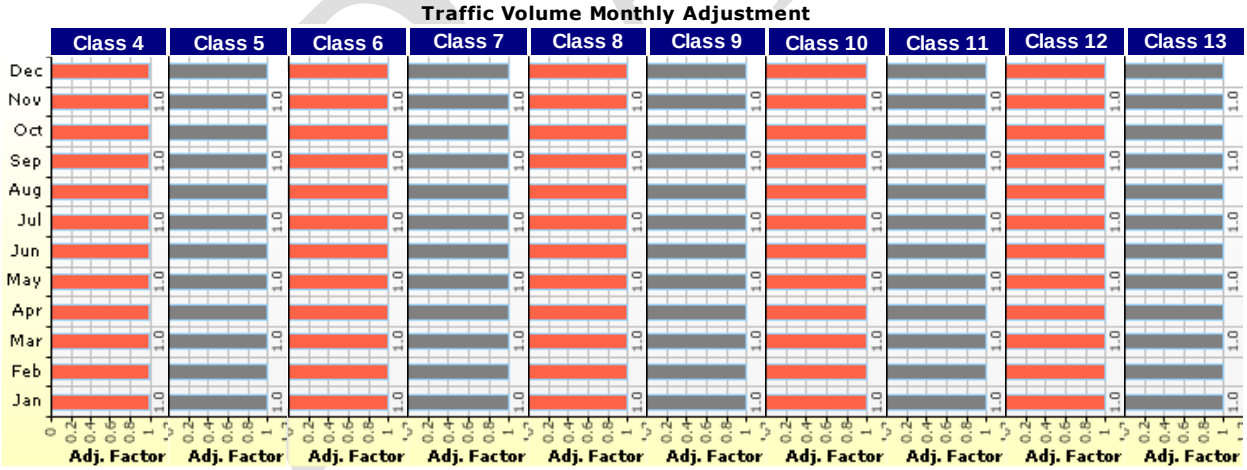
APPENDIX Q. GRAPHICAL AND TABULAR REPRESENTATIONS OF TRAFFIC INPUTS AND AXLE CONFIGURATION











Volume Monthly Adjustment Factors

Level 3: Default MAF

Month	Vehicle Class									
	4	5	6	7	8	9	10	11	12	13
January	1.0	1.0	1.0	1.0	1.0	1.0	1.0	1.0	1.0	1.0
February	1.0	1.0	1.0	1.0	1.0	1.0	1.0	1.0	1.0	1.0
March	1.0	1.0	1.0	1.0	1.0	1.0	1.0	1.0	1.0	1.0
April	1.0	1.0	1.0	1.0	1.0	1.0	1.0	1.0	1.0	1.0
May	1.0	1.0	1.0	1.0	1.0	1.0	1.0	1.0	1.0	1.0
June	1.0	1.0	1.0	1.0	1.0	1.0	1.0	1.0	1.0	1.0
July	1.0	1.0	1.0	1.0	1.0	1.0	1.0	1.0	1.0	1.0
August	1.0	1.0	1.0	1.0	1.0	1.0	1.0	1.0	1.0	1.0
September	1.0	1.0	1.0	1.0	1.0	1.0	1.0	1.0	1.0	1.0
October	1.0	1.0	1.0	1.0	1.0	1.0	1.0	1.0	1.0	1.0
November	1.0	1.0	1.0	1.0	1.0	1.0	1.0	1.0	1.0	1.0
December	1.0	1.0	1.0	1.0	1.0	1.0	1.0	1.0	1.0	1.0

Distributions by Vehicle Class

Vehicle Class	AADTT Distribution (%) (Level 3)	Growth Factor	
		Rate (%)	Function
Class 4	2.4%	3%	Linear
Class 5	22.7%	3%	Linear
Class 6	5.7%	3%	Linear
Class 7	1.4%	3%	Linear
Class 8	8.1%	3%	Linear
Class 9	55.2%	3%	Linear
Class 10	1.7%	3%	Linear
Class 11	2.2%	3%	Linear
Class 12	0.2%	3%	Linear
Class 13	0.4%	3%	Linear

Axle Configuration

Traffic Wander	
Mean wheel location (in)	18.0
Traffic wander standard deviation (in)	10.0
Design lane width (ft)	12.0

Axle Configuration	
Average axle width (ft)	8.5
Dual tire spacing (in)	12.0
Tire pressure (psi)	120.0

Average Axle Spacing	
Tandem axle spacing (in)	51.6
Tridem axle spacing (in)	49.2
Quad axle spacing (in)	49.2

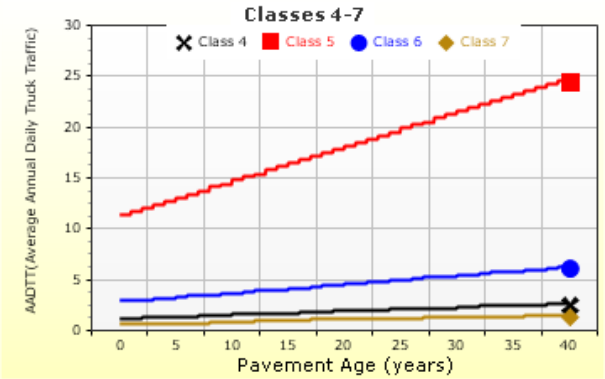
Wheelbase does not apply

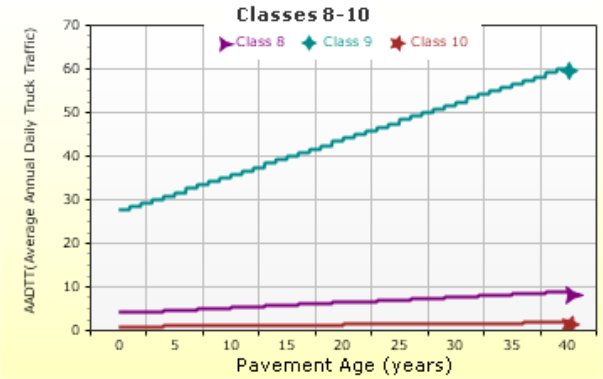
Number of Axles per Truck

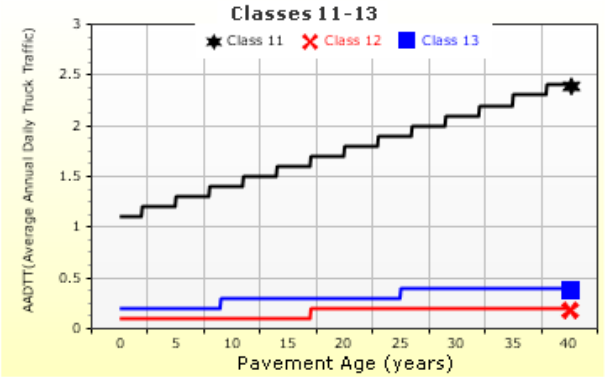
Vehicle Class	Single Axle	Tandem Axle	Tridem Axle	Quad Axle
Class 4	1.62	0.39	0	0
Class 5	2	0	0	0
Class 6	1.02	0.99	0	0
Class 7	1	0.26	0.83	0
Class 8	2.38	0.67	0	0
Class 9	1.13	1.93	0	0
Class 10	1.19	1.09	0.89	0
Class 11	4.29	0.26	0.06	0
Class 12	3.52	1.14	0.06	0
Class 13	2.15	2.13	0.35	0

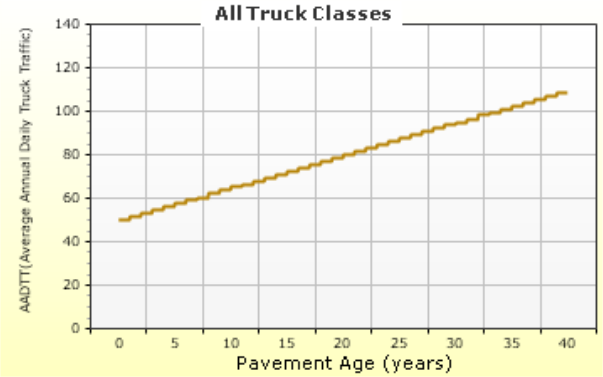
AADTT (Average Annual Daily Truck Traffic) Growth

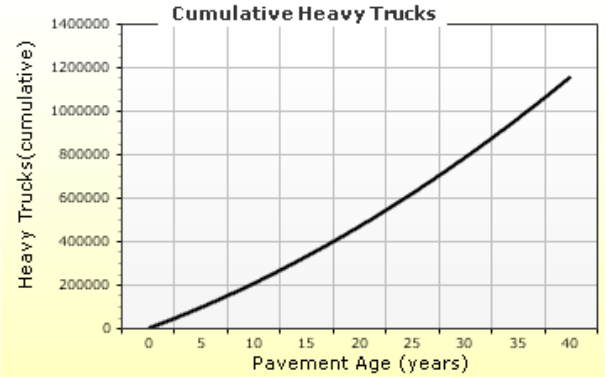
*** Traffic cap is not enforced**











APPENDIX R. ASPHALT LAYER PARAMETERS (LEVEL 3) IN PAVEMENT ME

HMA Design Properties

Use Multilayer Rutting Model	False
Using G* based model (not nationally calibrated)	False
Is NCHRP 1-37A HMA Rutting Model Coefficients	True
Endurance Limit	-
Use Reflective Cracking	True

Structure - ICM Properties	
AC surface shortwave absorptivity	0.85

Layer Name	**Layer Type**	**Interface Friction**
Layer 1 Flexible : Default asphalt concrete	Flexible (1)	1.00
Layer 2 Non-stabilized Base : A-1-a	Non-stabilized Base (4)	1.00
Layer 3 Non-stabilized Base : A-1-b	Non-stabilized Base (4)	1.00
Layer 4 Subgrade : A-1-b	Subgrade (5)	-

Master Curve Plot

Delta	2.8417502
Alpha	3.870018
Beta	-0.6501216
Gamma	0.313351
c	1.255882
SSE	0
Se/Sy	0

log(Reduce	**E* (psi)**	**14 oF**	**40 oF**	**70 oF**	**100 oF**	**130 oF**
-6.0271108	2682441.7	2682441.7				
-5.6291708	2477445	2477445				
-4.6291708	1949019.2	1949019.2				
-4.3281408	1790705.9	1790705.9				
-3.597245	1419160.5		1419160.5			
-3.1993049	1229267.8		1229267.8			
-2.1993049	809542.6		809542.6			
-1.8982749	702304.56		702304.56			
-1.39794	545336.95			545336.95		
-1	439474.08			439474.08		
0	242381.01			242381.01		
0.30103	200015.76			200015.76		
0.3203962	197523.86				197523.86	
0.7183362	152018.74				152018.74	
1.7183362	76682.67				76682.67	
2.0193662	62165.031				62165.031	
1.6808806	78707.012					78707.012
2.0788206	59637.836					59637.836
3.0788206	29842.823					29842.823
3.3798506	24350.865					24350.865

DRAFT

Shift Factor Plot

c	1.255882

Temp (F)	Shift	14 oF	40 oF	70 oF	100 oF	130 oF
14	4.6291708	4.6291708				
40	2.1993049		2.1993049			
70	0			0		
100	-1.7183362				-1.7183362	
130	-3.0788206					-3.0788206

Temperature Viscosity

Ao	10.035
VTSo	-3.35

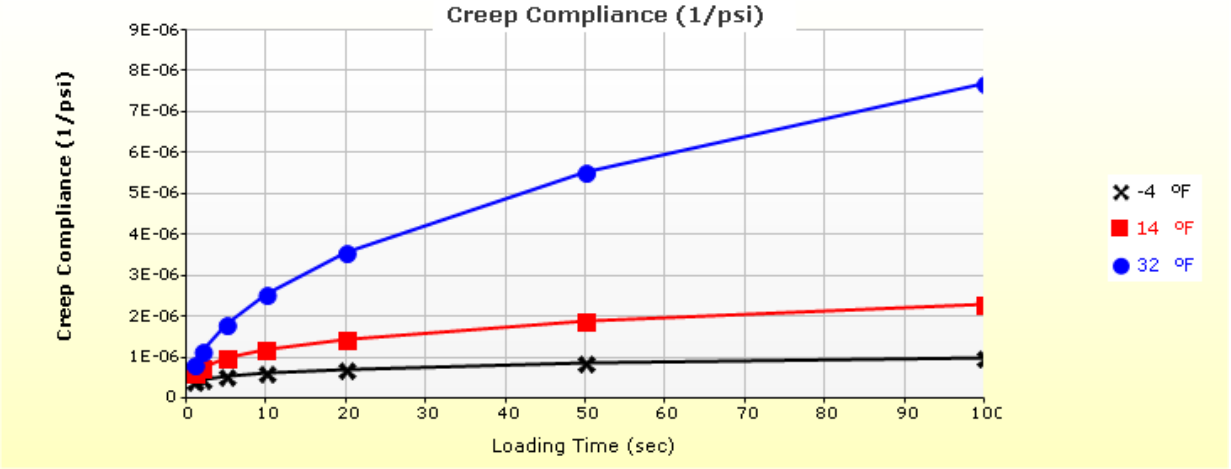
Log Temp	Log(Viscosity (cp))
2.6987093	9.87014833
2.72403	8.118944837
2.7479553	6.750714198
2.7706311	5.667424222

Thermal Cracking

Thermal Contraction	
Is thermal contraction calculated?	True
Mix coefficient of thermal contraction (in/in/ºF)	-
Aggregate coefficient of thermal contraction (in/in/ºF)	5.0e-006
Voids in Mineral Aggregate (%)	18.6

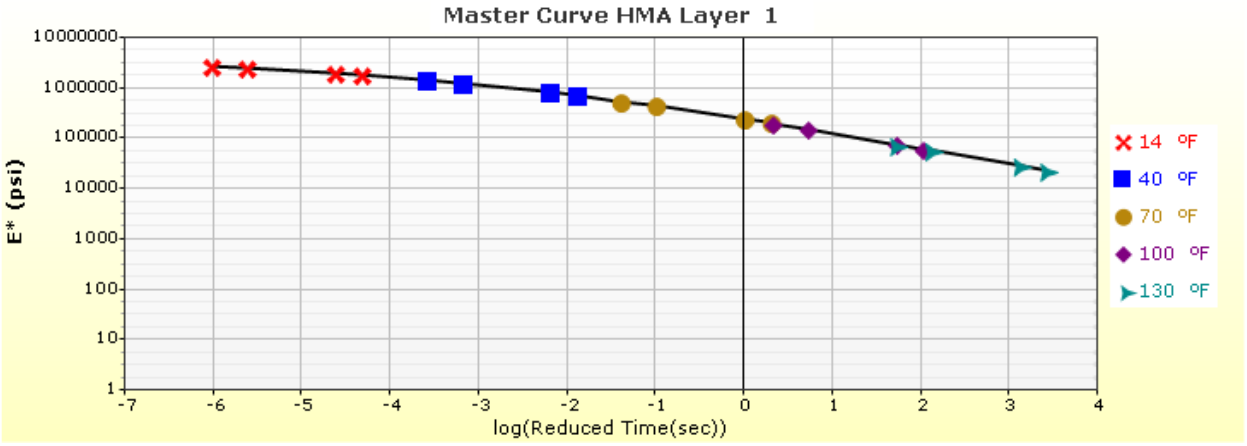
Indirect Tensile Strength (Input Level: 3)	
Test Temperature (ºF)	Indirect Tensilte Strength (psi)
14.0	473.35

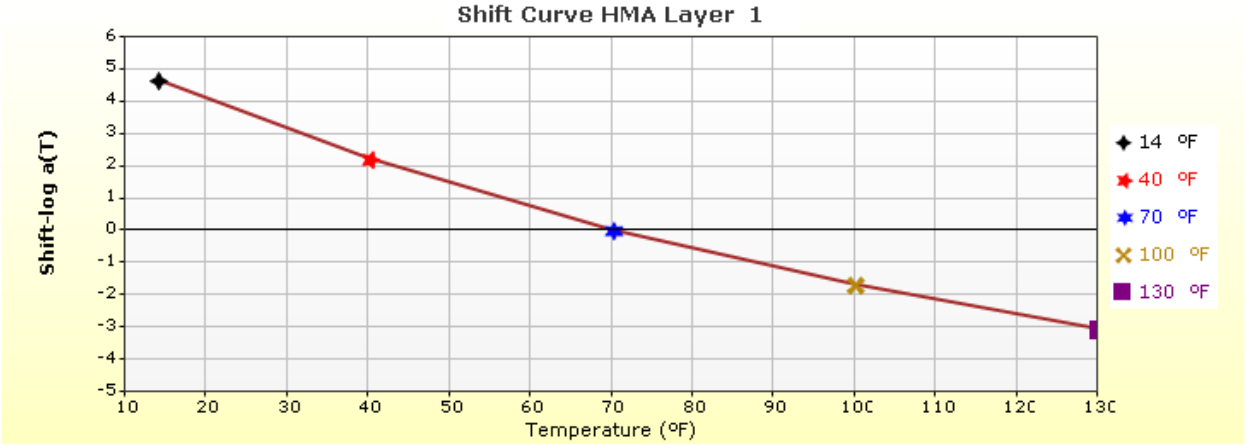
Creep Compliance (1/psi) (Input Level: 3)			
Loading time (sec)	-4 ºF	14 ºF	32 ºF
1	4.14e-007	6.27e-007	8.50e-007
2	4.72e-007	7.63e-007	1.19e-006
5	5.62e-007	9.89e-007	1.84e-006
10	6.42e-007	1.20e-006	2.56e-006
20	7.32e-007	1.46e-006	3.57e-006
50	8.71e-007	1.90e-006	5.55e-006
100	9.94e-007	2.31e-006	7.73e-006

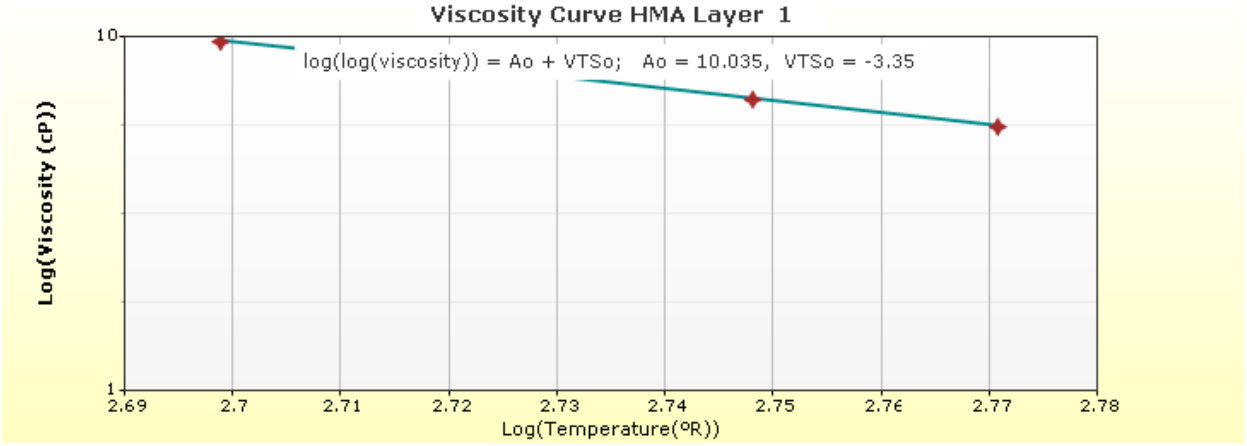


DRAFT

HMA Layer 1: Layer 1 Flexible : Default asphalt concrete







Layer 1 Flexible : Default asphalt concrete

Asphalt		
Thickness (in)	3.5	
Unit weight (pcf)	150.0	
Poisson's ratio	Is Calculated?	False
	Ratio	0.30
	Parameter A	-
	Parameter B	-

Asphalt Dynamic Modulus (Input Level: 3)

Gradation	Percent Passing
3/4-inch sieve	100
3/8-inch sieve	77
No.4 sieve	60
No.200 sieve	6

Asphalt Binder

Parameter	Value
Grade	Superpave Performance Grade
Binder Type	58-34
A	10.035
VTS	-3.35

General Info

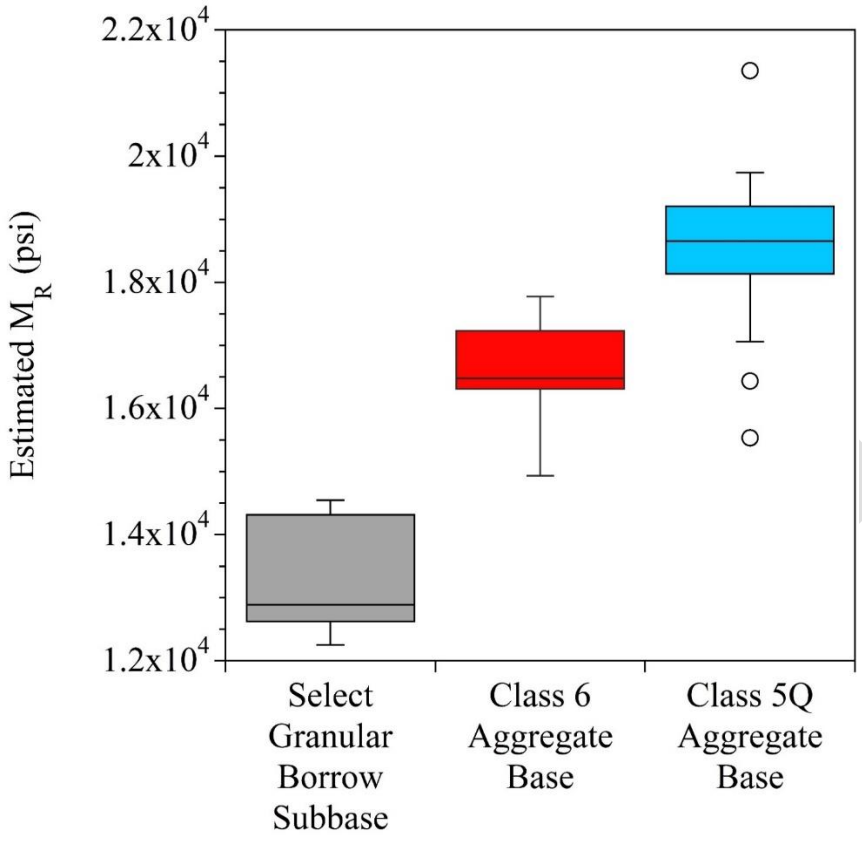
Name	Value
Reference temperature (ºF)	70
Effective binder content (%)	11.6
Air voids (%)	7
Thermal conductivity (BTU/hr-ft-ºF)	0.67
Heat capacity (BTU/lb-ºF)	0.23

Identifiers

Field	Value
Display name/identifier	Default asphalt concrete
Description of object	
Author	
Date Created	10/30/2010 12:00:00 AM
Approver	
Date approved	10/30/2010 12:00:00 AM
State	
District	
County	
Highway	
Direction of Travel	
From station (miles)	
To station (miles)	
Province	
User defined field 1	
User defined field 2	
User defined field 3	
Revision Number	0

DRAFT

APPENDIX S. ESTIMATION OF SM_R FOR SELECT GRANULAR BORROW, CLASS 6 AGGREGATE, AND CLASS 5Q AGGREGATE

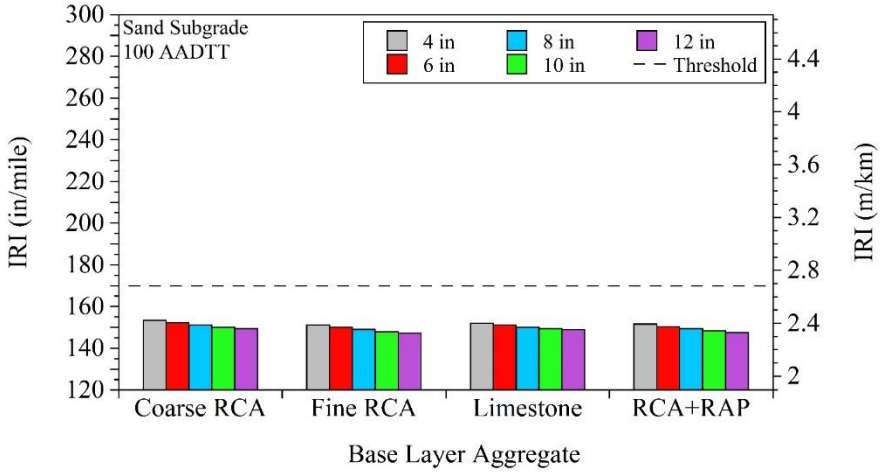


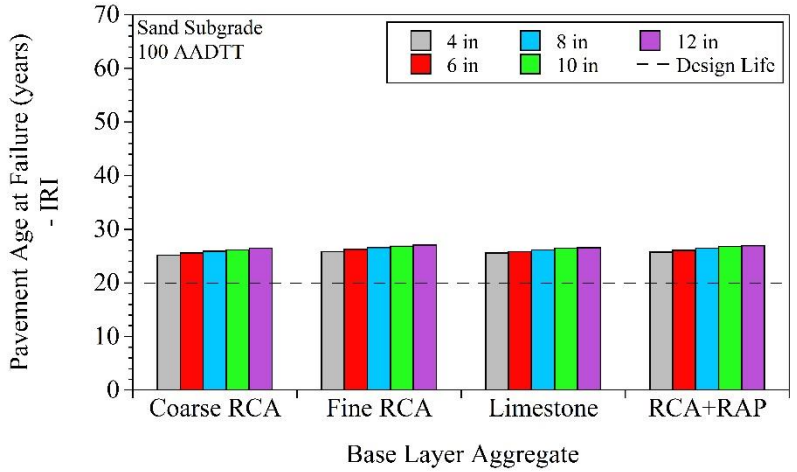
Median M_R values
Select granular borrow subbase = 12,888 psi
Class 6 aggregate base = 16,478.9 psi
Class 5Q aggregate base = 18,651.1 psi

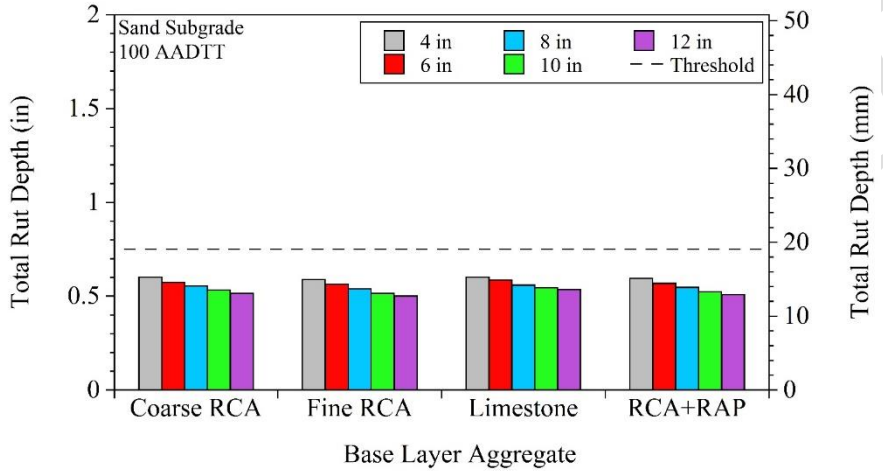
DRAFT

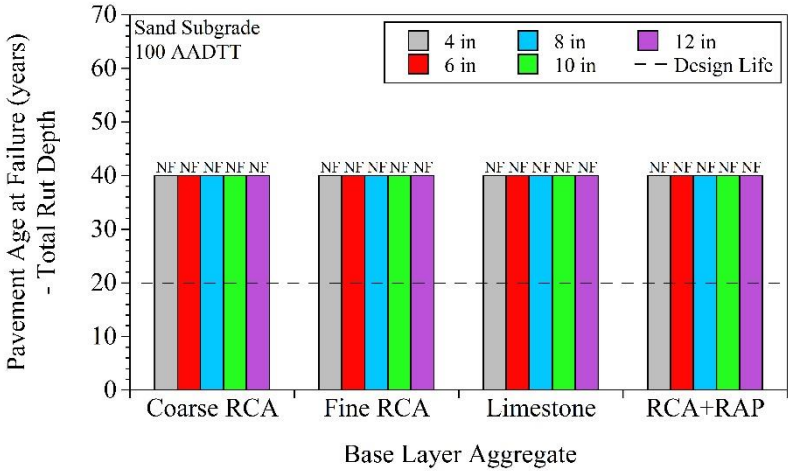
APPENDIX T. EFFECT OF AGGREGATE BASE LAYER THICKNESS ON PAVEMENT PERFORMANCE PREDICTIONS

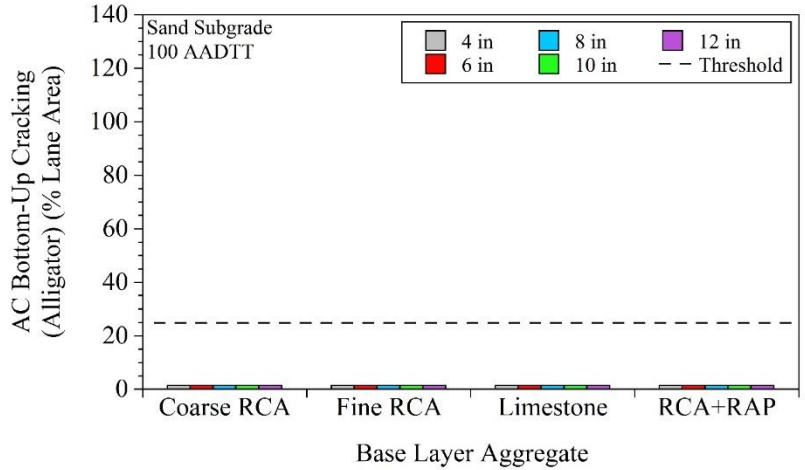
For pavement models that contained sand subgrade – 100 AADTT:

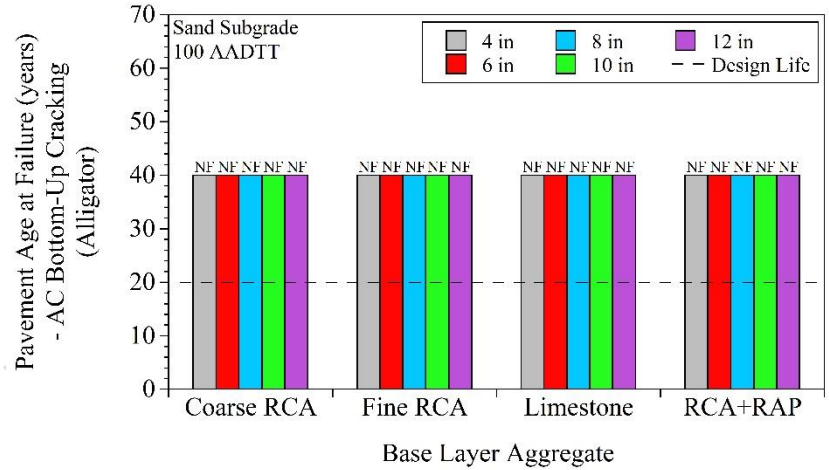


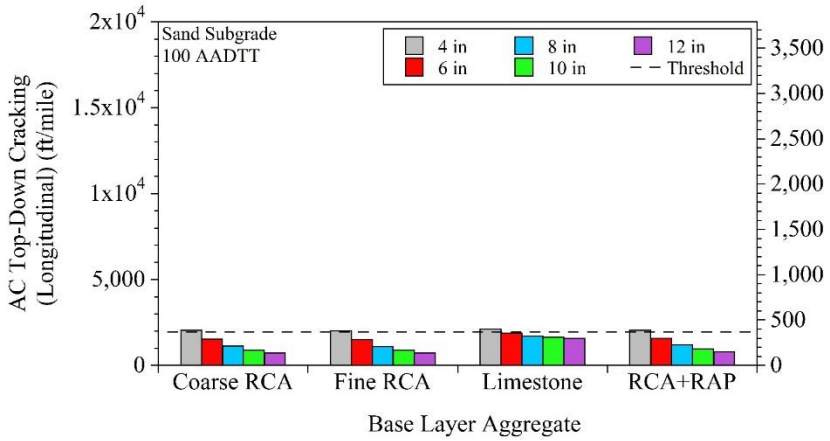


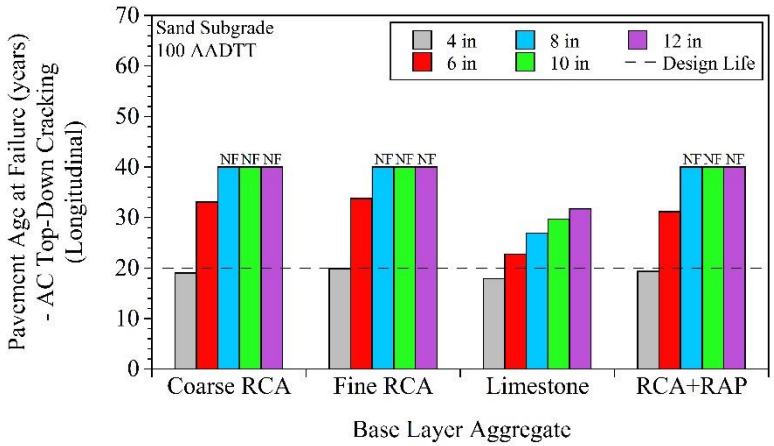




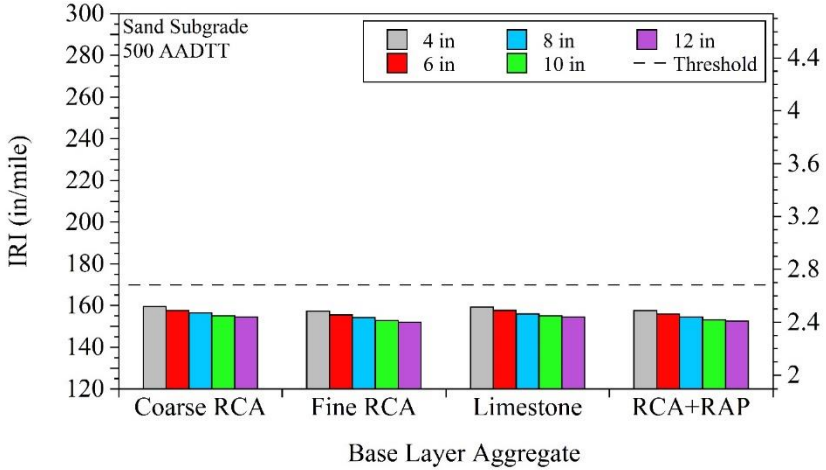

Sand Subgrade
100 AADTT
4 in
6 in
8 in
10 in
12 in
Threshold
AC Bottom-Up Cracking
(Alligator) (% Lane Area)
0
20
40
60
80
100
120
140
Coarse RCA
Fine RCA
Limestone
RCA+RAP
Base Layer Aggregate

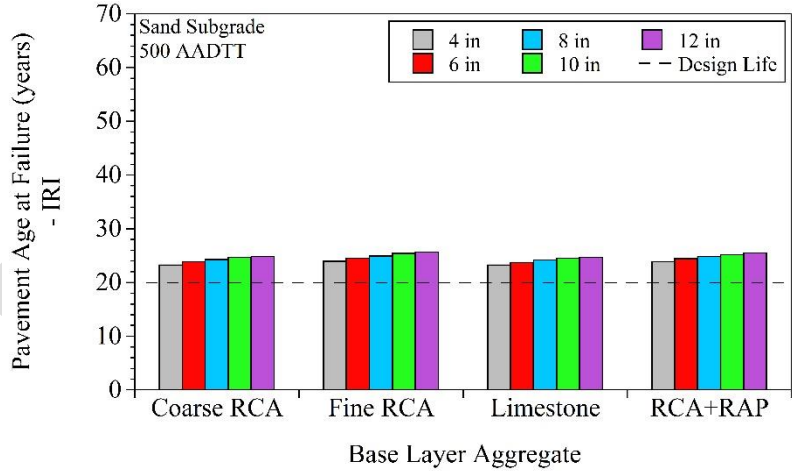

Sand Subgrade
100 AADTT
4 in
6 in
8 in
10 in
12 in
Design Life
Pavement Age at Failure (years)
- AC Bottom-Up Cracking
(Alligator)
0
10
20
30
40
50
60
70
NF NF NF NF NF
Coarse RCA
Fine RCA
Limestone
RCA+RAP
Base Layer Aggregate

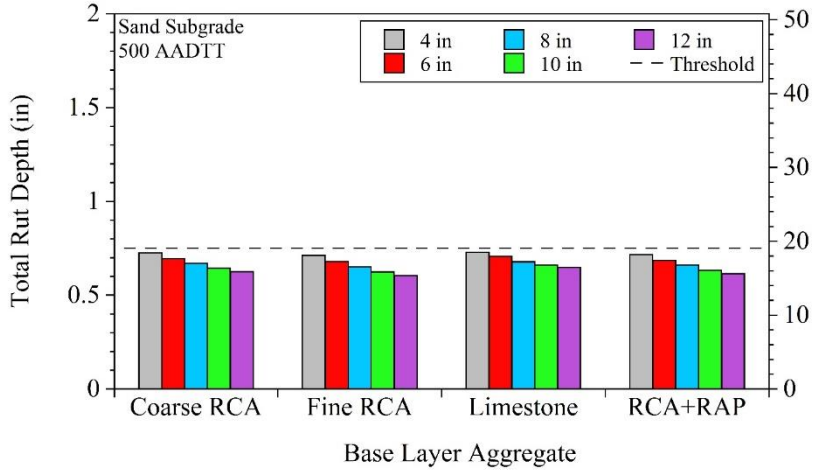

Sand Subgrade
100 AADTT
4 in
6 in
8 in
10 in
12 in
Threshold
AC Top-Down Cracking
(Longitudinal) (ft/mile)
0
5,000
1x10^4
1.5x10^4
2x10^4
AC Top-Down Cracking
(Longitudinal) (m/km)
0
500
1,000
1,500
2,000
2,500
3,000
3,500
Coarse RCA
Fine RCA
Limestone
RCA+RAP
Base Layer Aggregate

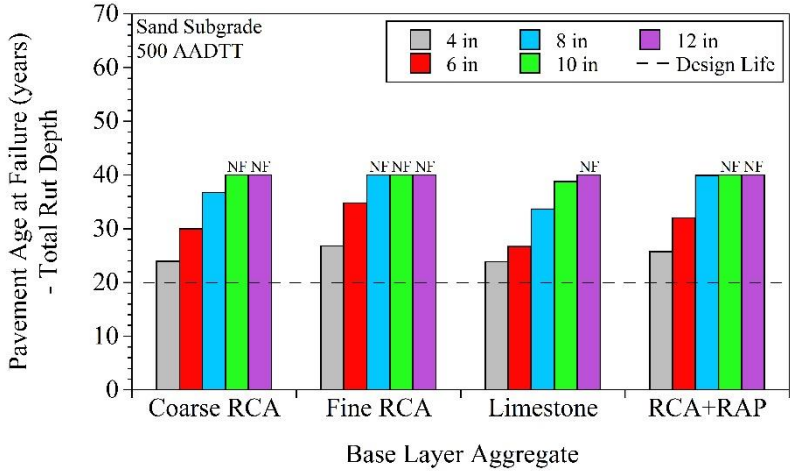

Sand Subgrade
100 AADTT
4 in
6 in
8 in
10 in
12 in
Design Life
Pavement Age at Failure (years)
- AC Top-Down Cracking
(Longitudinal)
0
10
20
30
40
50
60
70
NF NF NF
Coarse RCA
Fine RCA
Limestone
RCA+RAP
Base Layer Aggregate

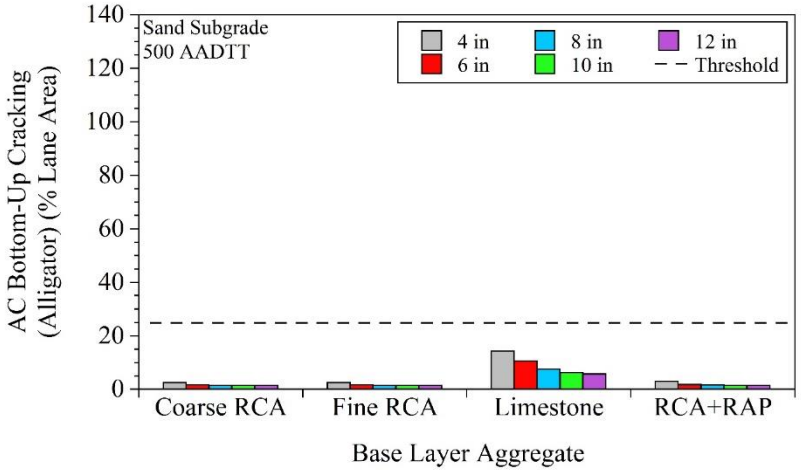
For pavements that contained sand subgrade – 500 AADTT:

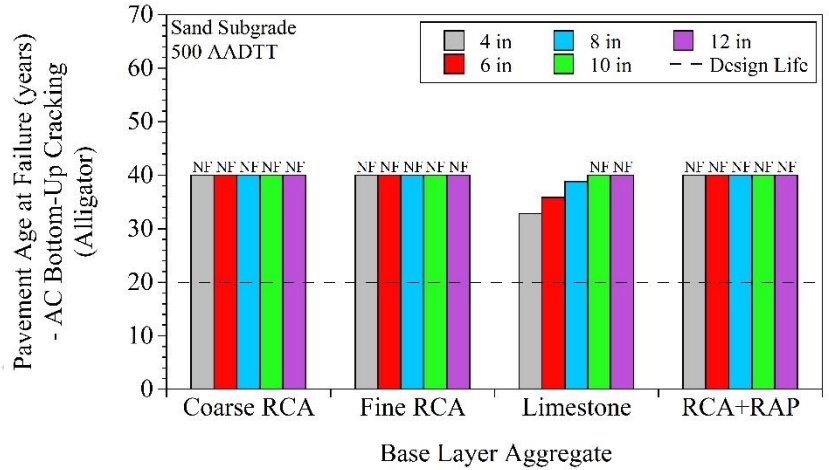


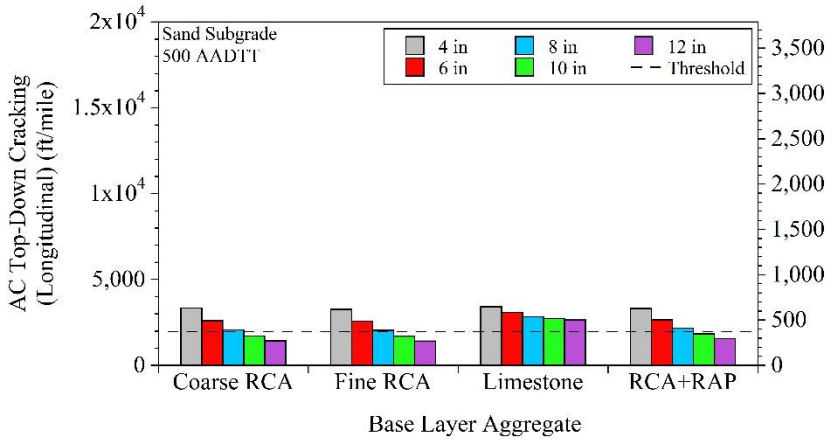


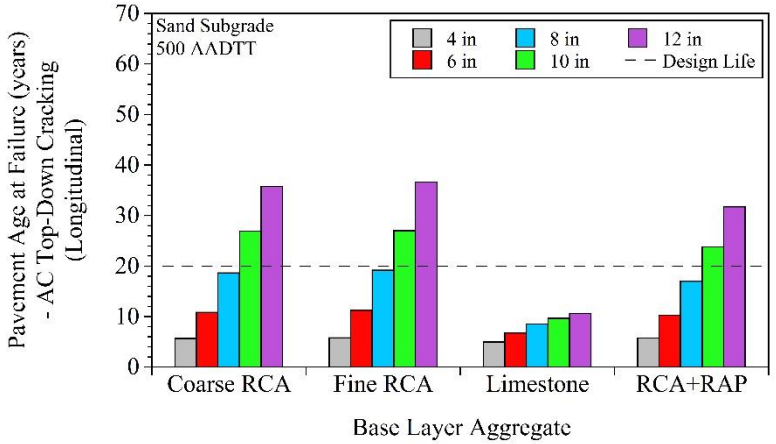




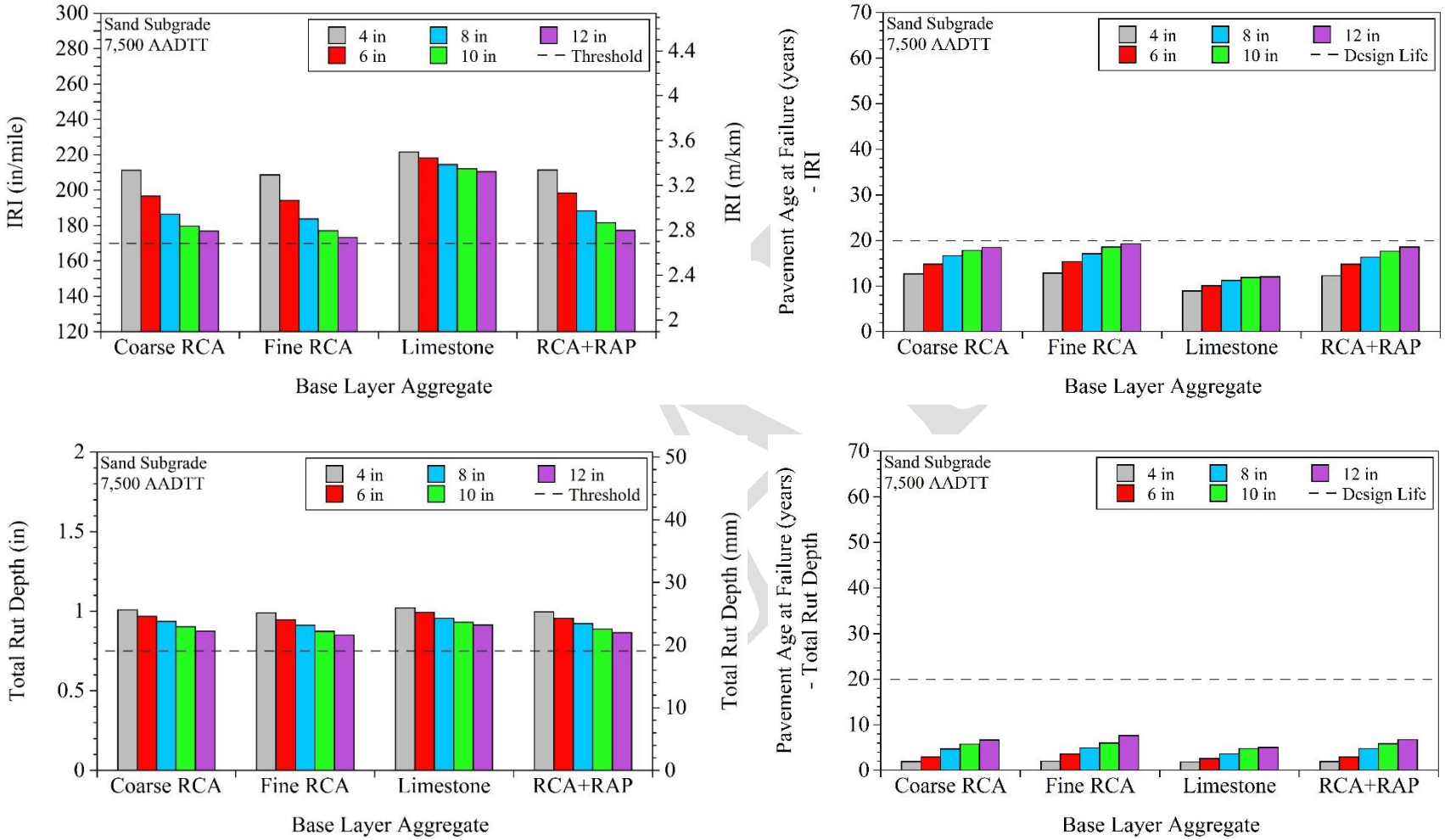

Sand Subgrade
500 AADTT
4 in
6 in
8 in
10 in
12 in
Threshold
AC Bottom-Up Cracking
(Alligator) (% Lane Area)
0
20
40
60
80
100
120
140
Coarse RCA
Fine RCA
Limestone
RCA+RAP
Base Layer Aggregate

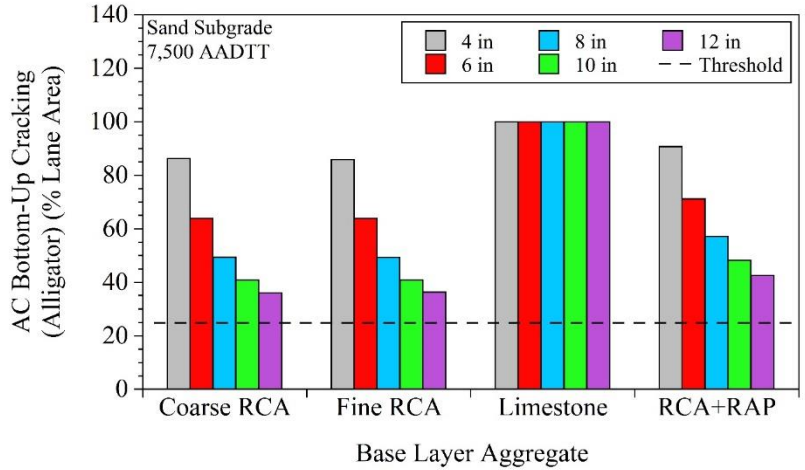

Sand Subgrade
500 AADTT
4 in
6 in
8 in
10 in
12 in
Design Life
Pavement Age at Failure (years)
- AC Bottom-Up Cracking
(Alligator)
NF NF NF NF NF
NF NF NF NF NF
NF NF
NF NF NF NF NF
0
10
20
30
40
50
60
70
Coarse RCA
Fine RCA
Limestone
RCA+RAP
Base Layer Aggregate

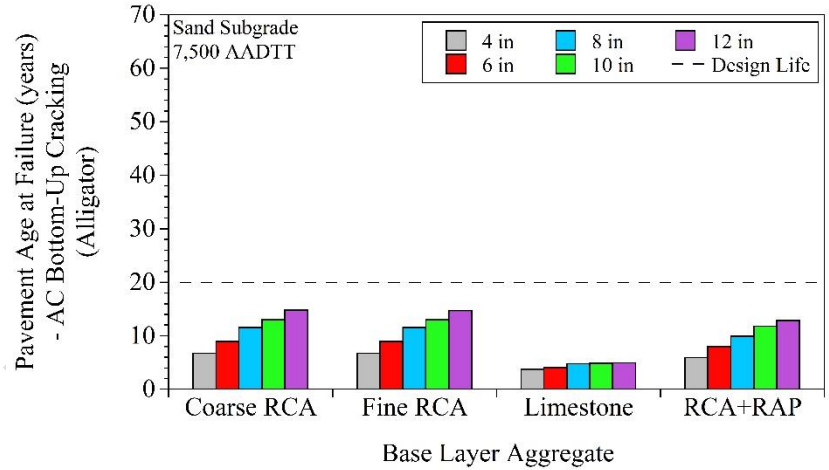

Sand Subgrade
500 AADTT
4 in
6 in
8 in
10 in
12 in
Threshold
AC Top-Down Cracking
(Longitudinal) (ft/mile)
AC Top-Down Cracking
(Longitudinal) (m/km)
0
5,000
1x10^4
1.5x10^4
2x10^4
0
500
1,000
1,500
2,000
2,500
3,000
3,500
Coarse RCA
Fine RCA
Limestone
RCA+RAP
Base Layer Aggregate

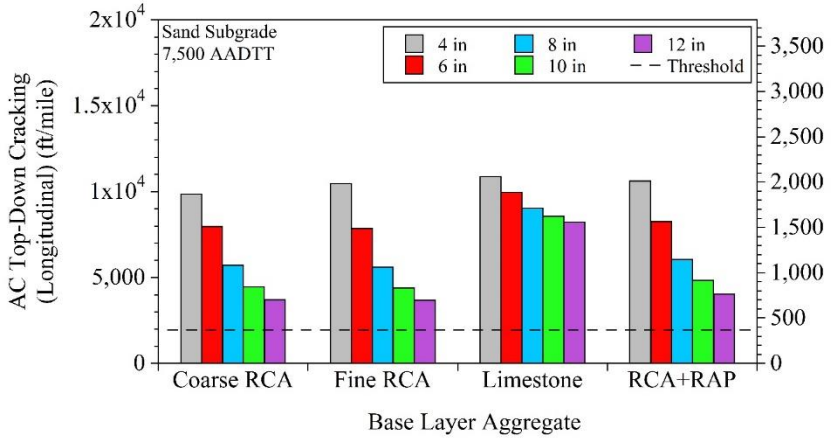

Sand Subgrade
500 AADTT
4 in
6 in
8 in
10 in
12 in
Design Life
Pavement Age at Failure (years)
- AC Top-Down Cracking
(Longitudinal)
0
10
20
30
40
50
60
70
Coarse RCA
Fine RCA
Limestone
RCA+RAP
Base Layer Aggregate

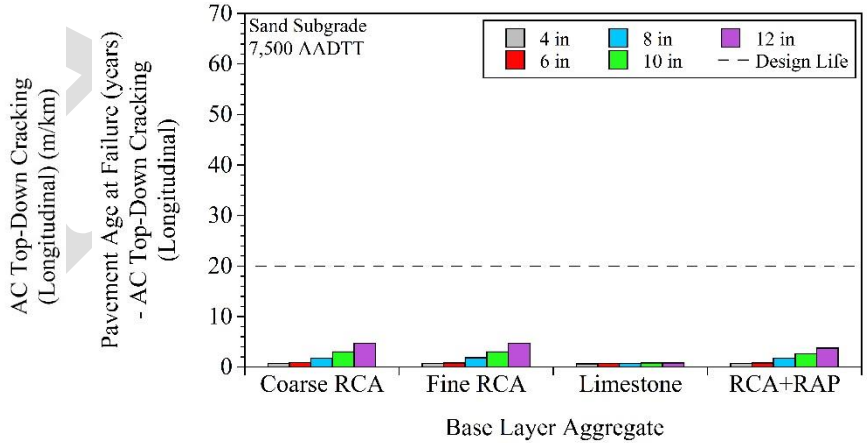
For pavements that contained sand subgrade – 7,500 AADTT:



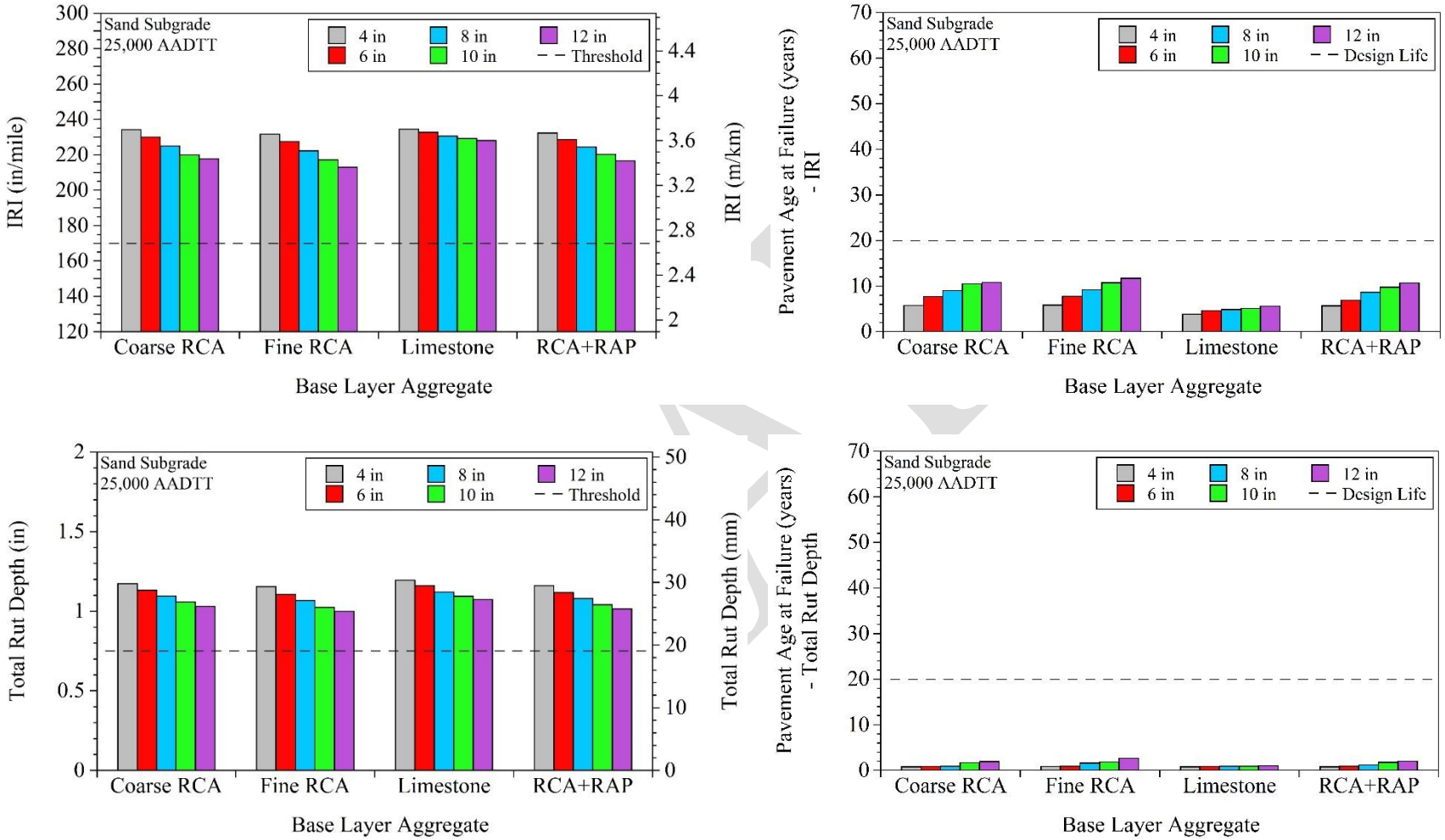

Sand Subgrade
7,500 AADTT
4 in
6 in
8 in
10 in
12 in
Threshold
AC Bottom-Up Cracking
(Alligator) (% Lane Area)
140
120
100
80
60
40
20
0
Coarse RCA
Fine RCA
Limestone
RCA+RAP
Base Layer Aggregate

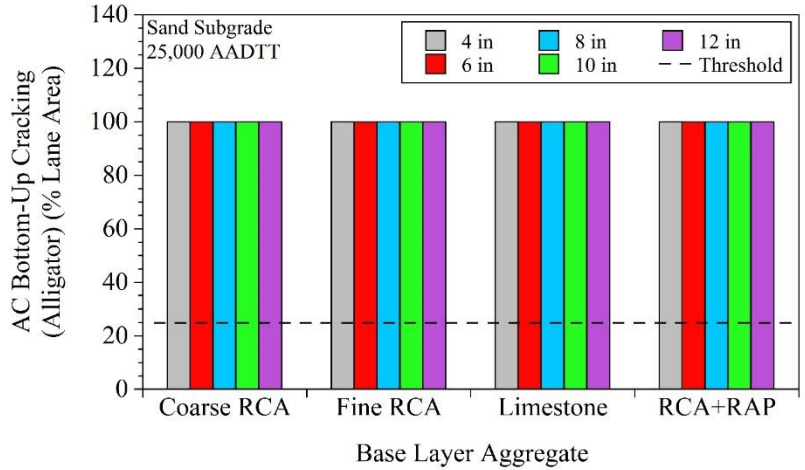

Sand Subgrade
7,500 AADTT
4 in
6 in
8 in
10 in
12 in
Design Life
Pavement Age at Failure (years)
- AC Bottom-Up Cracking
(Alligator)
70
60
50
40
30
20
10
0
Coarse RCA
Fine RCA
Limestone
RCA+RAP
Base Layer Aggregate

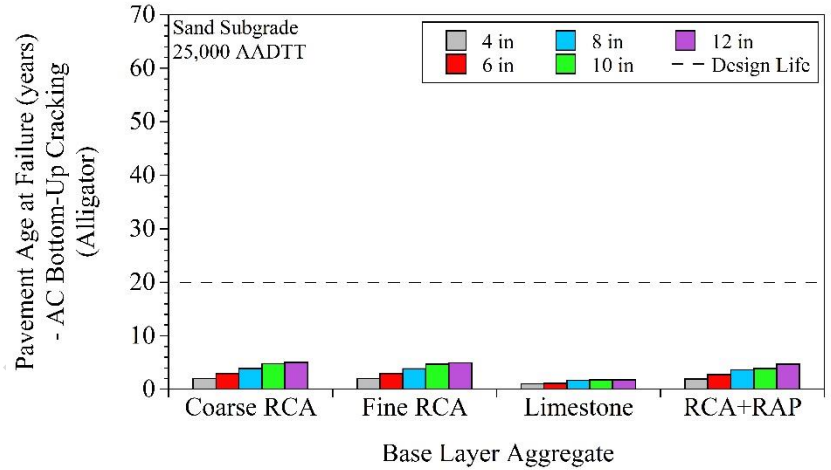

Sand Subgrade
7,500 AADTT
4 in
6 in
8 in
10 in
12 in
Threshold
AC Top-Down Cracking
(Longitudinal) (ft/mile)
2x10^4
1.5x10^4
1x10^4
5,000
0
3,500
3,000
2,500
2,000
1,500
1,000
500
0
Coarse RCA
Fine RCA
Limestone
RCA+RAP
Base Layer Aggregate

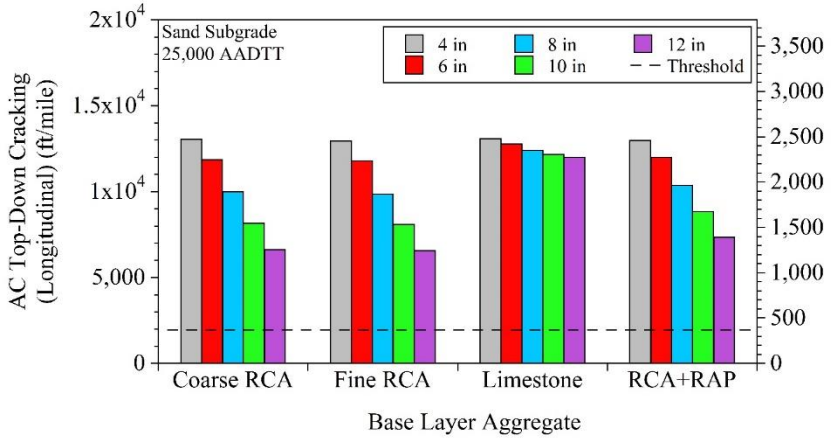

Sand Subgrade
7,500 AADTT
4 in
6 in
8 in
10 in
12 in
Design Life
AC Top-Down Cracking
(Longitudinal) (m/km)
Pavement Age at Failure (years)
- AC Top-Down Cracking
(Longitudinal)
70
60
50
40
30
20
10
0
Coarse RCA
Fine RCA
Limestone
RCA+RAP
Base Layer Aggregate

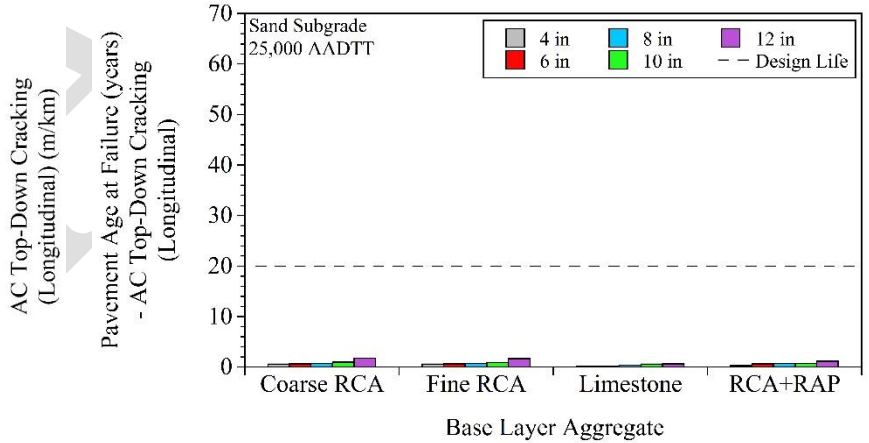
For pavements that contained sand subgrade – 25,000 AADTT:



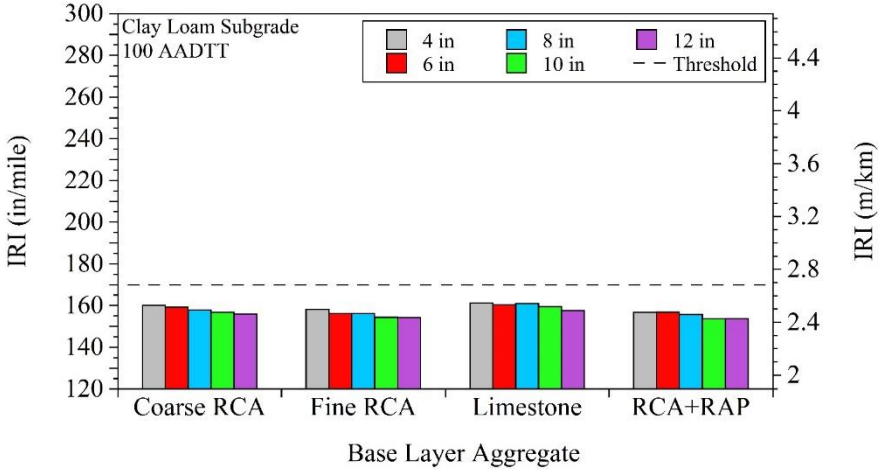

Sand Subgrade
25,000 AADTT
4 in
6 in
8 in
10 in
12 in
Threshold
AC Bottom-Up Cracking
(Alligator) (% Lane Area)
140
120
100
80
60
40
20
0
Coarse RCA
Fine RCA
Limestone
RCA+RAP
Base Layer Aggregate

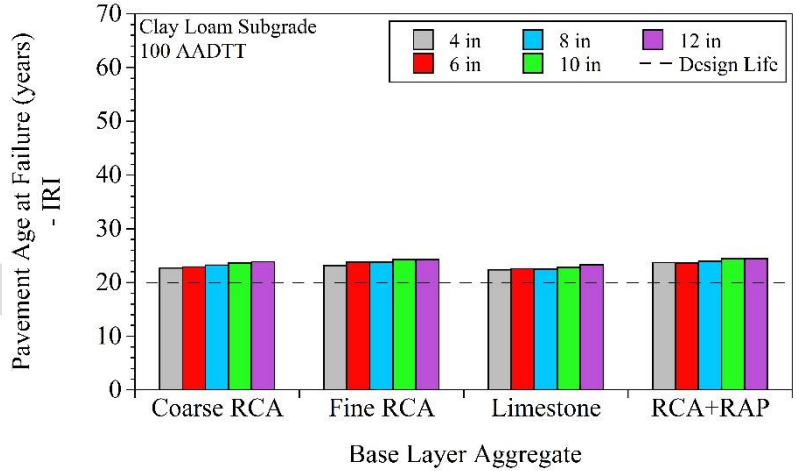

Sand Subgrade
25,000 AADTT
4 in
6 in
8 in
10 in
12 in
Design Life
Pavement Age at Failure (years)
- AC Bottom-Up Cracking
(Alligator)
70
60
50
40
30
20
10
0
Coarse RCA
Fine RCA
Limestone
RCA+RAP
Base Layer Aggregate

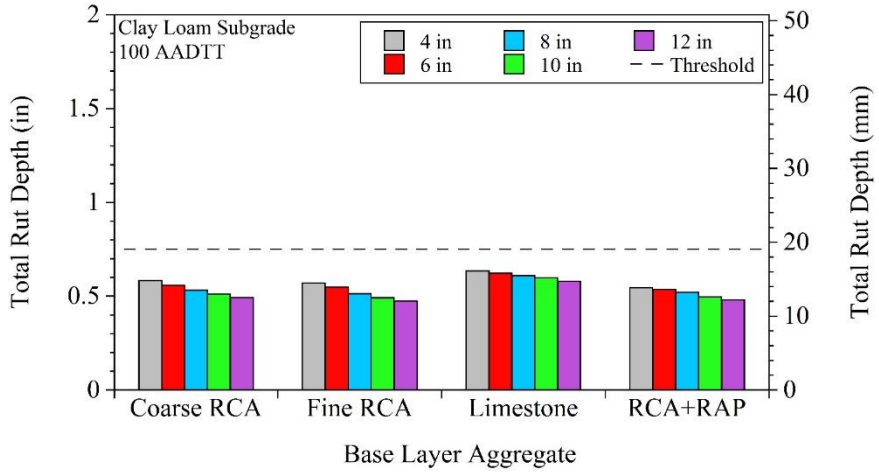

Sand Subgrade
25,000 AADTT
4 in
6 in
8 in
10 in
12 in
Threshold
AC Top-Down Cracking
(Longitudinal) (ft/mile)
2x10^4
1.5x10^4
1x10^4
5,000
0
3,500
3,000
2,500
2,000
1,500
1,000
500
0
Coarse RCA
Fine RCA
Limestone
RCA+RAP
Base Layer Aggregate

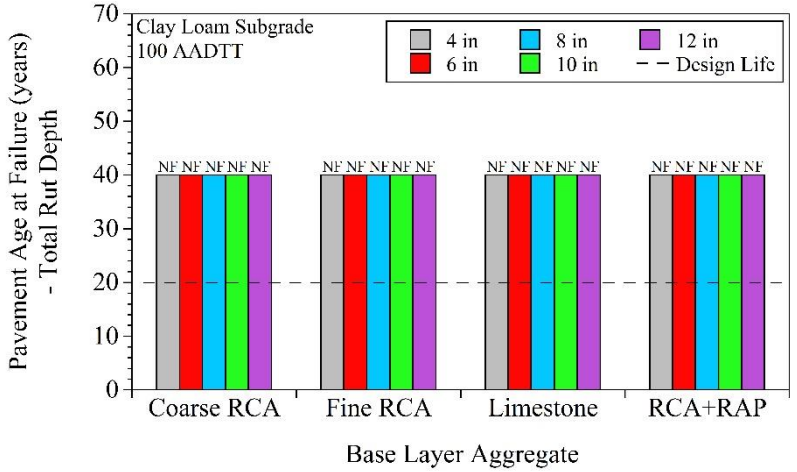

Sand Subgrade
25,000 AADTT
4 in
6 in
8 in
10 in
12 in
Design Life
AC Top-Down Cracking
(Longitudinal) (m/km)
Pavement Age at Failure (years)
- AC Top-Down Cracking
(Longitudinal)
70
60
50
40
30
20
10
0
Coarse RCA
Fine RCA
Limestone
RCA+RAP
Base Layer Aggregate

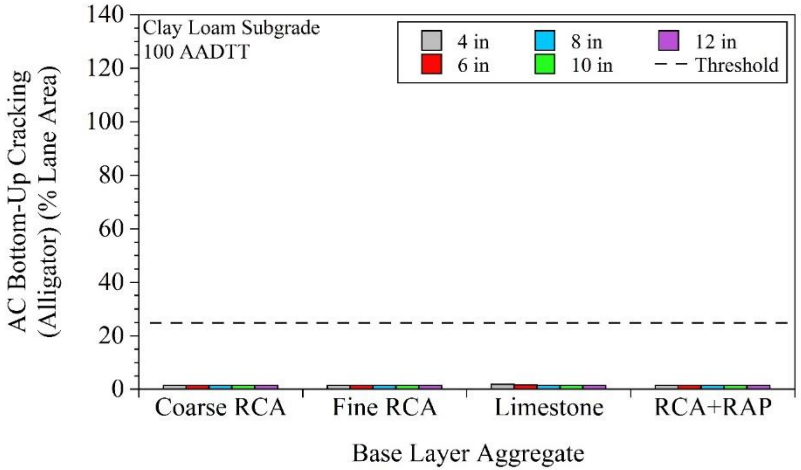
For pavements that contained clay loam subgrade – 100 AADTT:

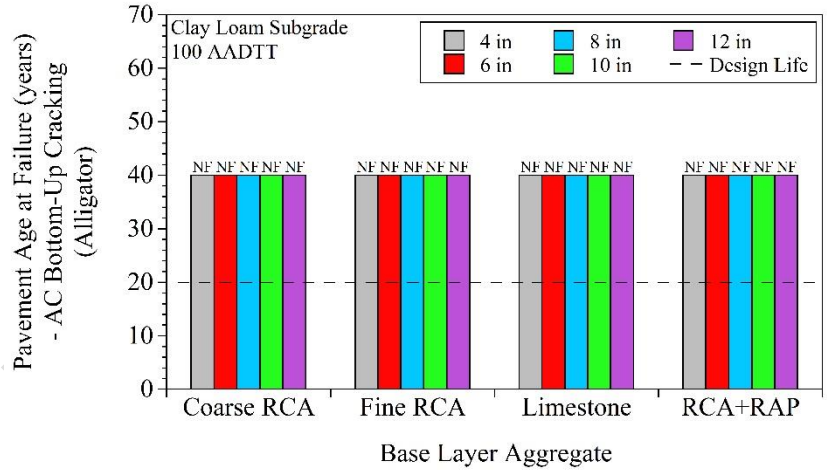




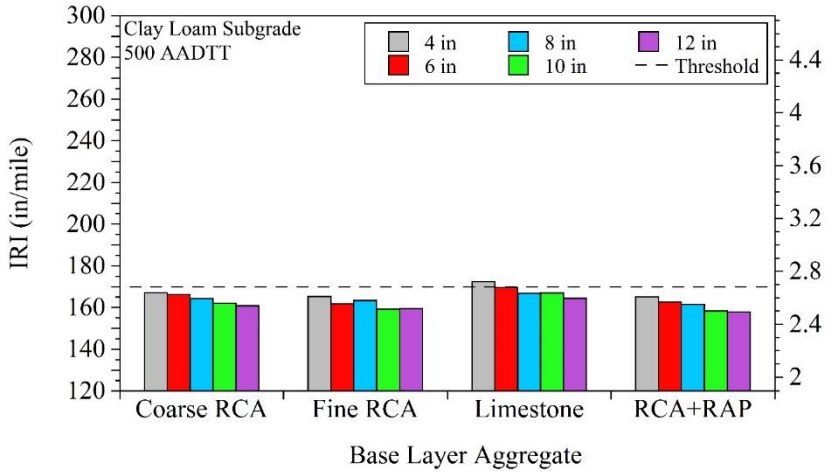


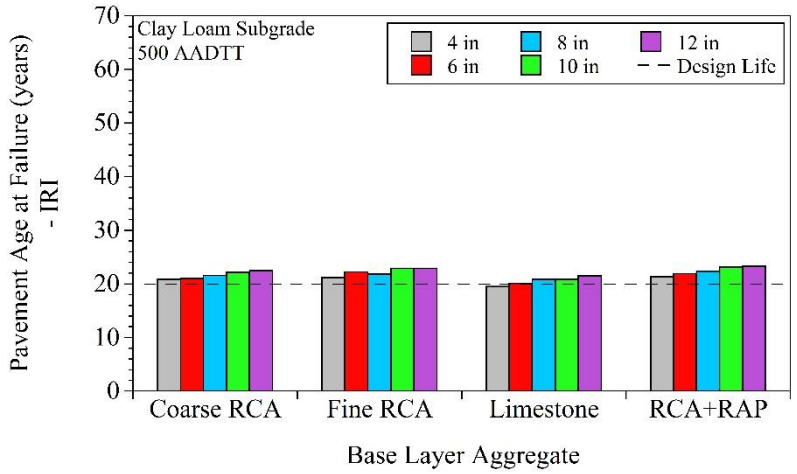


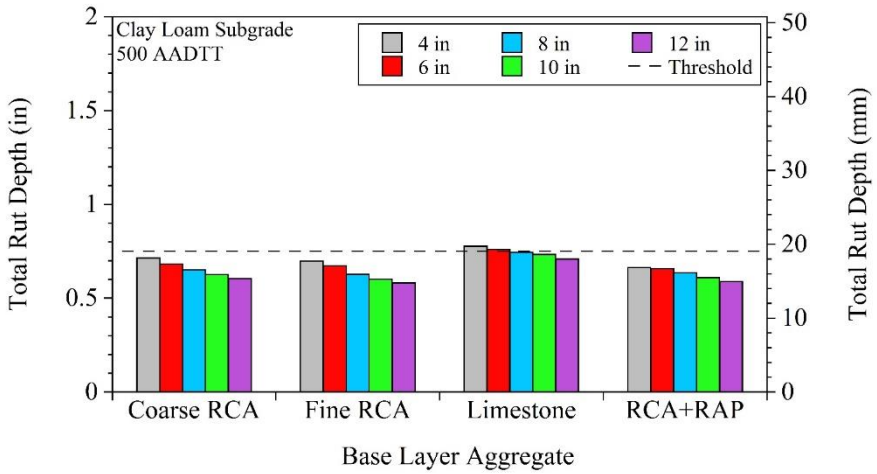


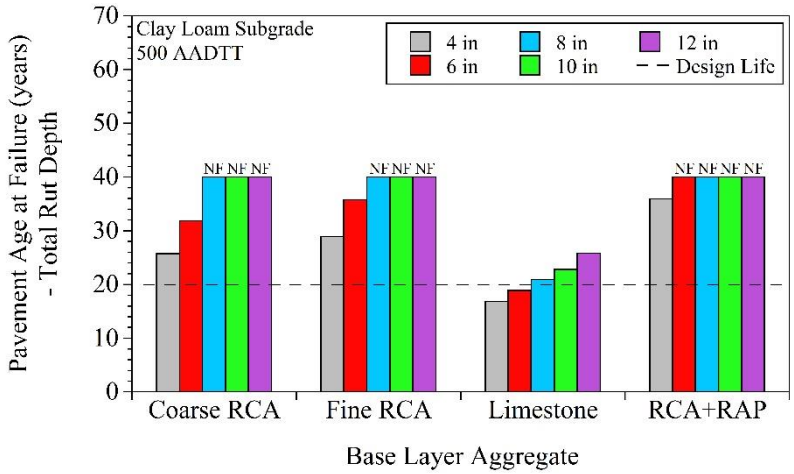


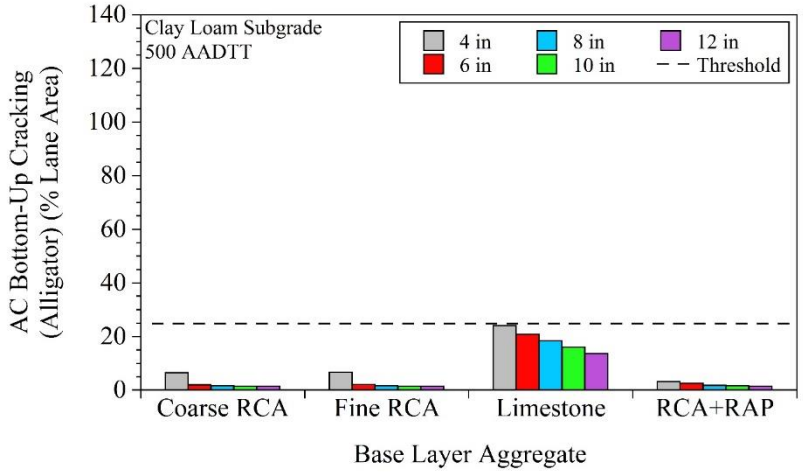
For pavements that contained clay loam subgrade – 500 AADTT:

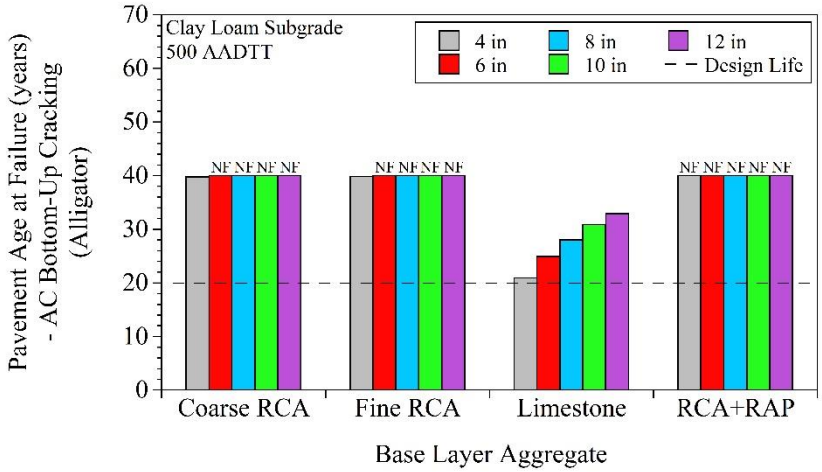




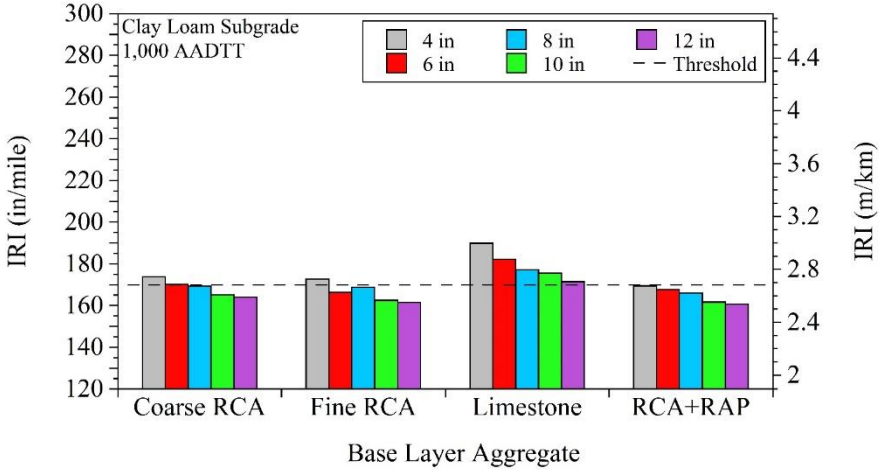

Clay Loam Subgrade
500 AADTT
4 in
6 in
8 in
10 in
12 in
Threshold
Total Rut Depth (in)
Total Rut Depth (mm)
Coarse RCA
Fine RCA
Limestone
RCA+RAP
Base Layer Aggregate

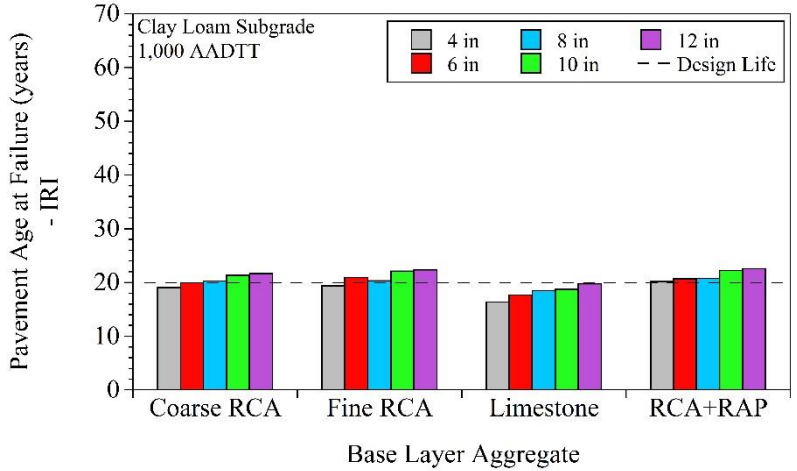

Clay Loam Subgrade
500 AADTT
4 in
6 in
8 in
10 in
12 in
Design Life
NF NF NF
Pavement Age at Failure (years)
- Total Rut Depth
Coarse RCA
Fine RCA
Limestone
RCA+RAP
Base Layer Aggregate

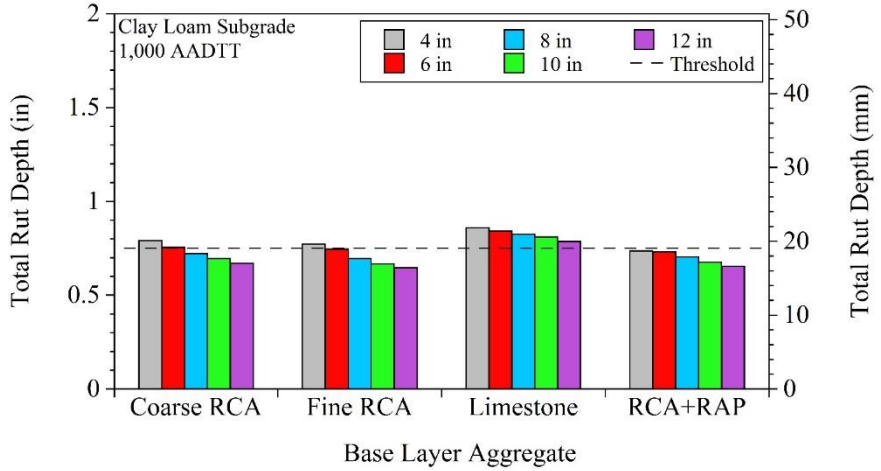

Clay Loam Subgrade
500 AADTT
4 in
6 in
8 in
10 in
12 in
Threshold
AC Bottom-Up Cracking
(Alligator) (% Lane Area)
Coarse RCA
Fine RCA
Limestone
RCA+RAP
Base Layer Aggregate

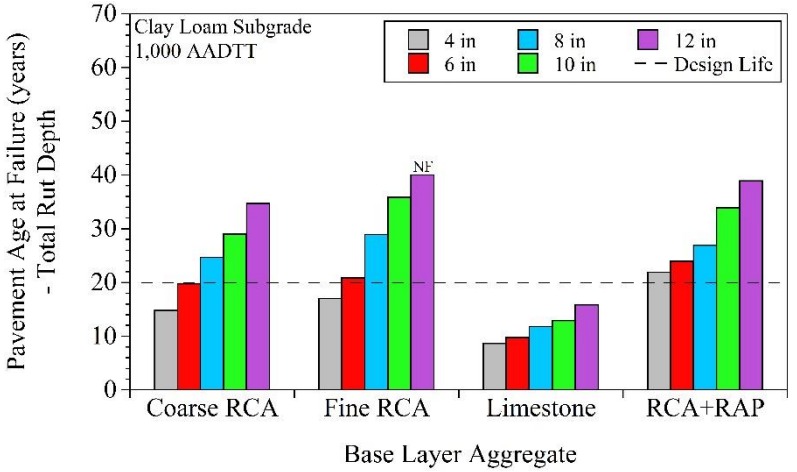

Clay Loam Subgrade
500 AADTT
4 in
6 in
8 in
10 in
12 in
Design Life
NF NF NF NF
Pavement Age at Failure (years)
- AC Bottom-Up Cracking
(Alligator)
Coarse RCA
Fine RCA
Limestone
RCA+RAP
Base Layer Aggregate

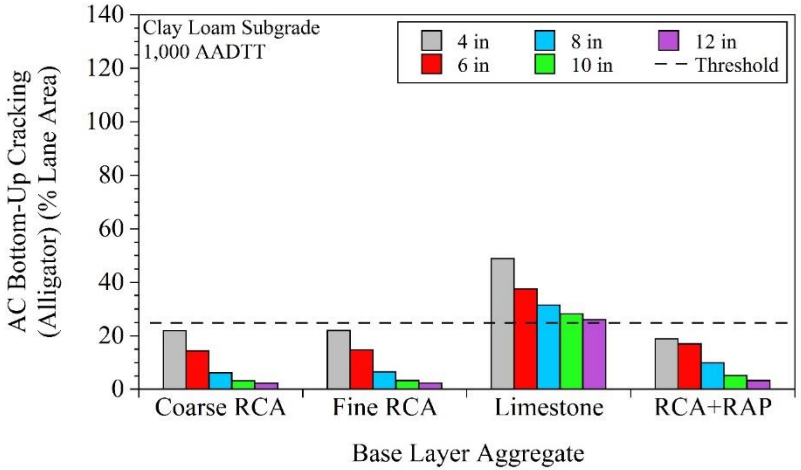
For pavements that contained clay loam subgrade – 1,000 AADTT:

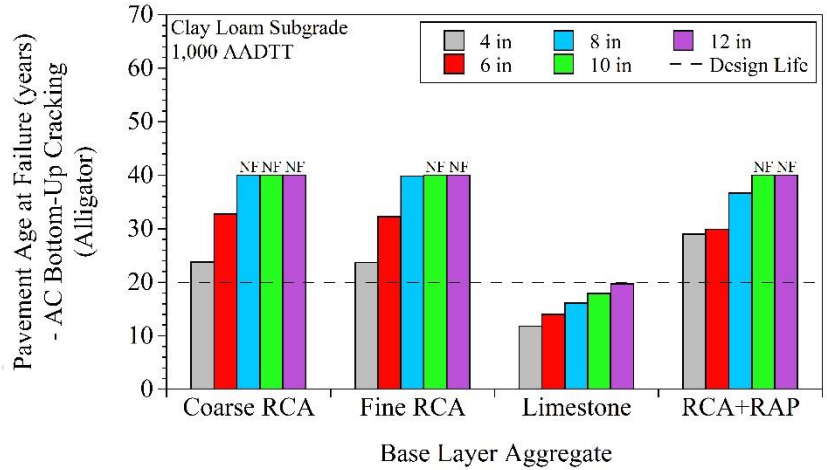




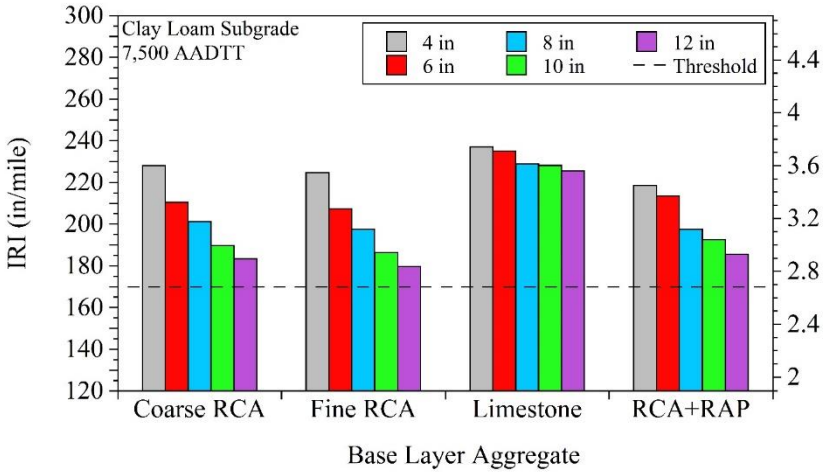


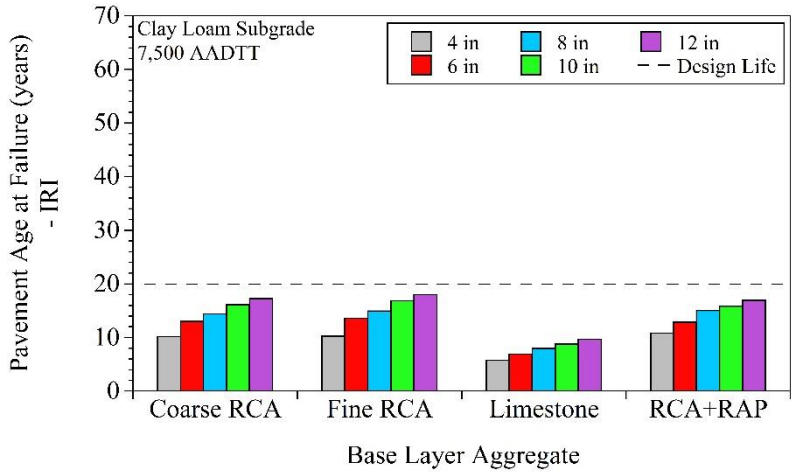


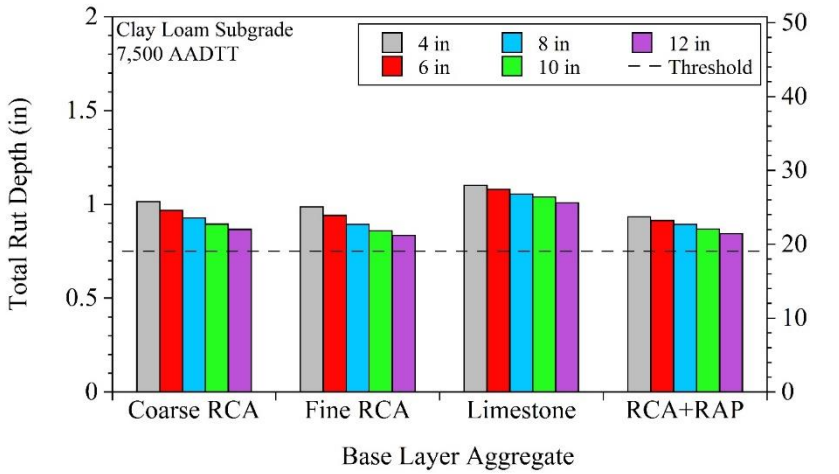


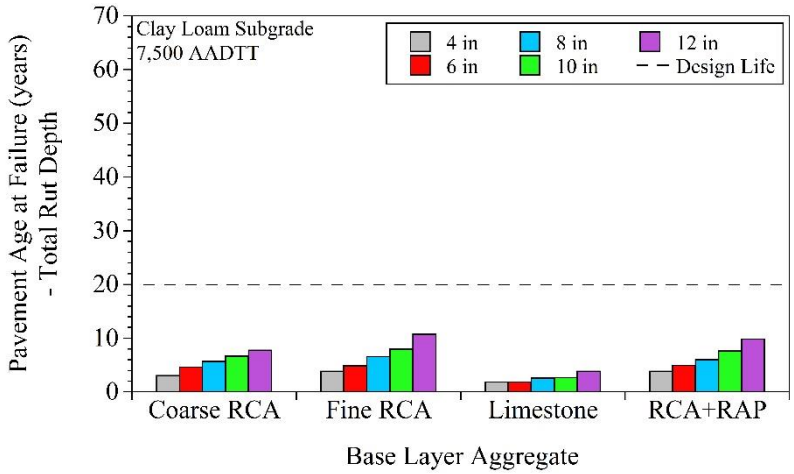


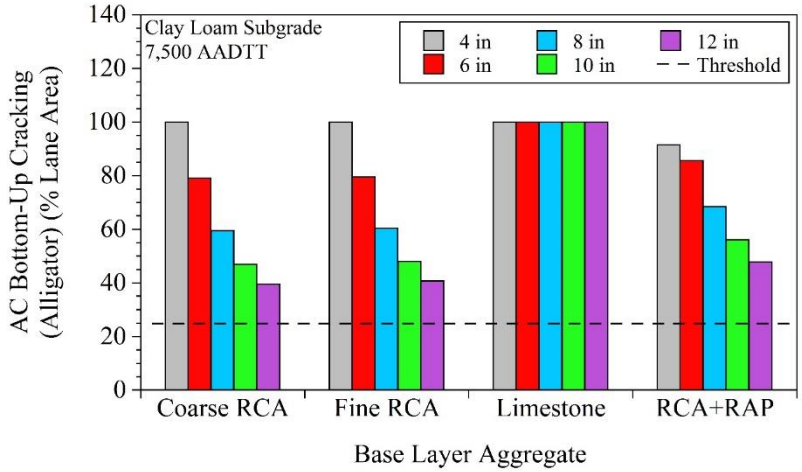
For pavements that contained clay loam subgrade – 7,500 AADTT:

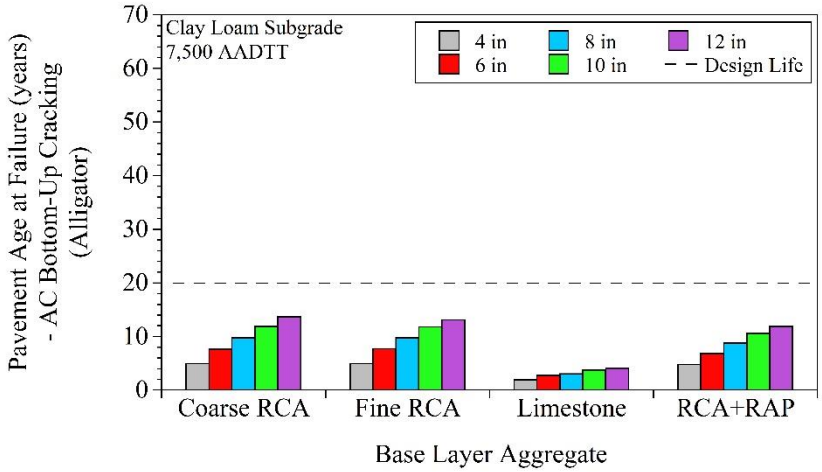




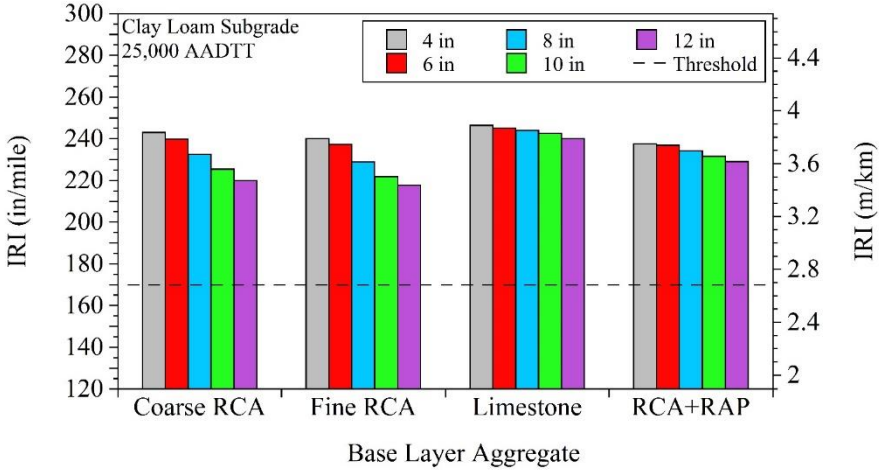

Clay Loam Subgrade
7,500 AADTT
4 in
6 in
8 in
10 in
12 in
Threshold
Total Rut Depth (in)
Total Rut Depth (mm)
Coarse RCA
Fine RCA
Limestone
RCA+RAP
Base Layer Aggregate

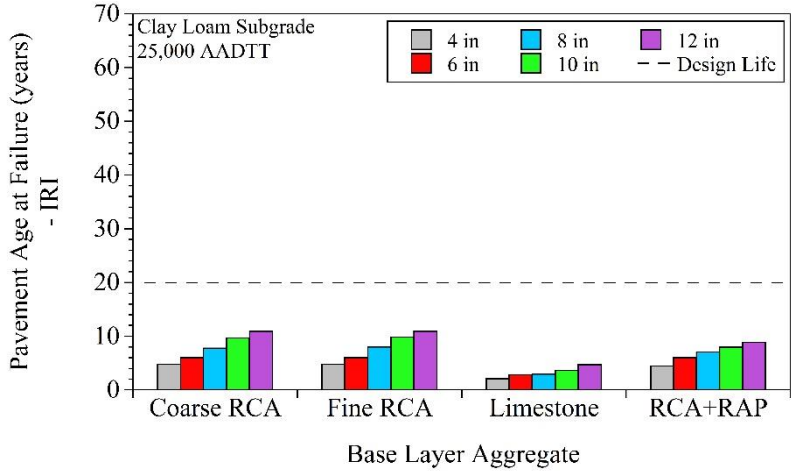

Clay Loam Subgrade
7,500 AADTT
4 in
6 in
8 in
10 in
12 in
Design Life
Pavement Age at Failure (years)
- Total Rut Depth
Coarse RCA
Fine RCA
Limestone
RCA+RAP
Base Layer Aggregate

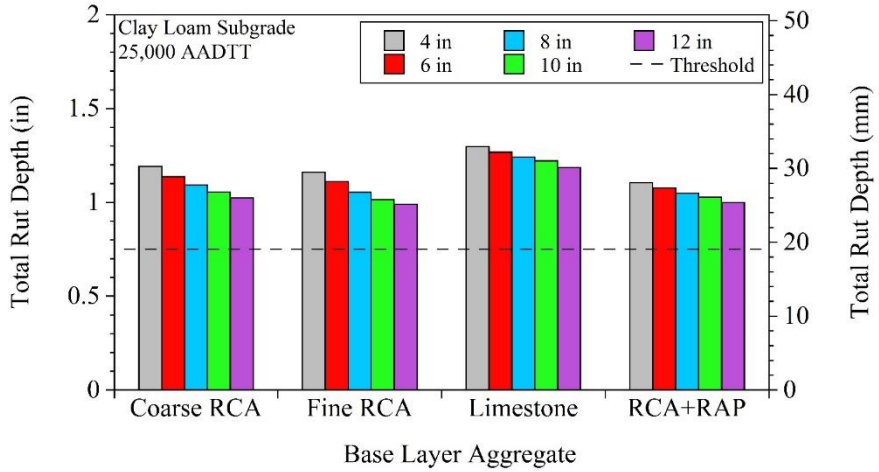

Clay Loam Subgrade
7,500 AADTT
4 in
6 in
8 in
10 in
12 in
Threshold
AC Bottom-Up Cracking
(Alligator) (% Lane Area)
Coarse RCA
Fine RCA
Limestone
RCA+RAP
Base Layer Aggregate

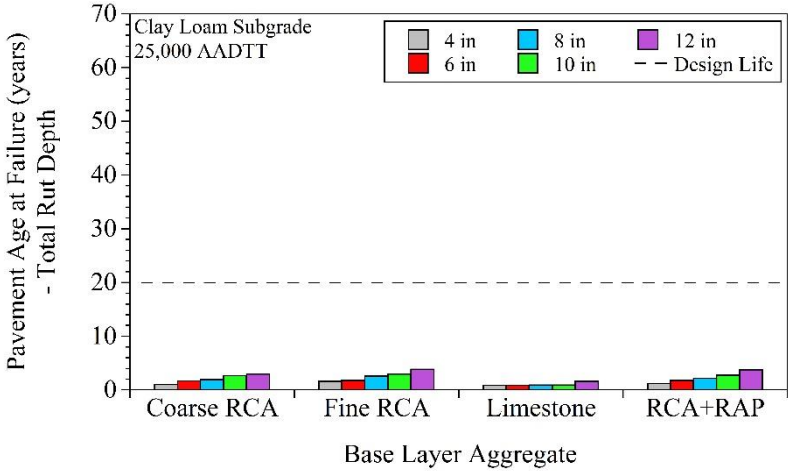

Clay Loam Subgrade
7,500 AADTT
4 in
6 in
8 in
10 in
12 in
Design Life
Pavement Age at Failure (years)
- AC Bottom-Up Cracking
(Alligator)
Coarse RCA
Fine RCA
Limestone
RCA+RAP
Base Layer Aggregate

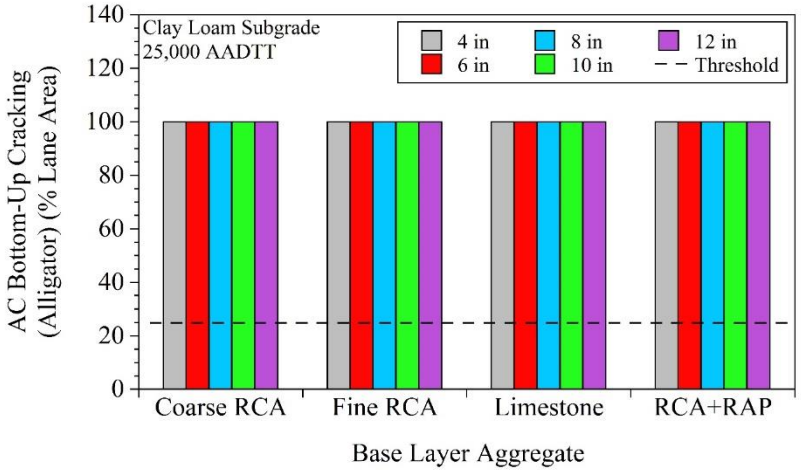
For pavements that contained clay loam subgrade – 25,000 AADTT:

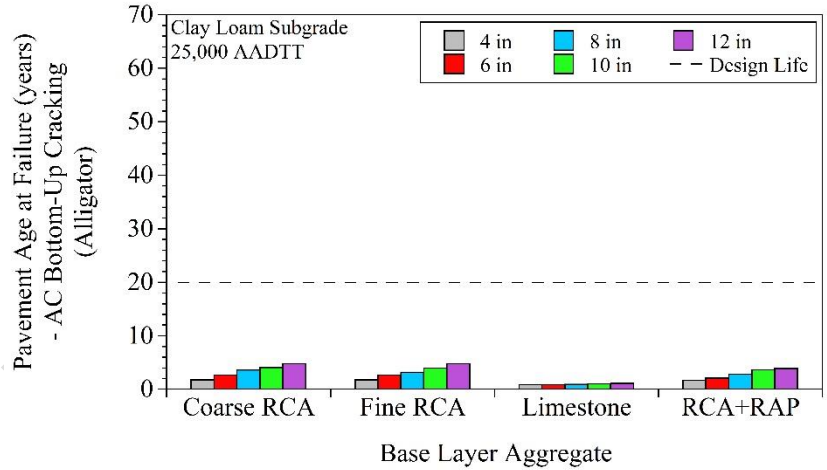








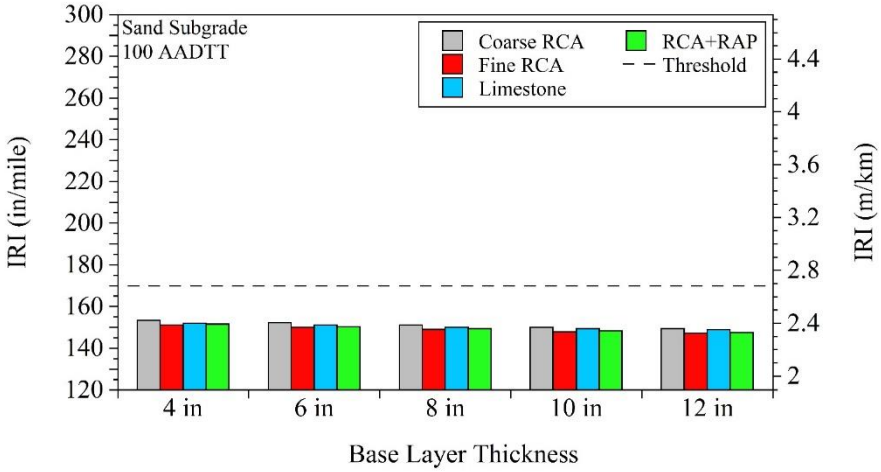

Clay Loam Subgrade
25,000 AADTT
4 in
6 in
8 in
10 in
12 in
Threshold
AC Bottom-Up Cracking
(Alligator) (% Lane Area)
0
20
40
60
80
100
120
140
Coarse RCA
Fine RCA
Limestone
RCA+RAP
Base Layer Aggregate

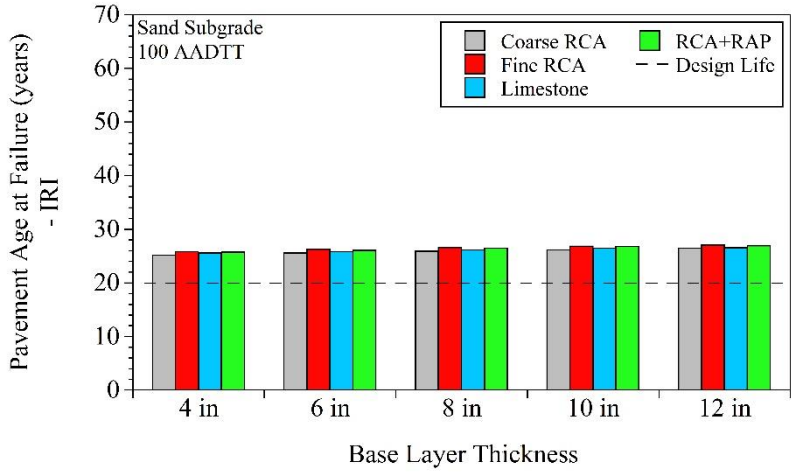

Clay Loam Subgrade
25,000 AADTT
4 in
6 in
8 in
10 in
12 in
Design Life
Pavement Age at Failure (years)
- AC Bottom-Up Cracking
(Alligator)
0
10
20
30
40
50
60
70
Coarse RCA
Fine RCA
Limestone
RCA+RAP
Base Layer Aggregate

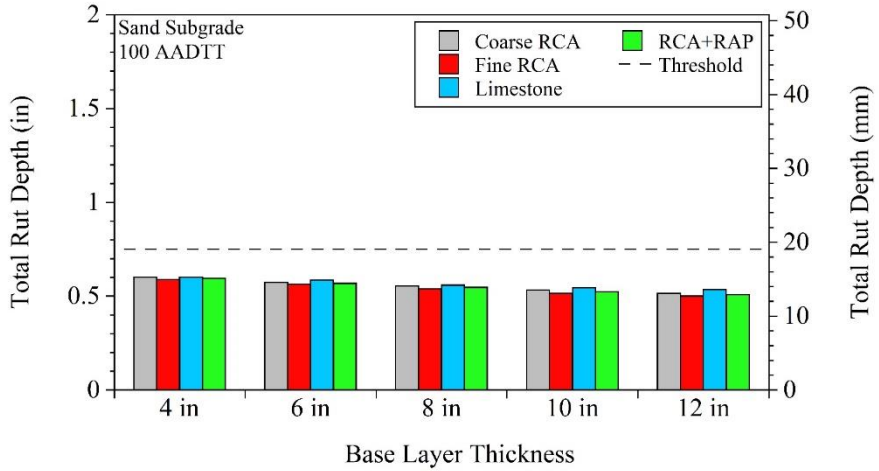
DRAFT

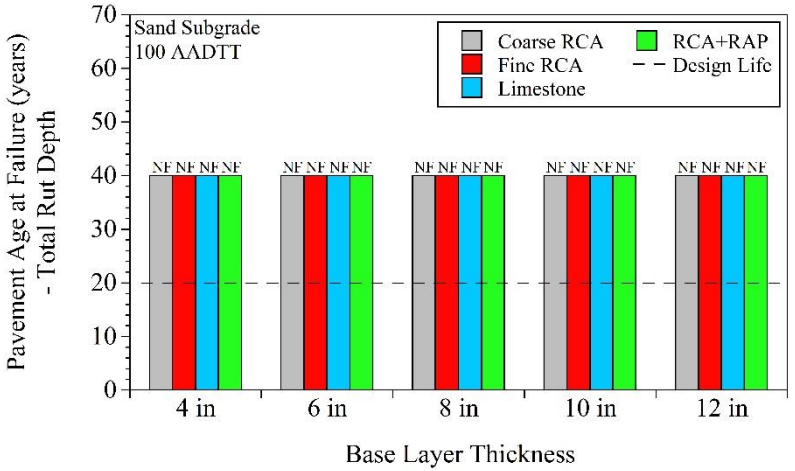
APPENDIX U. EFFECT OF BASE LAYER AGGREGATE TYPE ON PAVEMENT PERFORMANCE PREDICTIONS

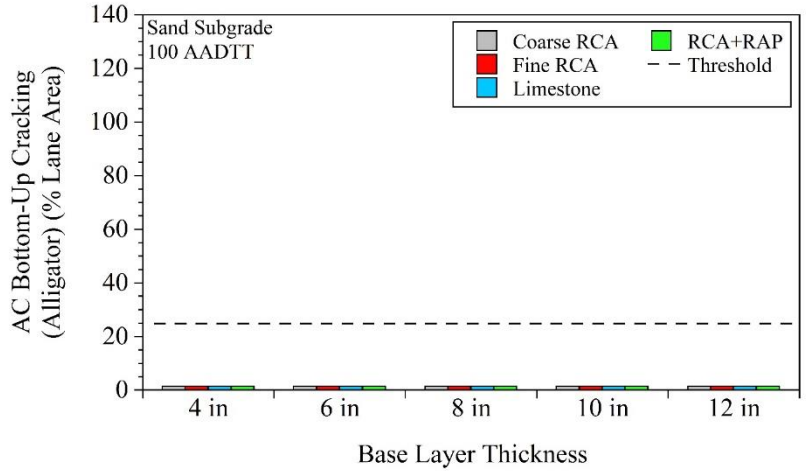
For pavements that contained sand subgrade – 100 AADTT:

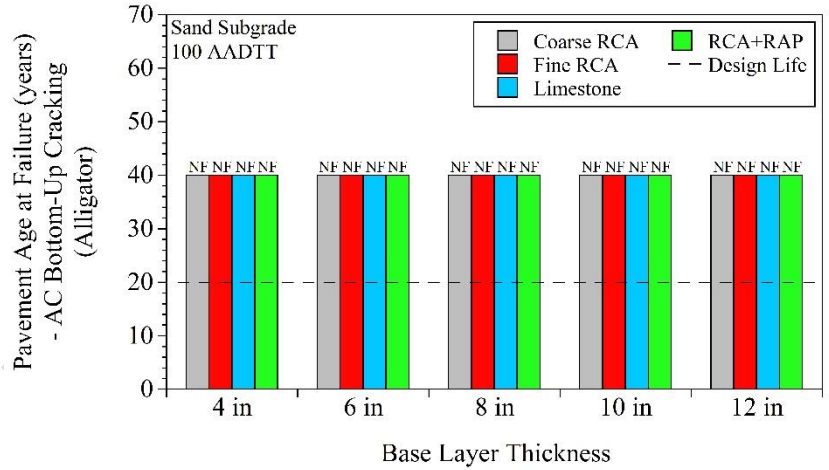


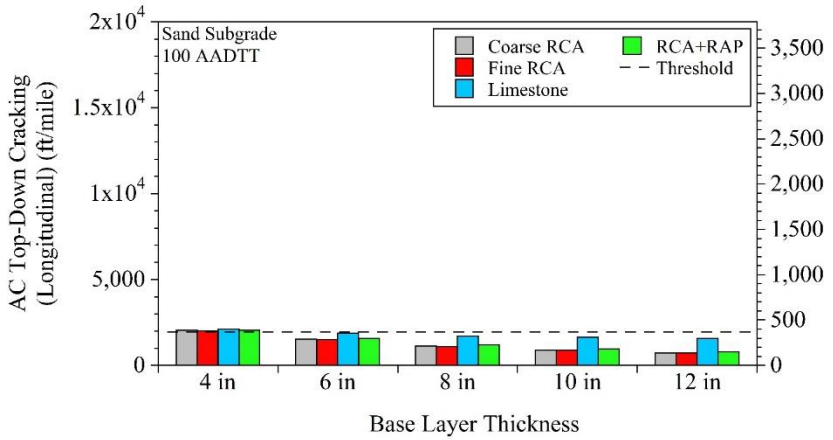


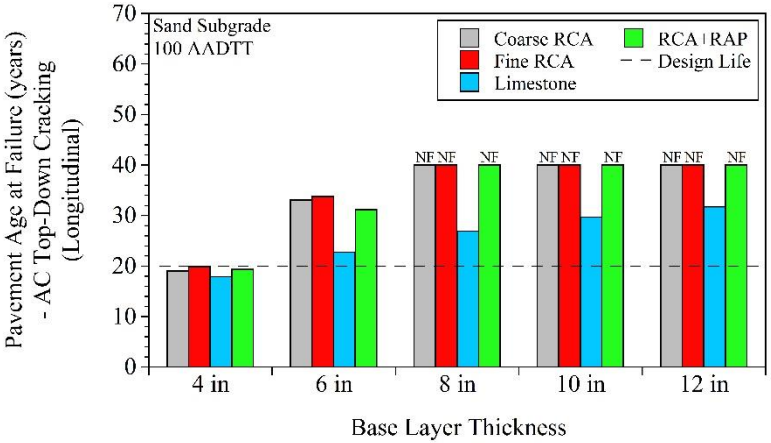




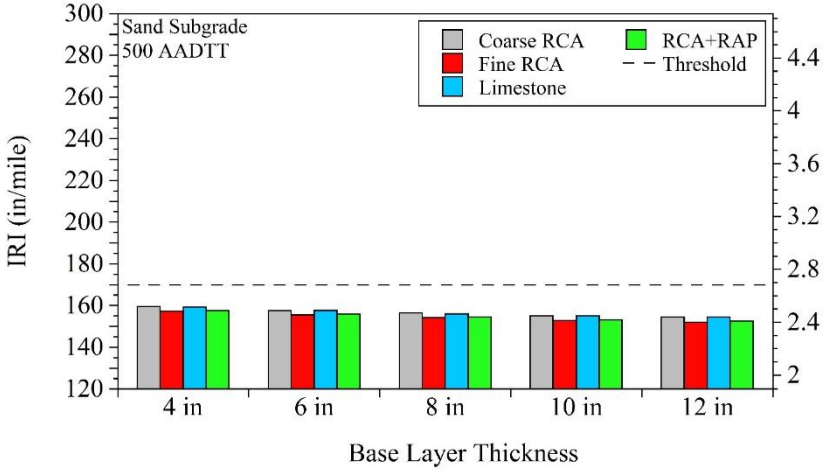

Sand Subgrade
100 AADTT
Coarse RCA
Fine RCA
Limestone
RCA+RAP
Threshold
AC Bottom-Up Cracking
(Alligator) (% Lane Area)
0
20
40
60
80
100
120
140
4 in
6 in
8 in
10 in
12 in
Base Layer Thickness

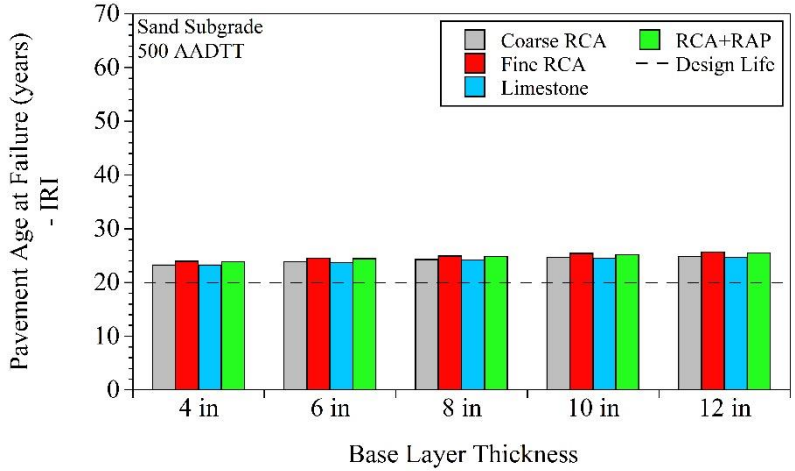

Sand Subgrade
100 AADTT
Coarse RCA
Fine RCA
Limestone
RCA+RAP
Design Life
Pavement Age at Failure (years)
- AC Bottom-Up Cracking
(Alligator)
NF NF NF NF
0
10
20
30
40
50
60
70
4 in
6 in
8 in
10 in
12 in
Base Layer Thickness

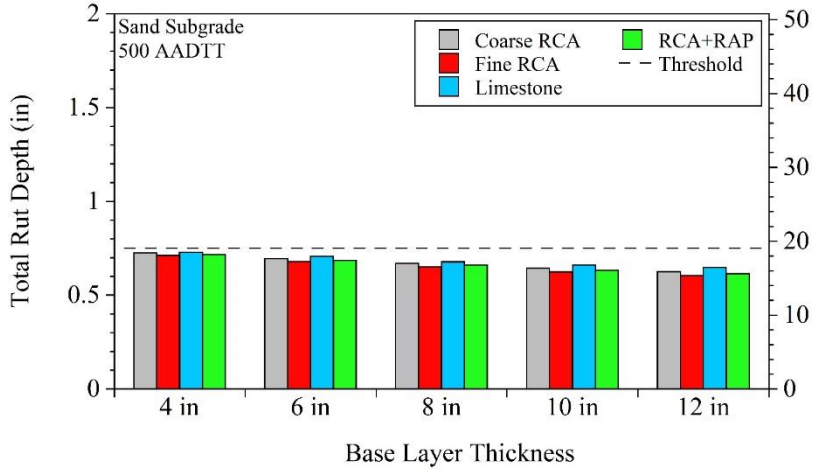

Sand Subgrade
100 AADTT
Coarse RCA
Fine RCA
Limestone
RCA+RAP
Threshold
AC Top-Down Cracking
(Longitudinal) (ft/mile)
0
5,000
1x10^4
1.5x10^4
2x10^4
0
500
1,000
1,500
2,000
2,500
3,000
3,500
AC Top-Down Cracking
(Longitudinal) (m/km)
4 in
6 in
8 in
10 in
12 in
Base Layer Thickness

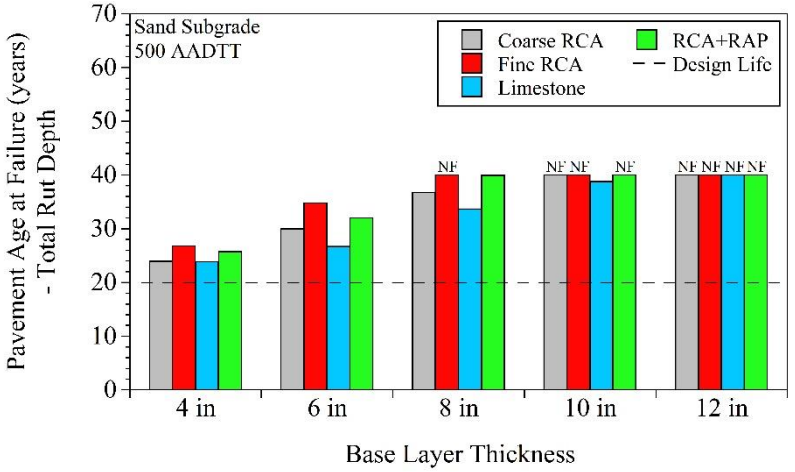

Sand Subgrade
100 AADTT
Coarse RCA
Fine RCA
Limestone
RCA+RAP
Design Life
Pavement Age at Failure (years)
- AC Top-Down Cracking
(Longitudinal)
NF NF NF
0
10
20
30
40
50
60
70
4 in
6 in
8 in
10 in
12 in
Base Layer Thickness

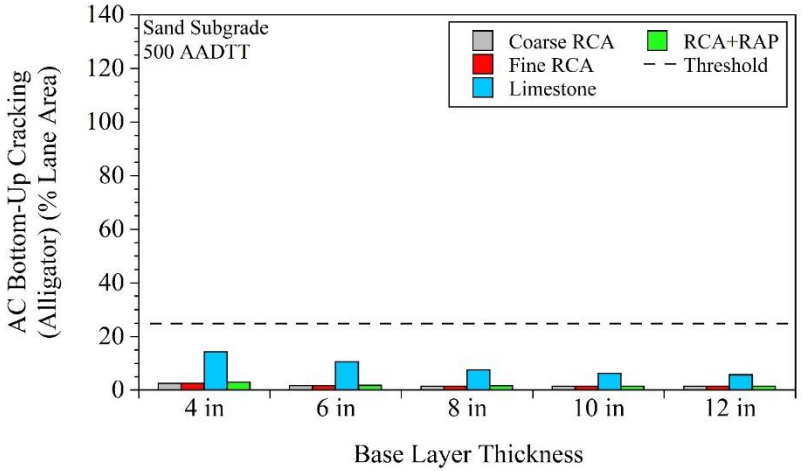
For pavements that contained sand subgrade – 500 AADTT:

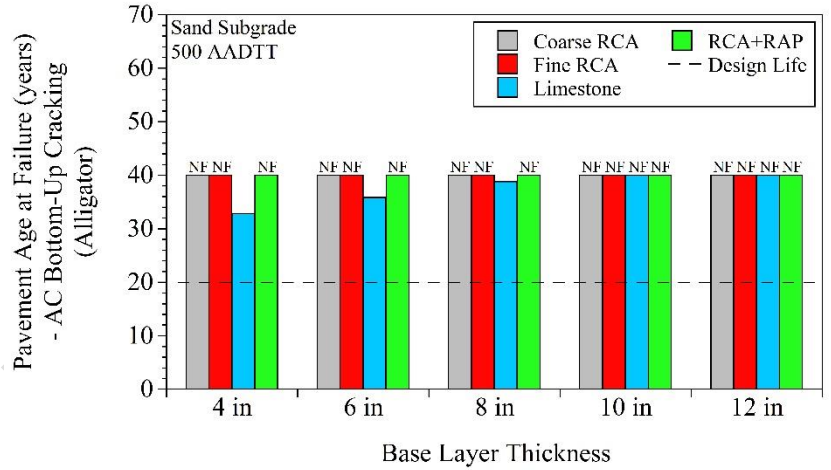


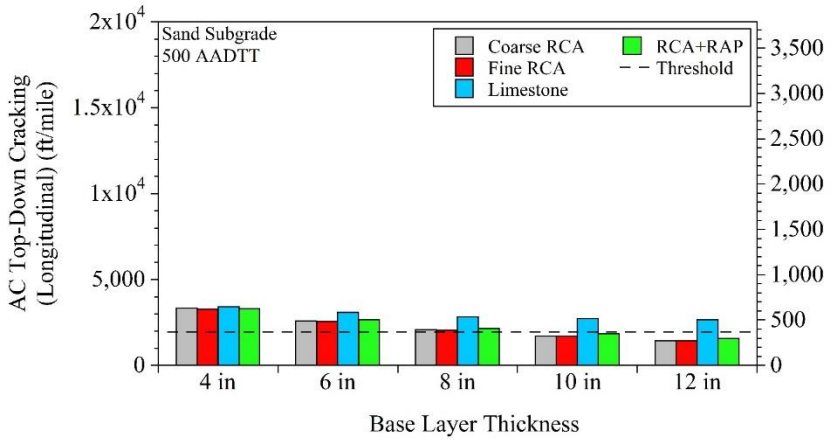


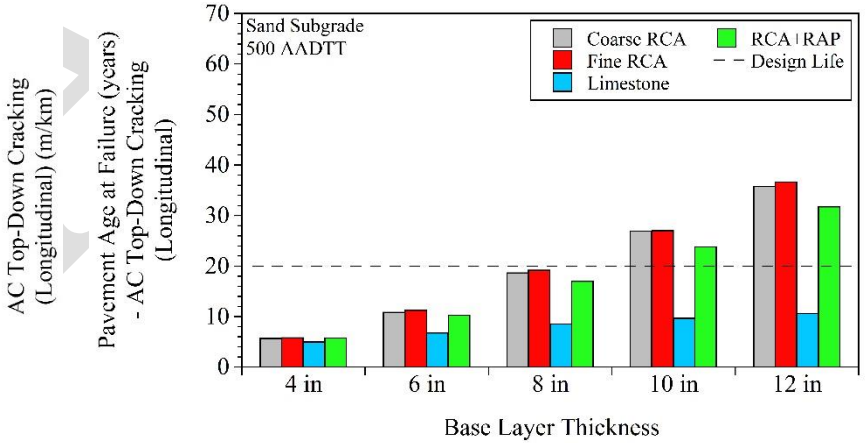




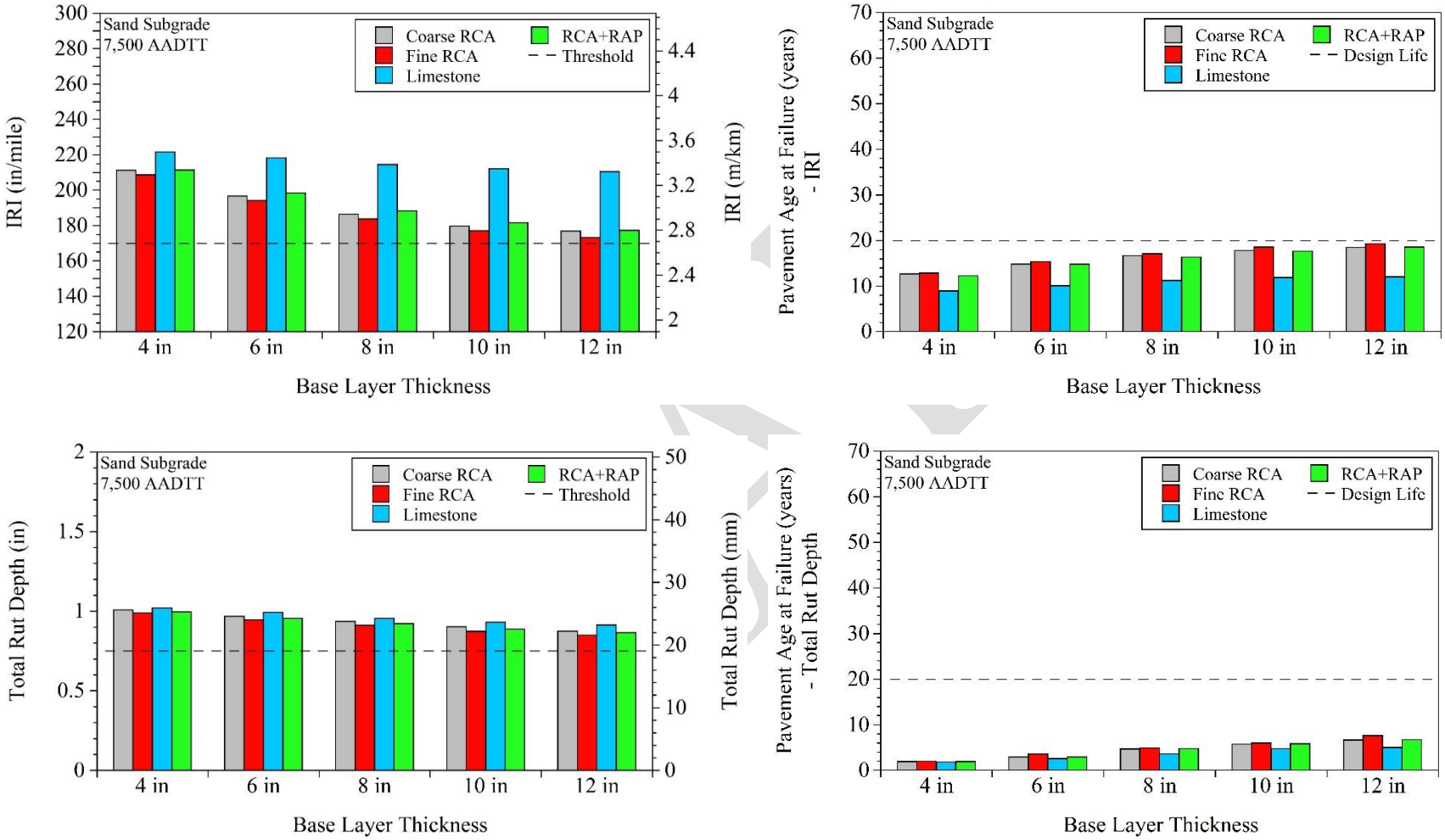

Sand Subgrade
500 AADTT
Coarse RCA
Fine RCA
Limestone
RCA+RAP
Threshold
AC Bottom-Up Cracking
(Alligator) (% Lane Area)
0
20
40
60
80
100
120
140
4 in
6 in
8 in
10 in
12 in
Base Layer Thickness

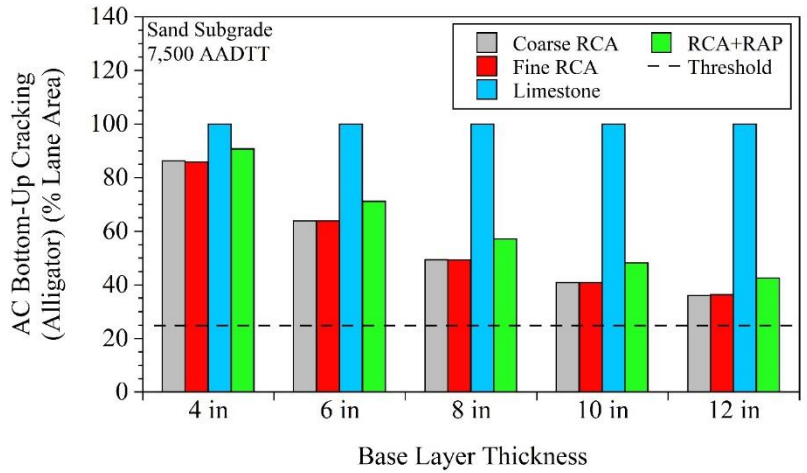

Sand Subgrade
500 AADTT
Coarse RCA
Fine RCA
Limestone
RCA+RAP
Design Life
Pavement Age at Failure (years)
- AC Bottom-Up Cracking
(Alligator)
NF NF NF
NF NF NF
NF NF NF
NF NF NF NF
NF NF NF NF
0
10
20
30
40
50
60
70
4 in
6 in
8 in
10 in
12 in
Base Layer Thickness

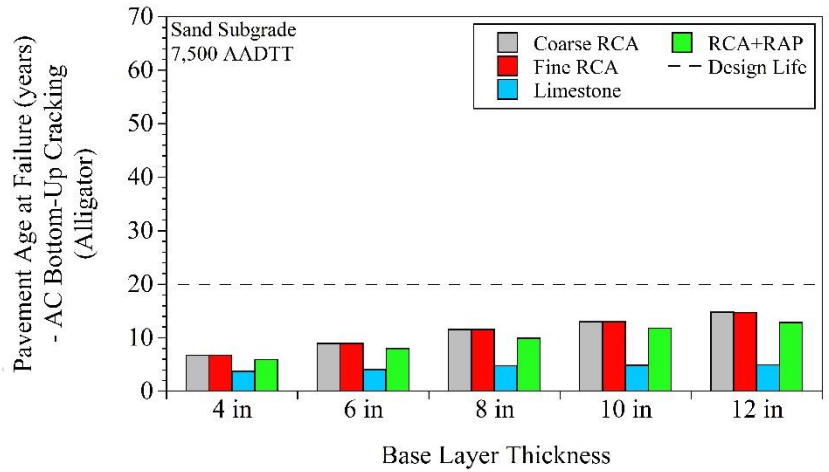

Sand Subgrade
500 AADTT
Coarse RCA
Fine RCA
Limestone
RCA+RAP
Threshold
AC Top-Down Cracking
(Longitudinal) (ft/mile)
0
5,000
1x10^4
1.5x10^4
2x10^4
0
500
1,000
1,500
2,000
2,500
3,000
3,500
AC Top-Down Cracking
(Longitudinal) (m/km)
4 in
6 in
8 in
10 in
12 in
Base Layer Thickness

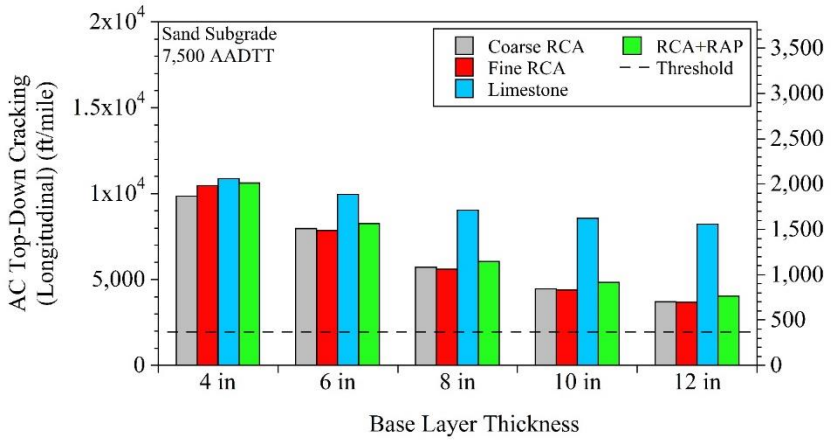

Sand Subgrade
500 AADTT
Coarse RCA
Fine RCA
Limestone
RCA+RAP
Design Life
Pavement Age at Failure (years)
- AC Top-Down Cracking
(Longitudinal)
0
10
20
30
40
50
60
70
4 in
6 in
8 in
10 in
12 in
Base Layer Thickness

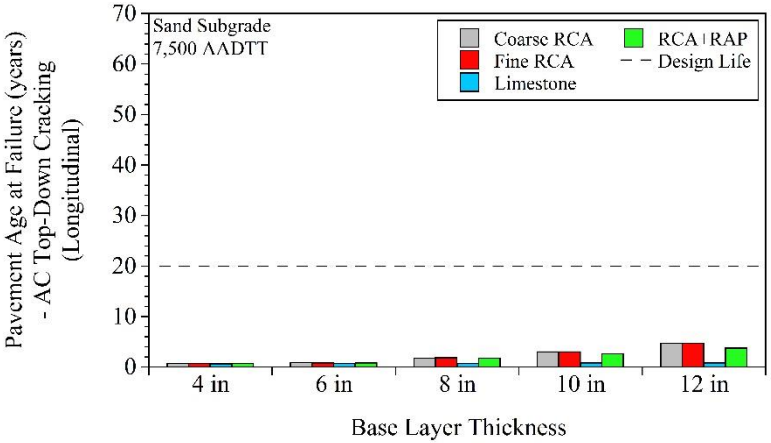
For pavements that contained sand subgrade – 7,500 AADTT:



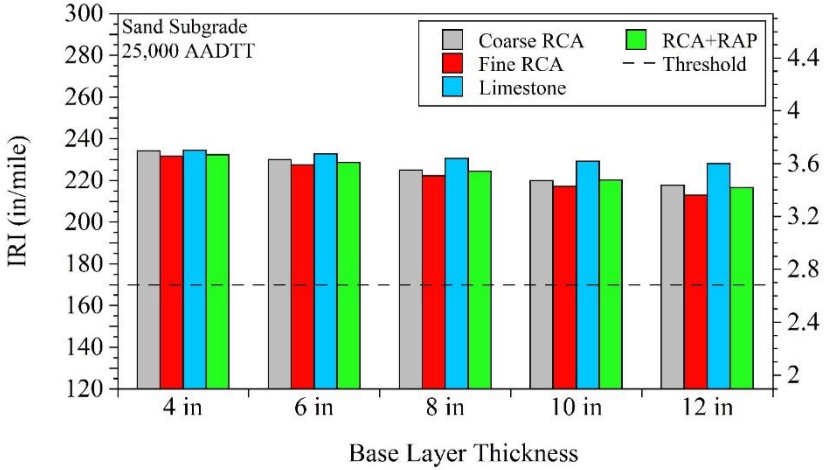

Sand Subgrade
7,500 AADTT
Coarse RCA
Fine RCA
Limestone
RCA+RAP
Threshold
AC Bottom-Up Cracking
(Alligator) (% Lane Area)
Base Layer Thickness
4 in
6 in
8 in
10 in
12 in

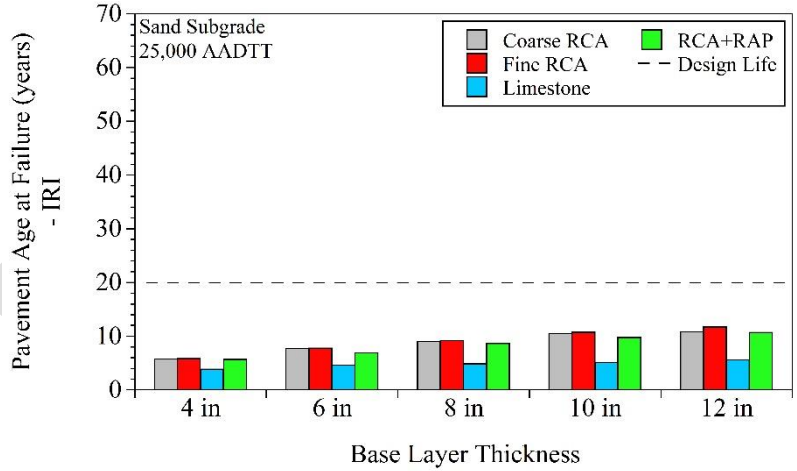

Sand Subgrade
7,500 AADTT
Coarse RCA
Fine RCA
Limestone
RCA+RAP
Design Life
Pavement Age at Failure (years)
- AC Bottom-Up Cracking
(Alligator)
Base Layer Thickness

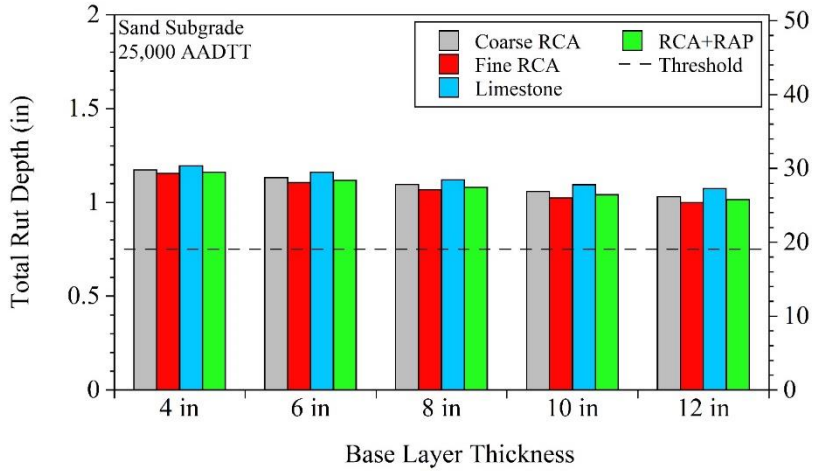

Sand Subgrade
7,500 AADTT
Coarse RCA
Fine RCA
Limestone
RCA+RAP
Threshold
AC Top-Down Cracking
(Longitudinal) (ft/mile)
AC Top-Down Cracking
(Longitudinal) (m/km)
Base Layer Thickness

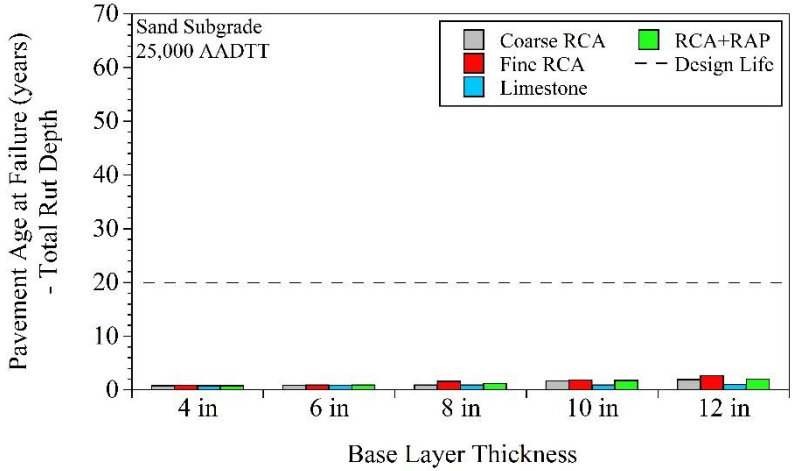

Sand Subgrade
7,500 AADTT
Coarse RCA
Fine RCA
Limestone
RCA+RAP
Design Life
Pavement Age at Failure (years)
- AC Top-Down Cracking
(Longitudinal)
Base Layer Thickness

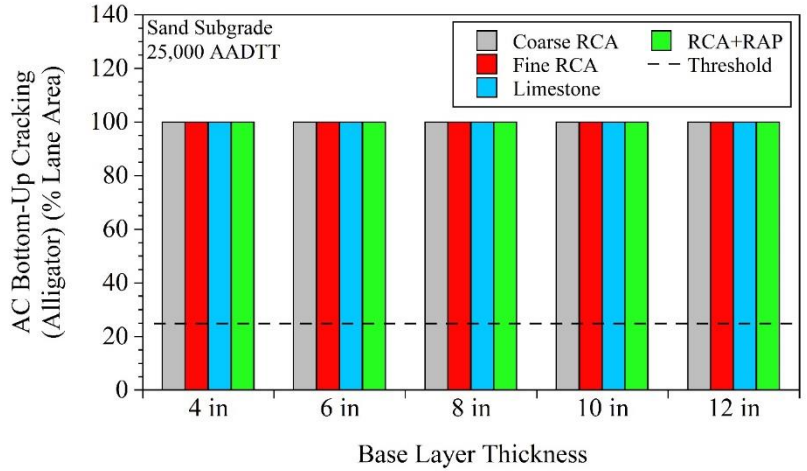
For pavements that contained sand subgrade – 25,000 AADTT:

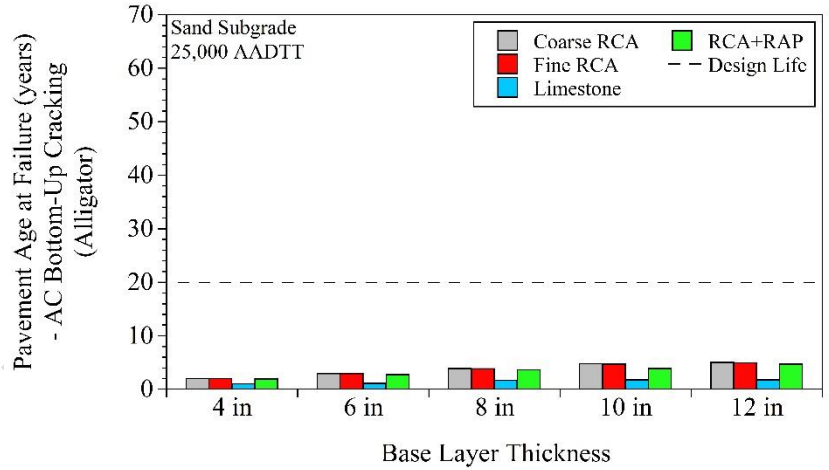


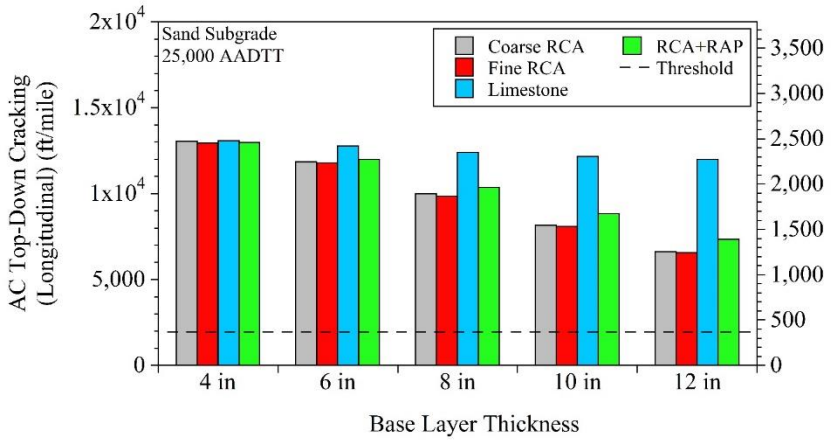


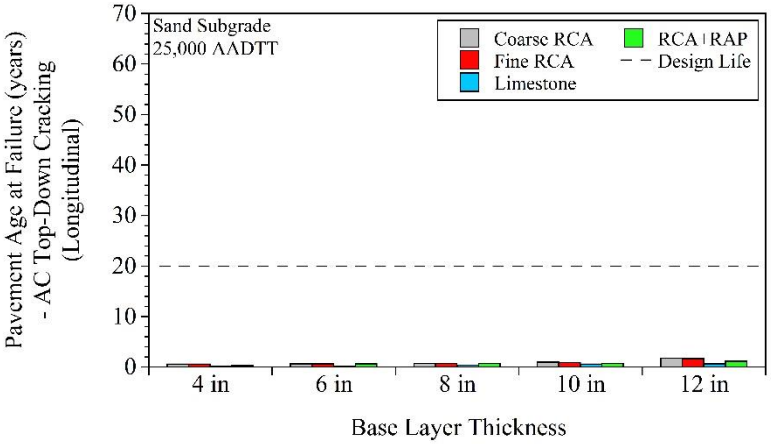




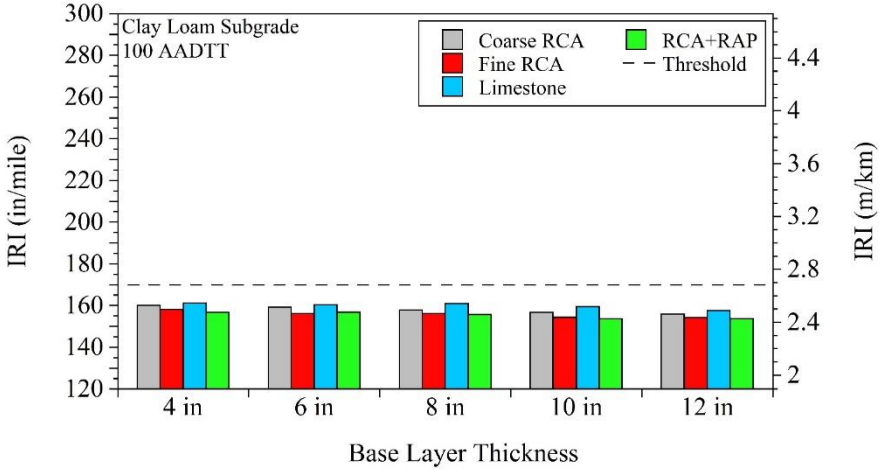

Sand Subgrade
25,000 AADTT
Coarse RCA
Fine RCA
Limestone
RCA+RAP
Threshold
AC Bottom-Up Cracking
(Alligator) (% Lane Area)
Base Layer Thickness
4 in
6 in
8 in
10 in
12 in

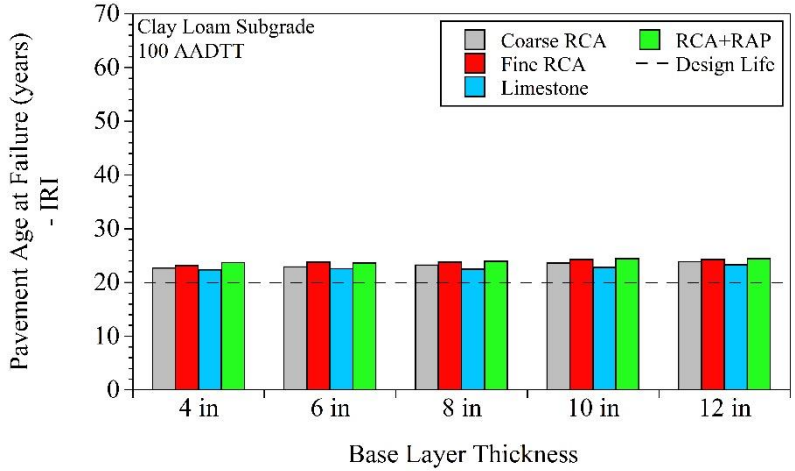

Sand Subgrade
25,000 AADTT
Coarse RCA
Fine RCA
Limestone
RCA+RAP
Design Life
Pavement Age at Failure (years)
- AC Bottom-Up Cracking
(Alligator)
Base Layer Thickness

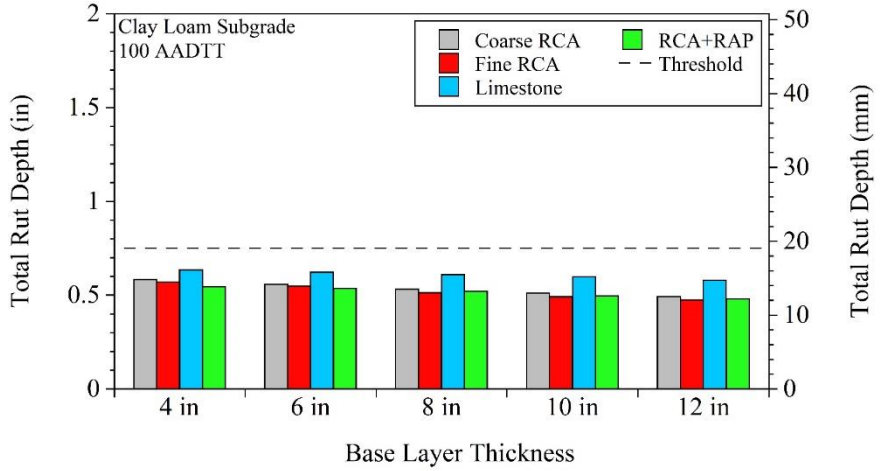

Sand Subgrade
25,000 AADTT
Coarse RCA
Fine RCA
Limestone
RCA+RAP
Threshold
AC Top-Down Cracking
(Longitudinal) (ft/mile)
AC Top-Down Cracking
(Longitudinal) (m/km)
Base Layer Thickness

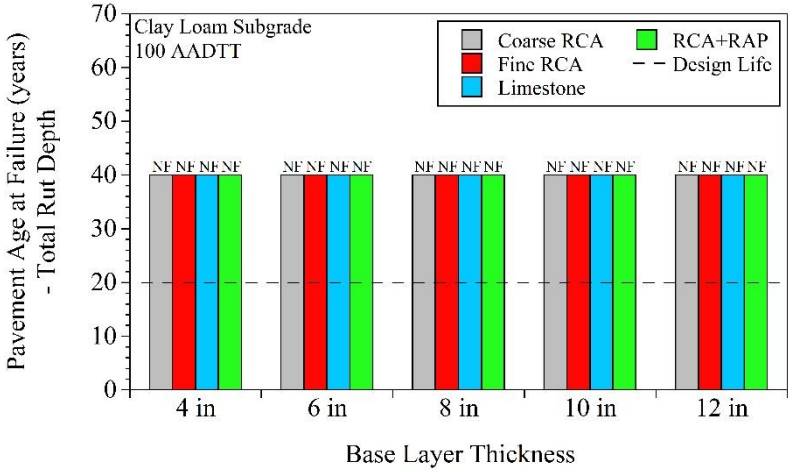

Sand Subgrade
25,000 AADTT
Coarse RCA
Fine RCA
Limestone
RCA+RAP
Design Life
Pavement Age at Failure (years)
- AC Top-Down Cracking
(Longitudinal)
Base Layer Thickness

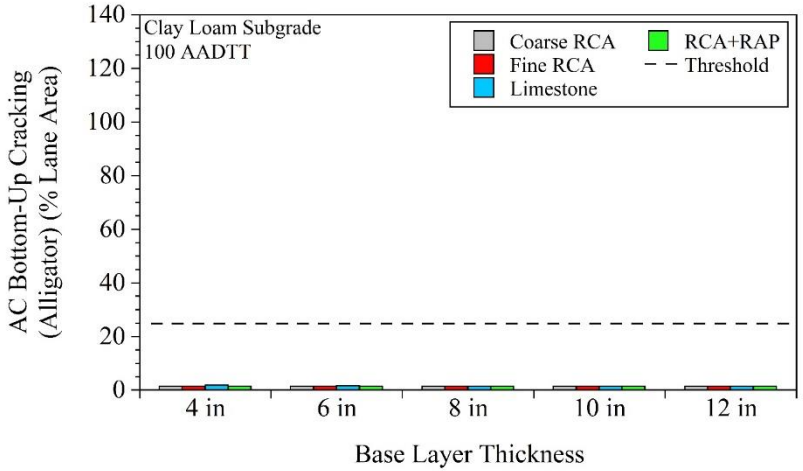
For pavements that contained clay loam subgrade – 100 AADTT:

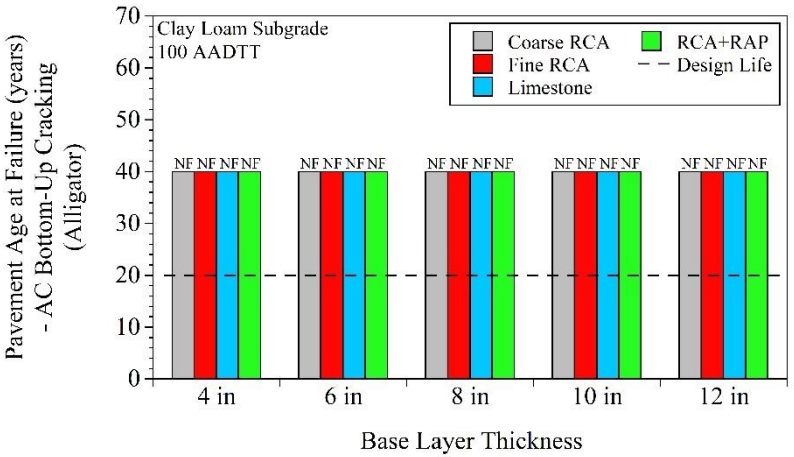




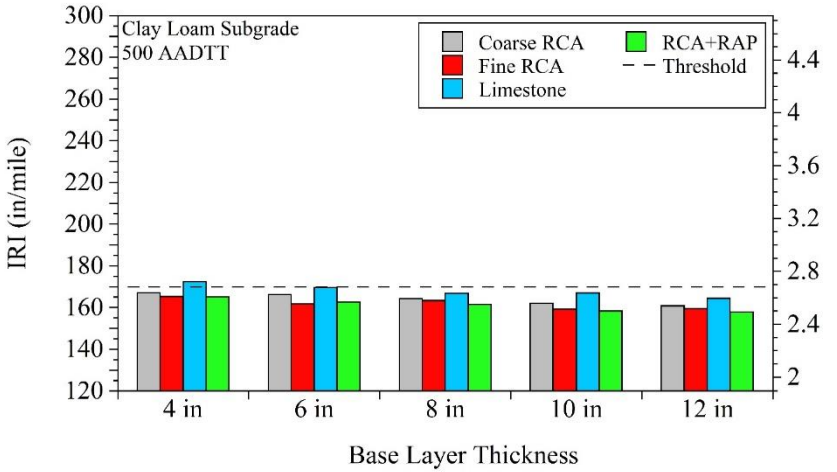


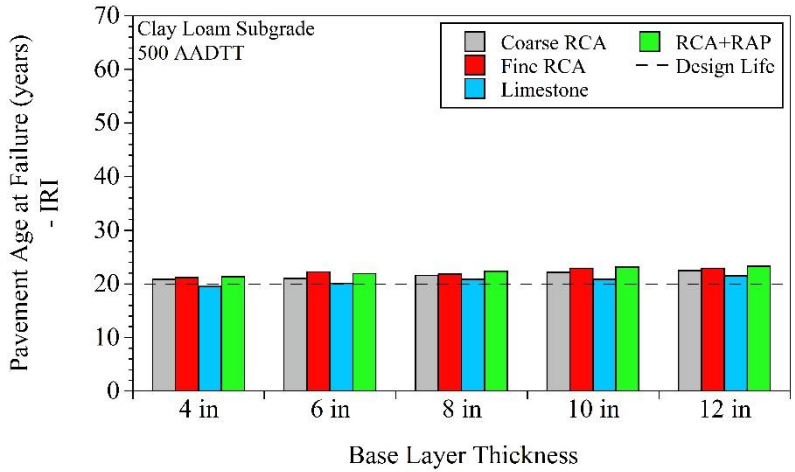


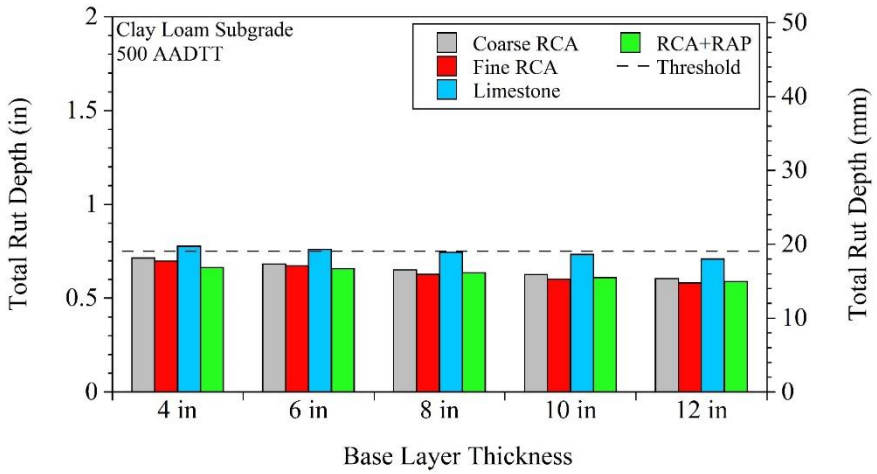


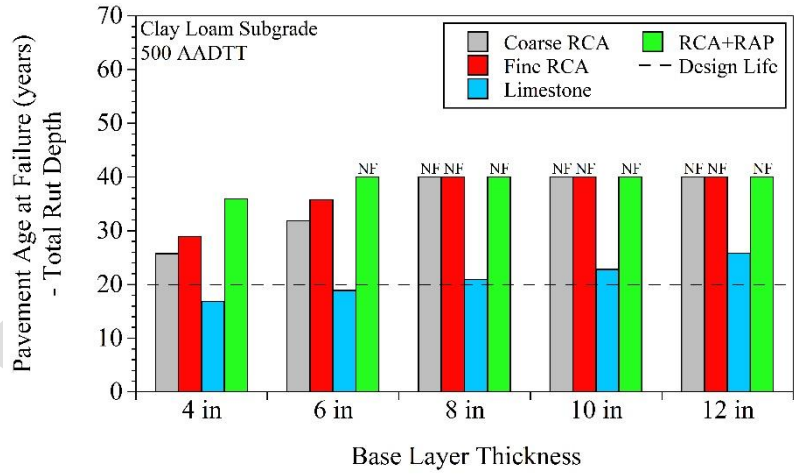


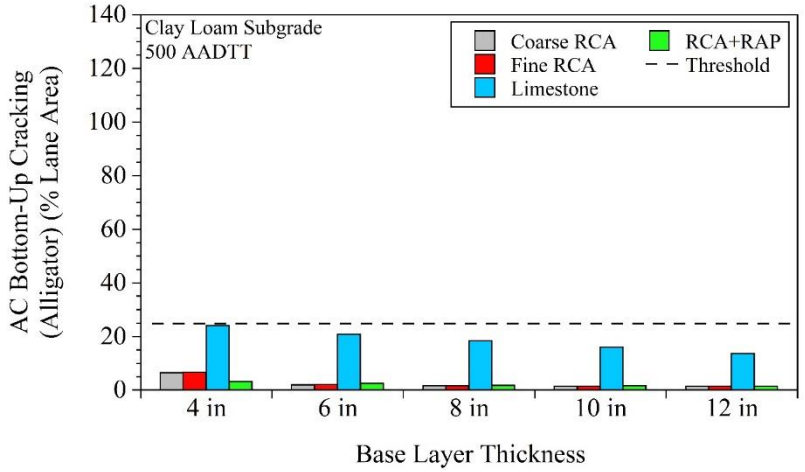
For pavements that contained clay loam subgrade – 500 AADTT:

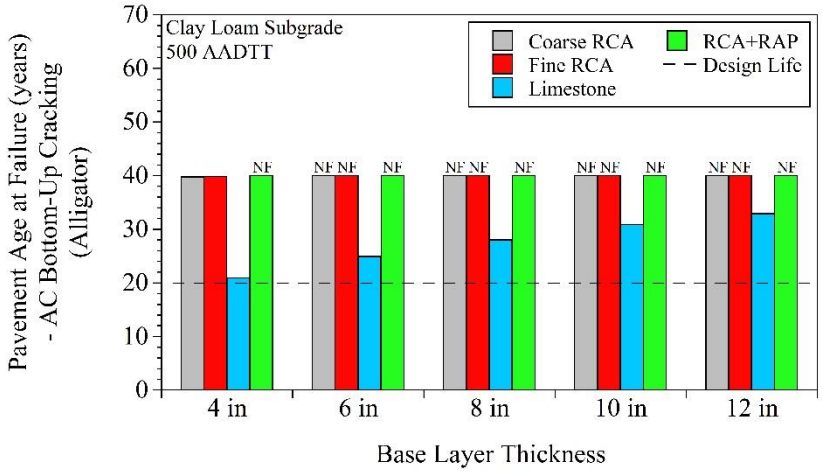




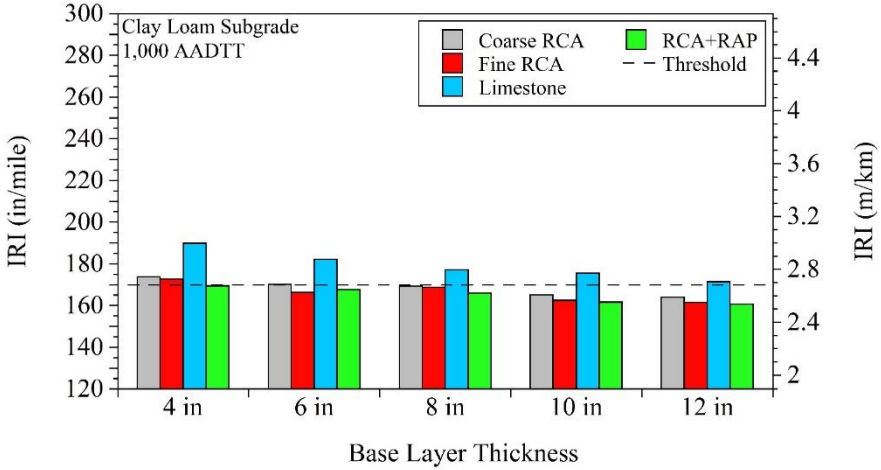

Clay Loam Subgrade
500 AADTT
Coarse RCA
Fine RCA
Limestone
RCA+RAP
Threshold
Total Rut Depth (in)
Total Rut Depth (mm)
Base Layer Thickness
4 in
6 in
8 in
10 in
12 in

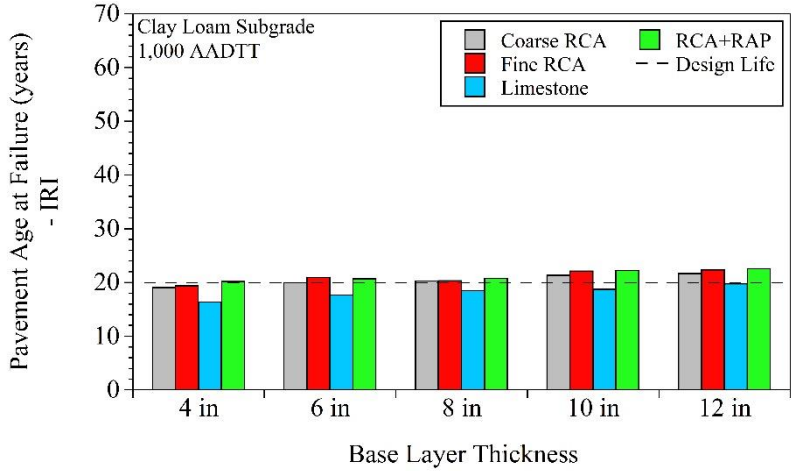

Clay Loam Subgrade
500 AADTT
Coarse RCA
Fine RCA
Limestone
RCA+RAP
Design Life
Pavement Age at Failure (years)
- Total Rut Depth
NF
Base Layer Thickness
4 in
6 in
8 in
10 in
12 in

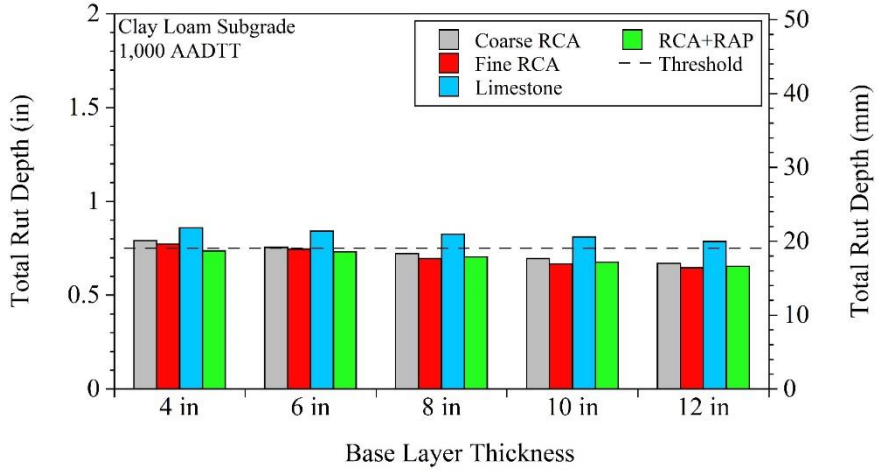

Clay Loam Subgrade
500 AADTT
Coarse RCA
Fine RCA
Limestone
RCA+RAP
Threshold
AC Bottom-Up Cracking
(Alligator) (% Lane Area)
Base Layer Thickness
4 in
6 in
8 in
10 in
12 in

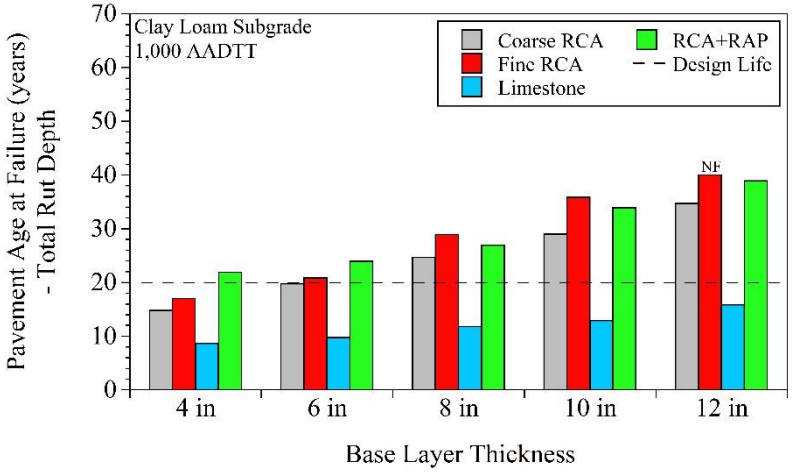

Clay Loam Subgrade
500 AADTT
Coarse RCA
Fine RCA
Limestone
RCA+RAP
Design Life
Pavement Age at Failure (years)
- AC Bottom-Up Cracking
(Alligator)
NF
Base Layer Thickness
4 in
6 in
8 in
10 in
12 in

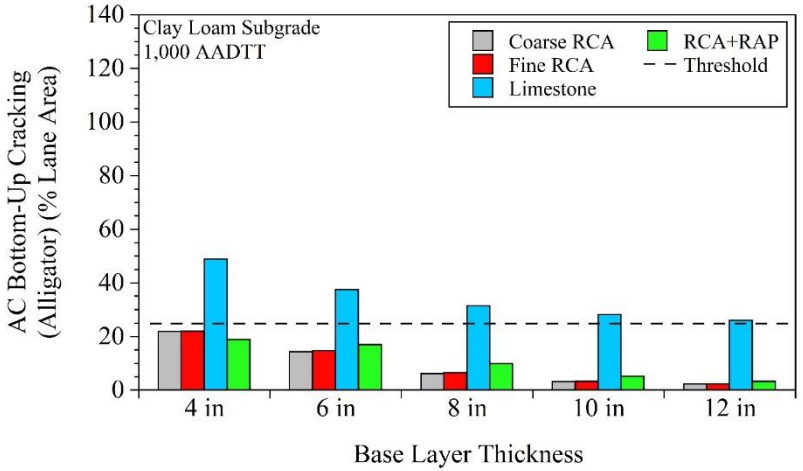
For pavements that contained clay loam subgrade – 1,000 AADTT:

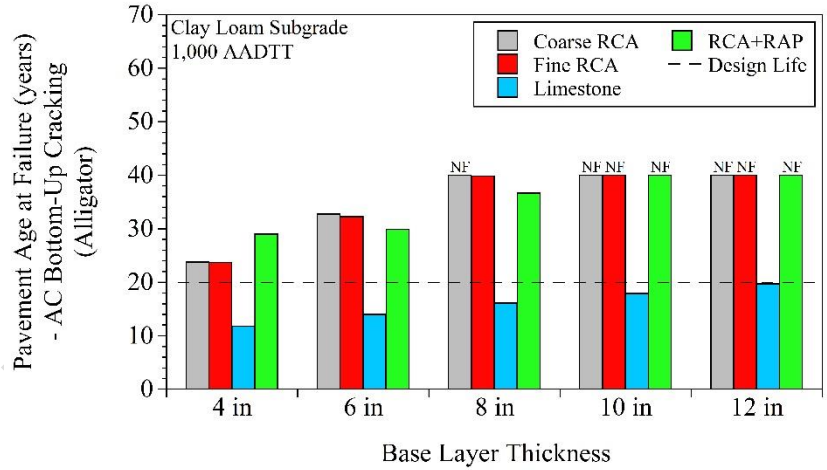




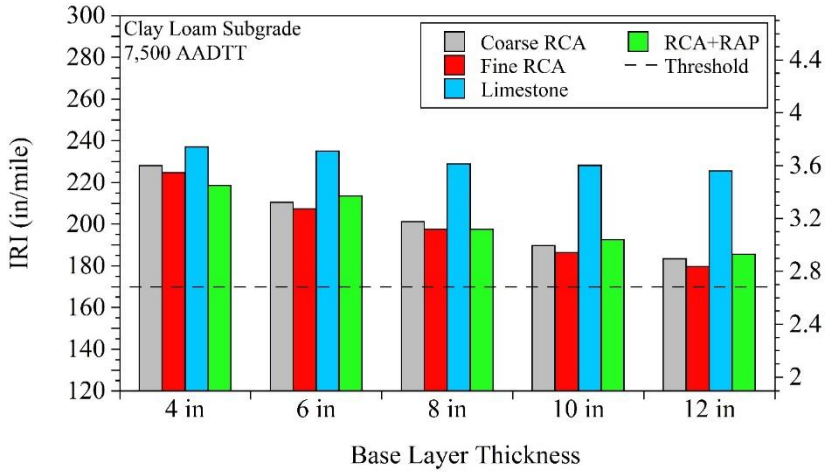


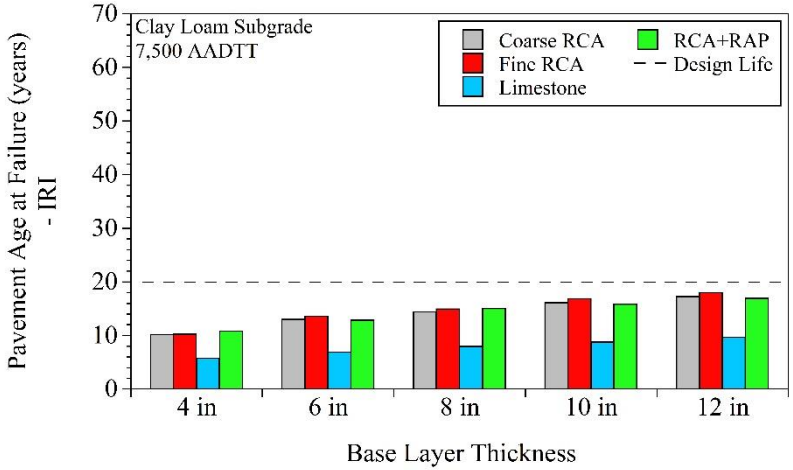


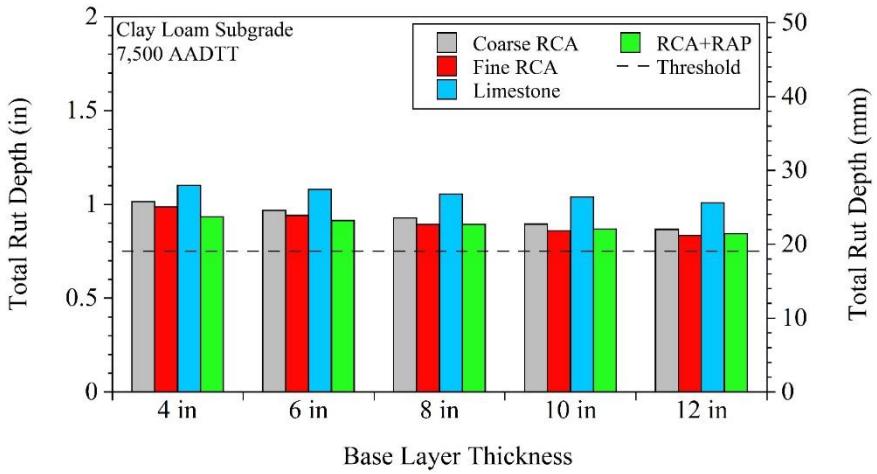


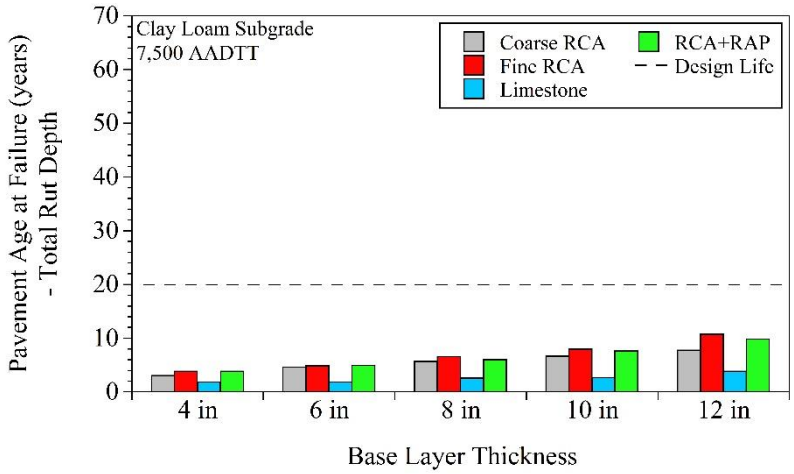


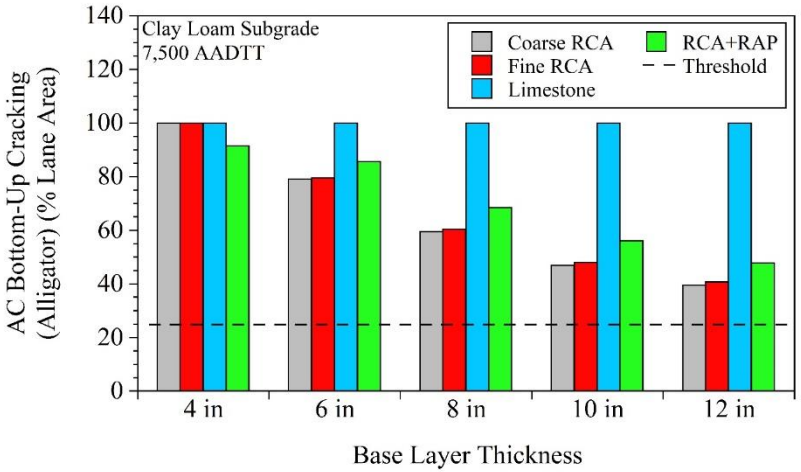
For pavements that contained clay loam subgrade – 7,500 AADTT:

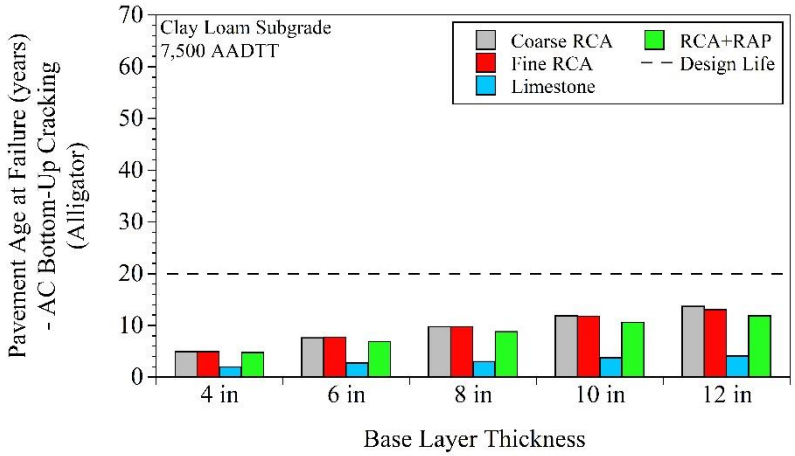




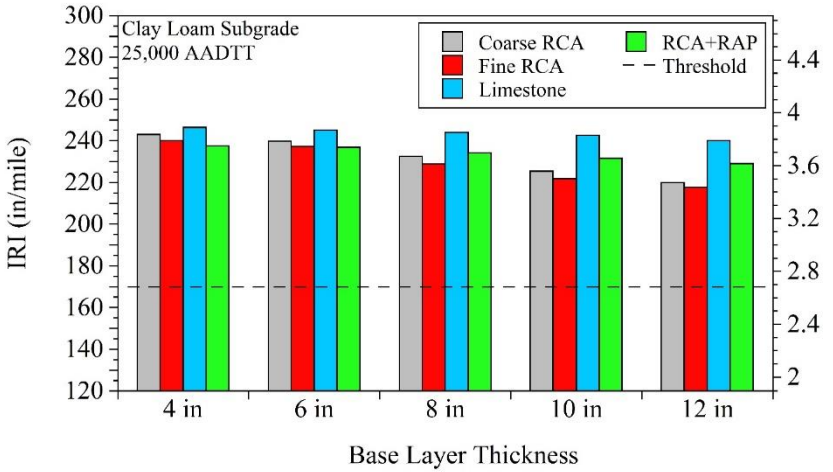

Clay Loam Subgrade
7,500 AADTT
Coarse RCA
Fine RCA
Limestone
RCA+RAP
Threshold
Total Rut Depth (in)
Total Rut Depth (mm)
0
0.5
1
1.5
2
0
10
20
30
40
50
4 in
6 in
8 in
10 in
12 in
Base Layer Thickness

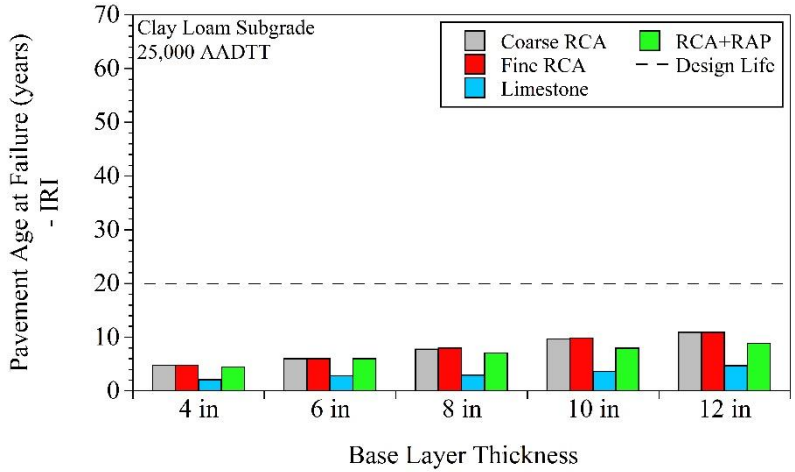

Clay Loam Subgrade
7,500 AADTT
Coarse RCA
Fine RCA
Limestone
RCA+RAP
Design Life
Pavement Age at Failure (years)
- Total Rut Depth
0
10
20
30
40
50
60
70
4 in
6 in
8 in
10 in
12 in
Base Layer Thickness

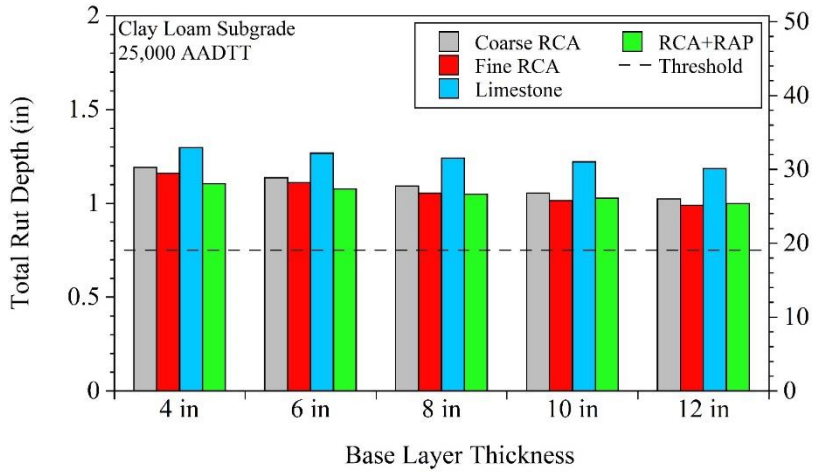

Clay Loam Subgrade
7,500 AADTT
Coarse RCA
Fine RCA
Limestone
RCA+RAP
Threshold
AC Bottom-Up Cracking
(Alligator) (% Lane Area)
0
20
40
60
80
100
120
140
4 in
6 in
8 in
10 in
12 in
Base Layer Thickness

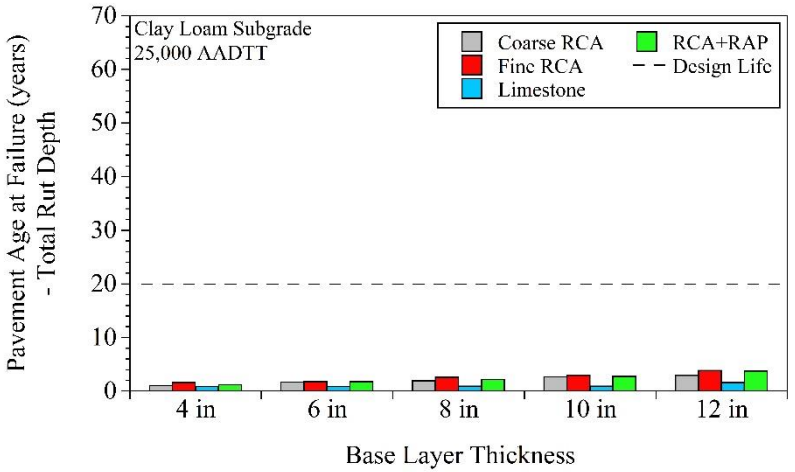

Clay Loam Subgrade
7,500 AADTT
Coarse RCA
Fine RCA
Limestone
RCA+RAP
Design Life
Pavement Age at Failure (years)
- AC Bottom-Up Cracking
(Alligator)
0
10
20
30
40
50
60
70
4 in
6 in
8 in
10 in
12 in
Base Layer Thickness

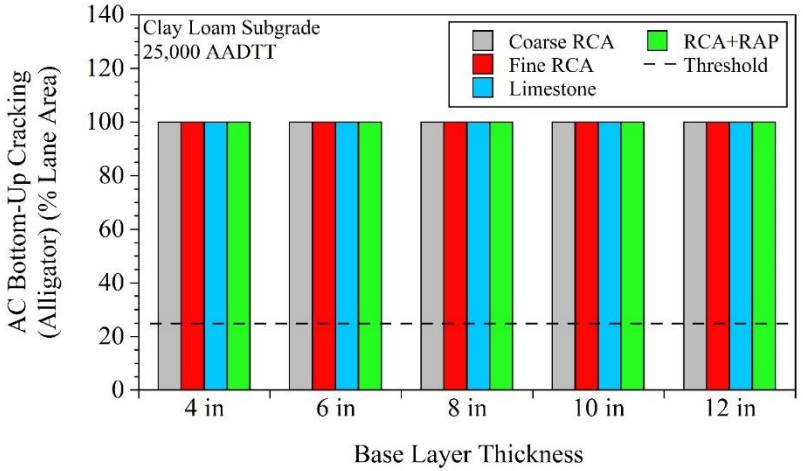
For pavements that contained clay loam subgrade – 25,000 AADTT:

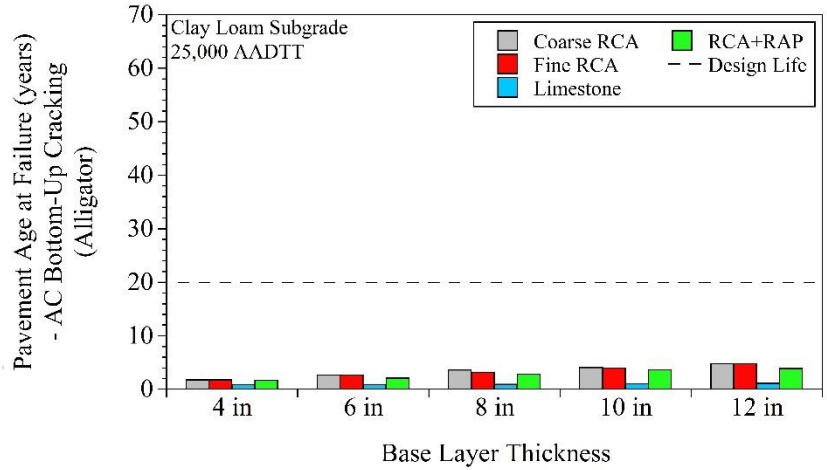








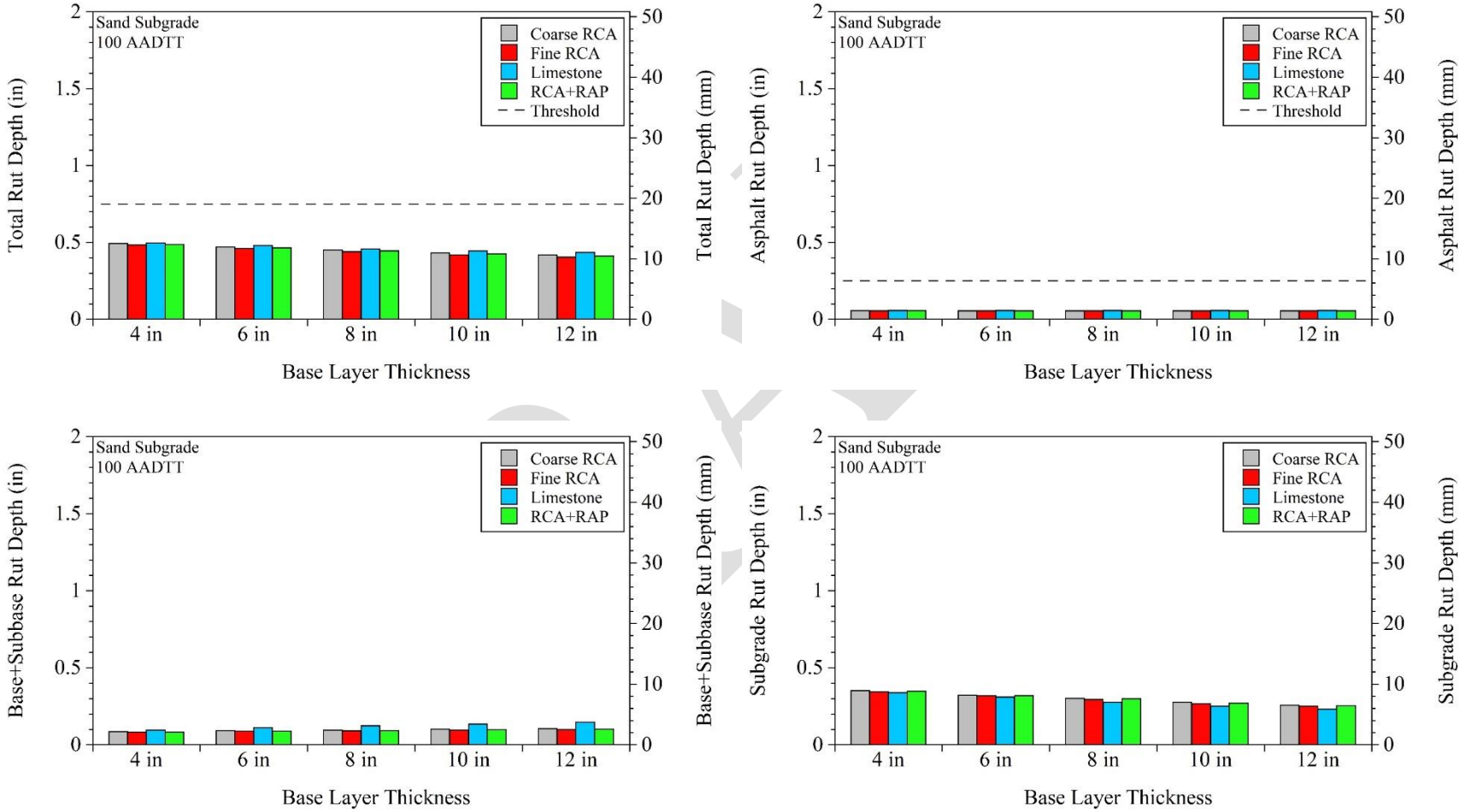

Clay Loam Subgrade
25,000 AADTT
Coarse RCA
Fine RCA
Limestone
RCA+RAP
Threshold
AC Bottom-Up Cracking
(Alligator) (% Lane Area)
0
20
40
60
80
100
120
140
4 in
6 in
8 in
10 in
12 in
Base Layer Thickness


Clay Loam Subgrade
25,000 AADTT
Coarse RCA
Fine RCA
Limestone
RCA+RAP
Design Life
Pavement Age at Failure (years)
- AC Bottom-Up Cracking
(Alligator)
0
10
20
30
40
50
60
70
4 in
6 in
8 in
10 in
12 in
Base Layer Thickness

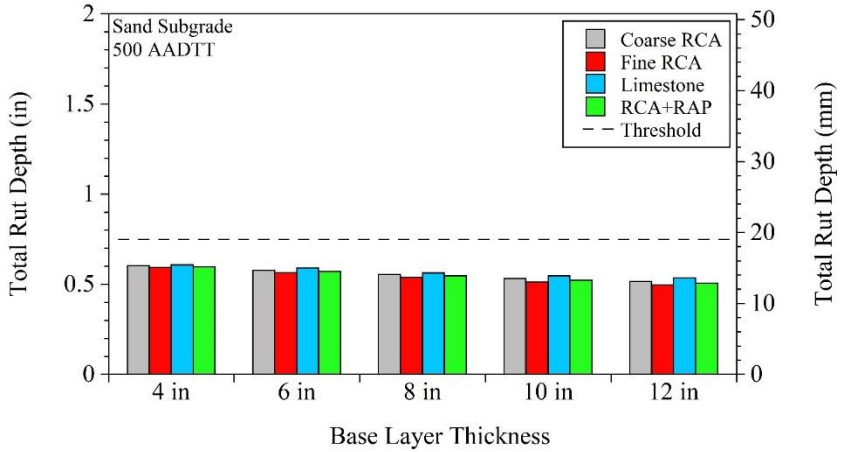
DRAFT

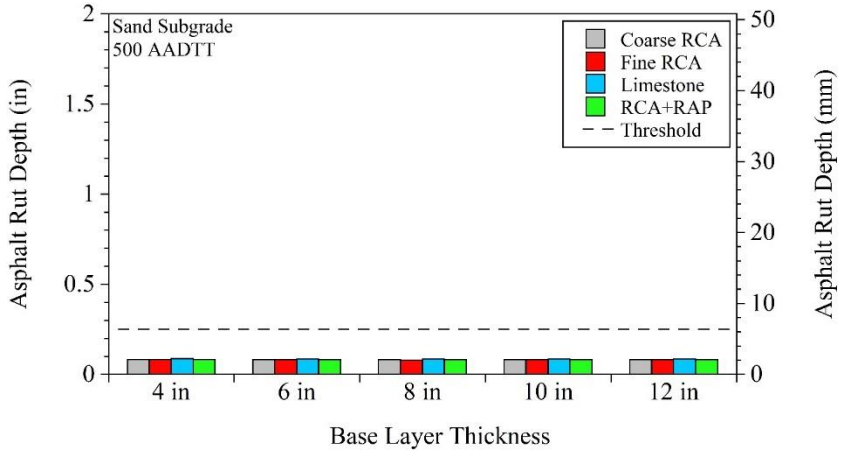
APPENDIX V. TOTAL, ASPHALT, BASE+SUBBASE, AND SUBGRADE LAYER RUTTING AT 50% RELIABILITY FOR RECYCLED AGGREGATE BASE (RAB) GROUP

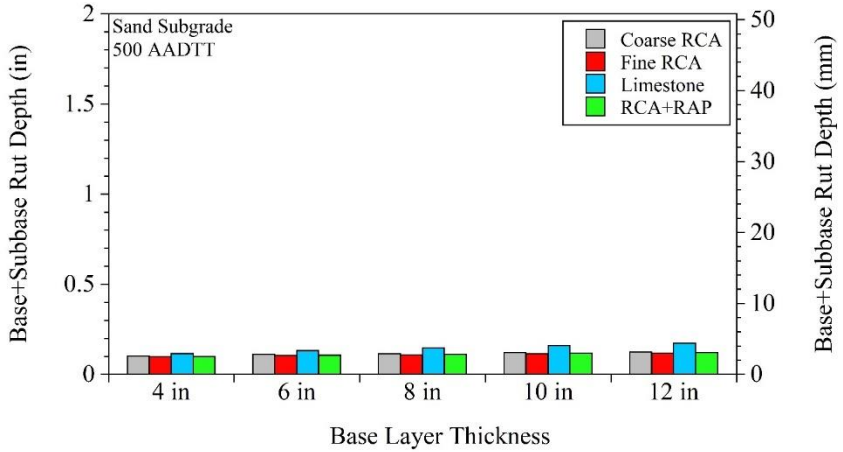
For pavements that contained sand subgrade – 100 AADTT:

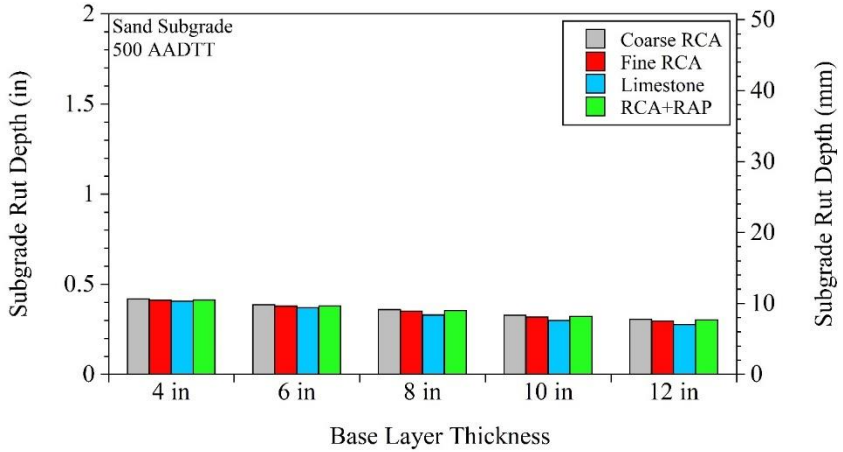


For pavements that contained sand subgrade – 500 AADTT:

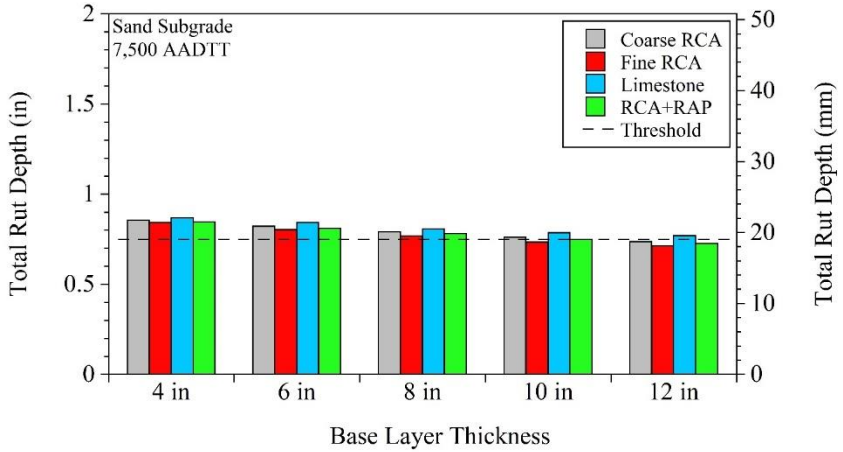


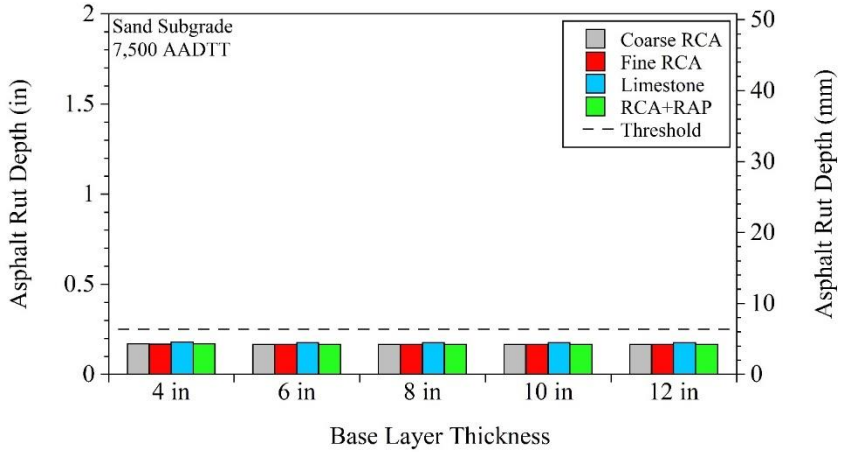


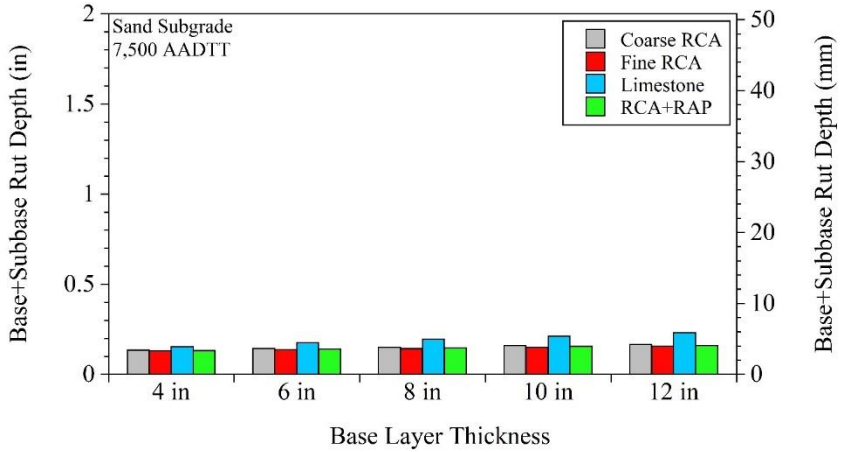


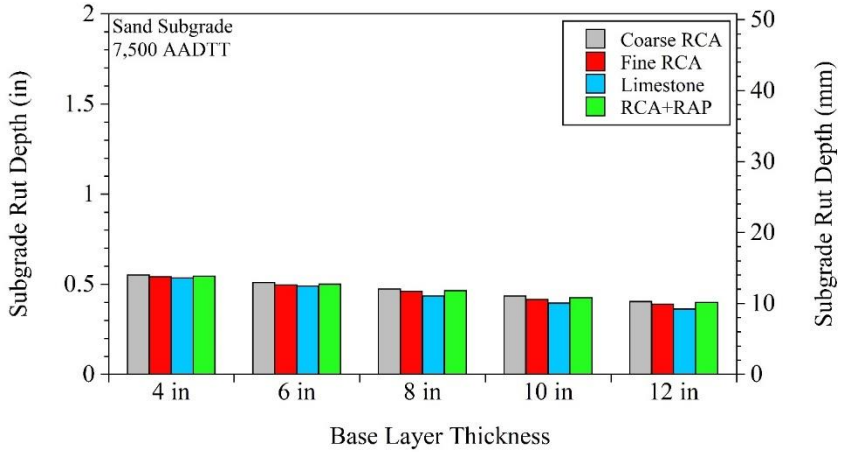


For pavements that contained sand subgrade – 7,500 AADTT:

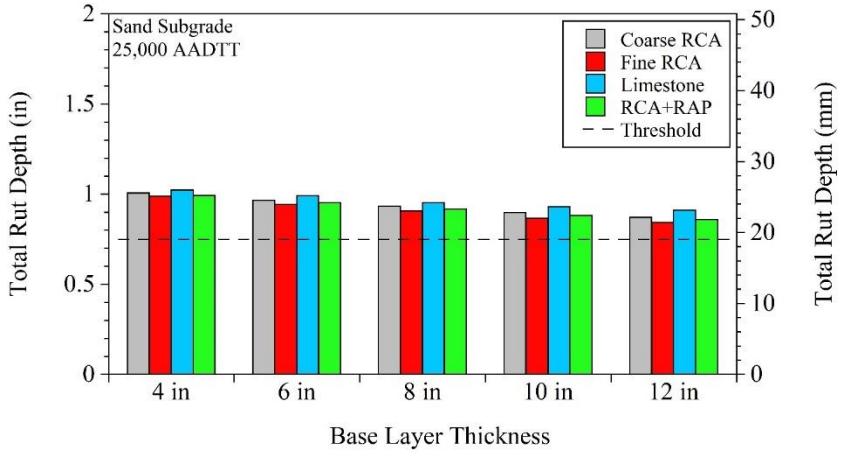


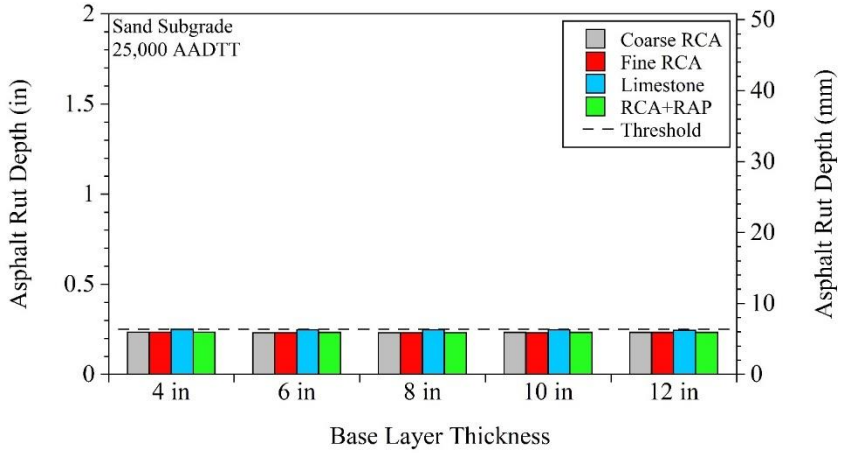


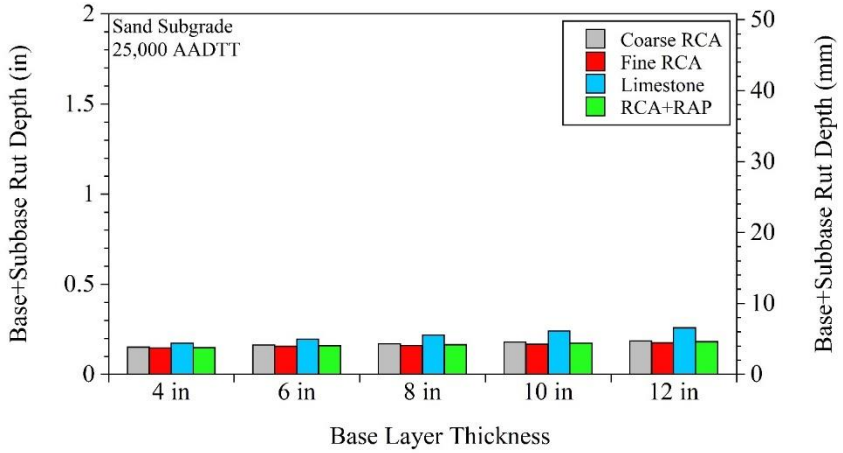


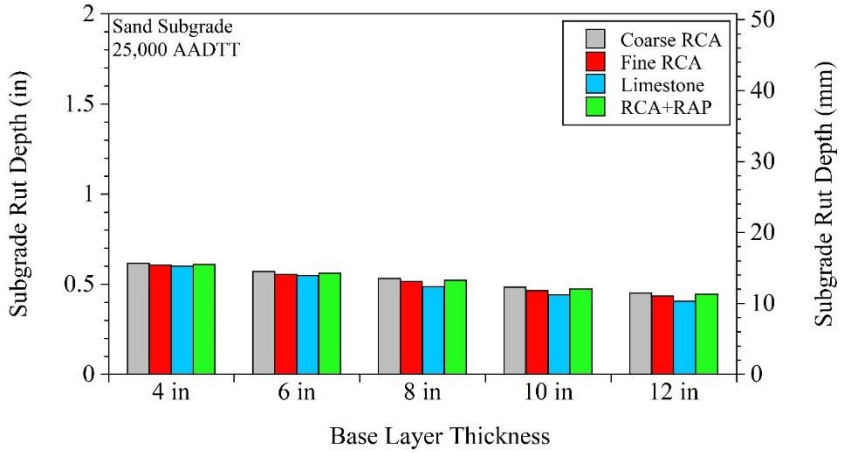


For pavements that contained sand subgrade – 25,000 AADTT:

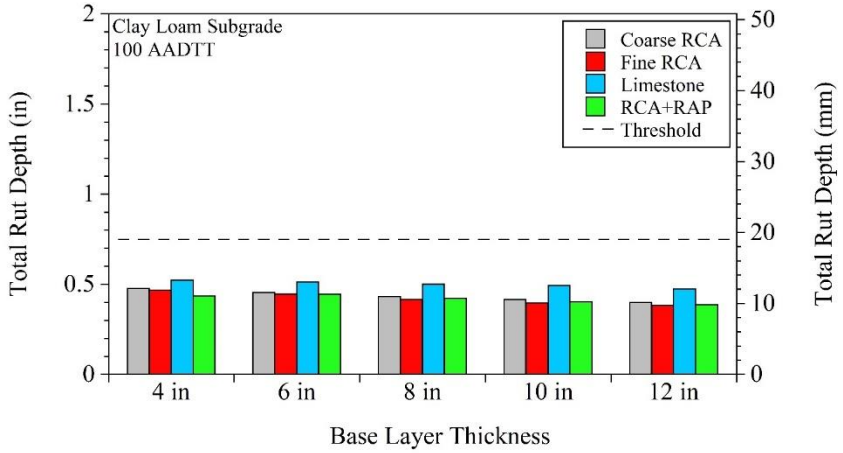


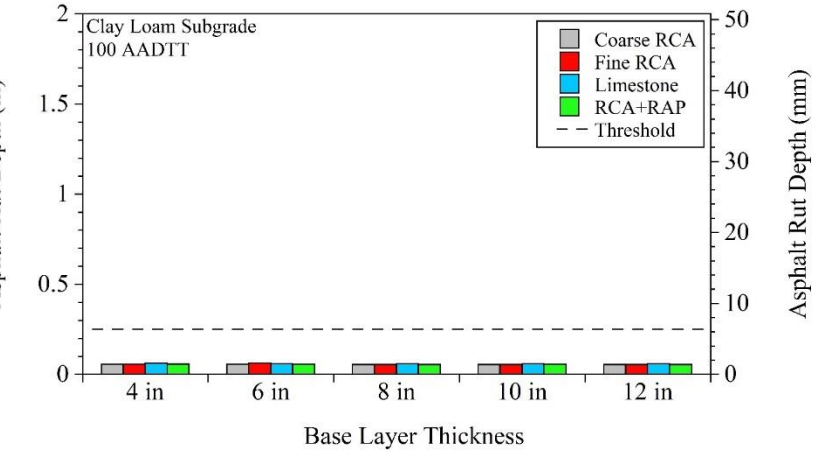


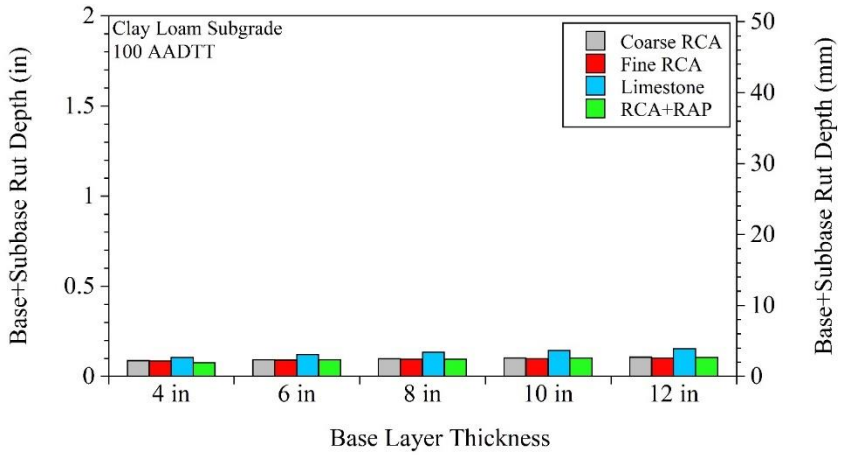


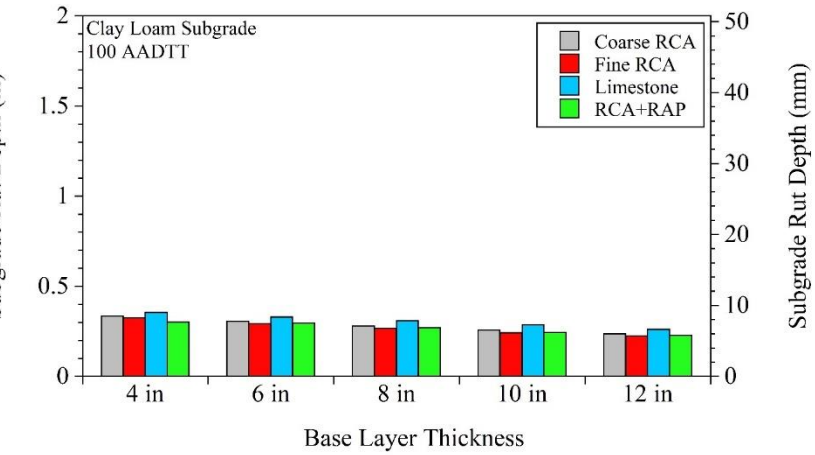


For pavements that contained clay loam subgrade – 100 AADTT:

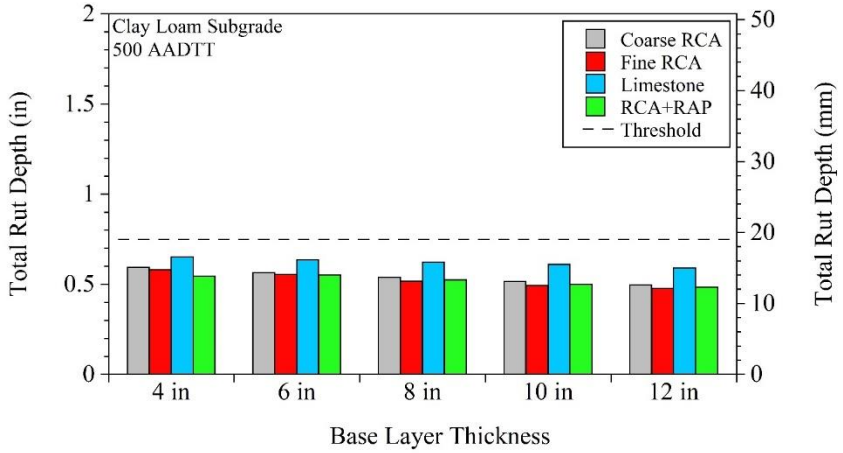


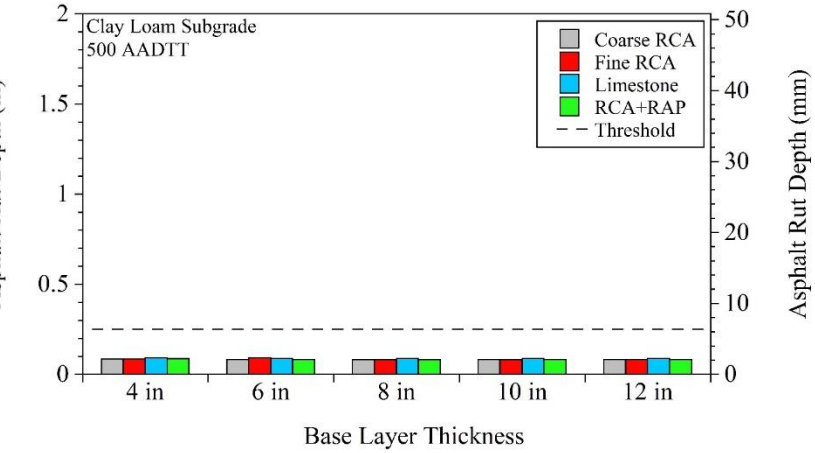


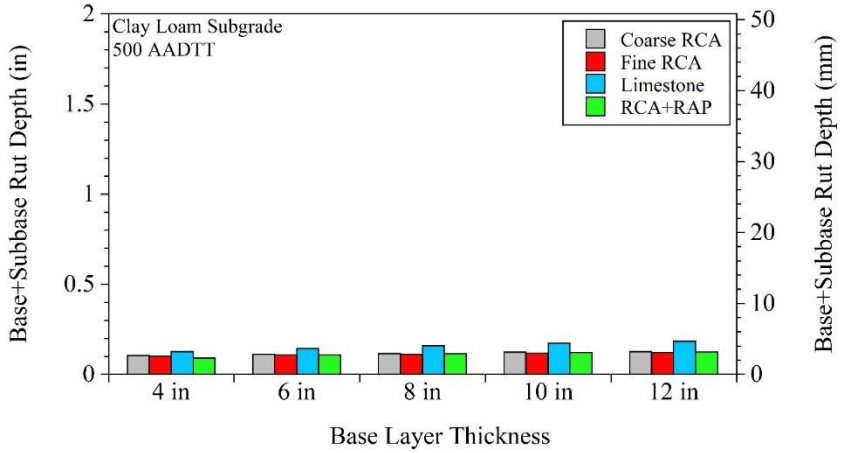


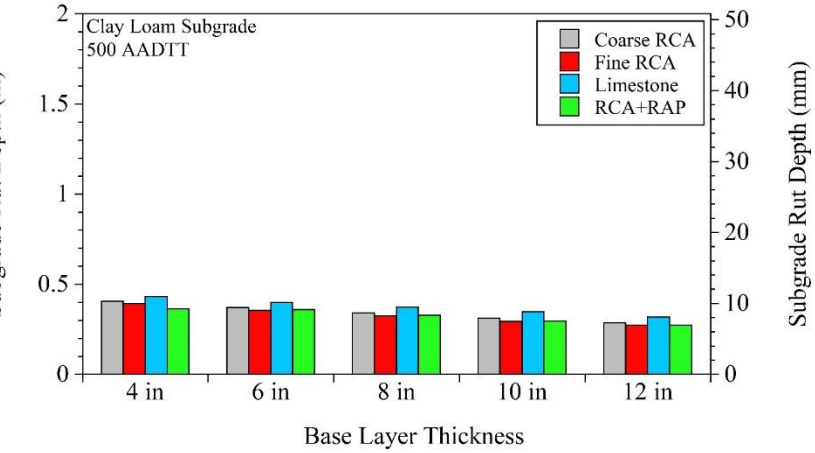


For pavements that contained clay loam subgrade – 500 AADTT:

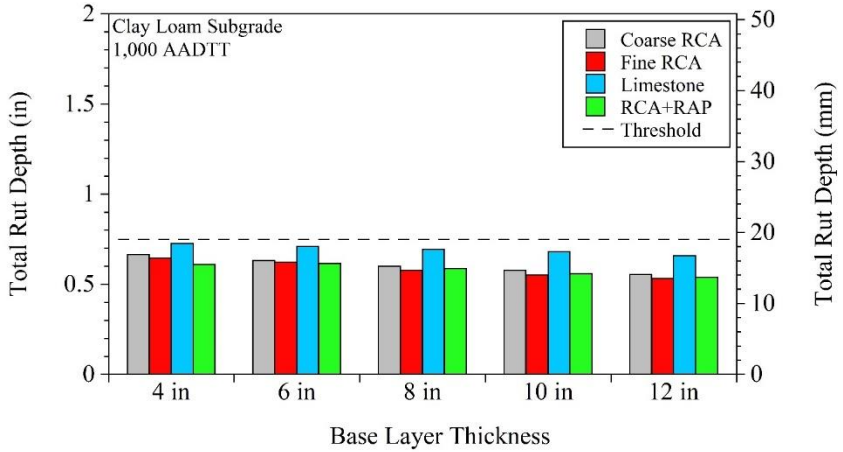


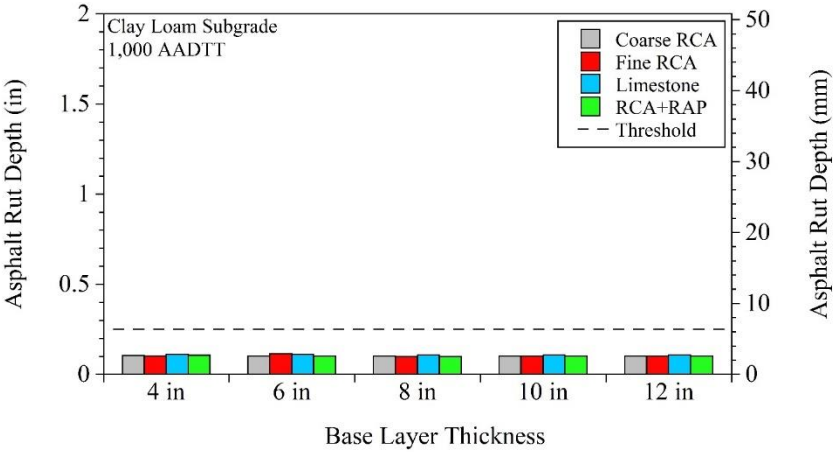


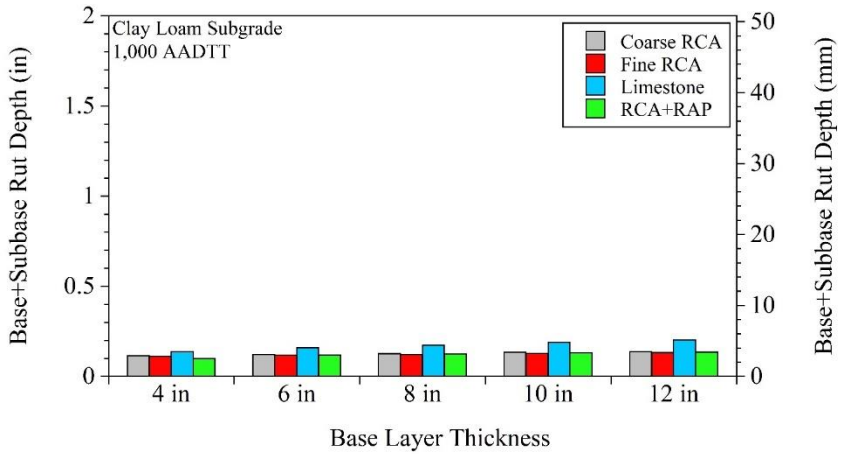


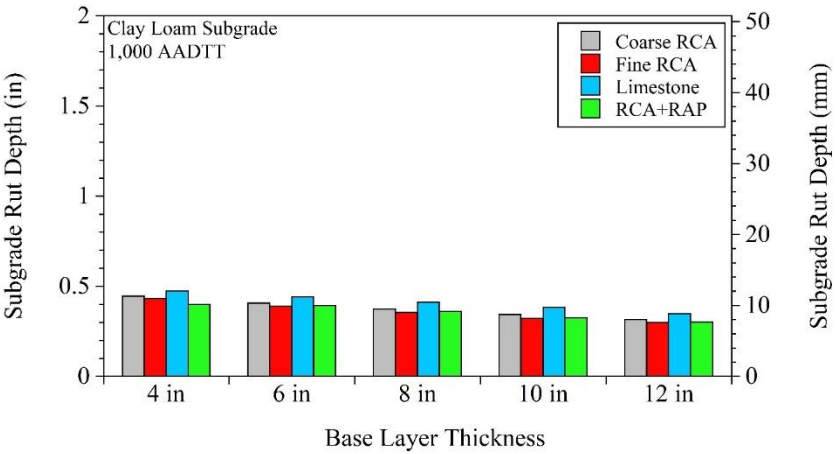


For pavements that contained clay loam subgrade – 1,000 AADTT:

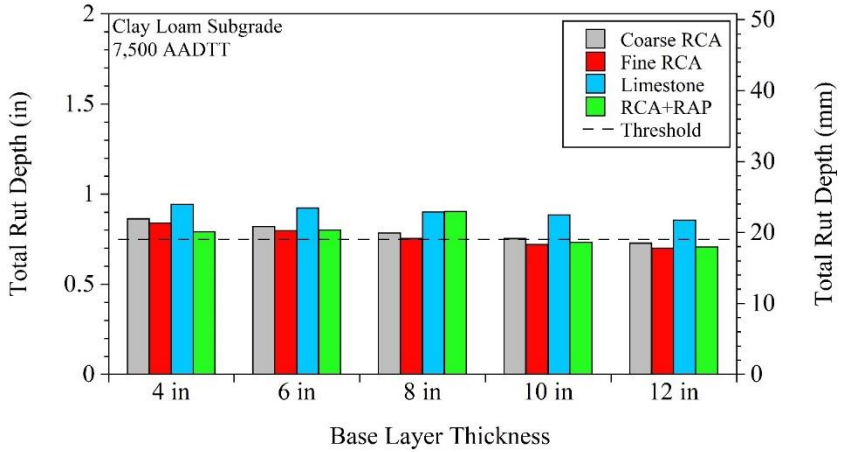


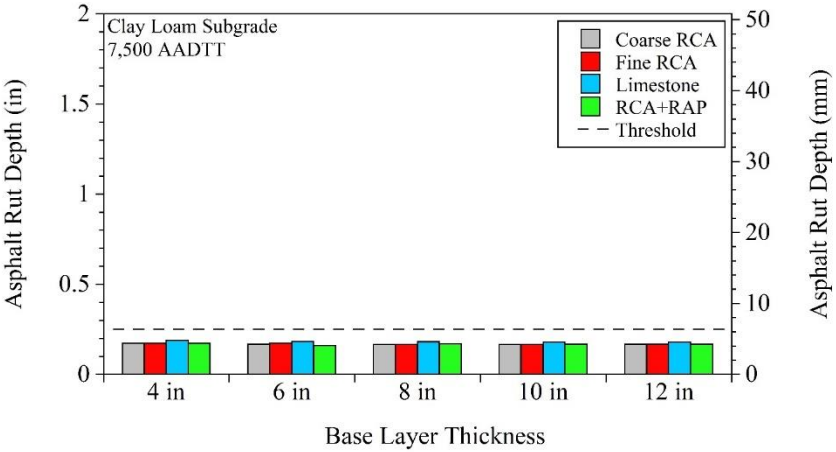


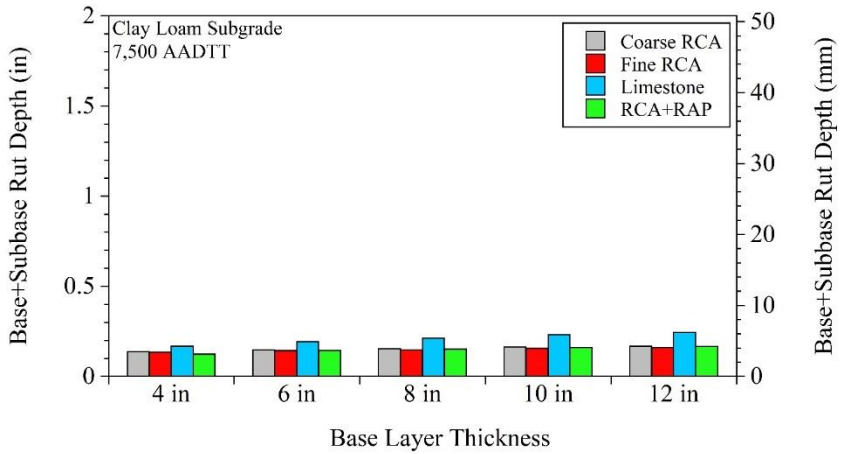


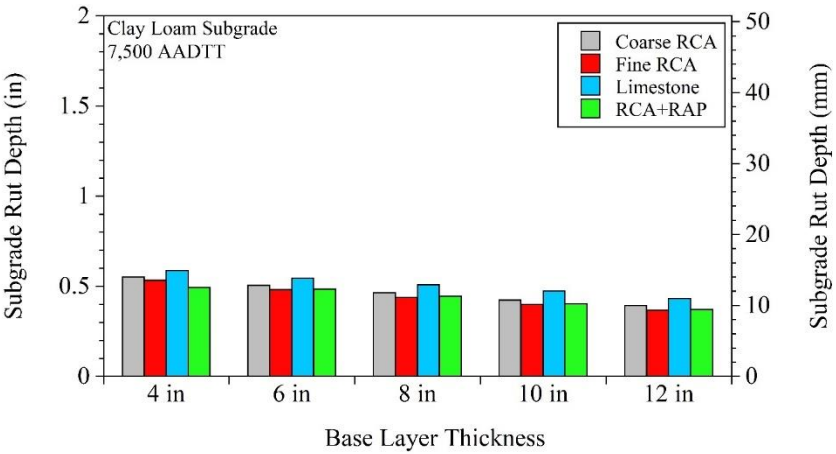


For pavements that contained clay loam subgrade – 7,500 AADTT:

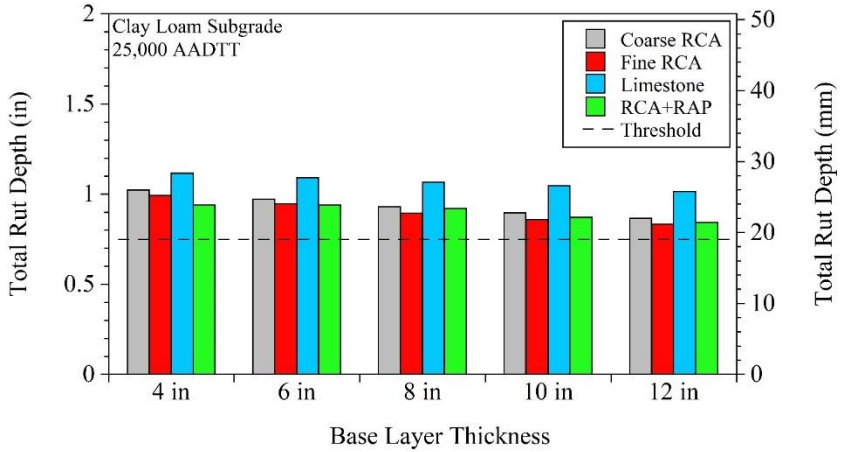


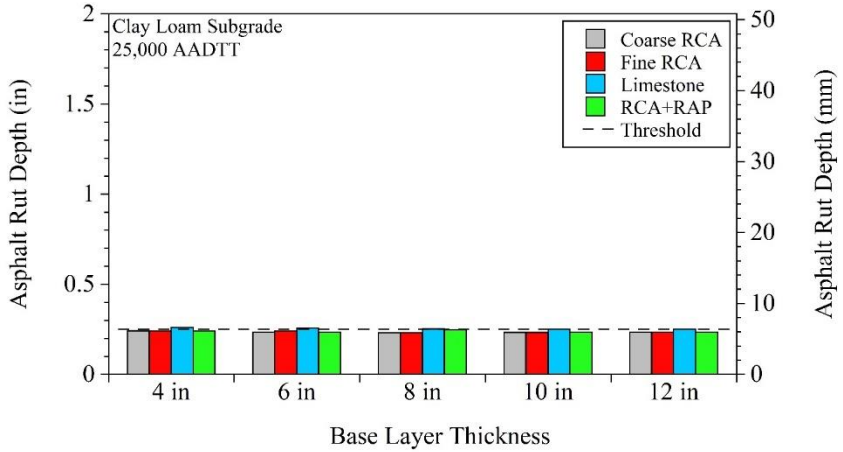


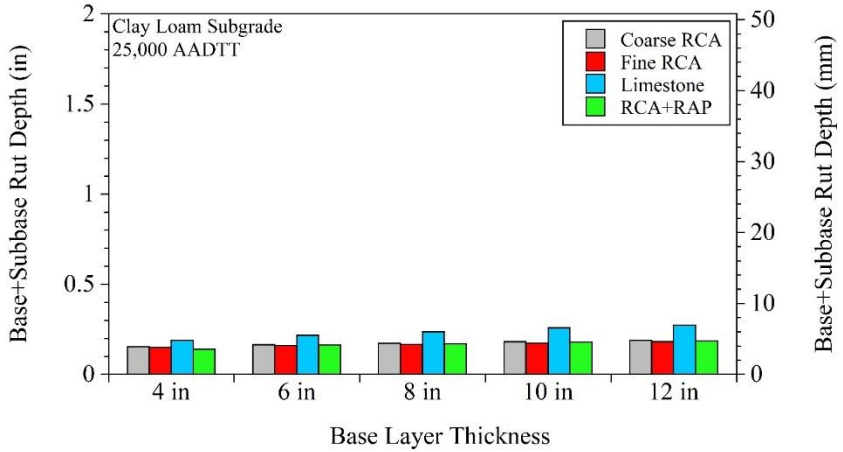


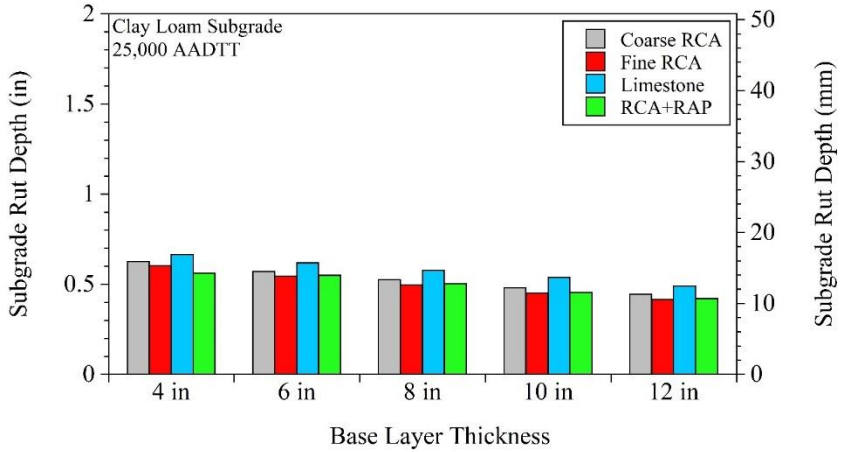


For pavements that contained clay loam subgrade – 25,000 AADTT:



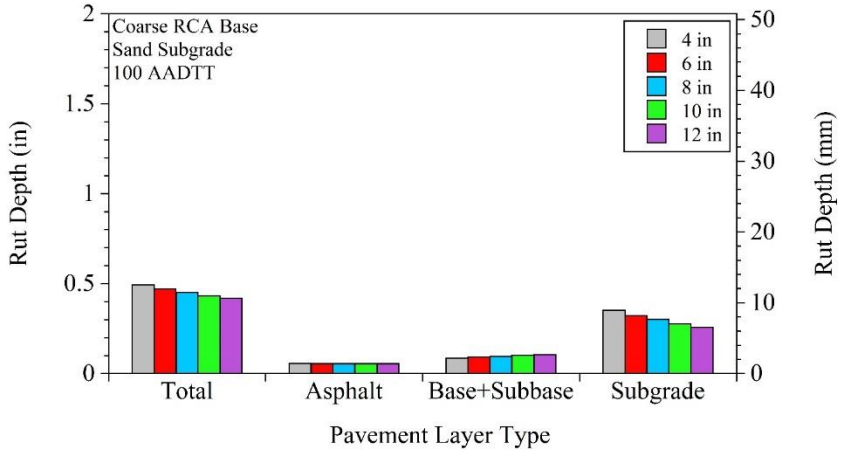


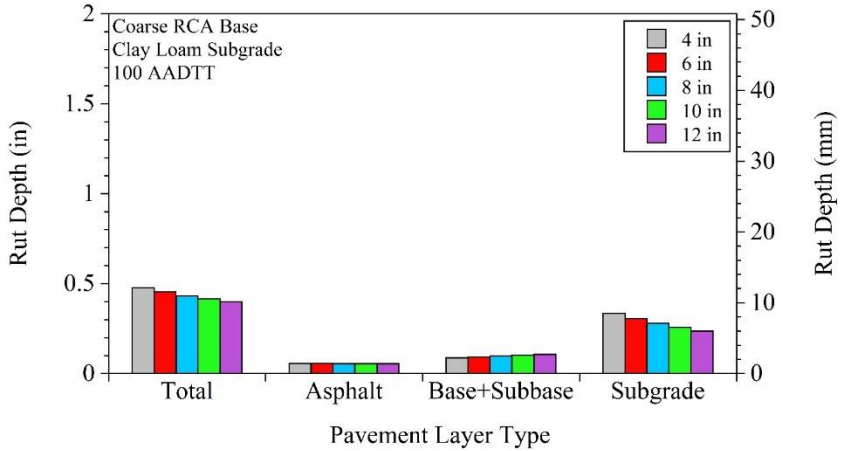




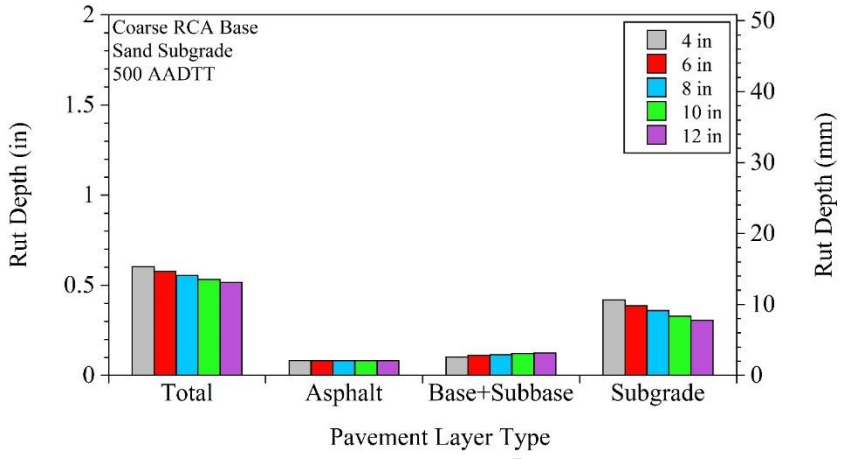
APPENDIX W. TOTAL AND LAYER RUTTING AT 50% RELIABILITY FOR RECYCLED AGGREGATE BASE (RAB) GROUP

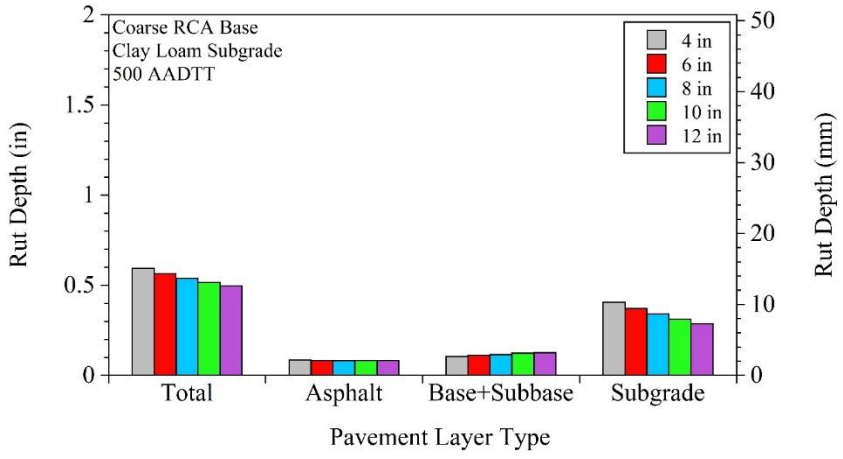
For pavements that contained coarse RCA base – 100 AADTT:



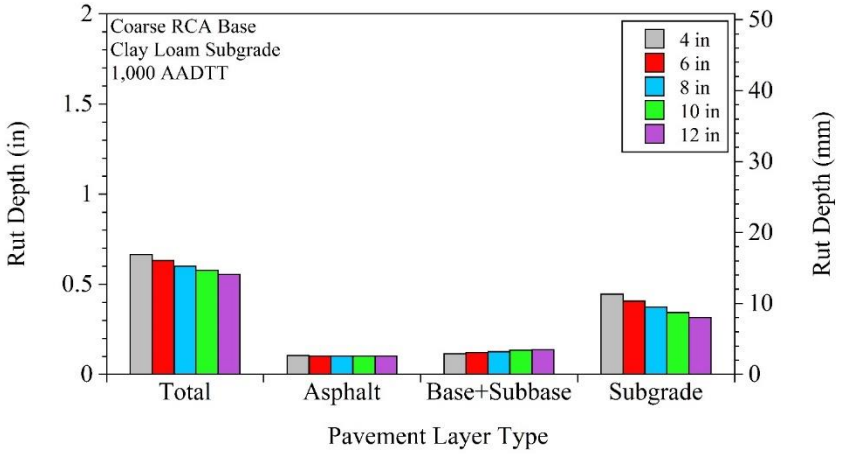


For pavements that contained coarse RCA base – 500 AADTT:

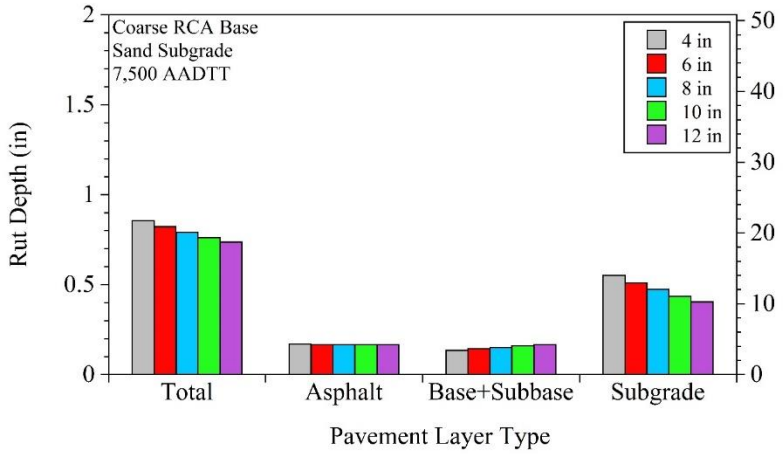


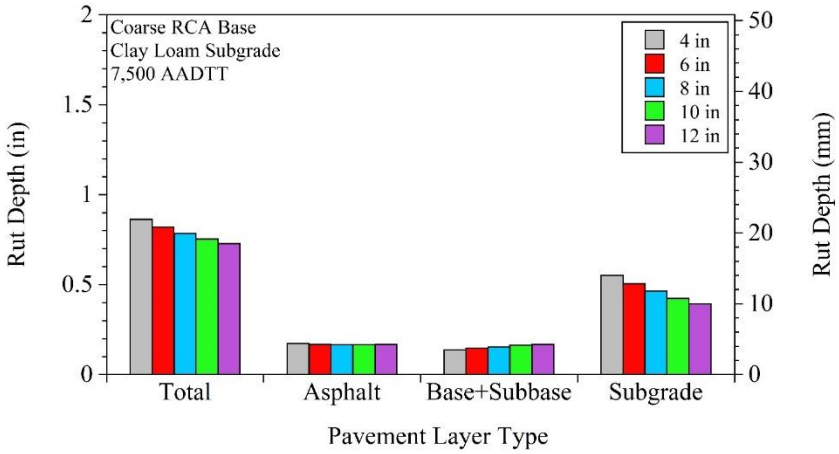


For pavements that contained coarse RCA base – 1,000 AADTT:



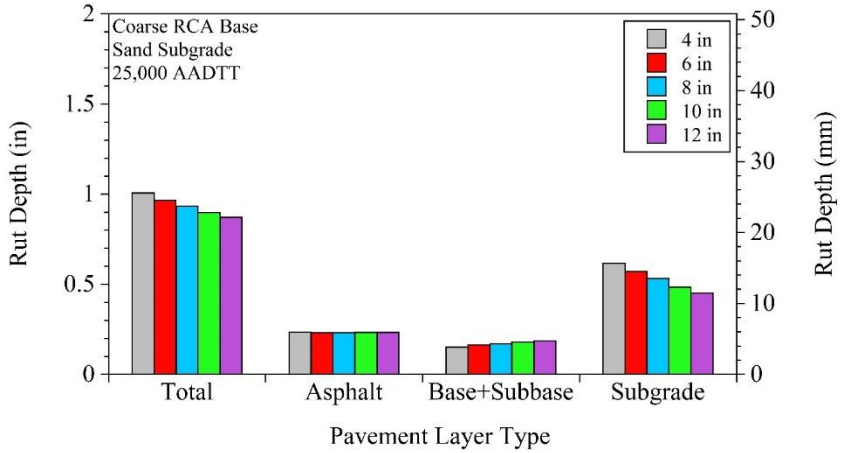
For pavements that contained coarse RCA base – 7,500 AADTT:

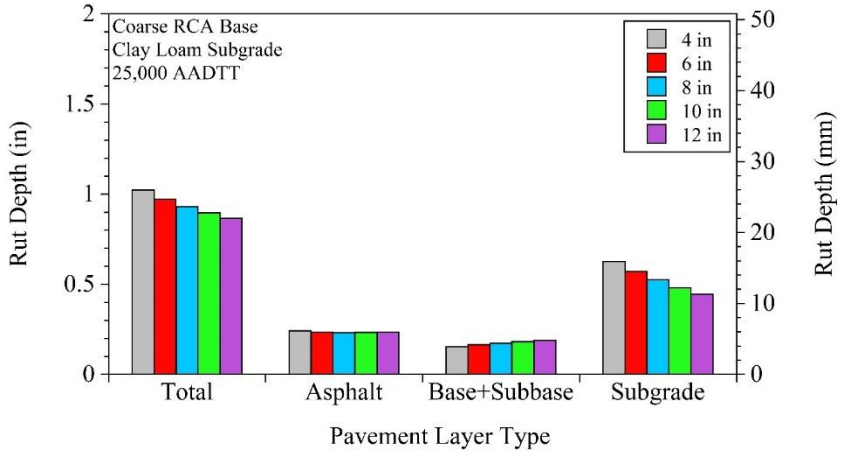




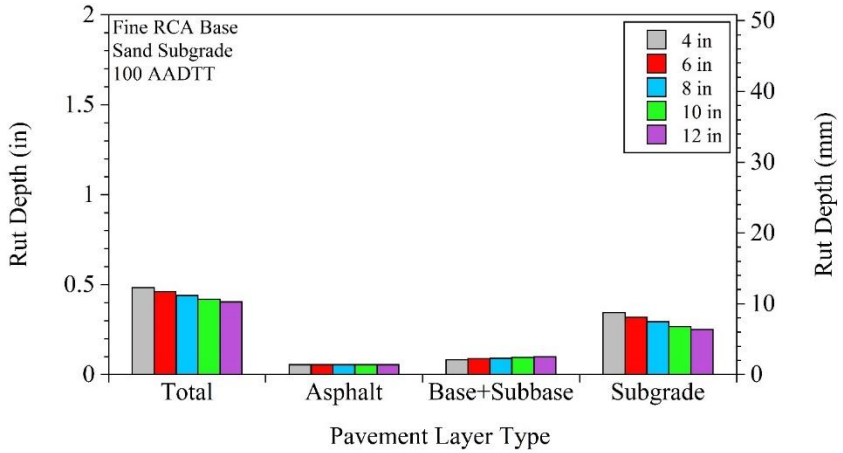
DRAFT

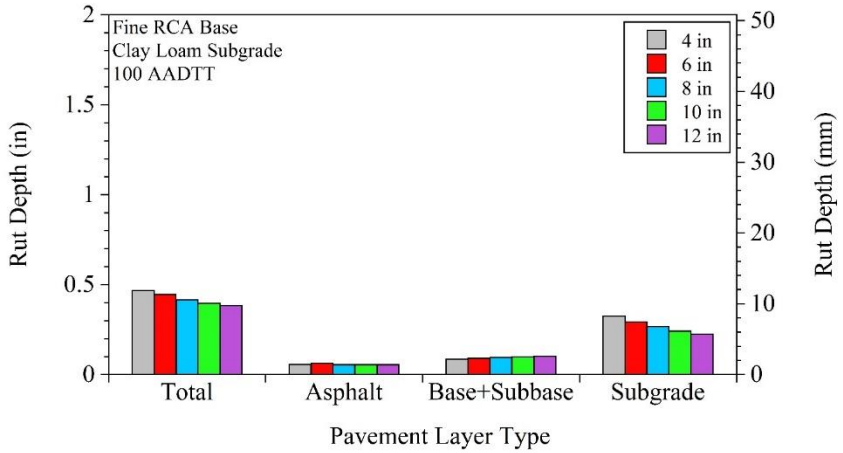
For pavements that contained coarse RCA base – 25,000 AADTT:



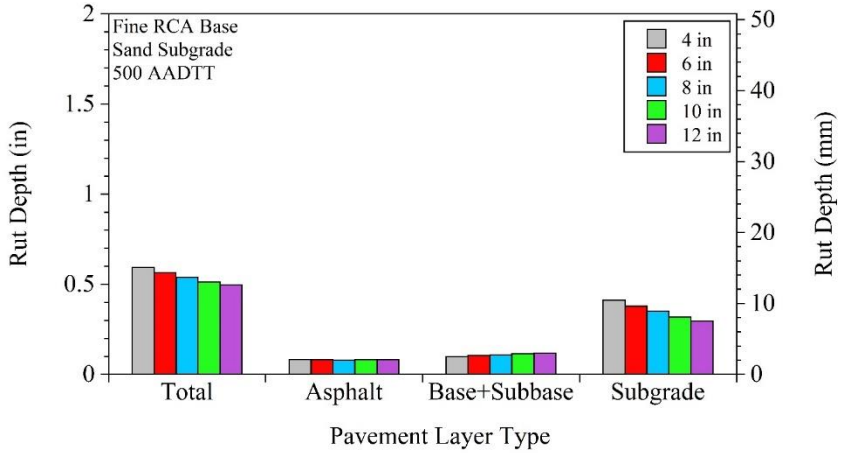


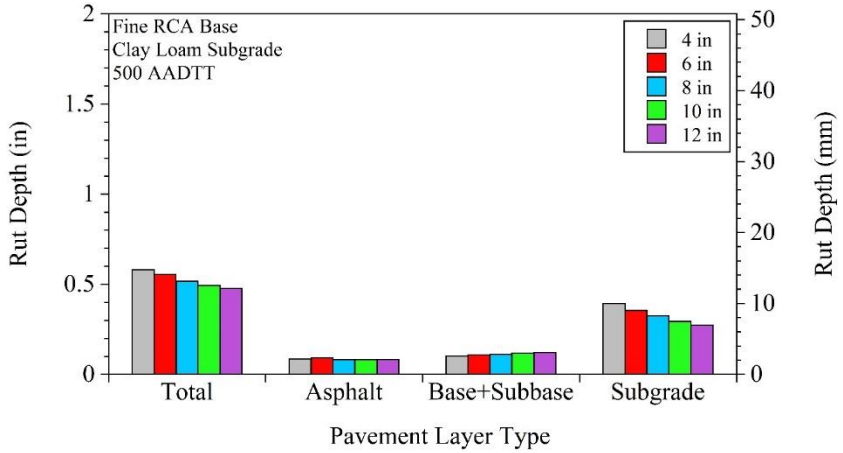
For pavements that contained fine RCA base – 100 AADTT:



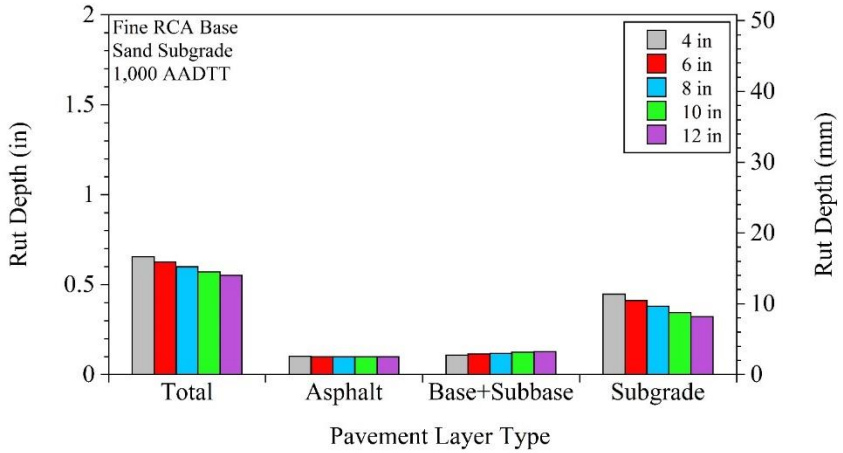


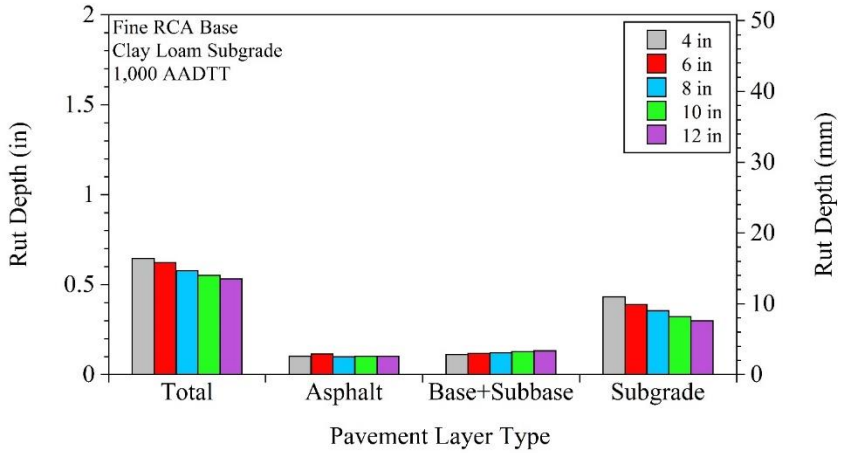
For pavements that contained fine RCA base – 500 AADTT:



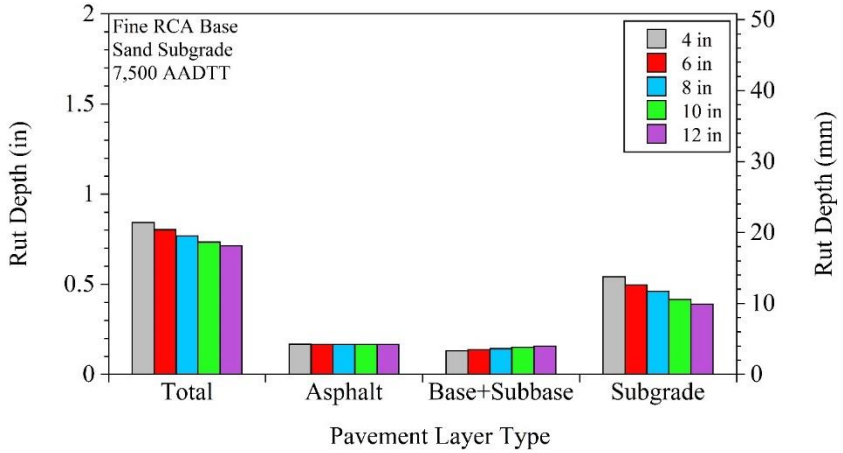


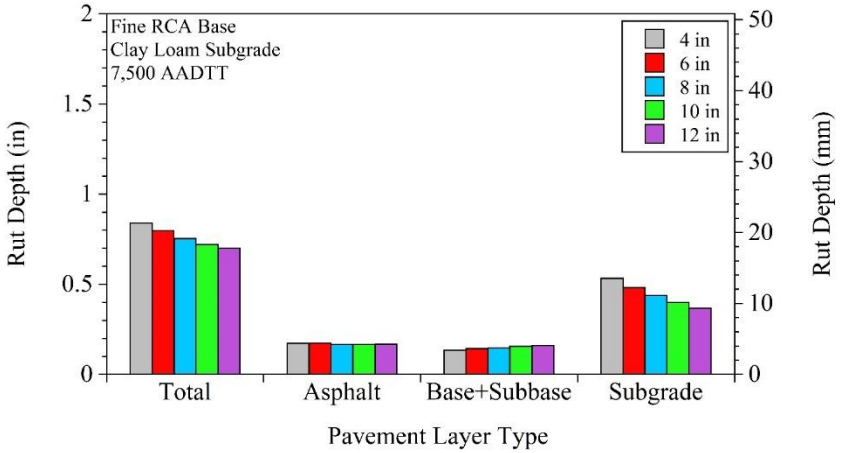
For pavements that contained fine RCA base – 1,000 AADTT:



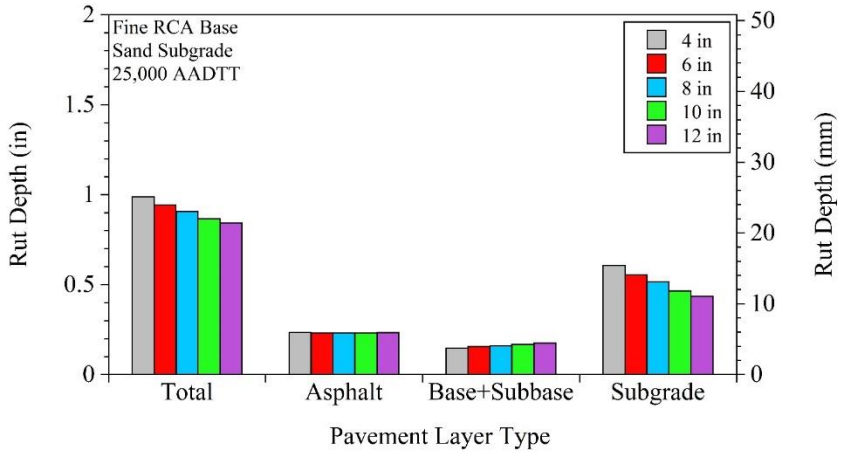


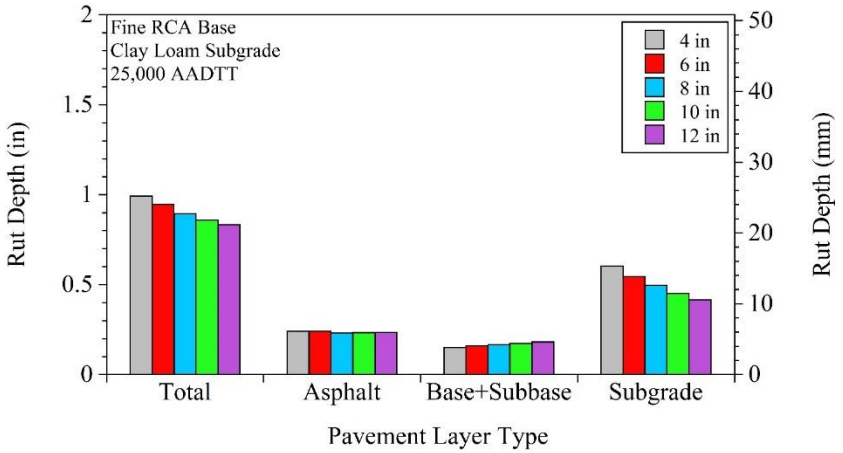
For pavements that contained fine RCA base – 7,500 AADTT:



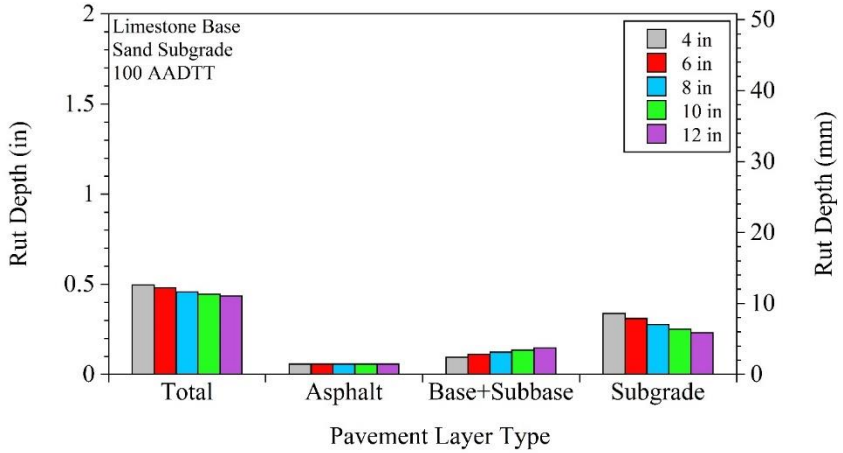


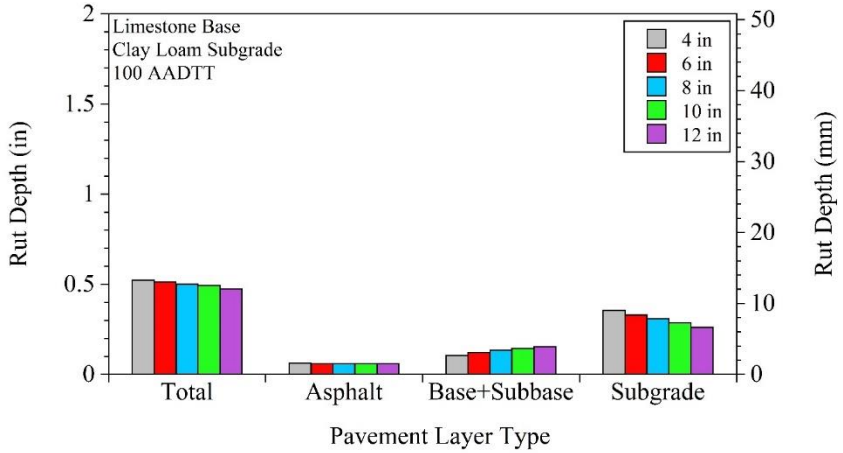
For pavements that contained fine RCA base – 25,000 AADTT:



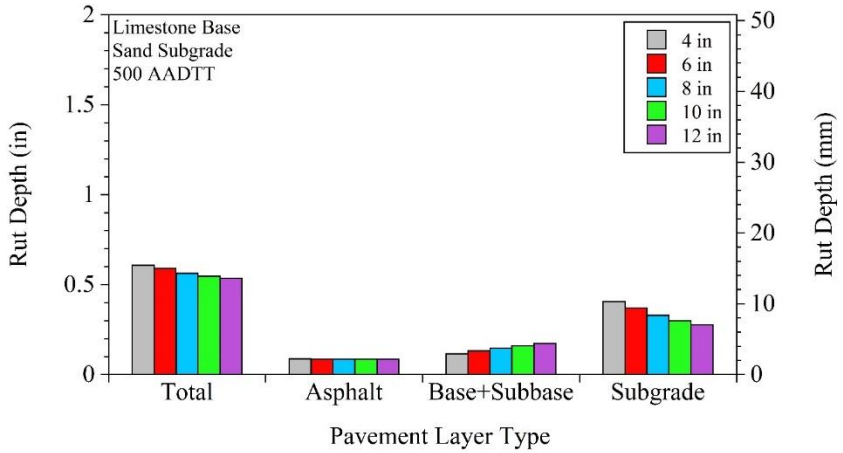


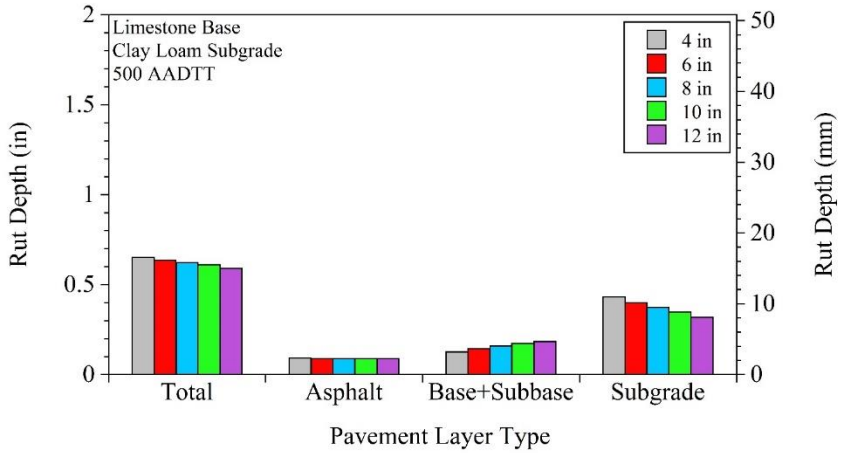
For pavements that contained limestone base – 100 AADTT:



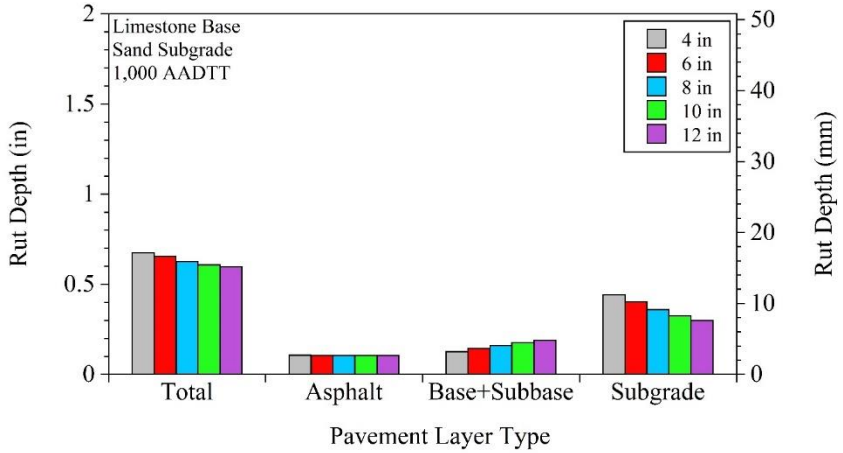


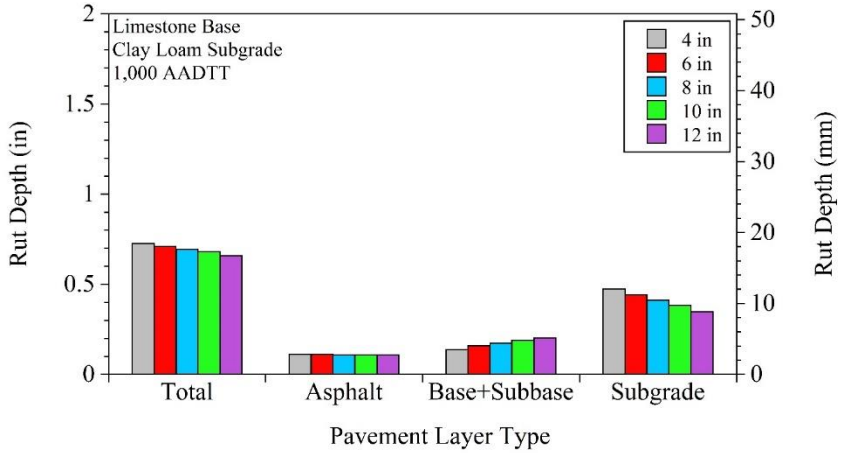
For pavements that contained limestone base – 500 AADTT:



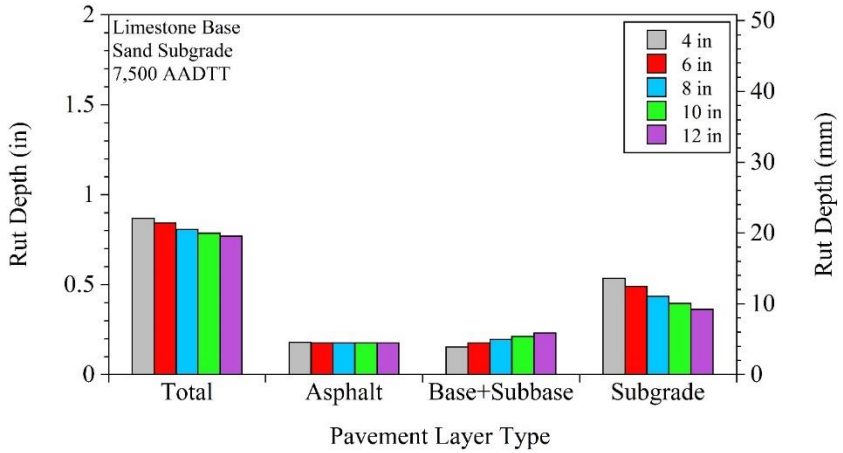


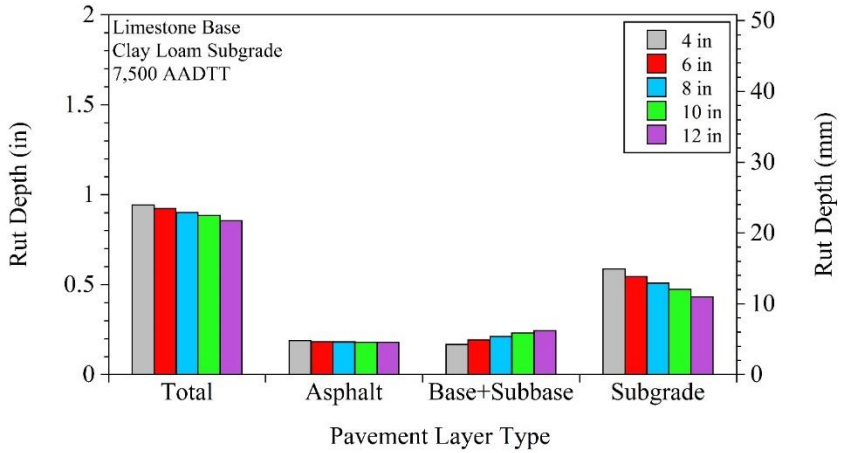
For pavements that contained limestone base – 1,000 AADTT:



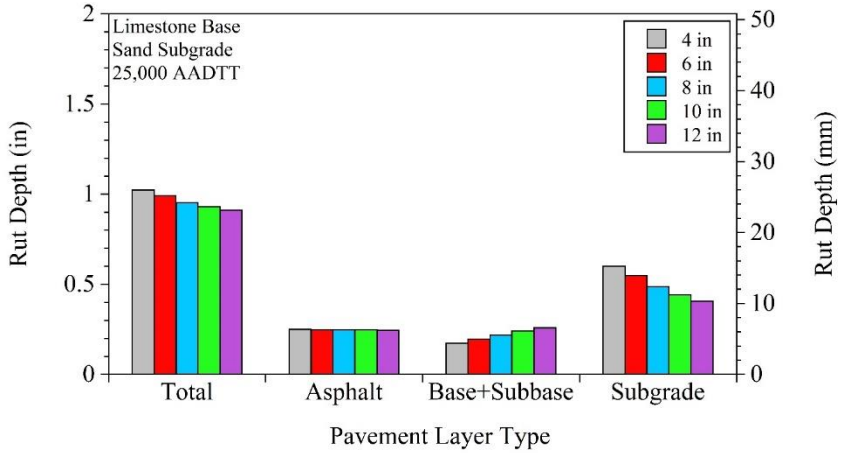


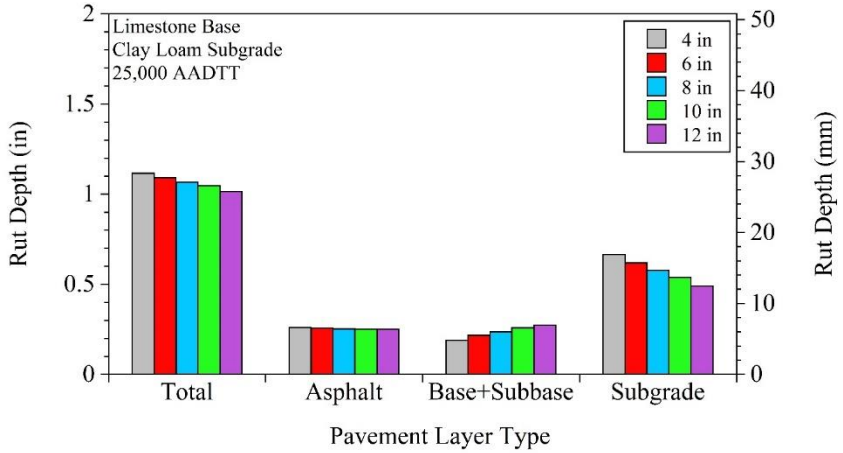
For pavements that contained limestone base – 7,500 AADTT:



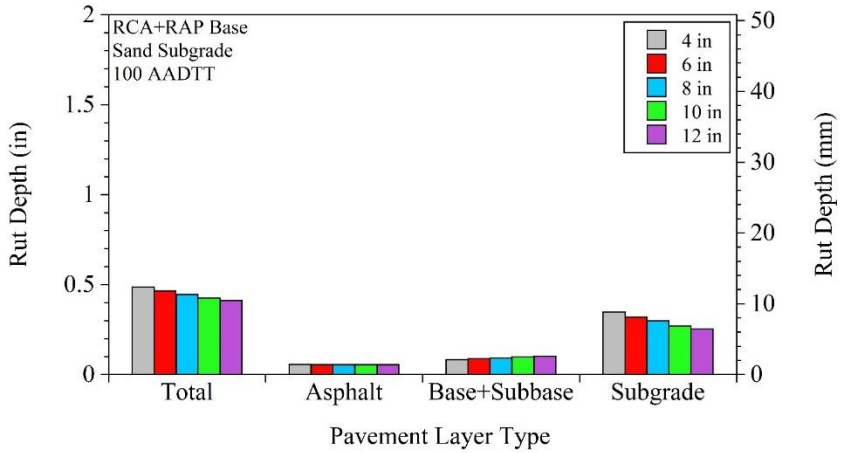


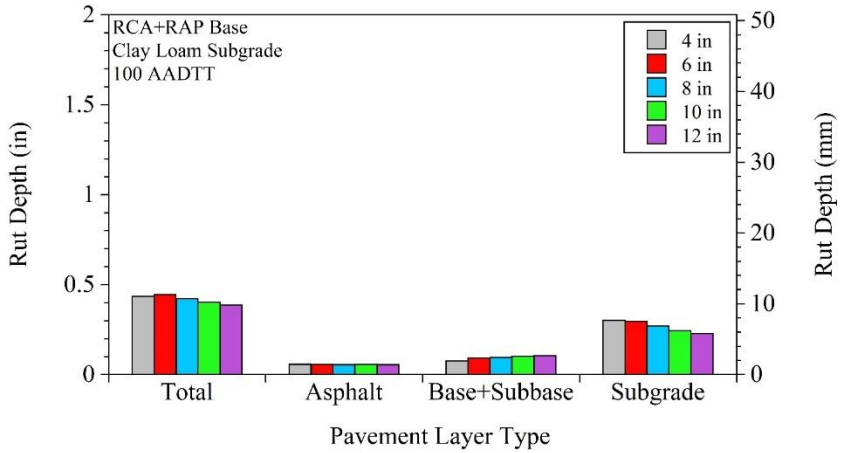
For pavements that contained limestone base – 25,000 AADTT:



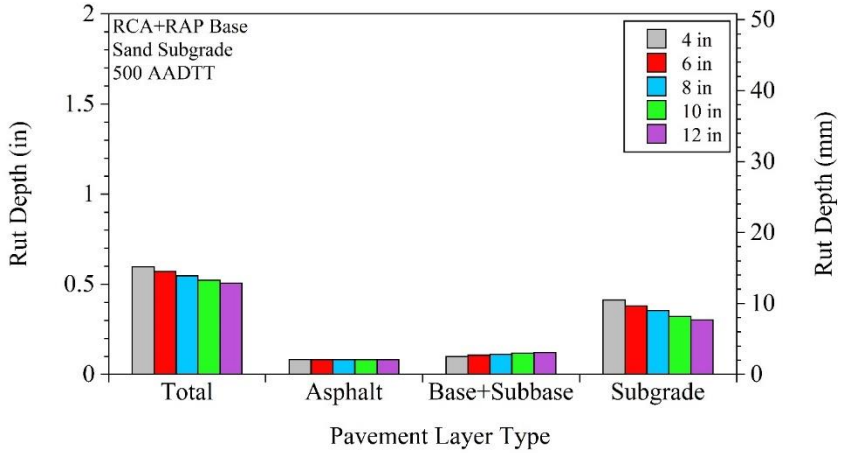


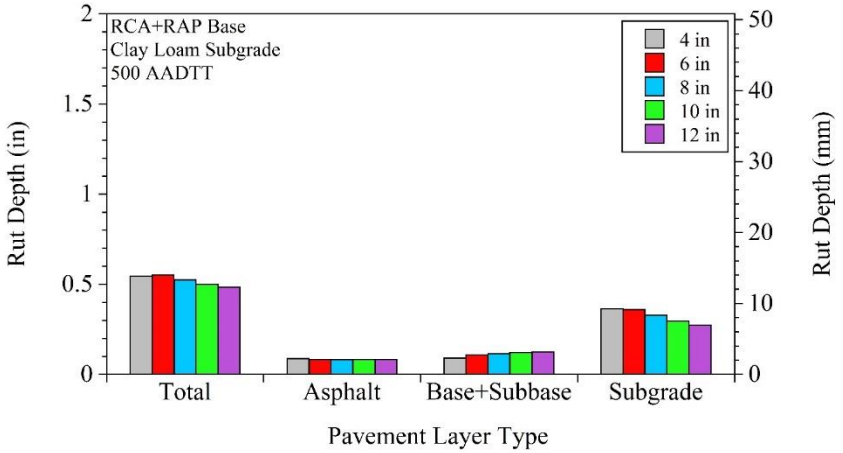
For pavements that contained RCA+RAP base – 100 AADTT:



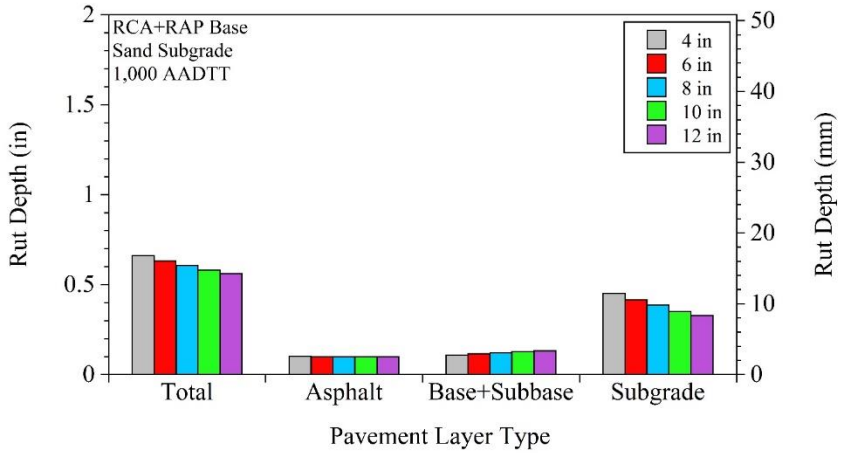


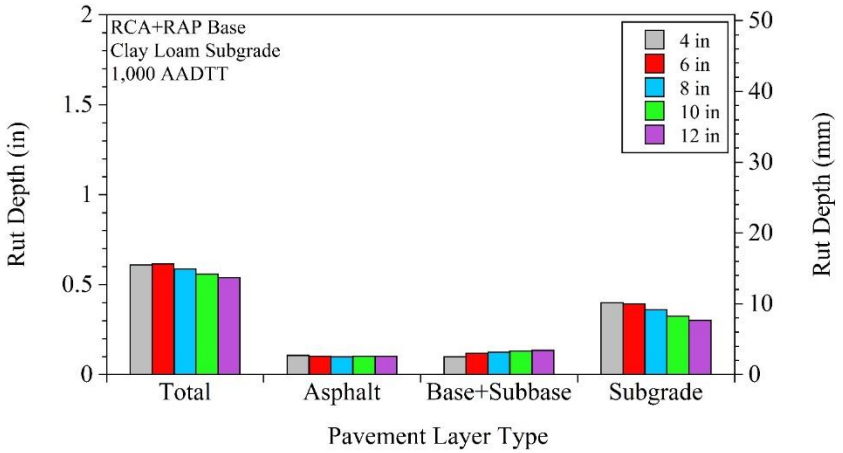
For pavements that contained RCA+RAP base – 500 AADTT:



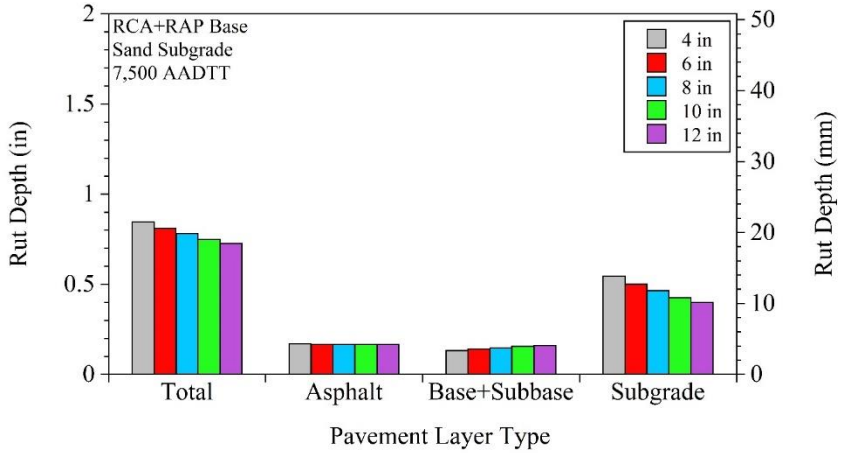


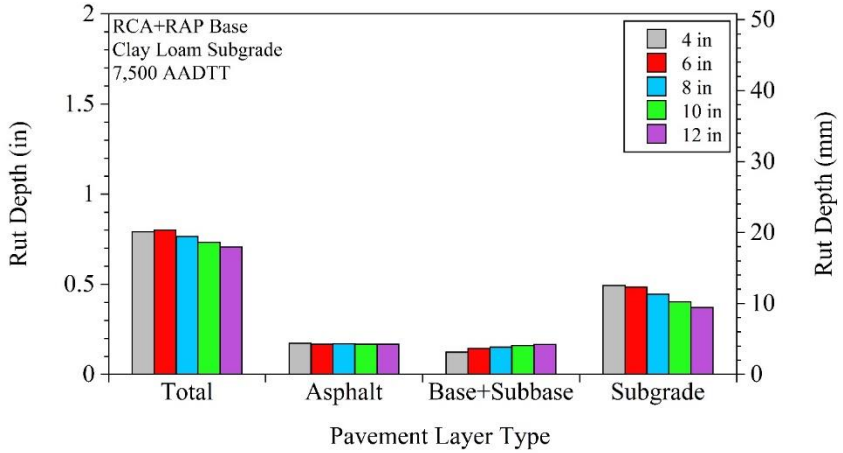
For pavements that contained RCA+RAP base – 1,000 AADTT:



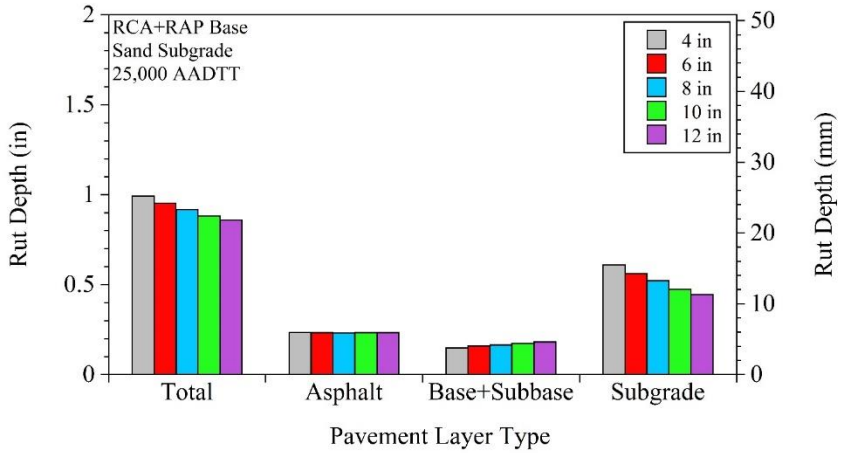


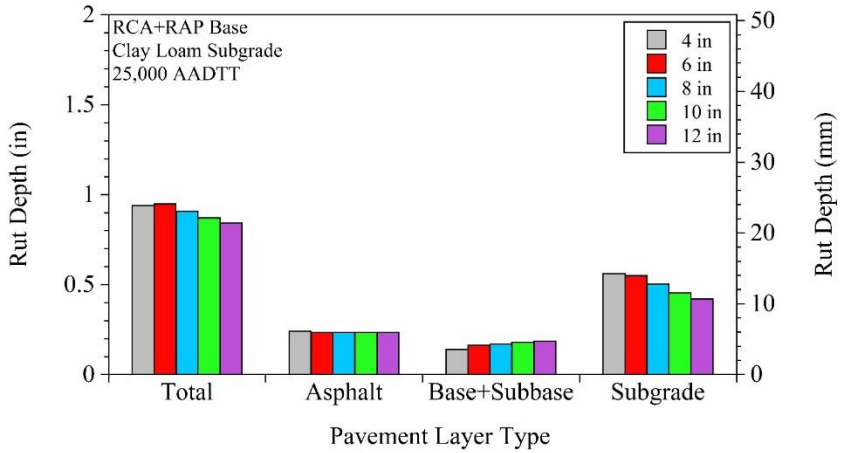
For pavements that contained RCA+RAP base – 7,500 AADTT:





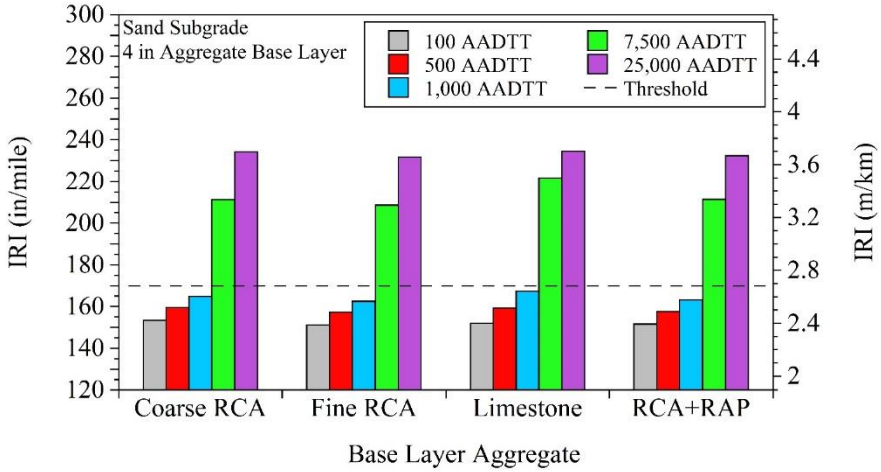
For pavements that contained RCA+RAP base – 25,000 AADTT:

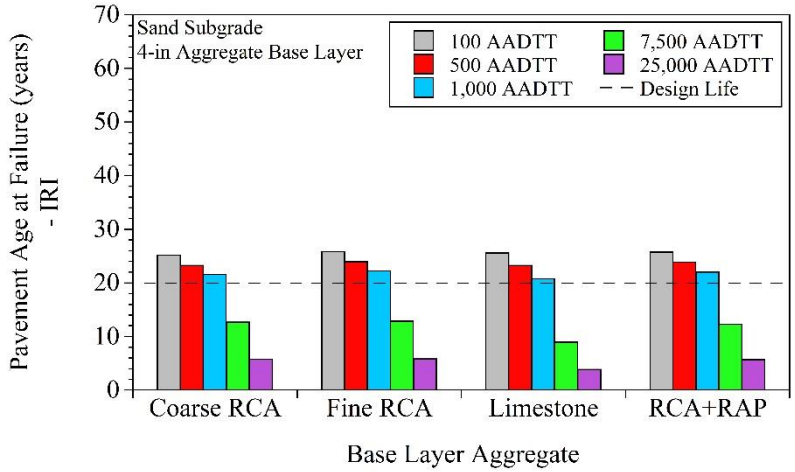


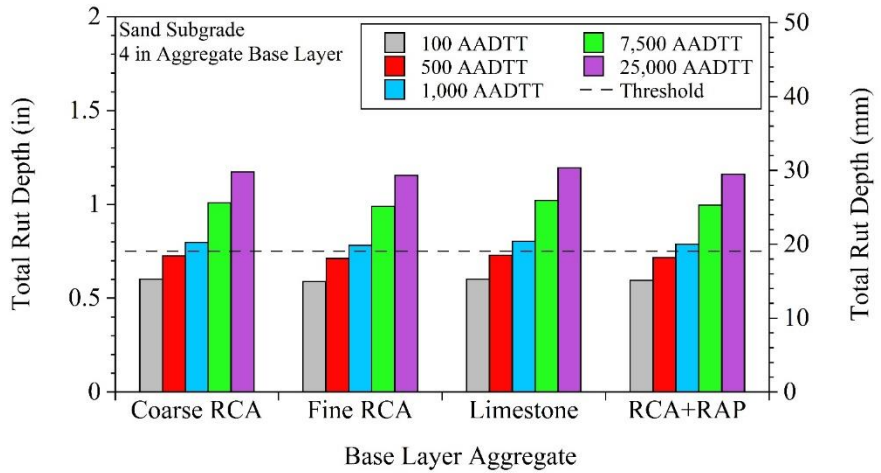


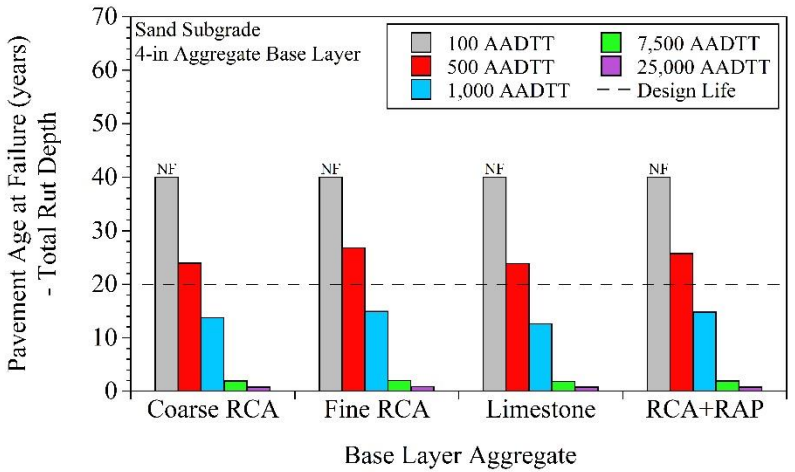
APPENDIX X. EFFECT OF TRAFFIC LEVEL ON PAVEMENT PERFORMANCE PREDICTIONS

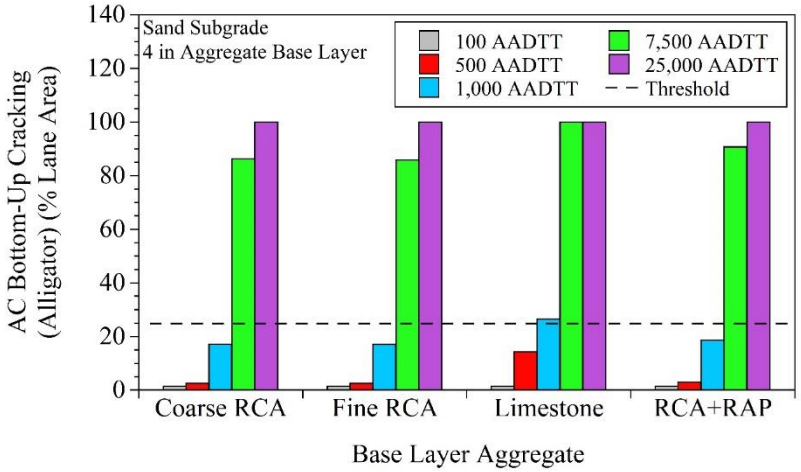
For pavements that contained sand subgrade and 4-in aggregate base:

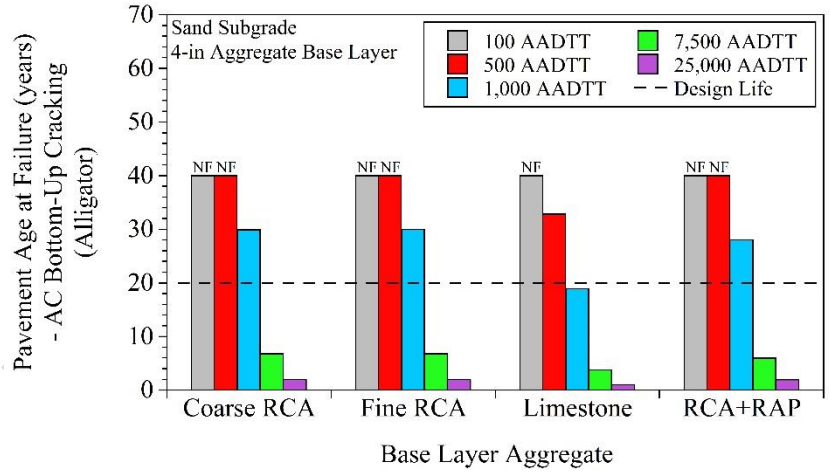


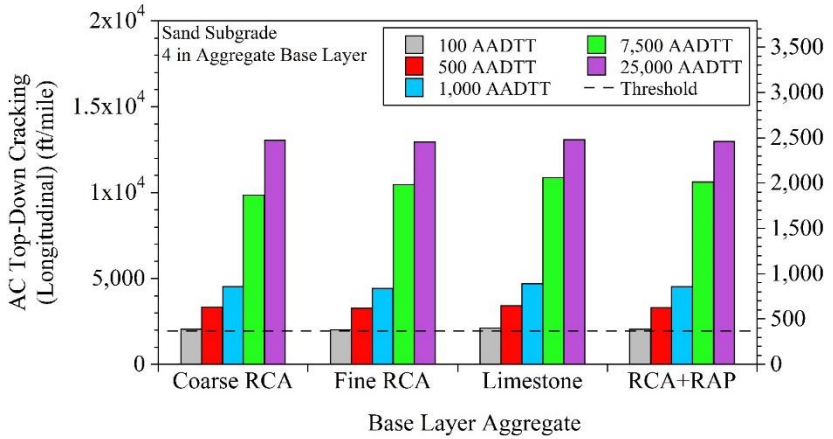


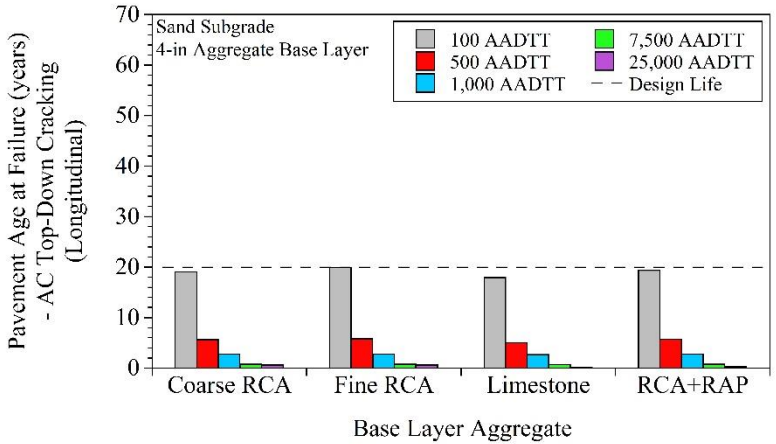




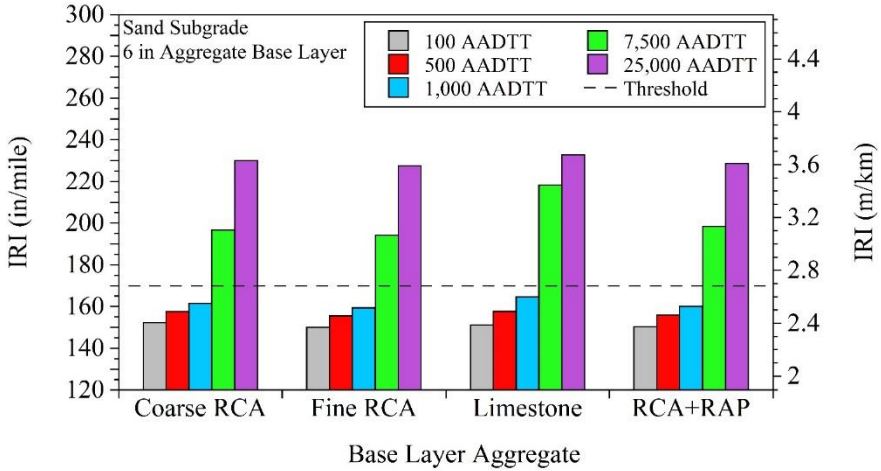

Sand Subgrade
4 in Aggregate Base Layer
100 AADTT
500 AADTT
1,000 AADTT
7,500 AADTT
25,000 AADTT
Threshold
AC Bottom-Up Cracking (Alligator) (% Lane Area)
0
20
40
60
80
100
120
140
Coarse RCA
Fine RCA
Limestone
RCA+RAP
Base Layer Aggregate

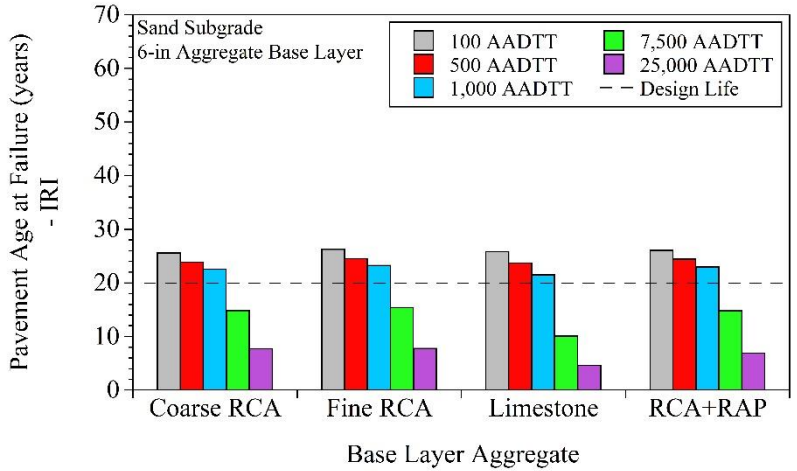

Sand Subgrade
4-in Aggregate Base Layer
100 AADTT
500 AADTT
1,000 AADTT
7,500 AADTT
25,000 AADTT
Design Life
Pavement Age at Failure (years) - AC Bottom-Up Cracking (Alligator)
NF NF
NF NF
NF
NF NF
0
10
20
30
40
50
60
70
Coarse RCA
Fine RCA
Limestone
RCA+RAP
Base Layer Aggregate

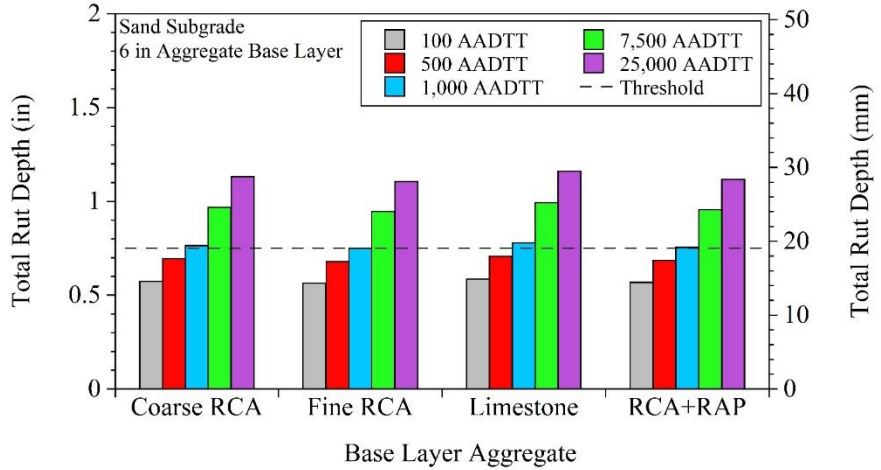

Sand Subgrade
4 in Aggregate Base Layer
100 AADTT
500 AADTT
1,000 AADTT
7,500 AADTT
25,000 AADTT
Threshold
AC Top-Down Cracking (Longitudinal) (ft/mile)
AC Top-Down Cracking (Longitudinal) (m/km)
0
5,000
1x10^4
1.5x10^4
2x10^4
0
500
1,000
1,500
2,000
2,500
3,000
3,500
Coarse RCA
Fine RCA
Limestone
RCA+RAP
Base Layer Aggregate

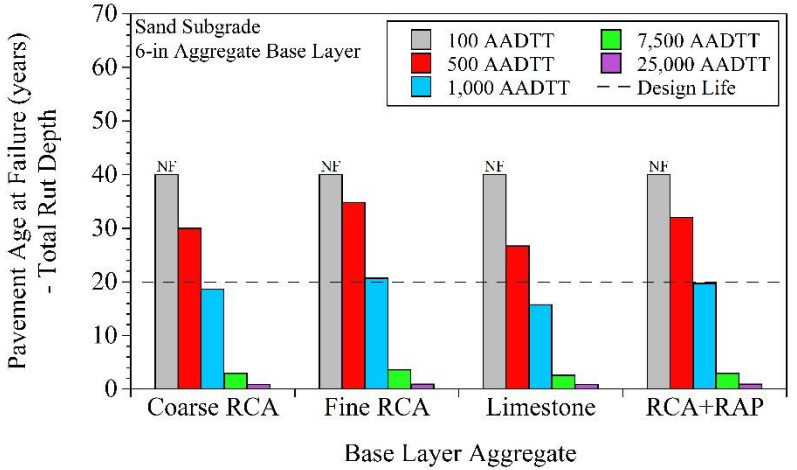

Sand Subgrade
4-in Aggregate Base Layer
100 AADTT
500 AADTT
1,000 AADTT
7,500 AADTT
25,000 AADTT
Design Life
Pavement Age at Failure (years) - AC Top-Down Cracking (Longitudinal)
0
10
20
30
40
50
60
70
Coarse RCA
Fine RCA
Limestone
RCA+RAP
Base Layer Aggregate

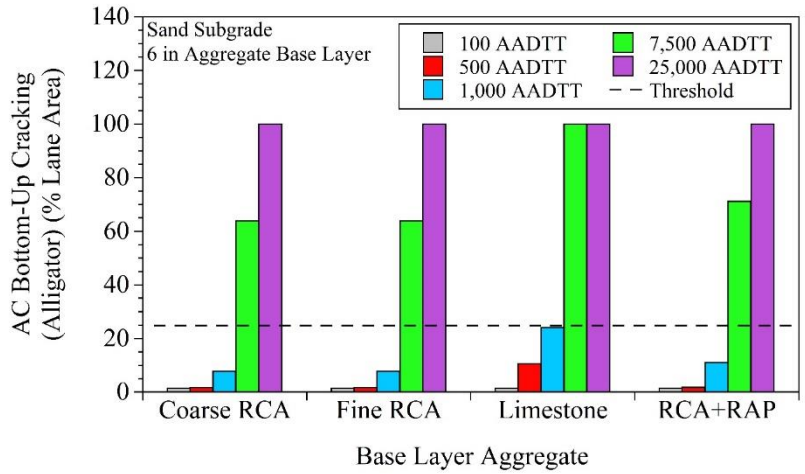
For pavements that contained sand subgrade and 6-in aggregate base:

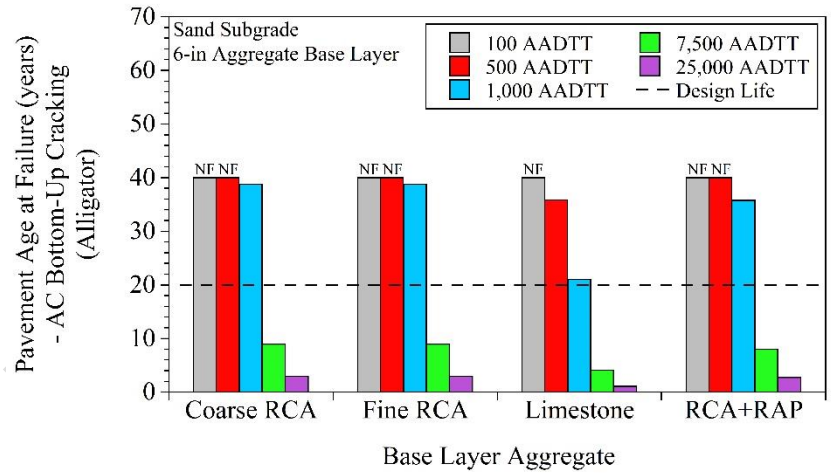


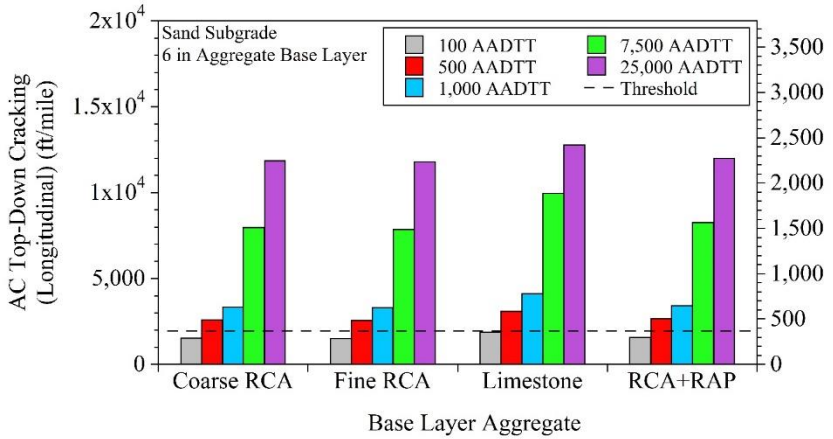


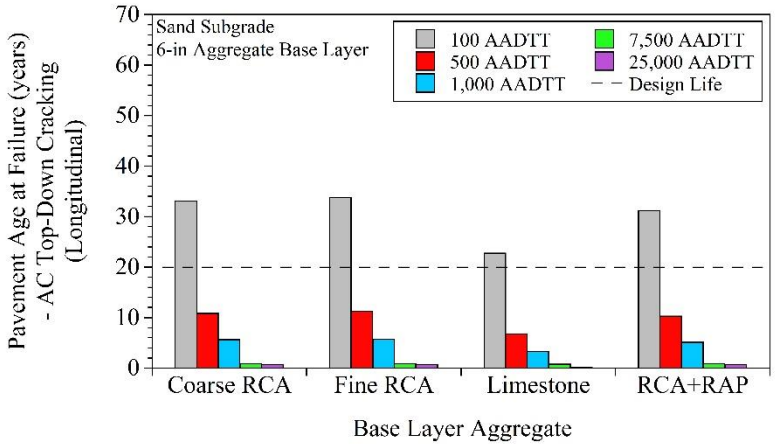




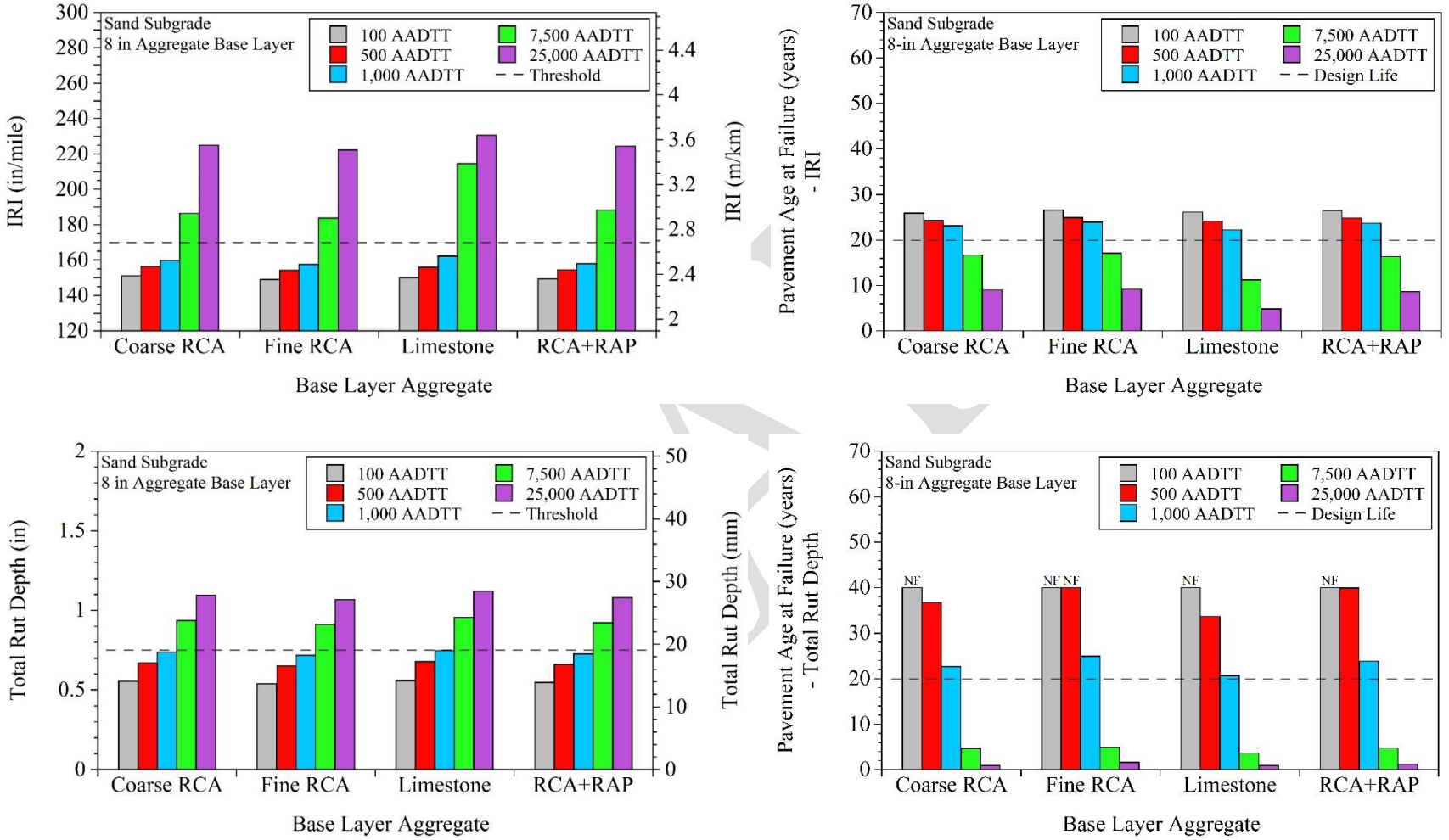

Sand Subgrade
6 in Aggregate Base Layer
100 AADTT
500 AADTT
1,000 AADTT
7,500 AADTT
25,000 AADTT
Threshold
AC Bottom-Up Cracking (Alligator) (% Lane Area)
0
20
40
60
80
100
120
140
Coarse RCA
Fine RCA
Limestone
RCA+RAP
Base Layer Aggregate

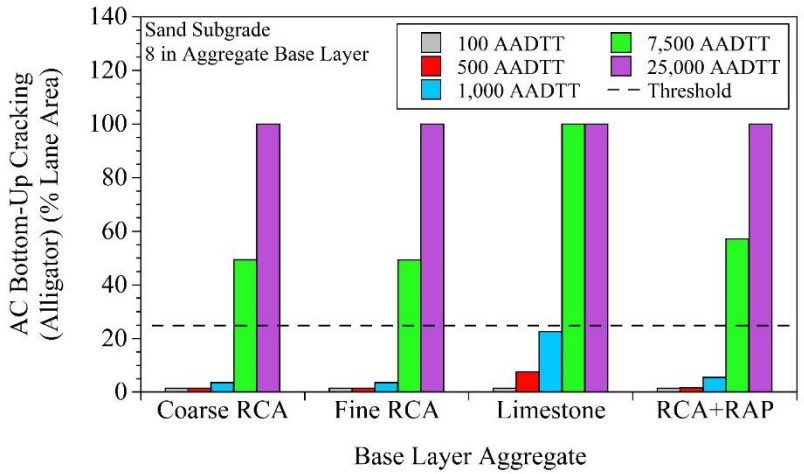

Sand Subgrade
6-in Aggregate Base Layer
100 AADTT
500 AADTT
1,000 AADTT
7,500 AADTT
25,000 AADTT
Design Life
Pavement Age at Failure (years) - AC Bottom-Up Cracking (Alligator)
NF NF
NF NF
NF
NF NF
0
10
20
30
40
50
60
70
Coarse RCA
Fine RCA
Limestone
RCA+RAP
Base Layer Aggregate

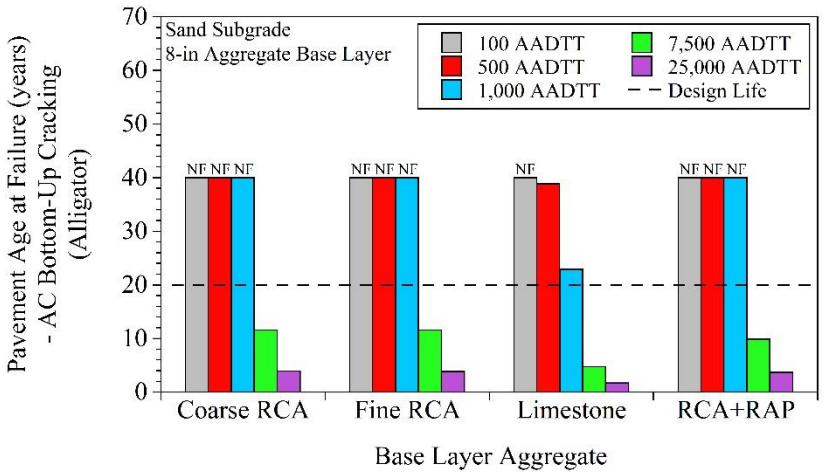

Sand Subgrade
6 in Aggregate Base Layer
100 AADTT
500 AADTT
1,000 AADTT
7,500 AADTT
25,000 AADTT
Threshold
AC Top-Down Cracking (Longitudinal) (ft/mile)
0
5,000
1x10^4
1.5x10^4
2x10^4
0
500
1,000
1,500
2,000
2,500
3,000
3,500
AC Top-Down Cracking (Longitudinal) (m/km)
Coarse RCA
Fine RCA
Limestone
RCA+RAP
Base Layer Aggregate

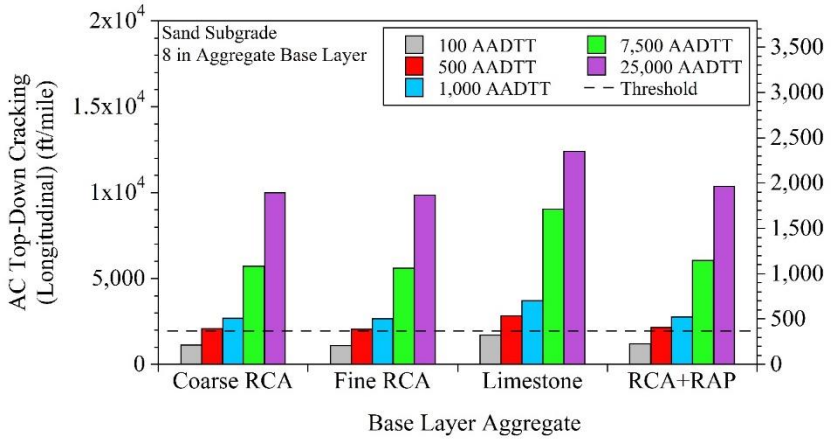

Sand Subgrade
6-in Aggregate Base Layer
100 AADTT
500 AADTT
1,000 AADTT
7,500 AADTT
25,000 AADTT
Design Life
Pavement Age at Failure (years) - AC Top-Down Cracking (Longitudinal)
0
10
20
30
40
50
60
70
Coarse RCA
Fine RCA
Limestone
RCA+RAP
Base Layer Aggregate

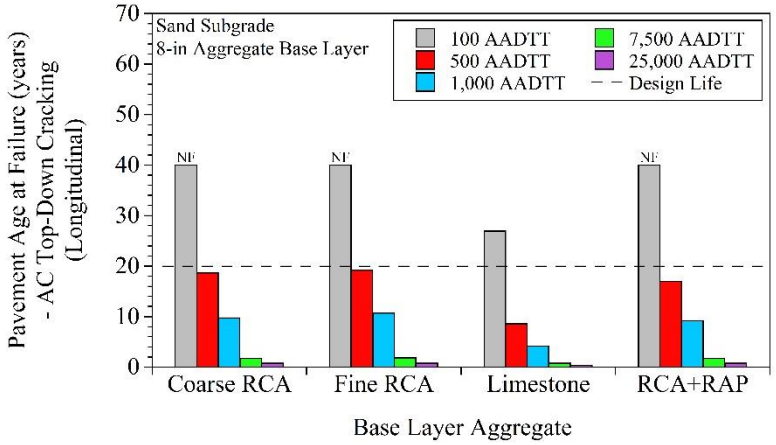
For pavements that contained sand subgrade and 8-in aggregate base:



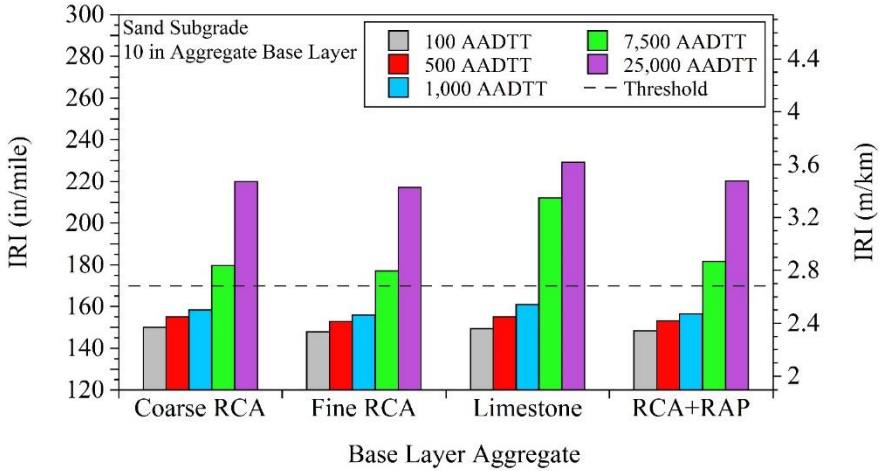

Sand Subgrade
8 in Aggregate Base Layer
100 AADTT
500 AADTT
1,000 AADTT
7,500 AADTT
25,000 AADTT
Threshold
AC Bottom-Up Cracking
(Alligator) (% Lane Area)
Coarse RCA
Fine RCA
Limestone
RCA+RAP
Base Layer Aggregate

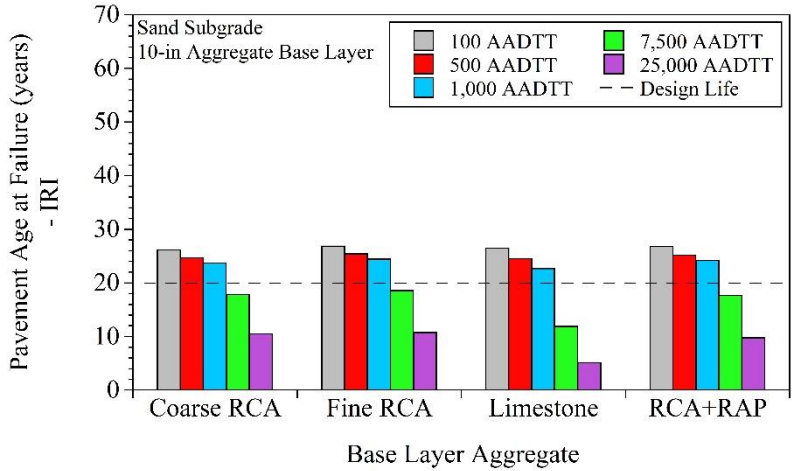

Sand Subgrade
8-in Aggregate Base Layer
100 AADTT
500 AADTT
1,000 AADTT
7,500 AADTT
25,000 AADTT
Design Life
NF
Pavement Age at Failure (years)
- AC Bottom-Up Cracking
(Alligator)
Coarse RCA
Fine RCA
Limestone
RCA+RAP
Base Layer Aggregate

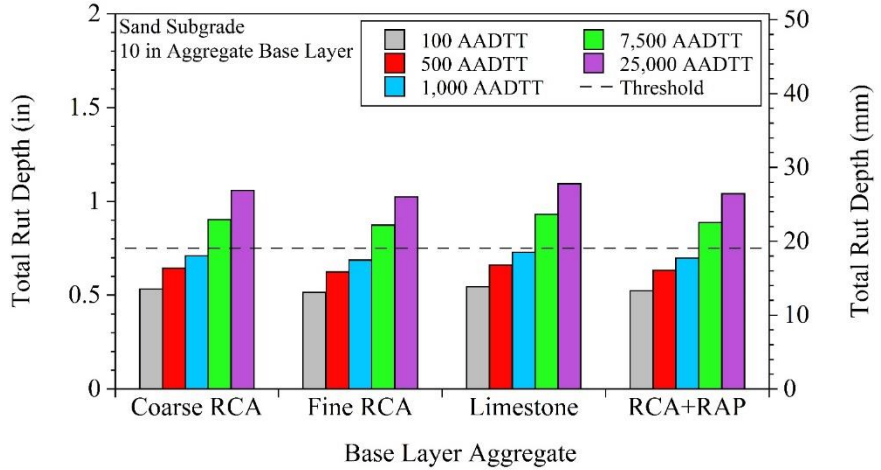

Sand Subgrade
8 in Aggregate Base Layer
100 AADTT
500 AADTT
1,000 AADTT
7,500 AADTT
25,000 AADTT
Threshold
AC Top-Down Cracking
(Longitudinal) (ft/mile)
AC Top-Down Cracking
(Longitudinal) (m/km)
Coarse RCA
Fine RCA
Limestone
RCA+RAP
Base Layer Aggregate

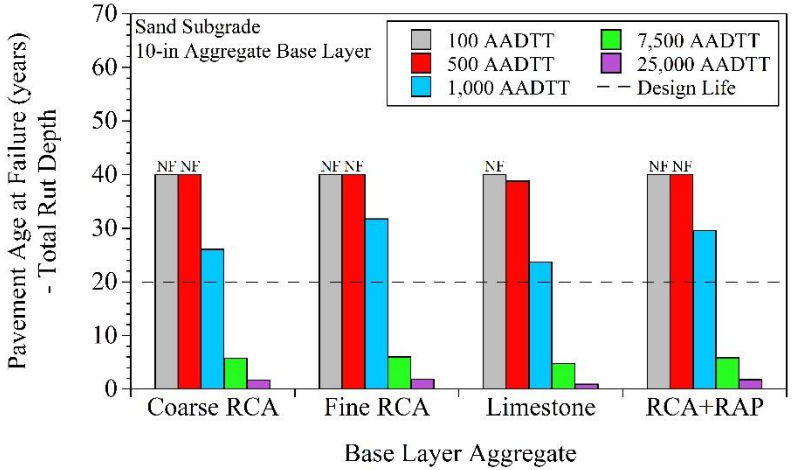

Sand Subgrade
8-in Aggregate Base Layer
100 AADTT
500 AADTT
1,000 AADTT
7,500 AADTT
25,000 AADTT
Design Life
NF
Pavement Age at Failure (years)
- AC Top-Down Cracking
(Longitudinal)
Coarse RCA
Fine RCA
Limestone
RCA+RAP
Base Layer Aggregate

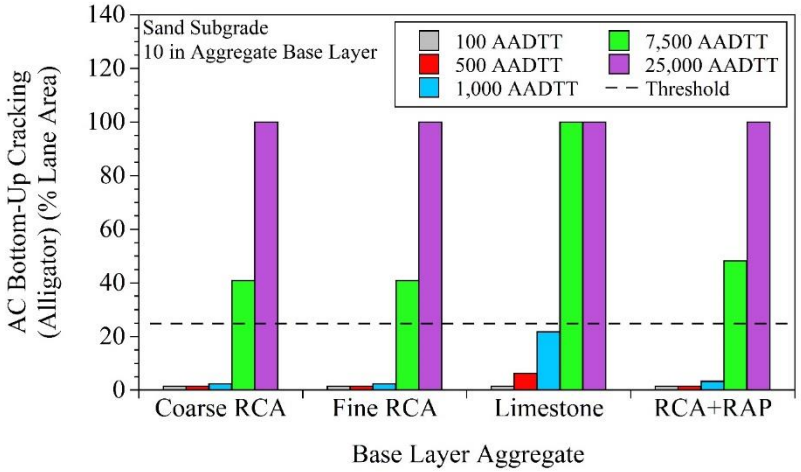
For pavements that contained sand subgrade and 10-in aggregate base:

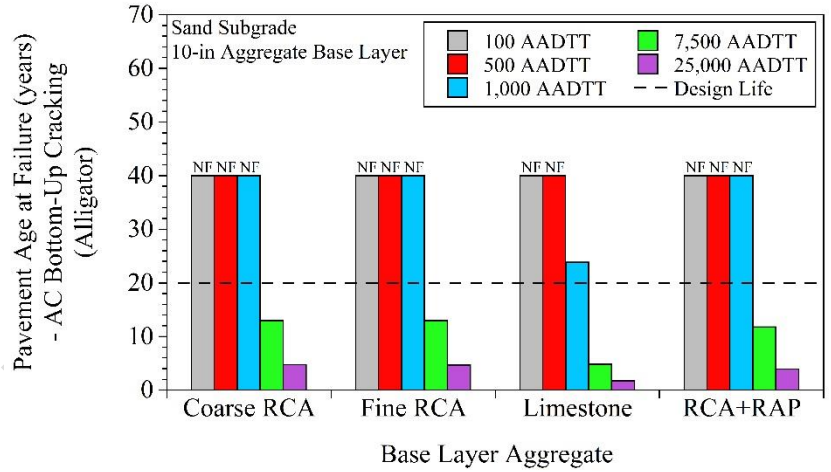


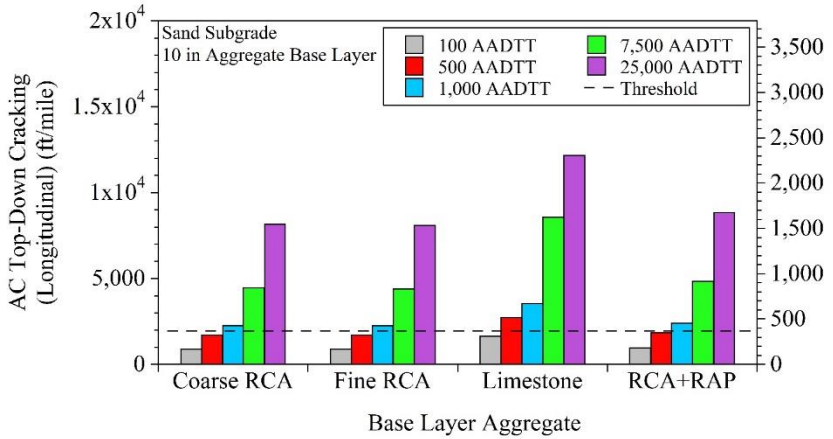


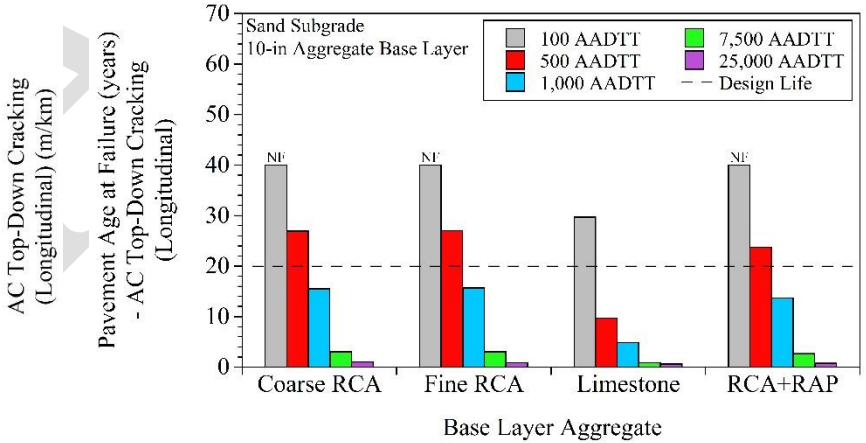




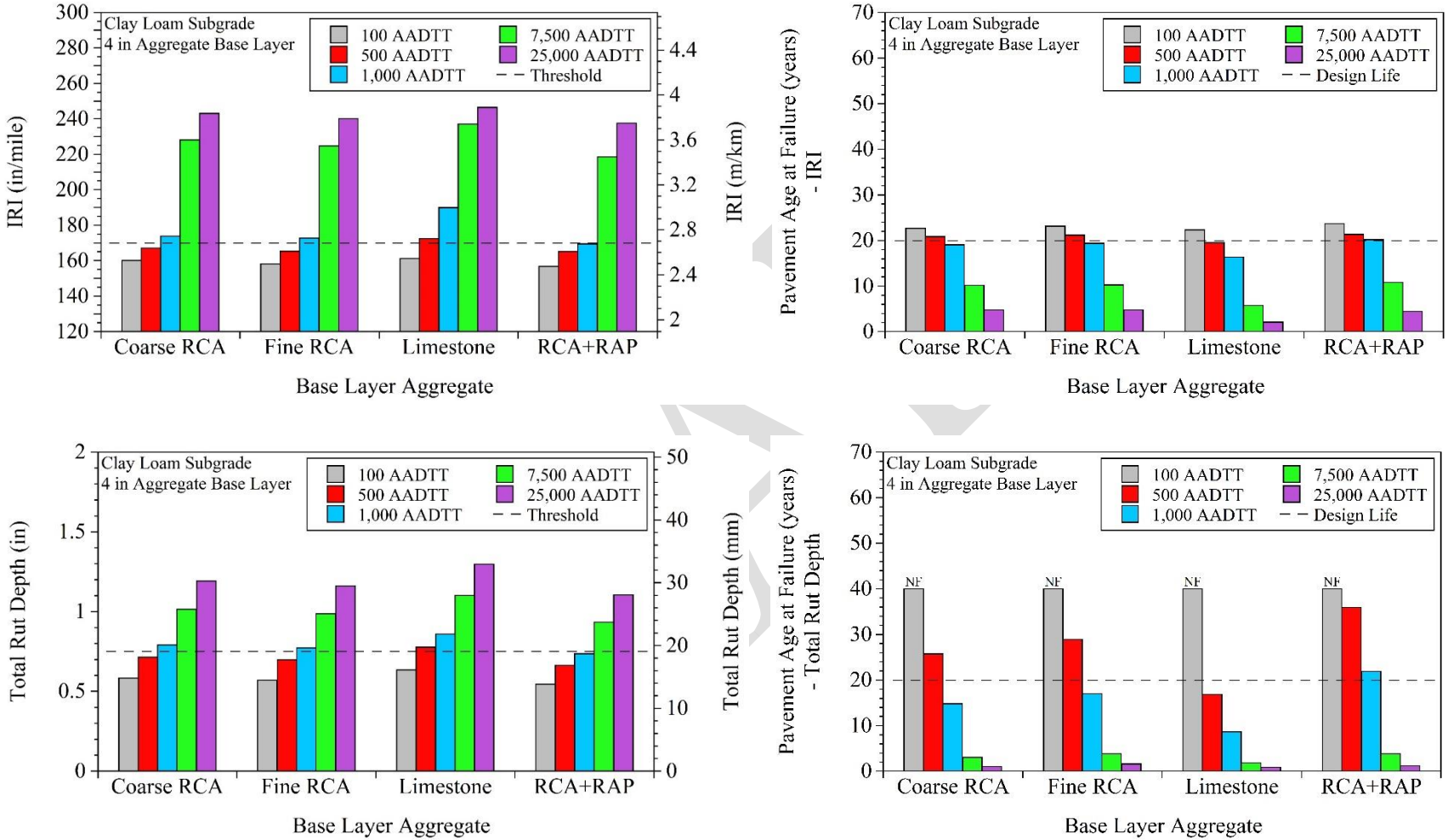

Sand Subgrade
10 in Aggregate Base Layer
100 AADTT
500 AADTT
1,000 AADTT
7,500 AADTT
25,000 AADTT
Threshold
AC Bottom-Up Cracking (Alligator) (% Lane Area)
0
20
40
60
80
100
120
140
Coarse RCA
Fine RCA
Limestone
RCA+RAP
Base Layer Aggregate

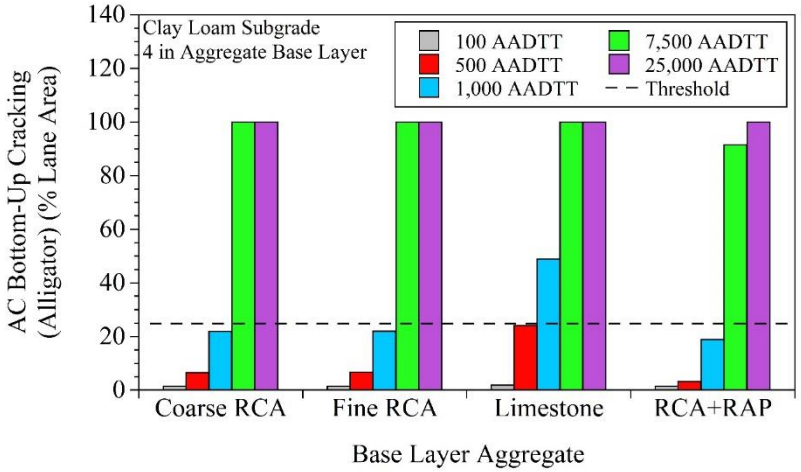

Sand Subgrade
10-in Aggregate Base Layer
100 AADTT
500 AADTT
1,000 AADTT
7,500 AADTT
25,000 AADTT
Design Life
Pavement Age at Failure (years) - AC Bottom-Up Cracking (Alligator)
NF NF NF
NF NF NF
NF NF
NF NF NF
0
10
20
30
40
50
60
70
Coarse RCA
Fine RCA
Limestone
RCA+RAP
Base Layer Aggregate

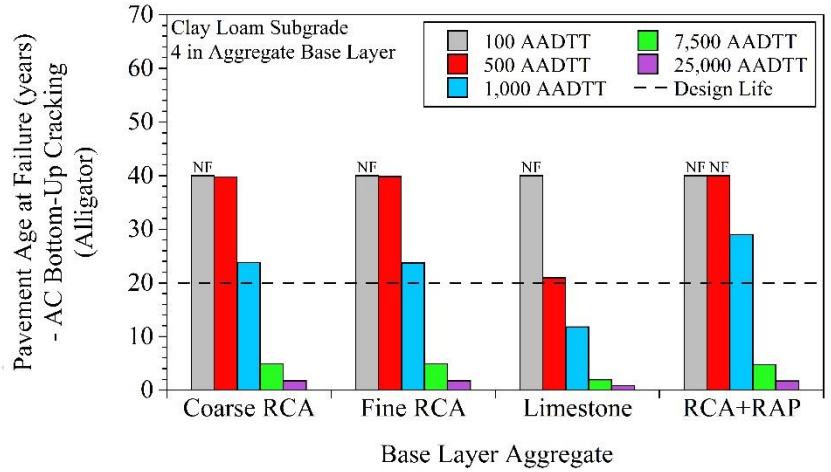

Sand Subgrade
10 in Aggregate Base Layer
100 AADTT
500 AADTT
1,000 AADTT
7,500 AADTT
25,000 AADTT
Threshold
AC Top-Down Cracking (Longitudinal) (ft/mile)
0
5,000
1x10^4
1.5x10^4
2x10^4
AC Top-Down Cracking (Longitudinal) (m/km)
0
500
1,000
1,500
2,000
2,500
3,000
3,500
Coarse RCA
Fine RCA
Limestone
RCA+RAP
Base Layer Aggregate


Sand Subgrade
10-in Aggregate Base Layer
100 AADTT
500 AADTT
1,000 AADTT
7,500 AADTT
25,000 AADTT
Design Life
Pavement Age at Failure (years) - AC Top-Down Cracking (Longitudinal)
NF
NF
NF
0
10
20
30
40
50
60
70
Coarse RCA
Fine RCA
Limestone
RCA+RAP
Base Layer Aggregate

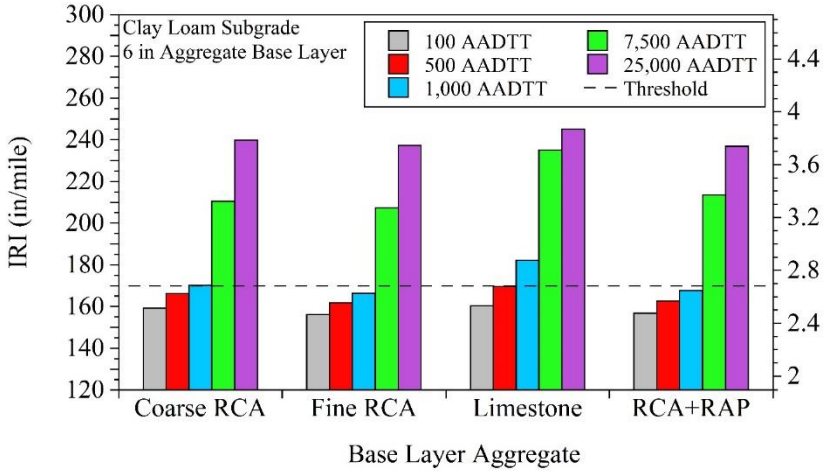
For pavements that contained clay loam subgrade and 4-in aggregate base:

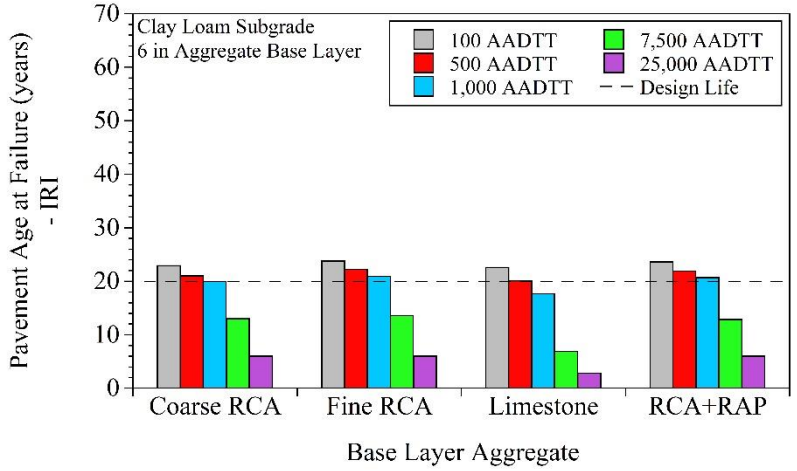


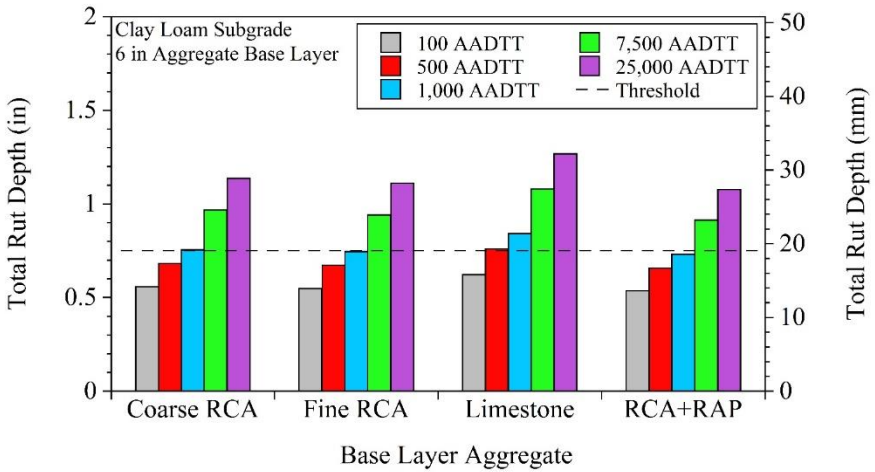


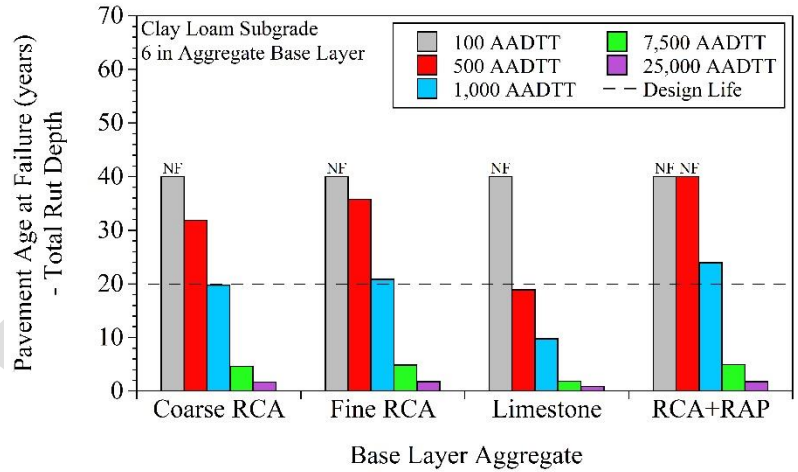


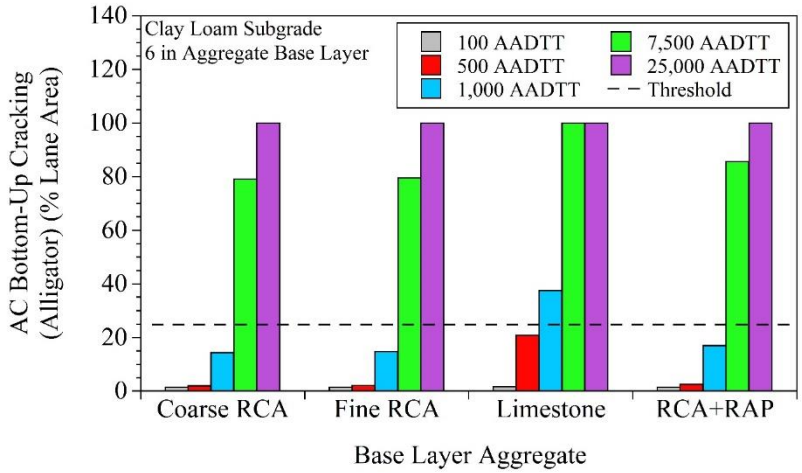
For pavements that contained clay loam subgrade and 6-in aggregate base:

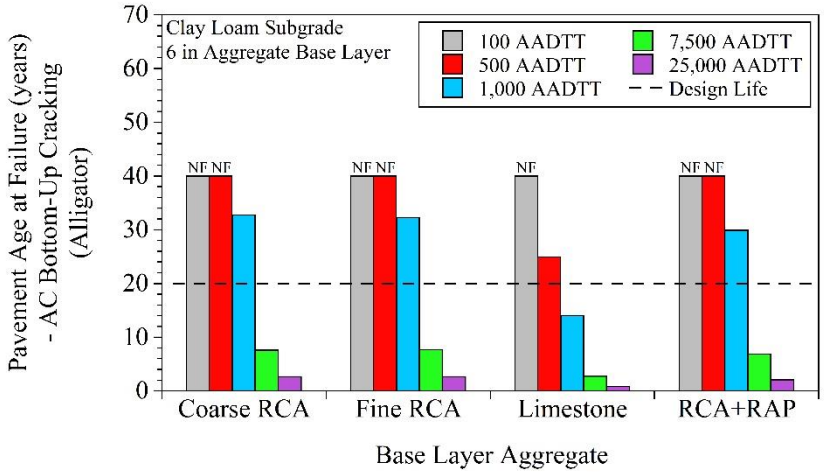




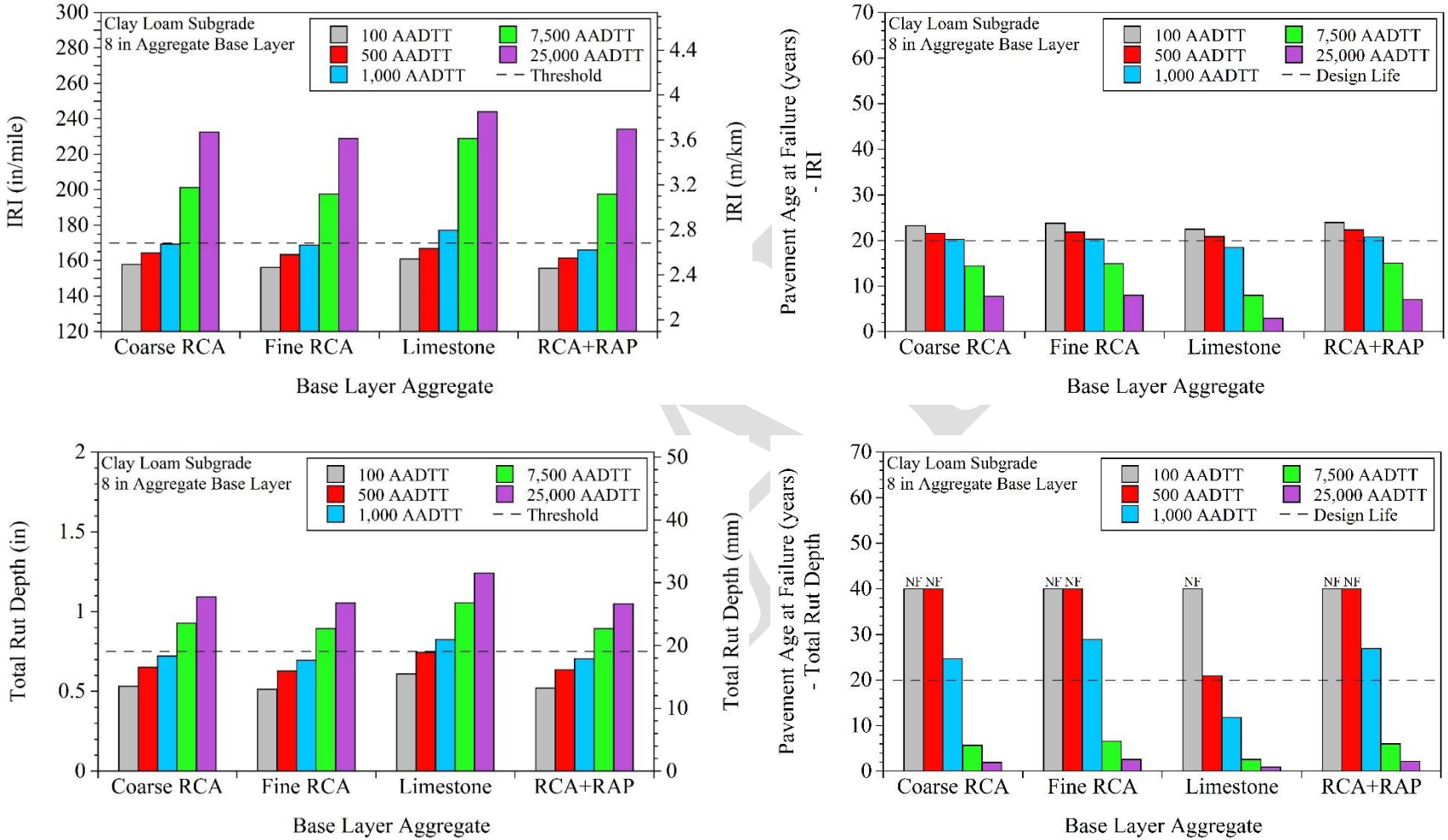

Clay Loam Subgrade
6 in Aggregate Base Layer
100 AADTT
500 AADTT
1,000 AADTT
7,500 AADTT
25,000 AADTT
Threshold
Total Rut Depth (in)
Total Rut Depth (mm)
Coarse RCA
Fine RCA
Limestone
RCA+RAP
Base Layer Aggregate

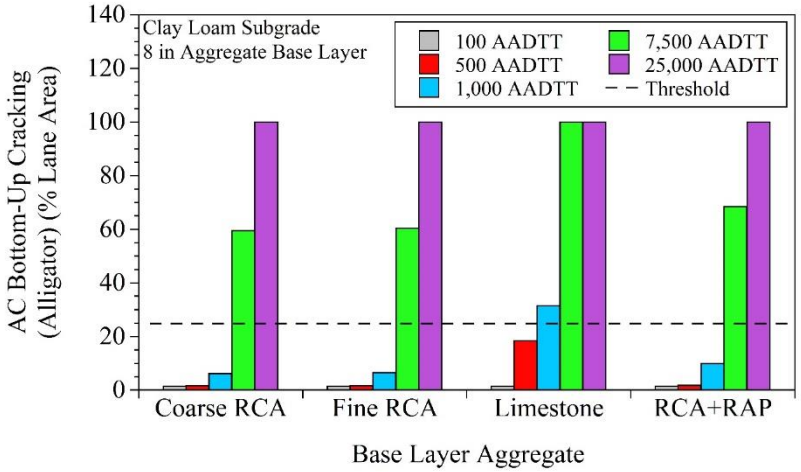

Clay Loam Subgrade
6 in Aggregate Base Layer
100 AADTT
500 AADTT
1,000 AADTT
7,500 AADTT
25,000 AADTT
Design Life
Pavement Age at Failure (years)
- Total Rut Depth
NF
Coarse RCA
Fine RCA
Limestone
RCA+RAP
Base Layer Aggregate

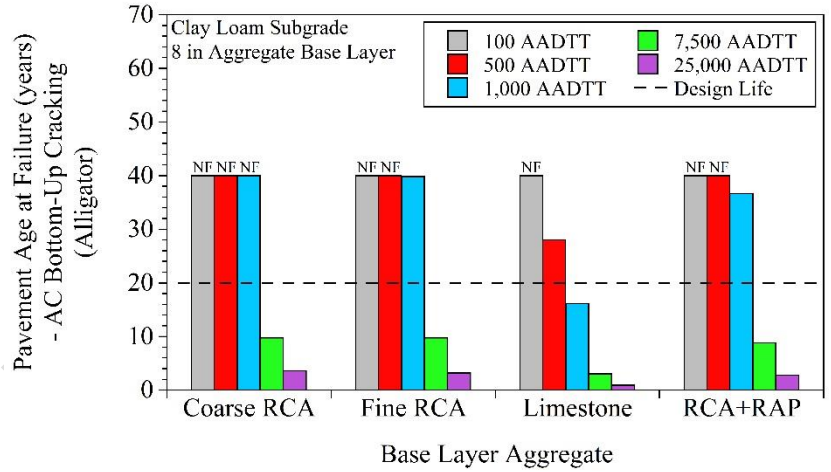

Clay Loam Subgrade
6 in Aggregate Base Layer
100 AADTT
500 AADTT
1,000 AADTT
7,500 AADTT
25,000 AADTT
Threshold
AC Bottom-Up Cracking
(Alligator) (% Lane Area)
Coarse RCA
Fine RCA
Limestone
RCA+RAP
Base Layer Aggregate


Clay Loam Subgrade
6 in Aggregate Base Layer
100 AADTT
500 AADTT
1,000 AADTT
7,500 AADTT
25,000 AADTT
Design Life
Pavement Age at Failure (years)
- AC Bottom-Up Cracking
(Alligator)
NF
Coarse RCA
Fine RCA
Limestone
RCA+RAP
Base Layer Aggregate

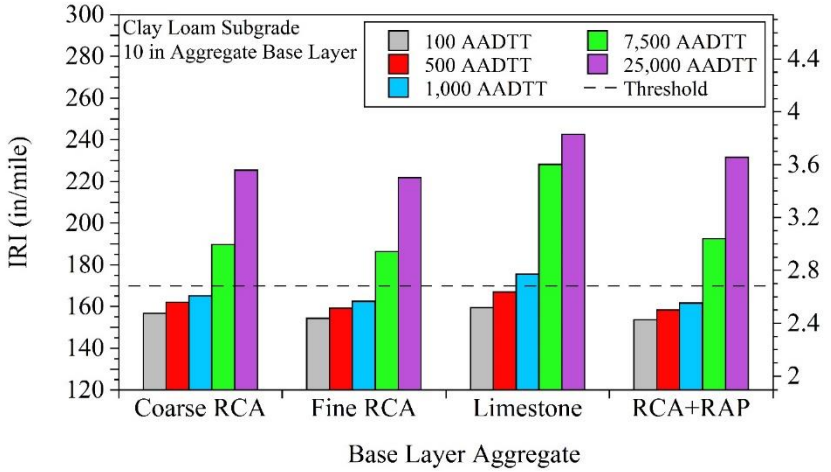
For pavements that contained clay loam subgrade and 8-in aggregate base:

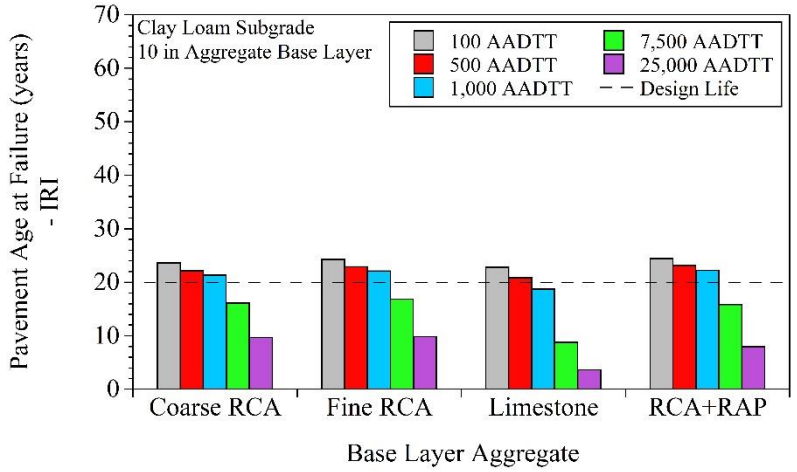


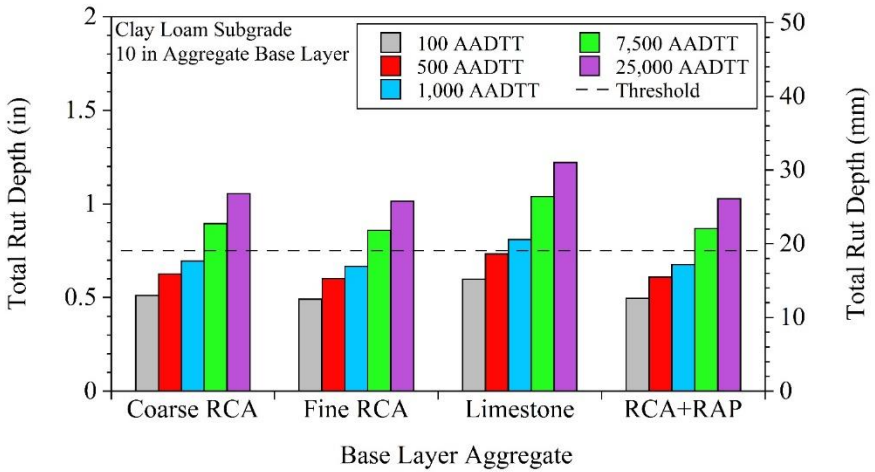


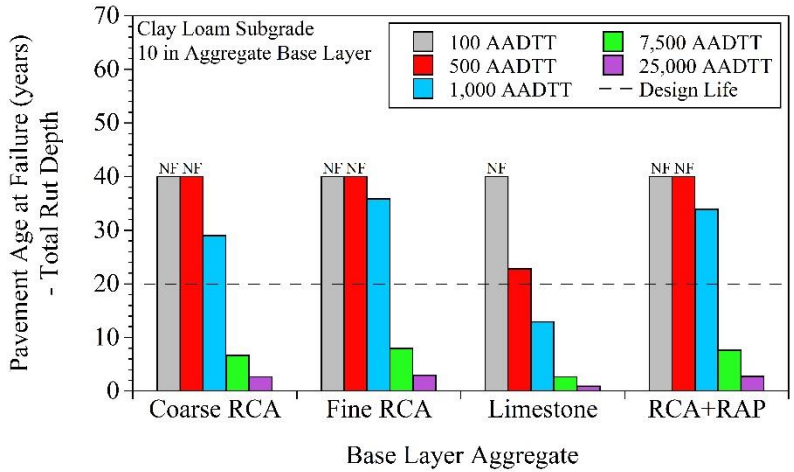


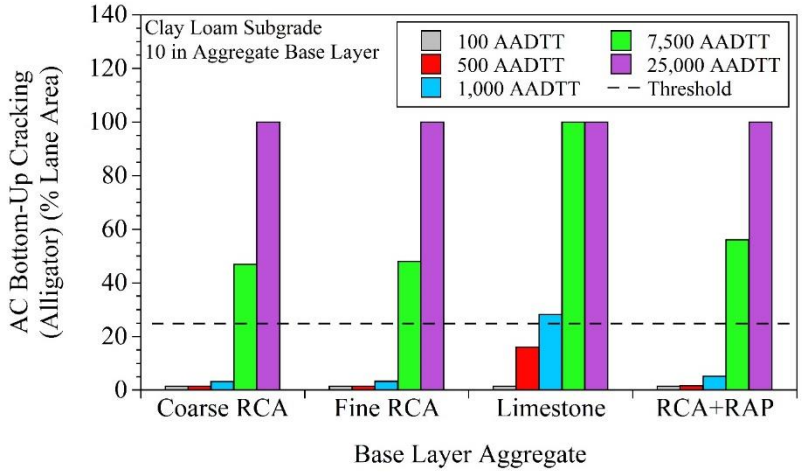
For pavements that contained clay loam subgrade and 10-in aggregate base:

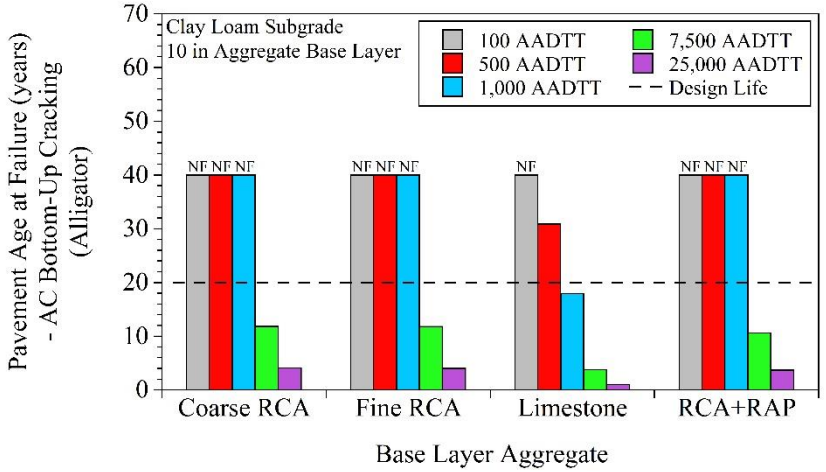




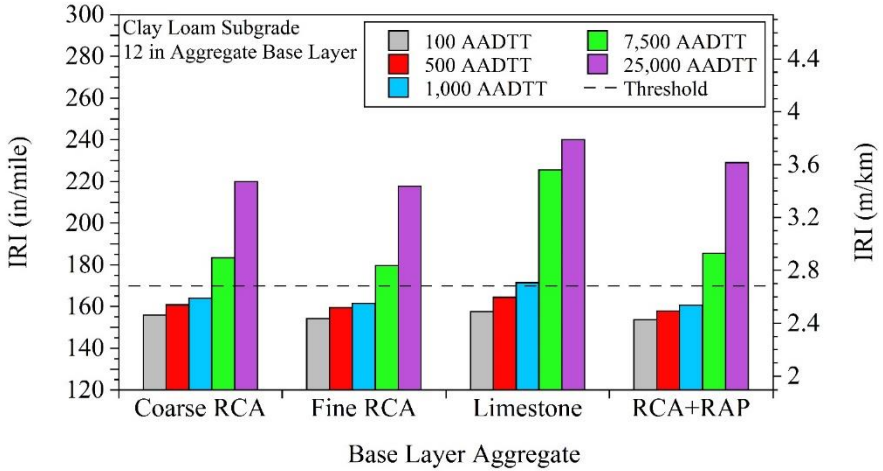

Clay Loam Subgrade
10 in Aggregate Base Layer
100 AADTT
500 AADTT
1,000 AADTT
7,500 AADTT
25,000 AADTT
Threshold
Total Rut Depth (in)
Total Rut Depth (mm)
Coarse RCA
Fine RCA
Limestone
RCA+RAP
Base Layer Aggregate

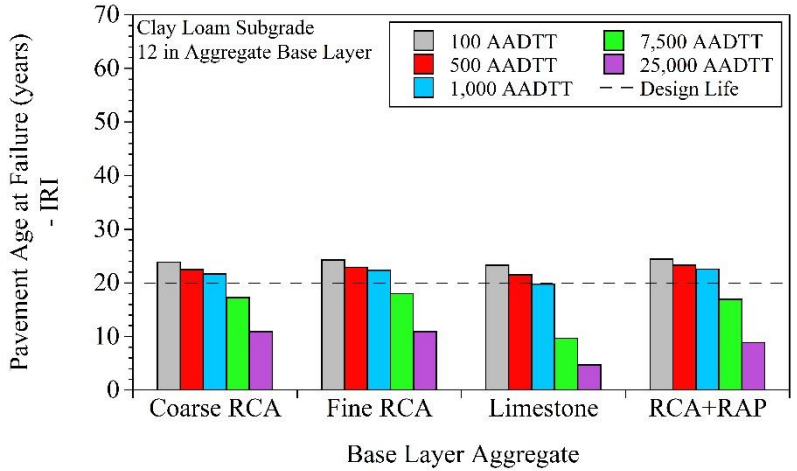

Clay Loam Subgrade
10 in Aggregate Base Layer
100 AADTT
500 AADTT
1,000 AADTT
7,500 AADTT
25,000 AADTT
Design Life
NF
Pavement Age at Failure (years)
- Total Rut Depth
Coarse RCA
Fine RCA
Limestone
RCA+RAP
Base Layer Aggregate

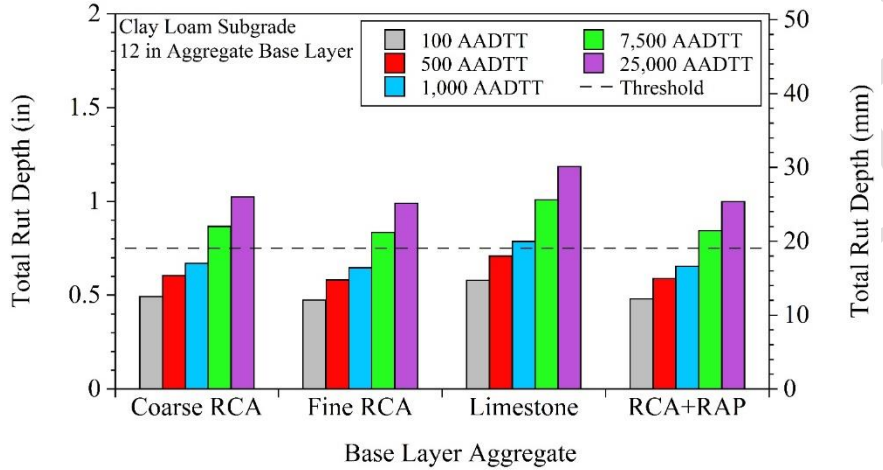

Clay Loam Subgrade
10 in Aggregate Base Layer
100 AADTT
500 AADTT
1,000 AADTT
7,500 AADTT
25,000 AADTT
Threshold
AC Bottom-Up Cracking
(Alligator) (% Lane Area)
Coarse RCA
Fine RCA
Limestone
RCA+RAP
Base Layer Aggregate

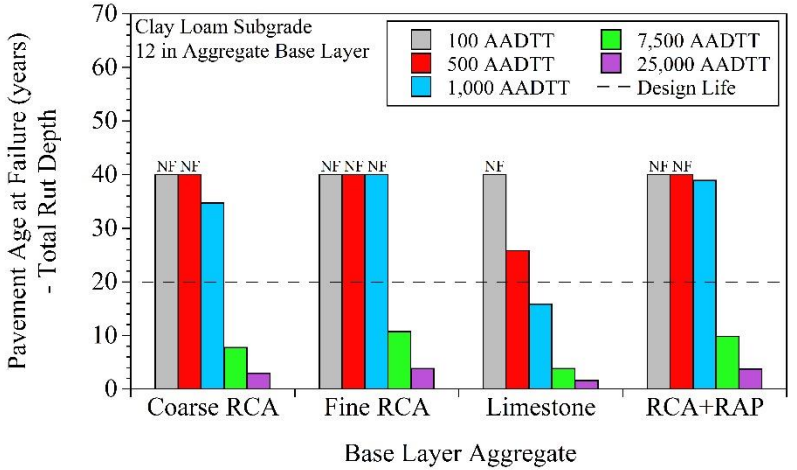

Clay Loam Subgrade
10 in Aggregate Base Layer
100 AADTT
500 AADTT
1,000 AADTT
7,500 AADTT
25,000 AADTT
Design Life
NF
Pavement Age at Failure (years)
- AC Bottom-Up Cracking
(Alligator)
Coarse RCA
Fine RCA
Limestone
RCA+RAP
Base Layer Aggregate

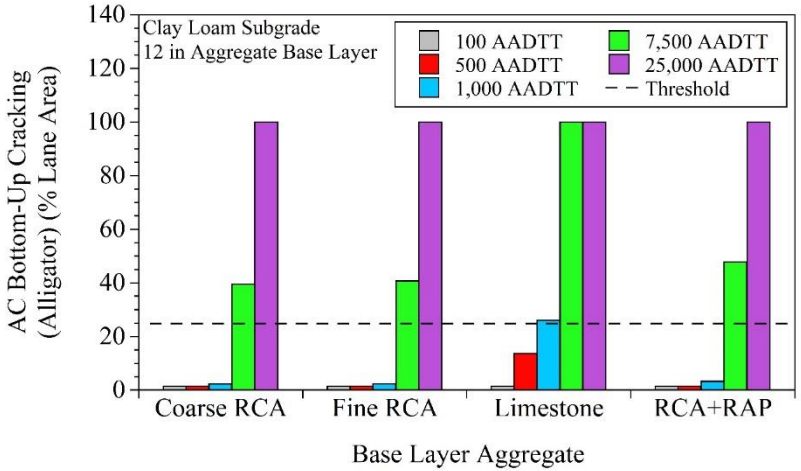
For pavements that contained clay loam subgrade and 12-in aggregate base:

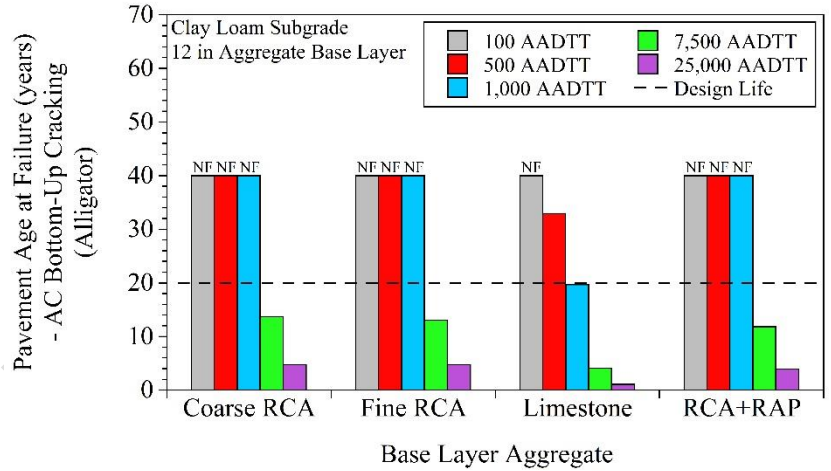








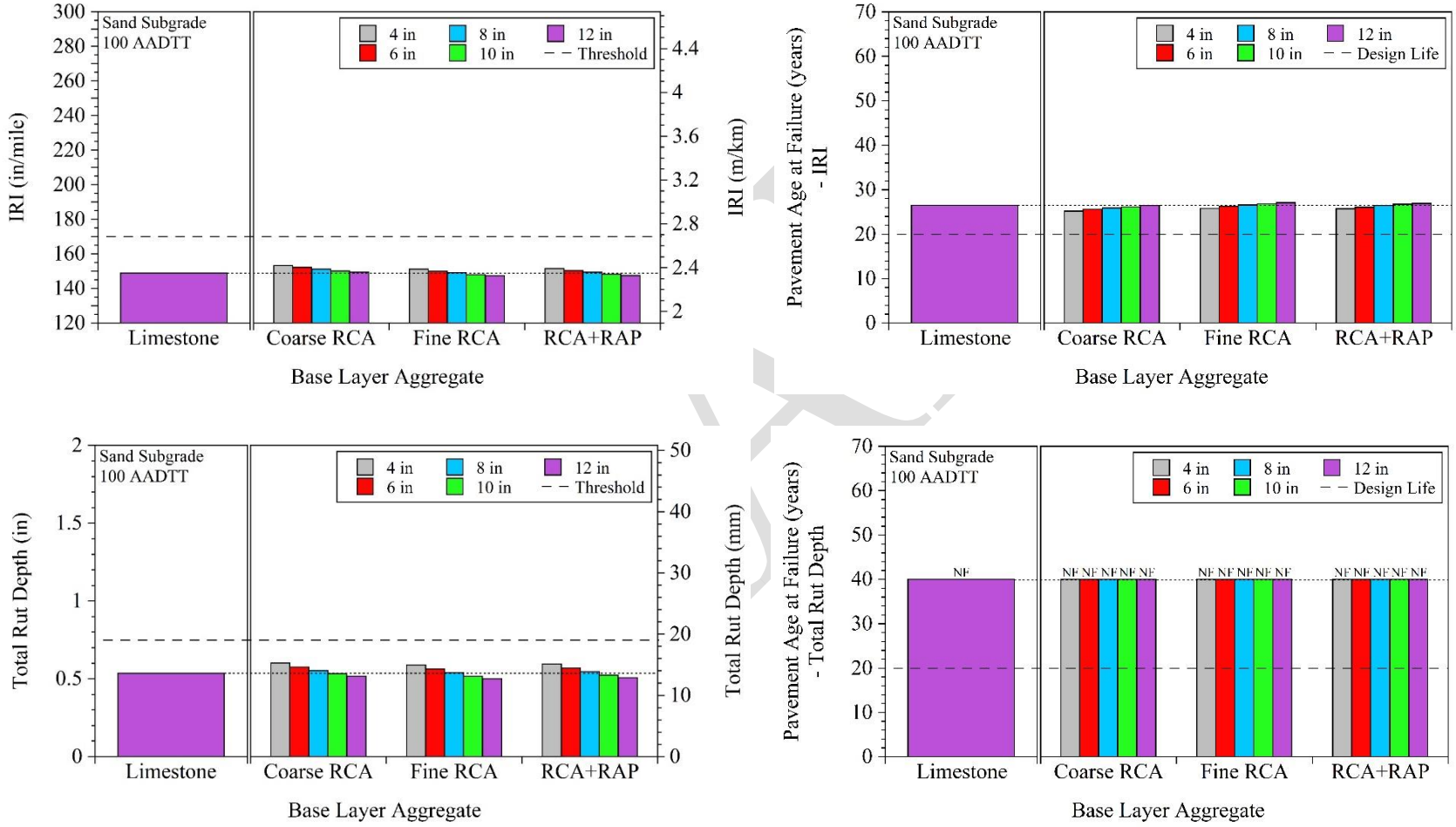

Clay Loam Subgrade
12 in Aggregate Base Layer
100 AADTT
500 AADTT
1,000 AADTT
7,500 AADTT
25,000 AADTT
Threshold
AC Bottom-Up Cracking
(Alligator) (% Lane Area)
0
20
40
60
80
100
120
140
Coarse RCA
Fine RCA
Limestone
RCA+RAP
Base Layer Aggregate

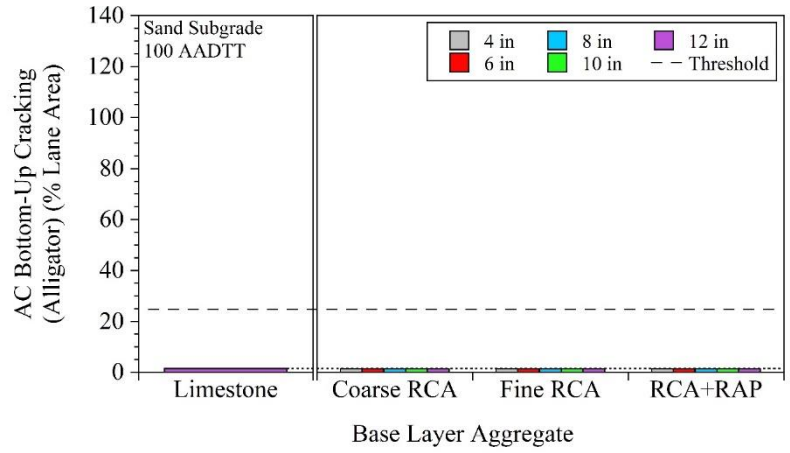

Clay Loam Subgrade
12 in Aggregate Base Layer
100 AADTT
500 AADTT
1,000 AADTT
7,500 AADTT
25,000 AADTT
Design Life
Pavement Age at Failure (years)
- AC Bottom-Up Cracking
(Alligator)
0
10
20
30
40
50
60
70
NF NF NF
NF NF NF
NF
NF NF NF
Coarse RCA
Fine RCA
Limestone
RCA+RAP
Base Layer Aggregate

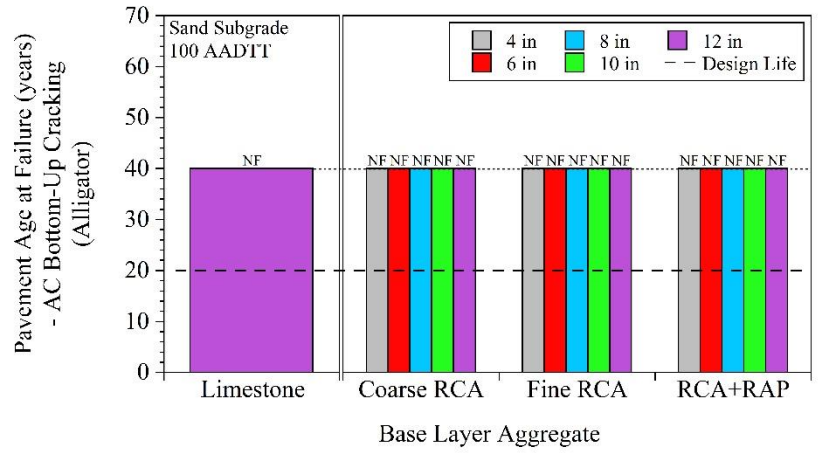
DRAFT

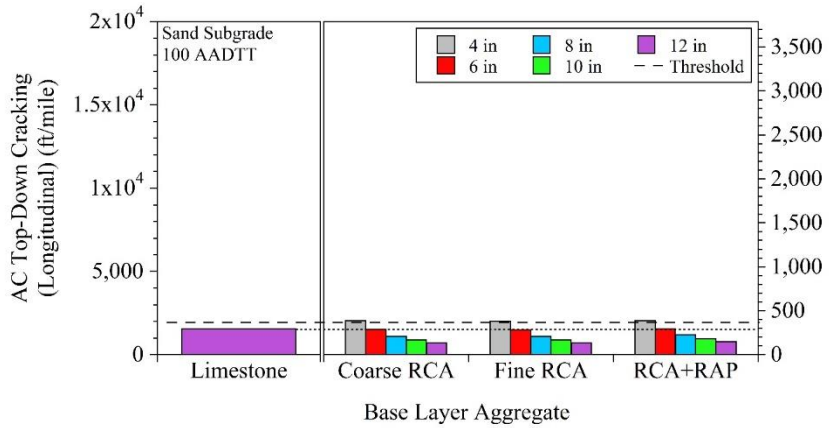
APPENDIX Y. RELATIVE AGGREGATE BASE LAYER THICKNESS

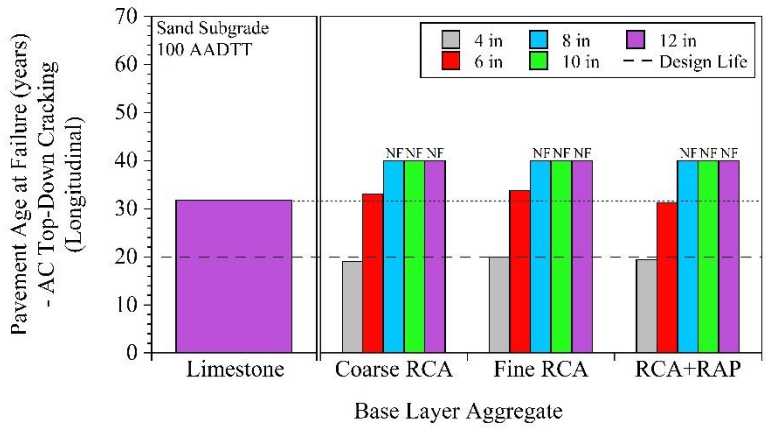
For pavements that contained sand subgrade – 100 AADTT:



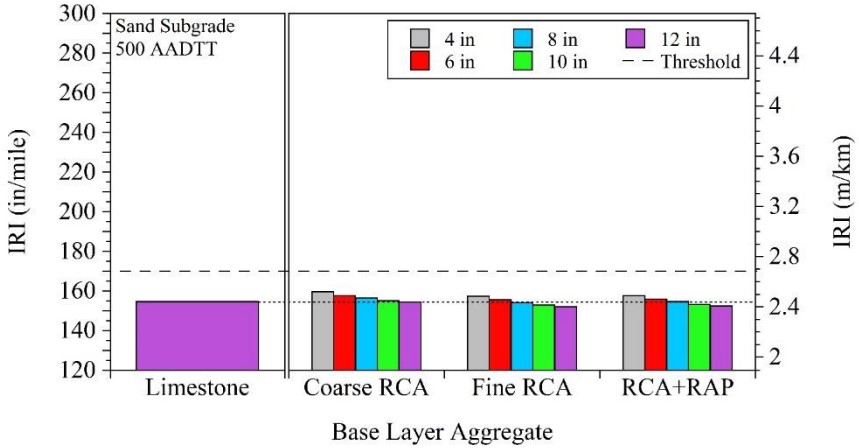

Sand Subgrade
100 AADTT
4 in
6 in
8 in
10 in
12 in
Threshold
AC Bottom-Up Cracking
(Alligator) (% Lane Area)
0
20
40
60
80
100
120
140
Limestone
Coarse RCA
Fine RCA
RCA+RAP
Base Layer Aggregate

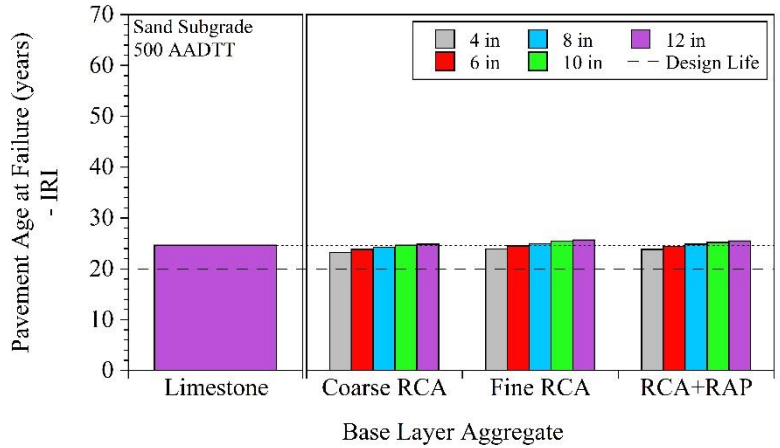

Sand Subgrade
100 AADTT
4 in
6 in
8 in
10 in
12 in
Design Life
Pavement Age at Failure (years)
- AC Bottom-Up Cracking
(Alligator)
0
10
20
30
40
50
60
70
NF
NF NF NF NF NF
NF NF NF NF NF
NF NF NF NF NF
Limestone
Coarse RCA
Fine RCA
RCA+RAP
Base Layer Aggregate

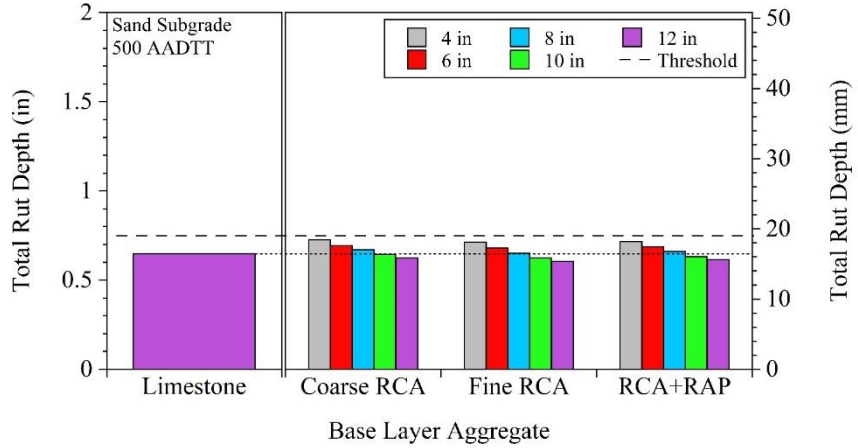

Sand Subgrade
100 AADTT
4 in
6 in
8 in
10 in
12 in
Threshold
AC Top-Down Cracking
(Longitudinal) (ft/mile)
0
5,000
1x10^4
1.5x10^4
2x10^4
AC Top-Down Cracking
(Longitudinal) (m/km)
0
500
1,000
1,500
2,000
2,500
3,000
3,500
Limestone
Coarse RCA
Fine RCA
RCA+RAP
Base Layer Aggregate

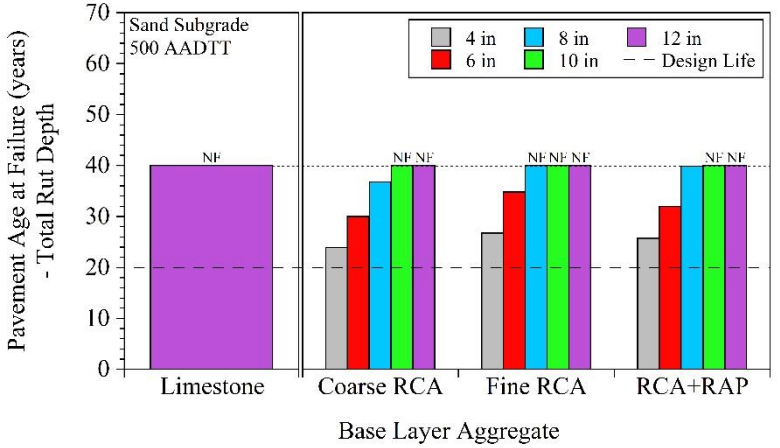

Sand Subgrade
100 AADTT
4 in
6 in
8 in
10 in
12 in
Design Life
Pavement Age at Failure (years)
- AC Top-Down Cracking
(Longitudinal)
0
10
20
30
40
50
60
70
NF NF NF
NF NF NF
NF NF NF
Limestone
Coarse RCA
Fine RCA
RCA+RAP
Base Layer Aggregate

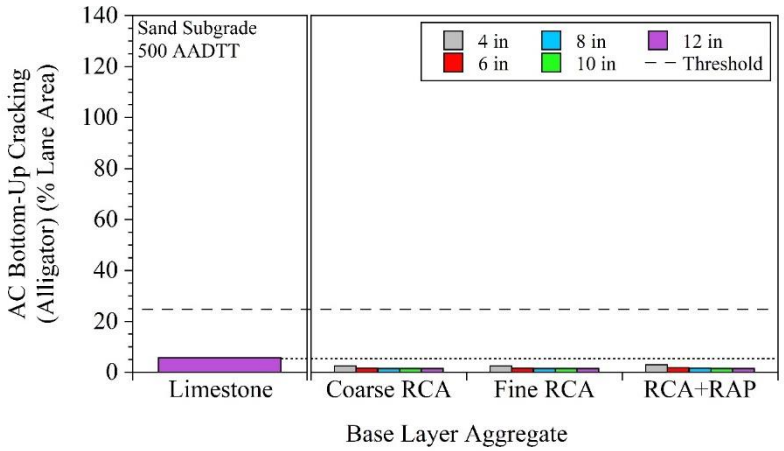
For pavements that contained sand subgrade – 500 AADTT:

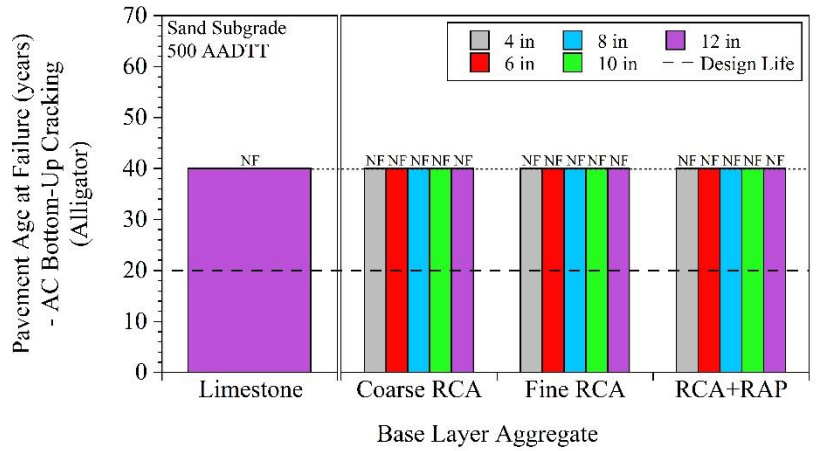


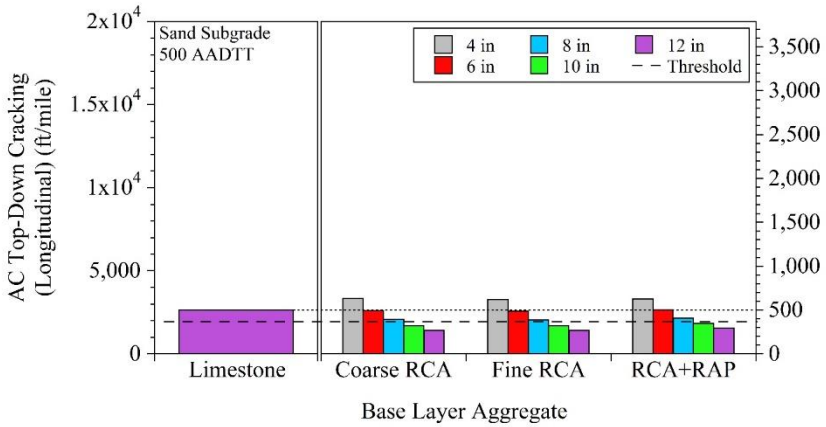


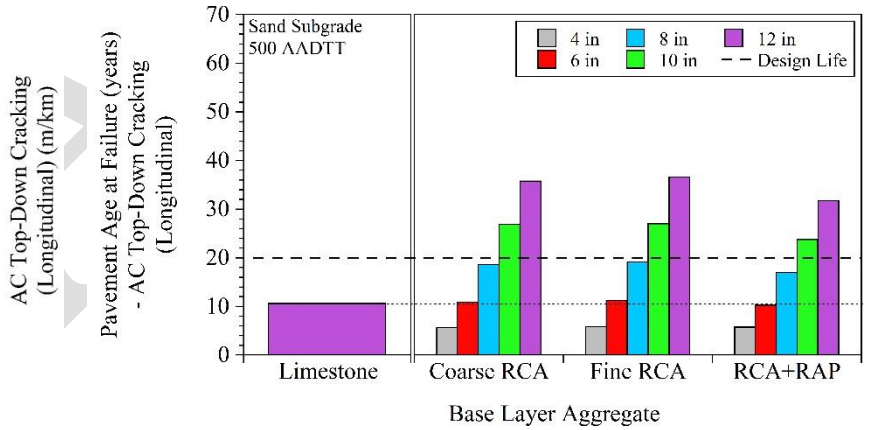




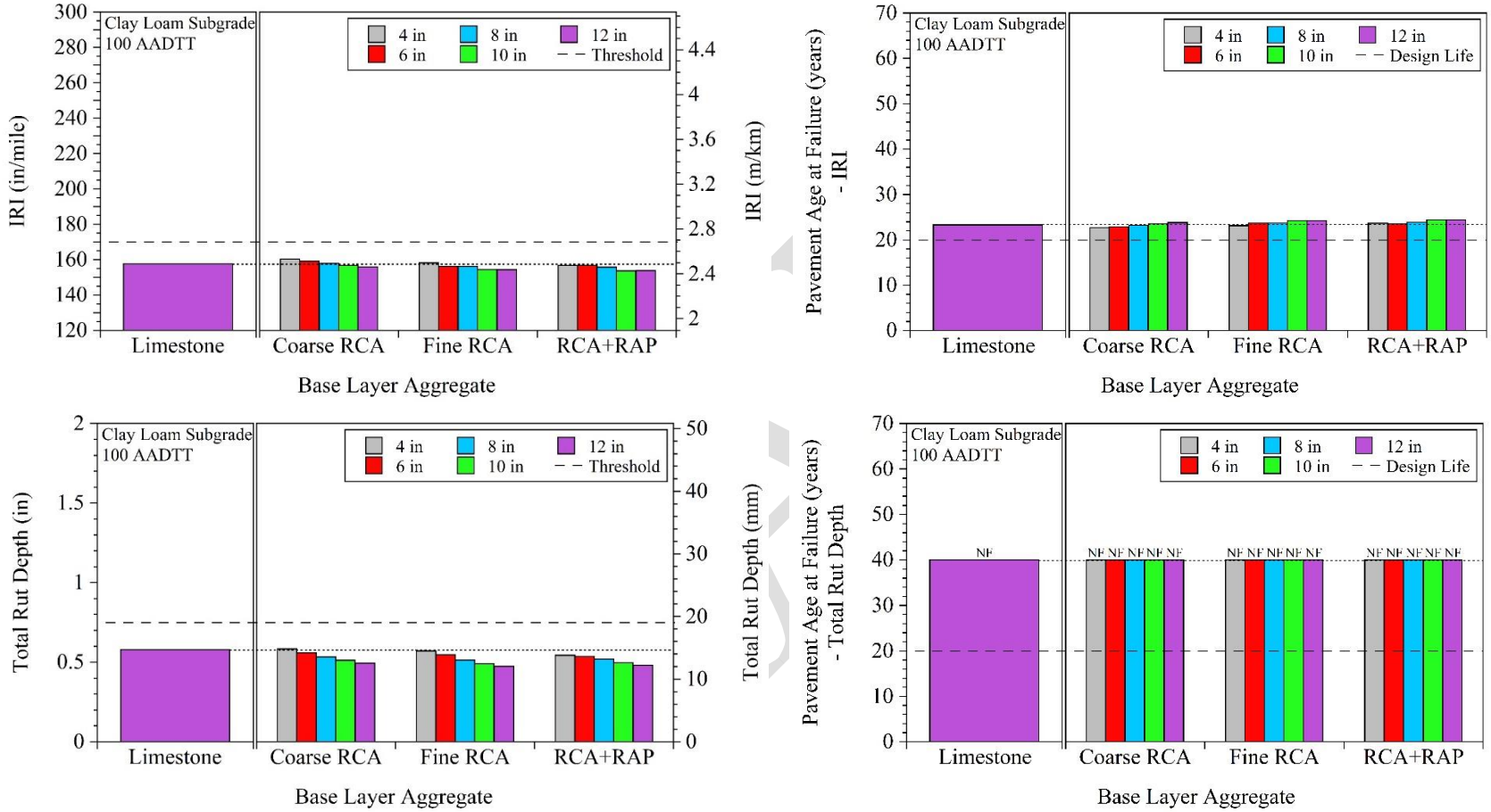

Sand Subgrade
500 AADTT
4 in
6 in
8 in
10 in
12 in
Threshold
AC Bottom-Up Cracking
(Alligator) (% Lane Area)
0
20
40
60
80
100
120
140
Limestone
Coarse RCA
Fine RCA
RCA+RAP
Base Layer Aggregate

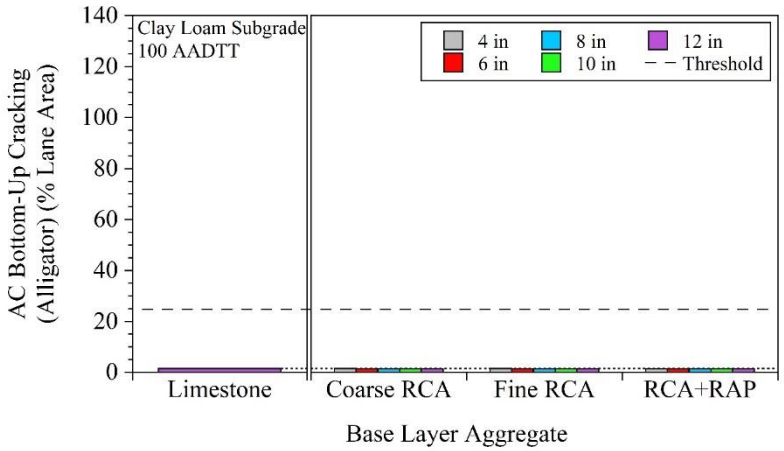

Sand Subgrade
500 AADTT
4 in
6 in
8 in
10 in
12 in
Design Life
Pavement Age at Failure (years)
- AC Bottom-Up Cracking
(Alligator)
0
10
20
30
40
50
60
70
NF
NF NF NF NF NF
NF NF NF NF NF
NF NF NF NF NF
Limestone
Coarse RCA
Fine RCA
RCA+RAP
Base Layer Aggregate

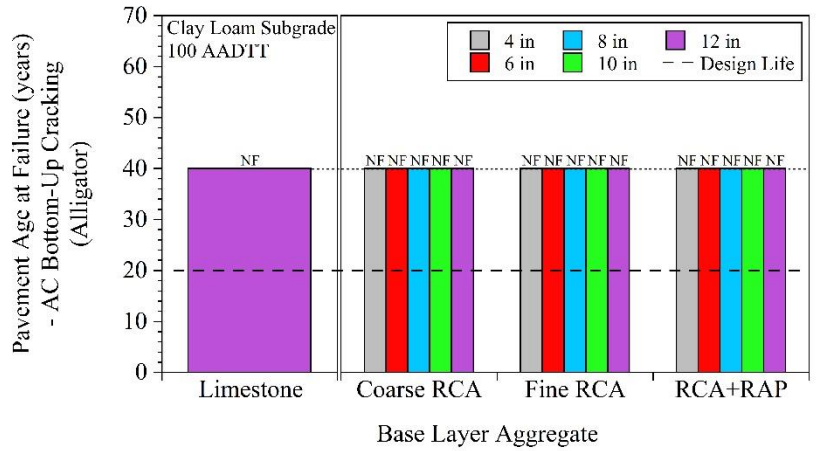

Sand Subgrade
500 AADTT
4 in
6 in
8 in
10 in
12 in
Threshold
AC Top-Down Cracking
(Longitudinal) (ft/mile)
0
5,000
1x10^4
1.5x10^4
2x10^4
0
500
1,000
1,500
2,000
2,500
3,000
3,500
Limestone
Coarse RCA
Fine RCA
RCA+RAP
Base Layer Aggregate


Sand Subgrade
500 AADTT
4 in
6 in
8 in
10 in
12 in
Design Life
AC Top-Down Cracking
(Longitudinal) (m/km)
Pavement Age at Failure (years)
- AC Top-Down Cracking
(Longitudinal)
0
10
20
30
40
50
60
70
Limestone
Coarse RCA
Fine RCA
RCA+RAP
Base Layer Aggregate

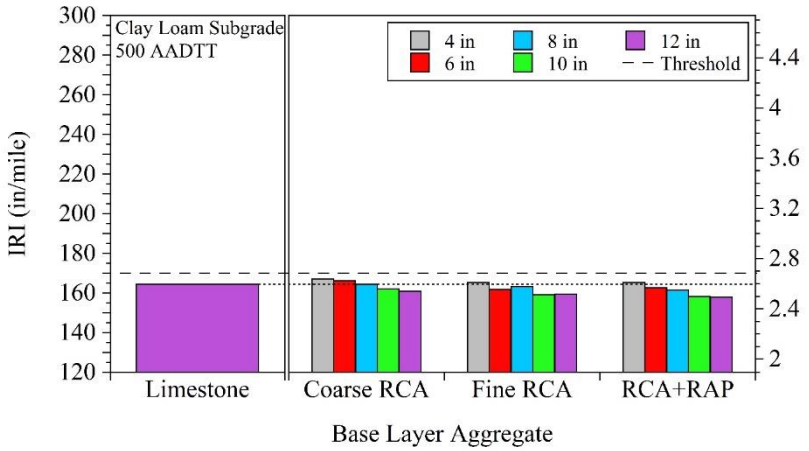
For pavements that contained clay loam subgrade – 100 AADTT:

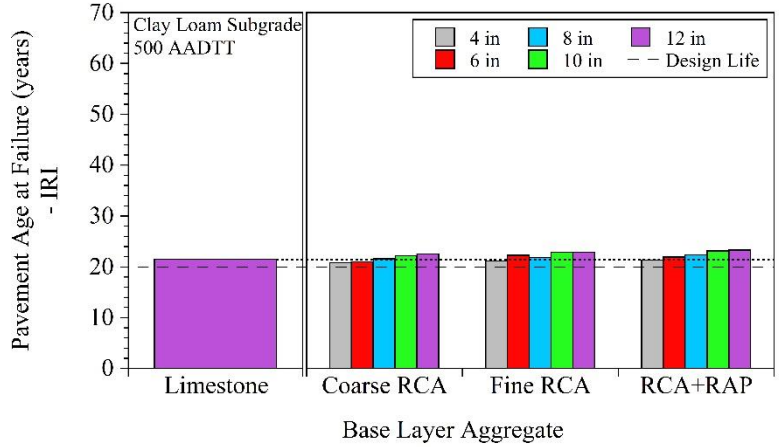


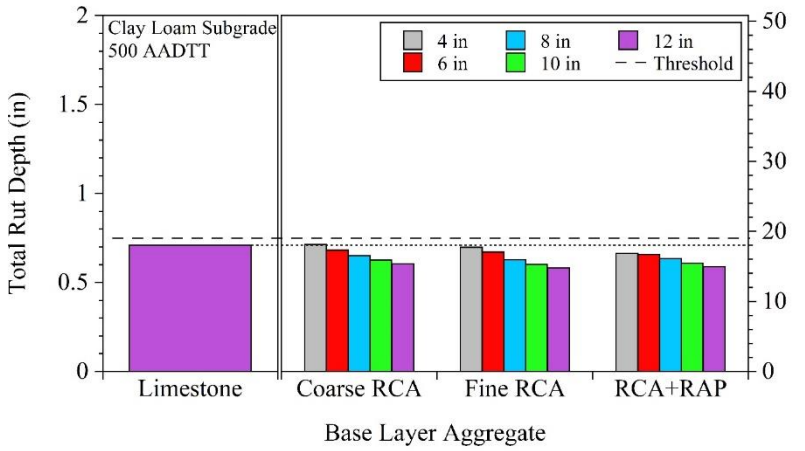


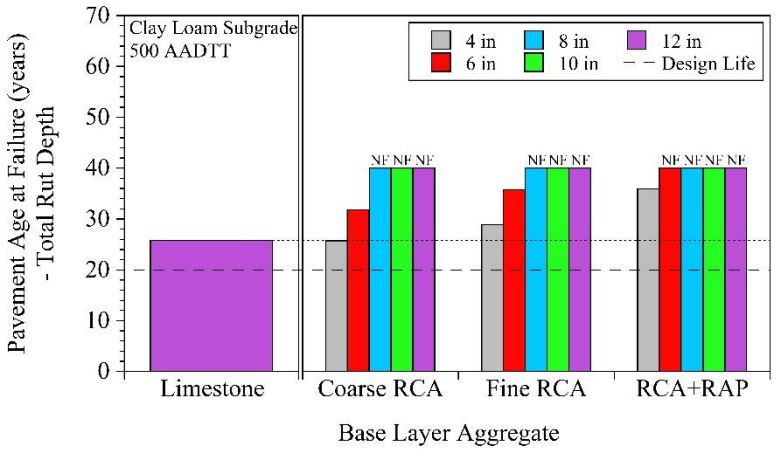


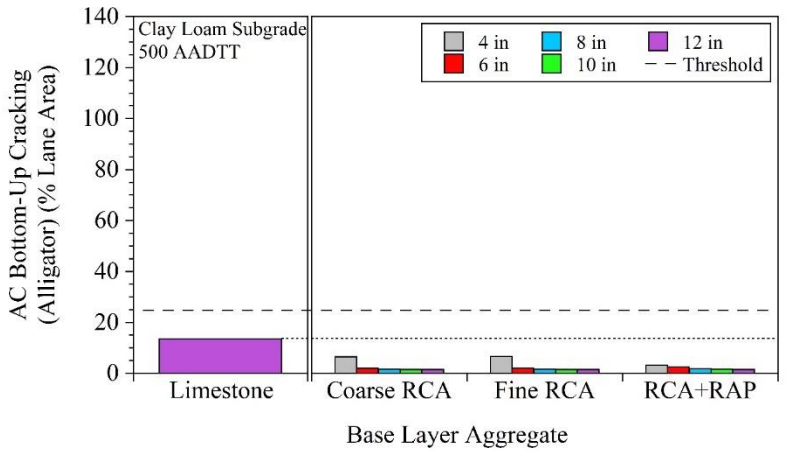
For pavements that contained clay loam subgrade – 500 AADTT:

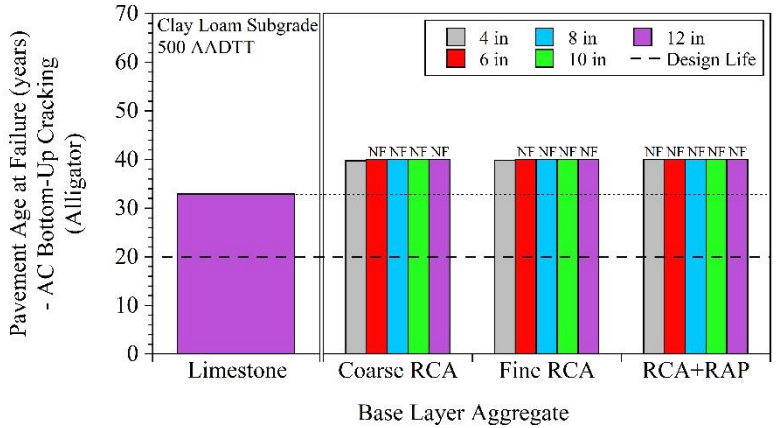




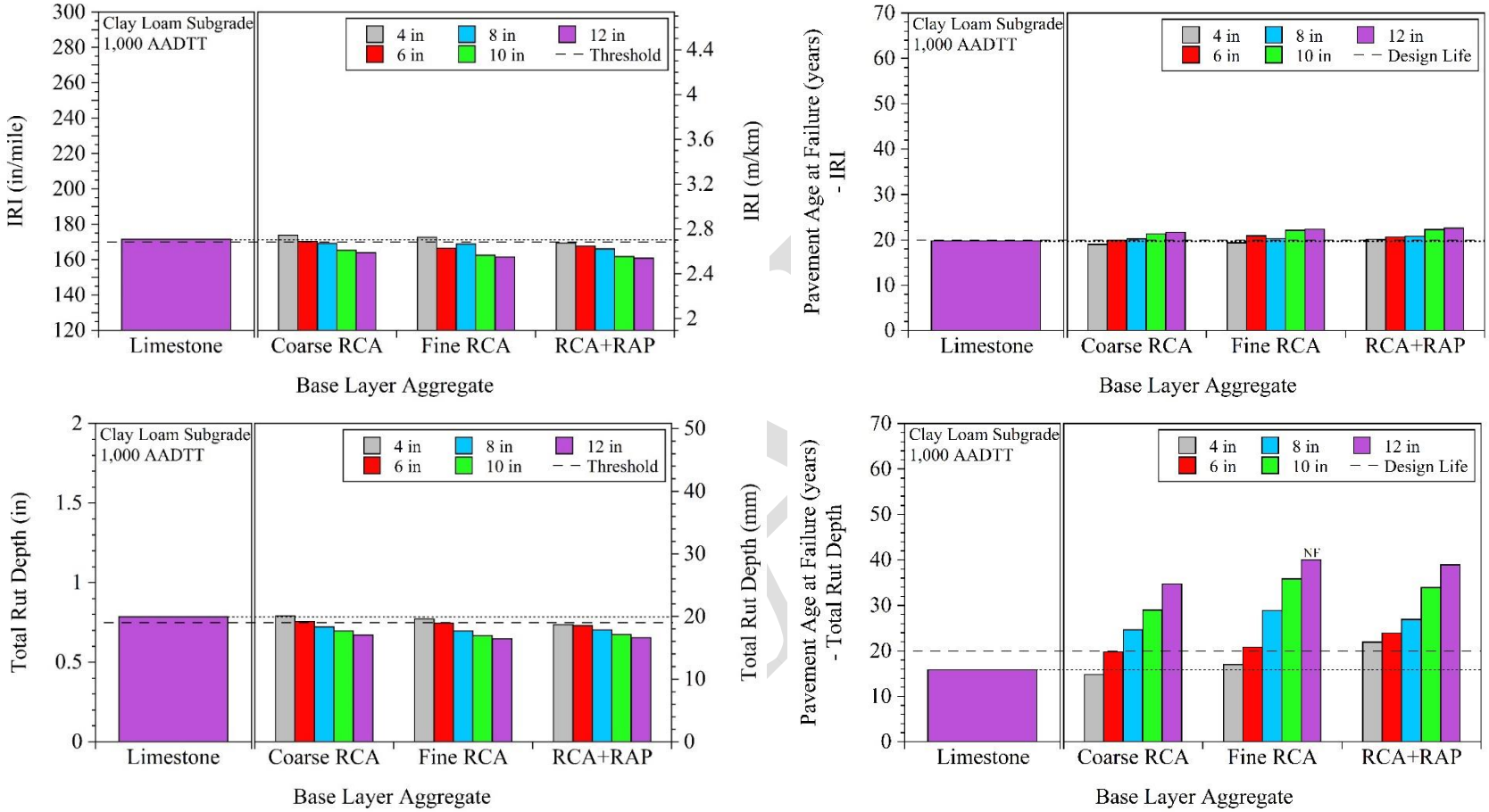

Clay Loam Subgrade
500 AADTT
4 in
6 in
8 in
10 in
12 in
Threshold
Total Rut Depth (in)
Total Rut Depth (mm)
Limestone
Coarse RCA
Fine RCA
RCA+RAP
Base Layer Aggregate

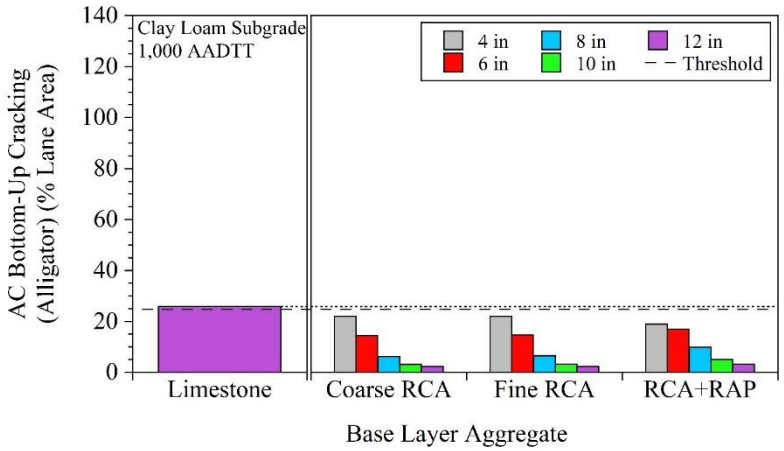

Clay Loam Subgrade
500 AADTT
4 in
6 in
8 in
10 in
12 in
Design Life
Pavement Age at Failure (years)
- Total Rut Depth
NF NF NF
NF NF NF
NF NF NF NF
Limestone
Coarse RCA
Fine RCA
RCA+RAP
Base Layer Aggregate

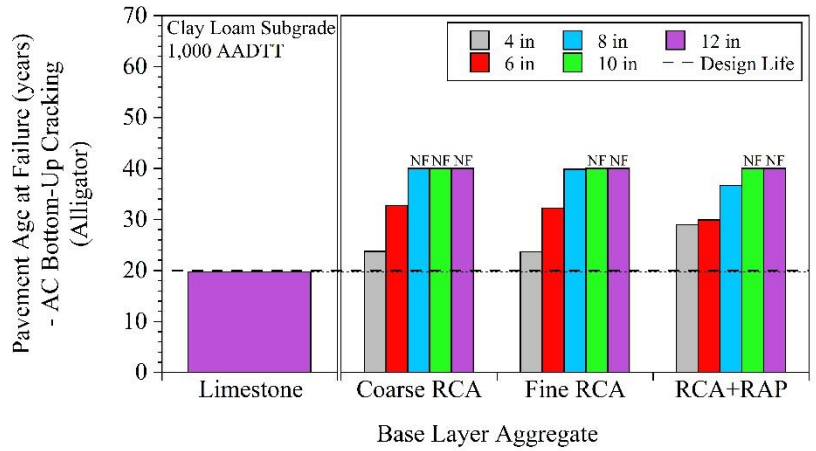

Clay Loam Subgrade
500 AADTT
4 in
6 in
8 in
10 in
12 in
Threshold
AC Bottom-Up Cracking
(Alligator) (% Lane Area)
Limestone
Coarse RCA
Fine RCA
RCA+RAP
Base Layer Aggregate


Clay Loam Subgrade
500 AADTT
4 in
6 in
8 in
10 in
12 in
Design Life
Pavement Age at Failure (years)
- AC Bottom-Up Cracking
(Alligator)
NF NF NF NF
NF NF NF NF
NF NF NF NF NF
Limestone
Coarse RCA
Finc RCA
RCA+RAP
Base Layer Aggregate

For pavements that contained clay loam subgrade – 1,000 AADTT:



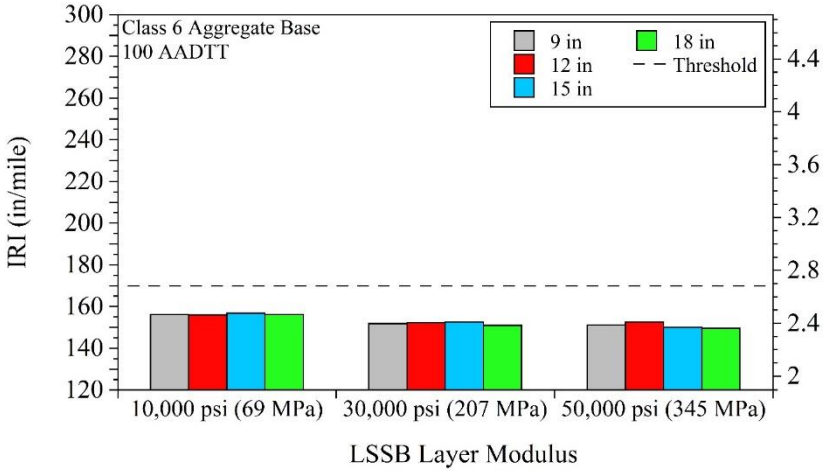

Clay Loam Subgrade
1,000 AADTT
4 in
6 in
8 in
10 in
12 in
Threshold
AC Bottom-Up Cracking
(Alligator) (% Lane Area)
140
120
100
80
60
40
20
0
Limestone
Coarse RCA
Fine RCA
RCA+RAP
Base Layer Aggregate

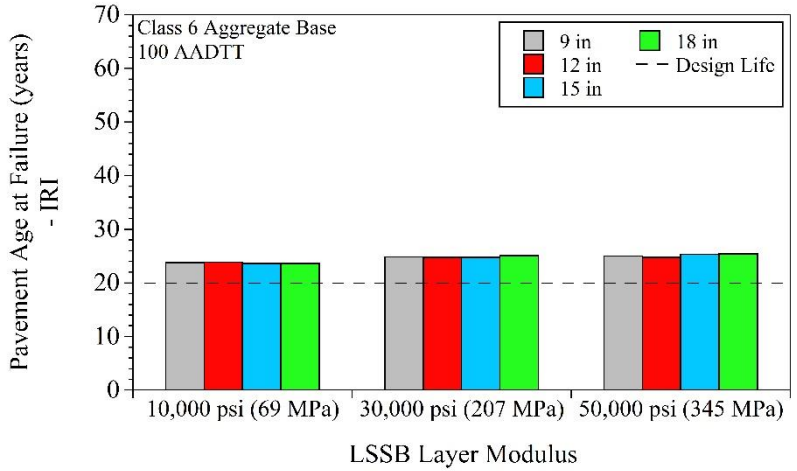

Clay Loam Subgrade
1,000 AADTT
4 in
6 in
8 in
10 in
12 in
Design Life
Pavement Age at Failure (years)
- AC Bottom-Up Cracking
(Alligator)
70
60
50
40
30
20
10
0
NF NF NF
NF NF
NF NF
Limestone
Coarse RCA
Fine RCA
RCA+RAP
Base Layer Aggregate

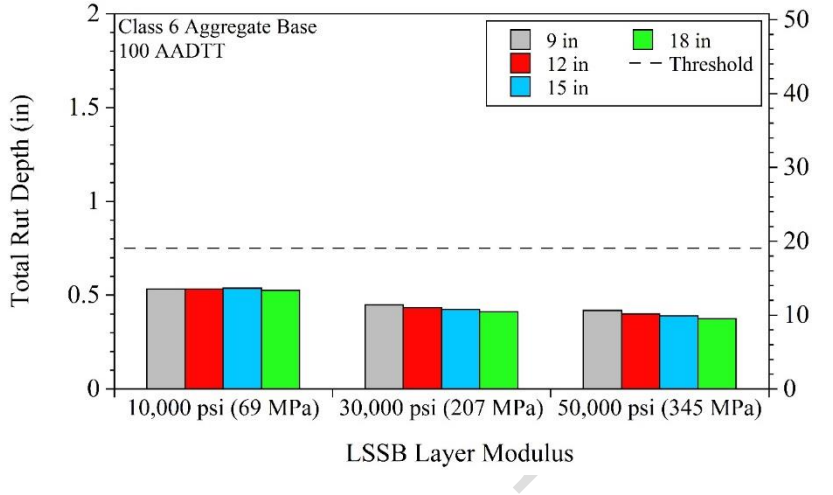
DRAFT

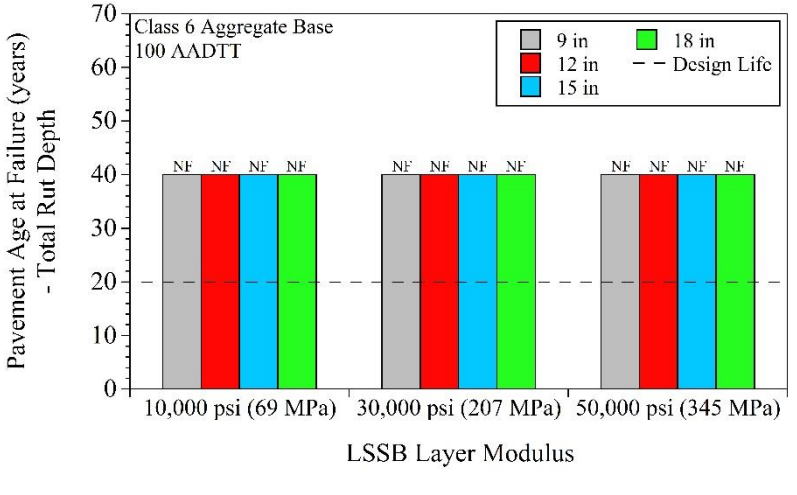
APPENDIX Z. EFFECT OF LARGE STONE SUBBASE (LSSB) THICKNESS ON PAVEMENT PERFORMANCE PREDICTIONS

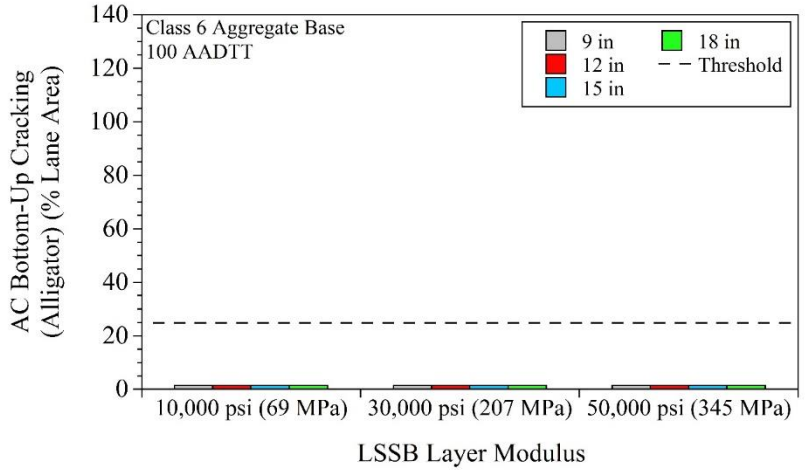
For pavement models that contained class 6 aggregate base – 100 AADTT:

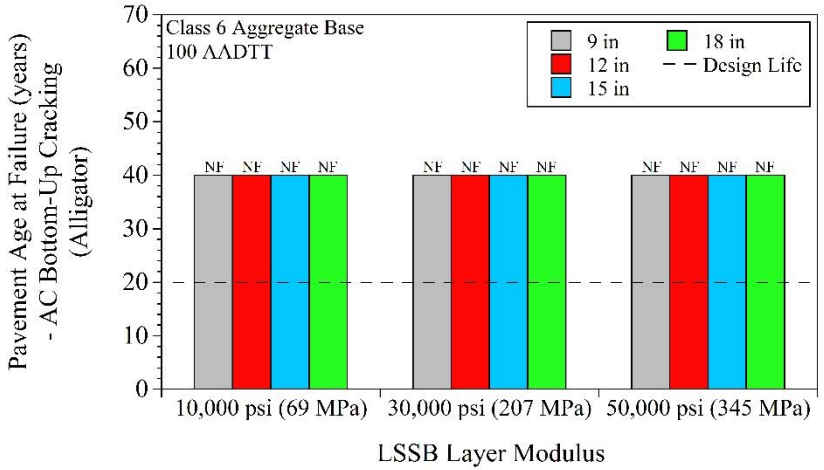




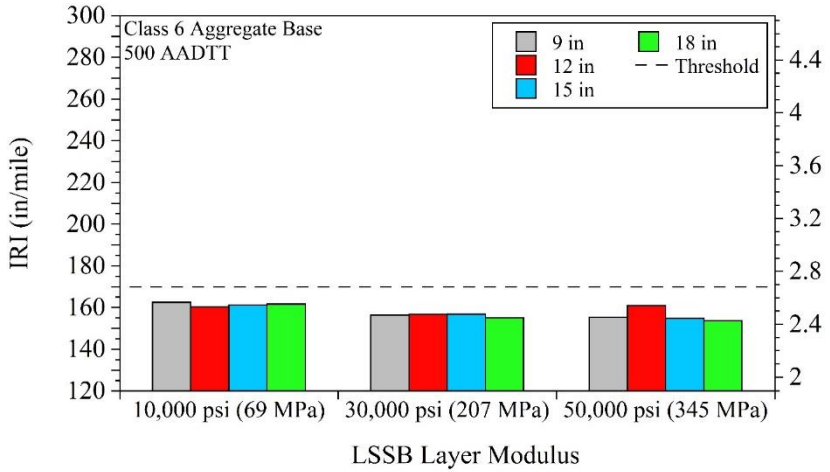


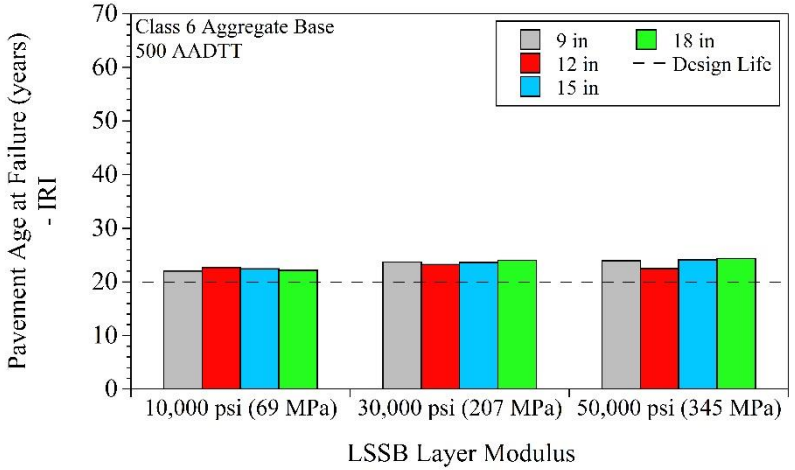


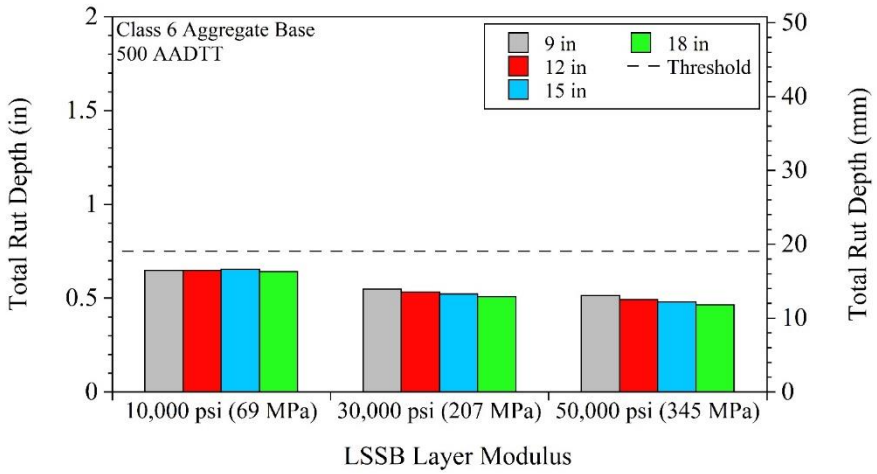


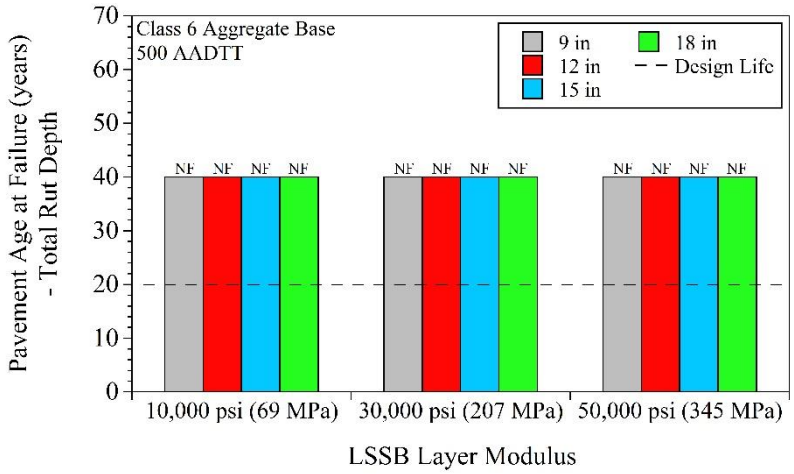


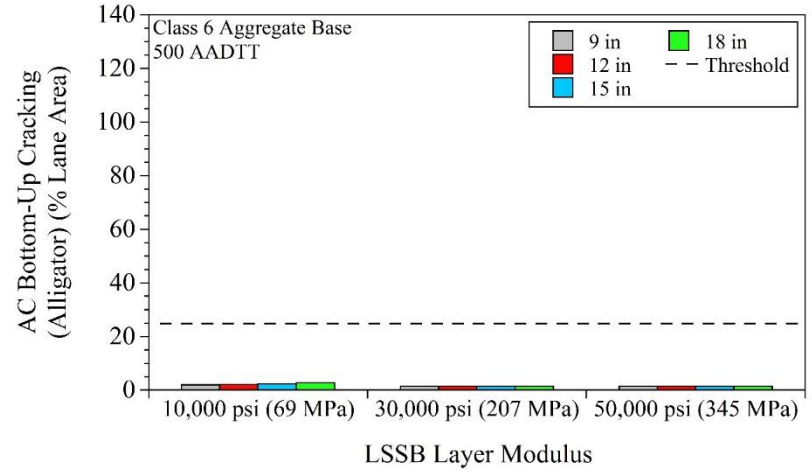
For pavement models that contained class 6 aggregate base – 500 AADTT:

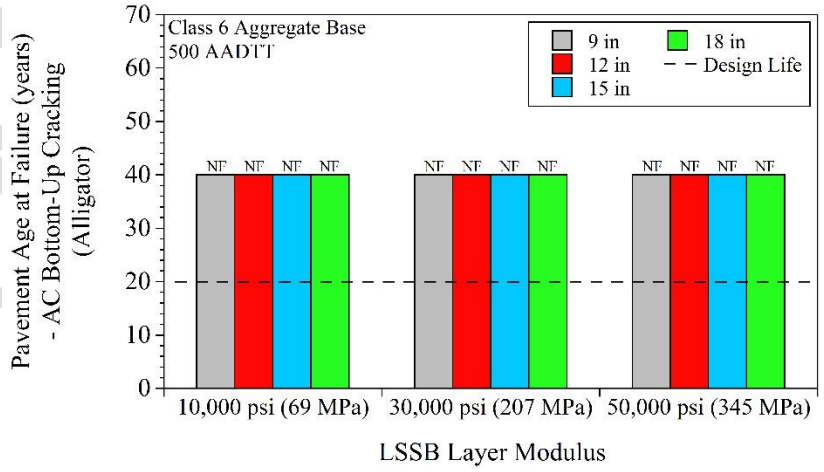




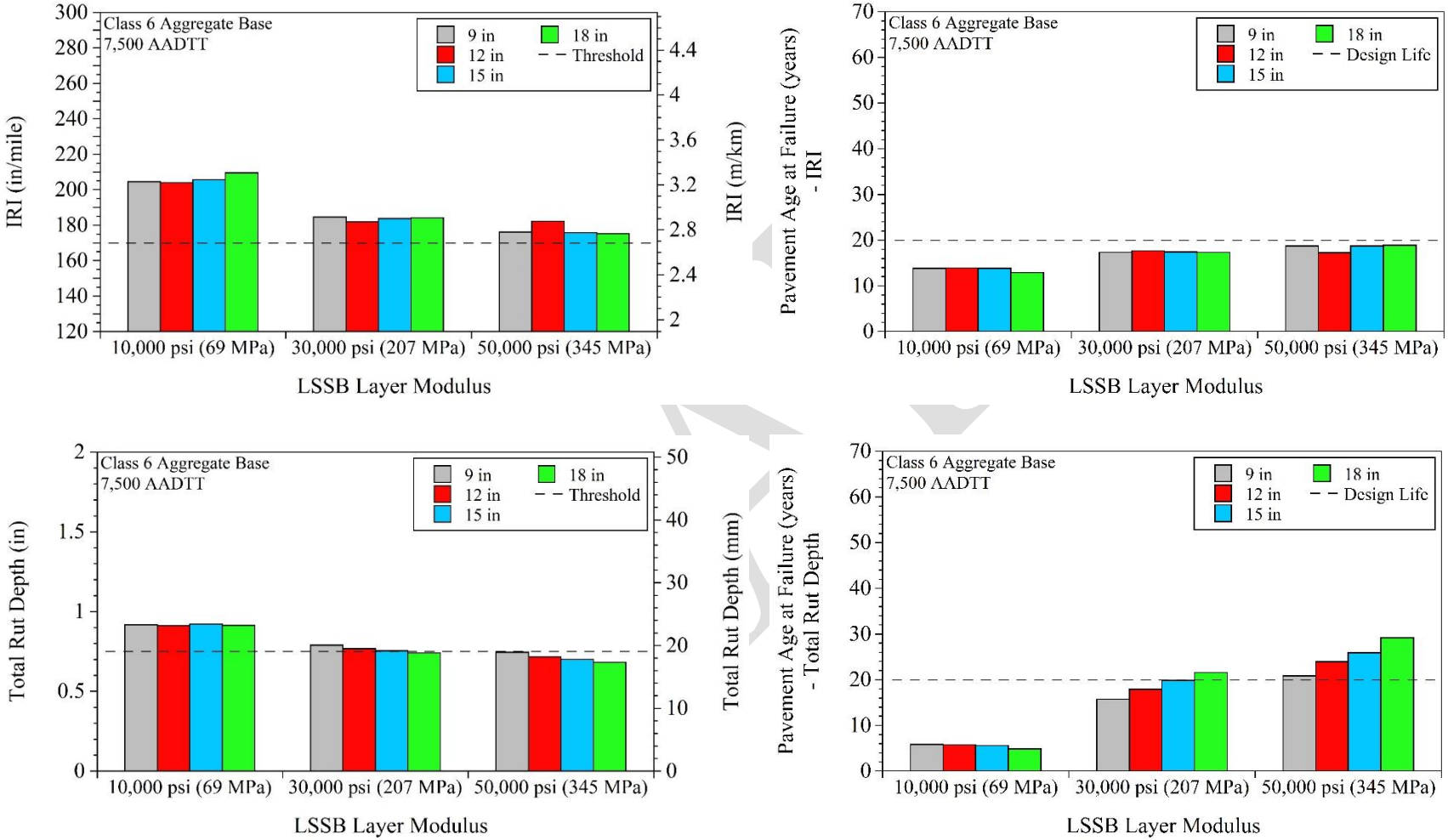

Class 6 Aggregate Base
500 AADTT
9 in
12 in
15 in
18 in
Threshold
Total Rut Depth (in)
Total Rut Depth (mm)
0
0.5
1
1.5
2
0
10
20
30
40
50
10,000 psi (69 MPa)
30,000 psi (207 MPa)
50,000 psi (345 MPa)
LSSB Layer Modulus

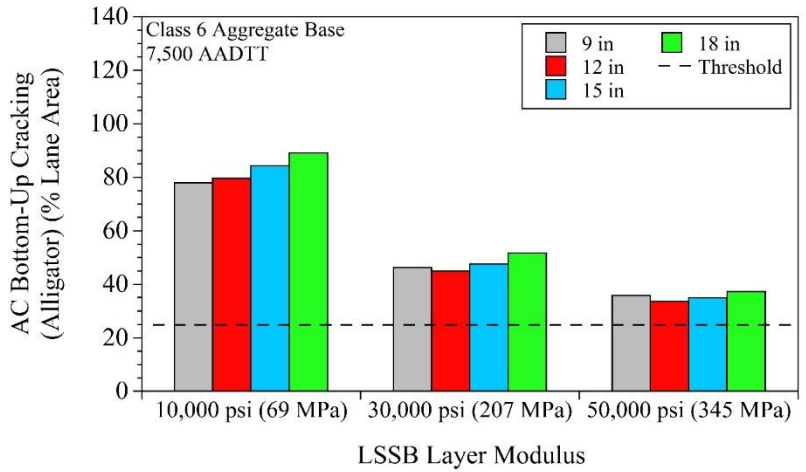

Class 6 Aggregate Base
500 AADTT
9 in
12 in
15 in
18 in
Design Life
Pavement Age at Failure (years)
- Total Rut Depth
0
10
20
30
40
50
60
70
NF
10,000 psi (69 MPa)
30,000 psi (207 MPa)
50,000 psi (345 MPa)
LSSB Layer Modulus

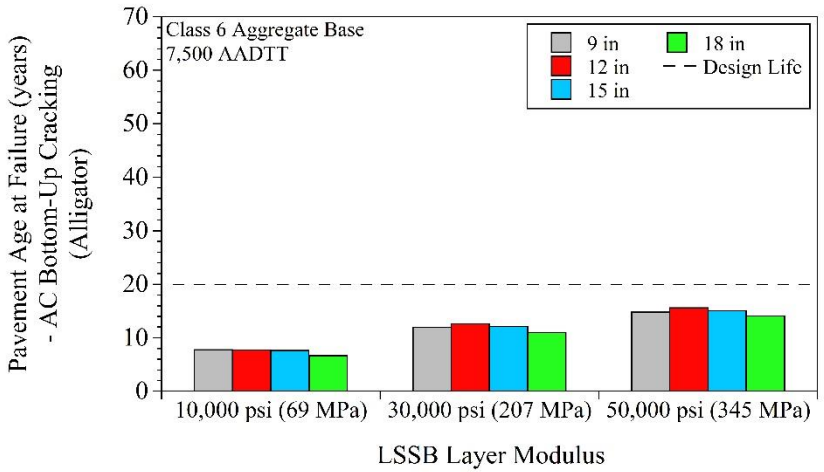

Class 6 Aggregate Base
500 AADTT
9 in
12 in
15 in
18 in
Threshold
AC Bottom-Up Cracking
(Alligator) (% Lane Area)
0
20
40
60
80
100
120
140
10,000 psi (69 MPa)
30,000 psi (207 MPa)
50,000 psi (345 MPa)
LSSB Layer Modulus


Class 6 Aggregate Base
500 AADTT
9 in
12 in
15 in
18 in
Design Life
Pavement Age at Failure (years)
- AC Bottom-Up Cracking
(Alligator)
0
10
20
30
40
50
60
70
NF
10,000 psi (69 MPa)
30,000 psi (207 MPa)
50,000 psi (345 MPa)
LSSB Layer Modulus

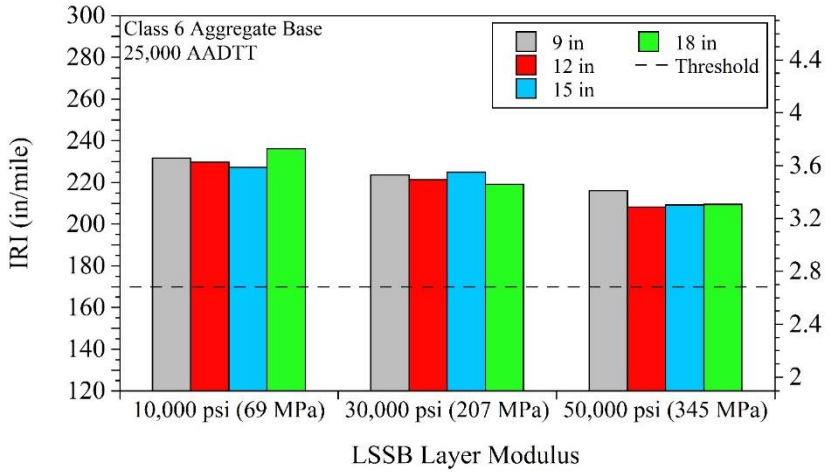
For pavement models that contained class 6 aggregate base – 7,500 AADTT:

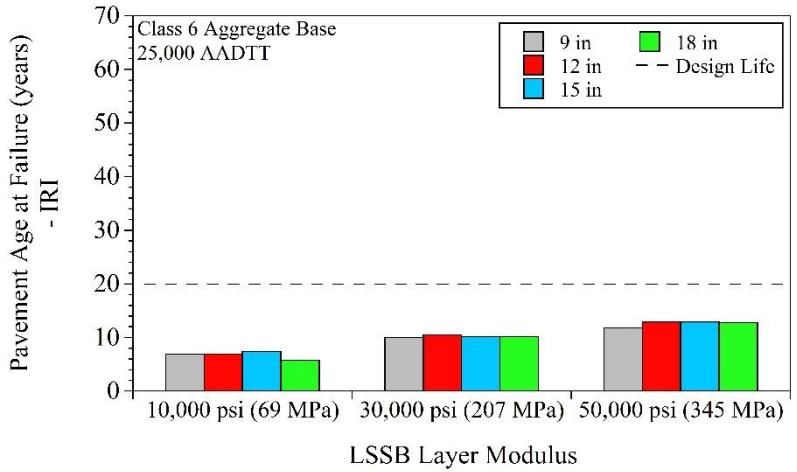


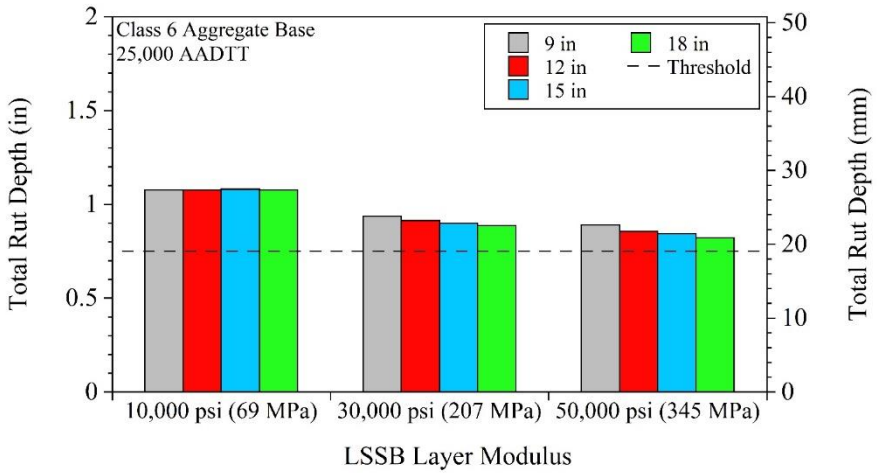


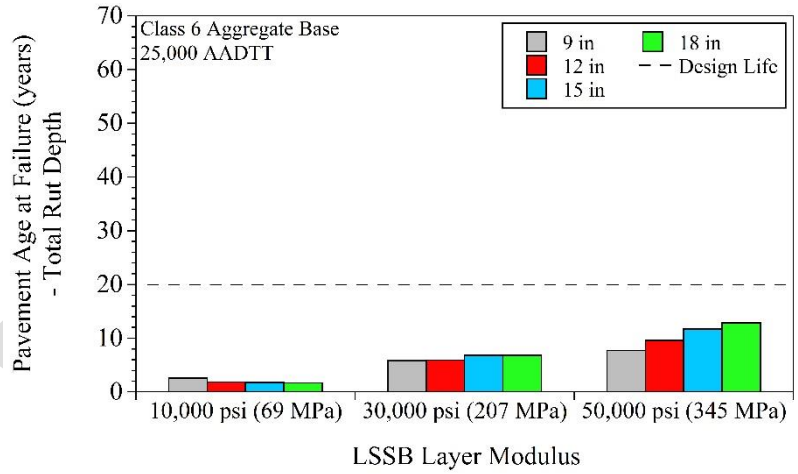


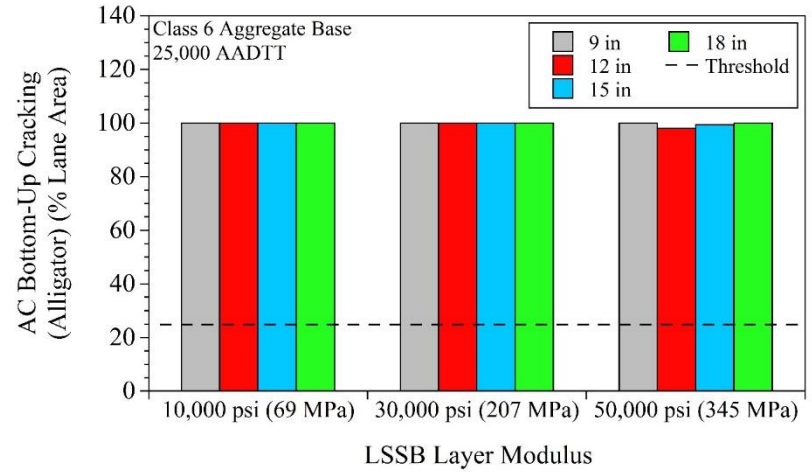
For pavement models that contained class 6 aggregate base – 25,000 AADTT:

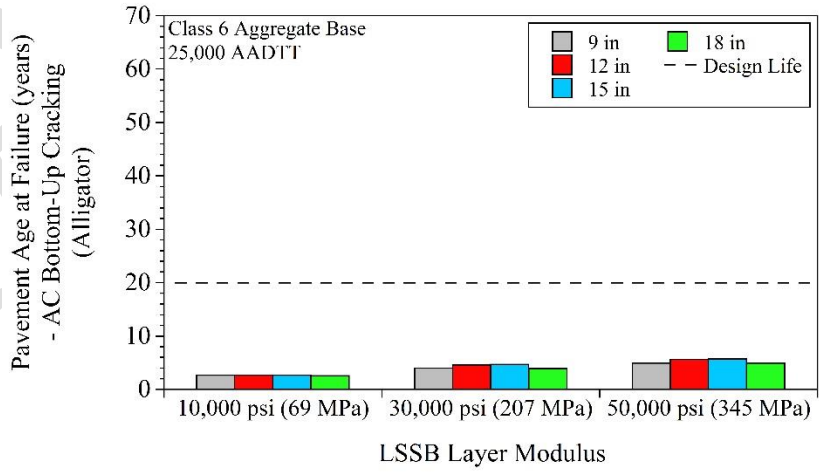




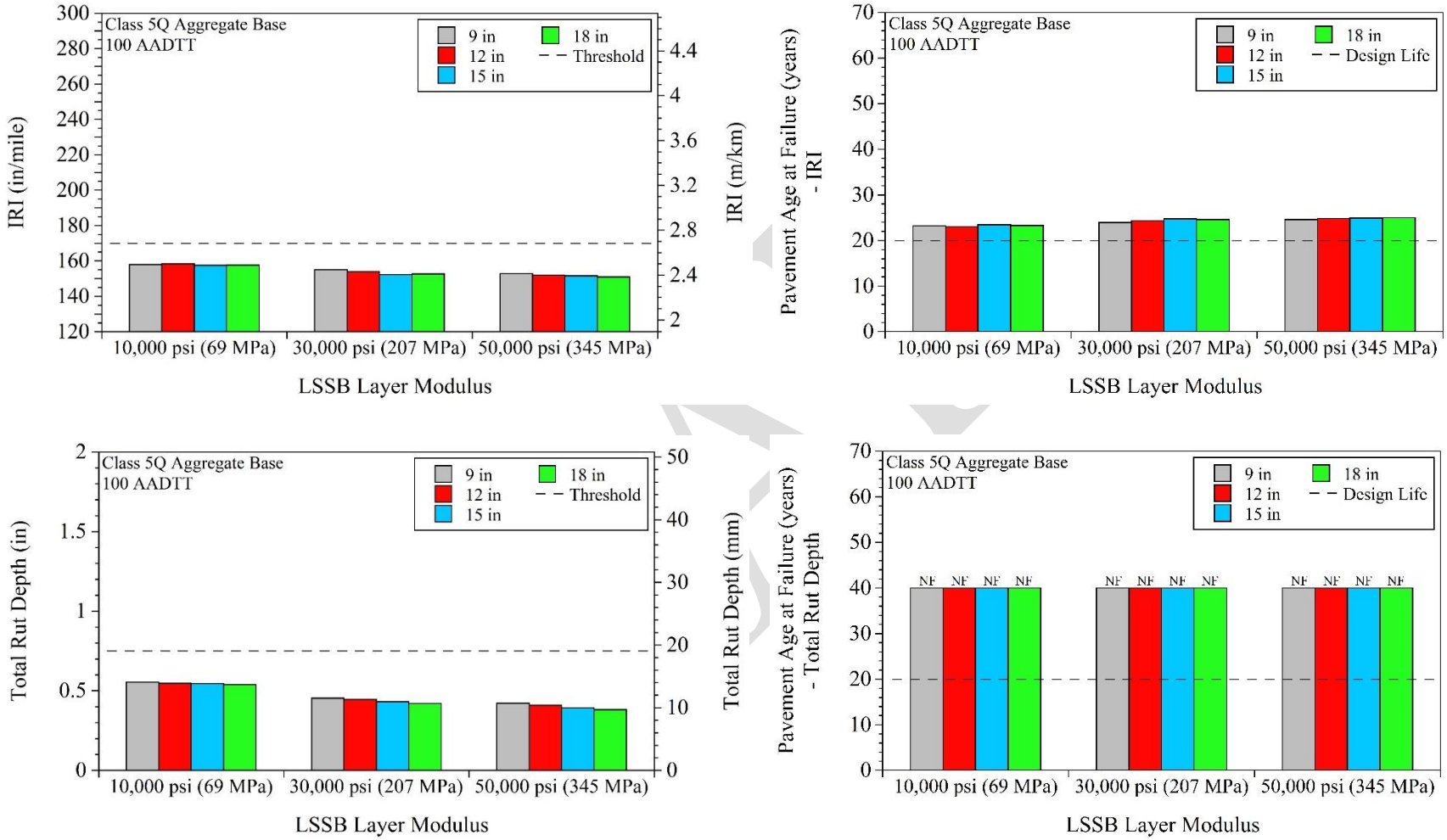

Class 6 Aggregate Base
25,000 AADTT
9 in
12 in
15 in
18 in
Threshold
Total Rut Depth (in)
Total Rut Depth (mm)
0
0.5
1
1.5
2
0
10
20
30
40
50
10,000 psi (69 MPa)
30,000 psi (207 MPa)
50,000 psi (345 MPa)
LSSB Layer Modulus

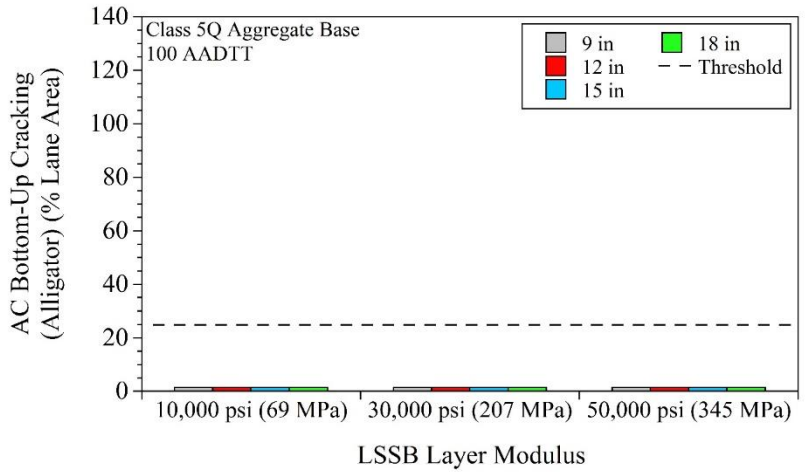

Class 6 Aggregate Base
25,000 AADTT
9 in
12 in
15 in
18 in
Design Life
Pavement Age at Failure (years)
- Total Rut Depth
0
10
20
30
40
50
60
70
10,000 psi (69 MPa)
30,000 psi (207 MPa)
50,000 psi (345 MPa)
LSSB Layer Modulus

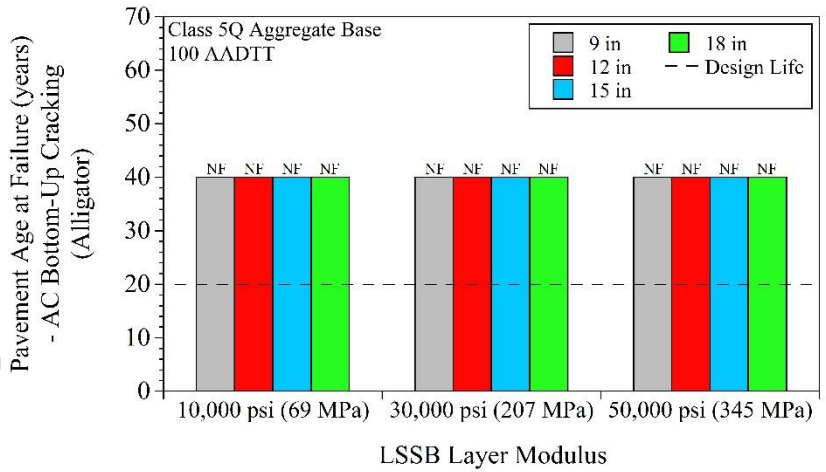

Class 6 Aggregate Base
25,000 AADTT
9 in
12 in
15 in
18 in
Threshold
AC Bottom-Up Cracking
(Alligator) (% Lane Area)
0
20
40
60
80
100
120
140
10,000 psi (69 MPa)
30,000 psi (207 MPa)
50,000 psi (345 MPa)
LSSB Layer Modulus


Class 6 Aggregate Base
25,000 AADTT
9 in
12 in
15 in
18 in
Design Life
Pavement Age at Failure (years)
- AC Bottom-Up Cracking
(Alligator)
0
10
20
30
40
50
60
70
10,000 psi (69 MPa)
30,000 psi (207 MPa)
50,000 psi (345 MPa)
LSSB Layer Modulus

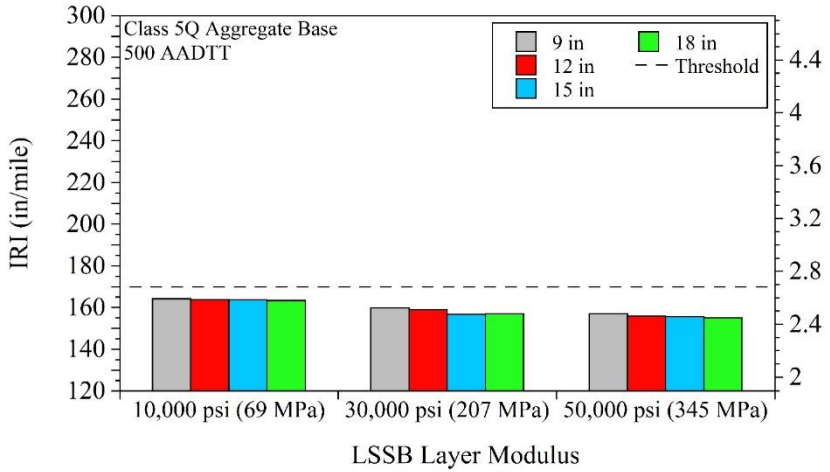
For pavement models that contained class 5Q aggregate base – 100 AADTT:

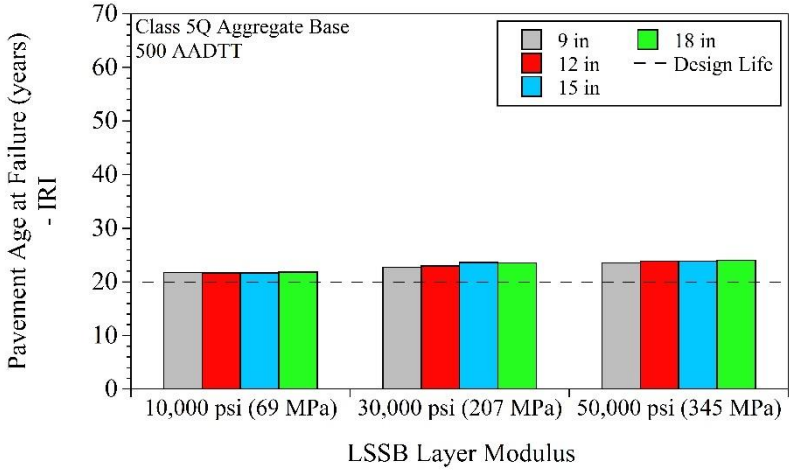


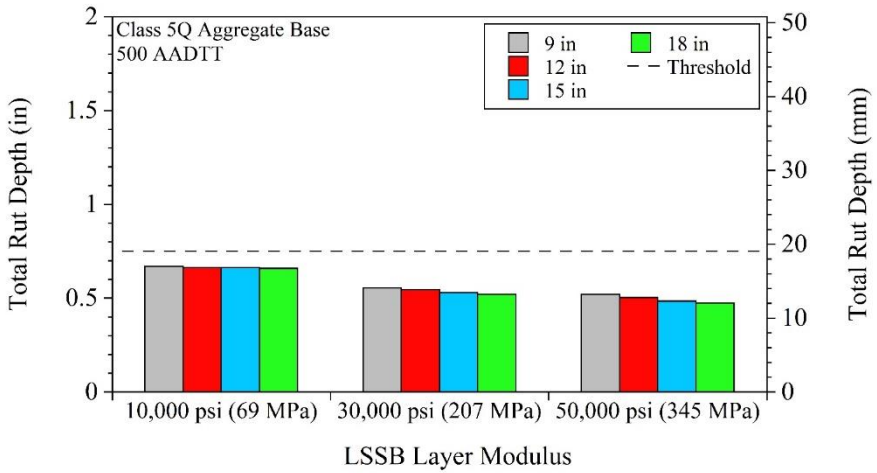


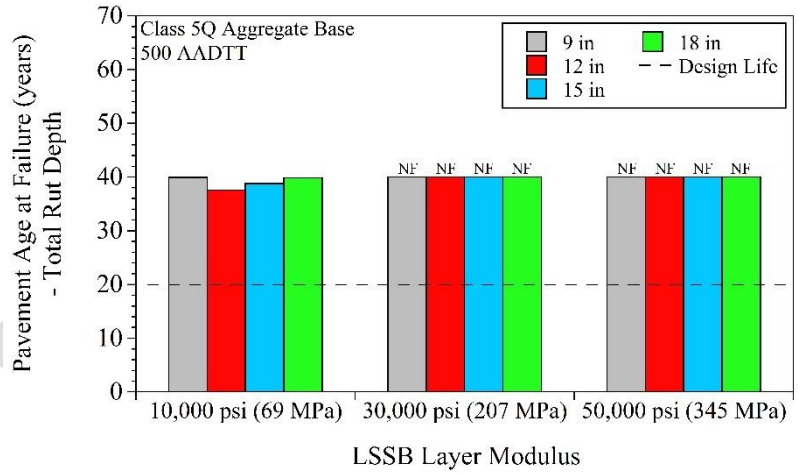


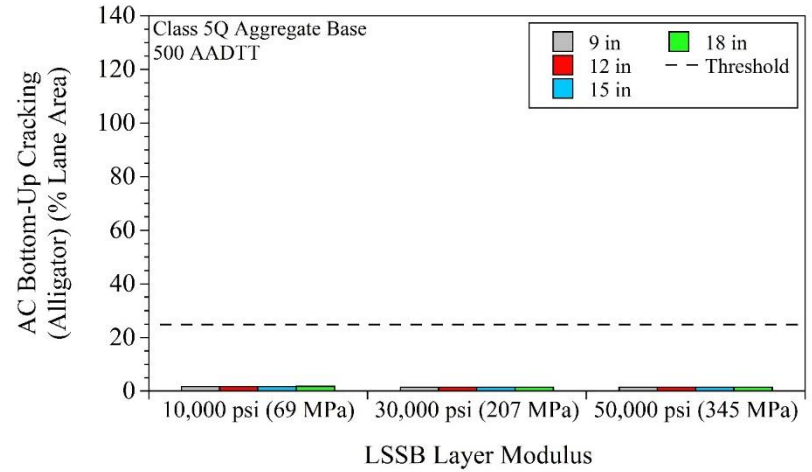
For pavement models that contained class 5Q aggregate base – 500 AADTT:

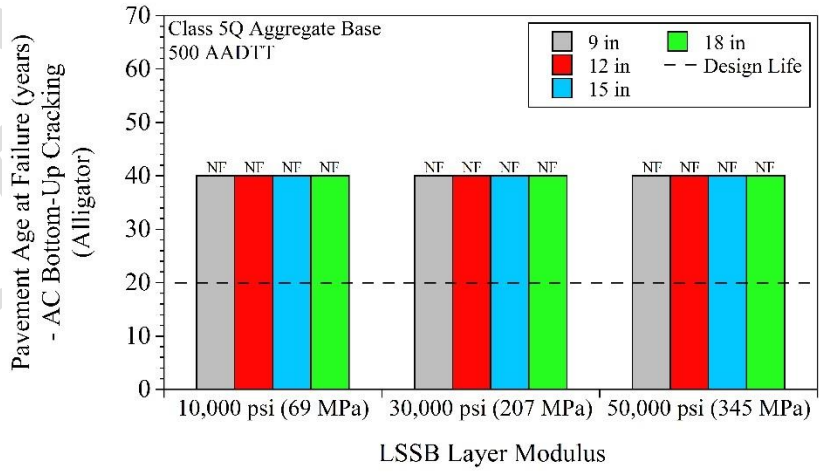




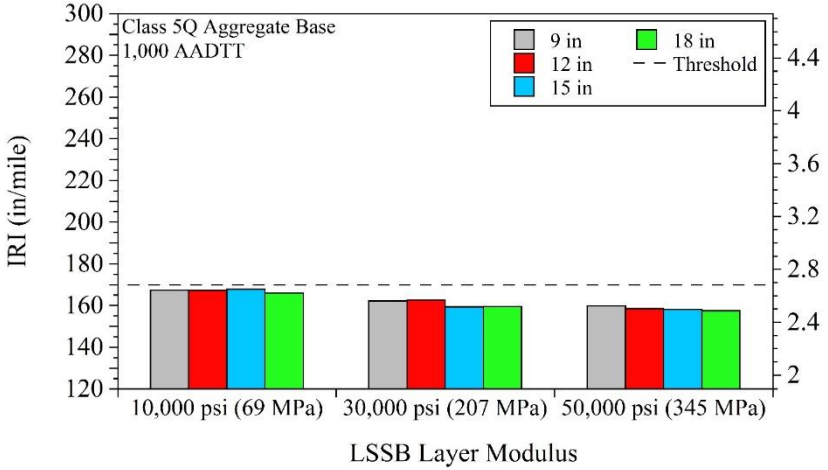

Class 5Q Aggregate Base
500 AADTT
9 in
12 in
15 in
18 in
Threshold
Total Rut Depth (in)
Total Rut Depth (mm)
0
0.5
1
1.5
2
0
10
20
30
40
50
10,000 psi (69 MPa)
30,000 psi (207 MPa)
50,000 psi (345 MPa)
LSSB Layer Modulus

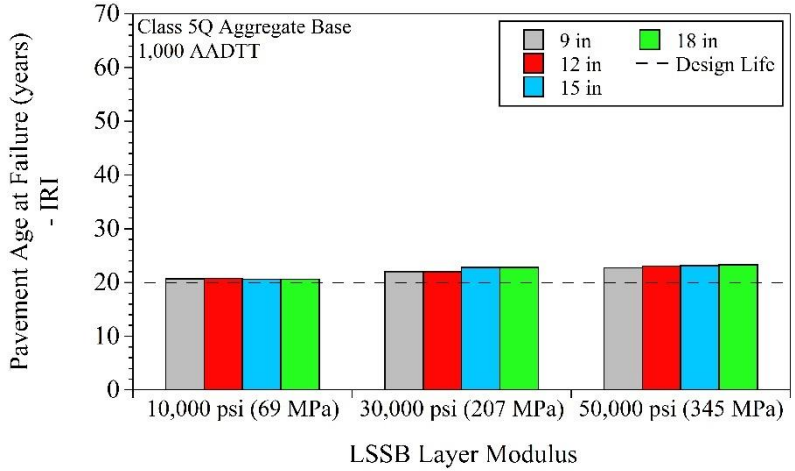

Class 5Q Aggregate Base
500 AADTT
9 in
12 in
15 in
18 in
Design Life
Pavement Age at Failure (years)
- Total Rut Depth
0
10
20
30
40
50
60
70
NF
10,000 psi (69 MPa)
30,000 psi (207 MPa)
50,000 psi (345 MPa)
LSSB Layer Modulus

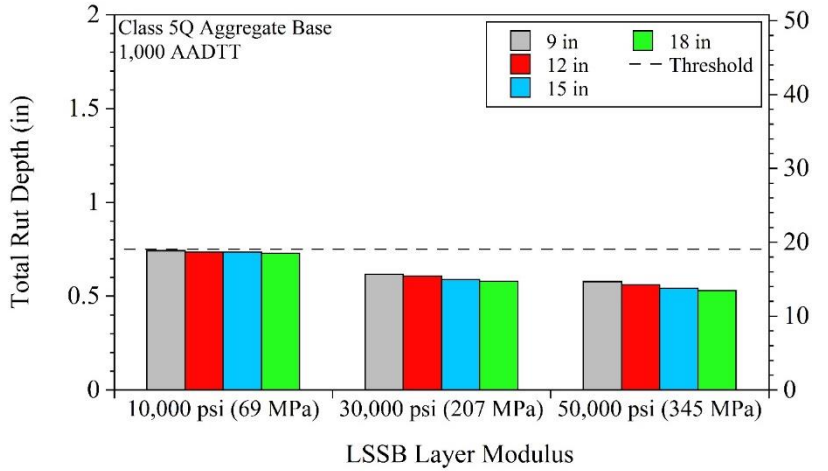

Class 5Q Aggregate Base
500 AADTT
9 in
12 in
15 in
18 in
Threshold
AC Bottom-Up Cracking
(Alligator) (% Lane Area)
0
20
40
60
80
100
120
140
10,000 psi (69 MPa)
30,000 psi (207 MPa)
50,000 psi (345 MPa)
LSSB Layer Modulus

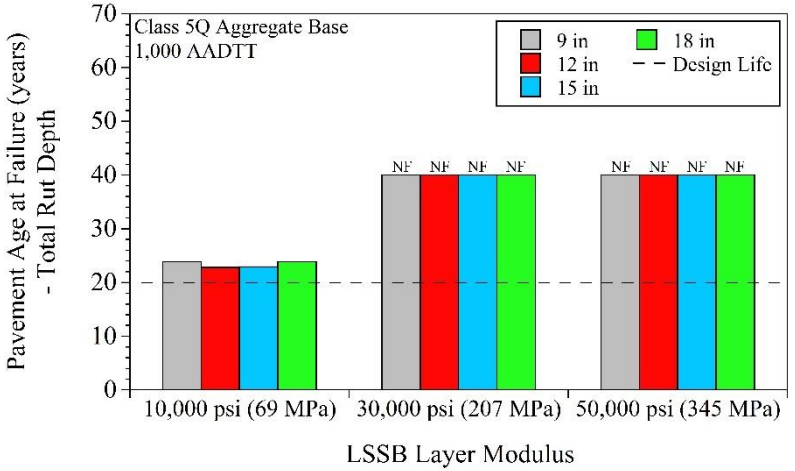

Class 5Q Aggregate Base
500 AADTT
9 in
12 in
15 in
18 in
Design Life
Pavement Age at Failure (years)
- AC Bottom-Up Cracking
(Alligator)
0
10
20
30
40
50
60
70
NF
10,000 psi (69 MPa)
30,000 psi (207 MPa)
50,000 psi (345 MPa)
LSSB Layer Modulus

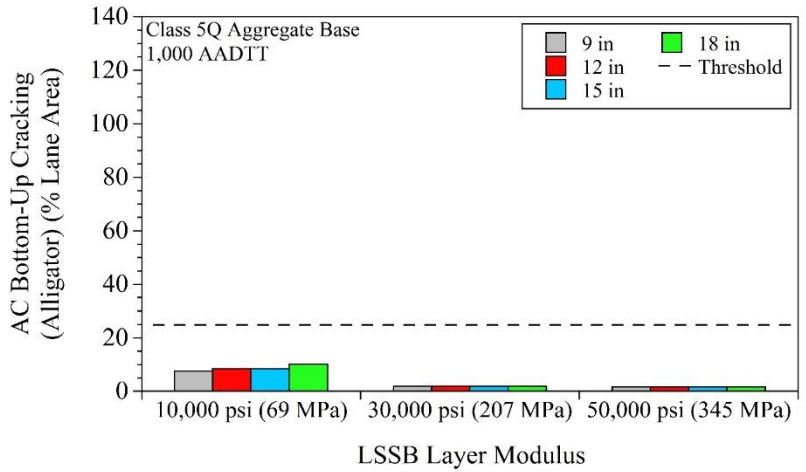
For pavement models that contained class 5Q aggregate base – 1,000 AADTT:

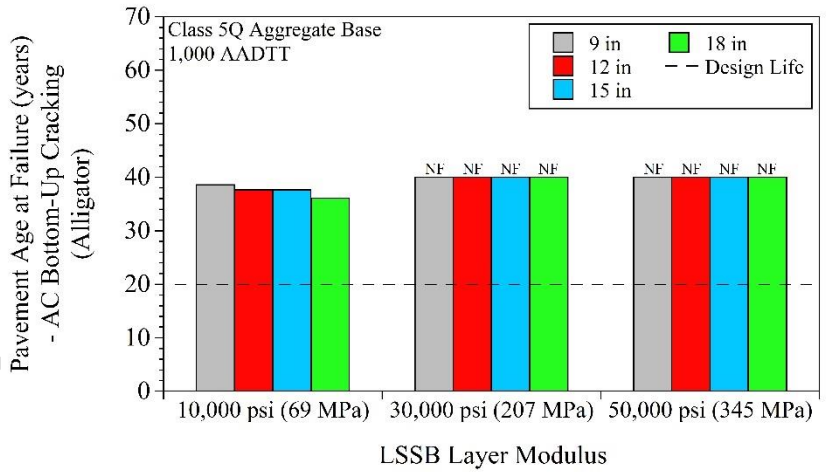




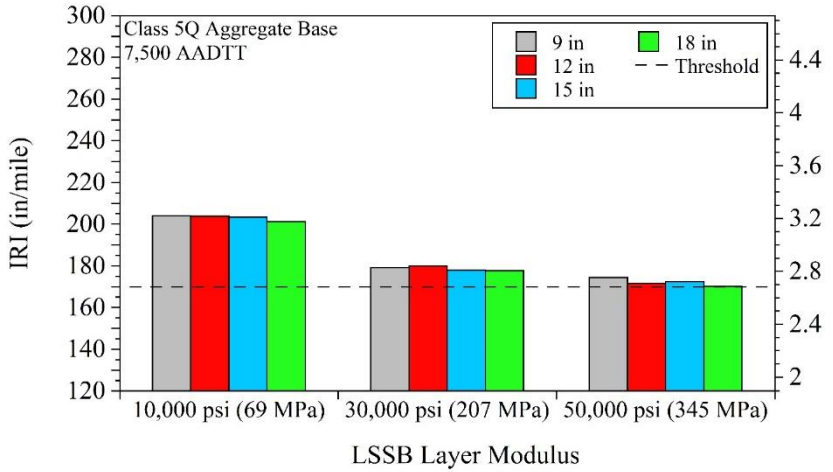


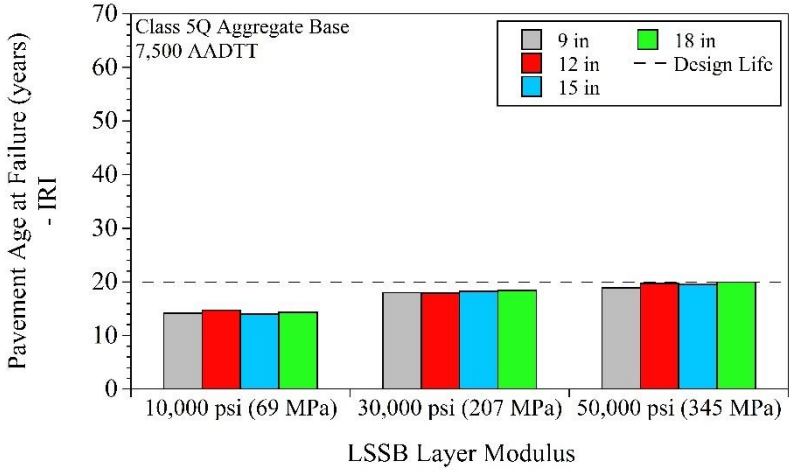


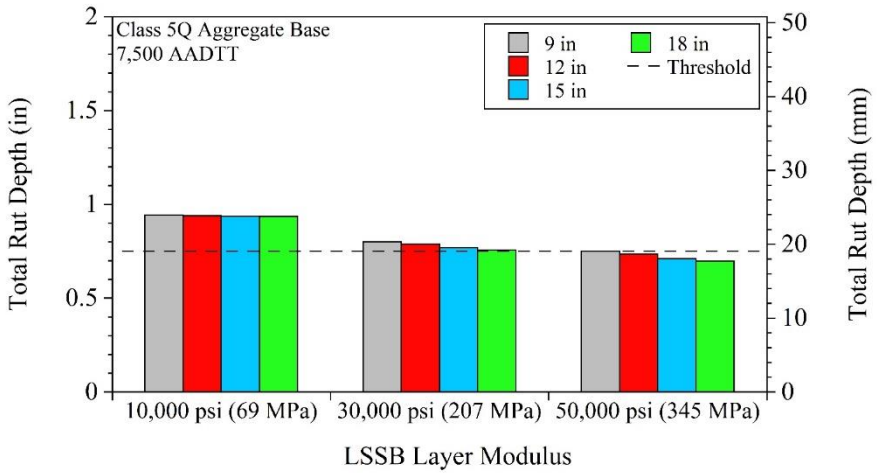


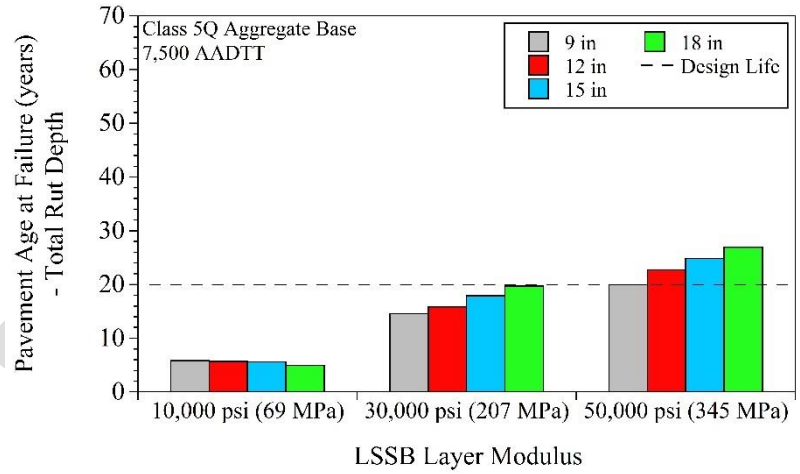


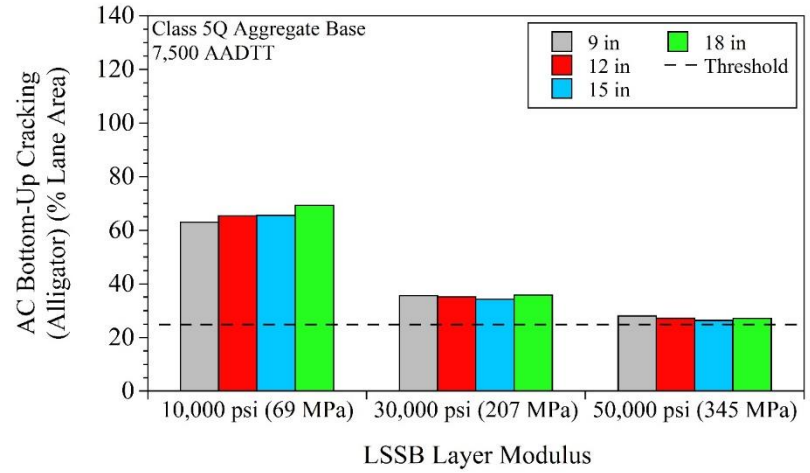
For pavement models that contained class 5Q aggregate base – 7,500 AADTT:

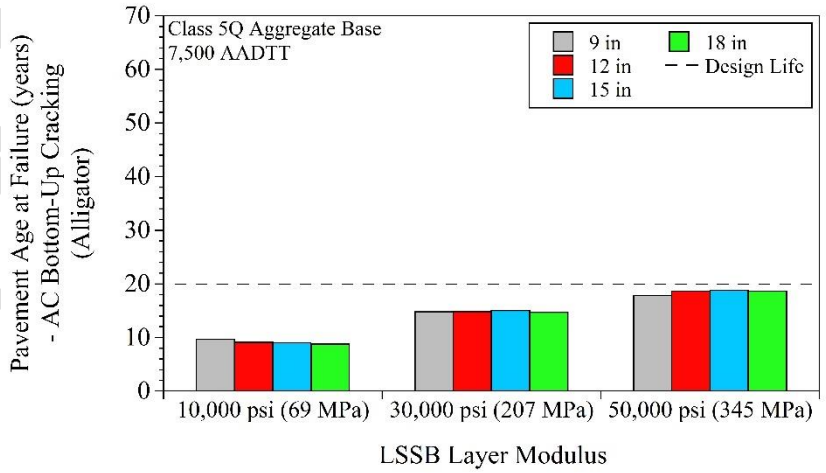




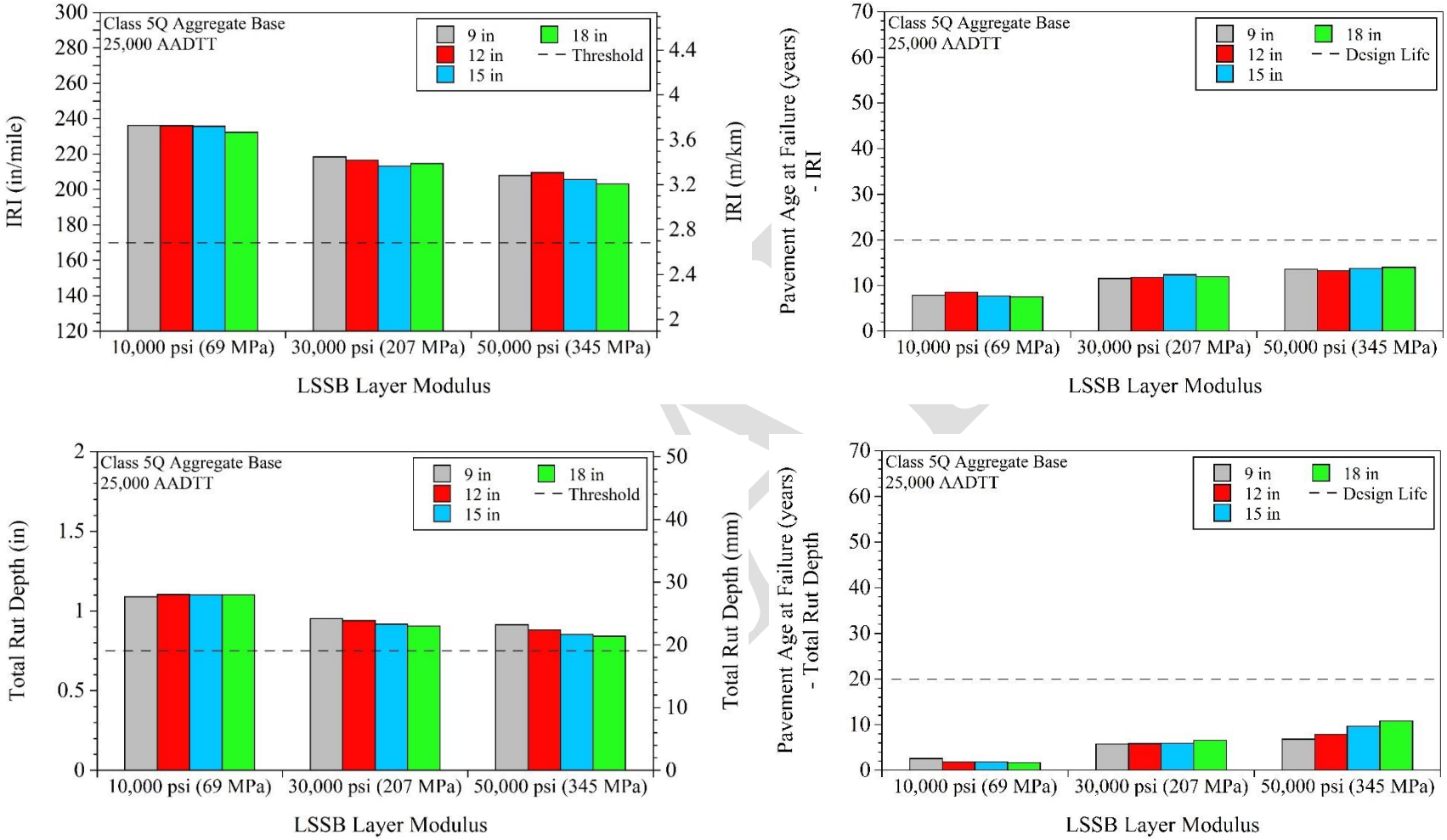

Class 5Q Aggregate Base
7,500 AADTT
9 in
12 in
15 in
18 in
Threshold
Total Rut Depth (in)
Total Rut Depth (mm)
10,000 psi (69 MPa)
30,000 psi (207 MPa)
50,000 psi (345 MPa)
LSSB Layer Modulus

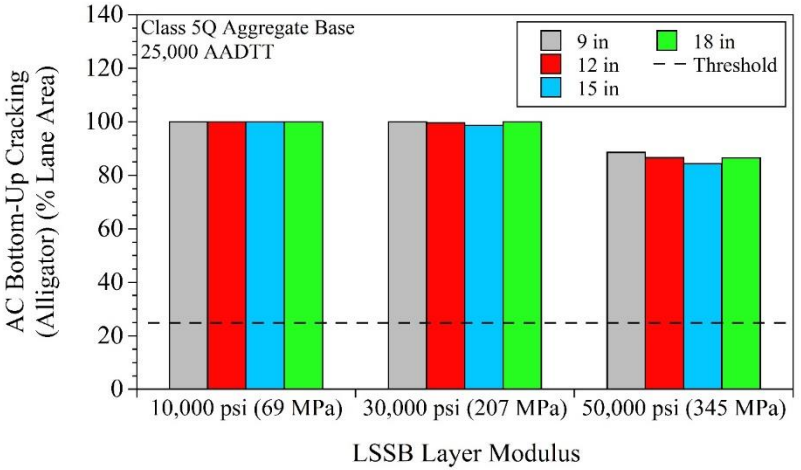

Class 5Q Aggregate Base
7,500 AADTT
9 in
12 in
15 in
18 in
Design Life
Pavement Age at Failure (years)
- Total Rut Depth
10,000 psi (69 MPa)
30,000 psi (207 MPa)
50,000 psi (345 MPa)
LSSB Layer Modulus

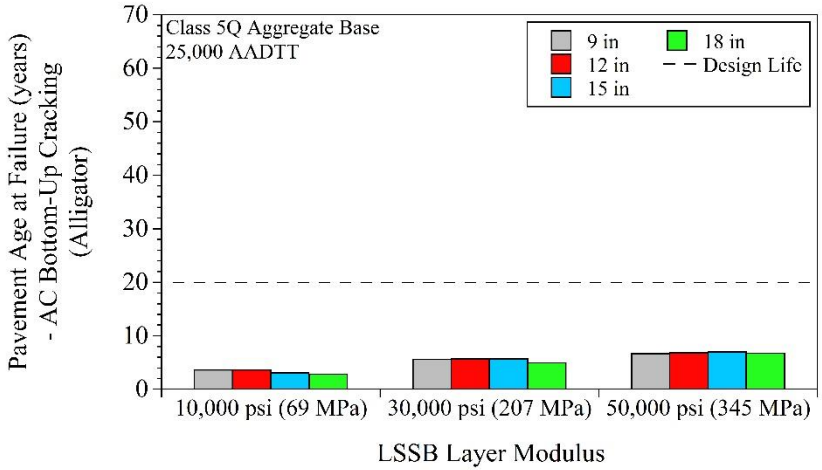

Class 5Q Aggregate Base
7,500 AADTT
9 in
12 in
15 in
18 in
Threshold
AC Bottom-Up Cracking
(Alligator) (% Lane Area)
10,000 psi (69 MPa)
30,000 psi (207 MPa)
50,000 psi (345 MPa)
LSSB Layer Modulus


Class 5Q Aggregate Base
7,500 AADTT
9 in
12 in
15 in
18 in
Design Life
Pavement Age at Failure (years)
- AC Bottom-Up Cracking
(Alligator)
10,000 psi (69 MPa)
30,000 psi (207 MPa)
50,000 psi (345 MPa)
LSSB Layer Modulus

For pavement models that contained class 5Q aggregate base – 25,000 AADTT:



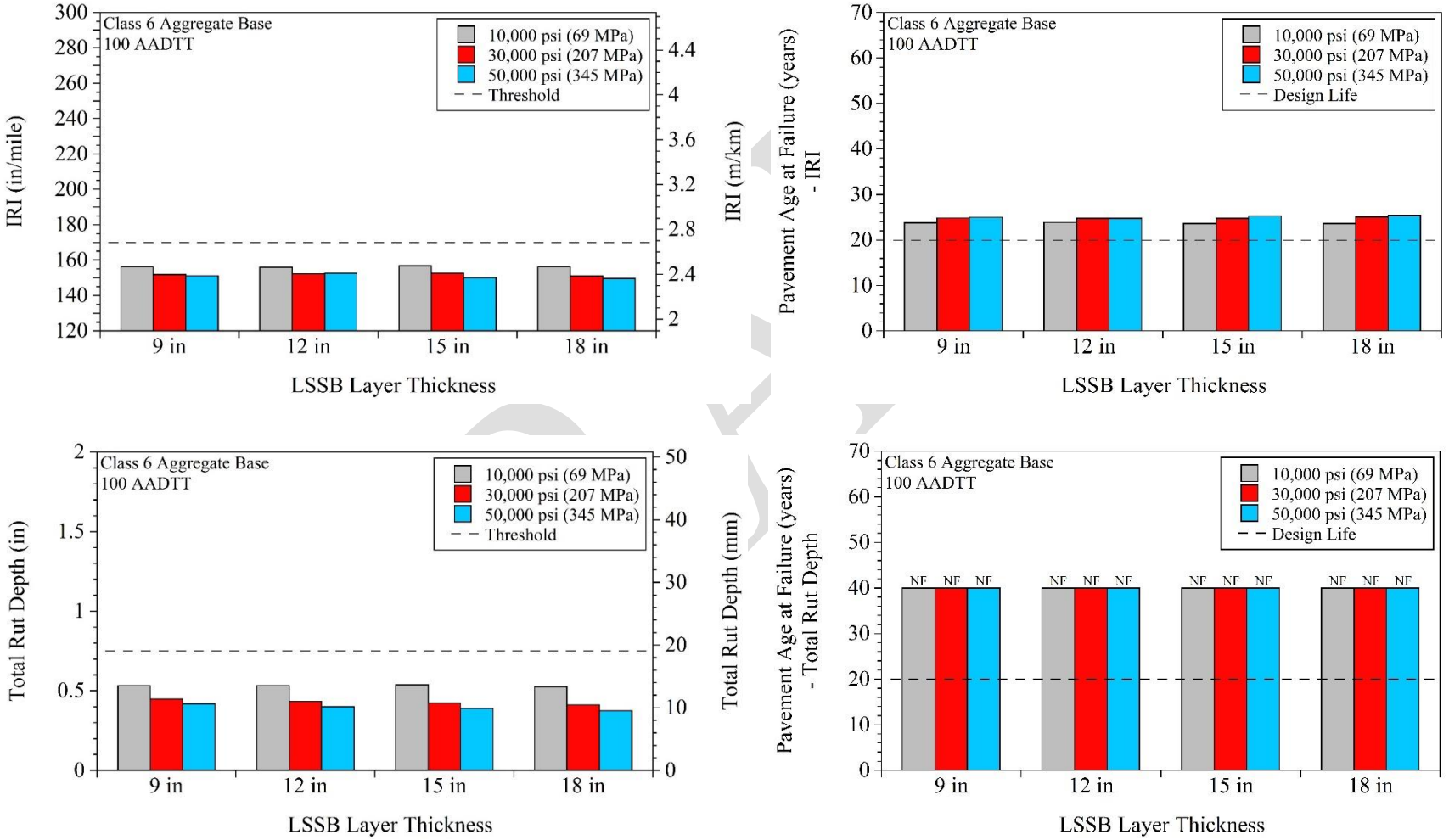

Class 5Q Aggregate Base
25,000 AADTT
9 in
12 in
15 in
18 in
Threshold
AC Bottom-Up Cracking
(Alligator) (% Lane Area)
0
20
40
60
80
100
120
140
10,000 psi (69 MPa)
30,000 psi (207 MPa)
50,000 psi (345 MPa)
LSSB Layer Modulus

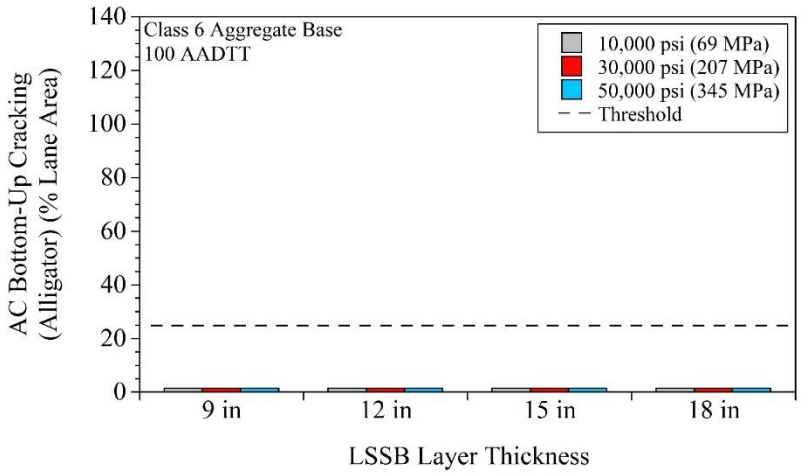

Class 5Q Aggregate Base
25,000 AADTT
9 in
12 in
15 in
18 in
Design Life
Pavement Age at Failure (years)
- AC Bottom-Up Cracking
(Alligator)
0
10
20
30
40
50
60
70
10,000 psi (69 MPa)
30,000 psi (207 MPa)
50,000 psi (345 MPa)
LSSB Layer Modulus

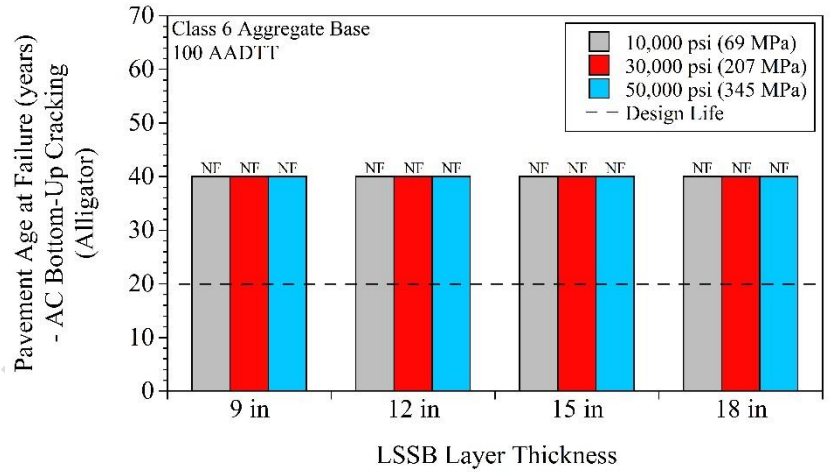
DRAFT

APPENDIX AA. EFFECT OF LARGE STONE SUBBASE (LSSB) LAYER MODULUS ON PAVEMENT PERFORMANCE PREDICTIONS

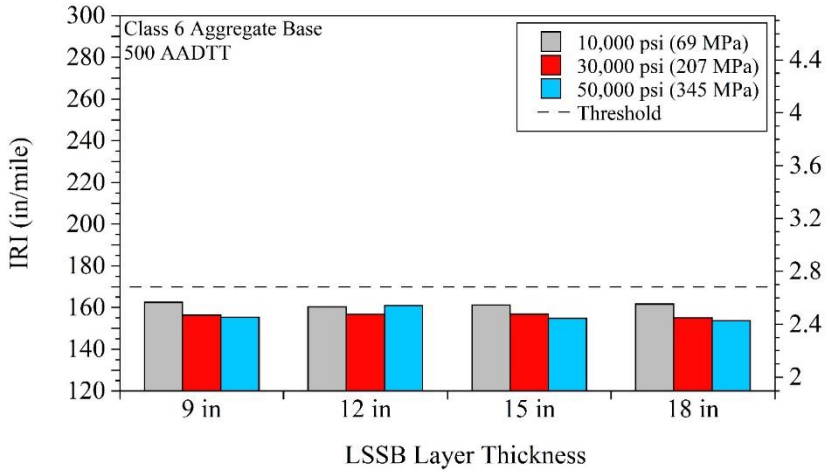
For pavement models that contained class 6 aggregate base – 100 AADTT:

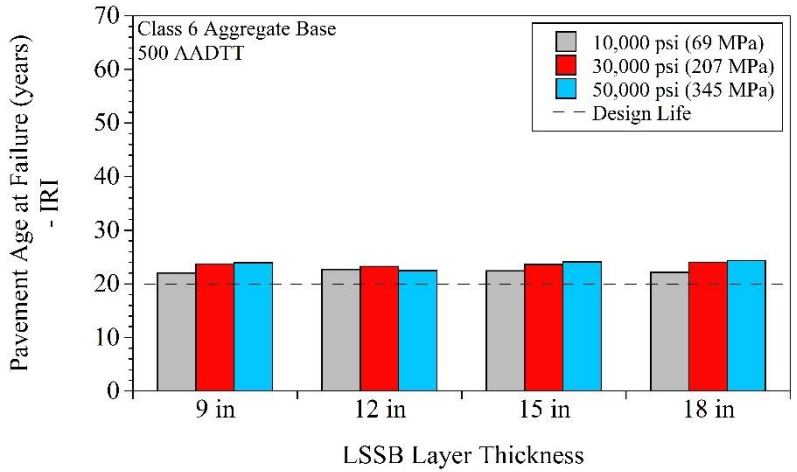


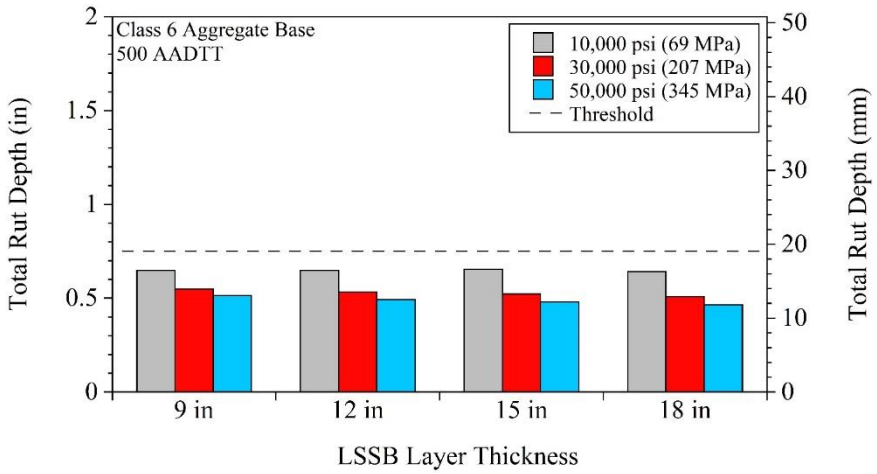


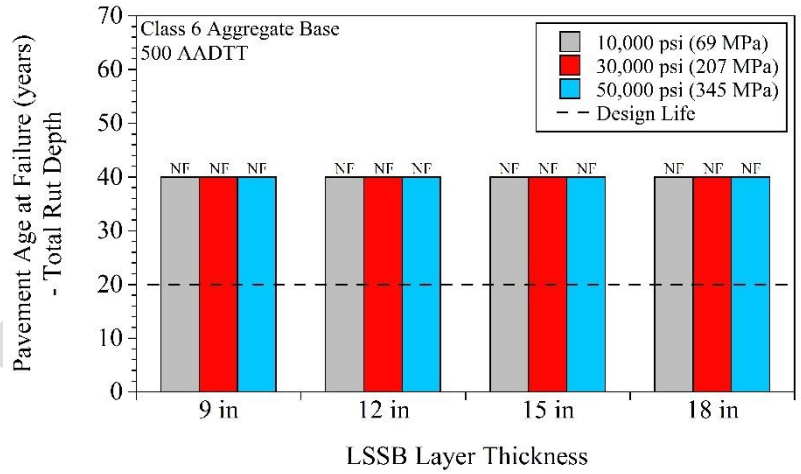


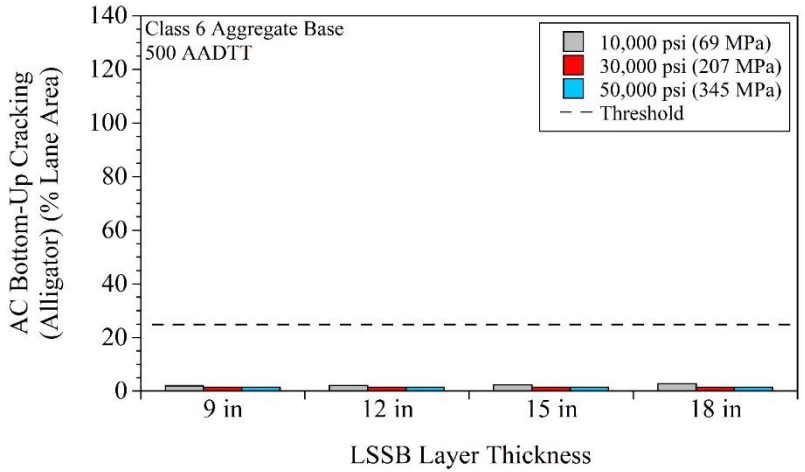
For pavement models that contained class 6 aggregate base – 500 AADTT:

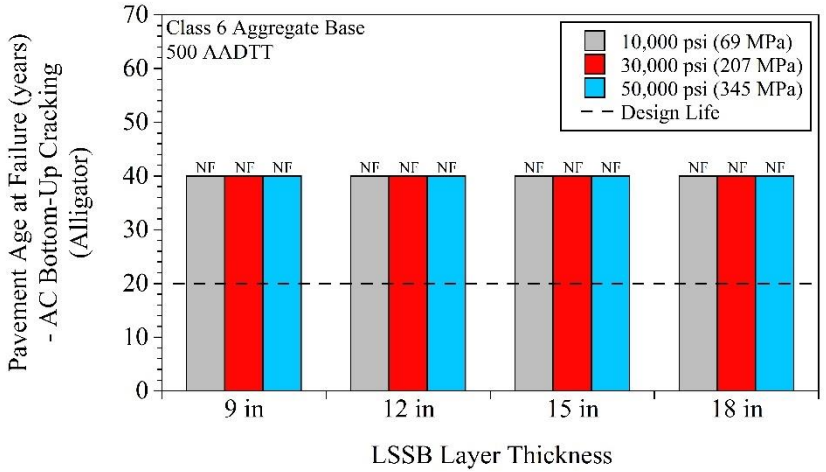




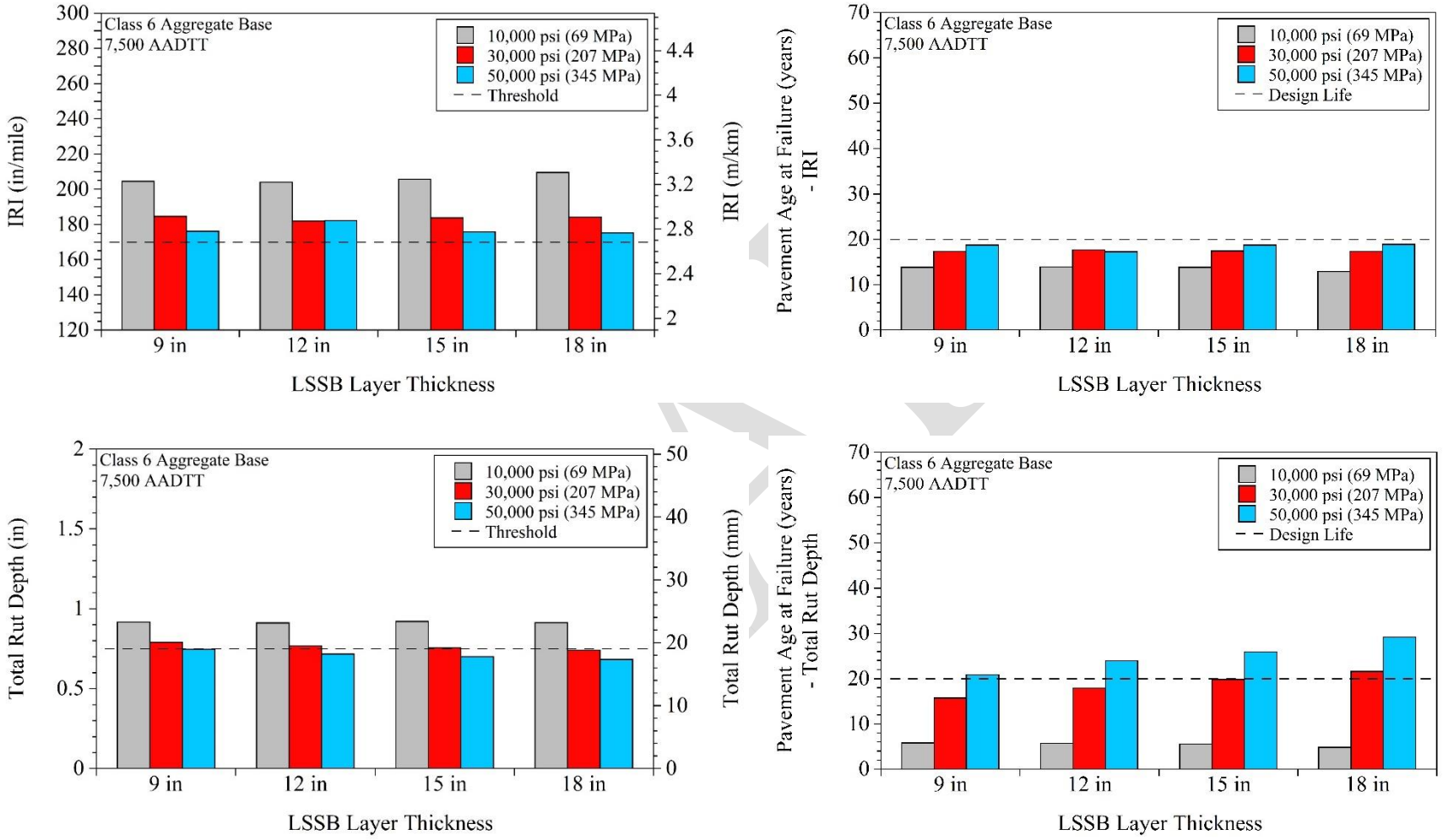

Class 6 Aggregate Base
500 AADTT
10,000 psi (69 MPa)
30,000 psi (207 MPa)
50,000 psi (345 MPa)
Threshold
Total Rut Depth (in)
Total Rut Depth (mm)
0
0.5
1
1.5
2
0
10
20
30
40
50
9 in
12 in
15 in
18 in
LSSB Layer Thickness

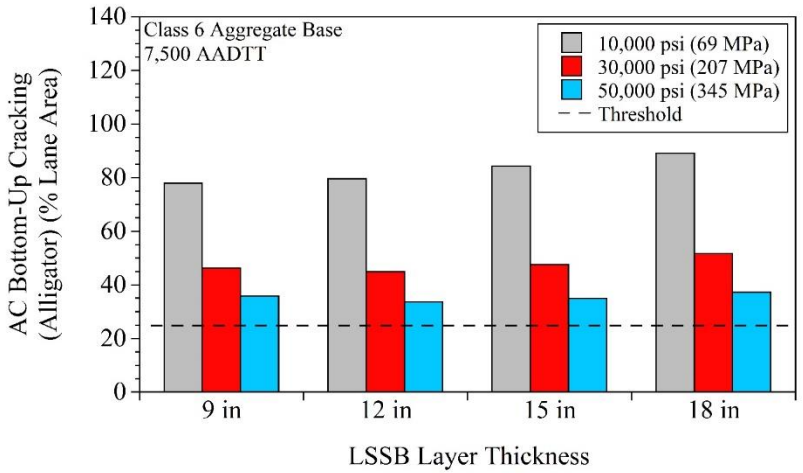

Class 6 Aggregate Base
500 AADTT
10,000 psi (69 MPa)
30,000 psi (207 MPa)
50,000 psi (345 MPa)
Design Life
Pavement Age at Failure (years)
- Total Rut Depth
0
10
20
30
40
50
60
70
NF
9 in
12 in
15 in
18 in
LSSB Layer Thickness

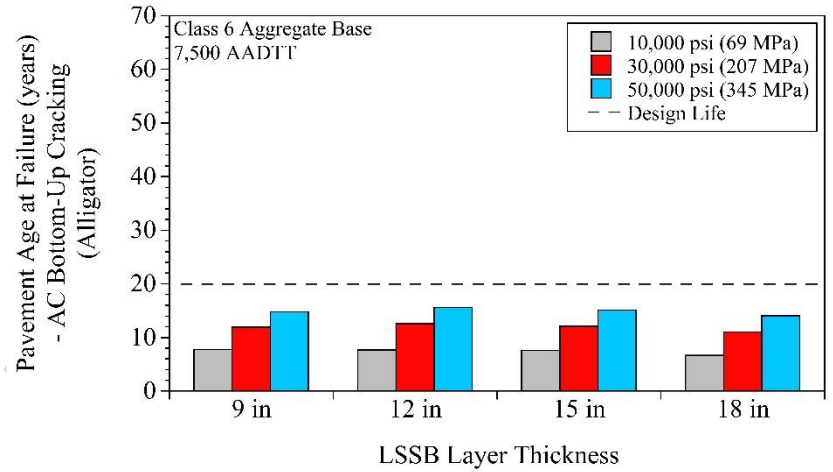

Class 6 Aggregate Base
500 AADTT
10,000 psi (69 MPa)
30,000 psi (207 MPa)
50,000 psi (345 MPa)
Threshold
AC Bottom-Up Cracking
(Alligator) (% Lane Area)
0
20
40
60
80
100
120
140
9 in
12 in
15 in
18 in
LSSB Layer Thickness


Class 6 Aggregate Base
500 AADTT
10,000 psi (69 MPa)
30,000 psi (207 MPa)
50,000 psi (345 MPa)
Design Life
Pavement Age at Failure (years)
- AC Bottom-Up Cracking
(Alligator)
0
10
20
30
40
50
60
70
NF
9 in
12 in
15 in
18 in
LSSB Layer Thickness

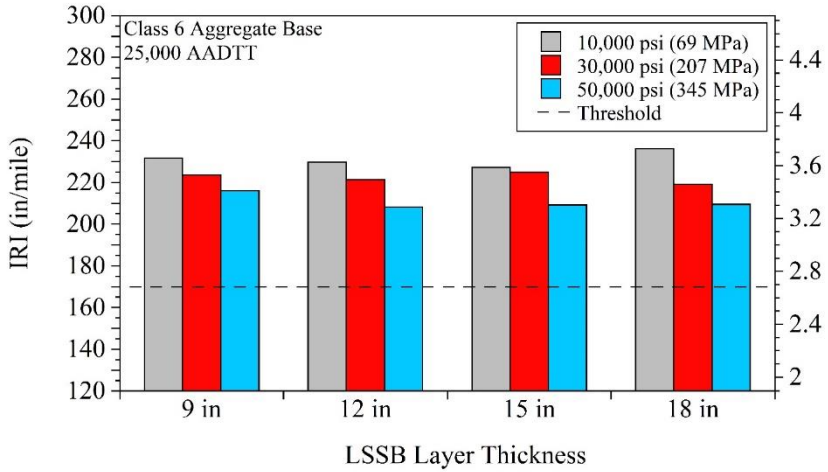
For pavement models that contained class 6 aggregate base – 7,500 AADTT:

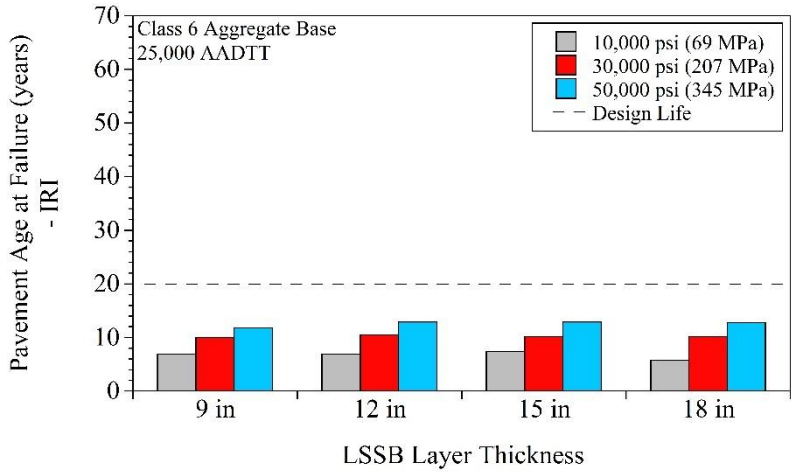


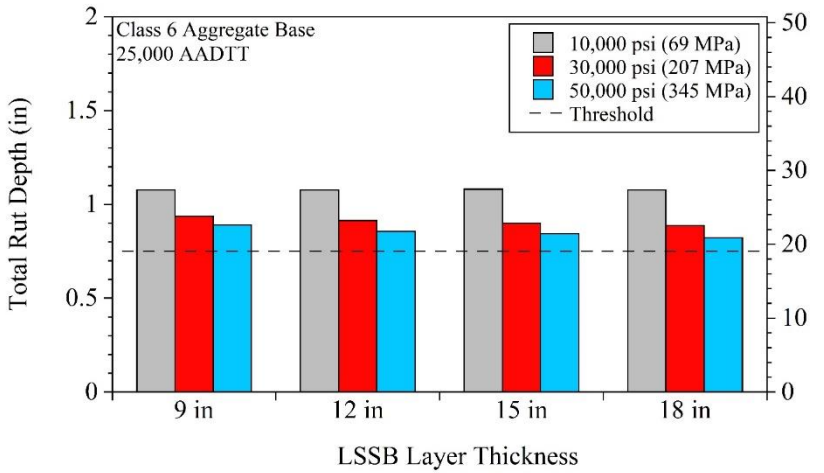


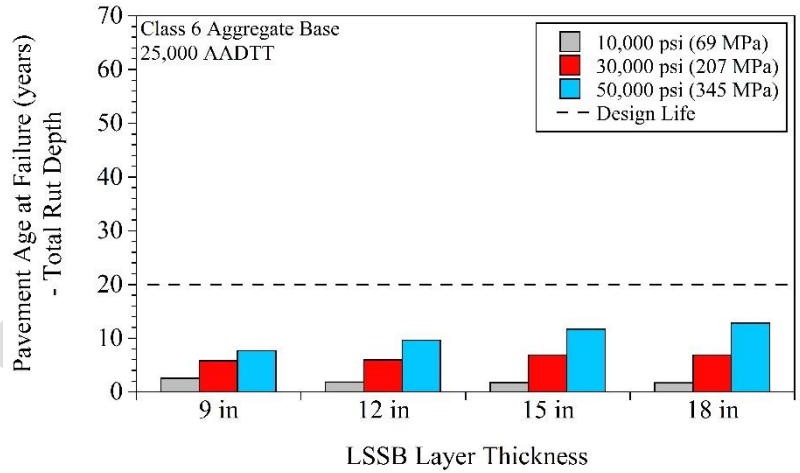


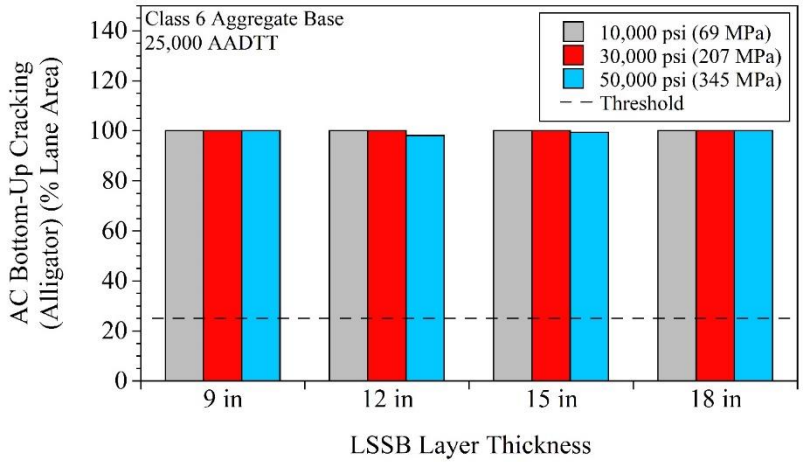
For pavement models that contained class 6 aggregate base – 25,000 AADTT:

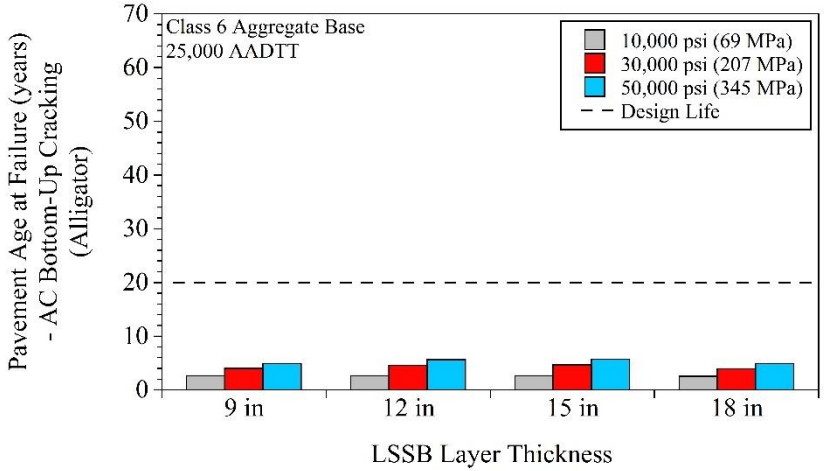




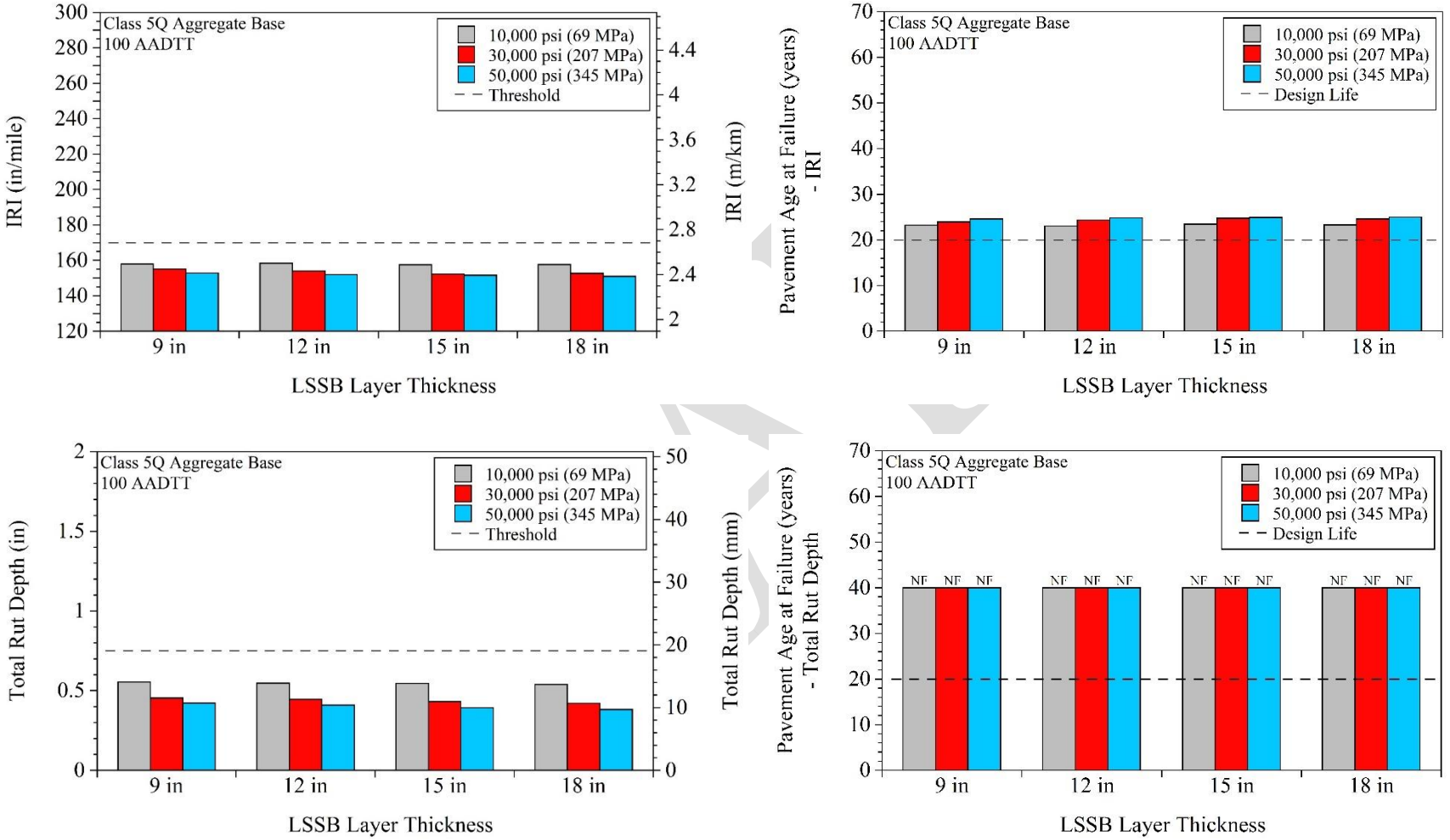

Class 6 Aggregate Base
25,000 AADTT
10,000 psi (69 MPa)
30,000 psi (207 MPa)
50,000 psi (345 MPa)
Threshold
Total Rut Depth (in)
Total Rut Depth (mm)
0
0.5
1
1.5
2
0
10
20
30
40
50
9 in
12 in
15 in
18 in
LSSB Layer Thickness

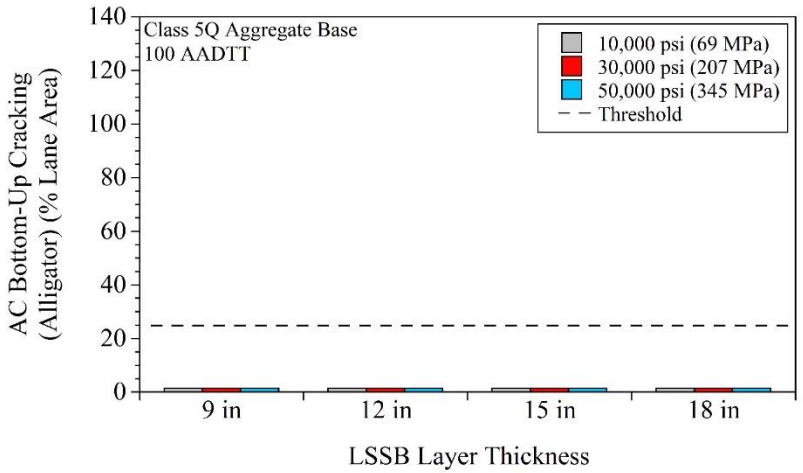

Class 6 Aggregate Base
25,000 AADTT
10,000 psi (69 MPa)
30,000 psi (207 MPa)
50,000 psi (345 MPa)
Design Life
Pavement Age at Failure (years)
- Total Rut Depth
0
10
20
30
40
50
60
70
9 in
12 in
15 in
18 in
LSSB Layer Thickness

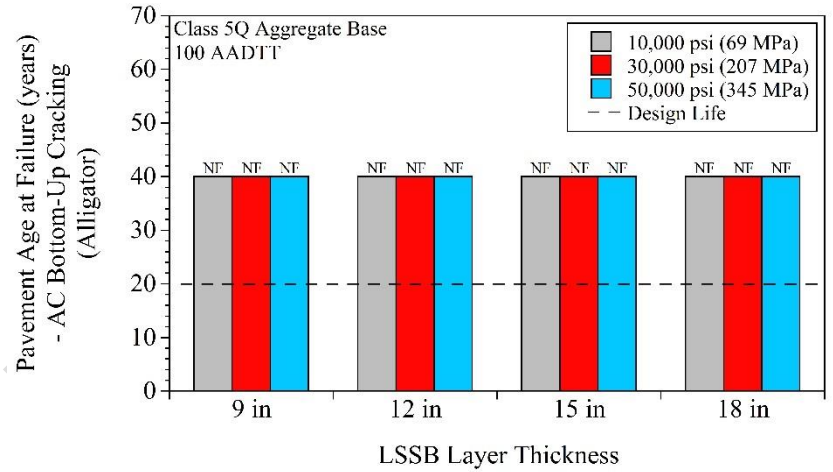

Class 6 Aggregate Base
25,000 AADTT
10,000 psi (69 MPa)
30,000 psi (207 MPa)
50,000 psi (345 MPa)
Threshold
AC Bottom-Up Cracking
(Alligator) (% Lane Area)
0
20
40
60
80
100
120
140
9 in
12 in
15 in
18 in
LSSB Layer Thickness


Class 6 Aggregate Base
25,000 AADTT
10,000 psi (69 MPa)
30,000 psi (207 MPa)
50,000 psi (345 MPa)
Design Life
Pavement Age at Failure (years)
- AC Bottom-Up Cracking
(Alligator)
0
10
20
30
40
50
60
70
9 in
12 in
15 in
18 in
LSSB Layer Thickness

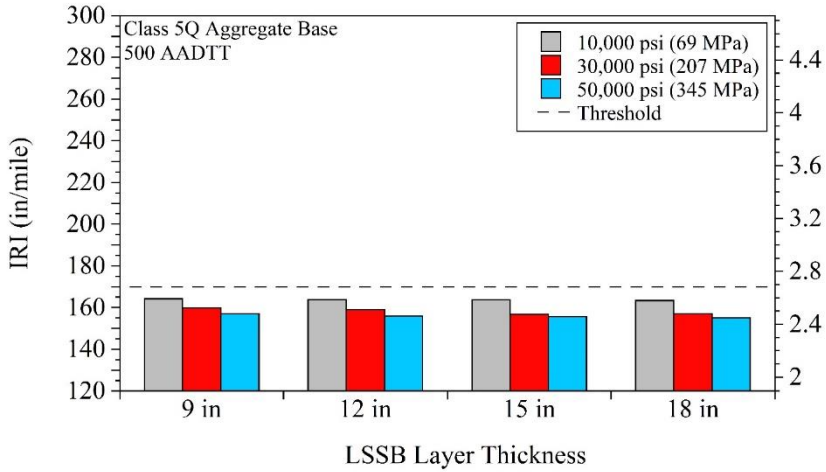
For pavement models that contained class 5Q aggregate base – 100 AADTT:

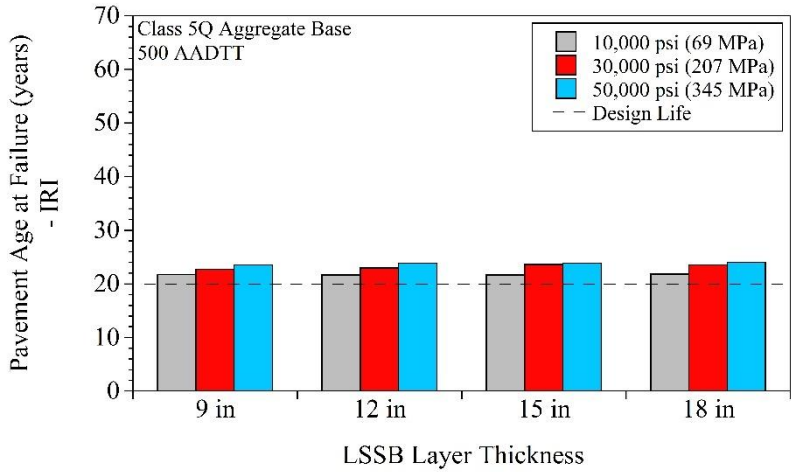


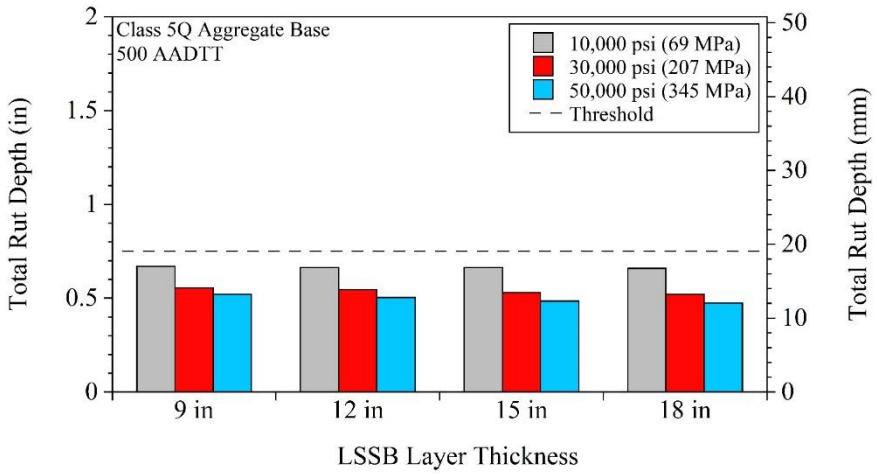


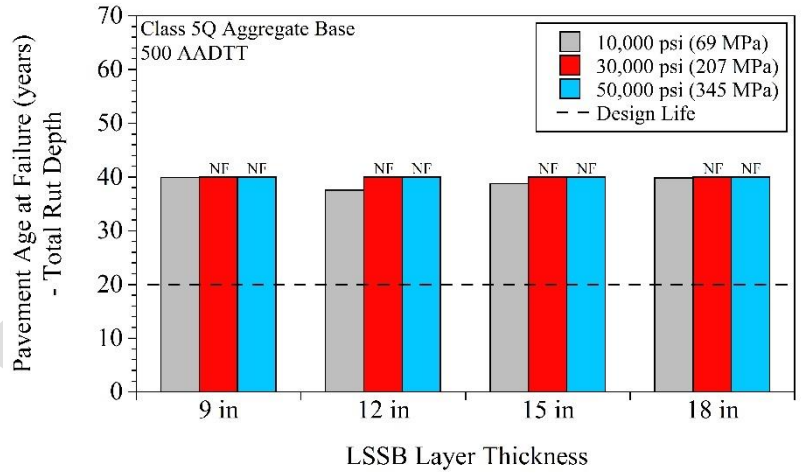


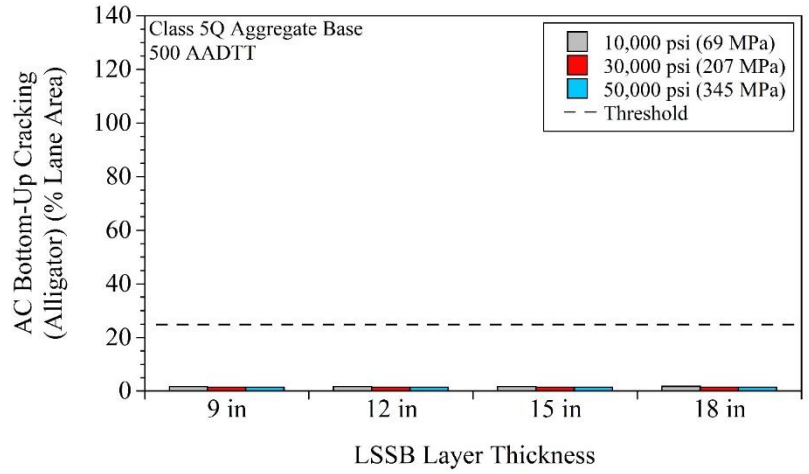
For pavement models that contained class 5Q aggregate base – 500 AADTT:

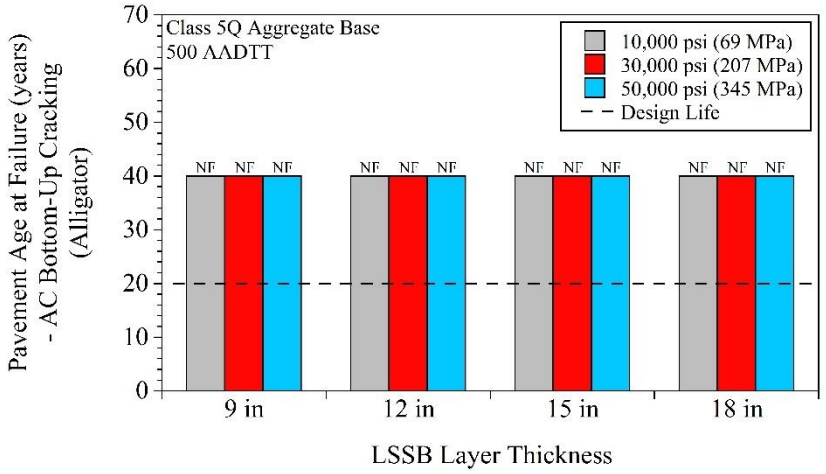




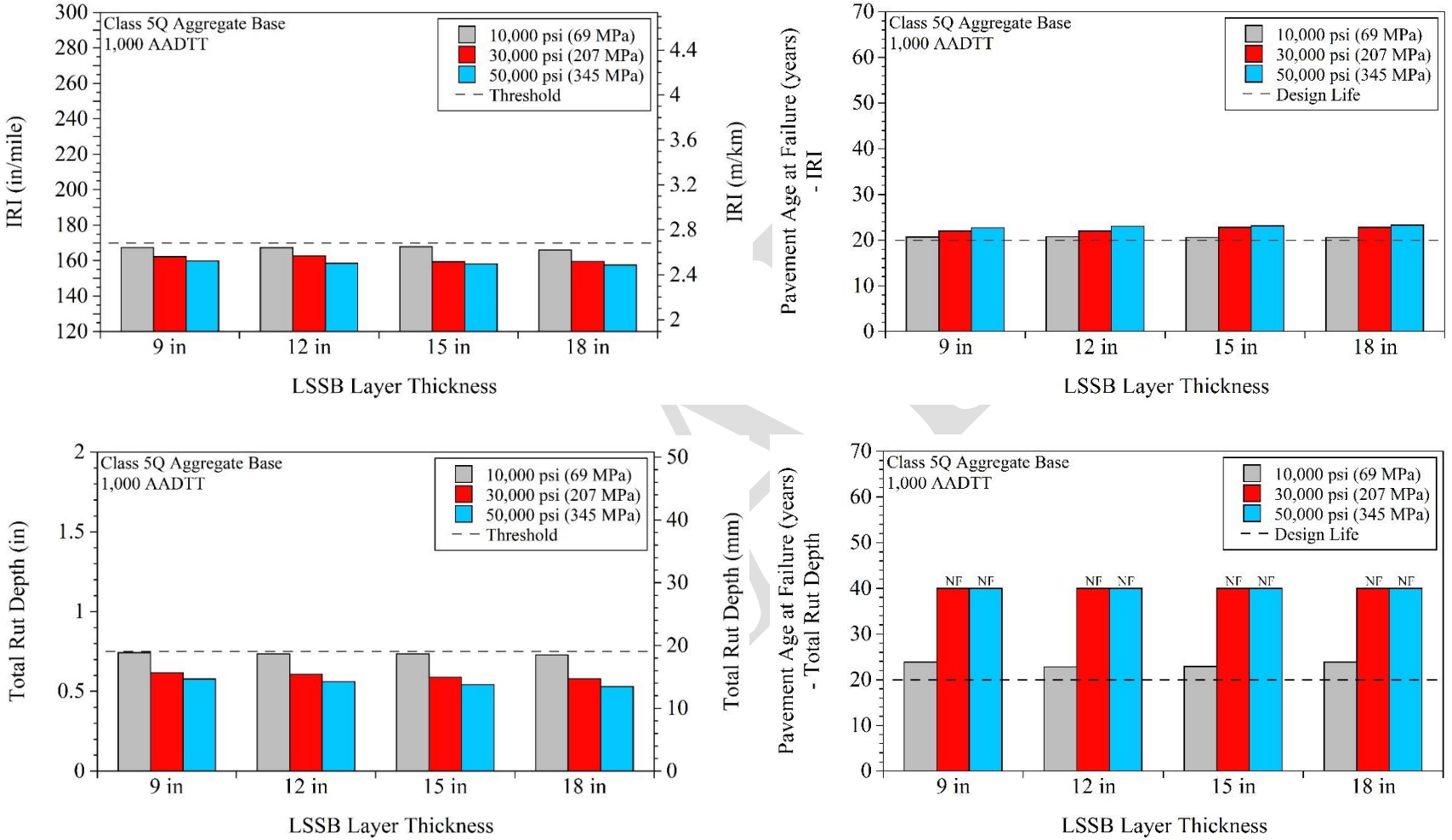

Class 5Q Aggregate Base
500 AADTT
10,000 psi (69 MPa)
30,000 psi (207 MPa)
50,000 psi (345 MPa)
Threshold
Total Rut Depth (in)
Total Rut Depth (mm)
0
0.5
1
1.5
2
0
10
20
30
40
50
9 in
12 in
15 in
18 in
LSSB Layer Thickness

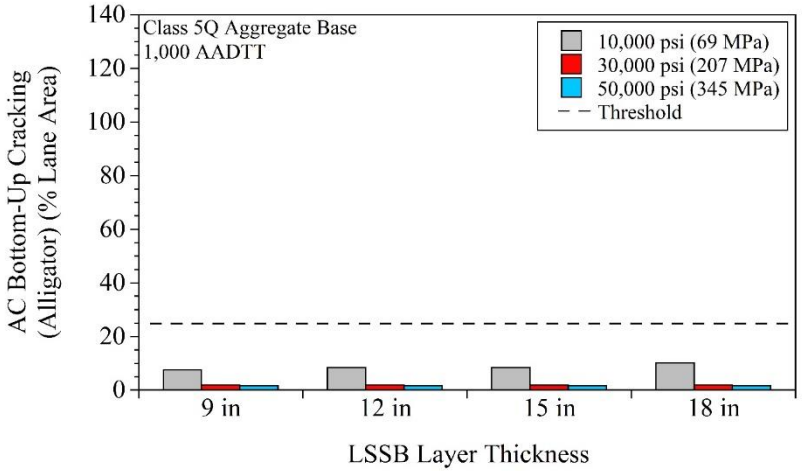

Class 5Q Aggregate Base
500 AADTT
10,000 psi (69 MPa)
30,000 psi (207 MPa)
50,000 psi (345 MPa)
Design Life
Pavement Age at Failure (years)
- Total Rut Depth
0
10
20
30
40
50
60
70
NF
9 in
12 in
15 in
18 in
LSSB Layer Thickness

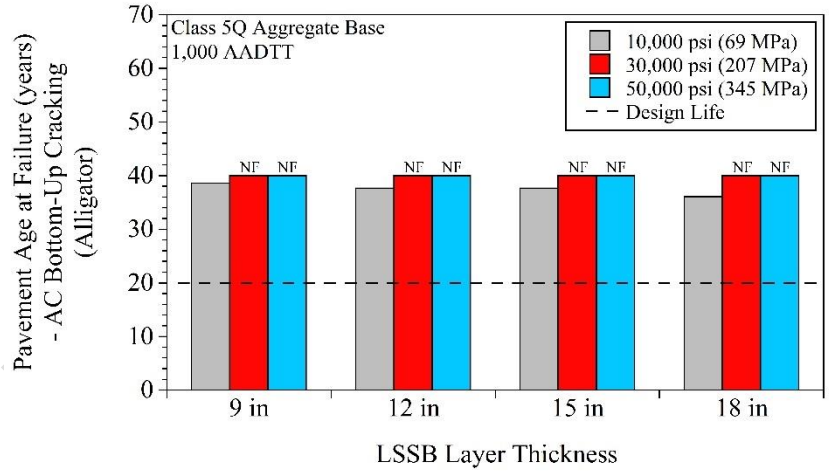

Class 5Q Aggregate Base
500 AADTT
10,000 psi (69 MPa)
30,000 psi (207 MPa)
50,000 psi (345 MPa)
Threshold
AC Bottom-Up Cracking
(Alligator) (% Lane Area)
0
20
40
60
80
100
120
140
9 in
12 in
15 in
18 in
LSSB Layer Thickness


Class 5Q Aggregate Base
500 AADTT
10,000 psi (69 MPa)
30,000 psi (207 MPa)
50,000 psi (345 MPa)
Design Life
Pavement Age at Failure (years)
- AC Bottom-Up Cracking
(Alligator)
0
10
20
30
40
50
60
70
NF
9 in
12 in
15 in
18 in
LSSB Layer Thickness

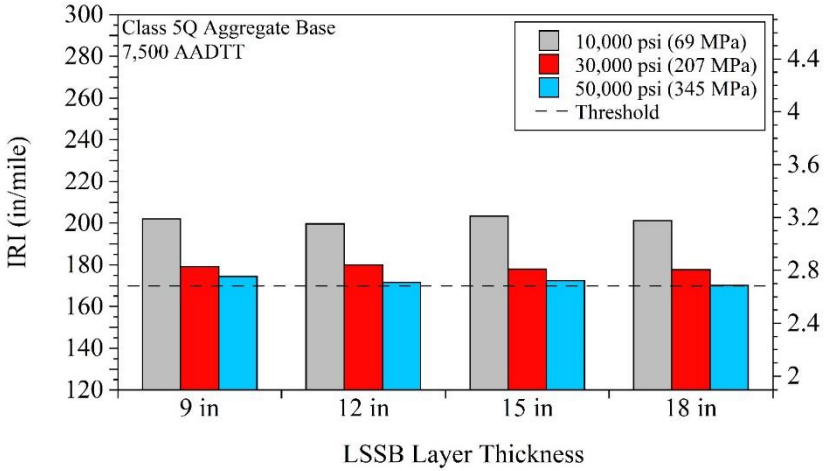
For pavement models that contained class 5Q aggregate base – 1,000 AADTT:

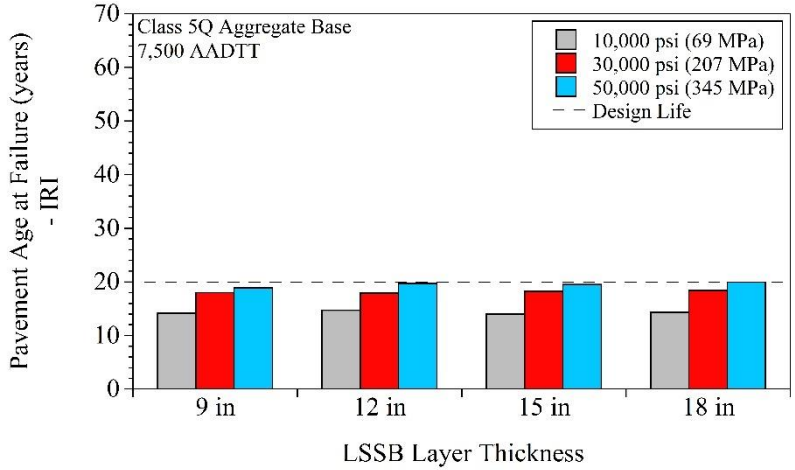


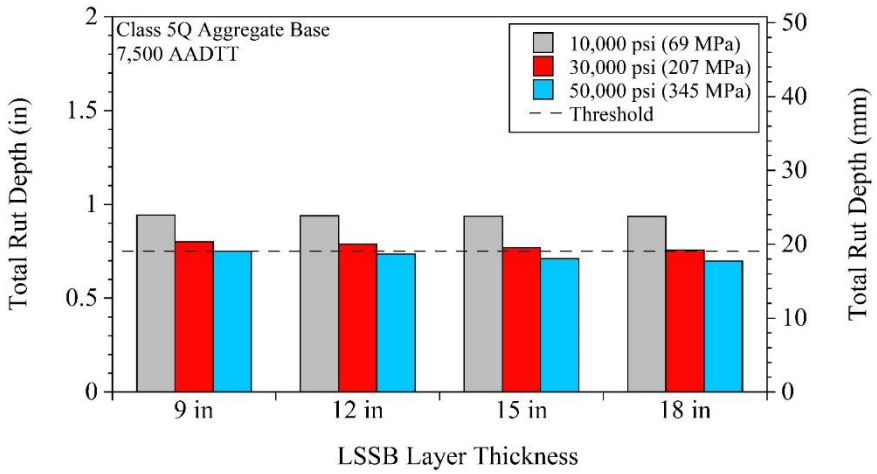


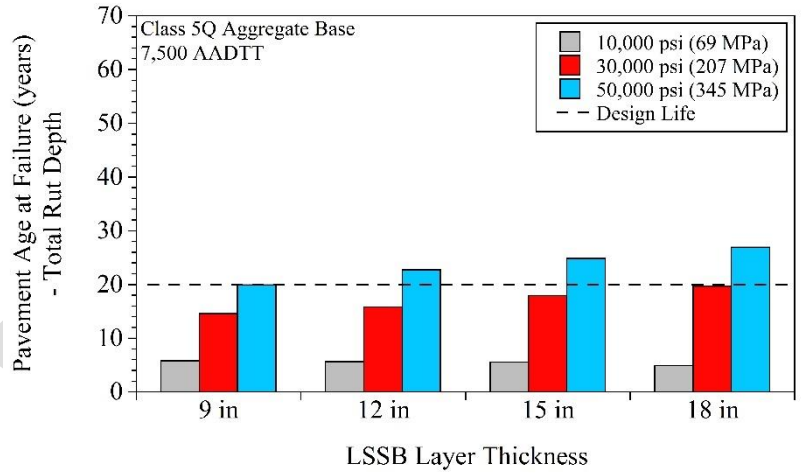


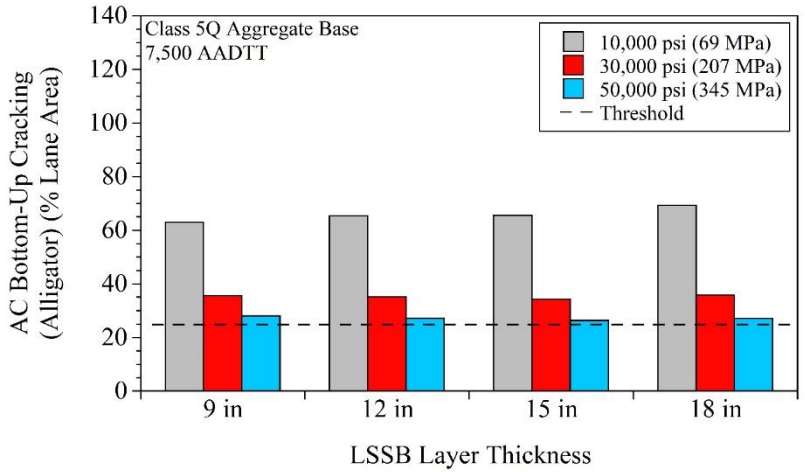
For pavement models that contained class 5Q aggregate base – 7,500 AADTT:

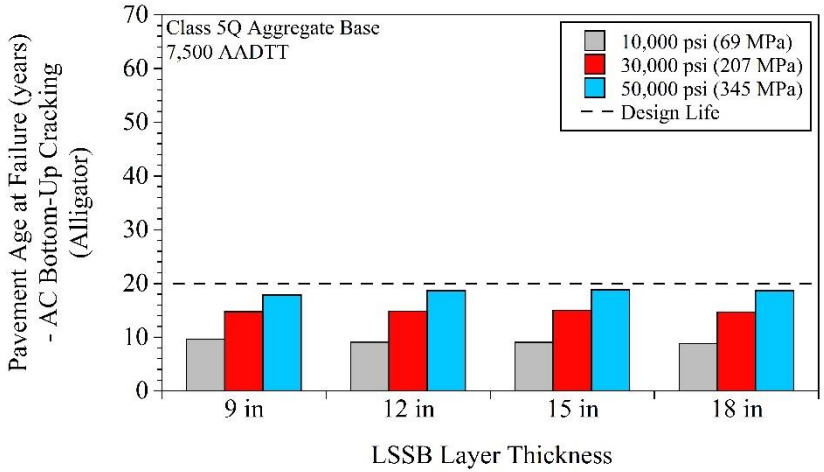




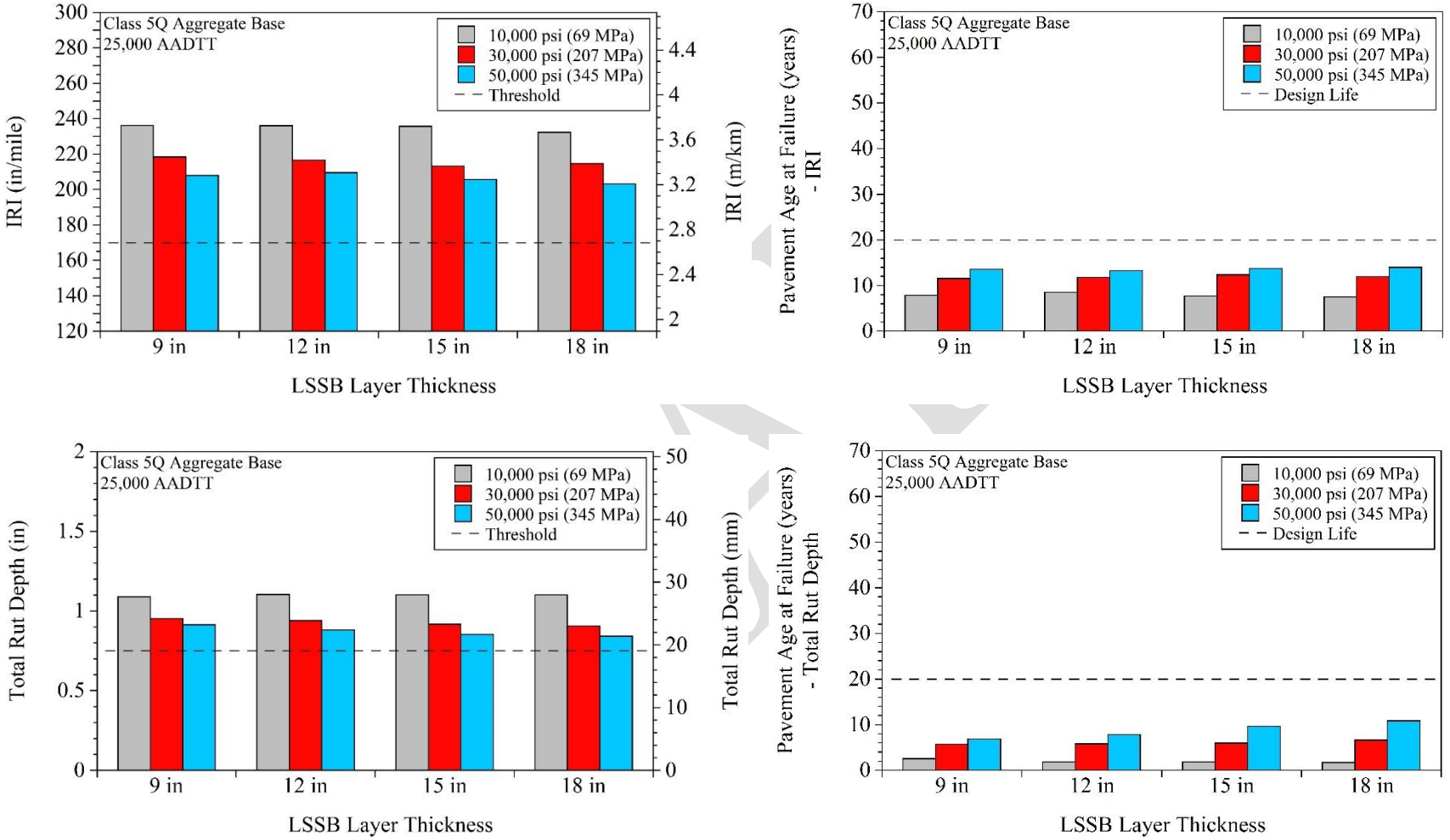

Class 5Q Aggregate Base
7,500 AADTT
10,000 psi (69 MPa)
30,000 psi (207 MPa)
50,000 psi (345 MPa)
Threshold
Total Rut Depth (in)
Total Rut Depth (mm)
9 in
12 in
15 in
18 in
LSSB Layer Thickness

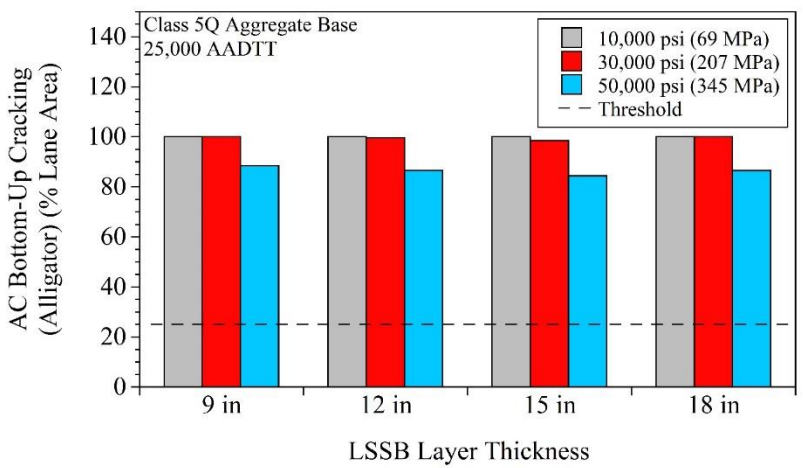

Class 5Q Aggregate Base
7,500 AADTT
10,000 psi (69 MPa)
30,000 psi (207 MPa)
50,000 psi (345 MPa)
Design Life
Pavement Age at Failure (years)
- Total Rut Depth
9 in
12 in
15 in
18 in
LSSB Layer Thickness

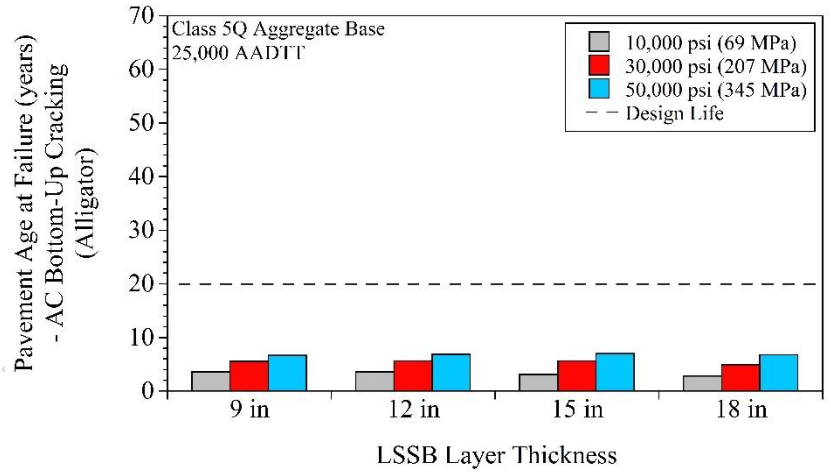

Class 5Q Aggregate Base
7,500 AADTT
10,000 psi (69 MPa)
30,000 psi (207 MPa)
50,000 psi (345 MPa)
Threshold
AC Bottom-Up Cracking
(Alligator) (% Lane Area)
9 in
12 in
15 in
18 in
LSSB Layer Thickness


Class 5Q Aggregate Base
7,500 AADTT
10,000 psi (69 MPa)
30,000 psi (207 MPa)
50,000 psi (345 MPa)
Design Life
Pavement Age at Failure (years)
- AC Bottom-Up Cracking
(Alligator)
9 in
12 in
15 in
18 in
LSSB Layer Thickness

For pavement models that contained class 5Q aggregate base – 25,000 AADTT:



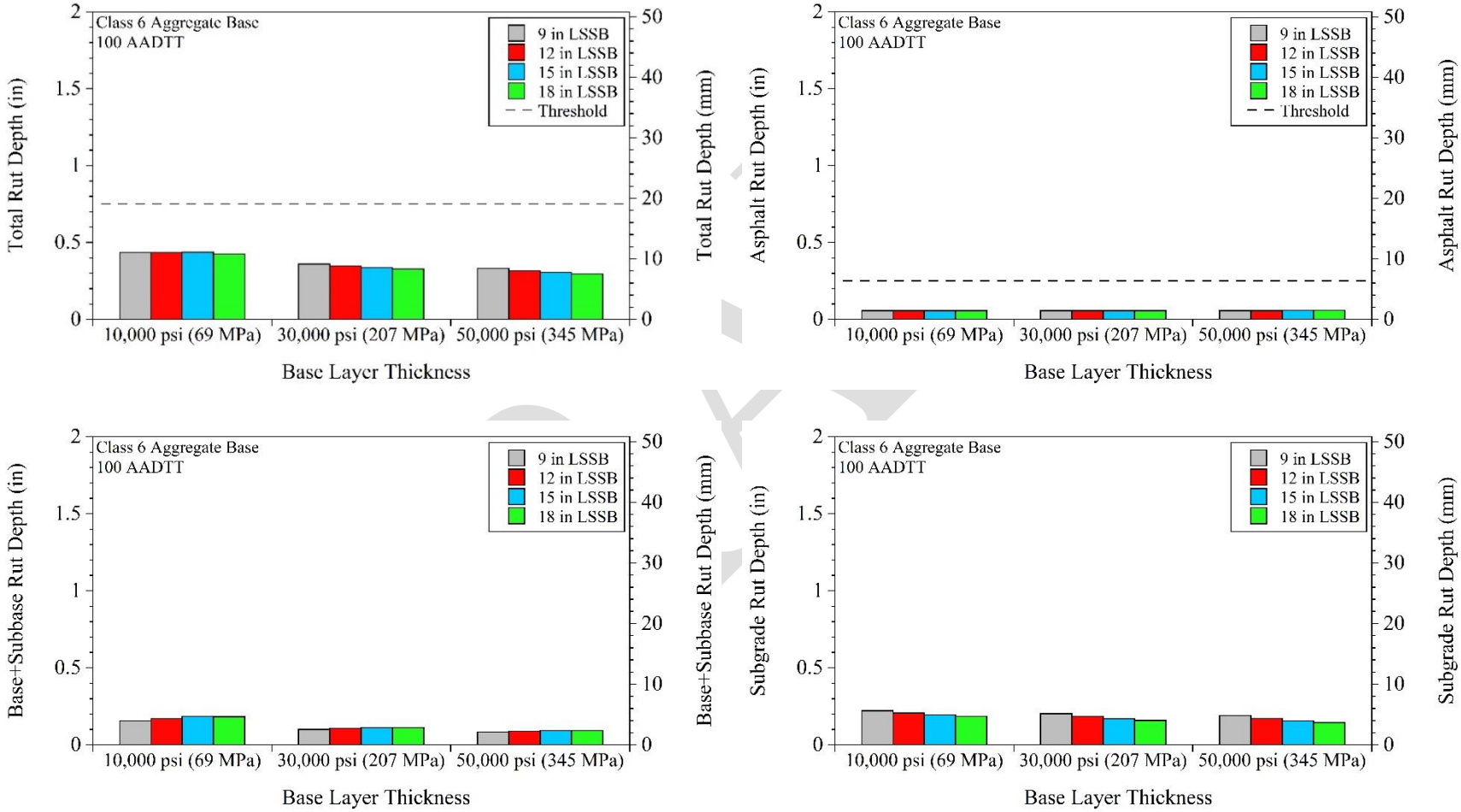

Class 5Q Aggregate Base
25,000 AADTT
10,000 psi (69 MPa)
30,000 psi (207 MPa)
50,000 psi (345 MPa)
Threshold
AC Bottom-Up Cracking
(Alligator) (% Lane Area)
0
20
40
60
80
100
120
140
9 in
12 in
15 in
18 in
LSSB Layer Thickness


Class 5Q Aggregate Base
25,000 AADTT
10,000 psi (69 MPa)
30,000 psi (207 MPa)
50,000 psi (345 MPa)
Design Life
Pavement Age at Failure (years)
- AC Bottom-Up Cracking
(Alligator)
0
10
20
30
40
50
60
70
9 in
12 in
15 in
18 in
LSSB Layer Thickness

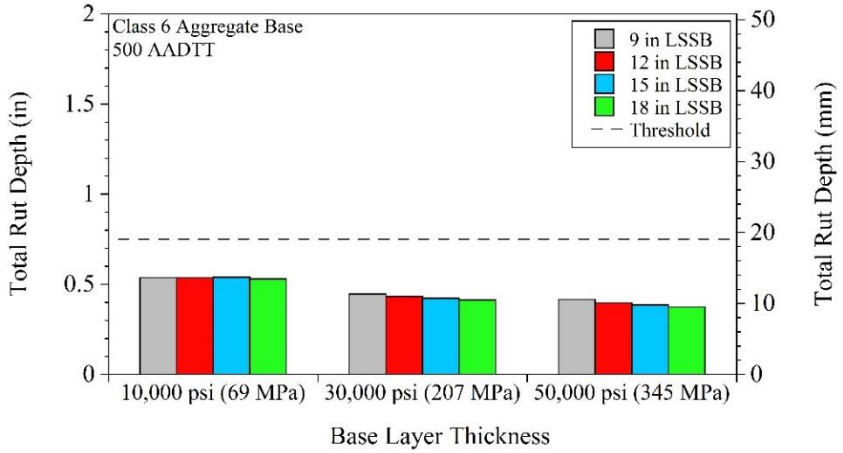
DRAFT

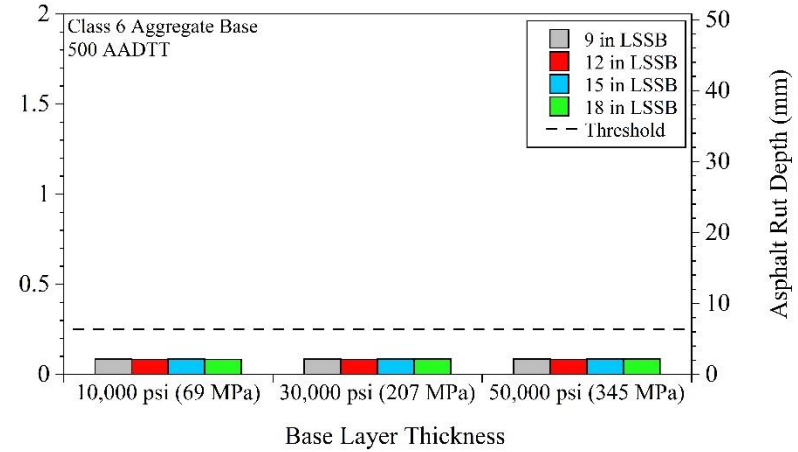
APPENDIX AB. TOTAL, ASPHALT, BASE+SUBBASE, AND SUBGRADE LAYER RUTTING AT 50% RELIABILITY FOR LARGE STONE SUBBASE (LSSB) GROUPS

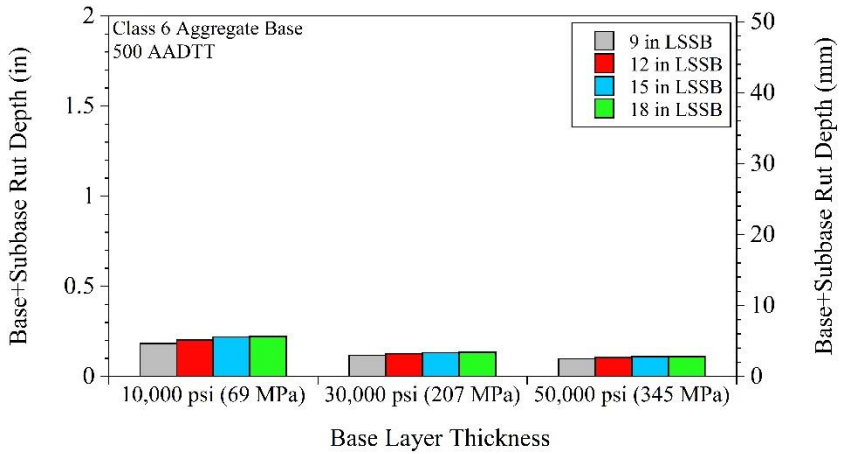
For pavements that contained class 6 aggregate – 100 AADTT:

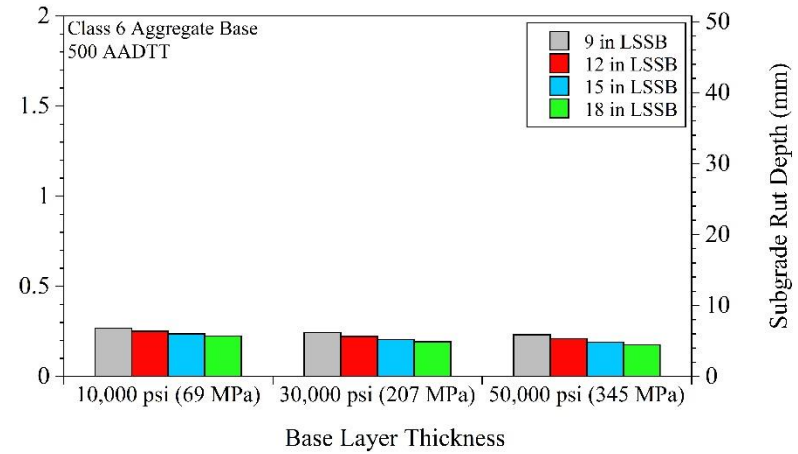


For pavements that contained class 6 aggregate – 500 AADTT:

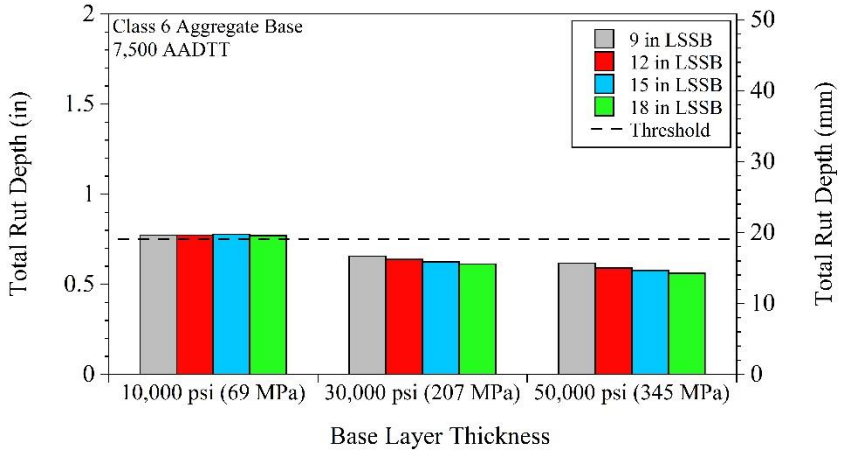


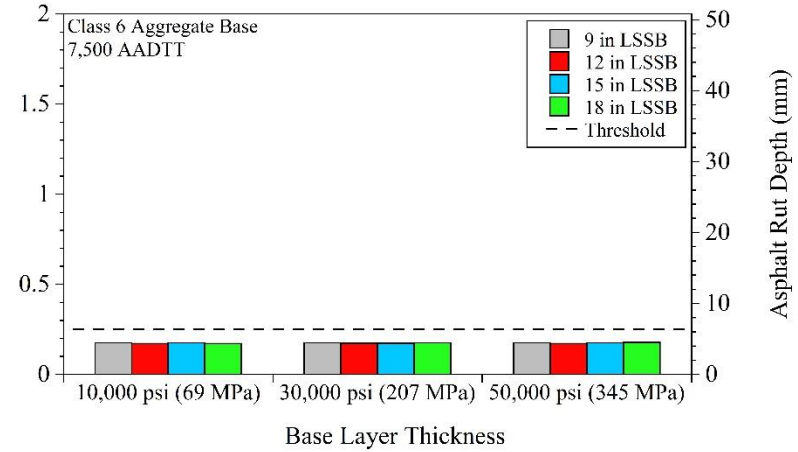


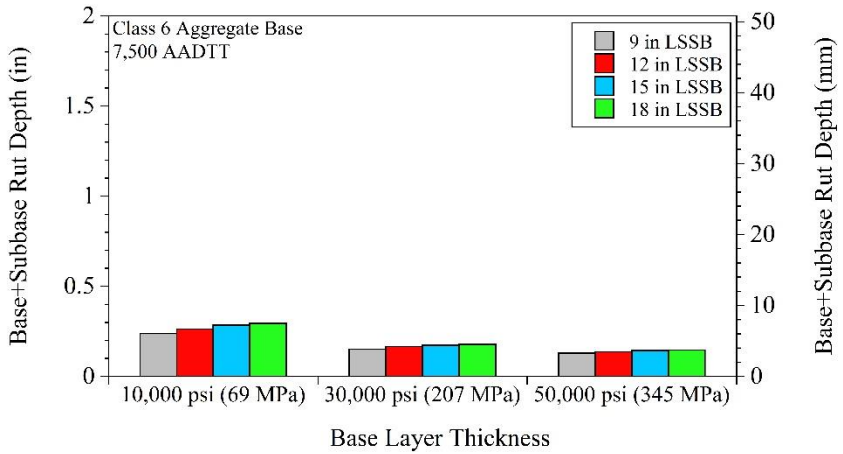


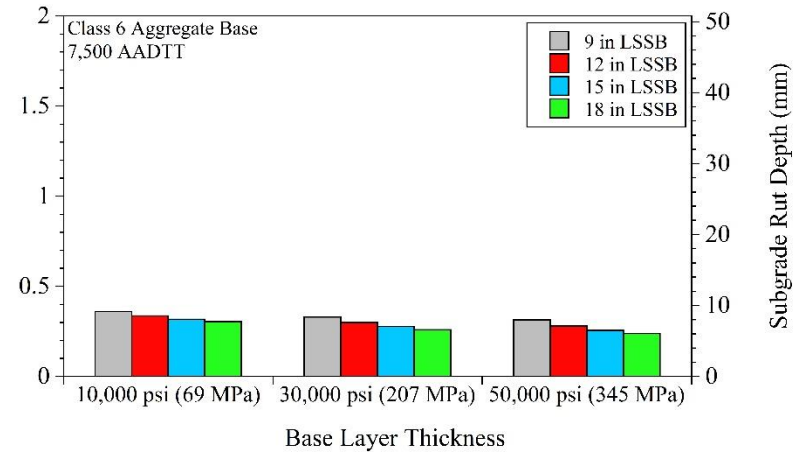


For pavements that contained class 6 aggregate – 7,500 AADTT:

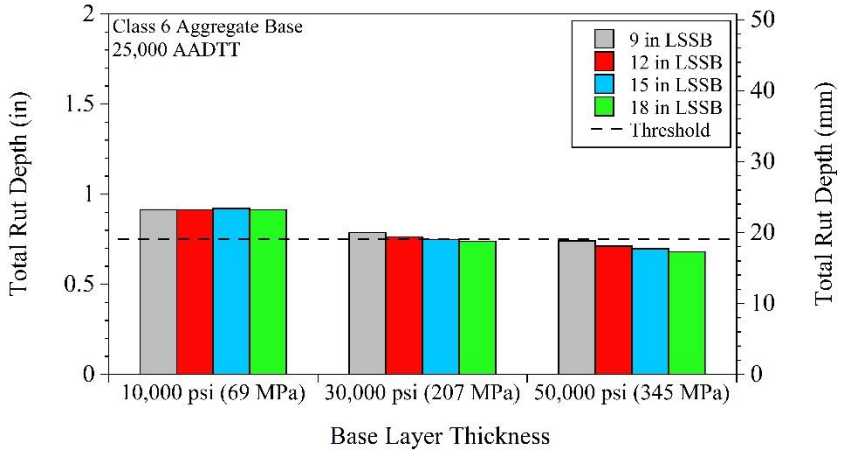


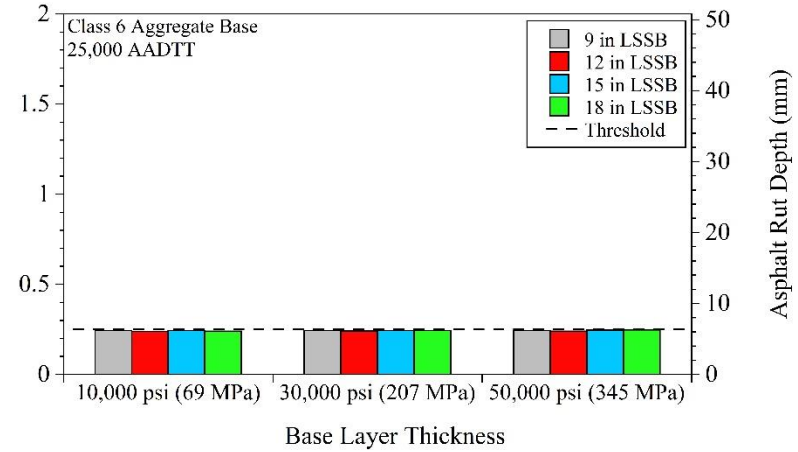


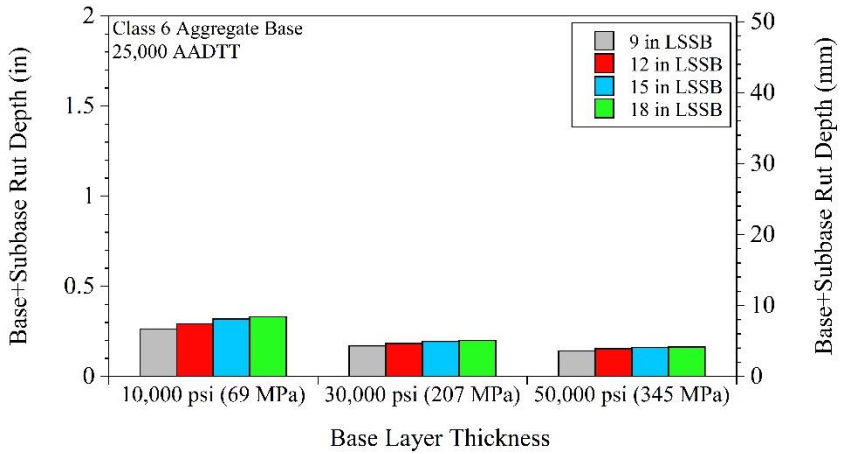


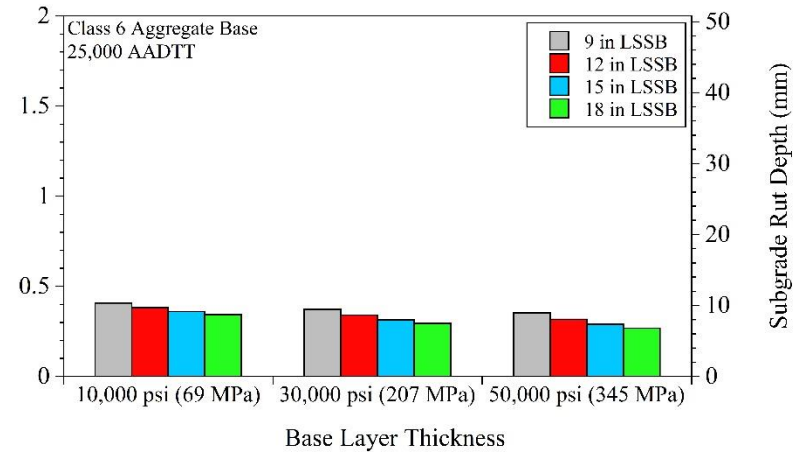


For pavements that contained class 6 aggregate – 25,000 AADTT:

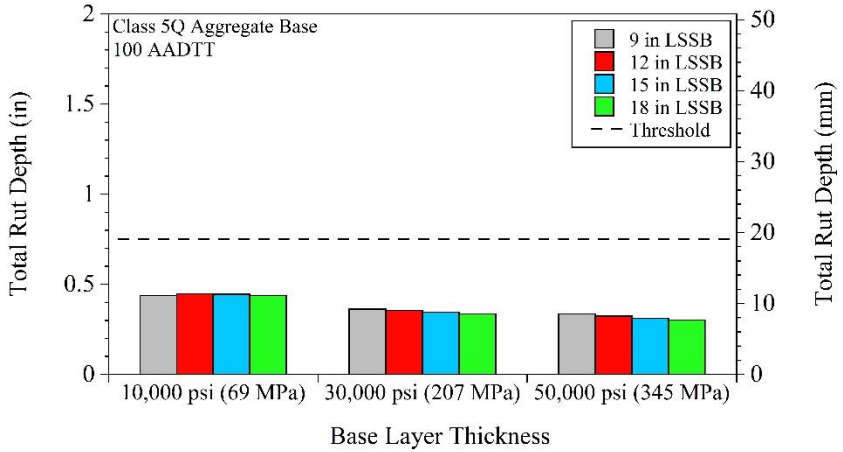


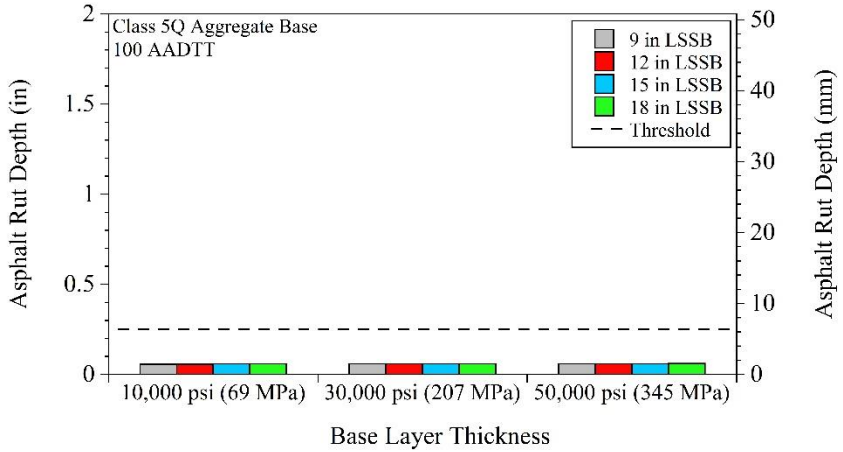


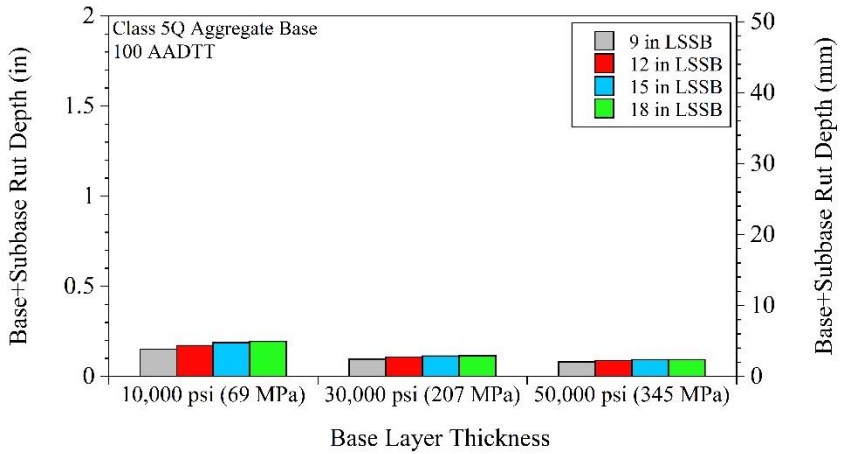


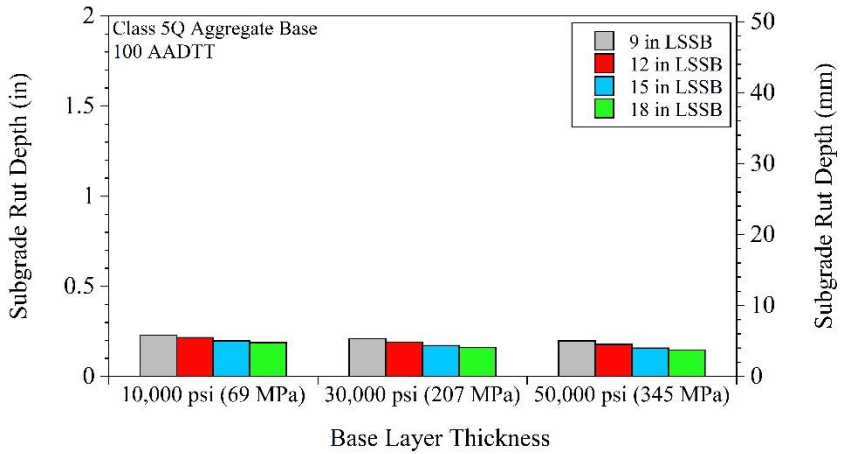


For pavements that contained class 5Q aggregate – 100 AADTT:

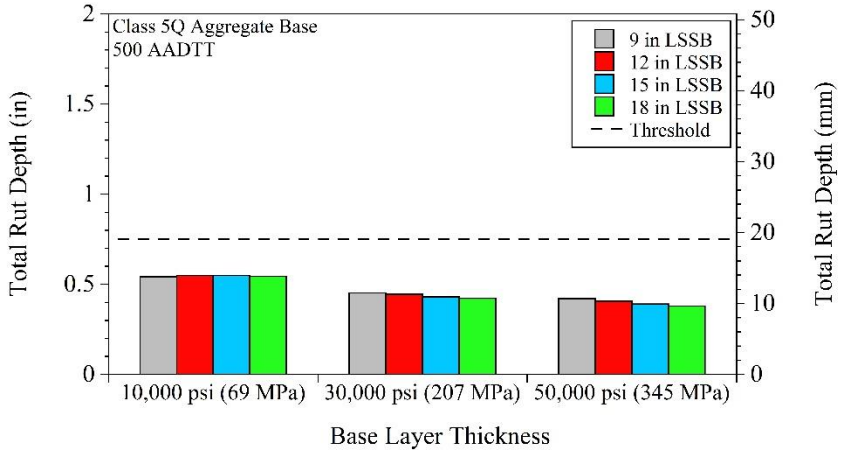


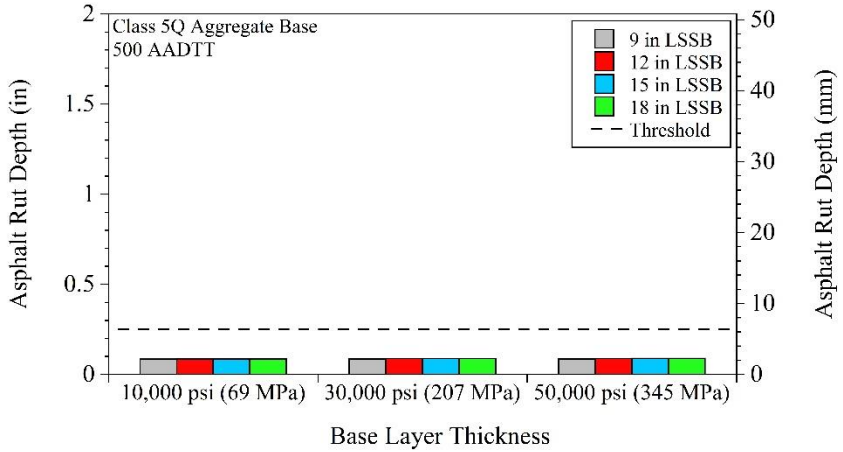


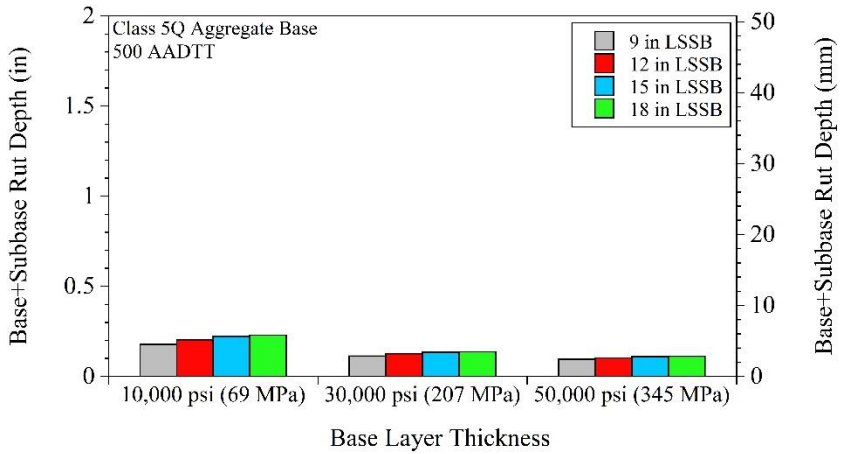


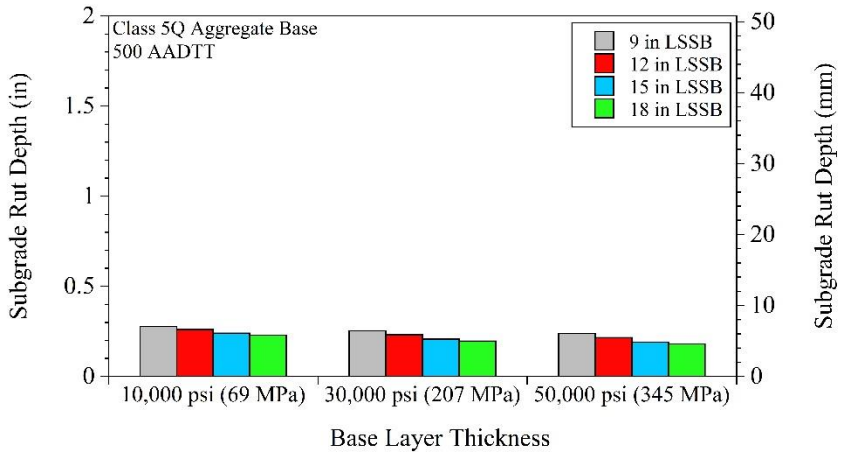


For pavements that contained class 5Q aggregate – 500 AADTT:

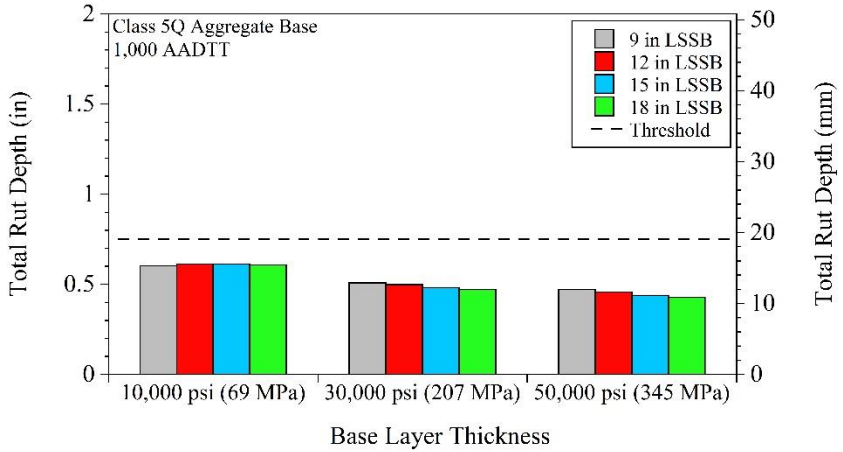


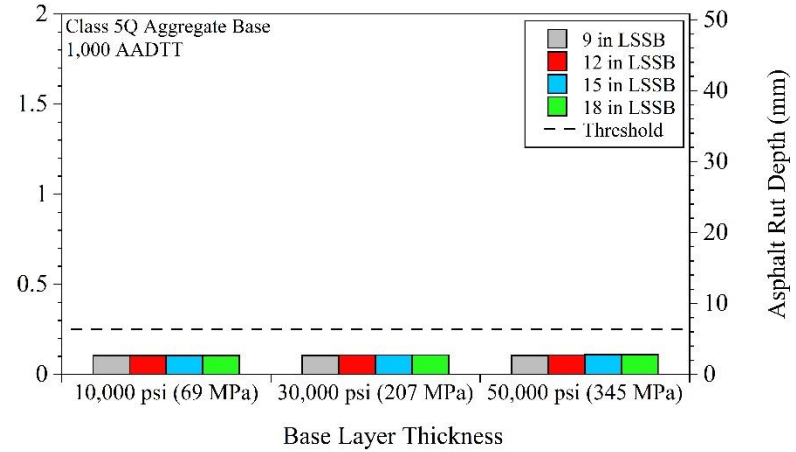


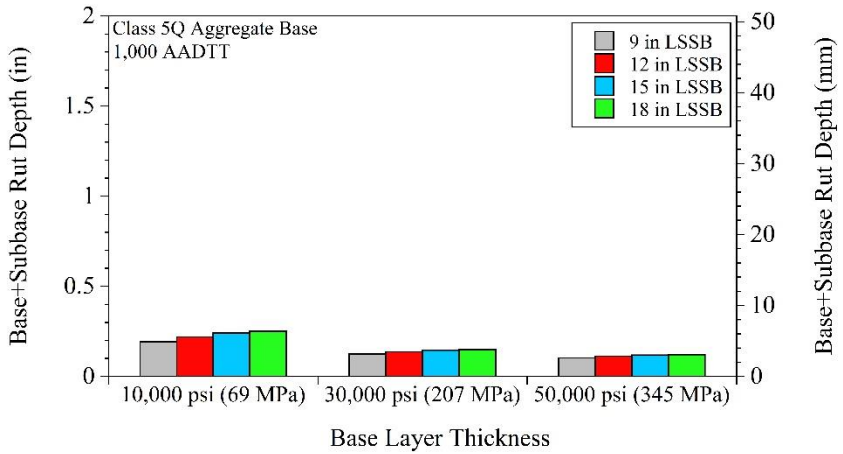


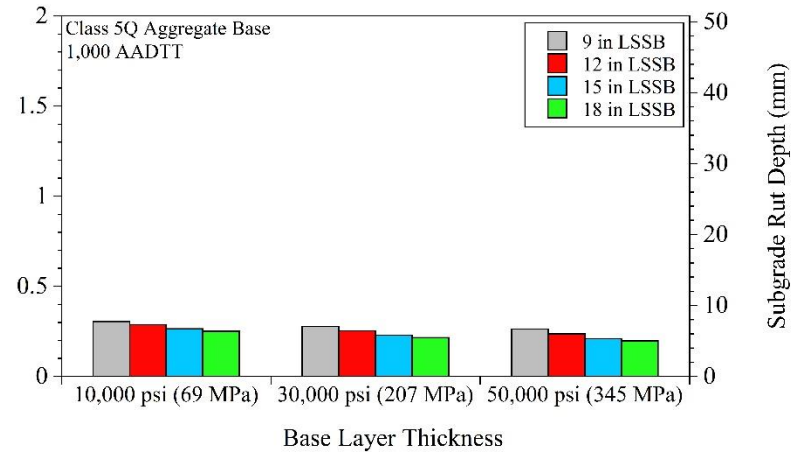


For pavements that contained class 5Q aggregate – 1,000 AADTT:

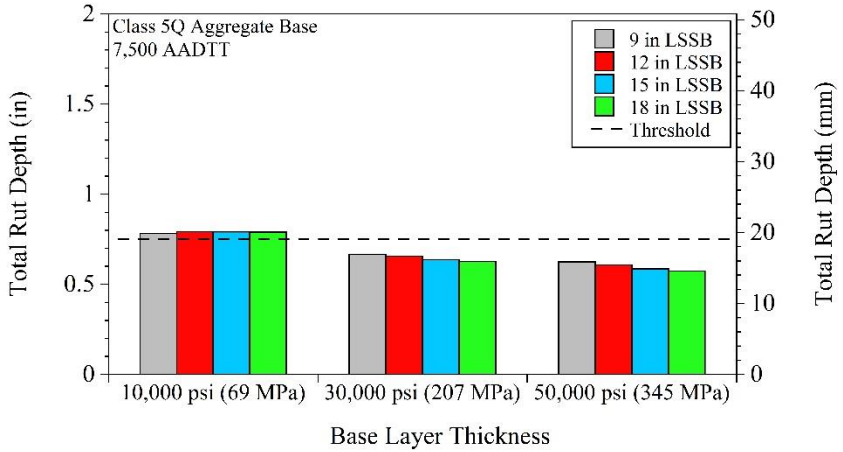


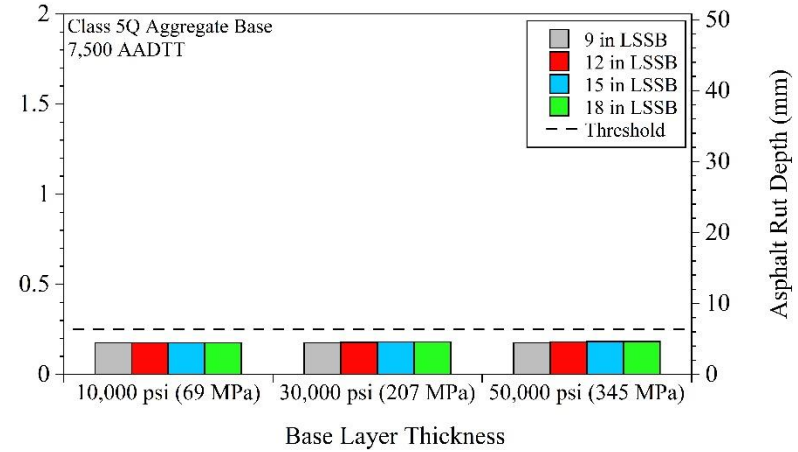


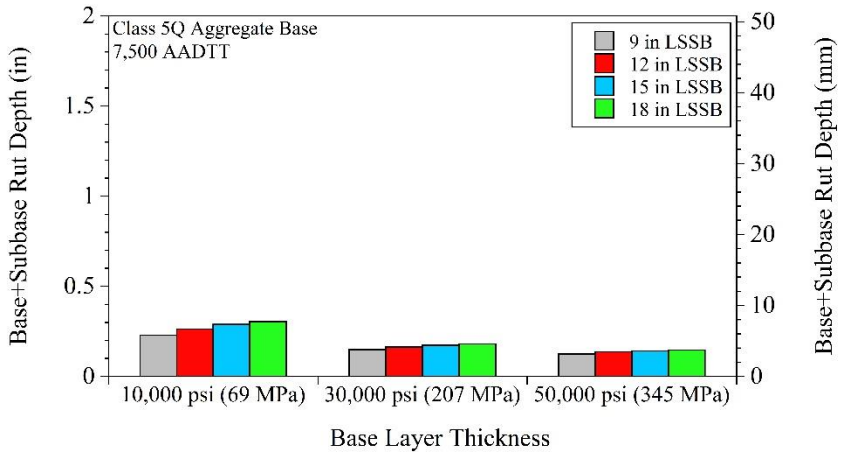


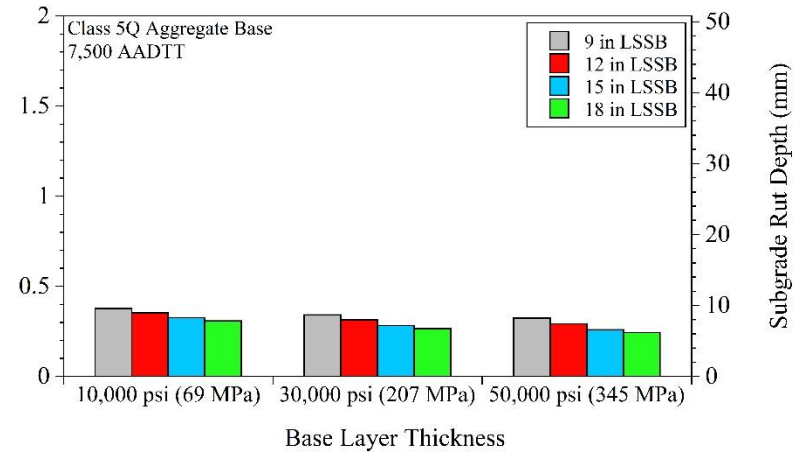


For pavements that contained class 5Q aggregate – 7,500 AADTT:

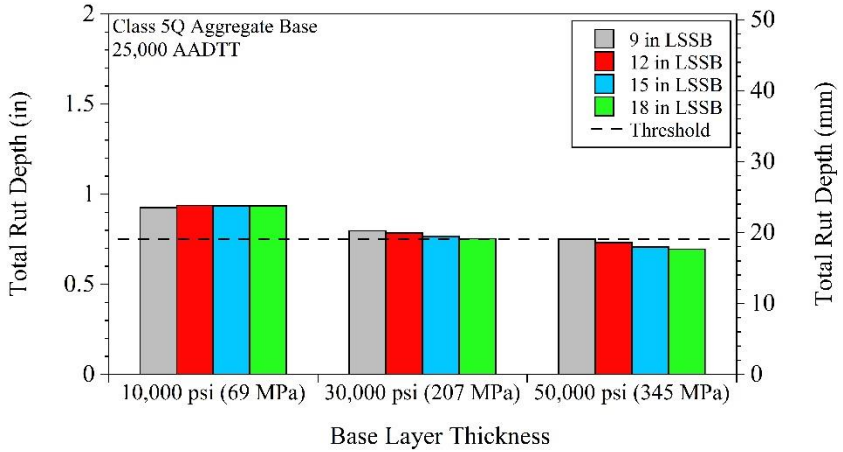


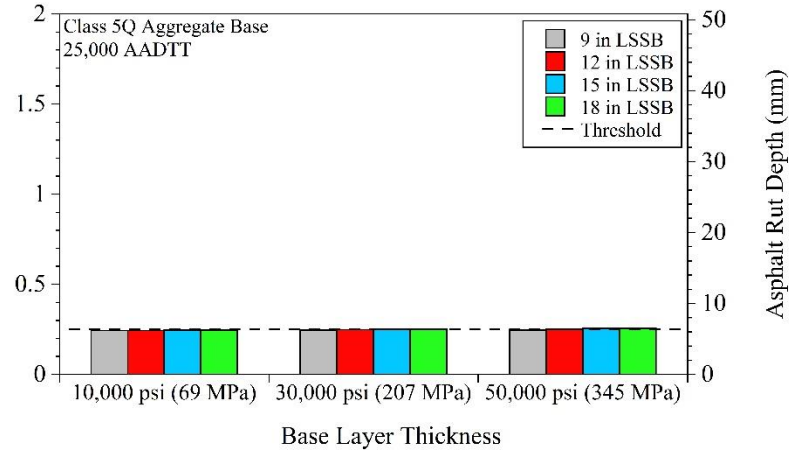


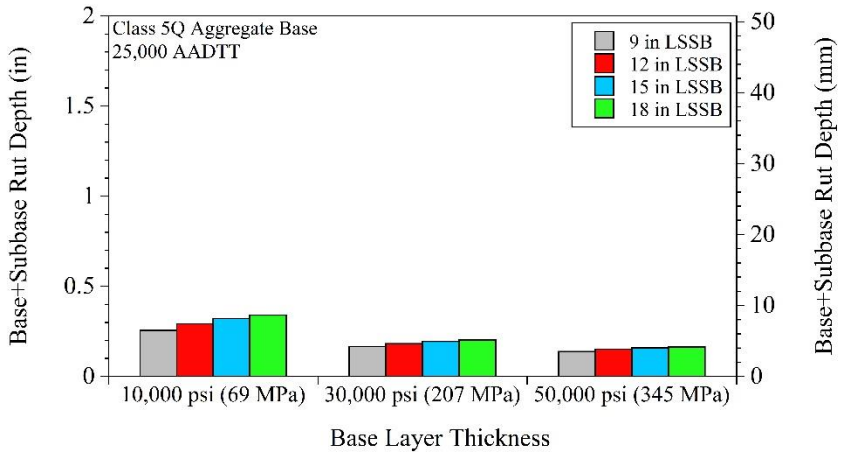


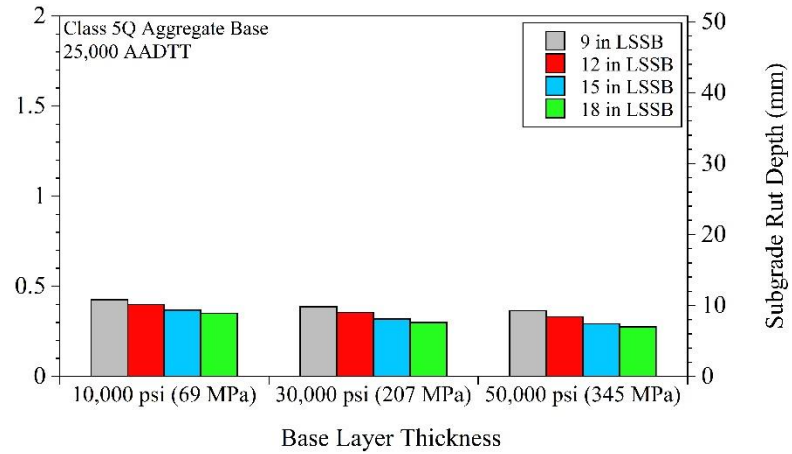


For pavements that contained class 5Q aggregate – 25,000 AADTT:



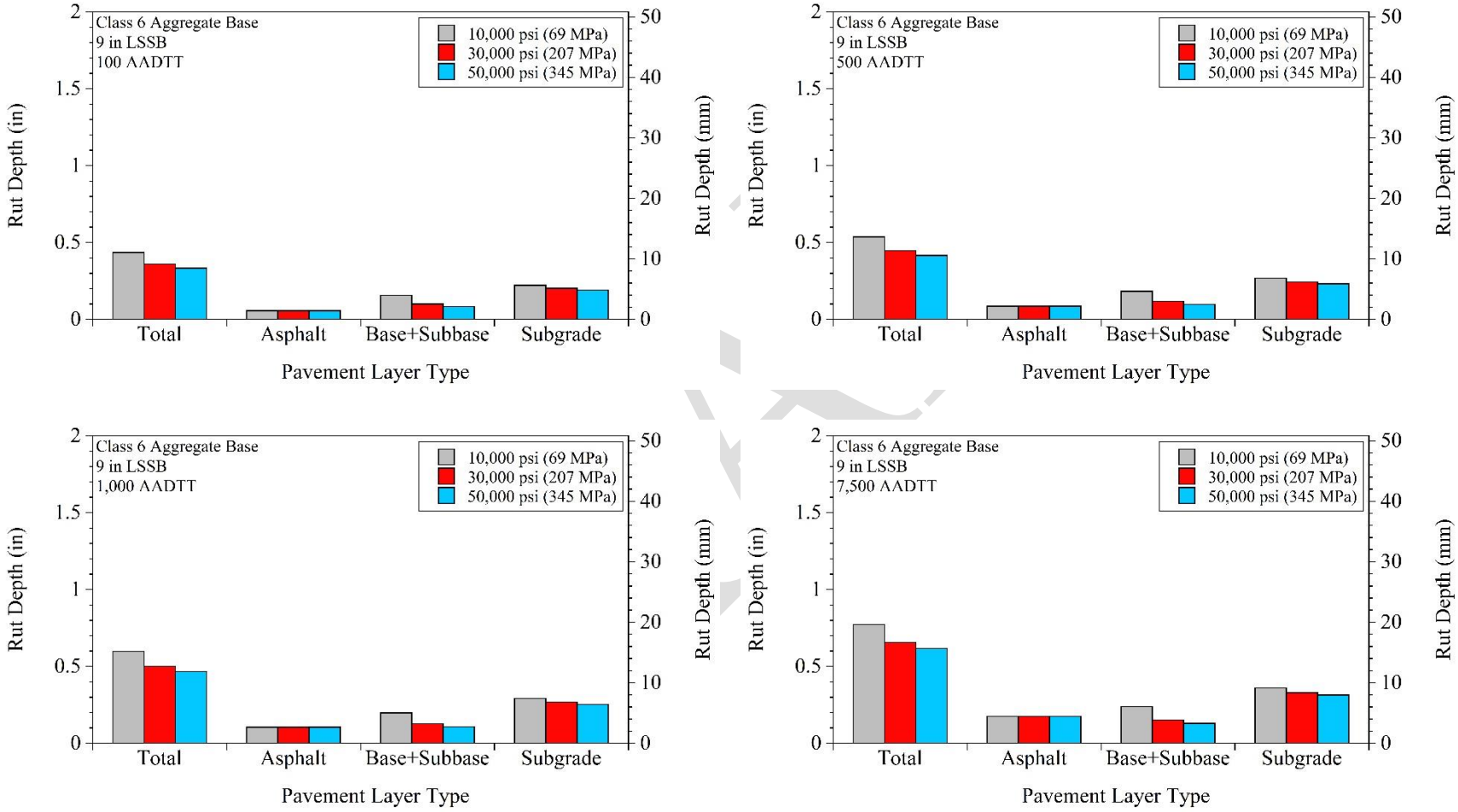


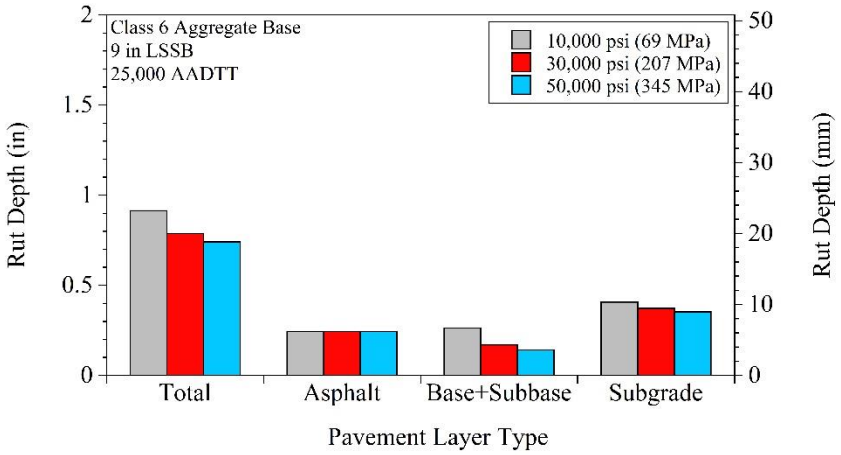




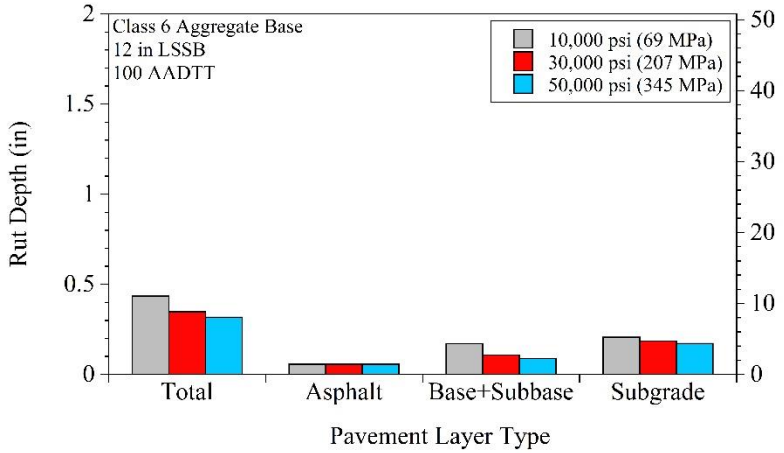
APPENDIX AC. TOTAL AND LAYER RUTTING AT 50% RELIABILITY FOR LARGE STONE SUBBASE (LSSB) GROUPS

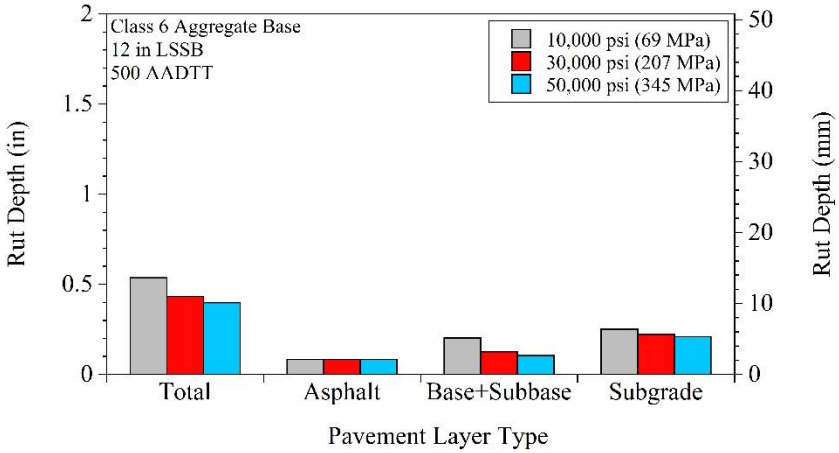
For pavements that contained class 6 aggregate and 9-in LSSB:



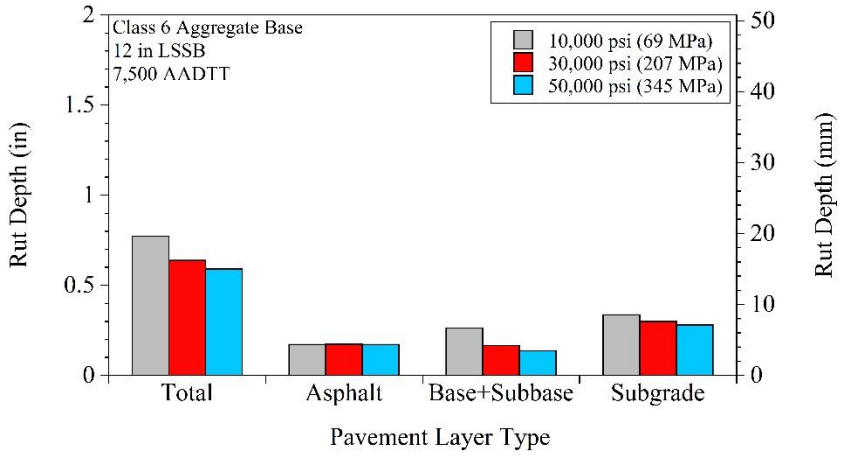


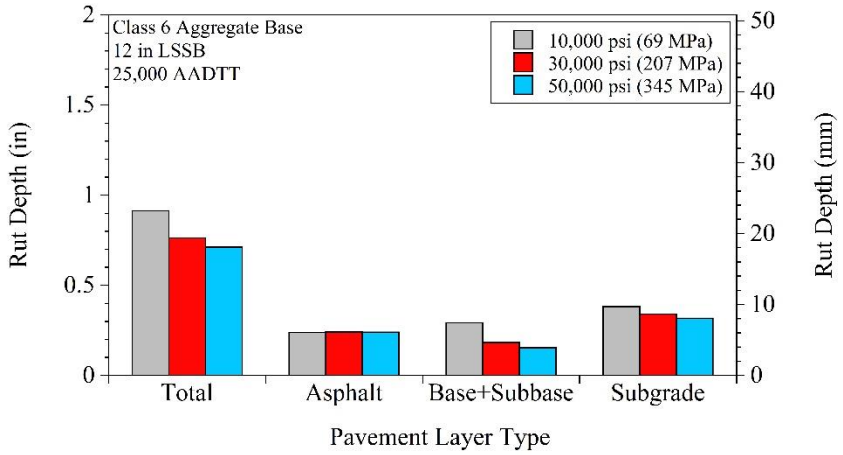
For pavements that contained class 6 aggregate and 12-in LSSB:



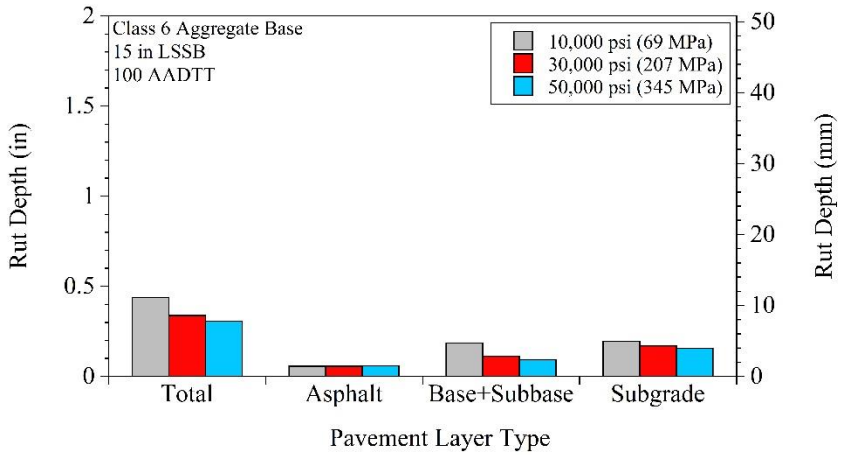


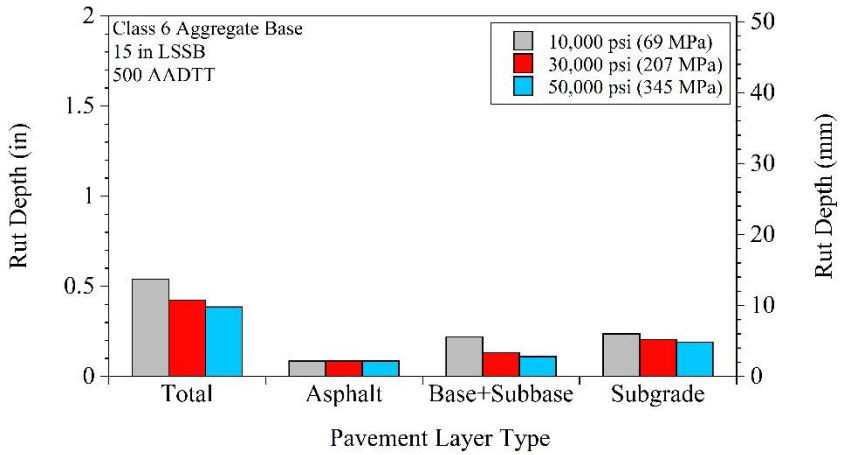
DRAFT

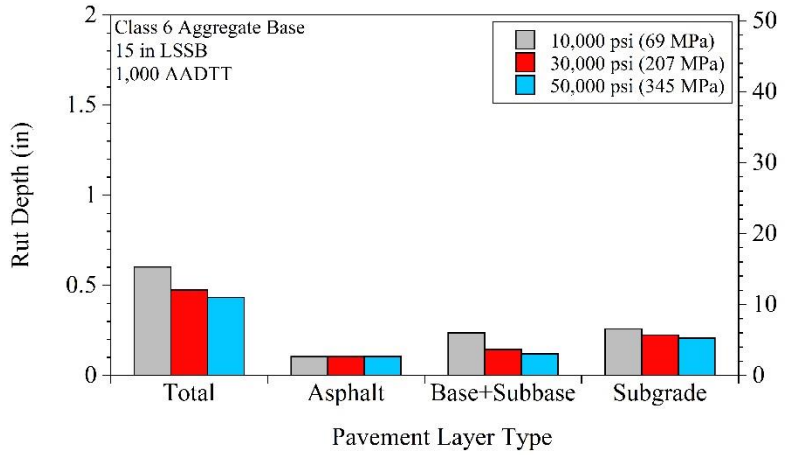


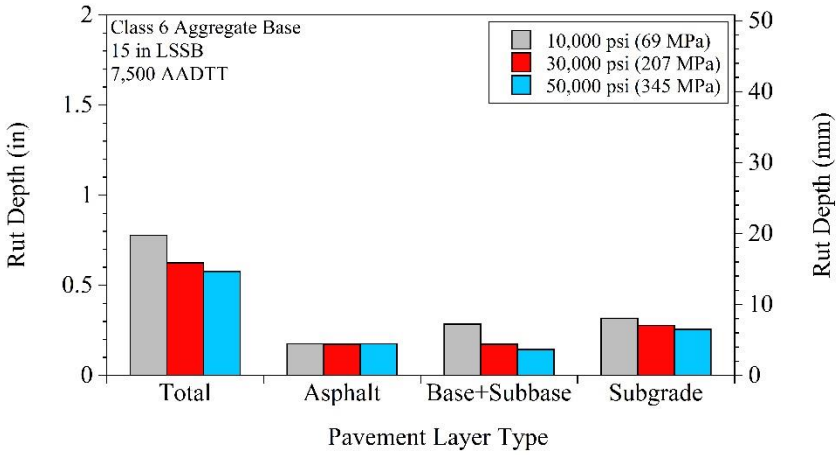


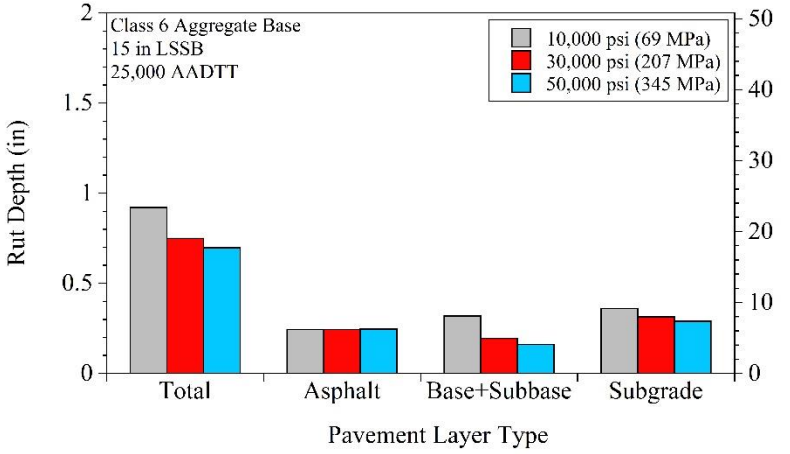
For pavements that contained class 6 aggregate and 15-in LSSB:





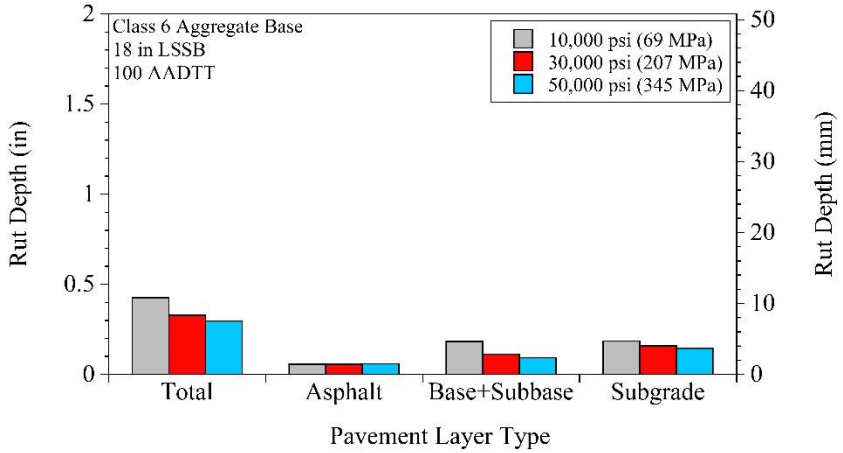

Class 6 Aggregate Base
15 in LSSB
1,000 AADTT
10,000 psi (69 MPa)
30,000 psi (207 MPa)
50,000 psi (345 MPa)
Rut Depth (in)
Rut Depth (mm)
Total
Asphalt
Base+Subbase
Subgrade
Pavement Layer Type

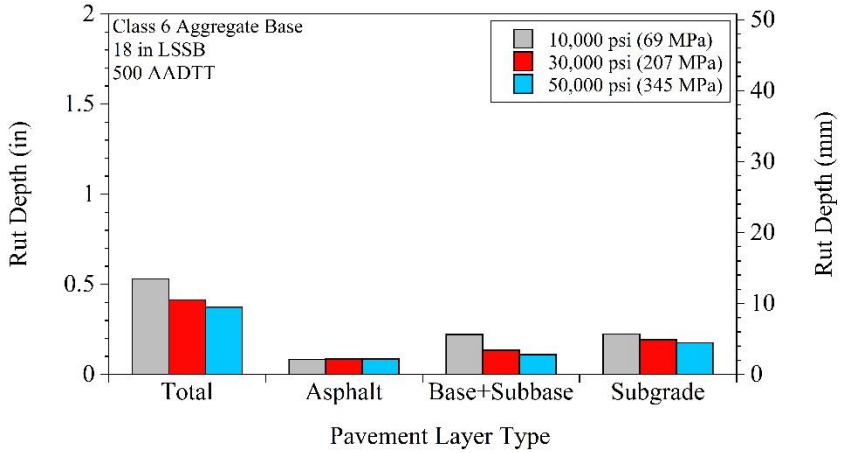

Class 6 Aggregate Base
15 in LSSB
7,500 AADTT
10,000 psi (69 MPa)
30,000 psi (207 MPa)
50,000 psi (345 MPa)
Rut Depth (in)
Rut Depth (mm)
Total
Asphalt
Base+Subbase
Subgrade
Pavement Layer Type

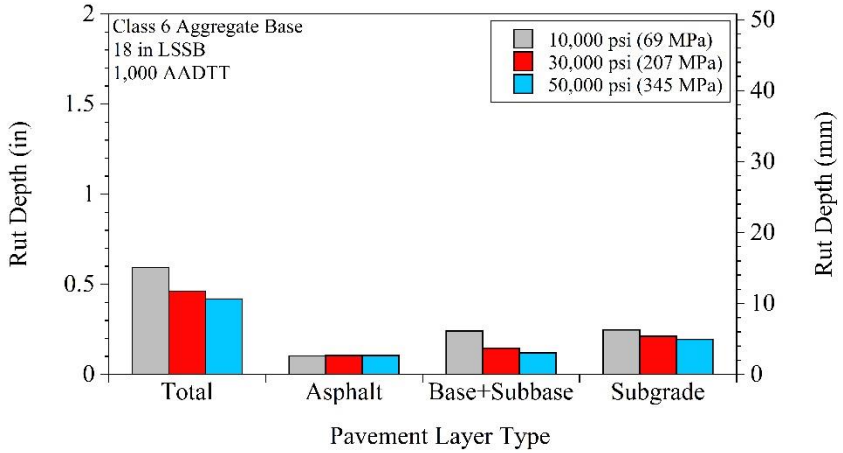

Class 6 Aggregate Base
15 in LSSB
25,000 AADTT
10,000 psi (69 MPa)
30,000 psi (207 MPa)
50,000 psi (345 MPa)
Rut Depth (in)
Rut Depth (mm)
Total
Asphalt
Base+Subbase
Subgrade
Pavement Layer Type

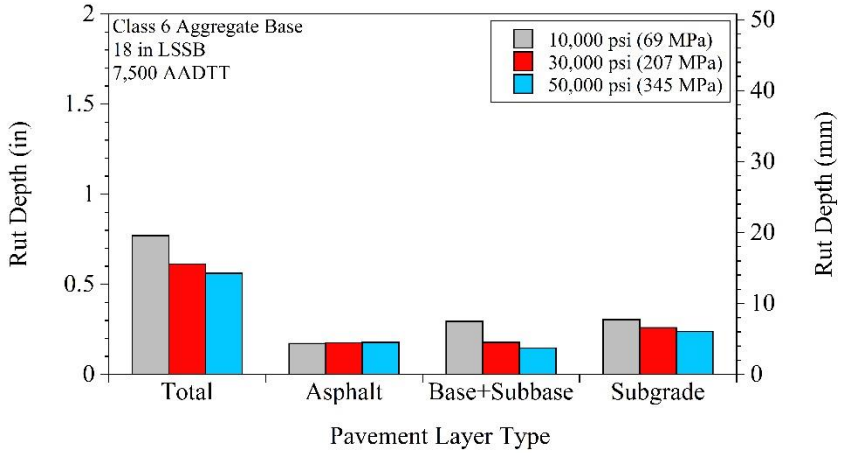
DRAFT

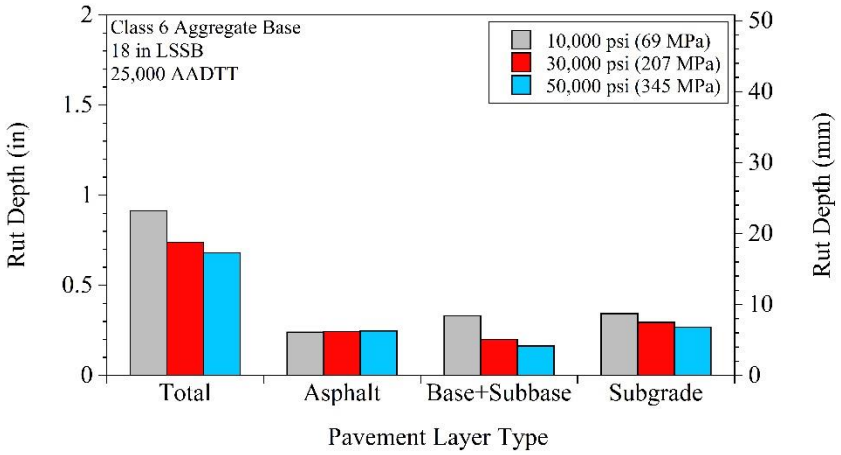
For pavements that contained class 6 aggregate and 18-in LSSB:



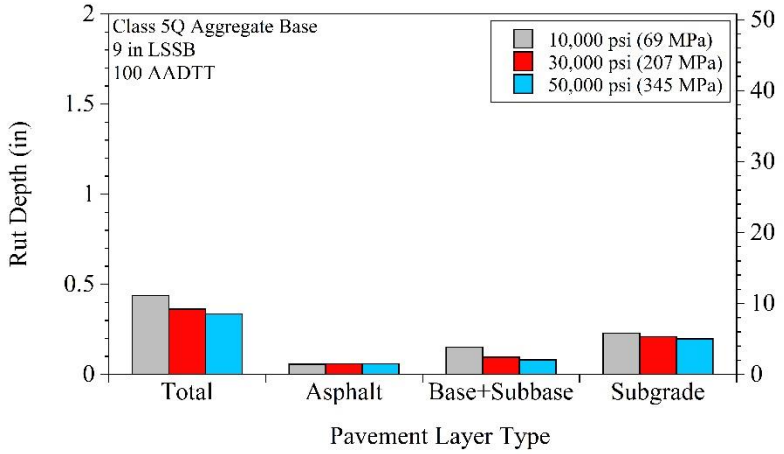


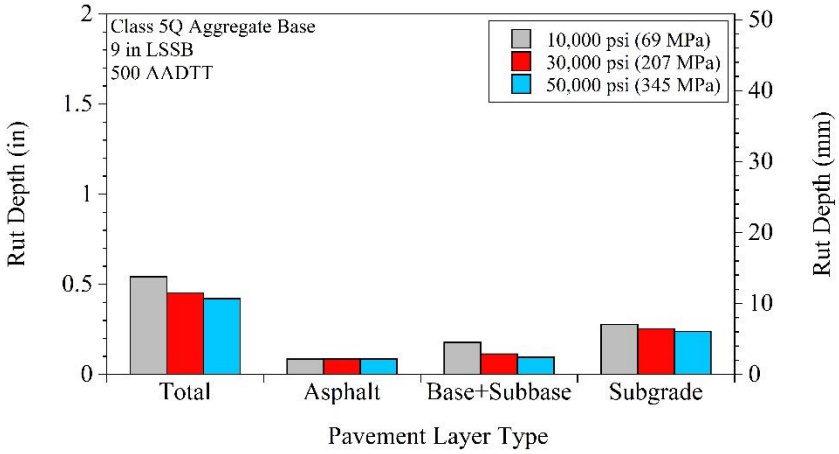




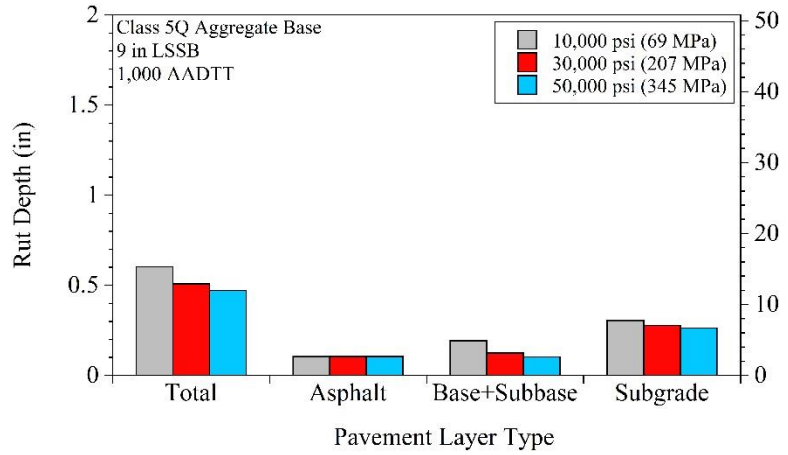


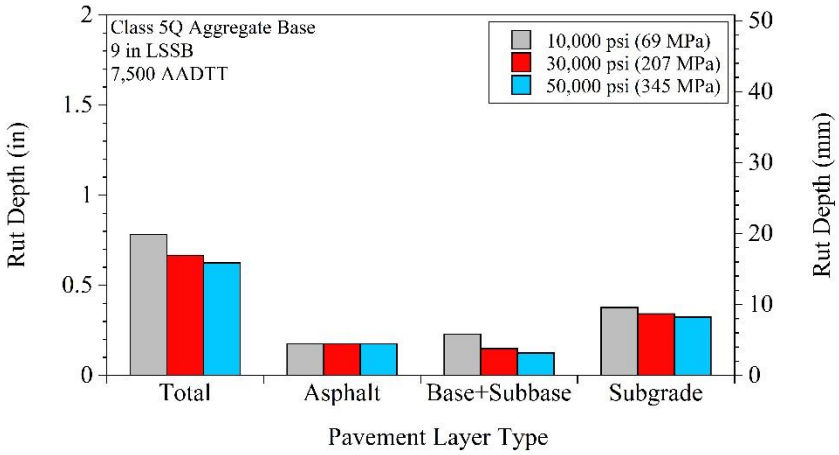
For pavements that contained class 5Q aggregate and 9-in LSSB:

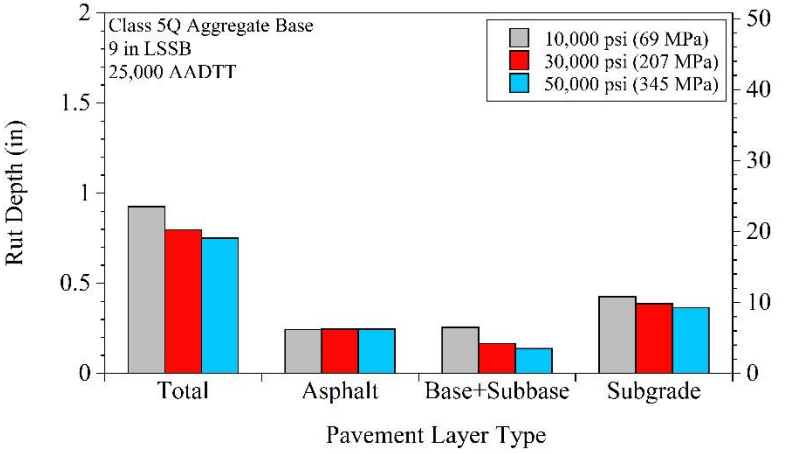




DRAFT

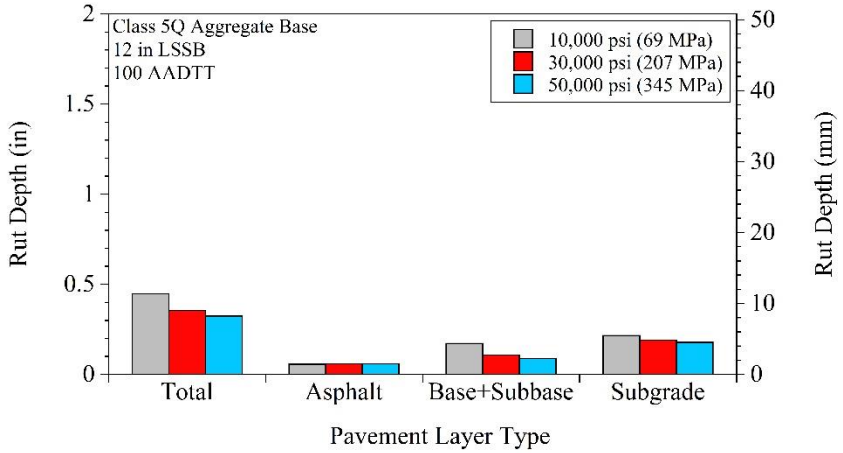

Class 5Q Aggregate Base
9 in LSSB
1,000 AADTT
10,000 psi (69 MPa)
30,000 psi (207 MPa)
50,000 psi (345 MPa)
Rut Depth (in)
Rut Depth (mm)
Total
Asphalt
Base+Subbase
Subgrade
Pavement Layer Type

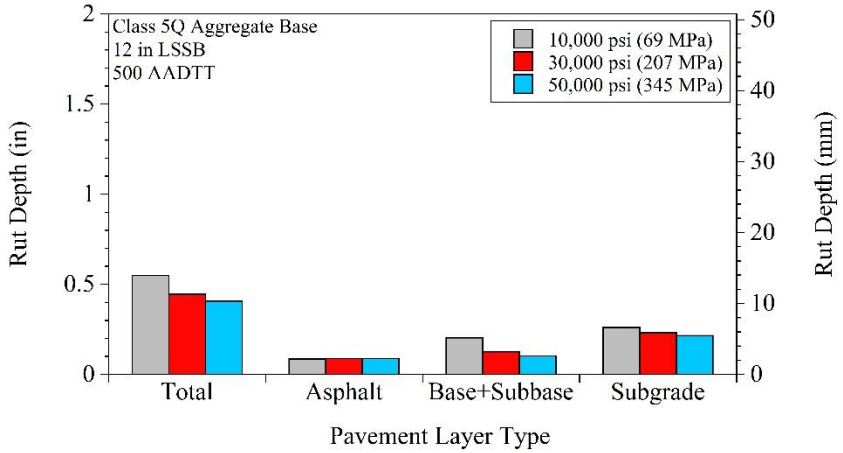

Class 5Q Aggregate Base
9 in LSSB
7,500 AADTT
10,000 psi (69 MPa)
30,000 psi (207 MPa)
50,000 psi (345 MPa)
Rut Depth (in)
Rut Depth (mm)
Total
Asphalt
Base+Subbase
Subgrade
Pavement Layer Type

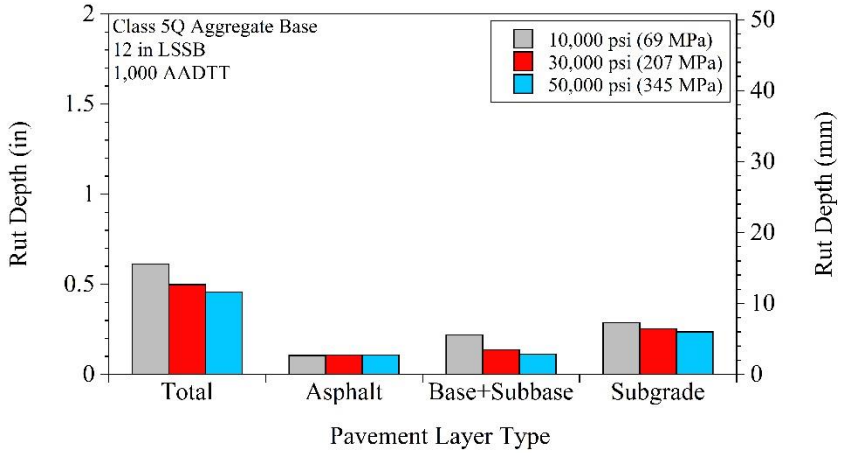

Class 5Q Aggregate Base
9 in LSSB
25,000 AADTT
10,000 psi (69 MPa)
30,000 psi (207 MPa)
50,000 psi (345 MPa)
Rut Depth (in)
Rut Depth (mm)
Total
Asphalt
Base+Subbase
Subgrade
Pavement Layer Type

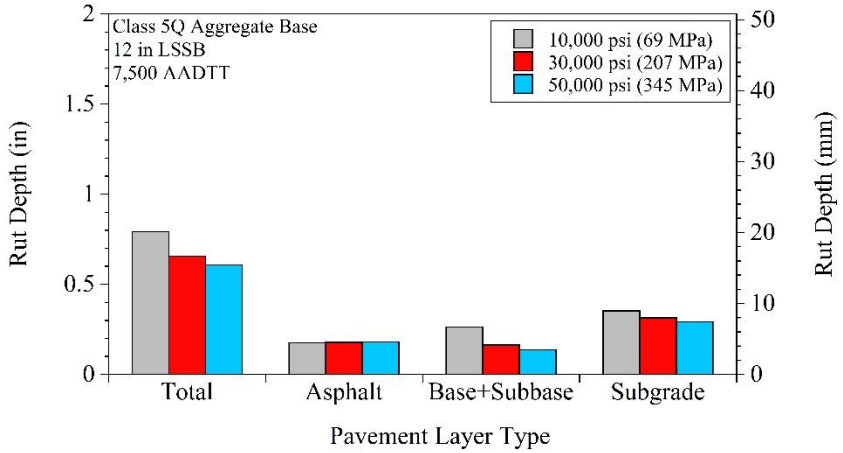
DRAFT

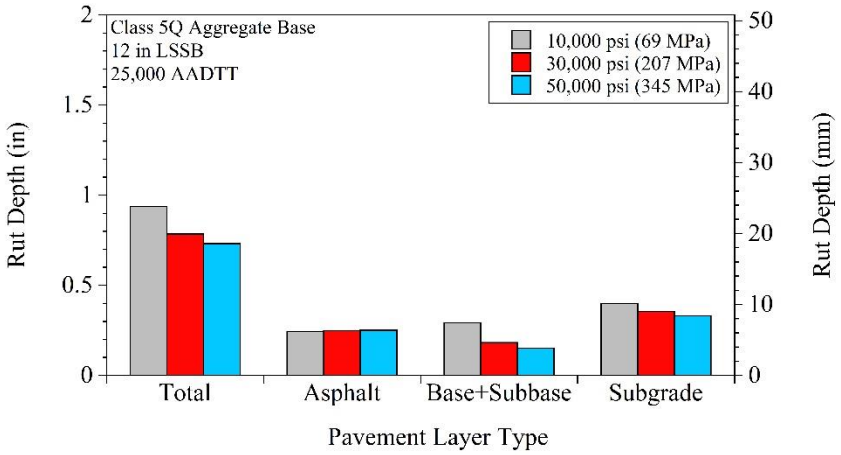
For pavements that contained class 5Q aggregate and 12-in LSSB:



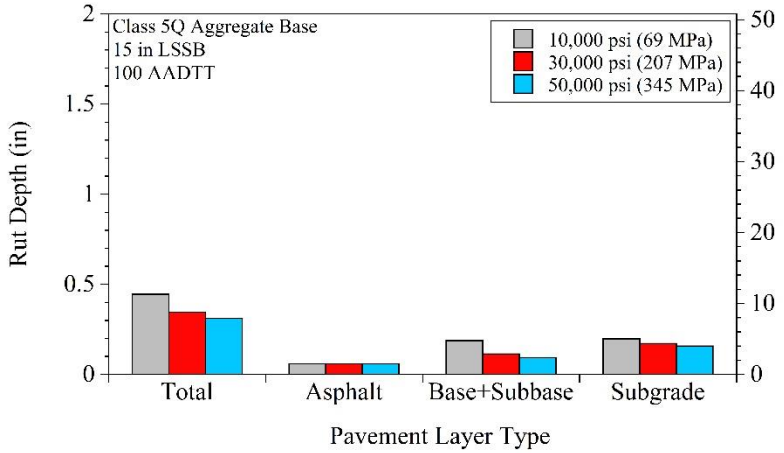


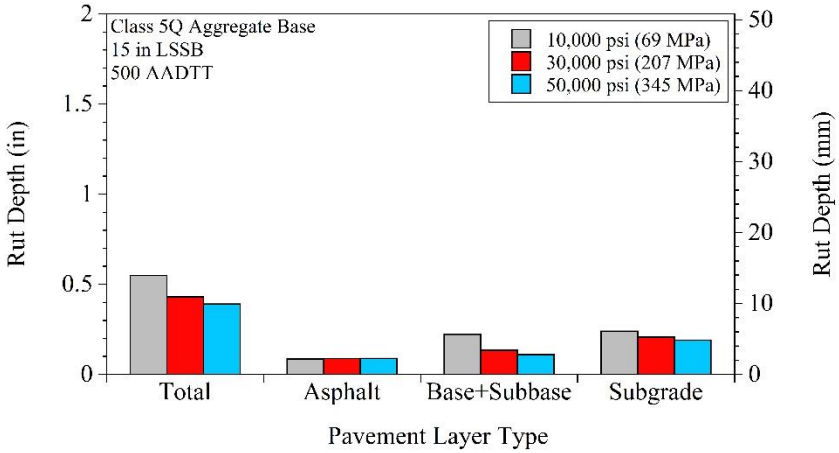




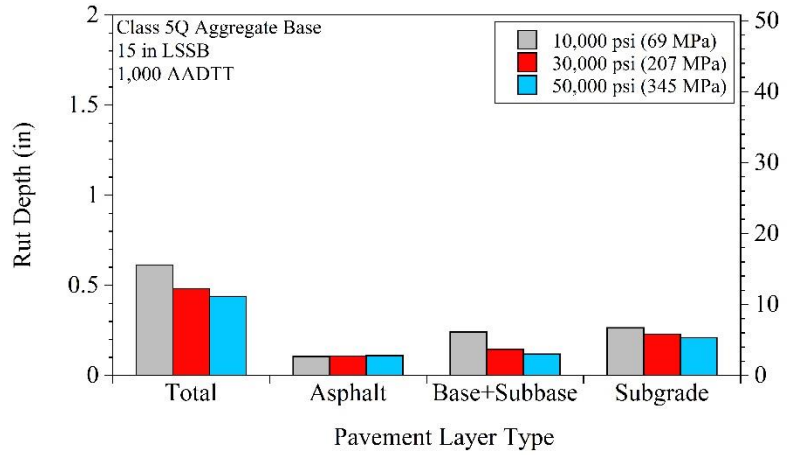


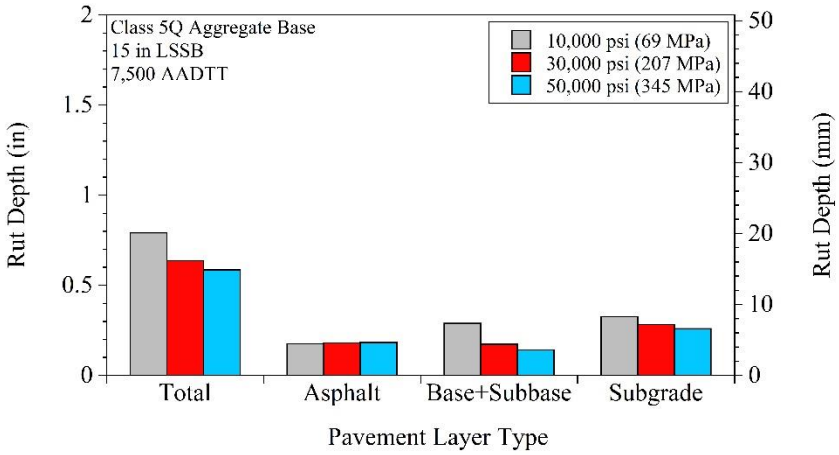
For pavements that contained class 5Q aggregate and 15-in LSSB:

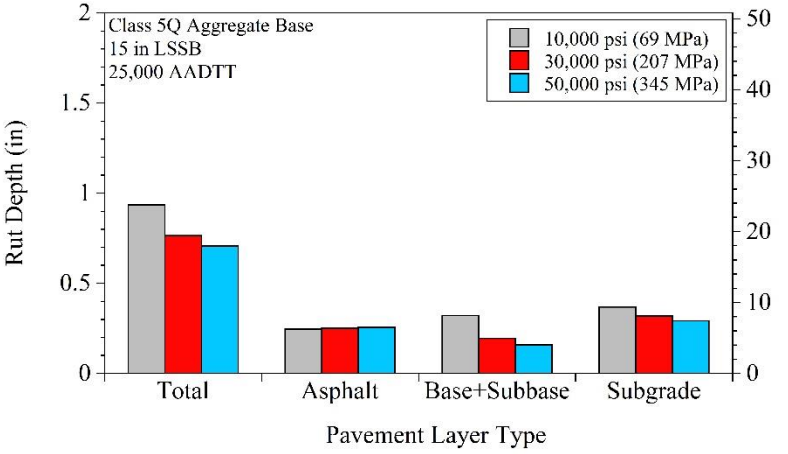




DRAFT

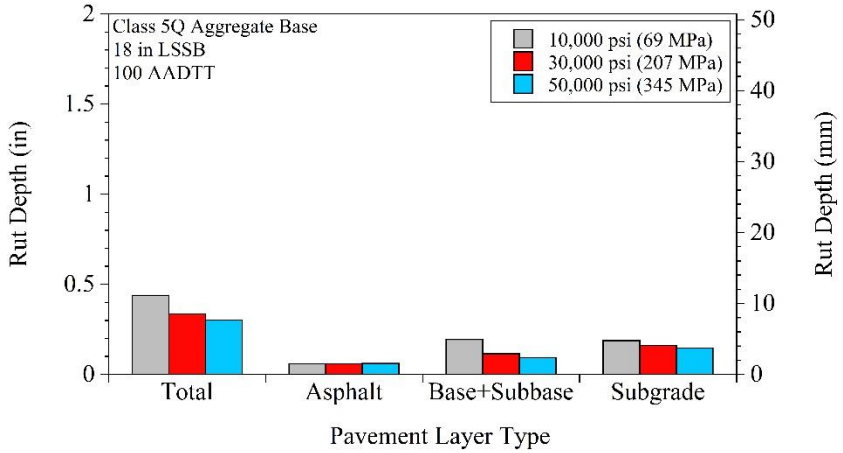

Class 5Q Aggregate Base
15 in LSSB
1,000 AADTT
10,000 psi (69 MPa)
30,000 psi (207 MPa)
50,000 psi (345 MPa)
Rut Depth (in)
Rut Depth (mm)
Total
Asphalt
Base+Subbase
Subgrade
Pavement Layer Type

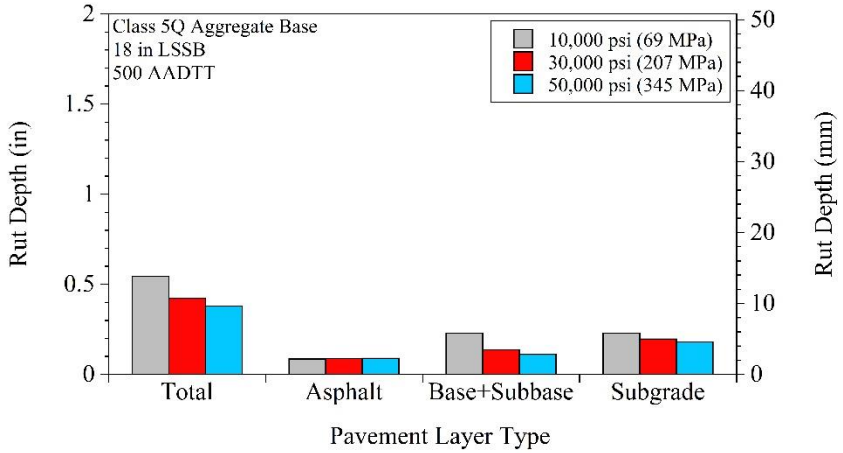

Class 5Q Aggregate Base
15 in LSSB
7,500 AADTT
10,000 psi (69 MPa)
30,000 psi (207 MPa)
50,000 psi (345 MPa)
Rut Depth (in)
Rut Depth (mm)
Total
Asphalt
Base+Subbase
Subgrade
Pavement Layer Type

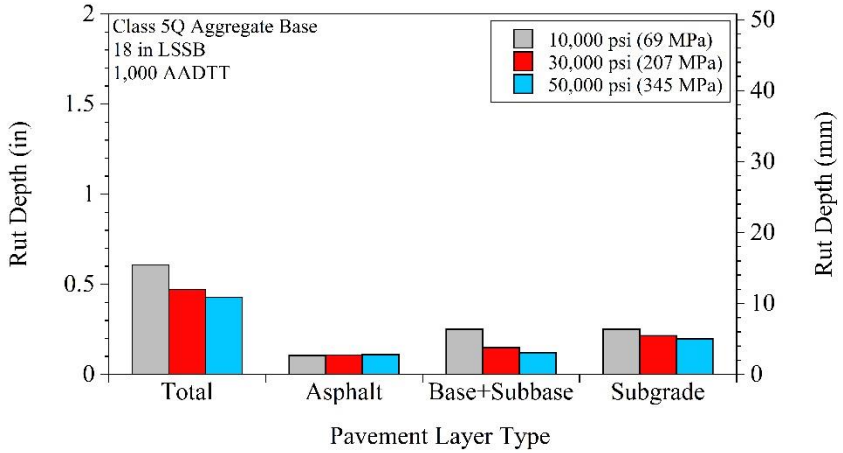

Class 5Q Aggregate Base
15 in LSSB
25,000 AADTT
10,000 psi (69 MPa)
30,000 psi (207 MPa)
50,000 psi (345 MPa)
Rut Depth (in)
Rut Depth (mm)
Total
Asphalt
Base+Subbase
Subgrade
Pavement Layer Type

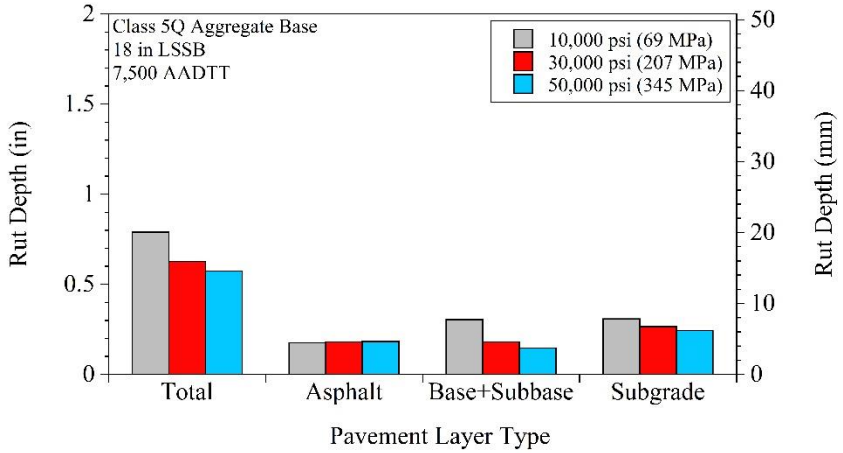
DRAFT

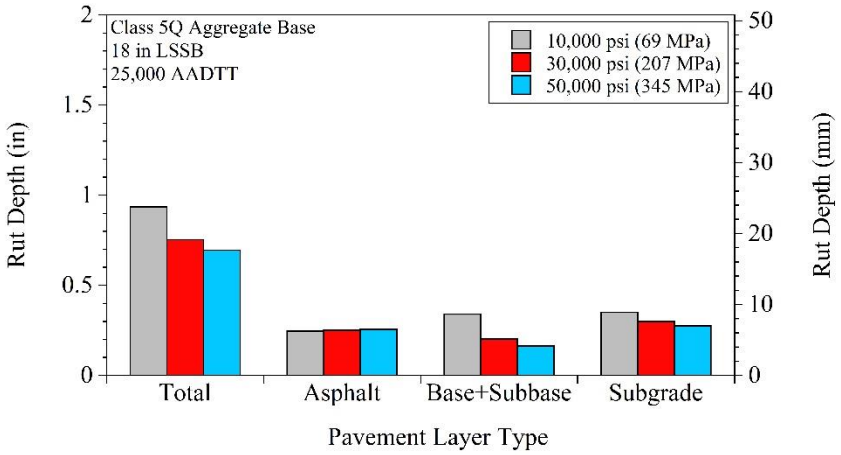
For pavements that contained class 5Q aggregate and 18-in LSSB:







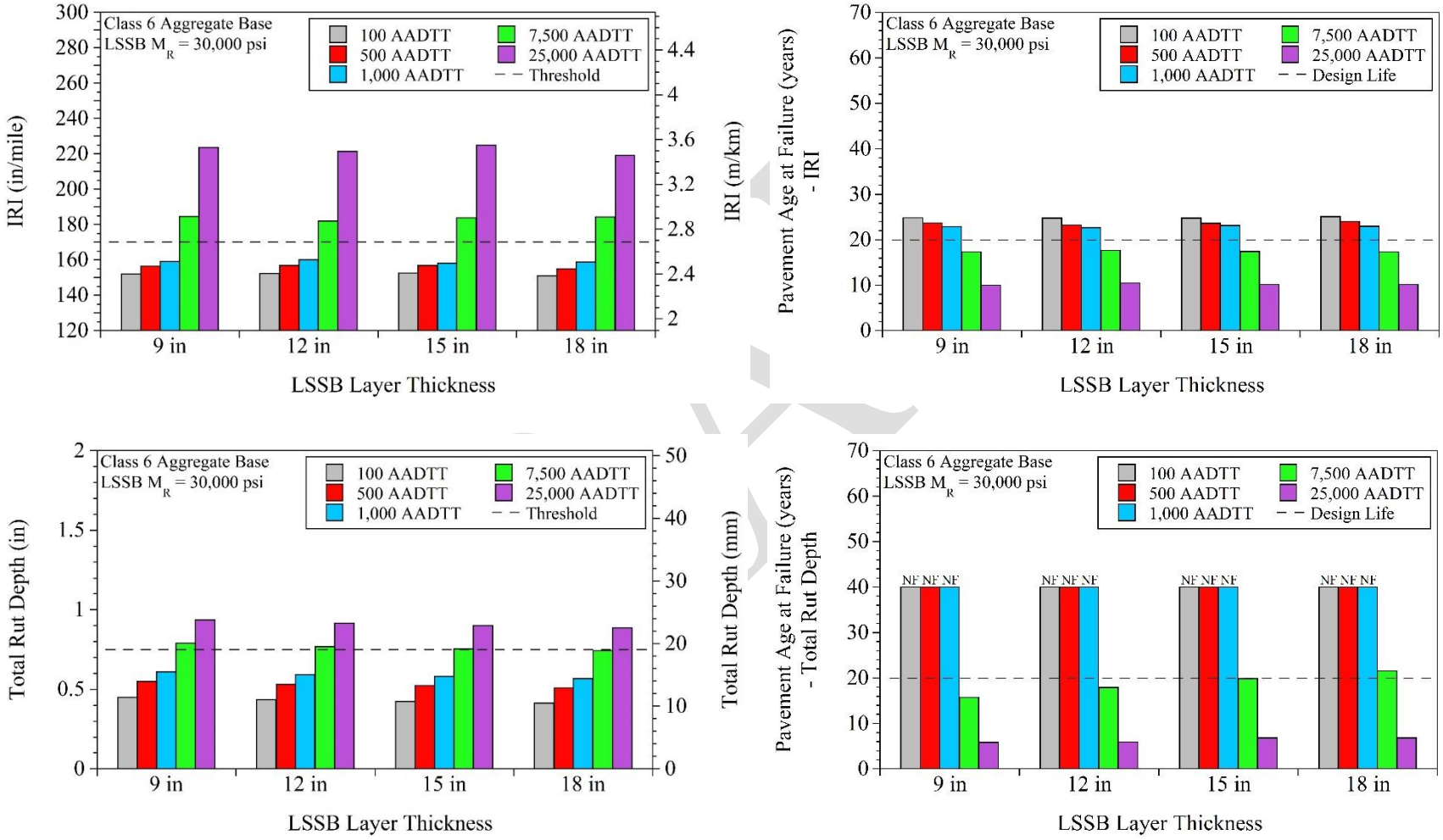


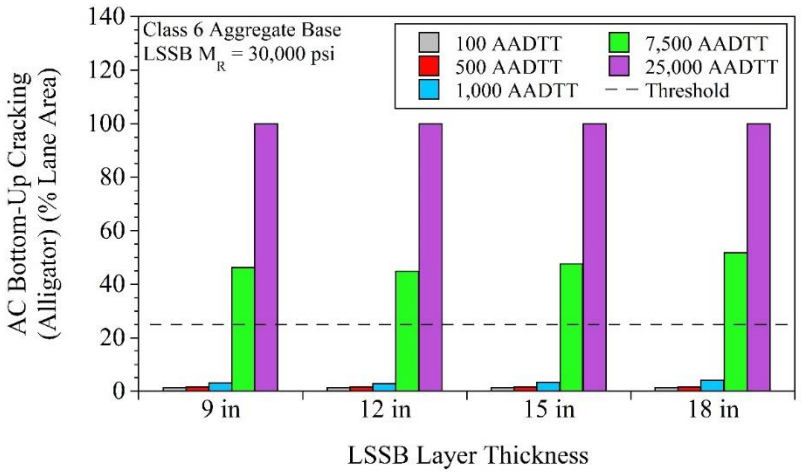

Class 5Q Aggregate Base
18 in LSSB
25,000 AADTT
10,000 psi (69 MPa)
30,000 psi (207 MPa)
50,000 psi (345 MPa)
Rut Depth (in)
Rut Depth (mm)
0
0.5
1
1.5
2
0
10
20
30
40
50
Total
Asphalt
Base+Subbase
Subgrade
Pavement Layer Type

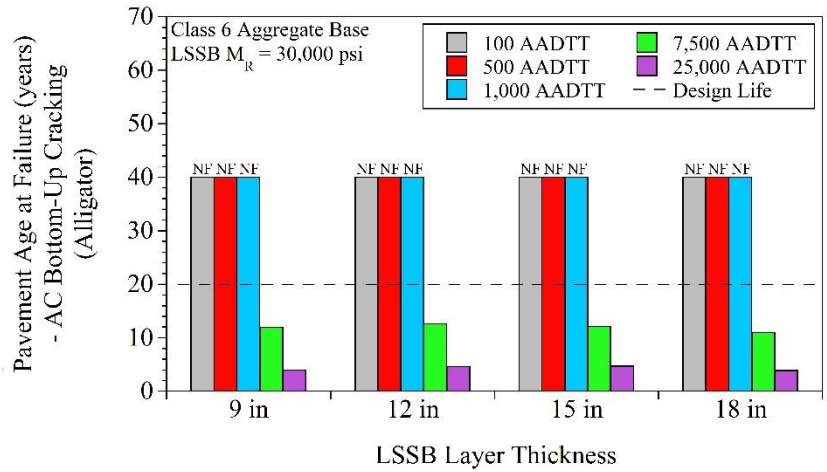
DRAFT

APPENDIX AD. EFFECT OF TRAFFIC LEVEL ON PAVEMENT PERFORMANCE PREDICTIONS

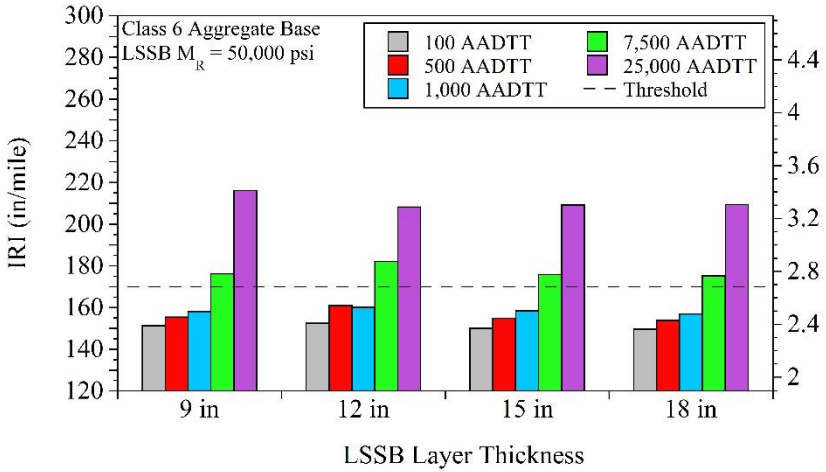
For pavements that contained class 6 aggregate and LSSB with M_R = 30,000 psi:

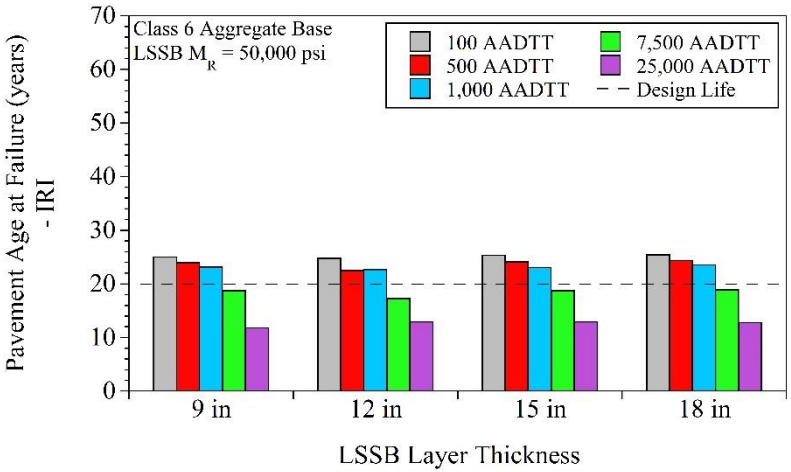


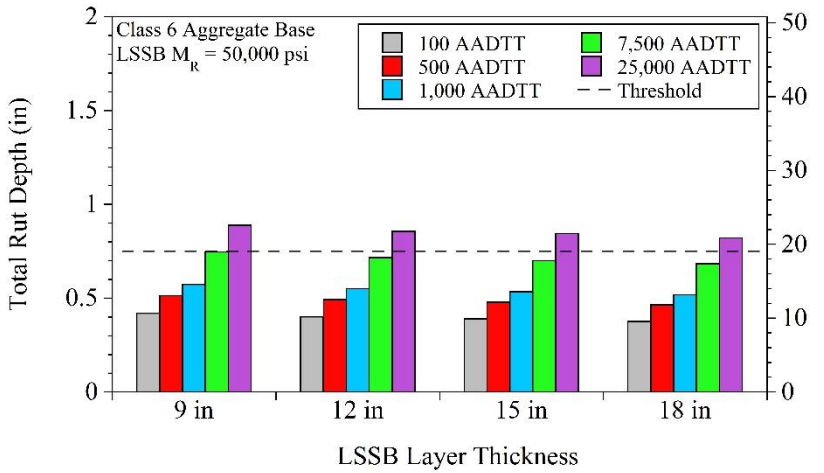


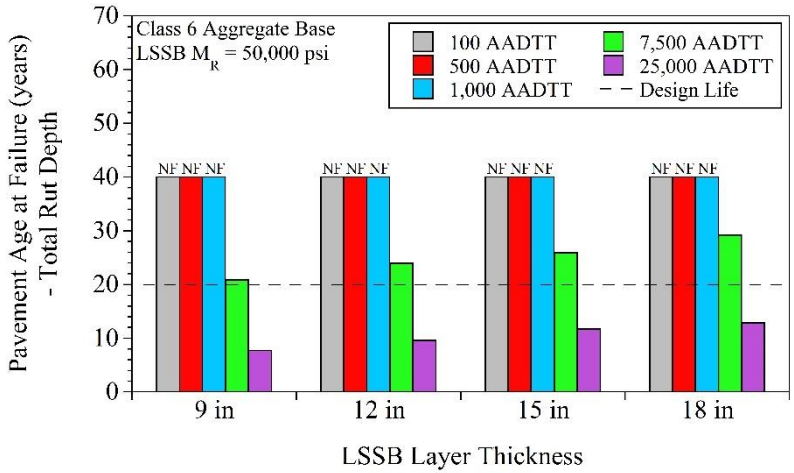


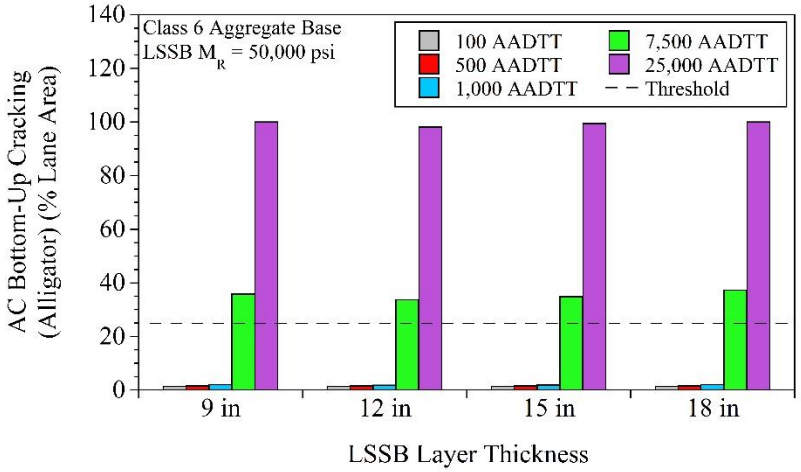
For pavements that contained class 6 aggregate and LSSB with M_R = 50,000 psi:

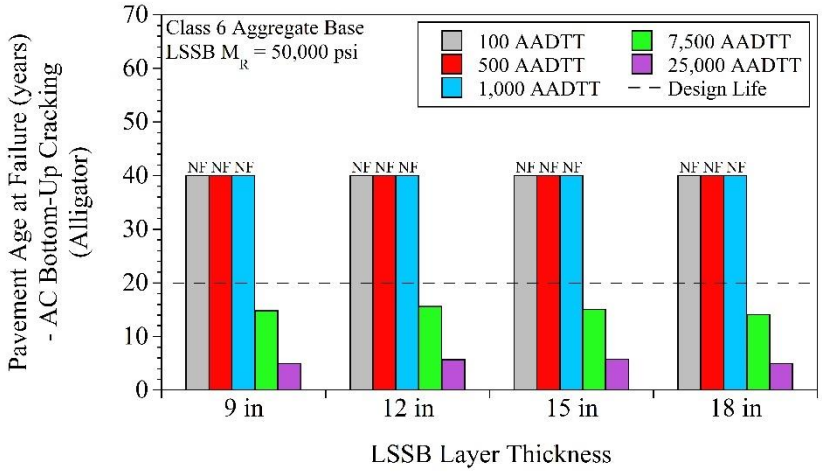




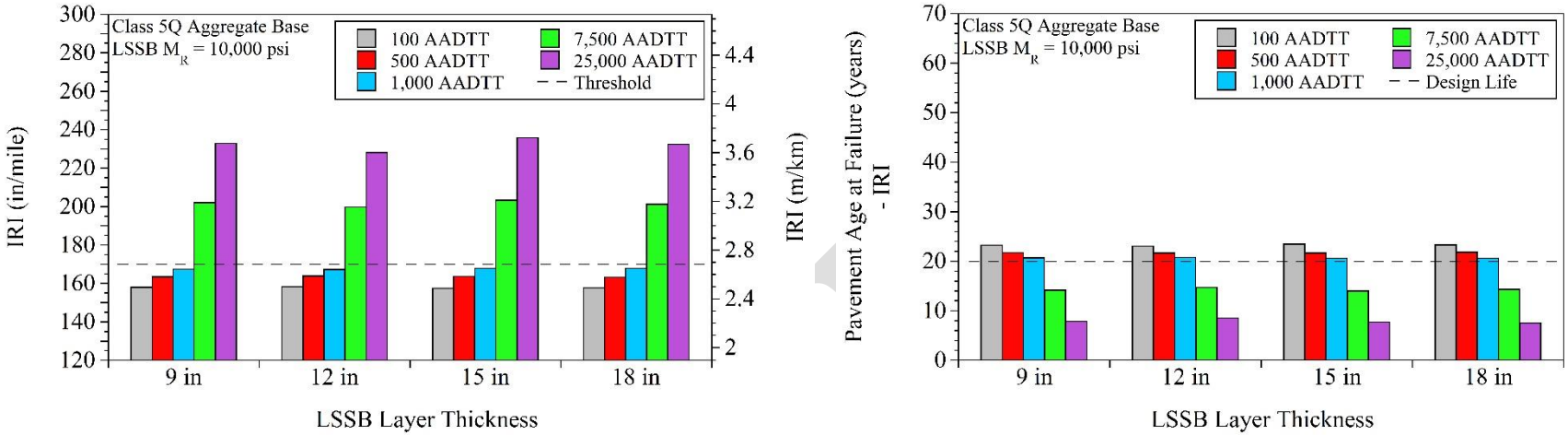

Class 6 Aggregate Base
LSSB M_R = 50,000 psi
100 AADTT
500 AADTT
1,000 AADTT
7,500 AADTT
25,000 AADTT
Threshold
Total Rut Depth (in)
Total Rut Depth (mm)
9 in
12 in
15 in
18 in
LSSB Layer Thickness

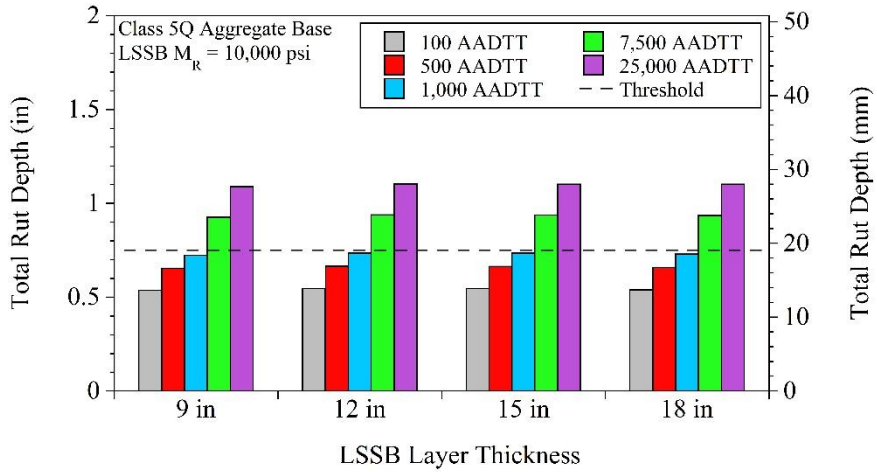

Class 6 Aggregate Base
LSSB M_R = 50,000 psi
100 AADTT
500 AADTT
1,000 AADTT
7,500 AADTT
25,000 AADTT
Design Life
Pavement Age at Failure (years)
- Total Rut Depth
NF NF NF
9 in
12 in
15 in
18 in
LSSB Layer Thickness

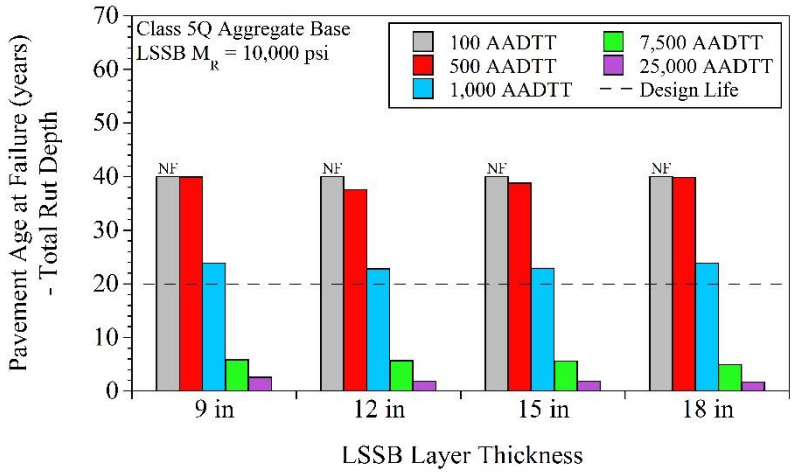

Class 6 Aggregate Base
LSSB M_R = 50,000 psi
100 AADTT
500 AADTT
1,000 AADTT
7,500 AADTT
25,000 AADTT
Threshold
AC Bottom-Up Cracking
(Alligator) (% Lane Area)
9 in
12 in
15 in
18 in
LSSB Layer Thickness

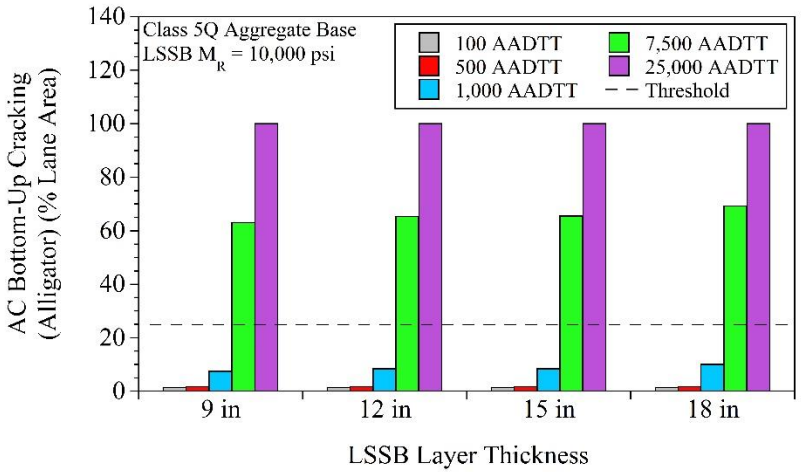

Class 6 Aggregate Base
LSSB M_R = 50,000 psi
100 AADTT
500 AADTT
1,000 AADTT
7,500 AADTT
25,000 AADTT
Design Life
Pavement Age at Failure (years)
- AC Bottom-Up Cracking
(Alligator)
NF NF NF
9 in
12 in
15 in
18 in
LSSB Layer Thickness

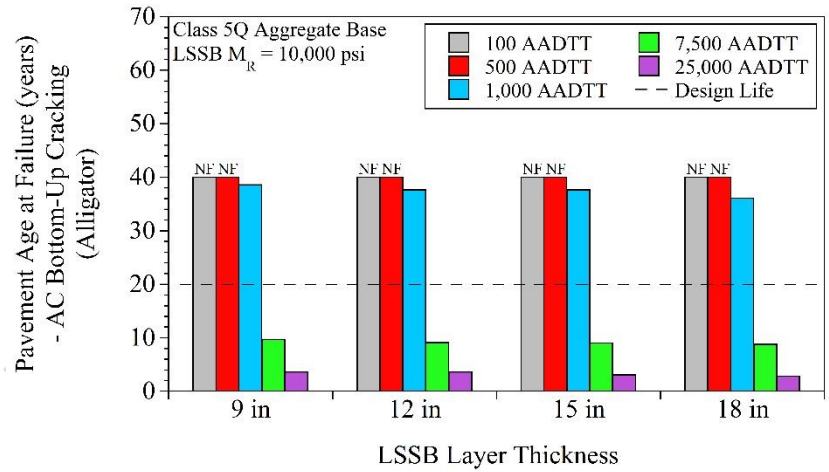
For pavements that contained class 5Q aggregate and LSSB with M_R = 10,000 psi:



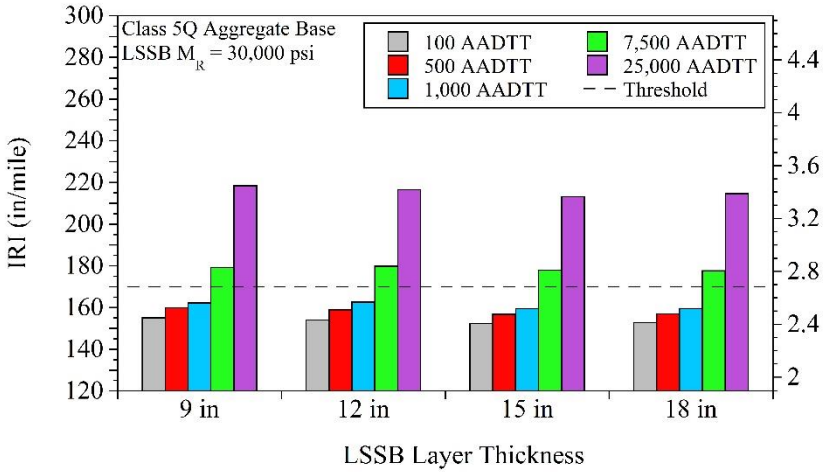


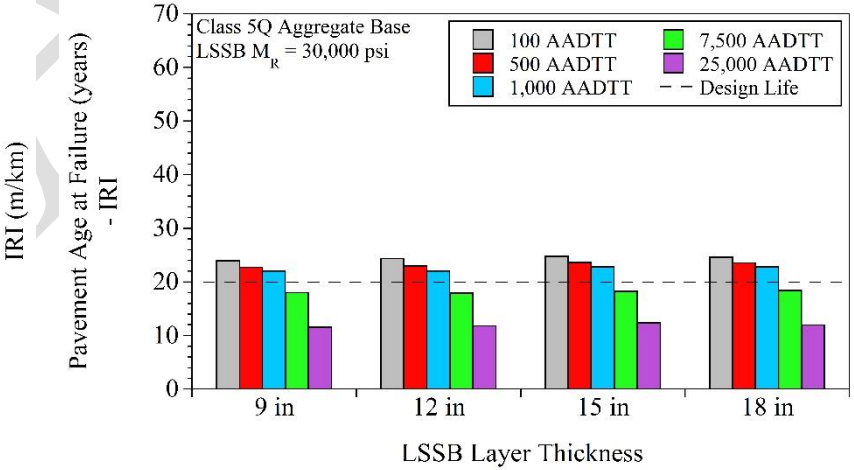


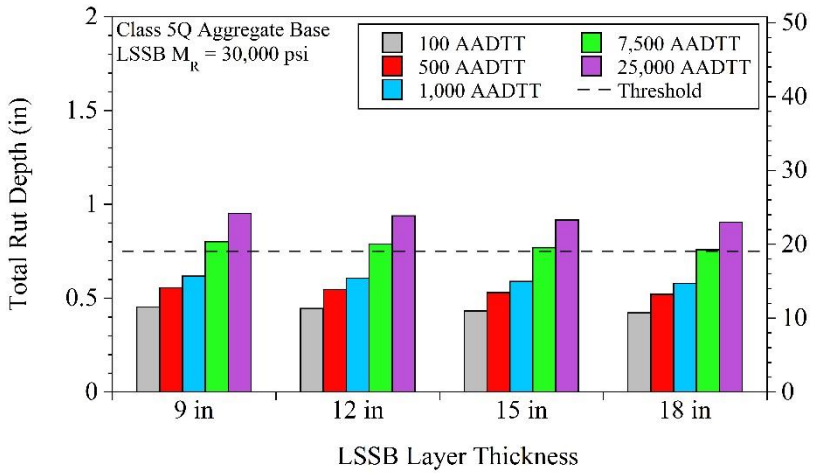


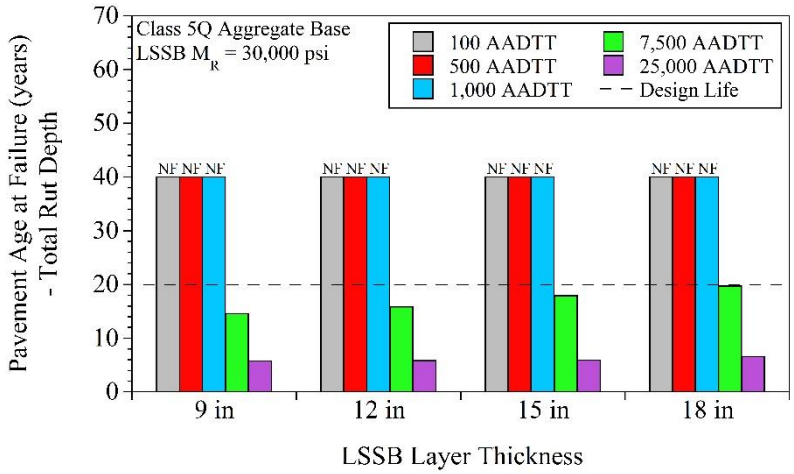


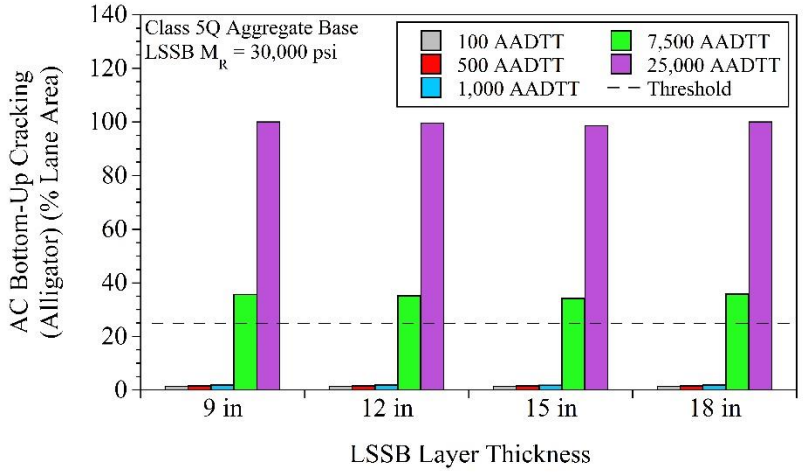
For pavements that contained class 5Q aggregate and LSSB with M_R = 30,000 psi:

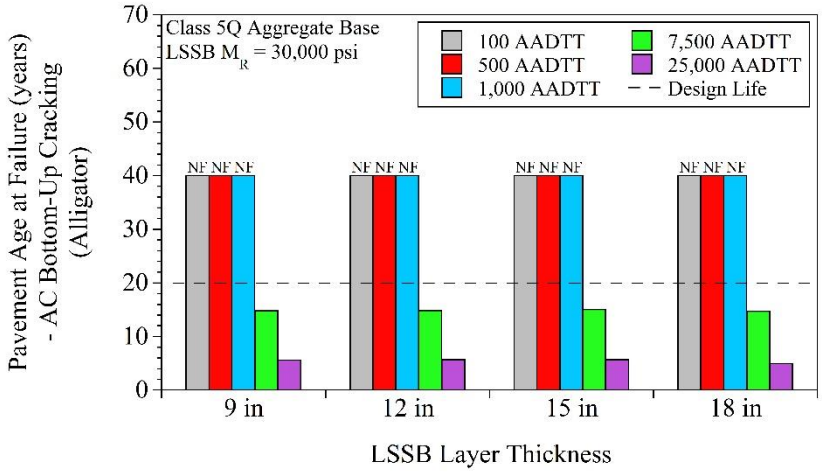




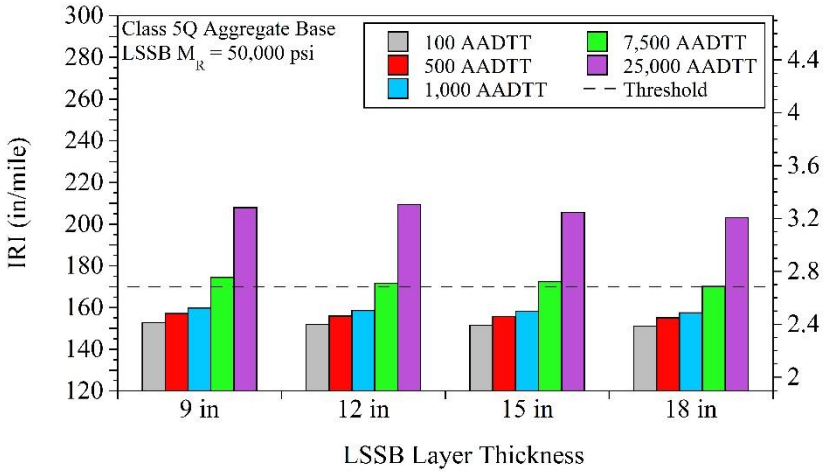

Class 5Q Aggregate Base
LSSB M_R = 30,000 psi
100 AADTT
500 AADTT
1,000 AADTT
7,500 AADTT
25,000 AADTT
Threshold
Total Rut Depth (in)
Total Rut Depth (mm)
9 in
12 in
15 in
18 in
LSSB Layer Thickness

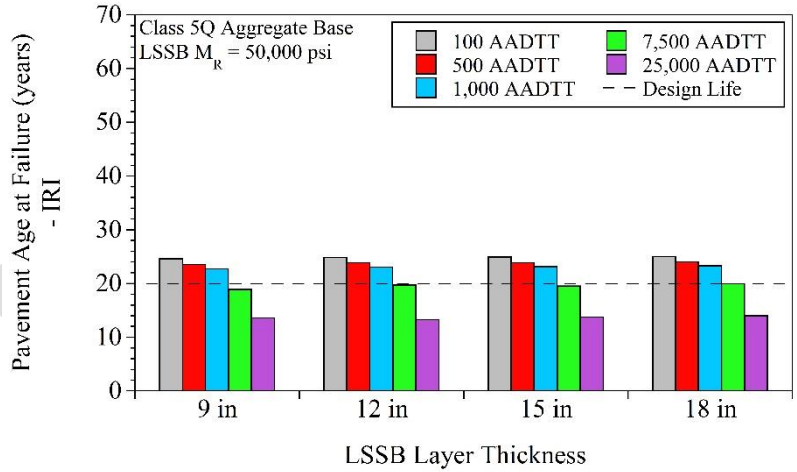

Class 5Q Aggregate Base
LSSB M_R = 30,000 psi
100 AADTT
500 AADTT
1,000 AADTT
7,500 AADTT
25,000 AADTT
Design Life
NF NF NF
Pavement Age at Failure (years)
- Total Rut Depth
9 in
12 in
15 in
18 in
LSSB Layer Thickness

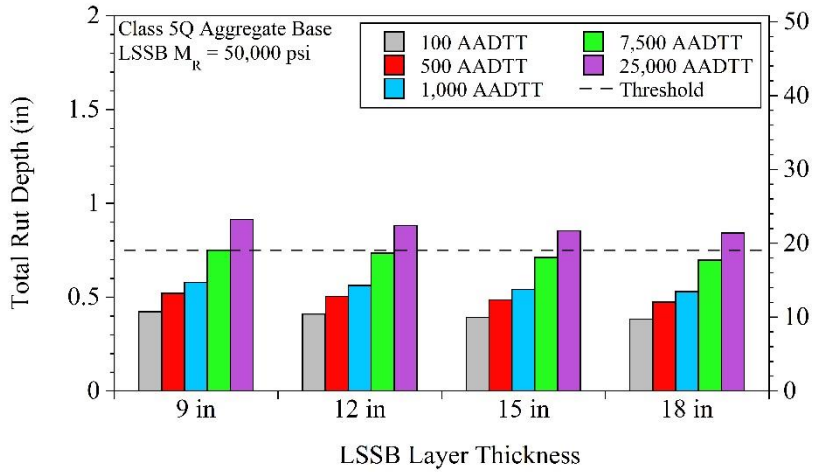

Class 5Q Aggregate Base
LSSB M_R = 30,000 psi
100 AADTT
500 AADTT
1,000 AADTT
7,500 AADTT
25,000 AADTT
Threshold
AC Bottom-Up Cracking
(Alligator) (% Lane Area)
9 in
12 in
15 in
18 in
LSSB Layer Thickness

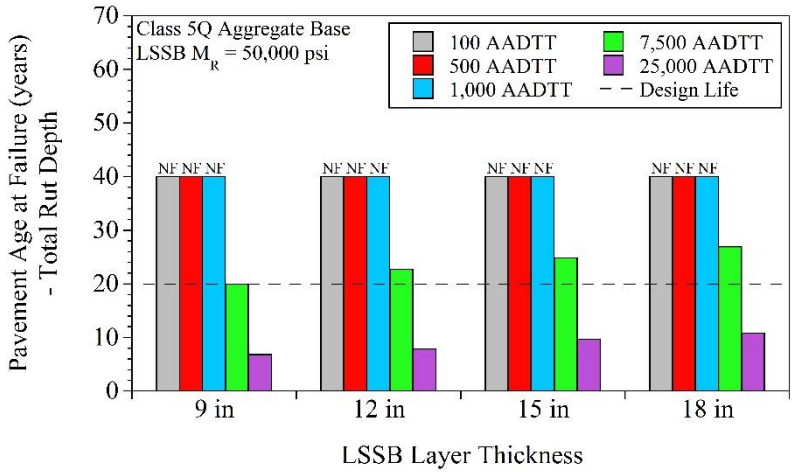

Class 5Q Aggregate Base
LSSB M_R = 30,000 psi
100 AADTT
500 AADTT
1,000 AADTT
7,500 AADTT
25,000 AADTT
Design Life
NF NF NF
Pavement Age at Failure (years)
- AC Bottom-Up Cracking
(Alligator)
9 in
12 in
15 in
18 in
LSSB Layer Thickness

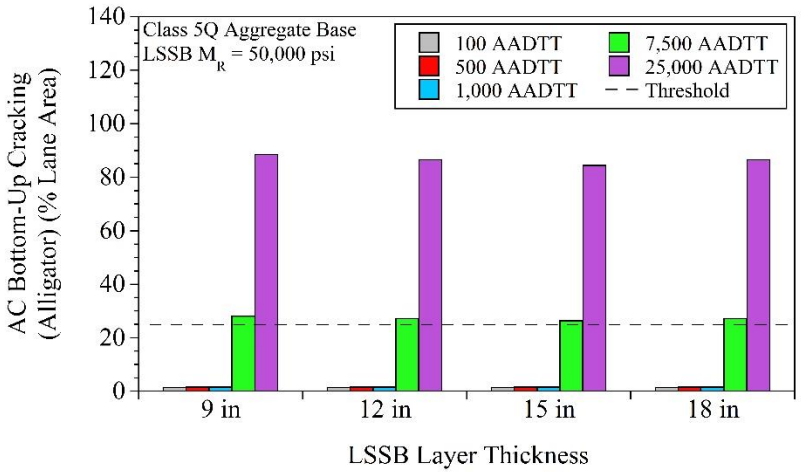
For pavements that contained class 5Q aggregate and LSSB with M_R = 50,000 psi:

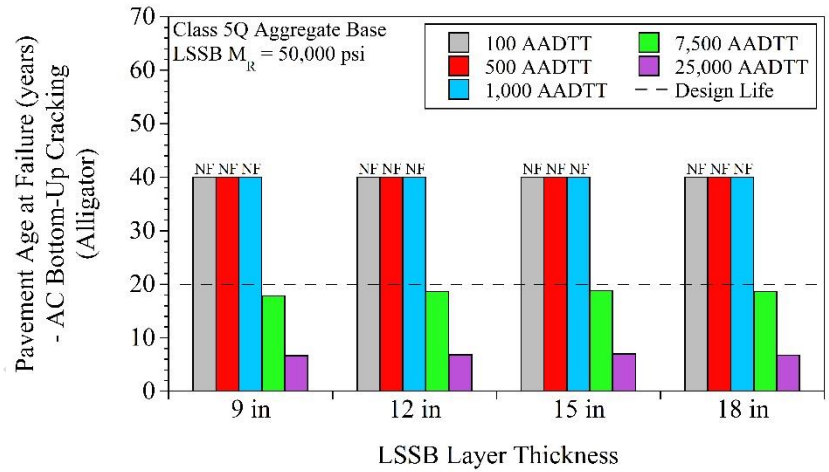








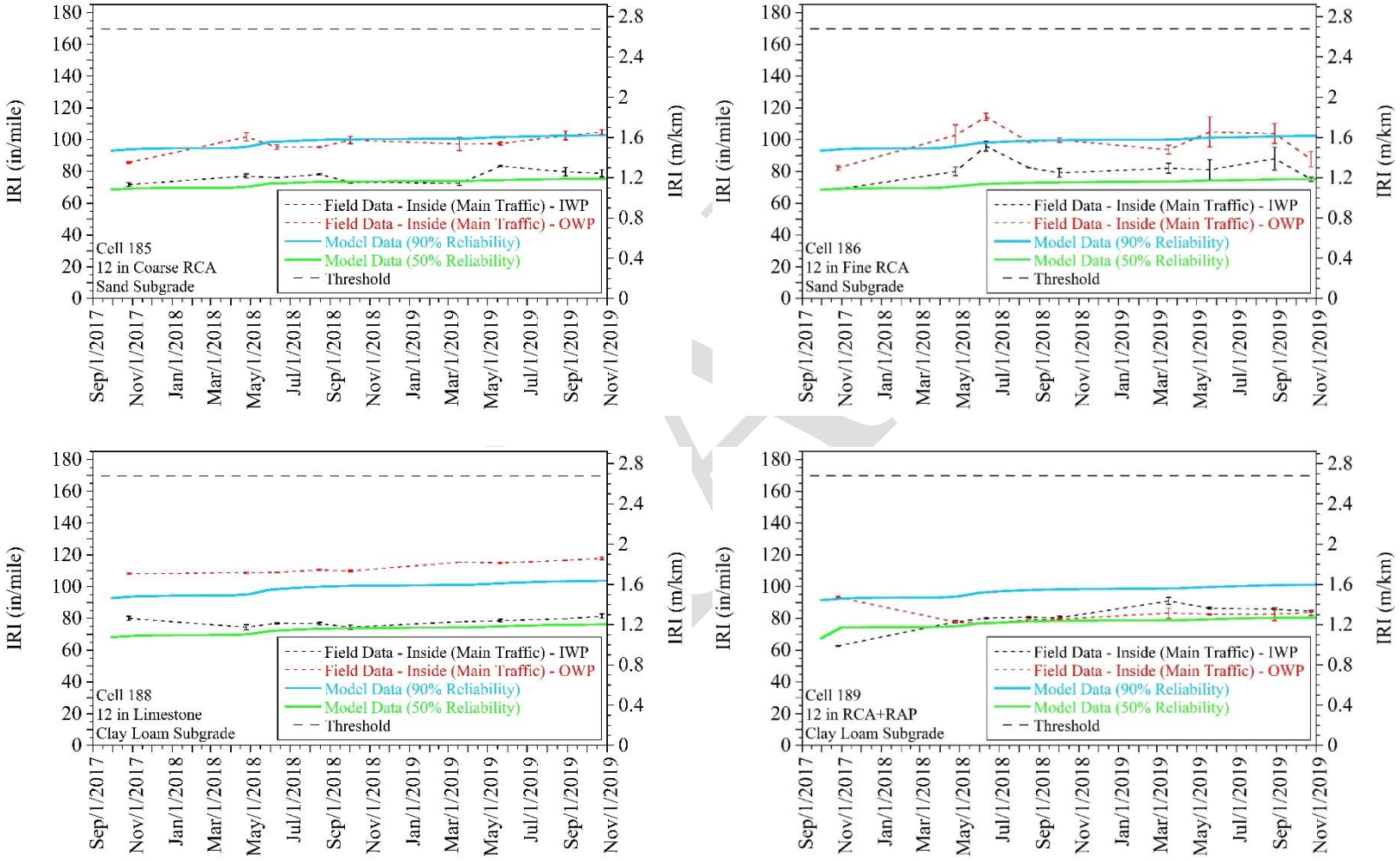

Class 5Q Aggregate Base
LSSB M_R = 50,000 psi
100 AADTT
500 AADTT
1,000 AADTT
7,500 AADTT
25,000 AADTT
Threshold
AC Bottom-Up Cracking
(Alligator) (% Lane Area)
0
20
40
60
80
100
120
140
9 in
12 in
15 in
18 in
LSSB Layer Thickness

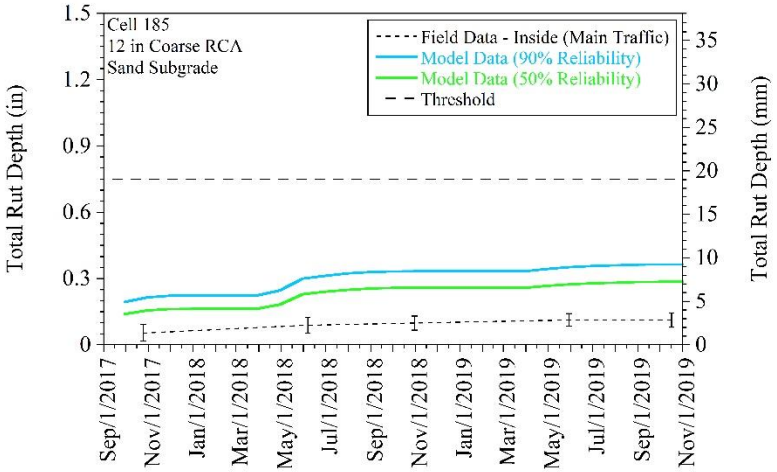

Class 5Q Aggregate Base
LSSB M_R = 50,000 psi
100 AADTT
500 AADTT
1,000 AADTT
7,500 AADTT
25,000 AADTT
Design Life
Pavement Age at Failure (years)
- AC Bottom-Up Cracking
(Alligator)
NF NF NF
0
10
20
30
40
50
60
70
9 in
12 in
15 in
18 in
LSSB Layer Thickness

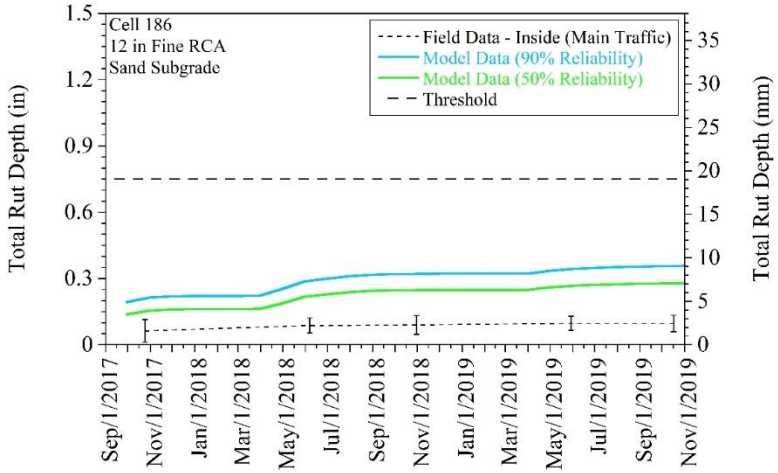
DRAFT

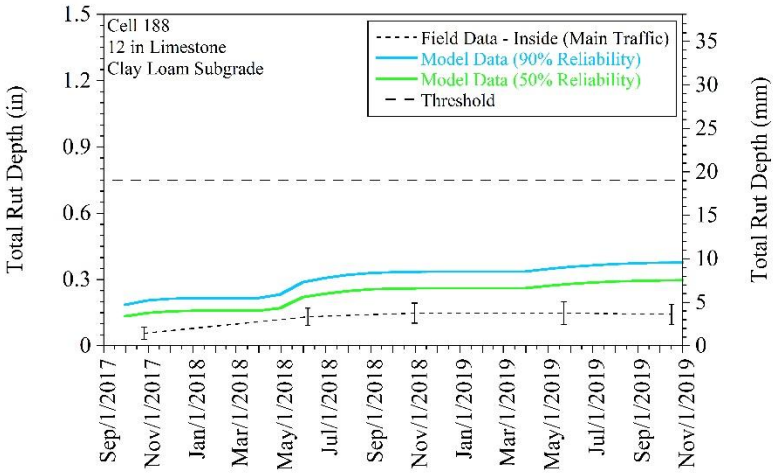
APPENDIX AE. COMPARISON BETWEEN FIELD DATA AND PAVEMENT ME MODELS

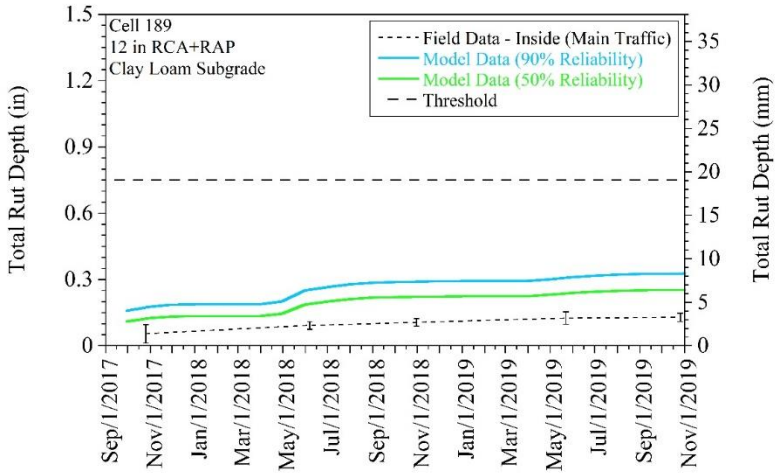
Recycled aggregate base (RAB) group:

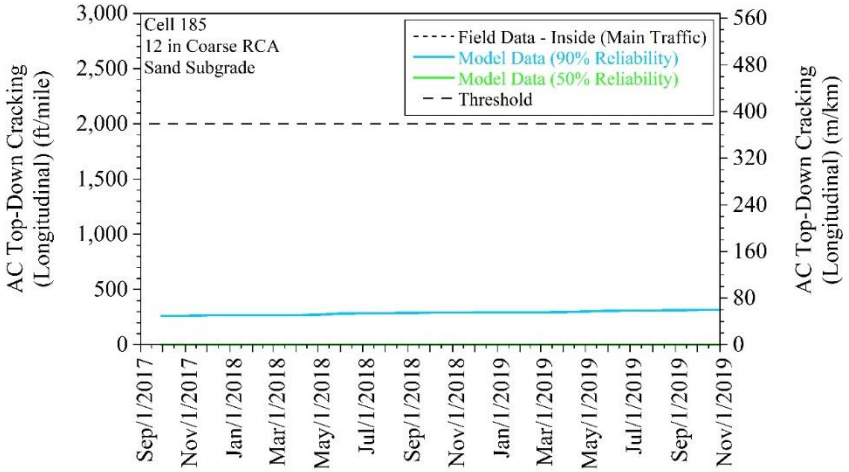


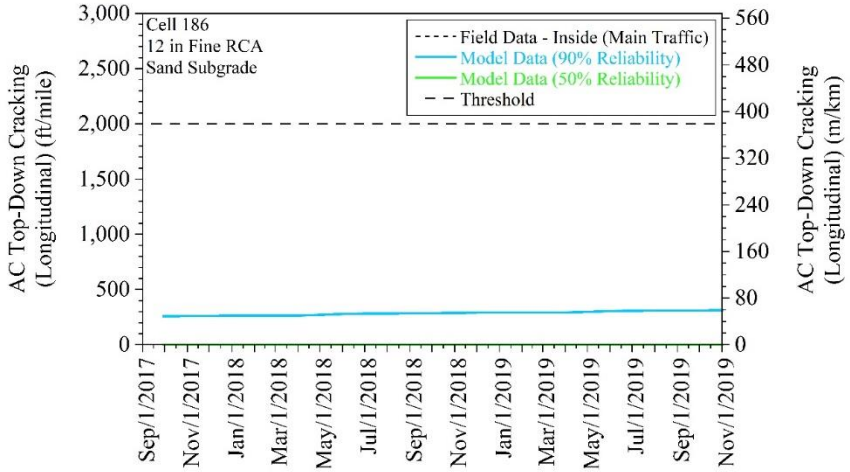

Cell 185
12 in Coarse RCA
Sand Subgrade
Field Data - Inside (Main Traffic)
Model Data (90% Reliability)
Model Data (50% Reliability)
Threshold
Total Rut Depth (in)
Total Rut Depth (mm)
Sep/1/2017
Nov/1/2017
Jan/1/2018
Mar/1/2018
May/1/2018
Jul/1/2018
Sep/1/2018
Nov/1/2018
Jan/1/2019
Mar/1/2019
May/1/2019
Jul/1/2019
Sep/1/2019
Nov/1/2019


Cell 186
12 in Fine RCA
Sand Subgrade
Field Data - Inside (Main Traffic)
Model Data (90% Reliability)
Model Data (50% Reliability)
Threshold
Total Rut Depth (in)
Total Rut Depth (mm)
Sep/1/2017
Nov/1/2017
Jan/1/2018
Mar/1/2018
May/1/2018
Jul/1/2018
Sep/1/2018
Nov/1/2018
Jan/1/2019
Mar/1/2019
May/1/2019
Jul/1/2019
Sep/1/2019
Nov/1/2019

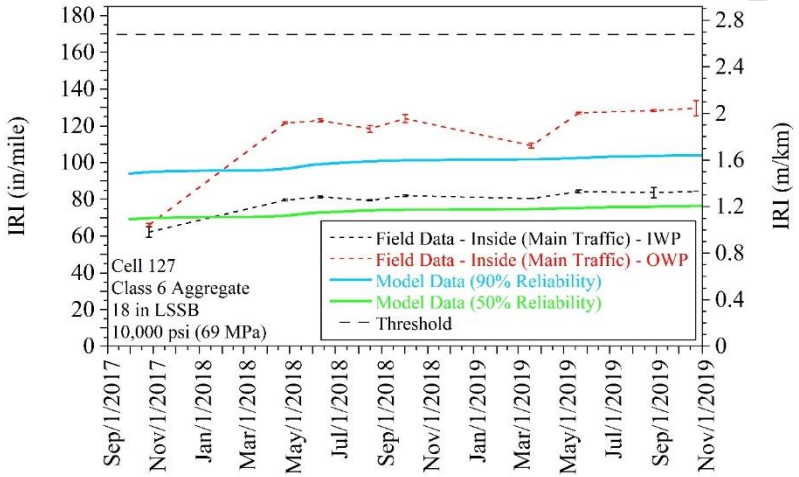

Cell 188
12 in Limestone
Clay Loam Subgrade
Field Data - Inside (Main Traffic)
Model Data (90% Reliability)
Model Data (50% Reliability)
Threshold
Total Rut Depth (in)
Total Rut Depth (mm)
Sep/1/2017
Nov/1/2017
Jan/1/2018
Mar/1/2018
May/1/2018
Jul/1/2018
Sep/1/2018
Nov/1/2018
Jan/1/2019
Mar/1/2019
May/1/2019
Jul/1/2019
Sep/1/2019
Nov/1/2019

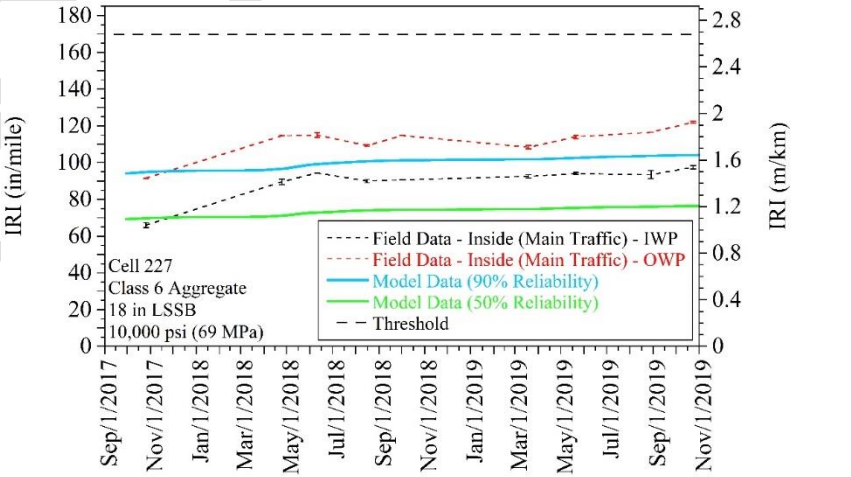

Cell 189
12 in RCA+RAP
Clay Loam Subgrade
Field Data - Inside (Main Traffic)
Model Data (90% Reliability)
Model Data (50% Reliability)
Threshold
Total Rut Depth (in)
Total Rut Depth (mm)
Sep/1/2017
Nov/1/2017
Jan/1/2018
Mar/1/2018
May/1/2018
Jul/1/2018
Sep/1/2018
Nov/1/2018
Jan/1/2019
Mar/1/2019
May/1/2019
Jul/1/2019
Sep/1/2019
Nov/1/2019

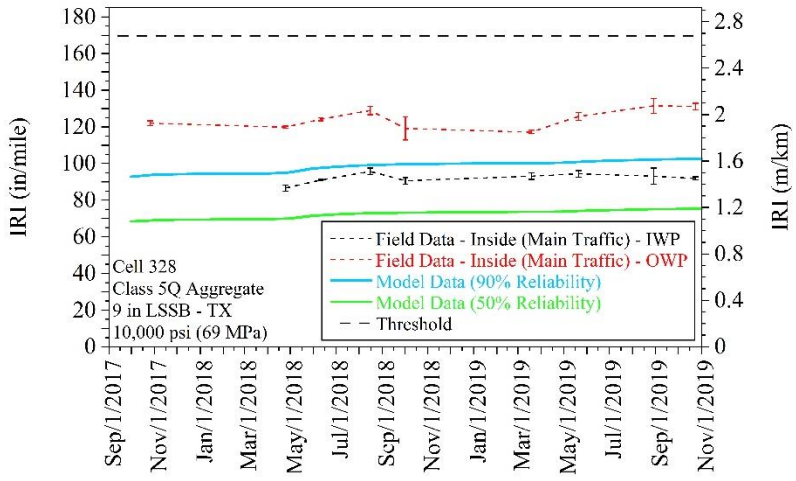


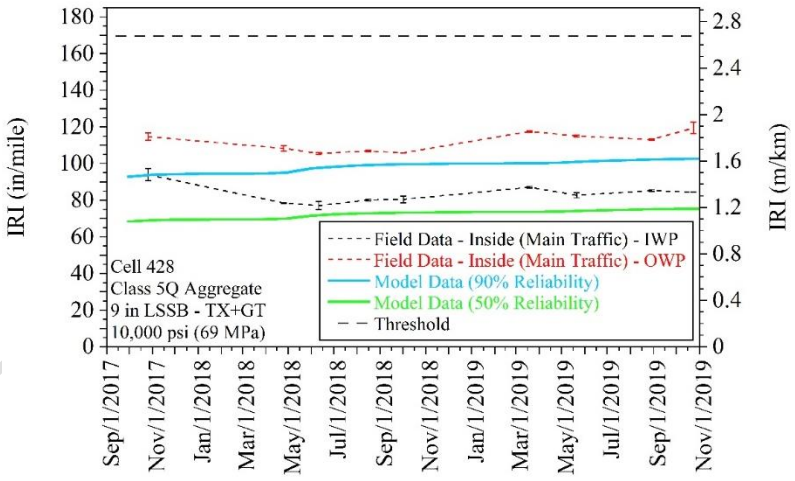


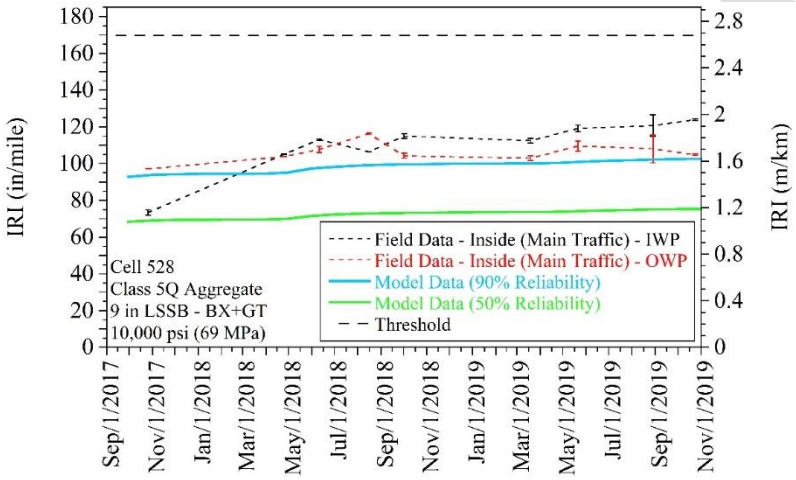
Large stone subbase (LSSB) groups – LSSB M_R = 10,000 psi:

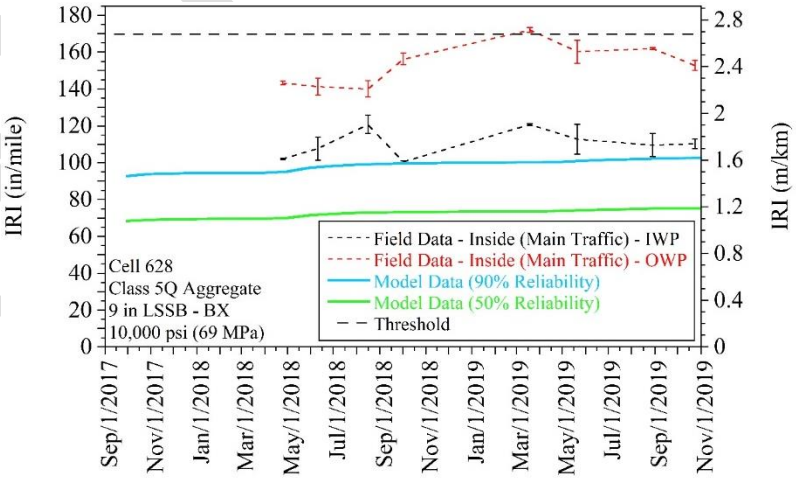


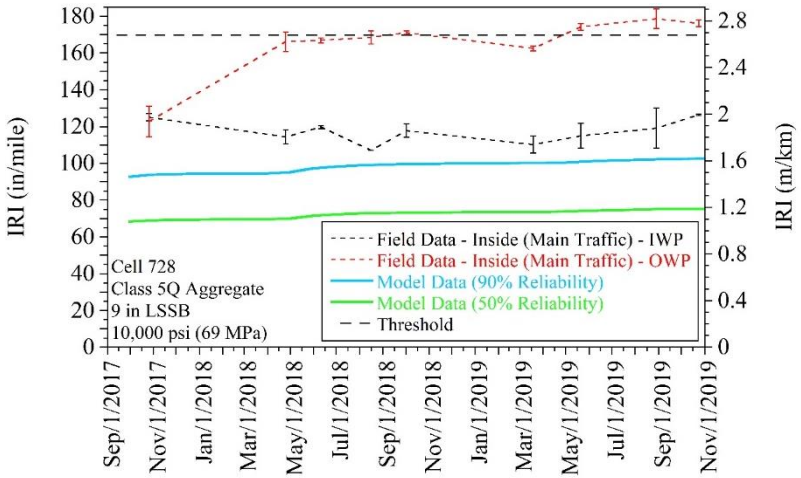


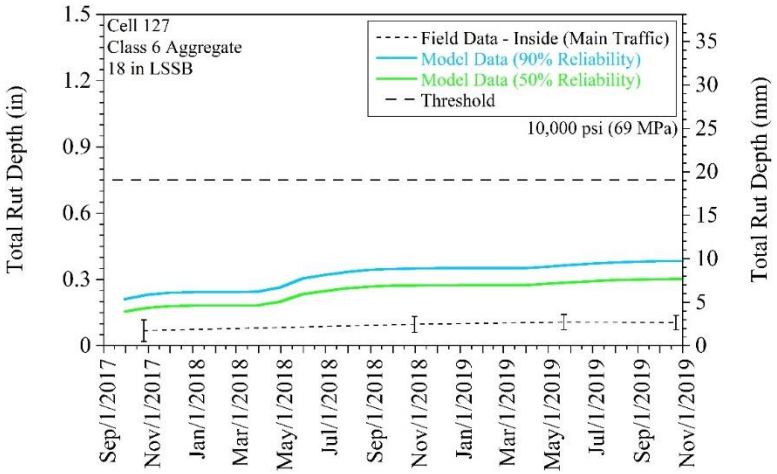

IRI (in/mile)
IRI (m/km)
Cell 328
Class 5Q Aggregate
9 in LSSB - TX
10,000 psi (69 MPa)
Field Data - Inside (Main Traffic) - IWP
Field Data - Inside (Main Traffic) - OWP
Model Data (90% Reliability)
Model Data (50% Reliability)
Threshold
Sep/1/2017
Nov/1/2017
Jan/1/2018
Mar/1/2018
May/1/2018
Jul/1/2018
Sep/1/2018
Nov/1/2018
Jan/1/2019
Mar/1/2019
May/1/2019
Jul/1/2019
Sep/1/2019
Nov/1/2019

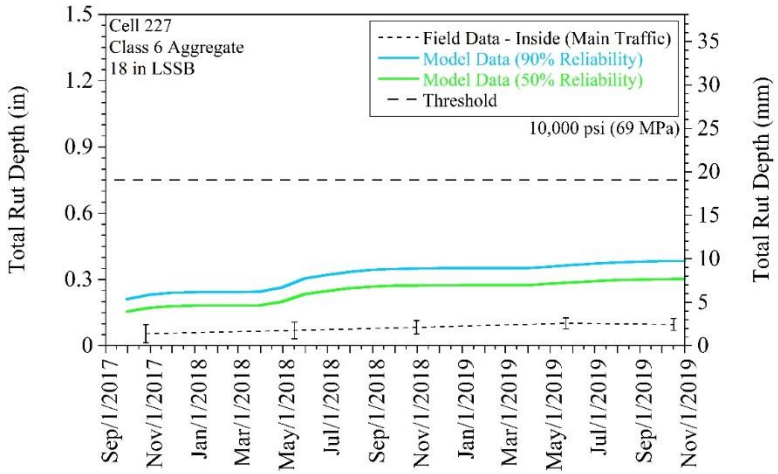

IRI (in/mile)
IRI (m/km)
Cell 428
Class 5Q Aggregate
9 in LSSB - TX+GT
10,000 psi (69 MPa)
Field Data - Inside (Main Traffic) - IWP
Field Data - Inside (Main Traffic) - OWP
Model Data (90% Reliability)
Model Data (50% Reliability)
Threshold
Sep/1/2017
Nov/1/2017
Jan/1/2018
Mar/1/2018
May/1/2018
Jul/1/2018
Sep/1/2018
Nov/1/2018
Jan/1/2019
Mar/1/2019
May/1/2019
Jul/1/2019
Sep/1/2019
Nov/1/2019

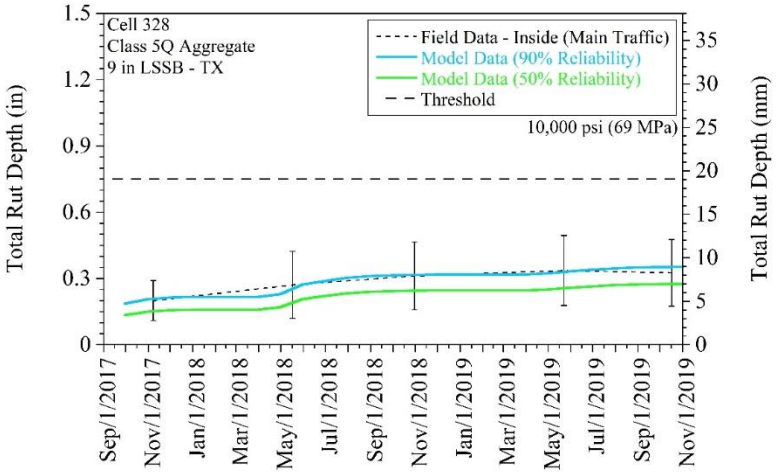

IRI (in/mile)
IRI (m/km)
Cell 528
Class 5Q Aggregate
9 in LSSB - BX+GT
10,000 psi (69 MPa)
Field Data - Inside (Main Traffic) - IWP
Field Data - Inside (Main Traffic) - OWP
Model Data (90% Reliability)
Model Data (50% Reliability)
Threshold
Sep/1/2017
Nov/1/2017
Jan/1/2018
Mar/1/2018
May/1/2018
Jul/1/2018
Sep/1/2018
Nov/1/2018
Jan/1/2019
Mar/1/2019
May/1/2019
Jul/1/2019
Sep/1/2019
Nov/1/2019

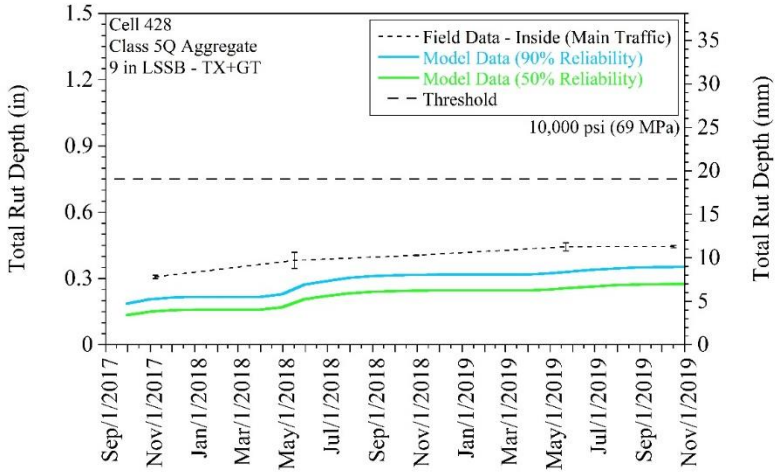

IRI (in/mile)
IRI (m/km)
Cell 628
Class 5Q Aggregate
9 in LSSB - BX
10,000 psi (69 MPa)
Field Data - Inside (Main Traffic) - IWP
Field Data - Inside (Main Traffic) - OWP
Model Data (90% Reliability)
Model Data (50% Reliability)
Threshold
Sep/1/2017
Nov/1/2017
Jan/1/2018
Mar/1/2018
May/1/2018
Jul/1/2018
Sep/1/2018
Nov/1/2018
Jan/1/2019
Mar/1/2019
May/1/2019
Jul/1/2019
Sep/1/2019
Nov/1/2019

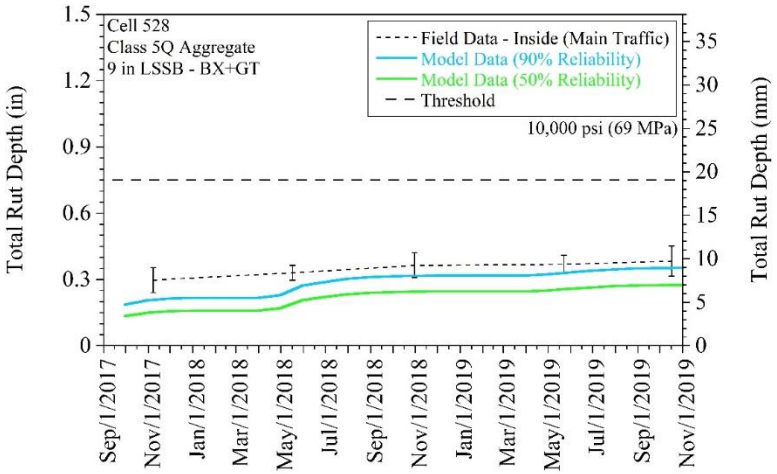

IRI (in/mile)
IRI (m/km)
Cell 728
Class 5Q Aggregate
9 in LSSB
10,000 psi (69 MPa)
Field Data - Inside (Main Traffic) - IWP
Field Data - Inside (Main Traffic) - OWP
Model Data (90% Reliability)
Model Data (50% Reliability)
Threshold
Sep/1/2017
Nov/1/2017
Jan/1/2018
Mar/1/2018
May/1/2018
Jul/1/2018
Sep/1/2018
Nov/1/2018
Jan/1/2019
Mar/1/2019
May/1/2019
Jul/1/2019
Sep/1/2019
Nov/1/2019

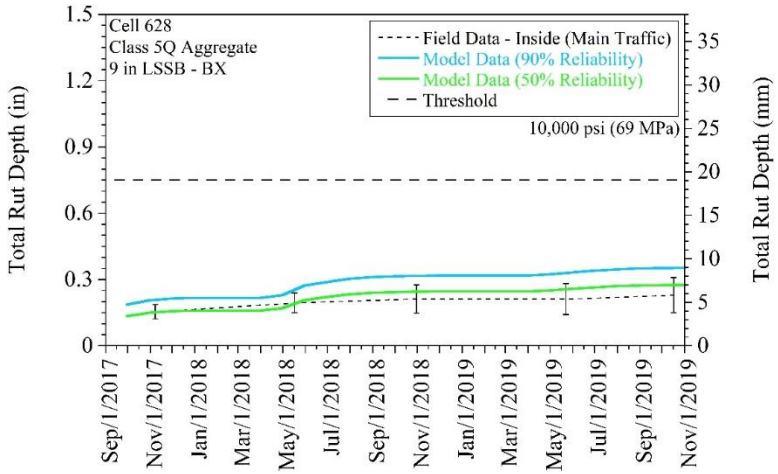

Total Rut Depth (in)
Total Rut Depth (mm)
Cell 127
Class 6 Aggregate
18 in LSSB
10,000 psi (69 MPa)
Field Data - Inside (Main Traffic)
Model Data (90% Reliability)
Model Data (50% Reliability)
Threshold
Sep/1/2017
Nov/1/2017
Jan/1/2018
Mar/1/2018
May/1/2018
Jul/1/2018
Sep/1/2018
Nov/1/2018
Jan/1/2019
Mar/1/2019
May/1/2019
Jul/1/2019
Sep/1/2019
Nov/1/2019

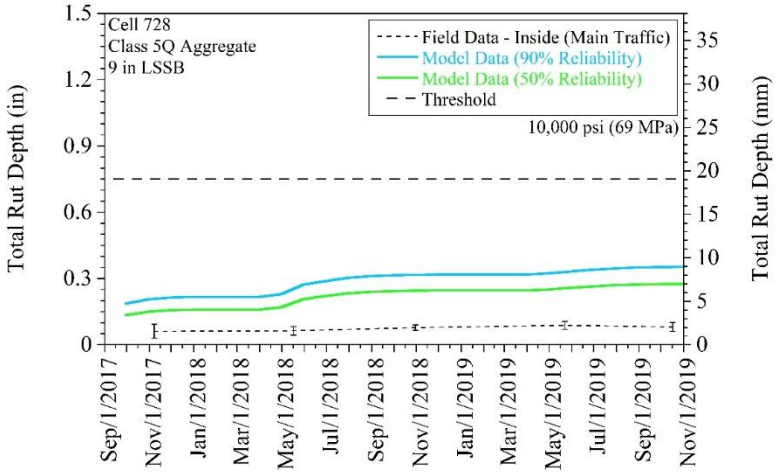

Total Rut Depth (in)
Total Rut Depth (mm)
Cell 227
Class 6 Aggregate
18 in LSSB
10,000 psi (69 MPa)
Field Data - Inside (Main Traffic)
Model Data (90% Reliability)
Model Data (50% Reliability)
Threshold
Sep/1/2017
Nov/1/2017
Jan/1/2018
Mar/1/2018
May/1/2018
Jul/1/2018
Sep/1/2018
Nov/1/2018
Jan/1/2019
Mar/1/2019
May/1/2019
Jul/1/2019
Sep/1/2019
Nov/1/2019


Cell 328
Class 5Q Aggregate
9 in LSSB - TX
Field Data - Inside (Main Traffic)
Model Data (90% Reliability)
Model Data (50% Reliability)
Threshold
10,000 psi (69 MPa)
Total Rut Depth (in)
Total Rut Depth (mm)
Sep/1/2017
Nov/1/2017
Jan/1/2018
Mar/1/2018
May/1/2018
Jul/1/2018
Sep/1/2018
Nov/1/2018
Jan/1/2019
Mar/1/2019
May/1/2019
Jul/1/2019
Sep/1/2019
Nov/1/2019

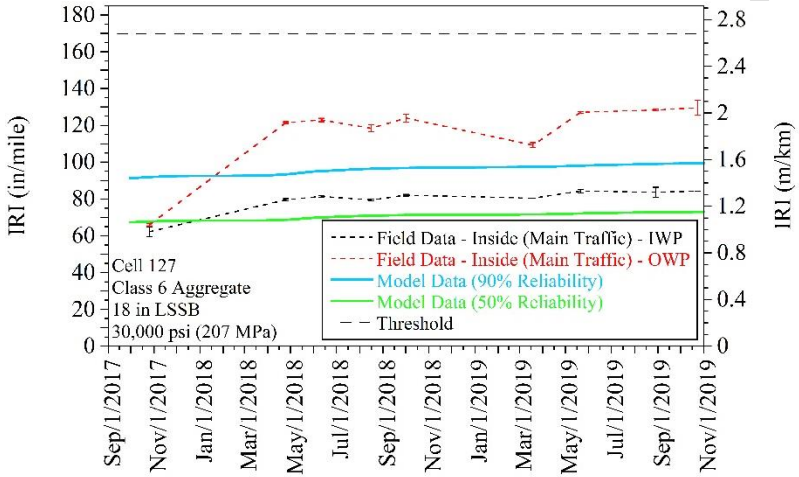

Cell 428
Class 5Q Aggregate
9 in LSSB - TX+GT
Field Data - Inside (Main Traffic)
Model Data (90% Reliability)
Model Data (50% Reliability)
Threshold
10,000 psi (69 MPa)
Total Rut Depth (in)
Total Rut Depth (mm)
Sep/1/2017
Nov/1/2017
Jan/1/2018
Mar/1/2018
May/1/2018
Jul/1/2018
Sep/1/2018
Nov/1/2018
Jan/1/2019
Mar/1/2019
May/1/2019
Jul/1/2019
Sep/1/2019
Nov/1/2019

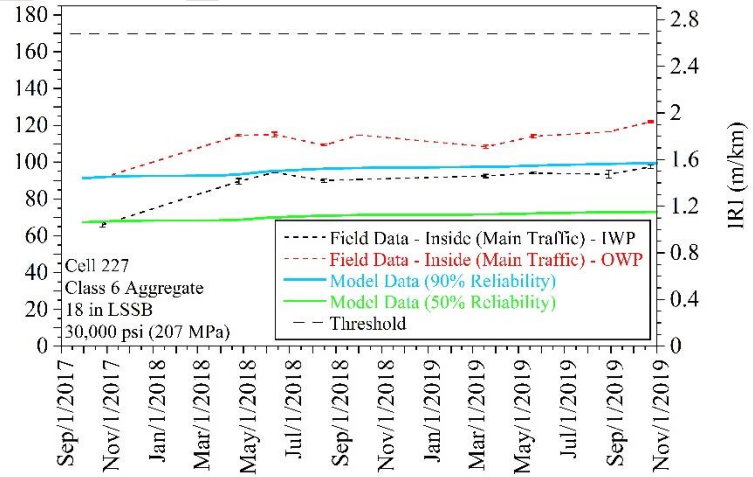

Cell 528
Class 5Q Aggregate
9 in LSSB - BX+GT
Field Data - Inside (Main Traffic)
Model Data (90% Reliability)
Model Data (50% Reliability)
Threshold
10,000 psi (69 MPa)
Total Rut Depth (in)
Total Rut Depth (mm)
Sep/1/2017
Nov/1/2017
Jan/1/2018
Mar/1/2018
May/1/2018
Jul/1/2018
Sep/1/2018
Nov/1/2018
Jan/1/2019
Mar/1/2019
May/1/2019
Jul/1/2019
Sep/1/2019
Nov/1/2019

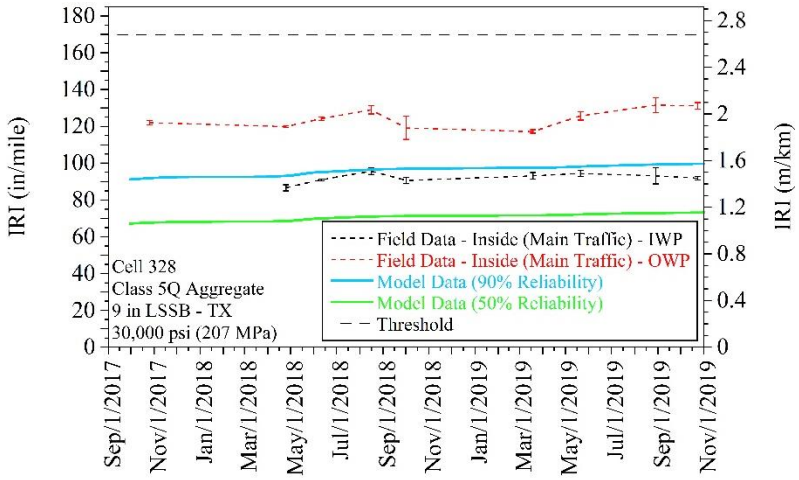

Cell 628
Class 5Q Aggregate
9 in LSSB - BX
Field Data - Inside (Main Traffic)
Model Data (90% Reliability)
Model Data (50% Reliability)
Threshold
10,000 psi (69 MPa)
Total Rut Depth (in)
Total Rut Depth (mm)
Sep/1/2017
Nov/1/2017
Jan/1/2018
Mar/1/2018
May/1/2018
Jul/1/2018
Sep/1/2018
Nov/1/2018
Jan/1/2019
Mar/1/2019
May/1/2019
Jul/1/2019
Sep/1/2019
Nov/1/2019

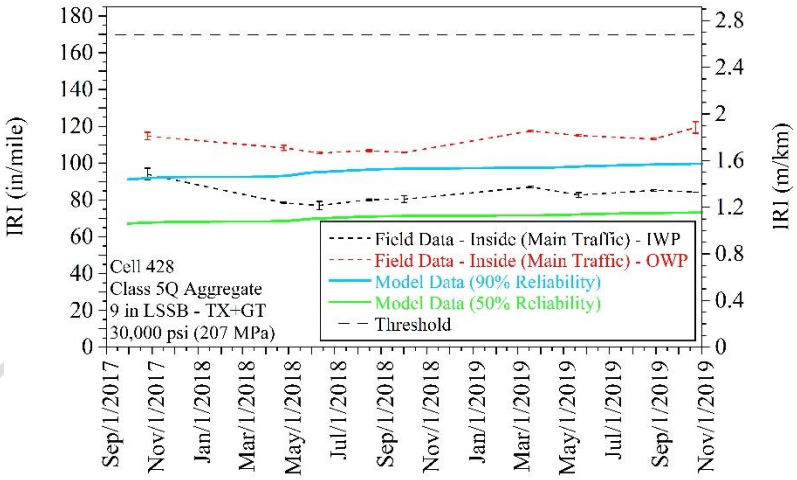


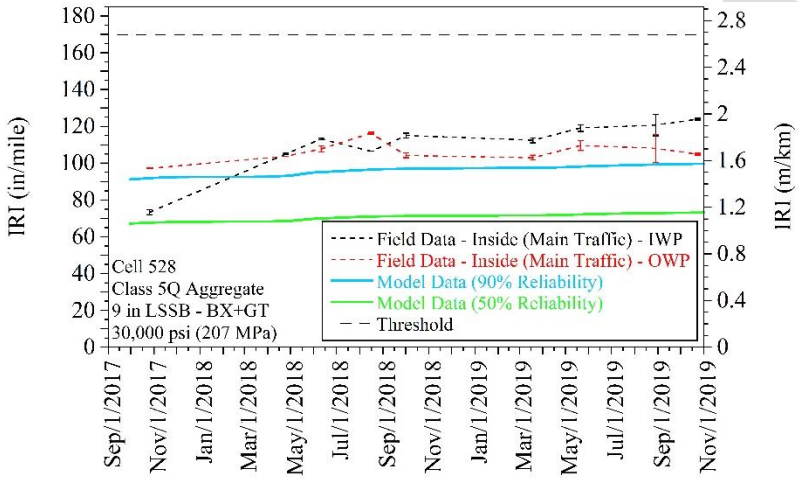
Large stone subbase (LSSB) groups – LSSB M_R = 30,000 psi:

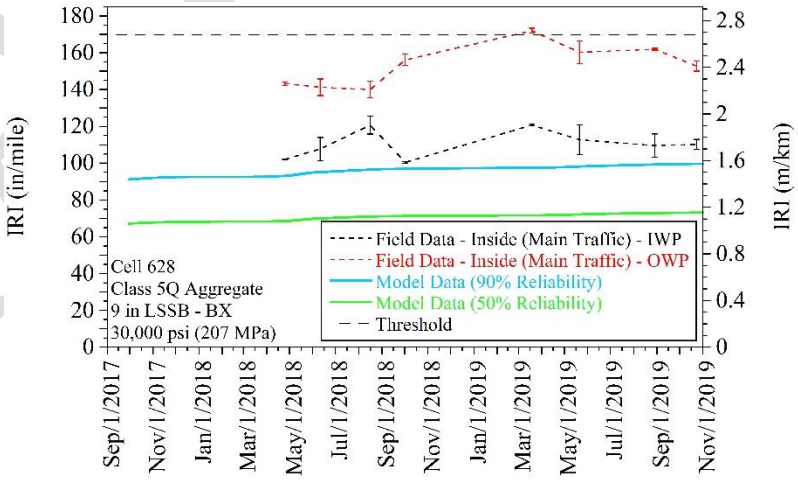


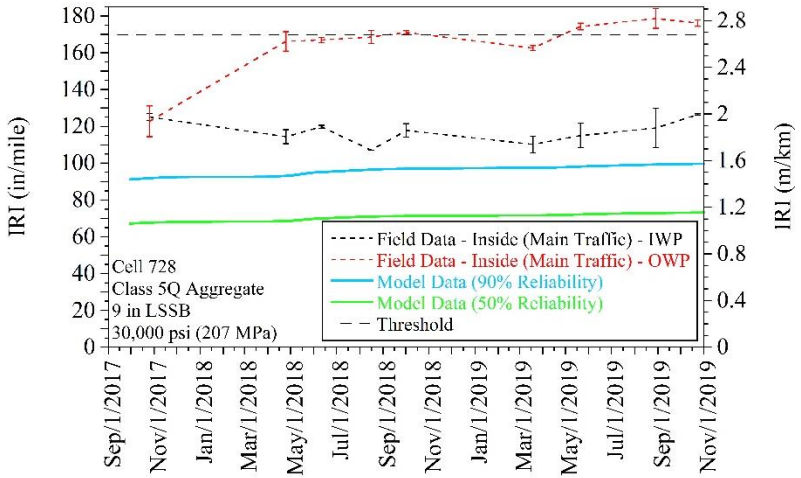


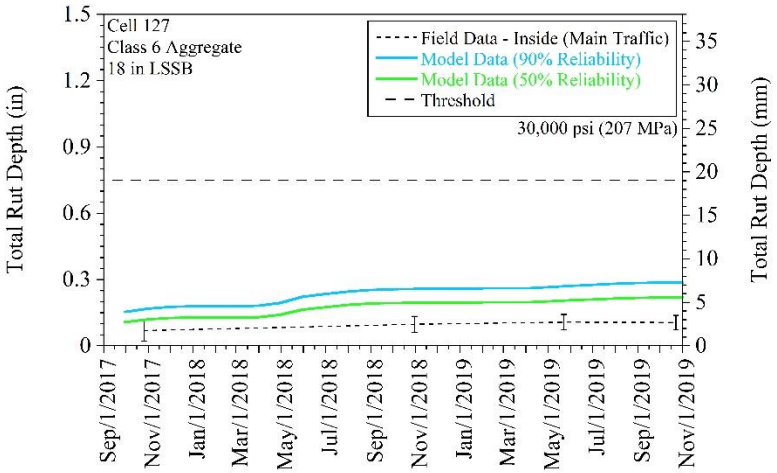

IRI (in/mile)
IRI (m/km)
Cell 328
Class 5Q Aggregate
9 in LSSB - TX
30,000 psi (207 MPa)
Field Data - Inside (Main Traffic) - IWP
Field Data - Inside (Main Traffic) - OWP
Model Data (90% Reliability)
Model Data (50% Reliability)
Threshold

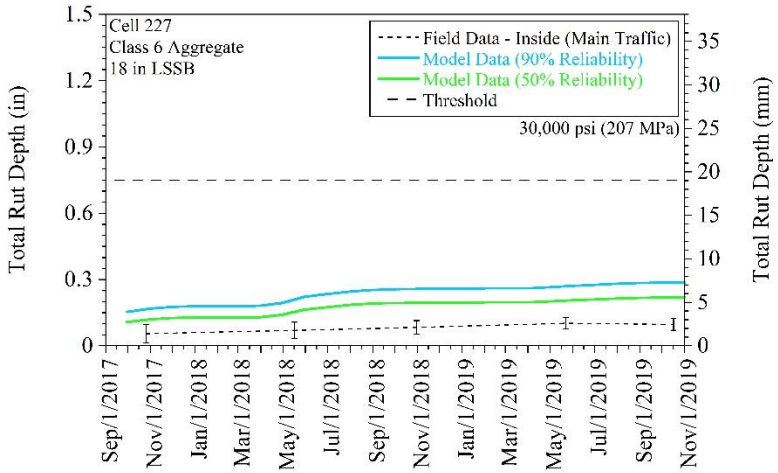

IRI (in/mile)
IRI (m/km)
Cell 428
Class 5Q Aggregate
9 in LSSB - TX+GT
30,000 psi (207 MPa)
Field Data - Inside (Main Traffic) - IWP
Field Data - Inside (Main Traffic) - OWP
Model Data (90% Reliability)
Model Data (50% Reliability)
Threshold

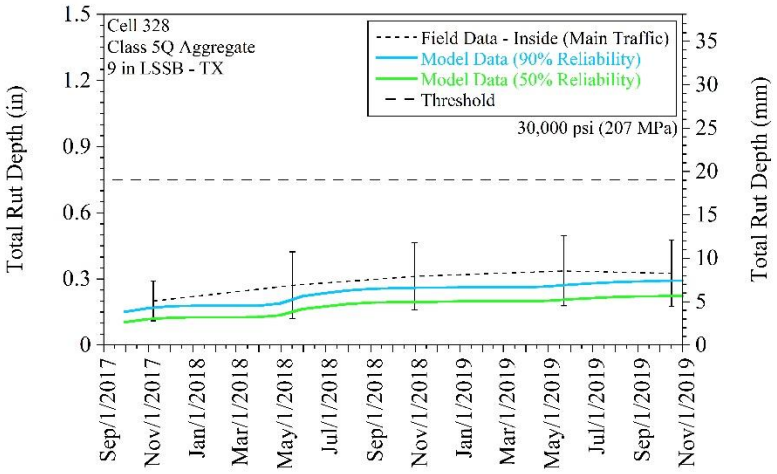

IRI (in/mile)
IRI (m/km)
Cell 528
Class 5Q Aggregate
9 in LSSB - BX+GT
30,000 psi (207 MPa)
Field Data - Inside (Main Traffic) - IWP
Field Data - Inside (Main Traffic) - OWP
Model Data (90% Reliability)
Model Data (50% Reliability)
Threshold

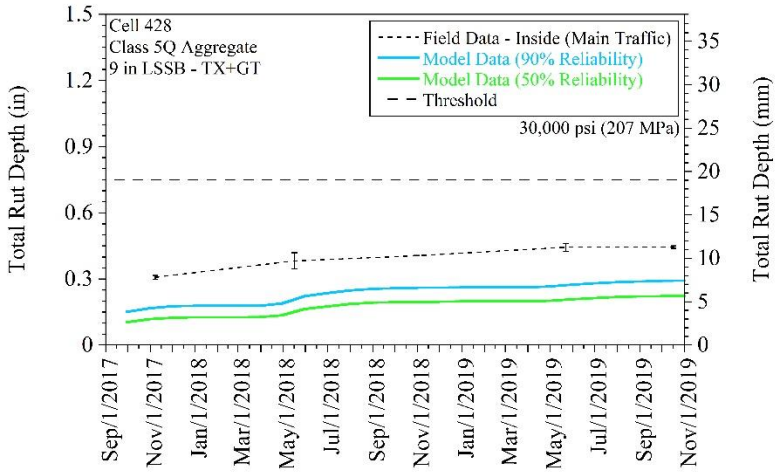

IRI (in/mile)
IRI (m/km)
Cell 628
Class 5Q Aggregate
9 in LSSB - BX
30,000 psi (207 MPa)
Field Data - Inside (Main Traffic) - IWP
Field Data - Inside (Main Traffic) - OWP
Model Data (90% Reliability)
Model Data (50% Reliability)
Threshold

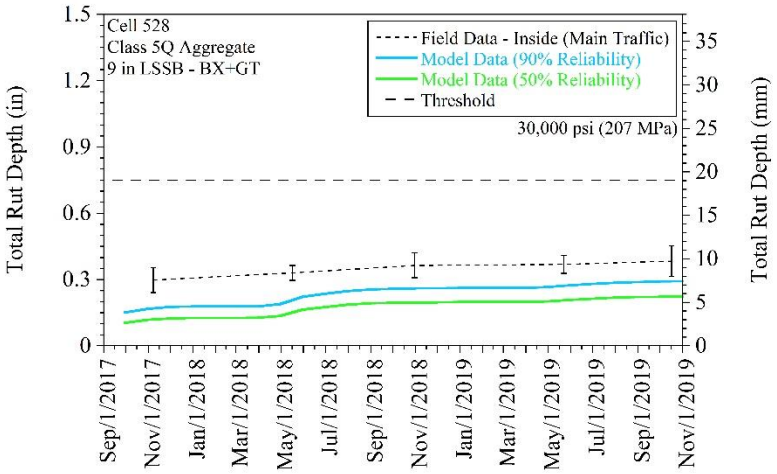

IRI (in/mile)
IRI (m/km)
Cell 728
Class 5Q Aggregate
9 in LSSB
30,000 psi (207 MPa)
Field Data - Inside (Main Traffic) - IWP
Field Data - Inside (Main Traffic) - OWP
Model Data (90% Reliability)
Model Data (50% Reliability)
Threshold
Sep/1/2017
Nov/1/2017
Jan/1/2018
Mar/1/2018
May/1/2018
Jul/1/2018
Sep/1/2018
Nov/1/2018
Jan/1/2019
Mar/1/2019
May/1/2019
Jul/1/2019
Sep/1/2019
Nov/1/2019

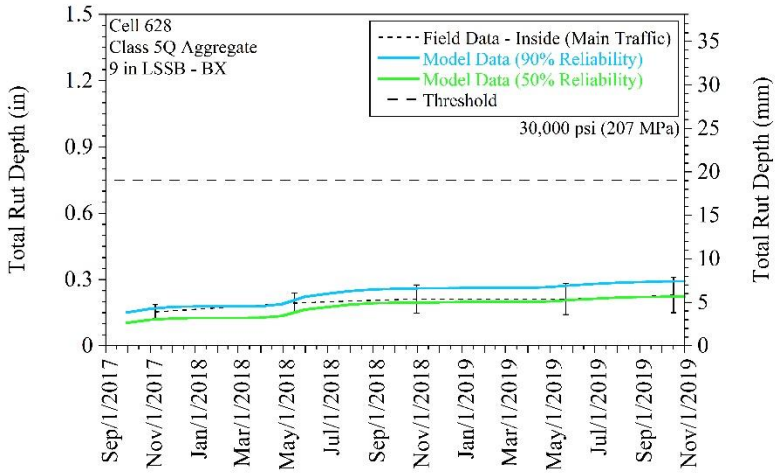

Total Rut Depth (in)
Total Rut Depth (mm)
Cell 127
Class 6 Aggregate
18 in LSSB
30,000 psi (207 MPa)
Field Data - Inside (Main Traffic)
Model Data (90% Reliability)
Model Data (50% Reliability)
Threshold
Sep/1/2017
Nov/1/2017
Jan/1/2018
Mar/1/2018
May/1/2018
Jul/1/2018
Sep/1/2018
Nov/1/2018
Jan/1/2019
Mar/1/2019
May/1/2019
Jul/1/2019
Sep/1/2019
Nov/1/2019

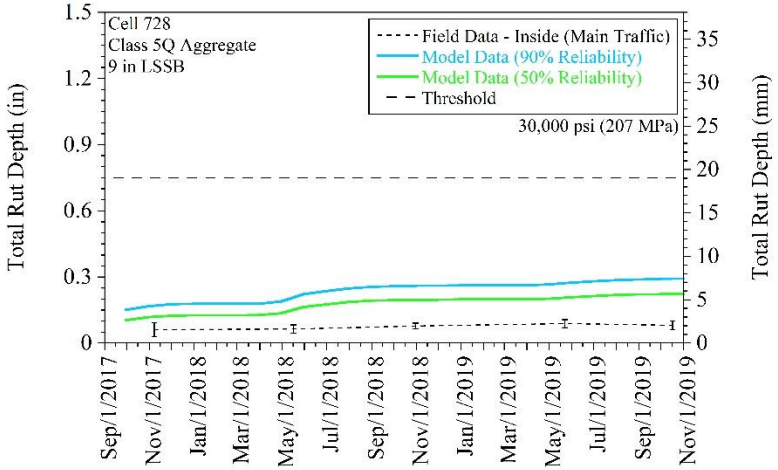

Total Rut Depth (in)
Total Rut Depth (mm)
Cell 227
Class 6 Aggregate
18 in LSSB
30,000 psi (207 MPa)
Field Data - Inside (Main Traffic)
Model Data (90% Reliability)
Model Data (50% Reliability)
Threshold
Sep/1/2017
Nov/1/2017
Jan/1/2018
Mar/1/2018
May/1/2018
Jul/1/2018
Sep/1/2018
Nov/1/2018
Jan/1/2019
Mar/1/2019
May/1/2019
Jul/1/2019
Sep/1/2019
Nov/1/2019


Cell 328
Class 5Q Aggregate
9 in LSSB - TX
Field Data - Inside (Main Traffic)
Model Data (90% Reliability)
Model Data (50% Reliability)
Threshold
30,000 psi (207 MPa)
Total Rut Depth (in)
Total Rut Depth (mm)
Sep/1/2017
Nov/1/2017
Jan/1/2018
Mar/1/2018
May/1/2018
Jul/1/2018
Sep/1/2018
Nov/1/2018
Jan/1/2019
Mar/1/2019
May/1/2019
Jul/1/2019
Sep/1/2019
Nov/1/2019

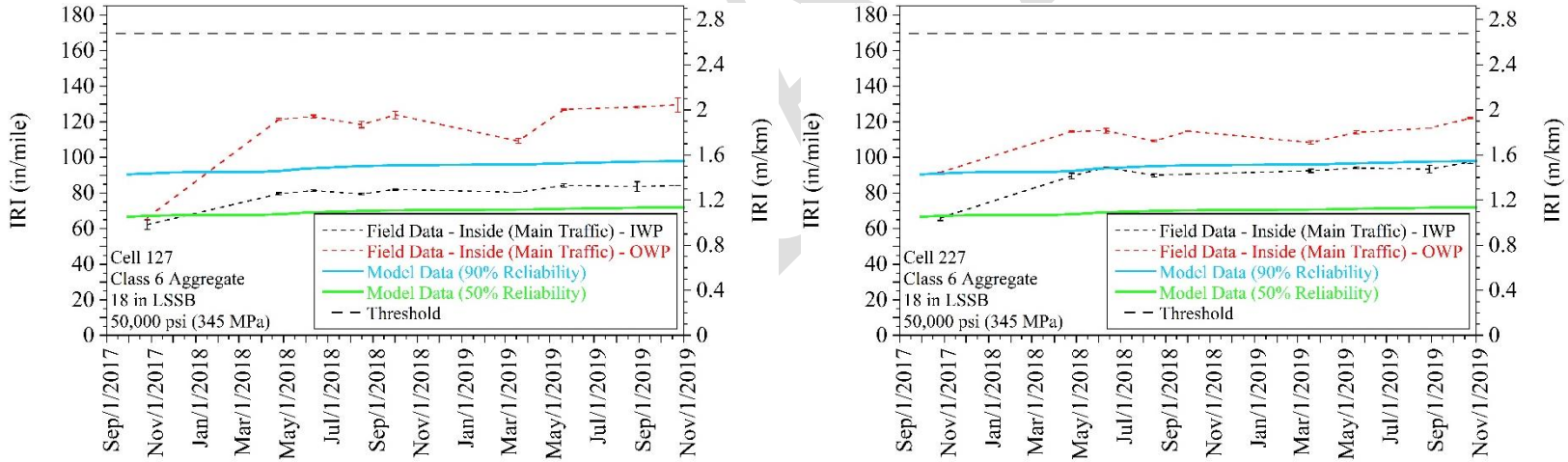

Cell 428
Class 5Q Aggregate
9 in LSSB - TX+GT
Field Data - Inside (Main Traffic)
Model Data (90% Reliability)
Model Data (50% Reliability)
Threshold
30,000 psi (207 MPa)
Total Rut Depth (in)
Total Rut Depth (mm)

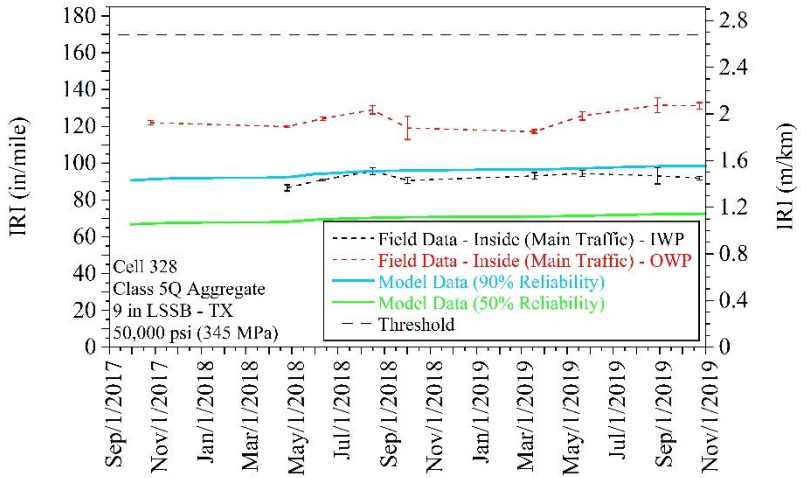

Cell 528
Class 5Q Aggregate
9 in LSSB - BX+GT
Field Data - Inside (Main Traffic)
Model Data (90% Reliability)
Model Data (50% Reliability)
Threshold
30,000 psi (207 MPa)
Total Rut Depth (in)
Total Rut Depth (mm)

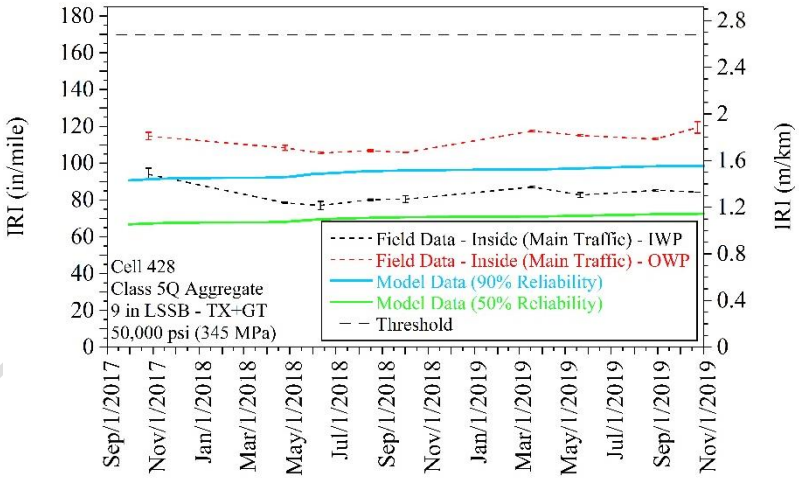

Cell 628
Class 5Q Aggregate
9 in LSSB - BX
Field Data - Inside (Main Traffic)
Model Data (90% Reliability)
Model Data (50% Reliability)
Threshold
30,000 psi (207 MPa)
Total Rut Depth (in)
Total Rut Depth (mm)

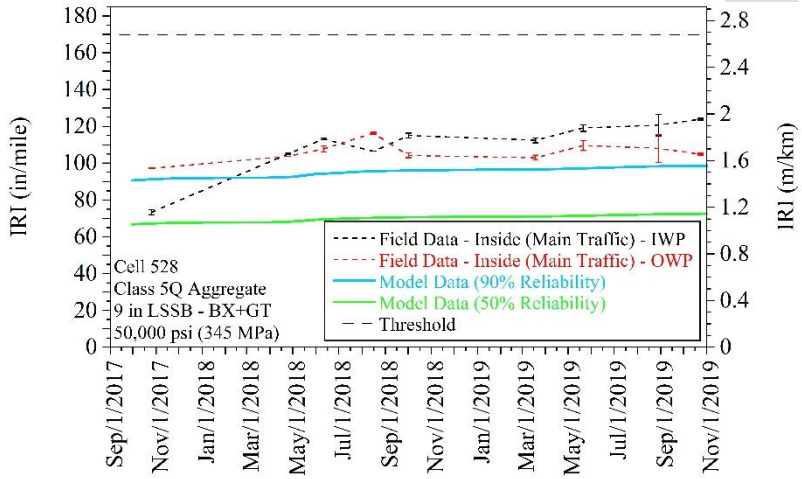


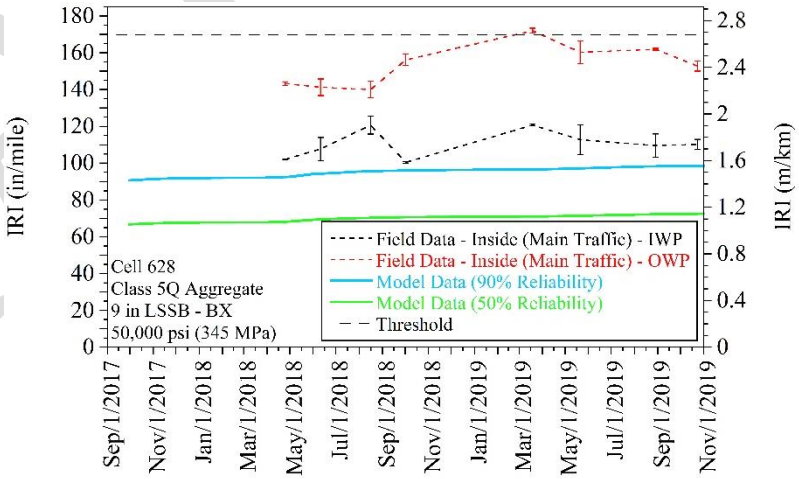
Large stone subbase (LSSB) groups – LSSB M_R = 50,000 psi:

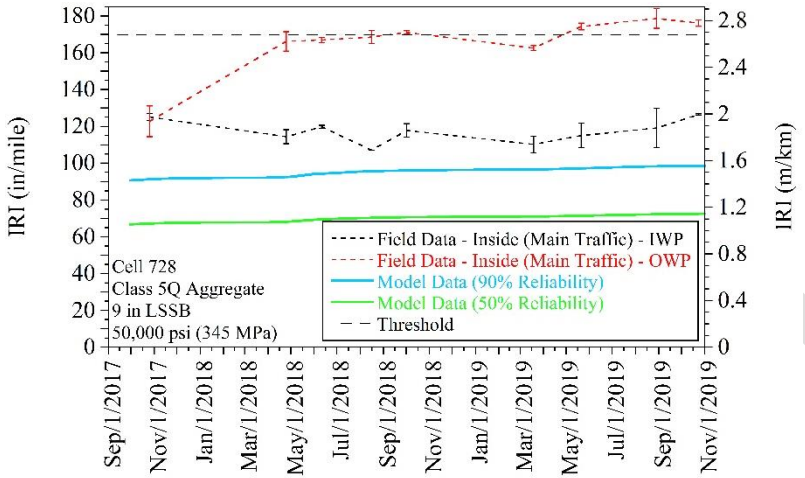


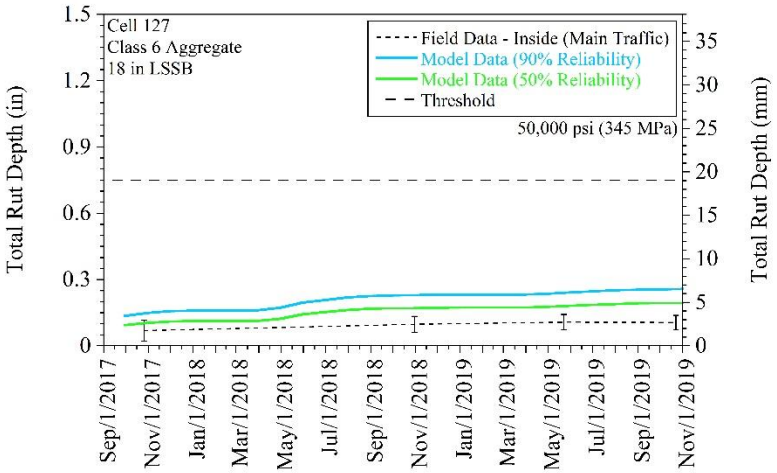

IRI (in/mile)
IRI (m/km)
Cell 328
Class 5Q Aggregate
9 in LSSB - TX
50,000 psi (345 MPa)
Field Data - Inside (Main Traffic) - IWP
Field Data - Inside (Main Traffic) - OWP
Model Data (90% Reliability)
Model Data (50% Reliability)
Threshold
Sep/1/2017
Nov/1/2017
Jan/1/2018
Mar/1/2018
May/1/2018
Jul/1/2018
Sep/1/2018
Nov/1/2018
Jan/1/2019
Mar/1/2019
May/1/2019
Jul/1/2019
Sep/1/2019
Nov/1/2019

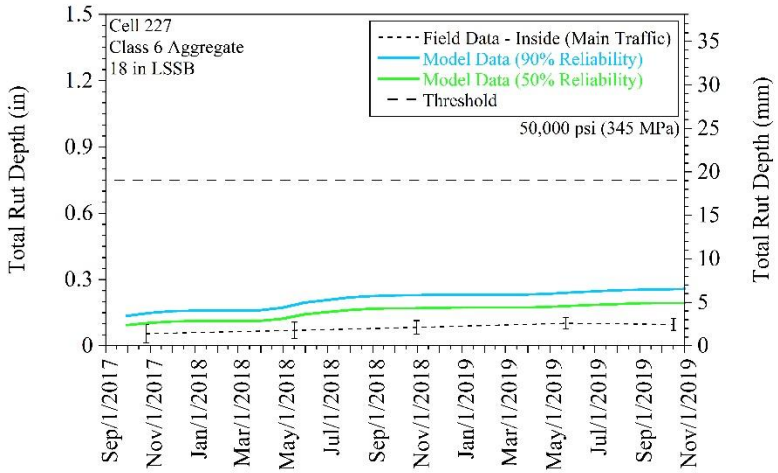

IRI (in/mile)
IRI (m/km)
Cell 428
Class 5Q Aggregate
9 in LSSB - TX+GT
50,000 psi (345 MPa)
Field Data - Inside (Main Traffic) - IWP
Field Data - Inside (Main Traffic) - OWP
Model Data (90% Reliability)
Model Data (50% Reliability)
Threshold
Sep/1/2017
Nov/1/2017
Jan/1/2018
Mar/1/2018
May/1/2018
Jul/1/2018
Sep/1/2018
Nov/1/2018
Jan/1/2019
Mar/1/2019
May/1/2019
Jul/1/2019
Sep/1/2019
Nov/1/2019

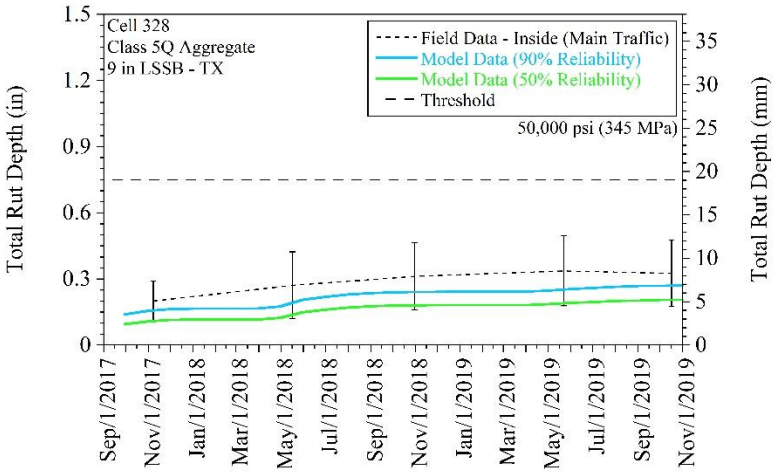

IRI (in/mile)
IRI (m/km)
Cell 528
Class 5Q Aggregate
9 in LSSB - BX+GT
50,000 psi (345 MPa)
Field Data - Inside (Main Traffic) - IWP
Field Data - Inside (Main Traffic) - OWP
Model Data (90% Reliability)
Model Data (50% Reliability)
Threshold
Sep/1/2017
Nov/1/2017
Jan/1/2018
Mar/1/2018
May/1/2018
Jul/1/2018
Sep/1/2018
Nov/1/2018
Jan/1/2019
Mar/1/2019
May/1/2019
Jul/1/2019
Sep/1/2019
Nov/1/2019

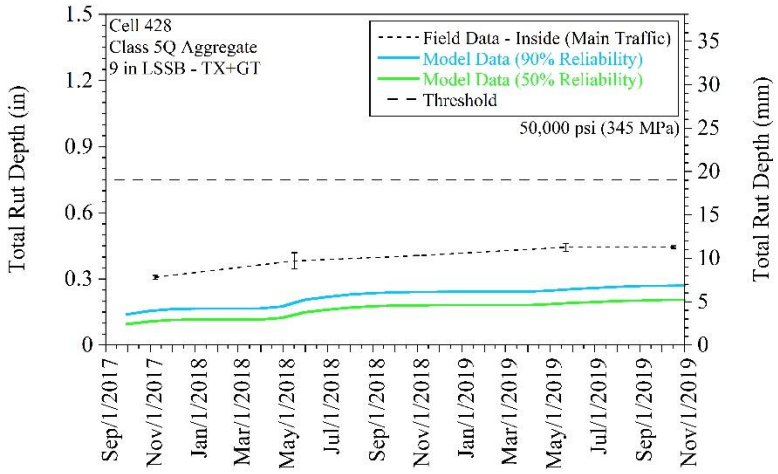

IRI (in/mile)
IRI (m/km)
Cell 628
Class 5Q Aggregate
9 in LSSB - BX
50,000 psi (345 MPa)
Field Data - Inside (Main Traffic) - IWP
Field Data - Inside (Main Traffic) - OWP
Model Data (90% Reliability)
Model Data (50% Reliability)
Threshold
Sep/1/2017
Nov/1/2017
Jan/1/2018
Mar/1/2018
May/1/2018
Jul/1/2018
Sep/1/2018
Nov/1/2018
Jan/1/2019
Mar/1/2019
May/1/2019
Jul/1/2019
Sep/1/2019
Nov/1/2019

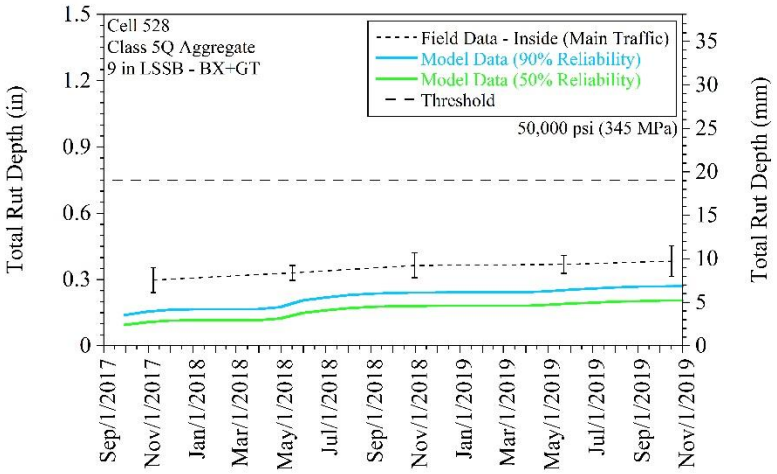

IRI (in/mile)
IRI (m/km)
Cell 728
Class 5Q Aggregate
9 in LSSB
50,000 psi (345 MPa)
Field Data - Inside (Main Traffic) - IWP
Field Data - Inside (Main Traffic) - OWP
Model Data (90% Reliability)
Model Data (50% Reliability)
Threshold

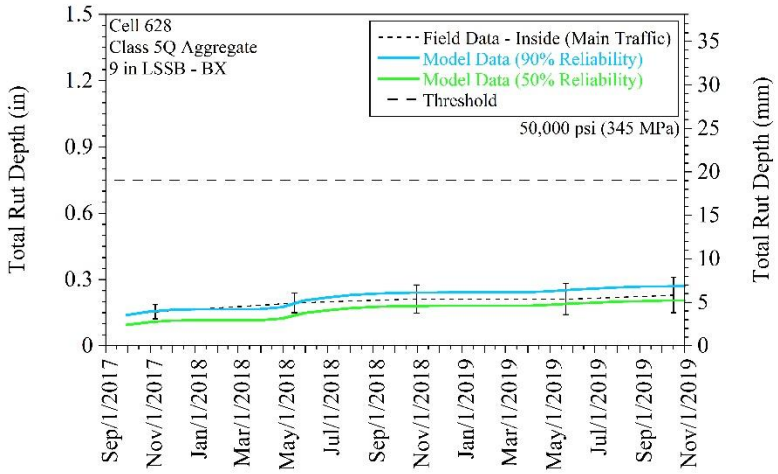

Total Rut Depth (in)
Total Rut Depth (mm)
Cell 127
Class 6 Aggregate
18 in LSSB
50,000 psi (345 MPa)
Field Data - Inside (Main Traffic)
Model Data (90% Reliability)
Model Data (50% Reliability)
Threshold

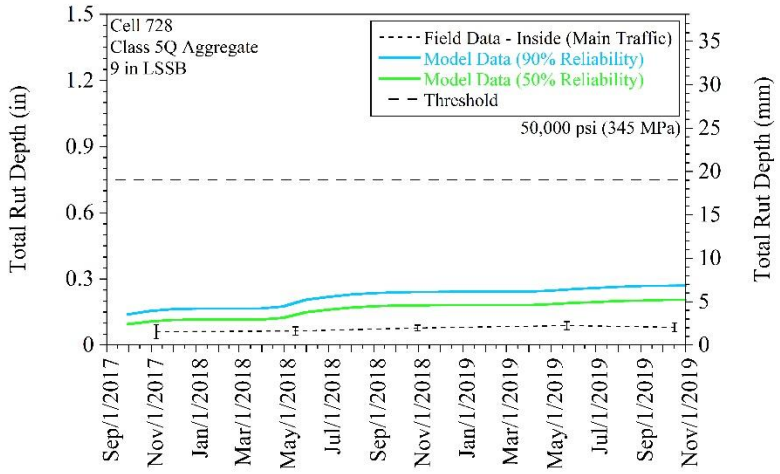

Total Rut Depth (in)
Total Rut Depth (mm)
Cell 227
Class 6 Aggregate
18 in LSSB
50,000 psi (345 MPa)
Field Data - Inside (Main Traffic)
Model Data (90% Reliability)
Model Data (50% Reliability)
Threshold


Cell 328
Class 5Q Aggregate
9 in LSSB - TX
Field Data - Inside (Main Traffic)
Model Data (90% Reliability)
Model Data (50% Reliability)
Threshold
50,000 psi (345 MPa)
Total Rut Depth (in)
Total Rut Depth (mm)
Sep/1/2017
Nov/1/2017
Jan/1/2018
Mar/1/2018
May/1/2018
Jul/1/2018
Sep/1/2018
Nov/1/2018
Jan/1/2019
Mar/1/2019
May/1/2019
Jul/1/2019
Sep/1/2019
Nov/1/2019


Cell 428
Class 5Q Aggregate
9 in LSSB - TX+GT
Field Data - Inside (Main Traffic)
Model Data (90% Reliability)
Model Data (50% Reliability)
Threshold
50,000 psi (345 MPa)
Total Rut Depth (in)
Total Rut Depth (mm)
Sep/1/2017
Nov/1/2017
Jan/1/2018
Mar/1/2018
May/1/2018
Jul/1/2018
Sep/1/2018
Nov/1/2018
Jan/1/2019
Mar/1/2019
May/1/2019
Jul/1/2019
Sep/1/2019
Nov/1/2019


Cell 528
Class 5Q Aggregate
9 in LSSB - BX+GT
Field Data - Inside (Main Traffic)
Model Data (90% Reliability)
Model Data (50% Reliability)
Threshold
50,000 psi (345 MPa)
Total Rut Depth (in)
Total Rut Depth (mm)
Sep/1/2017
Nov/1/2017
Jan/1/2018
Mar/1/2018
May/1/2018
Jul/1/2018
Sep/1/2018
Nov/1/2018
Jan/1/2019
Mar/1/2019
May/1/2019
Jul/1/2019
Sep/1/2019
Nov/1/2019


Cell 628
Class 5Q Aggregate
9 in LSSB - BX
Field Data - Inside (Main Traffic)
Model Data (90% Reliability)
Model Data (50% Reliability)
Threshold
50,000 psi (345 MPa)
Total Rut Depth (in)
Total Rut Depth (mm)
Sep/1/2017
Nov/1/2017
Jan/1/2018
Mar/1/2018
May/1/2018
Jul/1/2018
Sep/1/2018
Nov/1/2018
Jan/1/2019
Mar/1/2019
May/1/2019
Jul/1/2019
Sep/1/2019
Nov/1/2019


Cell 728
Class 5Q Aggregate
9 in LSSB
Field Data - Inside (Main Traffic)
Model Data (90% Reliability)
Model Data (50% Reliability)
Threshold
50,000 psi (345 MPa)
Total Rut Depth (in)
Total Rut Depth (mm)
1.5
1.2
0.9
0.6
0.3
0
35
30
25
20
15
10
5
0
Sep/1/2017
Nov/1/2017
Jan/1/2018
Mar/1/2018
May/1/2018
Jul/1/2018
Sep/1/2018
Nov/1/2018
Jan/1/2019
Mar/1/2019
May/1/2019
Jul/1/2019
Sep/1/2019
Nov/1/2019

DRAFT

APPENDIX AF. ASPHALT CONCRETE (AC) OVER AC OVERLAY DESIGNS

For cell 185 (overlay asphalt binder = Superpave PG 58-34):

Design Inputs

Design Life: 40 years
Design Type: ACC_ACC

Existing construction: August, 2017
Pavement construction: September, 2018
Traffic opening: September, 2018

Climate Data Sources: 45.5, -93.75; 45, -93.75; 45.5, -93.125; 45. -93.125; 45.5, -94.375; 45, -94.375

Design Structure

Layer type	Material Type	Thickness (in)
Flexible (OL)	Default asphalt concrete	4.0
Flexible (existing)	Default asphalt concrete	2.5
NonStabilized	A-1-a	12.0
NonStabilized	A-1-b	3.5
Subgrade	A-1-b	Semi-infinite

Volumetric at Construction:	
Effective binder content (%)	11.6
Air voids (%)	7.0

Traffic

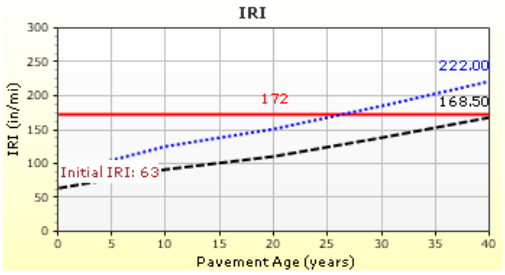
Age (year)	Heavy Trucks (cumulative)
2018 (initial)	1,000
2038 (20 years)	3,520,100
2058 (40 years)	8,683,820

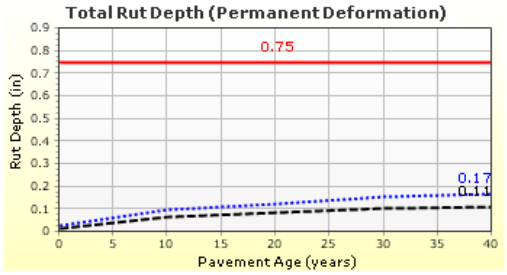
Design Outputs

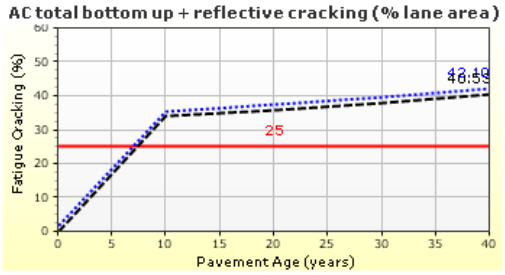
Distress Prediction Summary

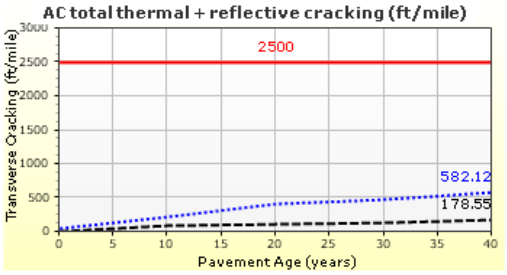
Distress Type	Distress @ Specified Reliability		Reliability (%)		Criterion Satisfied?
	Target	Predicted	Target	Achieved	
Terminal IRI (in/mile)	172.00	222.01	90.00	53.33	Fail
Permanent deformation - total pavement (in)	0.75	0.17	90.00	100.00	Pass
AC total fatigue cracking: bottom up + reflective (% lane area)	25.00	42.10	90.00	0.00	Fail
AC total transverse cracking: thermal + reflective (ft/mile)	2500.00	582.12	90.00	100.00	Pass
Permanent deformation - AC only (in)	0.25	0.16	90.00	99.96	Pass
AC bottom-up fatigue cracking (% lane area)	25.00	0.00	50.00	100.00	Pass
AC thermal cracking (ft/mile)	1000.00	103.59	50.00	100.00	Pass
AC top-down fatigue cracking (ft/mile)	2000.00	4257.96	90.00	60.88	Fail

Distress Charts











HMA Rehabilitation (Input Level: 3)

Milled thickness (in)	1.00
Structural rating	Fair
Environmental rating	Good
Total rut depth (in)	0.70

For cell 186 (overlay asphalt binder = Superpave PG 58-34):

Design Inputs

Design Life:	40 years	Existing construction:	August, 2017	Climate Data Sources	45.5, -93.75 45, -93.75 45.5, -93.125 45. -93.125 45.5, -94.375 45, -94.375
Design Type:	ACC_ACC	Pavement construction:	September, 2018		
		Traffic opening:	September, 2018		

Design Structure

Layer type	Material Type	Thickness (in)
Flexible (OL)	Default asphalt concrete	4.0
Flexible (existing)	Default asphalt concrete	2.5
NonStabilized	A-1-a	12.0
NonStabilized	A-1-b	3.5
Subgrade	A-1-b	Semi-infinite

Volumetric at Construction:	
Effective binder content (%)	11.6
Air voids (%)	7.0

Traffic

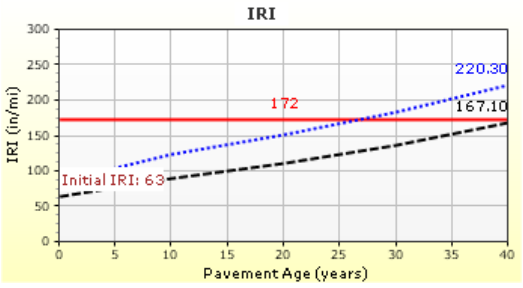
Age (year)	Heavy Trucks (cumulative)
2018 (initial)	1,000
2038 (20 years)	3,520,100
2058 (40 years)	8,683,820

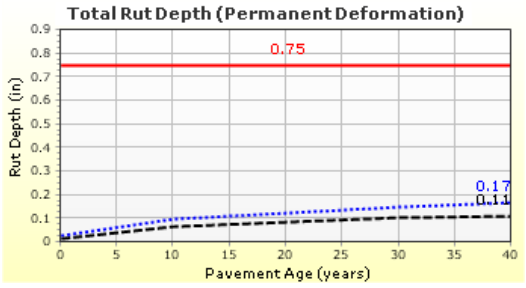
Design Outputs

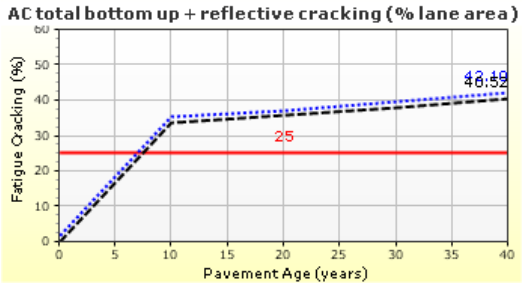
Distress Prediction Summary

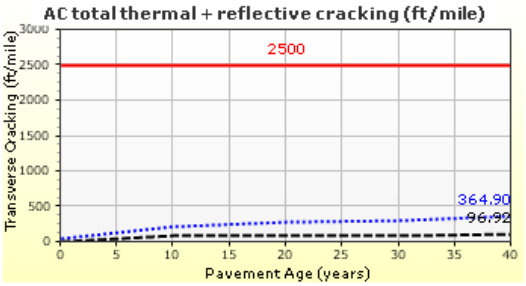
Distress Type	Distress @ Specified Reliability		Reliability (%)		Criterion Satisfied?
	Target	Predicted	Target	Achieved	
Terminal IRI (in/mile)	172.00	220.28	90.00	54.71	Fail
Permanent deformation - total pavement (in)	0.75	0.17	90.00	100.00	Pass
AC total fatigue cracking: bottom up + reflective (% lane area)	25.00	42.10	90.00	0.00	Fail
AC total transverse cracking: thermal + reflective (ft/mile)	2500.00	364.90	90.00	100.00	Pass
Permanent deformation - AC only (in)	0.25	0.16	90.00	99.96	Pass
AC bottom-up fatigue cracking (% lane area)	25.00	0.00	50.00	100.00	Pass
AC thermal cracking (ft/mile)	1000.00	21.96	50.00	100.00	Pass
AC top-down fatigue cracking (ft/mile)	2000.00	2646.38	90.00	82.52	Fail

Distress Charts











HMA Rehabilitation (Input Level: 3)

Milled thickness (in)	1.00
Structural rating	Fair
Environmental rating	Good
Total rut depth (in)	0.70

For cell 188 (overlay asphalt binder = Superpave PG 58-34):

Design Inputs

Design Life:	40 years	Existing construction:	August, 2017	Climate Data Sources	45.5, -93.75 45, -93.75 45.5, -93.125 45. -93.125 45.5, -94.375 45, -94.375
Design Type:	ACC_ACC	Pavement construction:	September, 2018		
		Traffic opening:	September, 2018		

Design Structure

Layer type	Material Type	Thickness (in)
Flexible (OL)	Default asphalt concrete	4.0
Flexible (existing)	Default asphalt concrete	2.5
NonStabilized	A-1-a	12.0
NonStabilized	A-1-b	3.5
Subgrade	A-6	Semi-infinite

Volumetric at Construction:	
Effective binder content (%)	11.6
Air voids (%)	7.0

Traffic

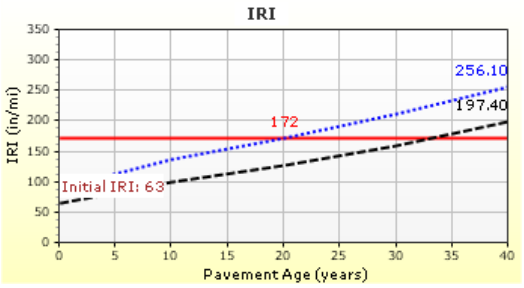
Age (year)	Heavy Trucks (cumulative)
2018 (initial)	1,000
2038 (20 years)	3,520,100
2058 (40 years)	8,683,820

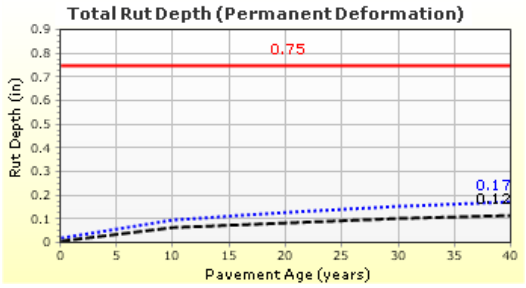
Design Outputs

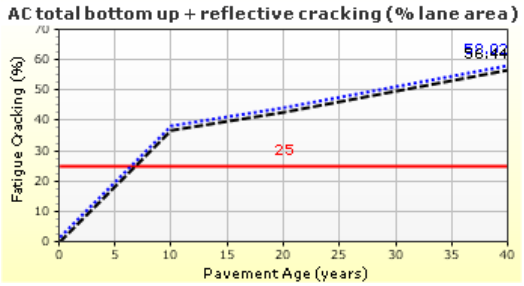
Distress Prediction Summary

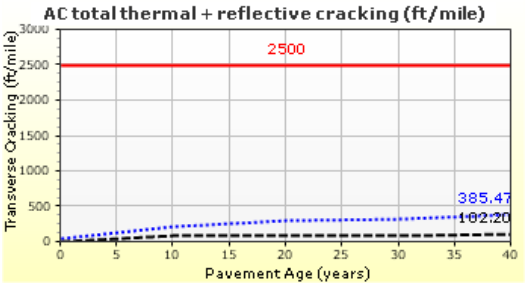
Distress Type	Distress @ Specified Reliability		Reliability (%)		Criterion Satisfied?
	Target	Predicted	Target	Achieved	
Terminal IRI (in/mile)	172.00	256.08	90.00	28.97	Fail
Permanent deformation - total pavement (in)	0.75	0.17	90.00	100.00	Pass
AC total fatigue cracking: bottom up + reflective (% lane area)	25.00	58.02	90.00	0.00	Fail
AC total transverse cracking: thermal + reflective (ft/mile)	2500.00	385.47	90.00	100.00	Pass
Permanent deformation - AC only (in)	0.25	0.15	90.00	100.00	Pass
AC bottom-up fatigue cracking (% lane area)	25.00	0.00	50.00	100.00	Pass
AC thermal cracking (ft/mile)	1000.00	27.24	50.00	100.00	Pass
AC top-down fatigue cracking (ft/mile)	2000.00	13803.87	90.00	0.03	Fail

Distress Charts











HMA Rehabilitation (Input Level: 3)

Milled thickness (in)	1.00
Structural rating	Fair
Environmental rating	Good
Total rut depth (in)	0.70

For cell 189 (overlay asphalt binder = Superpave PG 58-34):

Design Inputs

Design Life:	40 years	Existing construction:	August, 2017	Climate Data Sources	45.5, -93.75 45, -93.75 45.5, -93.125 45. -93.125 45.5, -94.375 45, -94.375
Design Type:	ACC_ACC	Pavement construction:	September, 2018		
		Traffic opening:	September, 2018		

Design Structure

Layer type	Material Type	Thickness (in)
Flexible (OL)	Default asphalt concrete	4.0
Flexible (existing)	Default asphalt concrete	2.5
NonStabilized	A-1-a	12.0
NonStabilized	A-1-b	3.5
Subgrade	A-6	Semi-infinite

Volumetric at Construction:	
Effective binder content (%)	11.6
Air voids (%)	7.0

Traffic

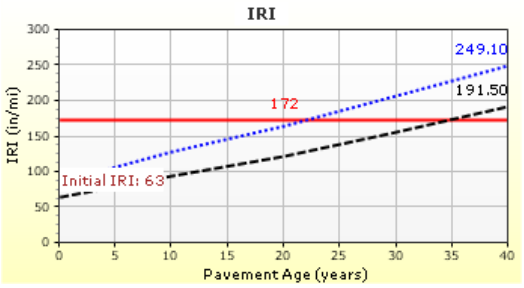
Age (year)	Heavy Trucks (cumulative)
2018 (initial)	1,000
2038 (20 years)	3,520,100
2058 (40 years)	8,683,820

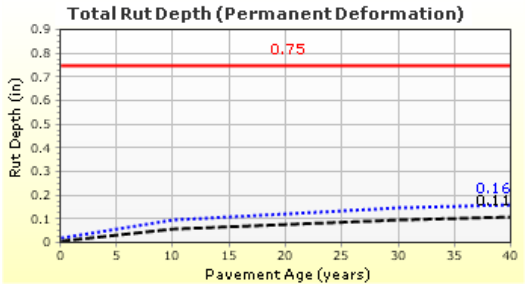
Design Outputs

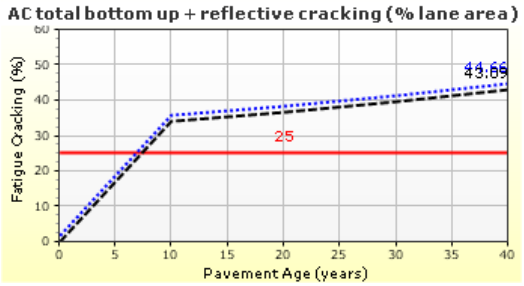
Distress Prediction Summary

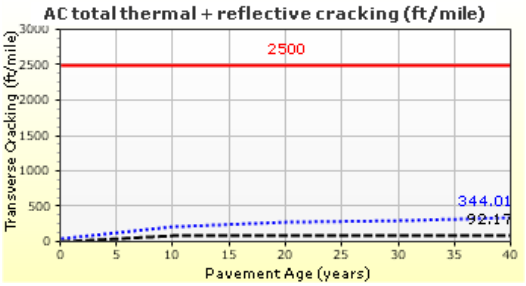
Distress Type	Distress @ Specified Reliability		Reliability (%)		Criterion Satisfied?
	Target	Predicted	Target	Achieved	
Terminal IRI (in/mile)	172.00	249.07	90.00	33.17	Fail
Permanent deformation - total pavement (in)	0.75	0.16	90.00	100.00	Pass
AC total fatigue cracking: bottom up + reflective (% lane area)	25.00	44.66	90.00	0.00	Fail
AC total transverse cracking: thermal + reflective (ft/mile)	2500.00	344.01	90.00	100.00	Pass
Permanent deformation - AC only (in)	0.25	0.16	90.00	99.98	Pass
AC bottom-up fatigue cracking (% lane area)	25.00	0.00	50.00	100.00	Pass
AC thermal cracking (ft/mile)	1000.00	17.21	50.00	100.00	Pass
AC top-down fatigue cracking (ft/mile)	2000.00	13803.16	90.00	0.03	Fail

Distress Charts











HMA Rehabilitation (Input Level: 3)

Milled thickness (in)	1.00
Structural rating	Fair
Environmental rating	Good
Total rut depth (in)	0.70

For cell 127/227 (overlay asphalt binder = Superpave PG 58-34) (LSSB M_R = 10,000 psi):

Design Inputs

Design Life:	40 years	Existing construction:	August, 2017	Climate Data Sources	45.5, -93.75 45, -93.75 45.5, -93.125 45. -93.125 45.5, -94.375 45, -94.375
Design Type:	ACC_ACC	Pavement construction:	September, 2018		
		Traffic opening:	September, 2018		

Design Structure

Layer type	Material Type	Thickness (in)
Flexible (OL)	Default asphalt concrete	4.0
Flexible (existing)	Default asphalt concrete	2.5
NonStabilized	A-1-a	6.0
NonStabilized	A-1-b	18.0
Subgrade	A-6	Semi-infinite

Volumetric at Construction:	
Effective binder content (%)	11.6
Air voids (%)	7.0

Traffic

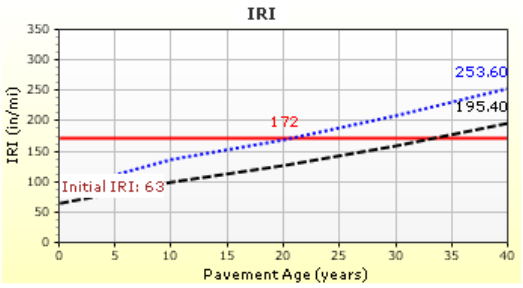
Age (year)	Heavy Trucks (cumulative)
2018 (initial)	1,000
2038 (20 years)	3,520,100
2058 (40 years)	8,683,820

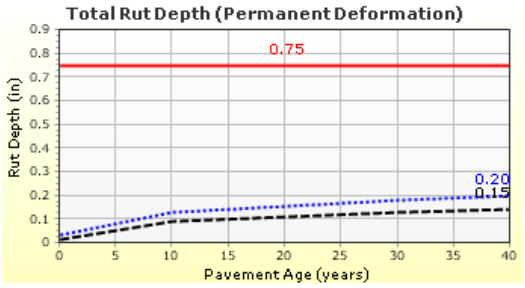
Design Outputs

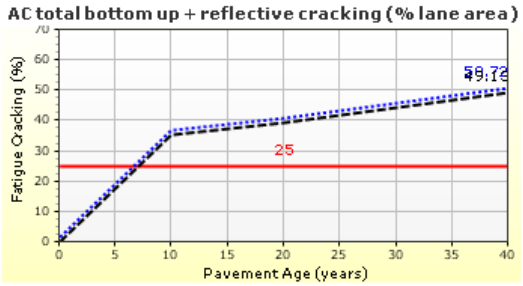
Distress Prediction Summary

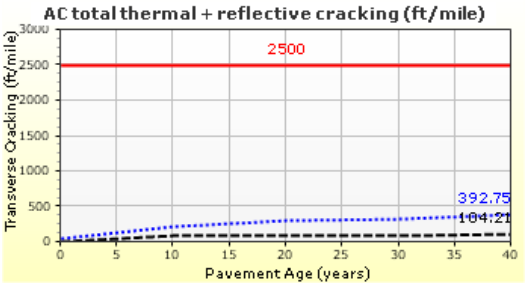
Distress Type	Distress @ Specified Reliability		Reliability (%)		Criterion Satisfied?
	Target	Predicted	Target	Achieved	
Terminal IRI (in/mile)	172.00	253.65	90.00	30.33	Fail
Permanent deformation - total pavement (in)	0.75	0.20	90.00	100.00	Pass
AC total fatigue cracking: bottom up + reflective (% lane area)	25.00	50.72	90.00	0.00	Fail
AC total transverse cracking: thermal + reflective (ft/mile)	2500.00	392.75	90.00	100.00	Pass
Permanent deformation - AC only (in)	0.25	0.15	90.00	99.99	Pass
AC bottom-up fatigue cracking (% lane area)	25.00	0.00	50.00	100.00	Pass
AC thermal cracking (ft/mile)	1000.00	29.25	50.00	100.00	Pass
AC top-down fatigue cracking (ft/mile)	2000.00	13701.19	90.00	0.03	Fail

Distress Charts











HMA Rehabilitation (Input Level: 3)

Milled thickness (in)	1.00
Structural rating	Fair
Environmental rating	Good
Total rut depth (in)	0.70

For cell 127/227 (overlay asphalt binder = Superpave PG 58-34) (LSSB M_R = 30,000 psi):

Design Inputs

Design Life:	40 years	Existing construction:	August, 2017	Climate Data Sources	45.5, -93.75 45, -93.75 45.5, -93.125 45. -93.125 45.5, -94.375 45, -94.375
Design Type:	ACC_ACC	Pavement construction:	September, 2018		
		Traffic opening:	September, 2018		

Design Structure

Layer type	Material Type	Thickness (in)
Flexible (OL)	Default asphalt concrete	4.0
Flexible (existing)	Default asphalt concrete	2.5
NonStabilized	A-1-a	6.0
NonStabilized	A-1-b	18.0
Subgrade	A-6	Semi-infinite

Volumetric at Construction:	
Effective binder content (%)	11.6
Air voids (%)	7.0

Traffic

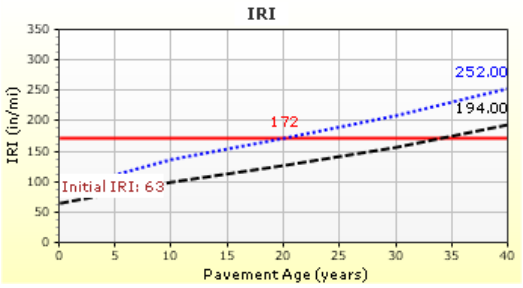
Age (year)	Heavy Trucks (cumulative)
2018 (initial)	1,000
2038 (20 years)	3,520,100
2058 (40 years)	8,683,820

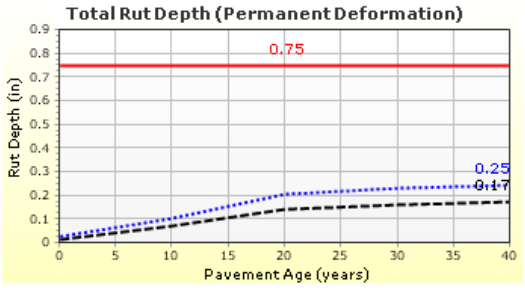
Design Outputs

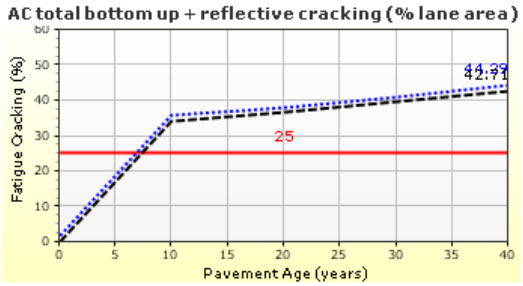
Distress Prediction Summary

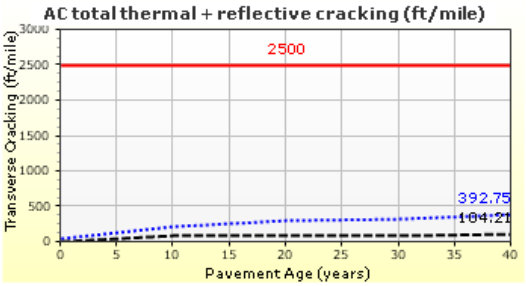
Distress Type	Distress @ Specified Reliability		Reliability (%)		Criterion Satisfied?
	Target	Predicted	Target	Achieved	
Terminal IRI (in/mile)	172.00	251.95	90.00	31.30	Fail
Permanent deformation - total pavement (in)	0.75	0.25	90.00	100.00	Pass
AC total fatigue cracking: bottom up + reflective (% lane area)	25.00	44.29	90.00	0.00	Fail
AC total transverse cracking: thermal + reflective (ft/mile)	2500.00	392.75	90.00	100.00	Pass
Permanent deformation - AC only (in)	0.25	0.23	90.00	94.41	Pass
AC bottom-up fatigue cracking (% lane area)	25.00	0.00	50.00	100.00	Pass
AC thermal cracking (ft/mile)	1000.00	29.25	50.00	100.00	Pass
AC top-down fatigue cracking (ft/mile)	2000.00	13803.55	90.00	0.03	Fail

Distress Charts









Threshold Value ····· @ Specified Reliability - - - @ 50% Reliability

HMA Rehabilitation (Input Level: 3)

Milled thickness (in)	1.00
Structural rating	Fair
Environmental rating	Good
Total rut depth (in)	0.70

For cell 127/227 (overlay asphalt binder = Superpave PG 58-34) (LSSB M_R = 50,000 psi):

Design Inputs

Design Life:	40 years	Existing construction:	August, 2017	Climate Data Sources	45.5, -93.75 45, -93.75 45.5, -93.125 45. -93.125 45.5, -94.375 45, -94.375
Design Type:	ACC_ACC	Pavement construction:	September, 2018		
		Traffic opening:	September, 2018		

Design Structure

Layer type	Material Type	Thickness (in)
Flexible (OL)	Default asphalt concrete	4.0
Flexible (existing)	Default asphalt concrete	2.5
NonStabilized	A-1-a	6.0
NonStabilized	A-1-b	18.0
Subgrade	A-6	Semi-infinite

Volumetric at Construction:	
Effective binder content (%)	11.6
Air voids (%)	7.0

Traffic

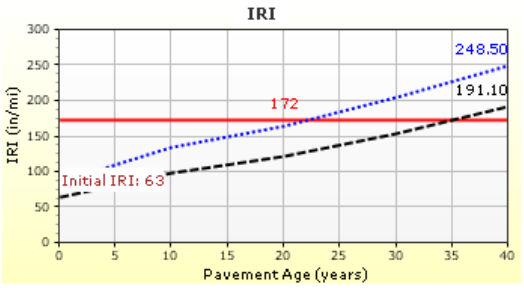
Age (year)	Heavy Trucks (cumulative)
2018 (initial)	1,000
2038 (20 years)	3,520,100
2058 (40 years)	8,683,820

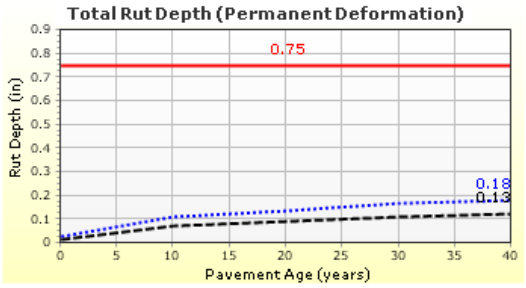
Design Outputs

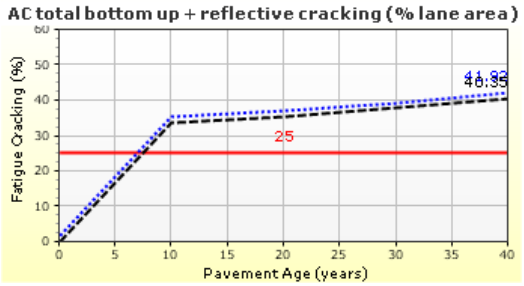
Distress Prediction Summary

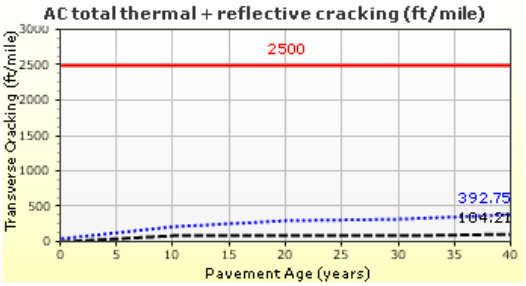
Distress Type	Distress @ Specified Reliability		Reliability (%)		Criterion Satisfied?
	Target	Predicted	Target	Achieved	
Terminal IRI (in/mile)	172.00	248.52	90.00	33.49	Fail
Permanent deformation - total pavement (in)	0.75	0.18	90.00	100.00	Pass
AC total fatigue cracking: bottom up + reflective (% lane area)	25.00	41.92	90.00	0.00	Fail
AC total transverse cracking: thermal + reflective (ft/mile)	2500.00	392.75	90.00	100.00	Pass
Permanent deformation - AC only (in)	0.25	0.17	90.00	99.93	Pass
AC bottom-up fatigue cracking (% lane area)	25.00	0.00	50.00	100.00	Pass
AC thermal cracking (ft/mile)	1000.00	29.25	50.00	100.00	Pass
AC top-down fatigue cracking (ft/mile)	2000.00	13697.57	90.00	0.03	Fail

Distress Charts











HMA Rehabilitation (Input Level: 3)

Milled thickness (in)	1.00
Structural rating	Fair
Environmental rating	Good
Total rut depth (in)	0.70

For cell 328/728 (overlay asphalt binder = Superpave PG 58-34) (LSSB M_R = 10,000 psi):

Design Inputs

Design Life:	40 years	Existing construction:	August, 2017	Climate Data Sources	45.5, -93.75 45, -93.75 45.5, -93.125 45. -93.125 45.5, -94.375 45, -94.375
Design Type:	ACC_ACC	Pavement construction:	September, 2018		
		Traffic opening:	September, 2018		

Design Structure

Layer type	Material Type	Thickness (in)
Flexible (OL)	Default asphalt concrete	4.0
Flexible (existing)	Default asphalt concrete	2.5
NonStabilized	A-1-a	6.0
NonStabilized	A-1-b	9.0
Subgrade	A-6	Semi-infinite

Volumetric at Construction:	
Effective binder content (%)	11.6
Air voids (%)	7.0

Traffic

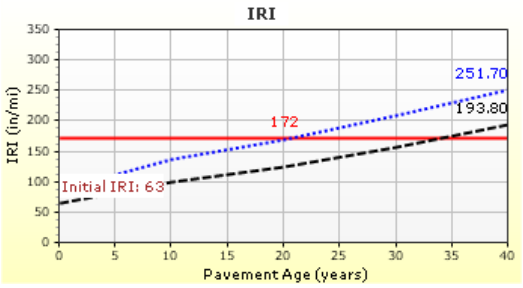
Age (year)	Heavy Trucks (cumulative)
2018 (initial)	1,000
2038 (20 years)	3,520,100
2058 (40 years)	8,683,820

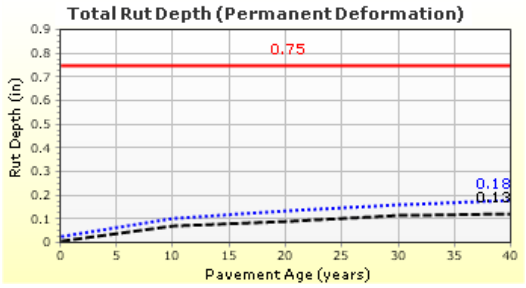
Design Outputs

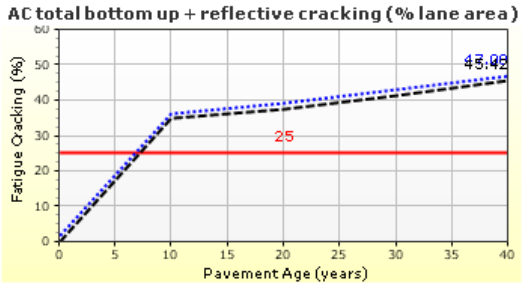
Distress Prediction Summary

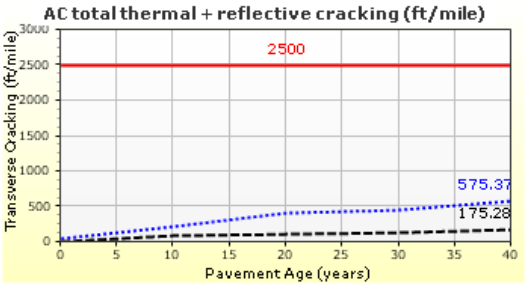
Distress Type	Distress @ Specified Reliability		Reliability (%)		Criterion Satisfied?
	Target	Predicted	Target	Achieved	
Terminal IRI (in/mile)	172.00	251.71	90.00	31.52	Fail
Permanent deformation - total pavement (in)	0.75	0.18	90.00	100.00	Pass
AC total fatigue cracking: bottom up + reflective (% lane area)	25.00	47.00	90.00	0.00	Fail
AC total transverse cracking: thermal + reflective (ft/mile)	2500.00	575.37	90.00	100.00	Pass
Permanent deformation - AC only (in)	0.25	0.15	90.00	99.99	Pass
AC bottom-up fatigue cracking (% lane area)	25.00	0.00	50.00	100.00	Pass
AC thermal cracking (ft/mile)	1000.00	100.32	50.00	100.00	Pass
AC top-down fatigue cracking (ft/mile)	2000.00	13701.82	90.00	0.03	Fail

Distress Charts











HMA Rehabilitation (Input Level: 3)

Milled thickness (in)	1.00
Structural rating	Fair
Environmental rating	Good
Total rut depth (in)	0.70

For cell 328/728 (overlay asphalt binder = Superpave PG 58-34) (LSSB M_R = 30,000 psi):

Design Inputs

Design Life:	40 years	Existing construction:	August, 2017	Climate Data Sources	45.5, -93.75 45, -93.75 45.5, -93.125 45. -93.125 45.5, -94.375 45, -94.375
Design Type:	ACC_ACC	Pavement construction:	September, 2018		
		Traffic opening:	September, 2018		

Design Structure

Layer type	Material Type	Thickness (in)
Flexible (OL)	Default asphalt concrete	4.0
Flexible (existing)	Default asphalt concrete	2.5
NonStabilized	A-1-a	6.0
NonStabilized	A-1-b	9.0
Subgrade	A-6	Semi-infinite

Volumetric at Construction:	
Effective binder content (%)	11.6
Air voids (%)	7.0

Traffic

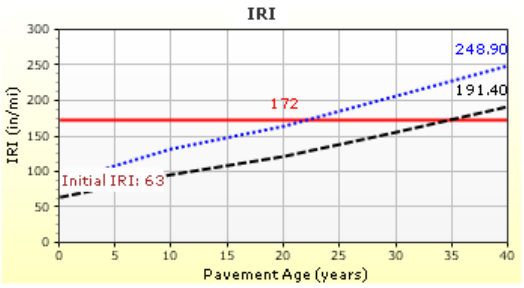
Age (year)	Heavy Trucks (cumulative)
2018 (initial)	1,000
2038 (20 years)	3,520,100
2058 (40 years)	8,683,820

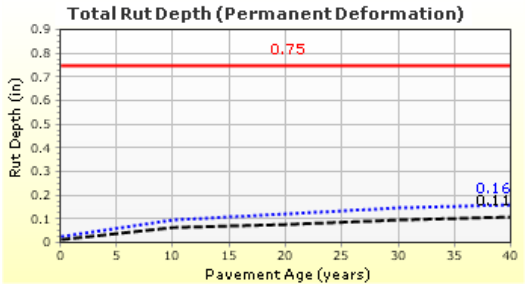
Design Outputs

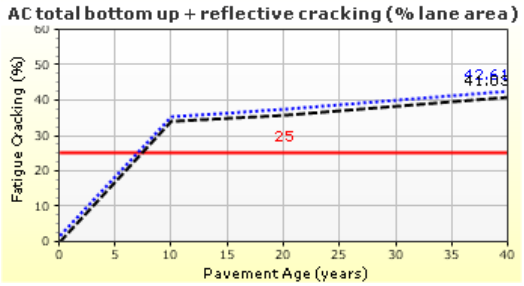
Distress Prediction Summary

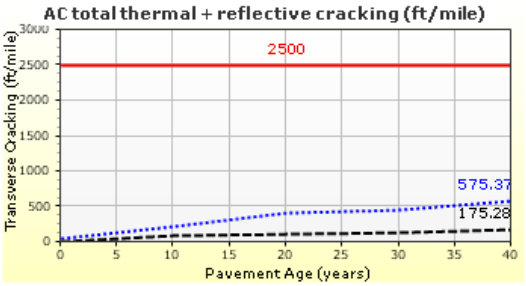
Distress Type	Distress @ Specified Reliability		Reliability (%)		Criterion Satisfied?
	Target	Predicted	Target	Achieved	
Terminal IRI (in/mile)	172.00	248.89	90.00	33.29	Fail
Permanent deformation - total pavement (in)	0.75	0.16	90.00	100.00	Pass
AC total fatigue cracking: bottom up + reflective (% lane area)	25.00	42.61	90.00	0.00	Fail
AC total transverse cracking: thermal + reflective (ft/mile)	2500.00	575.37	90.00	100.00	Pass
Permanent deformation - AC only (in)	0.25	0.16	90.00	99.97	Pass
AC bottom-up fatigue cracking (% lane area)	25.00	0.00	50.00	100.00	Pass
AC thermal cracking (ft/mile)	1000.00	100.32	50.00	100.00	Pass
AC top-down fatigue cracking (ft/mile)	2000.00	13803.87	90.00	0.03	Fail

Distress Charts









Threshold Value ····· @ Specified Reliability - - - @ 50% Reliability

HMA Rehabilitation (Input Level: 3)

Milled thickness (in)	1.00
Structural rating	Fair
Environmental rating	Good
Total rut depth (in)	0.70

For cell 328/728 (overlay asphalt binder = Superpave PG 58-34) (LSSB M_R = 50,000 psi):

Design Inputs

Design Life:	40 years	Existing construction:	August, 2017	Climate Data Sources	45.5, -93.75 45, -93.75 45.5, -93.125 45. -93.125 45.5, -94.375 45, -94.375
Design Type:	ACC_ACC	Pavement construction:	September, 2018		
		Traffic opening:	September, 2018		

Design Structure

Layer type	Material Type	Thickness (in)
Flexible (OL)	Default asphalt concrete	4.0
Flexible (existing)	Default asphalt concrete	2.5
NonStabilized	A-1-a	6.0
NonStabilized	A-1-b	9.0
Subgrade	A-6	Semi-infinite

Volumetric at Construction:	
Effective binder content (%)	11.6
Air voids (%)	7.0

Traffic

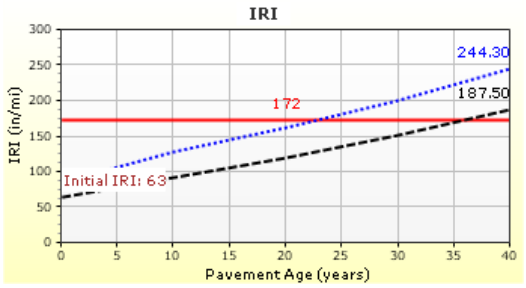
Age (year)	Heavy Trucks (cumulative)
2018 (initial)	1,000
2038 (20 years)	3,520,100
2058 (40 years)	8,683,820

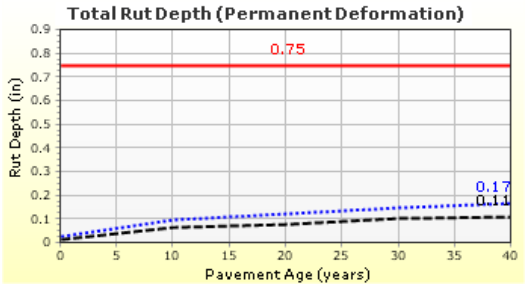
Design Outputs

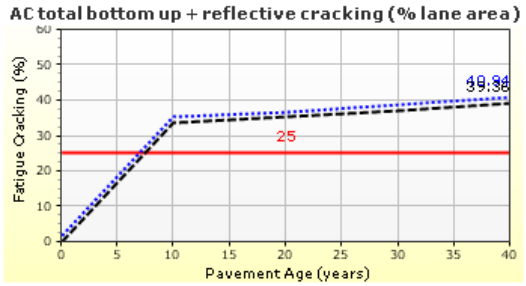
Distress Prediction Summary

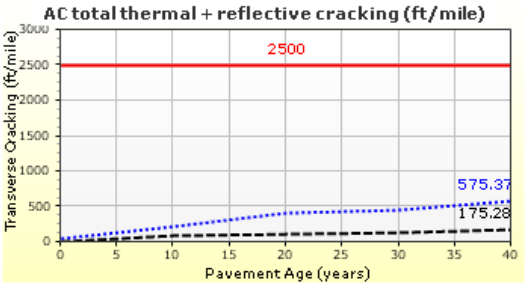
Distress Type	Distress @ Specified Reliability		Reliability (%)		Criterion Satisfied?
	Target	Predicted	Target	Achieved	
Terminal IRI (in/mile)	172.00	244.29	90.00	36.37	Fail
Permanent deformation - total pavement (in)	0.75	0.17	90.00	100.00	Pass
AC total fatigue cracking: bottom up + reflective (% lane area)	25.00	40.94	90.00	0.00	Fail
AC total transverse cracking: thermal + reflective (ft/mile)	2500.00	575.37	90.00	100.00	Pass
Permanent deformation - AC only (in)	0.25	0.16	90.00	99.95	Pass
AC bottom-up fatigue cracking (% lane area)	25.00	0.00	50.00	100.00	Pass
AC thermal cracking (ft/mile)	1000.00	100.32	50.00	100.00	Pass
AC top-down fatigue cracking (ft/mile)	2000.00	8559.50	90.00	7.63	Fail

Distress Charts











HMA Rehabilitation (Input Level: 3)

Milled thickness (in)	1.00
Structural rating	Fair
Environmental rating	Good
Total rut depth (in)	0.70